

School of Earth and Planetary Sciences

**The Tectonothermal Evolution of the Gascoyne
Province and its Role in Proterozoic Australia**

Agnieszka Marta Piechocka

This thesis is presented for the Degree of
Doctor of Philosophy
of
Curtin University

February 2019

Declaration

To the best of my knowledge and belief this thesis contains no material previously published by any other person except where due acknowledgment has been made.

This thesis contains no material which has been accepted for the award of any other degree or diploma in any university.

The author acknowledges that copyright of published works contained within this thesis resides with copyright holder(s) of those works. I warrant that I have obtained, where necessary, permission from the copyright owners to use of the third-party copyright material reproduced in the thesis (e.g., questionnaires, artwork, unpublished letters), or to use any of my own published work (e.g., journal articles) in which the copyright is held by another party (e.g., publisher, co-author).

Agnieszka Marta Piechocka

February 2019

Abstract

Intraplate reworking in Proterozoic Australia is typically attributed to elevated heat production in the crust and thermal softening beneath an insulating lid. However, it is unclear whether this model applies to all Proterozoic orogens. The Gascoyne Province forms the core of the Capricorn Orogen, and records nearly one billion years of Proterozoic intraplate crustal reworking of the West Australian Craton. Our understanding of the tectonothermal history of the province is largely the result of SHRIMP U-Pb zircon dating of felsic magmatism and high-grade metamorphism. Comparatively little is known about the low- to medium-temperature history of the province. The evolution of the northern part of the province is particularly unclear due to a lack of reliable geochronology. SHRIMP U-Pb phosphate geochronology was used to date low- to high-grade metamorphism and leucocratic magmatism associated with Proterozoic intraplate reworking in the Gascoyne Province. Additionally, $^{40}\text{Ar}/^{39}\text{Ar}$ mica geochronology was used to constrain the late reactivation history of the province. The U-Pb phosphate results show that regional metamorphism associated with two Paleoproterozoic reworking events is probably related to emplacement of magmas rather than to the presence of a thermal lid. Late Neoproterozoic reactivation of the province, which established the present crustal architecture, was the likely result of north-south compression, causing dextral-strike slip in the north and exhumation of the southern part of the province, rather than a collision from the west as previously proposed. The results demonstrate the benefit of using U-Pb phosphate geochronology to date geological processes in complex, low- to medium-grade Precambrian orogens.

Table of Contents

Declaration.....	iii
Abstract.....	v
Table of Contents.....	vii
List of Figures.....	xi
List of Tables.....	xiii
Acknowledgements.....	xv
List of Publications.....	xvii
Chapter 1 Introduction.....	1
1.1 Background.....	1
1.1.1 Current issues in resolving the tectonic history of the Gascoyne Province.....	4
1.2 Current knowledge of tectonism in the Gascoyne Province.....	5
1.2.1 Reworking events in the Gascoyne Province.....	5
1.2.2 Reactivation events in the Gascoyne Province.....	7
1.3 Thesis aims.....	8
1.4 Thesis structure.....	13
1.5 Chapters as a series of papers.....	15
1.6 References.....	17
Chapter 2 PAPER 1: SHRIMP U–Pb phosphate dating shows metamorphism was synchronous with magmatism during the Paleoproterozoic Capricorn Orogen.....	21
2.1 Abstract.....	22
2.2 Introduction.....	23
2.3 Regional Geology.....	26
2.3.1 Southern Capricorn Orogen.....	26
2.3.2 Central Capricorn Orogen.....	27
2.3.3 Northern Capricorn Orogen.....	29
2.4 Sample details.....	29
2.5 Analytical methods.....	31
2.6 Results.....	32
2.6.1 Monazite.....	32
2.6.2 Xenotime.....	40

2.7	Discussion	42
2.7.1	Previous U–Pb zircon and monazite constraints on Capricorn-aged metamorphism.....	43
2.7.2	New U–Pb monazite and xenotime constraints on the Capricorn Orogeny in the northern Gascoyne Province	44
2.7.3	A 1750–1730 Ma tectonothermal event in the northern Capricorn Orogen?.....	47
2.7.4	Regional correlations	49
2.7.5	New evidence for the drivers for metamorphism during the Capricorn Orogeny.....	50
2.8	Conclusions.....	51
2.9	Acknowledgements.....	51
2.10	References.....	52
Chapter 3	PAPER 2: The Mangaroon Orogeny: Synchronous c. 1.7 Ga magmatism and low-P, high-T metamorphism in the West Australian Craton.....	59
3.1	Abstract.....	60
3.2	Introduction.....	61
3.3	Regional Geology.....	62
3.4	Mangaroon Zone	65
3.4.1	Pooranoo Metamorphics	66
3.4.2	Durlacher Supersuite in the Mangaroon Zone	66
3.4.3	Deformation and metamorphism (D ₁ /M ₁ and D ₂ /M ₂).....	67
3.5	Sample descriptions and petrography	68
3.6	Analytical methods.....	75
3.6.1	In situ SHRIMP U–Pb monazite and xenotime geochronology	75
3.6.2	Whole-rock geochemistry	77
3.7	Results.....	77
3.7.1	U–Pb monazite and xenotime geochronology	77
3.8	Phase equilibria modelling.....	86
3.8.1	Results.....	88
3.9	Discussion.....	90
3.9.1	Duration of magmatism associated with the Mangaroon Orogeny.....	90
3.9.2	P–T–t conditions of early metamorphism	91
3.9.3	Timing, duration and causes of metamorphism	92
3.9.4	Temperatures and causes of granite emplacement.....	94
3.9.5	New age constraints on D ₁ /D ₂	95
3.9.6	Geodynamic setting of the Mangaroon Zone.....	96
3.9.7	Mangaroon Orogeny: high-grade core, low-grade halo	97

3.10	Conclusions.....	99
3.11	Acknowledgements.....	100
3.12	References.....	101
Chapter 4	PAPER 3: Monazite trumps zircon: applying SHRIMP U-Pb geochronology to systematically evaluate emplacement ages of leucocratic, low-temperature granites in a complex Precambrian orogen.....	109
4.1	Abstract.....	110
4.2	Introduction.....	111
4.3	Regional Geology.....	112
4.4	Sample descriptions and previous zircon geochronology.....	116
4.5	Analytical methods.....	120
4.6	Monazite geochronology results.....	121
4.7	Discussion.....	126
4.7.1	Assessment of magmatic monazite.....	128
4.7.2	Implications of the monazite geochronology.....	129
4.7.3	Zircon geochronology.....	131
4.7.4	Pegmatites.....	132
4.7.5	Monazite geochronology.....	132
4.7.6	An isolated granite.....	133
4.8	Conclusions.....	134
4.9	Acknowledgements.....	134
4.10	References.....	135
Chapter 5	PAPER 4: Neoproterozoic $^{40}\text{Ar}/^{39}\text{Ar}$ mica ages mark the termination of a billion years of intraplate reworking in the Capricorn Orogen, Western Australia.....	141
5.1	Abstract.....	142
5.2	Introduction.....	143
5.3	Intraplate reworking and reactivation in the Gascoyne Province.....	146
5.3.1	Reworking.....	146
5.3.2	Reactivation.....	146
5.4	Characteristics of fault and shear zone reactivation and sample details.....	147
5.4.1	The northern Gascoyne Province (Collins Fault).....	147
5.4.2	The central Gascoyne Province (Ti Tree Shear Zone).....	152
5.5	Geochronology methodology.....	153
5.5.1	$^{40}\text{Ar}/^{39}\text{Ar}$ mica geochronology.....	153
5.5.2	SHRIMP U–Pb xenotime geochronology.....	154

5.6	Geochronology Results	155
5.6.1	40Ar/39Ar mica age data	155
5.6.2	U–Pb xenotime age data.....	155
5.7	Discussion	162
5.7.1	⁴⁰ Ar/ ³⁹ Ar diffusion modelling of muscovite from the northern Gascoyne Province.....	162
5.7.2	Ages of mica growth or cooling?	165
5.7.3	The extent of the Neoproterozoic reactivation	167
5.7.4	Implications of reactivation of pre-existing crustal sutures and faults	169
5.7.5	From reworking to reactivation on an orogen scale	171
5.8	Conclusions	172
5.9	Acknowledgements	173
5.10	References	174
Chapter 6	Conclusion.....	179
	Bibliography	183
<hr/>		
	APPENDICES	201
<hr/>		
Appendix A	First Author Journal Publications	203
A.1	Paper 1 (published)	204
A.2	Paper 2 (published)	225
A.3	Paper 3 (published)	245
A.4	Paper 4 (published)	265
Appendix B	Supplementary Data (Chapter 3) – SHRIMP U–Pb Monazite and Xenotime Data.....	285
Appendix C	Supplementary Data (Chapter 3) – Mineral Chemistry Data and P–T Pseudosection	293
Appendix D	Supplementary Data (Chapter 4) – SHRIMP U–Pb Monazite Data.....	345
Appendix E	Supplementary Data (Chapter 5) – ⁴⁰Ar/³⁹Ar Mica Data	351

List of Figures

Figure 1.1	Regional Geology map of the Gascoyne Province	2
Figure 2.1	Regional Geology map of the Gascoyne Province, Capricorn Orogen	25
Figure 2.2	Field outcrop photos of selected samples from the northern Gascoyne Province	37
Figure 2.3	Petrographic images.....	38
Figure 2.4	Back-scattered electron (BSE) images of representative monazites and xenotime.....	38
Figure 2.5	U–Pb Concordia diagrams for (a–c) monazite and (d) and xenotime. (e) Th and U concentration of monazite from sample P01058.....	39
Figure 2.6	Summary diagram of tectonothermal events in the Gascoyne Province	43
Figure 2.7	Summary diagram of Capricorn aged geochronology from the Western Australian Craton.....	46
Figure 2.8	Diagram of Th versus U concentrations in xenotime	48
Figure 3.1	Regional geological setting of the Capricorn Orogen in relation to Australia (inset map) and simplified regional geology of the Gascoyne Province	63
Figure 3.2	Geology of the Mangaroon Zone.....	65
Figure 3.3	Field photos of granites and representative photomicrograph images of granitic sample 195890 in cross-polarised light. analysed in this study.	70
Figure 3.4	Field photos of pelitic samples analysed in this study.....	71
Figure 3.5	Representative photomicrograph images of analysed pelitic samples in plane-polarised light (PPL) and cross-polarised light (XPL).	72
Figure 3.6	Back-scattered electron (BSE) images of representative monazites and xenotime from samples analysed in situ.	80
Figure 3.7	U–Pb concordia diagrams for monazite from granitic samples A–C.	81
Figure 3.8	U–Pb concordia diagrams for monazite (A–F) and xenotime (G) from pelitic samples.....	82
Figure 3.9	P–T pseudosections for (a) GSWA 219749 and (b) GSWA 219742.....	89
Figure 3.10	Compilation diagram of Mangaroon-age geochronology from the Mangaroon Zone.....	91
Figure 3.11	Summary diagram showing P–T pseudosections from GSWA 219742 and 219749 plotted in P–T space.....	93
Figure 3.12	The Mangaroon orogeny high-grade core, low-grade halo in the West Australian Craton.....	98
Figure 4.1	Regional geological setting of the Capricorn Orogen.....	113
Figure 4.2	Local geology of sample areas.....	114

Figure 4.3	Representative photomicrograph images (cross polarised light).....	116
Figure 4.4	Field photos	119
Figure 4.5	SHRIMP U–Th–Pb analytical results for monazite from leucocratic granites in the Gascoyne Province.....	124
Figure 4.6	Back-scattered electron (BSE) images of representative in situ monazite ..	125
Figure 4.7	Cathodoluminescence image of representative zircon grains from sample 183287	127
Figure 4.8	Diagram of Th versus U concentrations in monazite.....	129
Figure 4.9	Zircon dates from Durlacher Supersuite granites in the northern Gascoyne Province	130
Figure 4.10	Monazite and zircon ages for leucocratic granites and pegmatites of the Thirty Three Supersuite.	133
Figure 5.1	Regional geological map of the Gascoyne Province, Capricorn Orogen...	144
Figure 5.2	Sample Detail.....	149
Figure 5.3	Plane polarized light and crossed polar photomicrographs of typical mica crystals	150
Figure 5.4	Outcrop photos of sample localities.....	152
Figure 5.5	A–F: $^{40}\text{Ar}/^{39}\text{Ar}$ age plateaus from mylonites within metagranites and quartz mylonites and a biotite schist from the Gascoyne Province...	159
Figure 5.6	A–B: $^{40}\text{Ar}/^{39}\text{Ar}$ muscovite age plateaus from a Paleoproterozoic metagranite from the Gascoyne Province.....	160
Figure 5.7	A–E: Representative backscattered electron images of xenotime from siltstone/mudstone samples.....	161
Figure 5.8	Modelled $^{40}\text{Ar}/^{39}\text{Ar}$ age spectra for 125 μm , 500 μm and 1000 μm radius muscovite grains	164
Figure 5.9	Summary diagram illustrating the spread of ages defined by $^{40}\text{Ar}/^{39}\text{Ar}$ mica and SHRIMP U–Pb xenotime geochronology.....	167
Figure 5.10	Interpreted crustal geology from the seismic lines 10GHA–CP3 and 10GA–CP3.....	170
Figure 5.11	Simplified time-space plot showing the distribution of reworking and reactivation events spanning the Gascoyne Province.	172
Figure B.1	Plot of ASI values for Durlacher granites from the Mangaroon Zone ...	286
Figure B.2	Calculated zircon saturation temperatures ($^{\circ}\text{C}$)	287
Figure B.3	Probability density diagrams and histograms	288
Figure C.1	Representative analysed garnet.....	295
Figure C.2	P–T pseudosection for sample 216533.	296

List of Tables

Table 1.1	The structural-metamorphic lithological zones making up the Gascoyne Province	3
Table 2.1	Summary table of samples, from the northern Gascoyne Province, Capricorn Orogen.	30
Table 2.2	Pb monazite data for samples GSWA 191938, P01085 and GSWA 219708.	34
Table 2.3	U–Pb xenotime data for sample GSWA 219706.	41
Table 3.1	Summary of granitic and pelitic samples from the Mangaroon Zone analysed in this study.	69
Table 3.2	Whole-rock geochemistry data for Mangaroon Zone Durlacher Supersuite granite samples, from this study and published data (GSWA 2016b).	78
Table 3.3	Whole-rock chemistry used to construct <i>P–T</i> pseudosections for samples GSWA 219742 and 219749.	87
Table 4.1	Selected whole-rock geochemistry data for leucocratic granite samples... ..	118
Table 4.2	Summary of field data, U–Pb zircon and U–Th–Pb monazite geochronology for leucocratic granite samples.	122
Table 5.1	Summary of field data and sample details from the Gascoyne Province, Capricorn Orogen.	148
Table 5.2	⁴⁰ Ar/ ³⁹ Ar muscovite and biotite results from the Gascoyne Province, Capricorn Orogen.	157
Table 5.3	SHRIMP U–Pb xenotime data from phyllite samples central Gascoyne Province, Capricorn Orogen.	158
Table 5.4	Diffusion parameters and time-temperature history used in the ArArDiff models (Jourdan and Eroglu, 2017) to generate synthetic age spectra for muscovite.	163
Table B.1	(Supplementary Table 1) U–Pb SHRIMP monazite and xenotime data tables	289
Table C.1	Cordierite composition from sample 219749.	297
Table C.2	Epidote composition from sample 216533.	300
Table C.3	Plagioclase composition from sample 216533, 219742, and 219749.	301
Table C.4	Garnet composition from sample 219742 and 216533.	306
Table C.5	Biotite composition from samples 216533, 219742 219749.	317
Table C.6	Perthitic k-feldspar composition from sample 219749.	334
Table C.7	Muscovite composition from samples 216533.	341
Table C.8	Data used to construct the pseudosection for sample 216533.	343

Table D.1	GSWA 139466: monazite: (Erong Granite, Moorarie Supersuite)	346
Table D.2	GSWA 169092: monazite: (Red Rock Bore Granite, Durlacher Supersuite)	347
Table D.3	GSWA 187401: monazite: (Perseverance Well Granite, Thirty Three Supersuite)	348
Table D.4	GSWA 183287: monazite: (Perseverance Well Granite, Thirty Three Supersuite)	349
Table E.1	Sample 216540B muscovite	352
Table E.2	Sample 183294 muscovite	353
Table E.3	Sample 183295 muscovite	354
Table E.4	Sample 216533 biotite	355
Table E.5	Sample 216533 biotite	356
Table E.6	Sample 195890B biotite.....	357
Table E.7	Sample 195890D muscovite	358
Table E.8	Sample 195890E muscovite.....	359

Acknowledgements

This PhD research would not have been possible without the participation and support of a number of people.

Firstly, I am thankful to my primary supervisor, Birger Rasmussen. You placed your trust in me and offered me this PhD opportunity. My sincere thanks for supporting me and giving me the freedom to explore a variety of techniques and allowing for the natural evolution of this thesis. Without you this project would not have been possible.

I am most grateful for the selfless ongoing support and encouragement from my supervisor Stephen Sheppard. Your patience and objective and constructive feedback kept me calm and focussed (most of the time) throughout the PhD process. This PhD would not have been completed without your immeasurable knowledge and significant contribution in helping me understand the broad topics that make up my thesis.

I would also express my thanks to my other supervisors. Jian-Wei Zi for the countless hours of assistance you provided with the SHRIMP and data interpretation. Ian Fitzsimons for the fair, honest and objective feedback helped me to focus and articulate my writing in a simplistic manner. Also, your assistance with funding the final six months of my PhD is acknowledged and greatly appreciated.

To my collaborative partners at the Geological Survey of Western Australia (GSWA): Fawna Korhonen, Simon Johnson and Michael Wingate, your input and support over the years helped me to gain a broader understanding. Michael and Simon, I am further grateful to you both for assisting me financially in the last months when funds were drying up. To Fred Jourdan for introducing me to the $^{40}\text{Ar}/^{39}\text{Ar}$ technique and assisting with the data interpretation. It was an enjoyable experience working with you.

I would also like to extend my thanks to the following people who helped along the way:

- Scott Jones and the field team at GSWA Carlisle, thank you for providing the field support which allowed me to collect my samples on multiple field trips.
- Hao Gao and Cristina Talavera your support at the SHRIMP lab is much appreciated.

- Celia Mayers, Zdenka Martelli and Adam Frew from the Argon lab, you provided me more time and assistance than I could have asked for. You made my experience with the Argon method very enjoyable.
- Chris Clark for covering some of my expenses during the later stages of my PhD.

I am very thankful for the overall support provided to me by the Geology Department at Curtin University.

Thanks to my family and friends for their support. Thank you for the understanding, patience and support throughout my PhD journey.

Finally, and most importantly, I dedicate this thesis to my husband Jimmy Trpceviski. Without your support this PhD would not have been possible. Our 10 year old golden Labrador, Ollie, you loyally sat by my side for days on end during periods of intense writing and gently reminding me to take breaks. Lastly, the imminent arrival of our son Izaak in December gave me the motivation to complete the final stages of this thesis. I look forward to the next chapter of our lives.

List of Publications

List of publications included as part of this thesis

This thesis is a compilation of research articles that were either accepted, under review or submitted at the time of thesis submission. Introductory Chapter 1 outlines the connection between the articles. All manuscripts have Statement of Authorships in Appendix A and published manuscripts are reprinted with the permission of the journal. This permission is included in corresponding Appendices.

Due to the formatting requirements of this thesis the manuscripts that make up Chapters 2–4 are formatted in a way to provide consistency throughout this thesis, therefore, the individual manuscripts will differ from their published formats.

Manuscript 1:

Piechocka, A. M., Zi, J.-W., Gregory, C. J., Sheppard, & Rasmussen, B. (2019). *SHRIMP U–Pb phosphate dating shows metamorphism was synchronous with magmatism during the Paleoproterozoic Capricorn Orogeny*. Australian Journal of Earth Sciences, 66, 973–990.

Manuscript 2:

Piechocka, A. M., Zi, J.-W., Wingate, M. T. D., Gregory, C. J., Sheppard, S., Korhonen, F. J., Fitzsimons, I. C. W., Johnson, T. E., and Rasmussen, B. (2019). *The Mangaroon Orogeny: Synchronous c. 1.7 Ga magmatism and low-P, high-T metamorphism in the West Australian Craton*. Precambrian Research, 333, 105425.

Manuscript 3:

Piechocka, A. M., Gregory, C. J., Zi, J.-W., Sheppard, S., Wingate, M. T. D., and Rasmussen, B. (2017). *Monazite trumps zircon: applying SHRIMP U–Pb geochronology to systematically evaluate emplacement ages of leucocratic, low-temperature granites in a complex Precambrian orogen*. Contributions to Mineralogy and Petrology 172, 1–17.

Manuscript 4:

Piechocka, A. M., Sheppard, S., Fitzsimons, I. C. W., Johnson, S. P., Rasmussen, B., and Jourdan, F. (2018). *Neoproterozoic $^{40}\text{Ar}/^{39}\text{Ar}$ mica ages mark the termination of a billion years of intraplate reworking in the Capricorn Orogen, Western Australia*. Precambrian Research, 310, 391–406.

List of additional publications relevant to this thesis

The following lists abstracts that were presented at conferences during the completion of this PhD. The material presented is relevant to this PhD.

1. Piechocka, A. M., Gregory, C. J., Zi, J.-W., Sheppard, S., Wingate, M. T. D., and Rasmussen, B. (2017). *Using U–Th–Pb monazite geochronology to constrain emplacement ages and melt production rates of leucocratic granites*. In Goldschmidt 2017 Conference Abstracts and TIGeR 2017 conference abstracts.
2. Piechocka, A. M., Zi, J.-W., Wingate, M. T. D., Gregory, C. J., Sheppard, S., Korhonen, F. J., Johnson S., P., Fitzsimons, I., C., W., and Rasmussen, B. (2017). *Low-P, high-T c. 1.69 Ga metamorphism in the West Australian Craton triggered by magma flux into the upper crust*. In Specialist Group in Tectonics and Structural Geology 2017, Conference Abstracts.
3. Piechocka, A. M., Sheppard, S., Johnson, S. P., Rasmussen, B., and Jourdan, F. (2017). *Death of an Orogen*. In Specialist Group in Tectonics and Structural Geology 2017, Conference Abstracts.
4. Piechocka, A. M., Sheppard, S., Fitzsimons, I. C. W., Johnson, S. P., Rasmussen, B., and Jourdan, F. (2018). *Neoproterozoic $^{40}\text{Ar}/^{39}\text{Ar}$ mica ages mark the termination of a billion years of intraplate reworking in the Capricorn Orogen, Western Australia*. In TIGeR 2018, Conference Abstracts.

Chapter 1

Introduction

1.1 Background

The Gascoyne Province forms the exposed western end of the Capricorn Orogen, of the West Australian Craton. The province was first defined by Williams (1986) as ‘...the deformed and high-grade metamorphic core zone of the early Proterozoic Capricorn orogen. It comprises voluminous granitoid intrusions, mantled-gneiss domes, metamorphosed and partly melted sedimentary rocks, and remobilised Archean basement gneiss’. Subsequent field studies combined with U–Pb SHRIMP geochronology have further developed our understanding of the timing of sediment deposition, and the timing and duration of magmatism and tectonic reworking in the Gascoyne Province since initiation of the Capricorn Orogen during two collisional events. The first collision was between the Archean Pilbara Craton and the Glenburgh Terrane during the 2215–2145 Ma Ophthalmia Orogeny (Rasmussen et al., 2005). The second event was the amalgamation of this combined entity with the Archean Yilgarn Craton during the 2005–1950 Ma Glenburgh Orogeny (Johnson et al., 2011; Occhipinti et al., 2004; Sheppard et al., 2004). The post-collisional tectonothermal history of the Capricorn Orogen is best preserved in the Gascoyne Province, which records nearly 1.5 billion years of episodic intraplate tectonism during four reworking and two reactivation events.

The Gascoyne Province is floored by Archean basement — known as the Glenburgh Terrane — which is exposed only in the southern parts of the province (the Chalba Shear Zone marks the northern exposed limit of the Glenburgh Terrane) (Figure 1.1), but likely extends beneath younger rocks to the northern edge of the province (Sheppard et al., 2010a). The Gascoyne Province is characterised by fault-bounded structural and metamorphic zones (Figure 1.1 and Table 1.1) and includes two suture zones, which represent two early collisional events that mark the amalgamation of the West Australian Craton. The post-collisional evolution of the Gascoyne Province involves the deposition of the 1842–1807 Ma Leake Springs Metamorphics followed by regional voluminous magmatism of the Moorarie Supersuite associated with the 1820–1770 Ma Capricorn Orogeny (Sheppard et al., 2010a; b). Subsequent deposition of the 1741–1682 Ma Pooranoo Metamorphics was followed by voluminous (but more geographically

restricted compared to the Moorarie Supersuite) magmatism of the Durlacher Supersuite associated with the 1680–1620 Ma Mangaroon Orogeny (Sheppard et al., 2005; 2010a).

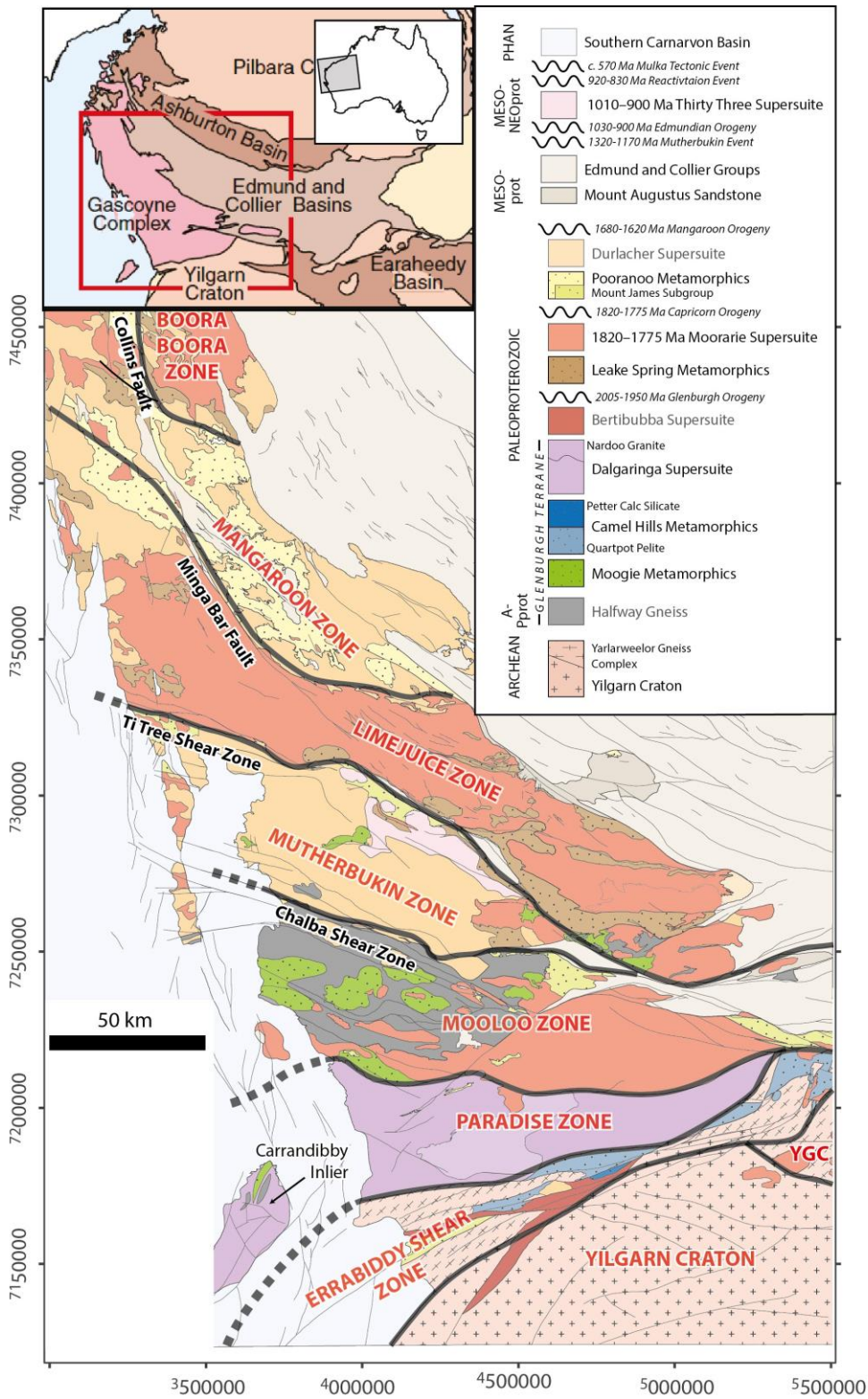


Figure 1.1 Regional Geology map of the Gascoyne Province showing the distinct structural-metamorphic zones (adapted from Sheppard et al., 2010b). YGC = Yarlweelor Gneiss Complex. Coordinate system is GDA 1994 MGA Zone 50.

Table 1.1 The structural-metamorphic lithological zones making up the Gascoyne Province as displayed in Figure 1.1 (after Sheppard et al., 2010b).

Zone	Description
Yilgarn Craton-Narryer Terrane	Characterised by granitic rocks older than 2.6 Ga with some gneisses older than 3.3 Ga. No Paleoproterozoic or younger reworking.
Yarlarweelor Gneiss Complex	Characterised by granitic rocks older than c. 2.6 Ga typical of the Yilgarn Craton, which have been intensely reworked during the 1820–1770 Ma Capricorn Orogeny. Contains voluminous Moorarie and Durlacher Supersuite granites.
Errabiddy Shear Zone	Zone of intense shearing and interleaving of lithologies from the Yilgarn Craton and Glenburgh Terrane. Intensely deformed and metamorphosed during the Glenburgh Orogeny.
Paradise Zone	Characterised by voluminous intermediate to felsic arc-related batholith of the Dalgaringa Supersuite (2005–1970 Ma). Deformed during the Glenburgh Orogeny.
Moolo Zone	Dominated by gneissic and siliclastic lithologies of the Glenburgh Terrane. Intensely reworked during the c. 1950 Ma Glenburgh Orogeny and overprinted by pervasive low grade metamorphism the 1820–1770 Ma Capricorn Orogeny. Contains abundant felsic intrusions of the Moorarie Supersuite.
Mutherbukin Zone	Dominated by voluminous felsic batholithic granites of the 1680–1620 Ma Durlacher Supersuite. Affected by multiple episodes of tectonic reworking during the 1320–1170 Mutherbukin Tectonic Event (Korhonen et al., 2017) and the 1030–955 Ma Edmundian Orogeny.
Limejuice Zone	Dominated by voluminous granites of the 1820–1775 Ma Moorarie Supersuite that comprise the Minnie Creek Batholith. Reworked during the 1820–1770 Ma Capricorn Orogeny.
Mangarooon Zone	Intensely deformed and metamorphosed during the 1680–1620 Ma Mangarooon Orogeny. Southern parts are characterised by migmatite melts (of the Pooranoo Metamorphics). Abundant intrusions of voluminous granite batholiths of the Durlacher Supersuite.
Boora Boora Zone	Dominated by medium-grade metasedimentary rock (of the Leake Springs Metamorphics) that may grade into the metasedimentary rocks of the Upper Wyloo Group. Foliated to gneissic granites of the Moorarie Supersuite.

The end of the Mangarooon Orogeny saw the deposition of the 1680–1465 Ma Edmund Basin. Following basin deposition another orogenic event the 1320–1170 Ma Mutherbukin Tectonic Event (Korhonen et al., 2015; 2017) affected the central parts of the province. Further sediment deposition occurred at 1170–1070 Ma known as the Collier Basin. The final reworking event also restricted to the central part of the province is the 1030–955 Ma Edmundian Orogeny, which includes the leucocratic pegmatites and magmatism of the Thirty Three Supersuite (Sheppard et al., 2007). Late fault reactivation occurred across the Gascoyne Province however geochronological constraints come

from a single shear zone, in the southern parts of the province, c. 570 Ma known as the Mulka Tectonic Event (Bodorkos and Wingate, 2007).

Initially, the Capricorn Orogeny was loosely constrained to between 2200 and 1600 Ma by Rb–Sr and Sm–Nd geochronology (Gee, 1979; Tyler and Thorne, 1990; Williams, 1986) and was considered to be the only event to have affected the Gascoyne Province. However, more recent SHRIMP U–Pb zircon geochronology combined with field mapping identified three events between 2200 and 1600 Ma. The oldest being the 2005–1950 Ma Glenburgh Orogeny (above) plus two post-collisional events being the 1820–1770 Ma Capricorn Orogeny (Sheppard et al., 2010a) and the 1680–1620 Ma Mangaroon Orogeny (Sheppard et al., 2005). Therefore, the tectonic history of the Gascoyne Province started to appear more complex than previously thought. Although two reworking events were identified in the Gascoyne Province it still remained unclear whether other mineral fabrics and deformation structures observed across the Gascoyne Province could all be correlated to either the Capricorn or Mangaroon Orogenies, or whether some deformation was the product of younger events.

1.1.1 Current issues in resolving the tectonic history of the Gascoyne Province

Traditionally, U–Pb zircon geochronology is employed to constrain high-grade metamorphism and felsic magmatism associated with orogenesis (e.g., Rowley et al., 1997; Hacker et al., 1998; Zhou et al. 2002), due to its high closure temperature $>900^{\circ}\text{C}$ (Cherniak and Watson 2001; Lee et al., 1997). This method was successful in identifying the Capricorn and Mangaroon Orogenies in the Gascoyne Province, but where temperatures during orogenic activity did not exceed 750°C , an alternative geochronometer is required because in these lower temperature environments it is difficult for new zircon growth to occur (e.g., Miller et al., 2003). For instance, monazite and xenotime have proven to be robust U–Pb geochronometers used to date low- to medium- to high temperature processes (e.g. Korhonen et al., 2015; Sheppard et al., 2007). Monazite is widely used mainly due to the following factors: new monazite growth occurs readily at a range of P – T conditions and has a closure temperature similar to zircon (Cherniak et al., 2004); monazite contains high U and Th and incorporates minor common Pb (Townsend et al., 2001); and, monazite, unlike zircon, generally does not contain inherited cores and is immune from radiogenic Pb loss at low temperatures (Grosse et al., 2009). Xenotime is also a robust U–Pb chronometer because it typically

contains high levels of uranium and low levels of lead and is resistant to isotopic resetting and metamictisation (Rasmussen 2005b). Xenotime has been successfully used to date a variety of geological processes including diagenesis (Rasmussen et al., 2007a), low- to medium grade metamorphism (Korhonen et al., 2015; Sheppard et al., 2007), high-grade metamorphism (Crowley and Parrish, 1999), igneous crystallisation (Heaman and Parrish, 1991), and hydrothermal processes (Rasmussen et al., 2005; Zi et al., 2015).

For the reasons stated above SHRIMP U–Pb monazite and xenotime geochronology was used in the central parts of the Gascoyne Province to identify two further orogenic events: the 1320–1170 Ma Mutherbukin Tectonic Event (Korhonen et al., 2015; 2017) and the 1030–955 Ma Edmundian Orogeny (Sheppard et al., 2007). Although, tectonic reworking was identified in the central parts of the Gascoyne Province, it is unknown whether the northern parts also experienced Meso- to Neoproterozoic reworking. A late reactivation event at c. 570 Ma was identified via $^{40}\text{Ar}/^{39}\text{Ar}$ laser mica geochronology (named the Mulka Tectonic Event; Bodorkos and Wingate, 2007). Similarly, it remains unknown whether other faults and shear zones across the Gascoyne Province were reactivated during the Mulka Tectonic event or during a separate event.

1.2 Current knowledge of tectonism in the Gascoyne Province

1.2.1 Reworking events in the Gascoyne Province

The earliest episode of reworking, the 1820–1770 Ma Capricorn Orogeny, is marked by the emplacement of voluminous felsic magmatic rocks and extensive deformation and metamorphism (Sheppard et al., 2010a). The footprint of the 1820–1770 Ma Capricorn Orogeny extends outside the Gascoyne Province to other parts of the Capricorn Orogen, including the Ashburton Basin and the Yarlaweelor Gneiss Complex (Sheppard et al., 2010a). It is characterised by extensive compressional deformation, mostly at low to medium metamorphic grade, magmatism, and some sedimentation (Sheppard et al., 2010a). The magmatism included voluminous felsic magmatic stocks, plutons and batholiths of the 1820–1775 Ma Moorarie Supersuite (Sheppard et al., 2010b). Although the magmatism was well constrained using U–Pb zircon geochronology a leucocratic pluton (Erong Granite) in the southern Gascoyne Province remains unassigned due to conflicting geochronology and field relationships. Sedimentation comprised deposition of the Upper Wyloo and Capricorn Groups in the Ashburton Basin and the protoliths to the Leake Springs Metamorphics in the Gascoyne

Province (Sheppard et al., 2010b). The Capricorn Orogeny was constrained through a combination of detailed field mapping and SHRIMP U–Pb zircon dating of felsic plutons and batholiths across the Gascoyne Province. The results revealed regional magmatism and three deformation episodes, constrained by the dated cross-cutting field relationships associated with the orogeny (Sheppard et al., 2010a). Scattered dates for metamorphism associated with the Capricorn Orogeny have been captured (Sheppard et al., 2010b), but there remains a lack of systematic dating of the regional metamorphism. Therefore it is unknown when metamorphism occurred in relation to the magmatism and deformation. The lack of precise geochronological constraints on the timing of metamorphism hampers the understanding of the drivers behind the Capricorn Orogeny.

The Capricorn Orogeny was followed by the 1680–1620 Ma Mangaroon Orogeny constrained by regional field mapping, SHRIMP U–Pb zircon geochronology and cross-cutting field relationships (Sheppard et al., 2005). The Mangaroon Orogeny is characterised by voluminous felsic magmatism (of the Durlacher Supersuite) and complex deformation and medium- to high-grade metamorphism with the peak conditions, recorded in the Mangaroon Zone, loosely estimated at <750 °C and <6 kbar based solely on mineral assemblages (Sheppard et al., 2005). Similar to the 1820–1775 Ma Moorarie Supersuite leucocratic plutons have been difficult to assign due to ambiguous U–Pb zircon geochronology results. In comparison to the Capricorn Orogeny, the Mangaroon Orogeny reworked a smaller portion of the Gascoyne Province with only the central and northern parts affected (i.e., from the Chalba Shear Zone to the Collins Fault). However, occurrences of fault reactivation related to the Mangaroon Orogeny are known from other parts of the Capricorn Orogen (Fielding et al., 2017; 2018 Rasmussen et al., 2007b). The lack of direct ages for metamorphism, an absence of pressure (*P*)–temperature (*T*) data, and uncertainty about the duration of granitic magmatism associated with the orogeny means that the drivers for orogenesis are unknown.

The next event was the Mesoproterozoic Mutherbukin Tectonic Event, which comprised deformation and metamorphism (Korhonen et al., 2017), but without magmatism, only in a 50 km-wide structural corridor (the Mutherbukin Zone) between the Ti Tree Shear Zone and Chalba Shear Zone. SHRIMP U–Pb monazite and xenotime geochronology combined with field mapping and *P*–*T* pseudosections constrained the *P*–*T*–*t* evolution of the Mutherbukin Tectonic event to 1320–1170 Ma at >650°C and 4.4–7 kbar (Korhonen et al., 2017). Thermal modelling suggested that the driver for the Mutherbukin Tectonic Event was thickening of radiogenic metasedimentary rocks, which

formed a thermal lid and generated radiogenic heat, prior to the onset of peak metamorphism (Korhonen et al., 2017). Of all the reworking events the Mutherbukin Tectonic Event is the best understood in terms of P – T – t conditions and drivers for orogenesis.

The youngest reworking event, the Meso–Neoproterozoic Edmundian Orogeny is restricted to a 20 km-wide structural corridor south of the Ti Tree Shear Zone (Sheppard et al., 2007). This orogeny was characterised by 1030–955 Ma deformation and greenschist to amphibolite facies metamorphism (estimated at 500–550°C and 3–4 kbar) and the intrusion of leucocratic magmatism and pegmatites of the Thirty Three Supersuite (Sheppard et al., 2007). Although the medium-grade reworking associated with the Edmundian Orogeny is known only from the central Gascoyne Province, low-grade deformation in the Errabiddy Shear Zone (Occhipinti and Reddy, 2009); and low-grade reactivation of structures in the adjacent Edmund Basin (Sheppard et al., 2007) occurred at the same time. SHRIMP U–Pb monazite and xenotime geochronology combined with field mapping was used to constrain the metamorphism and a single leucocratic pegmatite associated with the Edmundian Orogeny. However, the timing of the leucocratic magmatism remains poorly constrained due to earlier U–Pb zircon geochronology suggesting that magmatism occurred at c. 1640 Ma (Culver, 2001) although the granites cross-cut the metamorphic fabrics related to Edmundian Orogeny.

1.2.2 Reactivation events in the Gascoyne Province

The youngest dated reactivation event, the c. 570 Ma Mulka Tectonic Event, was identified by *in situ* laser $^{40}\text{Ar}/^{39}\text{Ar}$ mica dating (Bodorkos and Wingate, 2007) from the Chalba Shear Zone. The Chalba Shear Zone, in the southern Gascoyne Province, is characterised by dextral strike-slip kinematics and cross cuts c. 755 Ma dykes of the Mundine Well Dolerite Suite (Wingate and Giddings, 2000). Other undated shear zones in the area show the same kinematics and offset the c. 755 Ma dolerites suggesting that they also belong to the Mulka Tectonic Event. The Mulka Tectonic Event is interpreted as a terminal Proterozoic deformation event driven by far-field stress responses from active plate margins (Bodorkos and Wingate, 2007). In the northern Gascoyne Province, field observations show a major fault displacing 1680–1465 Ma sedimentary rocks and c. 755 Ma dolerites cross-cutting the faults, which suggests that fault reactivation there predates the Mulka Tectonic Event and post-dates the 1680–1620 Ma Mangaroon Orogeny. Therefore, the late fault reactivation of the Gascoyne Province remains poorly understood.

Although many studies have been conducted on resolving the tectonothermal evolution of the southern and parts of the central Gascoyne Province there remain large gaps in our knowledge about the tectonic evolution of the northern parts of the province.

1.3 Thesis aims

The previous contribution of SHRIMP U–Pb zircon, monazite and xenotime geochronology and $^{40}\text{Ar}/^{39}\text{Ar}$ mica geochronology in the central and southern parts of the Gascoyne Province have significantly increased our understanding of the tectonothermal evolution of the Capricorn Orogen. However, the same level of understanding is lacking in the northern parts of the province. Therefore, this PhD aims to contribute a similar level of understanding in the northern parts of the Gascoyne Province. In particular, the aims of this thesis were to constrain various low- to high-grade geological processes within a Proterozoic intraplate orogen. Constraining geological processes, such as the timing and duration of metamorphism, magmatism, and late fault reactivation, will provide further insight into the orogenic events and the potential tectonic drivers.

Although five tectonothermal events have been identified there remain gaps in the current understanding of certain aspects of the orogenic events. For instance, some of the crucial knowledge gaps, that form the basis of this thesis, include:

- The current understanding of the 1820–1770 Ma Capricorn Orogeny includes: geochronological constraints on the timing of regional magmatism; active deformation is constrained by dated cross-cutting field relationships; the grade of metamorphism ranges from low- to medium temperature with one region displaying higher temperature of metamorphism; and, a single date for metamorphism has been obtained. However, the direct ages and duration of metamorphism associated with the Capricorn Orogeny remain elusive. Furthermore, the P – T conditions remain unknown. The lack of constraints on the metamorphism means that the drivers for orogenesis remain poorly understood.
- The age of the 1680–1620 Ma Mangaroon Orogeny is constrained by dating accompanying felsic magmatism via U–Pb zircon dating. Magmatism associated with this event is known from the central and northern parts of the Gascoyne Province, however, metamorphic and deformation fabrics are known only from the Mangaroon Zone in the northern parts of the province. The direct ages of metamorphism and calculated P – T conditions remain unknown. Therefore, without

the constraints on metamorphism and lack of geochronology for magmatism, in the northern parts of the province, mean that the drivers for the Mangaroon Orogeny remain poorly understood.

- Although recent U–Pb monazite and xenotime dating in the central parts of the Gascoyne Province identified the 1030–955 Ma Edmundian Orogeny, age span of leucocratic magmatism associated with the Edmundian Orogeny remains poorly constrained. Previous U–Pb zircon geochronology yielded xenocrystic ages that were incompatible with the dated metamorphic fabrics. Therefore, the duration of this episode of magmatism has remained unknown.
- Previous U–Pb zircon geochronology proved to be a successful technique to constrain the Paleoproterozoic magmatism. However, several leucocratic granite samples (from the Moorarie and Durlacher Supersuites and Thirty Three Supersuite) either yielded xenocrystic zircon ages that were incompatible with the dated metamorphic fabrics or yielded multiple age populations. Therefore, several leucocratic plutons in the Gascoyne Province have remained unassigned to a known magmatic supersuite.
- While the late reactivation was identified at c. 570 Ma from mica dating at the Chalba Shear zone there is evidence in the northern parts of the Gascoyne province of earlier fault reactivation in the Mesoproterozoic or Neoproterozoic. For instance, field relationships in the northern parts of the Gascoyne Province show a major fault displacing rocks of the 1680–1465 Ma Edmund Group, with this fault then cut by c. 755 Ma dolerite dykes. This field relationship suggests that a period of fault reactivation post-dated the Mangaroon Orogeny and pre-dated the Mulka Tectonic Event.

To achieve the objectives of this thesis the sampling strategies are outlined below. To avoid repetition further sample details and map locations of samples are presented in the corresponding chapters.

1. To date Capricorn-aged metamorphism in the northern Gascoyne Province pelitic samples were collected for U–Pb phosphate geochronology from the Limejuice, Mangaroon and Boora Boora Zones (Chapter 2). Previous field mapping and zircon geochronology studies assigned deformation fabrics in the Boora Boora Zone and Limejuice Zones to the Capricorn Orogeny although the direct dates for metamorphism remained unknown. The northern Gascoyne Province is

characterised by altered and retrogressed lithologies, due to the overprinting of tectonothermal events, with only scattered occurrences of outcrop preserving original metamorphic minerals. Therefore, sampling was largely governed by suitable outcrop availability.

- GSWA 219708: garnet–biotite pelitic gneiss; GSWA 219706: feldspathic metasandstone; and GSWA 191938: quartz–muscovite–chlorite–garnet pelitic gneiss were collected from the Boora Boora and Limejuice Zones to date the direct timing of metamorphism.
 - P01058: quartz–muscovite–biotite–tourmaline schist. Due to the repeated tectonism, obliterating original metamorphic minerals and deformation fabrics, in the Mangaroon Zone, it was unclear from field observations which orogenic event produced the deformation. The quartz–muscovite–biotite–tourmaline schist was collected to test for either Mangaroon or Capricorn-aged metamorphism.
2. To date the direct timing of Mangaroon-aged metamorphism pelitic samples were collected from across the Mangaroon Zone. To date the timing of igneous crystallisation granitic samples were chosen. Sampling in the Mangaroon Zone was largely governed by suitable outcrop availability. To conduct the P – T history of metamorphism only three sample locations, that were also sampled for U–Pb phosphate geochronology, preserved suitable minerals to conduct phase equilibria modelling (Chapter 3 and Appendix C).
- GSWA 195890: muscovite–biotite metamonzogranite. This sample is characterised by zones of mylonitisation and was originally selected to date the mylonite formation using U–Pb phosphate geochronology. However, monazites associated with the mylonites were severely retrogressed and were deemed unsuitable for U–Pb dating. However, monazites in the less deformed parts of the sample were adequate for analysis (i.e., crystals consisted of $> 15 \mu\text{m}$ unaltered zones); therefore, were chosen to date the timing of igneous crystallisation.
 - P01085: biotite–muscovite syenogranite. This sample was collected to determine the field relationship between the granite pluton and intruding metasedimentary rocks (P16877: quartz–biotite–muscovite schist and P01081: quartz–muscovite–tourmaline schist), i.e., to date the timing of magmatism and the timing of metamorphism.

- GSWA 219741: tourmaline–muscovite monzogranite and GSWA 216538: biotite–muscovite–tourmaline pelitic gneiss. This deformed pelitic gneiss is meter-scale inclusion within the leucocratic monzogranite. The samples were chosen to date the field relationship, i.e., to date the timing of magmatism and the timing of metamorphism.
 - GSWA 219749: cordierite–sillimanite pelitic migmatite; GSWA 219742: sillimanite–biotite–pelitic gneiss; and GSWA 216533: garnet–biotite–epidote pelitic gneiss. These samples were selected for phase equilibria modelling and U–Pb phosphate geochronology.
3. To determine the duration of the magmatism associated with the Edmundian Orogeny leucocratic granitic samples assigned to the Neoproterozoic Thirty Three Supersuite, from the central Gascoyne, were collected for U–Pb monazite geochronology (Chapter 4).
- GSWA 183288: biotite–muscovite–tourmaline monzogranite; GSWA 183287: muscovite–tourmaline granodiorite; and GSWA 187401: tourmaline–muscovite monzogranite were chosen as these outcrops were most easily accessed.
4. Low-*T* leucocratic granites previously dated using U–Pb zircon geochronology that yielded dates incompatible with dated field relationships were resampled for U–Pb monazite geochronology to test whether the monazite would yield a more reliable age (Chapter 4).
- GSWA 139466: biotite–muscovite–granodiorite. This sample yielded a zircon age of 2621 ± 9 Ma which was inconsistent with dated field relationships i.e., the biotite–muscovite–granodiorite intruded 1965–1945 Ma granitic rocks and 2001–1950 Ma metasedimentary rocks.
 - GSWA 183287: muscovite–tourmaline granodiorite. This sample yielded zircon ages ranging from 2085–1309 Ma. The muscovite–tourmaline granodiorite cross-cut Neoproterozoic metamorphic fabrics; therefore, the zircons were interpreted as xenocrystic.
 - GSWA 169092: biotite–muscovite–monzogranite yielded two zircon age populations; therefore, the age of igneous crystallisation remained inconclusive.

5. With the exception of a single mica $^{40}\text{Ar}/^{39}\text{Ar}$ age (i.e., c. 570 Ma) obtained from a shear zone in the central Gascoyne Province the age of mylonite formation in the central and northern areas has remained unknown. To determine the timing of late mylonite formation and fault reactivation samples were collected from mylonite fault zones in the central and northern Gascoyne Province for $^{40}\text{Ar}/^{39}\text{Ar}$ mica geochronology (Chapter 5).
 - GSWA 183294 and 183295: quartz–muscovite mylonite; GSWA 195890: muscovite–biotite metamonzogranite (dextral kinematics); and GSWA 216540 B: muscovite–biotite metamonzogranite were collected from mylonite fault zones.
 - GSWA 216533: biotite–garnet schist. This outcrop, west of the main fault, is characterised by zones of mylonitisation and dextral kinematics. After monazite dating was used to date timing of metamorphism (during this thesis project) the timing of mylonitisation remained unclear.

This thesis utilises *in situ* Sensitive High Resolution Ion Microprobe (SHRIMP) U–Th–Pb monazite and xenotime geochronology and $^{40}\text{Ar}/^{39}\text{Ar}$ mica geochronology to date low- to high-grade orogenic processes in the Gascoyne Province. Monazite and xenotime U–Pb data were acquired using the SHRIMP II instrument at the John de Laeter Centre (JdLC) at Curtin University of Technology. The SHRIMP technique allows for U–Th–Pb isotopic analysis of selected minerals with a spatial resolution of 5–20 microns and simultaneous collection of Rare Earth Elements (REE).

Although U–Pb phosphate geochronology is a robust technique for resolving many geological processes, such as metamorphism and magmatism, dating the timing of movement of shear zones may not always be possible due to the complete retrogression of the monazite and xenotime found in rocks within major shear zones (Vernon and Clarke, 2008). This retrogression can be severe enough to destroy the existing phosphates, rendering them unsuitable for U–Pb geochronology. Therefore, an alternative technique is required to constrain the timing of fault movement and crustal uplift. In these instances $^{40}\text{Ar}/^{39}\text{Ar}$ mica geochronology can be successfully used to constrain deformation and cooling processes (e.g., Hansma et al., 2016; Scibiorski et al., 2015). Mica $^{40}\text{Ar}/^{39}\text{Ar}$ geochronology was acquired using the Argus VI Multi-Collector Noble Gas Mass Spectrometer at the Western Australian Argon Isotope Facility at the JdLC. The selected minerals were step heated, followed by gas purification and measurement of Ar isotopes.

In addition to acquiring geochronology data for this research project the construction of P – T pseudosections, using THERMOCALC software, was completed to determine P – T conditions of one orogenic event, the Mangaroon Orogeny.

1.4 Thesis structure

The introductory chapter (Chapter 1) notes the challenges of recognizing separate orogenic events in a complex Precambrian intraplate orogen subjected to repeated reworking by relying on field observations alone. A detailed account of the prolonged reworking and late reactivation history is included in this chapter (above) to emphasize the complex tectonothermal history of the Proterozoic Capricorn Orogen. However, with the application of appropriate geochronology methods, the geological processes can be dated, and the geological history resolved with confidence. The subsequent four chapters (Chapters 2–5), making up the body of the thesis, are presented as a compilation of published journal papers. In particular, this thesis begins with constraining the timing and duration of metamorphism, using U–Pb monazite and xenotime geochronology, related to two Paleoproterozoic reworking events (Chapters 2 and 3), including the first reworking event since the initiation of the intraplate orogen. Chapter 4 examines the issues of relying on U–Pb zircon geochronology alone to constrain leucocratic magmatism. Here we show how using U–Pb monazite geochronology yielded more reliable results that were compatible with field relationships allowing for the duration of magmatism to be constrained. The body of the thesis concludes by establishing a Neoproterozoic widespread reactivation event that potentially marks a change in crustal behaviour which symbolises stabilisation of the orogen (Chapter 5).

Due to the prolonged and repeated reworking history of the Proterozoic Capricorn Orogen determining the timing and duration of metamorphism associated with the first reworking event, the 1820–1770 Ma Capricorn Orogeny, has been challenging. Chapter 2 presents new SHRIMP U–Pb monazite and xenotime geochronology, from the northern Gascoyne Province, from a metasandstone, a quartz–muscovite–chlorite–garnet pelitic schist, a quartz–muscovite–biotite tourmaline schist and a garnet–biotite pelitic gneiss. The new geochronology data allowed the duration of metamorphism and the relationship to magmatism to be resolved and, therefore, provided clues as to the drivers for metamorphism.

The second orogenic event known from the Gascoyne Province is the 1680–1620 Ma Mangaroon Orogeny. The aim of Chapter 3 was to obtain the first direct dates, and P – T conditions, of the medium- to high-grade metamorphism, and to resolve the age of

magmatism in the Mangaroon Zone associated with the Mangaroon Orogeny. This chapter presents new P – T – t information for the orogeny in the Mangaroon Zone derived from a combination of *in situ* SHRIMP U–Pb monazite and xenotime dating, along with modelled P – T pseudosections. For the metamorphic study the pelitic samples include a cordierite–sillimanite pelitic migmatite, sillimanite–biotite pelitic gneiss, garnet–biotite–epidote pelitic gneiss, quartz–muscovite–tourmaline gneiss, quartz–biotite–muscovite schist, and a biotite–muscovite–tourmaline pelitic gneiss. For the magmatic aspect of this chapter crustal granites studied include monzogranites, granodiorites, and a syenogranite. The new data reveal the P – T conditions of peak metamorphism which points to a magmatic source as a driver for the metamorphism.

The final reworking event at 1030–955 Ma, restricted to the center of the Gascoyne Province, consists of purely leucocratic magmatism. Small occurrences of leucocratic magmatism are also known from the Paleoproterozoic Moorarie and Durlacher Supersuites. Chapter 4 highlights the issue of using U–Pb zircon geochronology, alone, to date low-temperature leucocratic granites and demonstrates how SHRIMP U–Pb monazite geochronology yields more reliable results. For instance, existing U–Pb zircon geochronology from leucocratic granite samples associated with the Thirty Three Supersuite and Moorarie Supersuite of magmatism yielded results that were incompatible with dated field relationships. Furthermore, zircon geochronology results from a leucocratic pluton, in the northern parts of the Gascoyne Province, associated with the Durlacher Supersuite yielded multiple concordant ages making it difficult to constrain the timing of magmatism in this part of the province. The new data allowed the timing and duration of the youngest supersuite to be constrained reliably for the first time. Secondly, the results enabled a previously unassigned leucocratic pluton to be correlated with the Moorarie Supersuite. Finally, the duration of magmatism associated with the Durlacher Supersuite in the northern parts of the Gascoyne Province was established with confidence.

The Gascoyne Province was subjected to several episodes of fault reactivation following the final reworking event. However, only the timing of the youngest reactivation event at c. 570 Ma has been reliably constrained using $^{40}\text{Ar}/^{39}\text{Ar}$ mica geochronology. Field relationships suggest a period of fault reactivation occurred sometime between 1465 and 755 Ma in the northern Gascoyne Province. The aim of Chapter 5 is to date the timing of low-grade fault reactivation in the northern and central Gascoyne Province. This chapter presents new $^{40}\text{Ar}/^{39}\text{Ar}$ mica and SHRIMP U–Pb xenotime geochronology from major faults across the Gascoyne Province resolving the reactivation history. The new

geochronology data combined with field structural observations revealed that compressional forces drove the Neoproterozoic fault reactivation.

The thesis concludes with Chapter 6 outlining the main conclusions of this work and provides recommendations for future work to further increase the understanding of the intraplate evolution of the Capricorn Orogen. Due to the nature of this thesis, as a compilation of papers, there is some repetition throughout this document.

1.5 Chapters as a series of papers

The titles of chapters representing papers, and their publication status, are listed below:

- **Chapter 2 (Paper 1):** SHRIMP U–Pb phosphate dating shows metamorphism was synchronous with magmatism of the Paleoproterozoic Capricorn Orogeny.

Reference:

Piechocka, A. M., Zi, J.-W., Gregory, C. J., Sheppard, & Rasmussen, B. (2019). *SHRIMP U–Pb phosphate dating shows metamorphism was synchronous with magmatism during the Paleoproterozoic Capricorn Orogeny*. *Australian Journal of Earth Sciences*, 66, 973–990.

- **Chapter 3 (Paper 2):** Low-P, high-T c. 1.69 Ga metamorphism in the West Australian Craton triggered by magma flux into the upper crust.

Reference:

Piechocka, A. M., Zi, J.-W., Wingate, M. T. D., Gregory, C. J., Sheppard, S., Korhonen, F. J., Fitzsimons, I., C. W., Johnson, T. E., and Rasmussen, B. (2019). *The Mangaroon Orogeny: Synchronous c. 1.7 Ga magmatism and low-P, high-T metamorphism in the West Australian Craton*. *Precambrian Research*, 333, 105425.

- **Chapter 4 (Paper 3):** Monazite trumps zircon: applying SHRIMP U–Pb geochronology to systematically evaluate emplacement ages of leucocratic, low-temperature granites in a complex Precambrian orogen.

Reference:

Piechocka, A. M., Gregory, C. J., Zi, J.-W., Sheppard, S., Wingate, M. T. D., & Rasmussen, B. (2017). *Monazite trumps zircon: applying SHRIMP U–Pb geochronology to systematically evaluate emplacement ages of leucocratic, low-temperature granites in a complex Precambrian orogen*. *Contributions to Mineralogy and Petrology*, 172, 1–17.

- **Chapter 5 (Paper 4):** Neoproterozoic $^{40}\text{Ar}/^{39}\text{Ar}$ mica ages mark the termination of a billion years of intraplate reworking in the Capricorn Orogen, Western Australia.

Reference:

Piechocka, A. M., Sheppard, S., Fitzsimons, I. C. W., Johnson, S. P., Rasmussen, B. & Jourdan, F. (2018). *Neoproterozoic $^{40}\text{Ar}/^{39}\text{Ar}$ mica ages mark the termination of a billion years of intraplate reworking in the Capricorn Orogen, Western Australia*. *Precambrian Research*, 310, 391–406.

1.6 References

- Bodorkos, S., & Wingate, M. T. D. (2007). The contribution of geochronology to GSWA's mapping programs: current perspectives and future directions: Geological Survey of Western Australia, Record 2007/2, p. 10–11.
- Cherniak, D. J., & Watson, E. B. (2001). Pb diffusion in zircon: *Chemical Geology* 172, 5–24.
- Cherniak, D. J., Watson, E. B., Grove, M., & Harrison, T. M. (2004). Pb diffusion in monazite: a combined RBS/SIMS study: *Geochimica et Cosmochimica Acta* 68, 829–840.
- Crowley, J. L., & Parrish, R. R. (1999). U–Pb isotopic constraints on diachronous metamorphism in the northern Monashee complex, southern Canadian Cordillera: *Journal of Metamorphic Geology* 17, 483–502.
- Culver, K. E. (2001). Structure, metamorphism and geochronology of the northern margin of the Gurun Gutta Granite, central Gascoyne Complex, Western Australia. Curtin University of Technology, Perth BSc. (Hons) thesis (unpublished).
- Cutten, H. N., Johnson, S. P., Thorne, A.M., Wingate, M.T.D., Kirkland, C.L., Belousova, E.A., Blay, O. A., & Zwingmann, H. (2016). Deposition, provenance, inversion history and mineralization of the Proterozoic Edmund and Collier Basins, Capricorn Orogen. Geological Survey of Western Australia Report 127, pp. 80.
- Fielding, I. O. H., Johnson, S. P., Zi, J. W., Rasmussen, B., Muhling, J. R., Dunkley, D. J., Sheppard, S., Wingate, M. T. D., & Rogers, J. R. (2017). Using In Situ SHRIMP U-Pb Monazite and Xenotime Geochronology to Determine the Age of Orogenic Gold Mineralization: An Example from the Paulsens Mine, Southern Pilbara Craton: *Economic Geology* 112, 1205–1230.
- Fielding, I. O. H., Johnson, S. P., Zi, J.-W., Sheppard, S., & Rasmussen, B. (2018). Neighbouring orogenic gold deposits may be the products of unrelated mineralizing events: *Ore Geology Reviews* 95, 593–603.
- Gee, R. D. (1979). Structure and tectonic style of the Western Australian Shield: *Tectonophysics* 58, 327–369.
- Grosse, P., Söllner, F., Báez, M. A., Toselli, A. J., Rossi, J. N., & de la Rosa, J. D. (2009). Lower Carboniferous post-orogenic granites in central-eastern Sierra de Velasco, Sierras Pampeanas, Argentina: U–Pb monazite geochronology, geochemistry and Sr–Nd isotopes: *International Journal of Earth Sciences* 98, 1001–1025.
- Hacker, B. R., Ratschbacher, L., Webb, L., Ireland, T., Walker, D., & Shuwen, D. (1998). U–Pb zircon ages constrain the architecture of the ultrahigh-pressure Qinling–Dabie Orogen, China: *Earth and Planetary Science Letters* 161, 215–230.

- Hansma, J., Tohver, E., Schrank, C., Jourdan, F., & Adams, D. (2016). The timing of the Cape Orogeny: New $^{40}\text{Ar}/^{39}\text{Ar}$ age constraints on deformation and cooling of the Cape Fold Belt, South Africa: *Gondwana Research* 32, 122–137.
- Heaman, L., and Parrish, R. (1991). U–Pb geochronology of accessory minerals. In: Heaman, L. Ludden, J. N. (Eds.), *Applications of radiogenic isotope systems to problems in geology: Short Course Handbook-Mineralogical Association of Canada* 19, 59–102.
- Johnson, S. P., Sheppard, S., Rasmussen, B., Wingate, M. T. D., Kirkland, C. L., Muhling, J. R., Fletcher, I. R., & Belousova, E. A. (2011). Two collisions, two sutures: Punctuated pre-1950Ma assembly of the West Australian Craton during the Ophthalmian and Glenburgh Orogenies: *Precambrian Research* 189, 239–262.
- Korhonen, F. J., & Johnson, S. P. (2015). The role of radiogenic heat in prolonged intraplate reworking: The Capricorn Orogen explained?: *Earth and Planetary Science Letters* 428, 22–32.
- Korhonen, F. J., Johnson, S. P., Wingate, M. T. D., Kirkland, C. L., Fletcher, I. R., Dunkley, D. J., Roberts, M. P., Sheppard, S., Muhling, J. R., & Rasmussen, B. (2017). Radiogenic heating and craton-margin plate stresses as drivers for intraplate orogeny: *Journal of Metamorphic Geology* 35, 631–661.
- Lee, J. K. W., Williams, I. S., & Ellis, D. J. (1997). Pb, U and Th diffusion in natural zircon: *Nature* 390, 159–162.
- Occhipinti, S. A., & Reddy, S. M. (2009). Neoproterozoic reworking of the Paleoproterozoic Capricorn Orogen of Western Australia and implications for the amalgamation of Rodinia. *Geological Society, London, Special Publications* 327, 445–456.
- Occhipinti, S. A., Sheppard, S., Passchier, C., Tyler, I. M., & Nelson, D. R. (2004). Paleoproterozoic crustal accretion and collision in the southern Capricorn Orogen: the Glenburgh Orogeny: *Precambrian Research* 128, 237–255.
- Rasmussen, B. (2005). Radiometric dating of sedimentary rocks: the application of diagenetic xenotime geochronology: *Earth-Science Reviews* 68, 197–243.
- Rasmussen, B., Fletcher, I. R., & Muhling, J. R. (2007a). In situ U–Pb dating and element mapping of three generations of monazite: Unravelling cryptic tectonothermal events in low-grade terranes. *Geochimica et Cosmochimica Acta*, 71, 670–690.
- Rasmussen, B., Fletcher, I. R., Muhling, J. R., Thorne, W. S., & Broadbent, G. C. (2007b). Prolonged history of episodic fluid flow in giant hematite ore bodies: Evidence from in situ U–Pb geochronology of hydrothermal xenotime: *Earth and Planetary Science Letters* 258, 249–259.

- Rasmussen, B., Fletcher, I. R., & Sheppard, S. (2005). Isotopic dating of the migration of a low-grade metamorphic front during orogenesis: *Geology* 33, 773–776.
- Rowley, D. B., Xue, F., Tucker, R. D., Peng, Z. X., Baker, J., & Davis, A. (1997). Ages of ultrahigh pressure metamorphism and protolith orthogneisses from the eastern Dabie Shan: U/Pb zircon geochronology: *Earth and Planetary Science Letters* 151, 191–203.
- Scibiorski, E., Tohver, E., & Jourdan, F. (2015). Rapid cooling and exhumation in the western part of the Mesoproterozoic Albany-Fraser Orogen, Western Australia: *Precambrian Research* 265, 232–248.
- Scrimgeour, I. R. (2003). Developing a revised framework for the Arunta Region, in *Annual Geoscience Exploration Seminar (AGES) 2003: Northern Territory Geological Survey, Record 2003-001*, p. 1–3.
- Sheppard, S., Bodorkos, S., Johnson, S. P., Wingate, M. T. D., & Kirkland, C. L. (2010a). The Paleoproterozoic Capricorn Orogeny: Intracontinental Reworking Not Continent-Continent Collision: Geological Survey of Western Australia, Report 108, p. 33.
- Sheppard, S., Johnson, S. P., Wingate, M. T. D., Kirkland, C. L., & Pirajno, F. (2010b). Explanatory notes for the Gascoyne Province: Geological Survey of Western Australia, 1:100 000 Explanatory Notes, p. 336.
- Sheppard, S., Occhipinti, S. A., & Nelson, D. R. (2005). Intracontinental reworking in the Capricorn Orogen, Western Australia: the 1680–1620 Ma Mangaroon Orogeny: *Australian Journal of Earth Sciences*, 52, 443–460.
- Sheppard, S., Occhipinti, S. A., & Tyler, I. M. (2004). A 2005–1970 Ma Andean-type batholith in the southern Gascoyne Complex, Western Australia: *Precambrian Research*, 128, 257–277.
- Sheppard, S., Rasmussen, B., Muhling, J. R., Farrell, T. R., & Fletcher, I. R. (2007). Grenvillian-aged orogenesis in the Paleoproterozoic Gascoyne Complex, Western Australia: 1030–950 Ma reworking of the Proterozoic Capricorn Orogen: *Journal of Metamorphic Geology*, 25, 477–494.
- Townsend, K. J., Miller, C. F., D'Andrea, J. L., Ayers, J. C., Harrison, T. M., & Coath, C. D. (2001). Low temperature replacement of monazite in the Ireteba granite, Southern Nevada: geochronological implications: *Chemical Geology* 172, 95–112.
- Tyler, I. M., & Thorne, A. M. (1990). The northern margin of the Capricorn Orogen Western Australia an example of an Early Proterozoic collision zone: *Journal of Structural Geology*, 12, 685–701.

- Vernon, R. H., & Clarke, G. L. (2008). *Principles of metamorphic petrology*. New York, USA: Cambridge Press University.
- Williams, S. J. (1986). *Geology of the Gascoyne Province, western Australia: Geological Survey of Western Australia, Report 15*, p. 85.
- Wingate, M. T. D., & Giddings, J. W. (2000). Age and palaeomagnetism of the Mundine Well dyke swarm, Western Australia: implications for an Australia-Laurentia connection at 755 Ma: *Precambrian Research* 100, 335–357.
- Zhou, M.-F., Yan, D.-P., Kennedy, A. K., Li, Y., & Ding, J. (2002). SHRIMP U–Pb zircon geochronological and geochemical evidence for Neoproterozoic arc-magmatism along the western margin of the Yangtze Block, South China: *Earth and Planetary Science Letters* 196, 51–67.
- Zi, J.-W., Rasmussen, B., Muhling, J. R., Fletcher, I. R., Thorne, A. M., Johnson, S. P., Cutten, H. N., Dunkley, D. J., & Korhonen, F. J. (2015). In situ U–Pb geochronology of xenotime and monazite from the Abra polymetallic deposit in the Capricorn Orogen, Australia: Dating hydrothermal mineralization and fluid flow in a long-lived crustal structure: *Precambrian Research* 260, 91–112.

Chapter 2

PAPER 1: SHRIMP U–Pb phosphate dating shows metamorphism was synchronous with magmatism during the Paleoproterozoic Capricorn Orogeny

Authors:

Agnieszka M. Piechocka¹, Jian-Wei Zi^{2, 3}, Courtney J Gregory¹, Stephen Sheppard⁴, Birger Rasmussen^{3,5}

¹School of Earth and Planetary Sciences, Curtin University, Kent Street, Bentley, WA 6102, Australia

²John de Laeter Centre, Curtin University, Kent Street, Bentley, WA 6102, Australia

³State Key Laboratory of Geological Processes and Mineral Resources, China University of Geosciences, Wuhan, 430074, China

⁴Calidus Resources Ltd, Suite 12, 11 Ventnor Avenue, West Perth, WA, 6005, Australia

⁵School of Earth Sciences, The University of Western Australia, Nedlands, WA 6009, Australia

Keywords:

intraplate orogeny, U–Pb geochronology, monazite, xenotime, Proterozoic, Capricorn Orogen

2.1 Abstract

Unlike many Phanerozoic orogens, where the primary effects of orogenic events can be easily determined, Precambrian orogens are commonly characterised by repeated tectonothermal events making it challenging to decipher the geological history. The Capricorn Orogen is a complex Precambrian intraplate orogen located within the Western Australian Craton that has been subjected to four separate reworking tectonic events between 1820 Ma and 900 Ma. Although direct U–Pb ages for metamorphism have been obtained for the younger events, there is only limited geochronological data for the oldest event — the 1820 Ma to 1770 Ma Capricorn Orogeny. This is primarily because of multiple episodes of deformation and metamorphism overprinting and obscuring the original tectonic fabrics and destroying metamorphic chronometers. In this study, we use *in situ* U–Pb monazite and xenotime geochronology, from a feldspathic metasandstone, a quartz–muscovite–chlorite–garnet pelitic schist, a quartz–muscovite–tourmaline schist and a garnet–biotite–plagioclase pelitic gneiss, to obtain the first direct age constraints for metamorphism during the Capricorn Orogeny in the northern Gascoyne Province. Metamorphism was synchronous with the 1820–1775 Ma regional magmatism in the northern part, and possibly in the southern part, of the Gascoyne Province. Furthermore, our results hint at a late stage hydrothermal fluid event at c. 1750–1730 Ma, post-dating the magmatism in the northern Gascoyne Province.

2.2 Introduction

Determining the timing of geological processes in Proterozoic intraplate orogens can be challenging, especially in cases where the orogen has been subjected to a prolonged history of tectonic reworking and reactivation (e.g. Hand and Buick, 2001). The Proterozoic Capricorn Orogen of Western Australia is an orogen that records nearly a billion years of intraplate reworking (Korhonen et al., 2017; Occhipinti et al., 2001; Piechocka et al., 2017; Sheppard et al., 2005; Sheppard et al., 2007; Sheppard et al., 2010a). The Capricorn Orogen is at least 1000 km long and 500 km wide and includes the southern margin of the Pilbara Craton and the northern edge of the Yilgarn Craton (Figure 2.1). It is divided into several tectonic units that include the Gascoyne Province, Glenburgh Terrane, Narryer Terrane, Errabiddy Shear Zone, and numerous Paleoproterozoic basins with sedimentary ± volcanic fill (Cawood and Tyler, 2004).

Early studies suggested that the fabrics and metamorphic assemblages in the Gascoyne Province and Paleoproterozoic basins were the product of a single protracted Capricorn Orogeny (Tyler and Thorne 1990). Furthermore, it was thought that the Capricorn Orogeny spanned roughly 400 million years from 2000 Ma to 1600 Ma (Tyler and Thorne 1990). Subsequent U–Pb zircon geochronology suggested that the fabrics and metamorphic assemblages in the Capricorn Orogen belonged to two earlier collisional events: a collision between the Pilbara Craton and the Glenburgh Terrane during the 2.2 Ga Ophthalmia Orogeny (Rasmussen et al., 2005) and a second collision between the combined Pilbara–Glenburgh Terrane with the northern Yilgarn Craton during the 1.95 Ga Glenburgh Orogeny (Johnson et al., 2011; Occhipinti et al., 2004; Sheppard et al., 2004), thus forming the West Australian Craton. Further U–Pb zircon geochronology identified two reworking events: the Capricorn and Mangaroon orogenies.

The 1820–1770 Ma Capricorn Orogeny was constrained through a combination of detailed field mapping and dating of granites across the Gascoyne Province (Sheppard et al., 2010a; 2010b). Although scattered dates for metamorphism associated with the Capricorn Orogeny have been captured (Korhonen et al., 2015; Wingate et al., 2010), there remains a lack of robust and systematic dating of regional metamorphism. Similarly, the 1680–1620 Ma Mangaroon Orogeny was identified by routine SHRIMP U–Pb zircon dating of granites across the Gascoyne Province combined with regional field mapping in the Mangaroon Zone (Sheppard et al., 2005).

U–Pb monazite and xenotime geochronology identified a further two reworking events at 1320–1170 Ma and 1030–900 Ma (Korhonen et al., 2017; Piechocka et al., 2017; Sheppard et al., 2007). SHRIMP U–Pb monazite and xenotime geochronology combined with field mapping and P – T pseudosections constrained the P – T – t evolution of the 1320–1170 Ma Mutherbukin Tectonic Event (Korhonen et al., 2017). Similarly, field mapping combined with SHRIMP U–Pb monazite and xenotime geochronology to directly date the metamorphism and magmatism identified the 1030–900 Ma Edmundian Orogeny (Piechocka et al., 2017; Sheppard et al., 2007). This reworking was followed by two reactivation episodes at 920–830 Ma (Piechocka et al., 2018) and c. 570 Ma (Bodorkos and Wingate 2007).

The 1820–1770 Ma Capricorn Orogeny has the biggest geographic footprint of the orogenic events, extending outside the Gascoyne Province to other parts of the Capricorn Orogen, including the Ashburton Basin and the Yarlalweelor Gneiss Complex (Occhipinti et al., 2001; Sheppard et al., 2010a, 2010b). SHRIMP U–Pb zircon dating has shown that 1820–1775 Ma magmatism is both widespread and voluminous, and bracketing relationships indicate that magmatism was accompanied by deformation and metamorphism associated with the Capricorn Orogeny (Occhipinti et al., 2001; Sheppard et al., 2010a, b). Despite all the SHRIMP U–Pb zircon and phosphate dating, direct ages for metamorphism have remained elusive and hindered our understanding of the duration and likely causes of the metamorphism associated with the 1820–1770 Ma Capricorn Orogeny.

Here we present the first reliable *in situ* U–Pb monazite and xenotime geochronology for the metamorphism associated with the Capricorn Orogeny in the northern Gascoyne Province, providing new insights into the duration and regional extent of this Paleoproterozoic tectonothermal event. Although the P – T conditions remain unknown, we propose that magmatism was the likely cause of the regional metamorphism. A secondary outcome of this study is the suggestion of a younger age grouping that could reflect a late stage deformation and hydrothermal fluid flow event linked to recently published ages from orogenic gold deposits in the Ashburton Basin to the north.

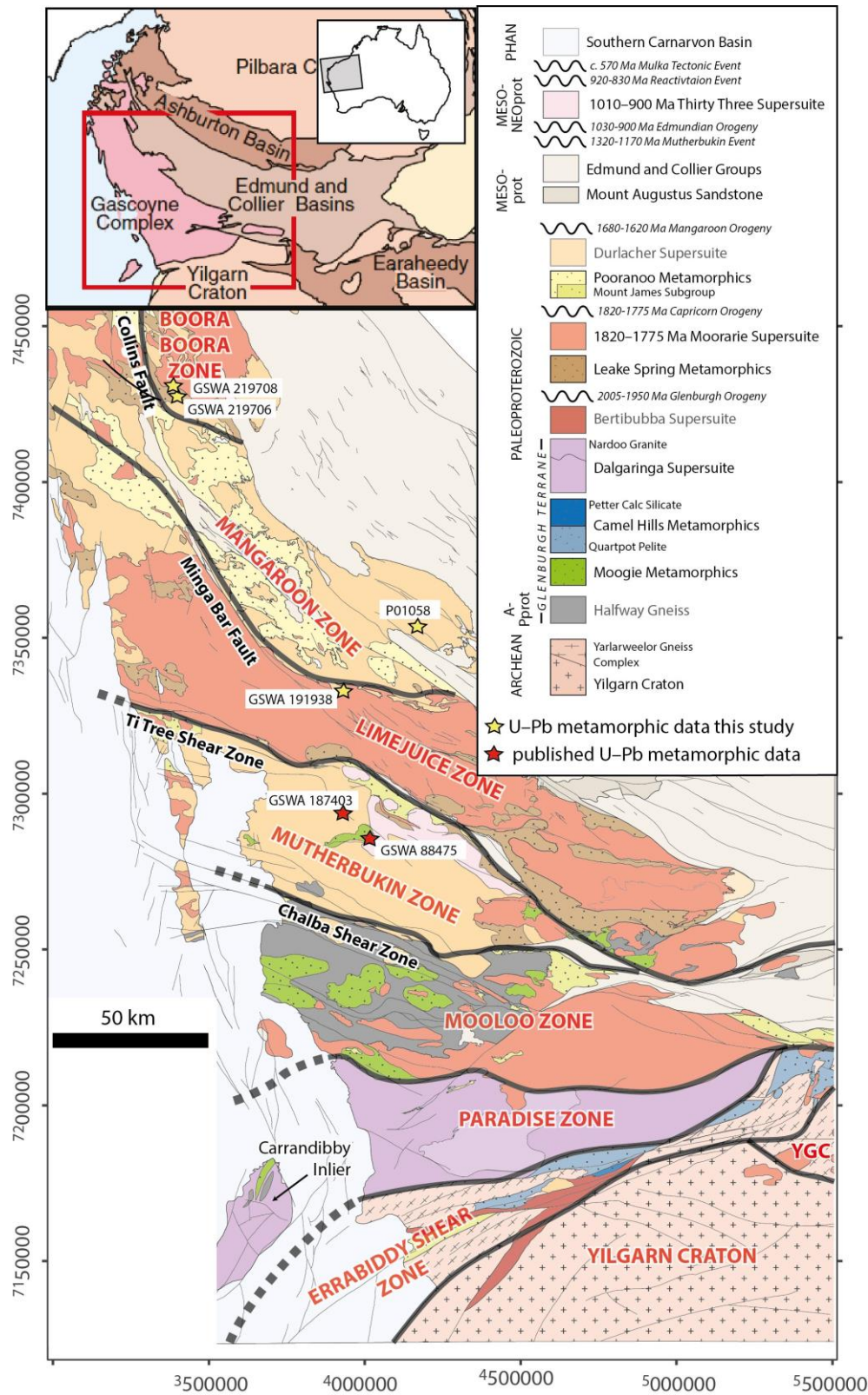


Figure 2.1 Regional Geology map of the Gascoyne Province, Capricorn Orogen showing the distinct structural-metamorphic zones and sample locations related to this study and published supporting samples (adapted from Sheppard et al., 2010b). YGC = Yarlarweelor Gneiss Complex. Coordinate system is GDA 1994 MGA Zone 50.

2.3 Regional Geology

Of all the lithotectonic units of the Capricorn Orogen, the Gascoyne Province records the most complex and protracted tectonothermal history. The province is characterised by fault-bounded structural and metamorphic zones (Sheppard et al., 2010b) (Figure 2.1), each recording distinct deformation fabrics and mineral assemblages. The Gascoyne Province includes the Errabiddy Shear Zone, Paradise Zone, Mooloo Zone, Mutherbukin Zone, Limejuice Zone, Mangaroon Zone and the Boora Boora Zone (Figure 2.1). Three episodes of deformation associated with the 1820–1770 Ma Capricorn Orogeny have been recognised and are referred to as D_{1n} , D_{2n} and D_{3n} (Sheppard et al., 2010a; 2010b). The maximum age constraint comes from the age of the oldest igneous intrusion of the Moorarie Supersuite at c. 1820 Ma while the minimum age constraint is derived from metamorphic zircon rims dated at c. 1770 Ma (Sheppard et al., 2010b). The timing of these events has been constrained by SHRIMP U–Pb zircon dating of felsic igneous rocks that were overprinted by, or cut, the individual events. D_{1n} and D_{2n} are known to have affected the entire Gascoyne Province and D_{3n} is known only from the Limejuice Zone (Sheppard et al., 2010b). The metamorphic grade ranges from greenschist to upper amphibolite facies (Sheppard et al., 2010b). Although deformation and metamorphism associated with D_{1n} – D_{3n} are thought to have been broadly coeval with the emplacement of 1820–1775 Ma granites (Sheppard et al., 2010b), there are no direct constraints on the start or end of metamorphism.

In this paper, the northern Gascoyne Province refers to the Mangaroon Zone and the Boora Boora Zone. While the northern Capricorn Orogen refers to the Boora Boora Zone, Ashburton Basin and the southern margin of the Pilbara Craton. The central Capricorn Orogen consists of the Mutherbukin and Limejuice zones. The southern Capricorn Orogen refers to the Yarlarweelor Gneiss Complex, Errabiddy Shear Zone, Paradise Zone and Mooloo Zone.

2.3.1 Southern Capricorn Orogen

In the southern Capricorn Orogen, the Capricorn Orogeny overprints the earlier metamorphism and deformation associated with the 1950 Ma Glenburgh Orogeny (Johnson et al., 2010). In the Yarlarweelor Gneiss Complex in the southern part of the Capricorn Orogen, gneissic fabrics, upright folds and metamorphic assemblages up to amphibolite facies, accompanied by magmatism record deformation and metamorphism associated with the Capricorn Orogeny (Sheppard et al., 2010a). In the Errabiddy Shear

Zone, the southernmost zone of the Gascoyne Province, earlier 1950 Ma structures are overprinted by greenschist facies metamorphic assemblages, upright folds and anastomosing shear zones considered to be an extension of the Capricorn Orogeny (Sheppard et al., 2010a). The upper amphibolite to granulite facies metamorphism associated with the 1950 Ma Glenburgh Orogeny affected the Paradise Zone (Johnson et al., 2010), however, retrogression fabrics in the Paradise Zone may be related to the Capricorn Orogeny (Sheppard et al., 2010a).

The geochronological constraints on D_{1n} in the Yarlalweelor Gneiss Complex come from the youngest deformed intrusions dated at 1813 ± 8 Ma (GSWA 142849; Nelson, 1998a) and the oldest undeformed granites dated at 1808 ± 6 Ma (GSWA 142851; Nelson 1998b; Sheppard et al., 2010b). In the Glenburgh Terrane, foliated granodiorite dated at 1811 ± 6 Ma, 1810 ± 9 Ma, and 1804 ± 5 Ma, is intruded by an undeformed granite dated at 1800 ± 7 Ma (Sheppard et al., 2010b). Therefore, the first recognisable event, D_{1n} , occurred between c. 1813 and 1800 Ma.

The Yarlalweelor Gneiss Complex also provides a geochronological constraint on D_{2n} . The youngest granite (Kerba Granite) determined from field relationships is dated at 1808 ± 6 Ma (GSWA 142849; Nelson 1998a) and is cut by D_{2n} structures, providing a maximum age for the deformation (Sheppard et al., 2010b). The minimum age constraint for D_{2n} and the deformation and metamorphism associated with D_{3n} are known from the central Gascoyne Province in the Limejuice Zone (see below).

2.3.2 Central Capricorn Orogen

In the central part of the Gascoyne Province, greenschist-facies retrogression of garnet to chloritoid, and sillimanite to sericite, with abundant chloritoid across the Mooloo Zone (Figure 2.1) indicate that peak P – T associated with Capricorn metamorphism was 425–500 °C and <4 kbar (Sheppard et al., 2010a). The timing of deformation is constrained by deformed granite dated at 1810 Ma and undeformed granite dated at 1800 Ma (Sheppard et al., 2010a).

Capricorn-aged metamorphism, in the Mutherbukin Zone, is recorded by U–Pb zircon dating from a single quartzite sample (GSWA 187403), and U–Pb monazite and xenotime geochronology from a metasomatic schist (GSWA 88475) (see Figure 2.1 for locations). Metamorphic zircon rims on detrital grains from the quartzite yielded 1772 ± 6 Ma (GSWA 187403; Wingate et al., 2010). The zircons in sample GSWA 187403 are

anhedral to subhedral, and clear and colourless to dark brown. Concentric zoning in the zircon cores is truncated at grain boundaries (Fig. 1 of Wingate et al., 2010). The 1772 ± 6 Ma age from zircon rims could be related to D_{3n} (Johnson et al., 2010; Sheppard et al., 2010a). More recently, monazite from a metasomatic schist from the Mutherbukin Zone (Figure 2.1), yielded a U–Pb date of 1780 ± 2 Ma interpreted as the timing of new monazite growth. Xenotime from the same sample yielded two age groupings: 1805 ± 9 Ma (four analyses from two spots on one grain), interpreted as possible new xenotime growth, and a single analysis at 1725 ± 11 Ma (1σ), interpreted as fine-scale recrystallisation (GSWA 88475: Korhonen et al., 2015). The link between the recent phosphate results and the tectonic fabrics and mineral assemblages associated with the Capricorn Orogeny is unclear.

Deformation fabrics associated with D_{3n} are currently only known from the Limejuice Zone, north of the Mutherbukin Zone, and consist of a low-grade crenulation, and a mineral assemblage of muscovite–chlorite–quartz in pelitic rocks and quartz–muscovite in psammitic rocks (Sheppard et al., 2010b), suggesting greenschist facies metamorphism. If the zircons in sample GSWA 187403 (discussed above) had grown under low-grade metamorphic conditions they would typically display zircon outgrowths surrounding the zircon crystal (e.g., Fig. 3 of Rasmussen, 2005). Therefore, it is likely that the zircons in GSWA 187403, in the Mutherbukin Zone, formed under higher than greenschist facies temperatures as seen in the Limejuice Zone.

In the Limejuice Zone, field observations show granites with a gneissic fabric parallel to the fabric in the metasedimentary rocks are intruded by undeformed granites (Sheppard et al., 2010b). For instance, a deformed granite with crystallisation age of 1788 ± 7 Ma (GSWA 190662; Wingate et al., 2011) is intruded by undeformed granite dated at 1791 ± 4 Ma and 1786 ± 6 Ma (Sheppard et al., 2010b; GSWA 190660; Wingate et al., 2012a; GSWA 188974; Wingate et al., 2017). Therefore, D_{2n} is constrained between 1808 Ma (the maximum age for D_{2n} as defined in the Yarlalweelor Gneiss Complex) and 1786 Ma. Due to the presence of relict peak assemblages of andalusite–cordierite–biotite–muscovite–plagioclase in amphibolites and pelitic gneisses the P – T conditions were assumed to be of high-temperature and low-pressure (Sheppard et al., 2010a).

Although deformation associated with the Capricorn Orogeny has been constrained by U–Pb zircon dates that bracket deformed and undeformed granites, there remains a lack of direct ages for metamorphism associated with the orogeny.

2.3.3 Northern Capricorn Orogen

Two episodes of deformation in the northern Capricorn Orogen are recognised as D_{1a} and D_{2a} (Krapez and McNaughton, 1999; Martin et al., 2005; Sheppard et al., 2010a; Thorne and Seymour, 1991; Tyler and Thorne, 1990). The age of D_{1a} is constrained between c. 1805 and c. 1790 Ma (Martin et al., 2005 p.14). The age of D_{2a} is loosely defined at between c. 1790 and c. 1620 Ma with the younger age limit possibly related to the 1680–1620 Ma Mangaroon Orogeny rather than the Capricorn Orogeny (Sheppard et al., 2010a). Considering that the geochronological constraints in the Boora Boora Zone and Ashburton Basin are similar in age to D_{1n} and D_{2n} fabrics in other parts of the Gascoyne Province, D_{1a} and D_{2a} may be related to the Capricorn Orogeny (Krapez and McNaughton, 1999; Sheppard et al., 2010a; 2010b).

2.4 Sample details

Earlier work focussed in the southern Gascoyne Province revealed that the Capricorn Orogeny appeared to be associated with the retrogression of medium- to high-grade assemblages of the older Glenburgh Orogeny (Johnson et al., 2010). The effect of this retrogression was the destruction of metamorphic monazite and xenotime, rendering them unsuitable for SHRIMP dating. However, the northern Gascoyne Province has provided the ideal location to date the timing of Capricorn-age metamorphism due to the preservation of monazite and xenotime in the samples.

The sampling strategy for this study was to collect samples for U–Pb phosphate geochronology from the northern Gascoyne Province to test whether Capricorn-aged metamorphism is preserved in the Limejuice, Mangaroon and Boora Boora zones (Figure 2.1). In particular, the Mangaroon Zone is characterised by fabrics and metamorphism associated with the 1680–1620 Ma Mangaroon Orogeny (Sheppard et al., 2005), and is the only zone where Capricorn-aged deformation or metamorphism has not been previously recorded (Sheppard et al., 2010a; 2010b). A quartz–muscovite–biotite–tourmaline schist (sample P01058) was collected from the Mangaroon Zone. Three further samples were collected from either side of the Mangaroon Zone: a quartz–muscovite–chlorite–garnet pelitic schist (GSWA 191938) was collected from the Limejuice Zone and two samples (GSWA 219708: garnet–biotite pelitic gneiss and GSWA 219706: feldspathic metasandstone) were collected from the Boora Boora Zone (Figure 2.1). Outcrop and petrographic descriptions of the samples are provided in the results section. A summary of samples is provided in Table 2.1.

Table 2.1 Summary table of samples, from the northern Gascoyne Province, Capricorn Orogen.

Sample ID	Eastings	Northing	Rock type	Location	Structure	Mineral	$^{207}\text{Pb}^*/^{206}\text{Pb}^*$ age (Ma)
GSWA 219706	342310	7427355	Feldspathic metasandstone	Boora Boora Zone	Lineation: 70°/350°	xenotime	1817 ± 17 and 1750 ± 18 [#]
GSWA 191938	393576, 393574	7333031, 7333018	Quartz–muscovite–chlorite–garnet pelitic schist	Northern Gascoyne (northern Minnie Creek Batholith)	Metamorphic foliation: 140°/90°	monazite	1798 ± 7
P01058	413508	7355209	Quartz–muscovite–biotite–tourmaline schist	Mangaroon Zone	Metamorphic foliation: 322°/72° (NE)	monazite	1782 ± 3 and 1730 ± 18
GSWA 219708	342168	7429822	Garnet–biotite pelitic gneiss	Boora Boora Zone	Axis of crenulation: 35°/315°	monazite	1778 ± 6 and 1751 ± 26

Notes:

$^{207}\text{Pb}^*/^{206}\text{Pb}^*$ ages quoted at 95% confidence unless otherwise stated.

[#] Quoted as 2 sigma weighted average.

2.5 Analytical methods

In situ U–Pb monazite and xenotime geochronology results

Four samples were collected from the northern Gascoyne Province for SHRIMP U–Pb monazite and xenotime geochronology. For samples P01058 and GSWA 191938, 219708 and 219706, typically several polished thin sections were imaged using a scanning electron microscope (SEM) in back-scattered electron (BSE) mode fitted with an energy dispersive X-ray spectrometer (EDS) to identify suitable monazite and xenotime grains for *in situ* SHRIMP geochronology. Monazite and xenotime grains >10 µm across were drilled out in 3 mm-diameter plugs and cast in a single 25 mm epoxy mount. In all sessions the reference standards for Pb/U and Pb/Th calibrations and for $^{207}\text{Pb}/^{206}\text{Pb}$ fractionation monitoring were in separate mounts that were cleaned and Au-coated with the sample mounts prior to analysis.

U–Pb analyses of monazite were conducted using a SHRIMP II ion microprobe in the John de Laeter Centre at Curtin University, Perth. Optical and BSE images were used to guide placement of the primary ion beam during SHRIMP analysis. The SHRIMP analytical procedures followed established methodologies for monazite (Fletcher et al. 2010) and xenotime (Fletcher et al. 2000, 2004). During all analytical sessions, an O_2^- primary beam, with a spot size of 10 to 15 µm, was focussed through a 30 to 50 µm Kohler aperture with a beam intensity of 0.18 to 0.45 nA. The secondary ion beam was focused through a 100-µm collector slit onto an electron multiplier to produce mass peaks with flat tops and a mass resolution (1% peak heights) of >5,200. A post-collector retardation lens was used to reduce background counts produced from stray ions.

Monazite was analysed with a 13-peak run table as defined by Fletcher et al (2010), which includes mass stations for the estimation of La, Ce and Nd (REEPO_2^+), and Y (YCeO^+). Count times per scan for Pb isotopes 204, background position 204.045, 206, 207, and 208 were 10, 10, 10, 30, and 10 seconds, respectively. The primary Pb/U and Th/Pb standard used was French (known as MAD 1, Foster et al., 2000). Matrix effects on Pb/U data from U and Th were determined using Z2234 standard (Stern and Sanborn, 1998). Standard Z2908 (moderate U and Th contents; provided by Richard Stern) was used to monitor $^{207}\text{Pb}/^{206}\text{Pb}$ fractionation of the SHRIMP II instrument.

Xenotime was analysed with a 9-peak run table. The primary Pb/U standard MG-1 (Fletcher et al., 2004) was used for Pb/U, Pb/Th and U, Th and Pb abundance calibrations. The secondary standards were XENO1 (Stern and Rainbird, 2001) used for

$^{207}\text{Pb}/^{206}\text{Pb}$ normalisation and used in conjunction with MG-1 for matrix corrections to Pb/U and Pb/Th, and XENO2 (Stern and Rainbird, 2001) used to monitor matrix effects.

Squid-2.50.11.02.03 software (Ludwig, 2009) was used for initial data reduction, including correction for common Pb. Common Pb corrections were based on individual measured ^{204}Pb abundances and assuming crustal common Pb at the approximate age of the samples modelled by Stacey and Kramers (1975). Corrections for matrix effects in Pb/U and Pb/Th, from U and Th in xenotime (Fletcher et al., 2004) and from U, Th, Pb, and REE in monazite and for instrumental mass fractionation in $^{207}\text{Pb}/^{206}\text{Pb}$ (Fletcher et al. 2010) were applied to the sample data. Weighted mean dates are reported with 95% confidence limits, unless otherwise stated, whereas individual analyses are presented with 1σ uncertainties.

2.6 Results

2.6.1 Monazite

Sample GSWA 191938: quartz–muscovite–chlorite–garnet pelitic schist

This sample is a strongly foliated quartz–muscovite–chlorite–garnet schist (Figure 2.2a). In thin section the foliation is defined by laths of muscovite and chlorite. The monazites are subhedral and anhedral, and range in size from 15 to 30 μm occurring as inclusions in quartz, plagioclase and garnet (Figure 2.4b–c) and within the matrix. One thin section was examined to locate suitable monazite crystals for dating. Five analyses were carried out on three monazite crystals (Table 2.2), all showing low discordance (<5%) and low common Pb ($f_{206} < 1\%$). The five analytical spots show Th concentrations typically ranging from 46,000 to 130,000 ppm and U concentrations from 3000 to 4000 ppm. The five analyses yield $^{207}\text{Pb}^*/^{206}\text{Pb}^*$ indistinguishable dates between 1805 and 1793 Ma with a weighted mean of 1798 ± 7 Ma (MSWD = 0.31), which is interpreted as the timing of monazite growth (Figure 2.5a).

Sample P01058: quartz–muscovite–biotite–tourmaline schist

This sample is a strongly crenulated quartz–muscovite–biotite–tourmaline schist (Figure 2.2b–c and Figure 2.3a). The monazite crystals are typically subhedral and range in size from 10 to 50 μm and are aligned with quartz and within muscovite (Figure 2.4d–e). One thin section was examined to locate suitable monazite crystals for dating. Twenty-three analyses were carried out on nine monazite crystals (Table 2.2). One analysis is

excluded from the final age calculation due to high common Pb ($f_{206} > 1\%$). A further one analysis is excluded as it is deemed to be a statistical outlier (i.e., it is greater than 2.5 standard deviations from the mean). Eighteen analytical spots from 16 crystals, show Th concentrations typically ranging from 25,000 to 80,000 ppm and U concentrations from 2,000 to 3,000 ppm. The eighteen analyses yield $^{207}\text{Pb}^*/^{206}\text{Pb}^*$ dates between 1792 and 1769 Ma with a weighted mean of 1782 ± 3 Ma (MSWD = 1.7), which is interpreted as the timing of monazite growth (Figure 2.5b). The remaining three analyses of two crystals yielded a $^{207}\text{Pb}^*/^{206}\text{Pb}^*$ weighted mean of 1730 ± 18 Ma (MSWD = 1.8) (Figure 2.5b). The Th and U concentrations of this group form a distinct population (Figure 2.5e).

Table 2.2 U–Pb monazite data for samples GSWA 191938, P01085 and GSWA 219708.

Grain spot	²³⁸ U (ppm)	²³² Th (ppm)	²³² Th / ²³⁸ U	<i>f</i> ₂₀₆ (%)	²³⁸ U/ ²⁰⁶ Pb* ±1s	²⁰⁷ Pb*/ ²⁰⁶ Pb* ±1s	²⁰⁸ Pb*/ ²³² Th ±1s	Disc (%)	²⁰⁷ Pb*/ ²⁰⁶ Pb* date (Ma) ±1s		
GSWA 191938 quartz–muscovite–chlorite–garnet pelitic schist											
<i>main group</i>											
0673G.1-1	3217	70730	22	0.09	3.20	0.11031	0.00062	0.0019	3	1805	10
0673G.2-1	2884	75870	26	0.06	3.10	0.11014	0.00048	0.0020	0	1802	8
0673H.1-1	2967	53354	18	0.18	3.17	0.10997	0.00045	0.0020	2	1799	7
0673A.1-1	2008	130250	65	0.02	3.19	0.10975	0.00072	0.0020	2	1795	12
0673B.1-1	4608	46518	10	0.06	3.19	0.10961	0.00041	0.0019	2	1793	7
P01085 quartz–muscovite–biotite–tourmaline schist											
<i>older group</i>											
1005H.2-2	2289	60040	26	0.04	3.27	0.10955	0.00026	0.0013	4	1792	4
1005I.4-2	2108	28215	13	0.06	3.21	0.10942	0.00028	0.0013	2	1790	5
1005E.2-1	2012	38879	19	0.05	3.30	0.10936	0.00033	0.0016	5	1789	6
1005I.3-1	2403	51326	21	0.02	3.20	0.10923	0.00027	0.0014	2	1787	5
1005D.1-1	3471	77110	22	0.05	3.38	0.10922	0.00033	0.0015	6	1786	6
1005C.3-1	2424	50106	21	0.03	3.22	0.10911	0.00029	0.0014	2	1785	5
1005J.1-1	3119	66705	21	0.05	3.13	0.10901	0.00024	0.0014	0	1783	4
1005C.3-2	1984	49871	25	0.09	3.35	0.10895	0.00033	0.0015	6	1782	5
1005B.1-1	2259	25137	11	0.01	3.23	0.10891	0.00028	0.0014	2	1781	5
1005H.2-1	2427	33935	14	0.03	3.27	0.10890	0.00029	0.0015	3	1781	5
1005I.1-1	2489	34382	14	0.03	3.21	0.10890	0.00046	0.0013	2	1781	8
1005G.1-1	2474	35373	14	0.03	3.20	0.10889	0.00027	0.0013	2	1781	5
1005C.2-1	2572	41842	16	0.03	3.17	0.10884	0.00026	0.0016	1	1780	4
1005F.2-1	2634	52995	20	0.06	3.26	0.10853	0.00051	0.0014	3	1775	9
1005E.1-1	2673	43606	16	0.04	3.30	0.10844	0.00028	0.0013	4	1773	5
1005C.1-1	2573	39549	15	0.03	3.30	0.10841	0.00026	0.0017	4	1773	4
1005I.4-1	2509	30378	12	0.04	3.14	0.10838	0.00026	0.0013	0	1772	4
1005F.1-1	2496	46880	19	0.05	3.21	0.10816	0.00043	0.0014	1	1769	7

Grain spot	^{238}U (ppm)	^{232}Th (ppm)	$^{232}\text{Th}/^{238}\text{U}$	f_{206} (%)	$^{238}\text{U}/^{206}\text{Pb}^*$ $\pm 1s$	$^{207}\text{Pb}^*/^{206}\text{Pb}^*$ $\pm 1s$	$^{208}\text{Pb}^*/^{232}\text{Th}$ $\pm 1s$	Disc (%)	$^{207}\text{Pb}^*/^{206}\text{Pb}^*$ date (Ma) $\pm 1s$			
<i>Statistical outlier/Pb loss</i>												
1005I.2-1	2683	19222	7	0.03	3.13	0.10804	0.00025	0.0943	0.0013	-1	1767	4
<i>younger group</i>												
1005I.1-2	3338	32650	10	0.06	3.19	0.10637	0.00106	0.0960	0.0013	-1	1738	18
1005J.1-2	5336	50274	9	0.04	3.42	0.10598	0.00019	0.0885	0.0012	5	1731	3
1005J.2-1	3407	42682	13	0.11	3.25	0.10480	0.00060	0.0952	0.0015	-1	1711	11
$f_{206} > 1\%$												
1005H.1-1	1993	55964	28	1.64	3.08	0.11157	0.00864	0.0910	0.0016	1	1825	140
219708 garnet–biotite pelitic gneiss												
<i>older group</i>												
1605G.1-1	1710	25773	15	0.02	3.09	0.10924	0.00027	0.1084	0.0067	-1	1787	5
1605B.1-1	2310	32351	14	0.03	3.00	0.10911	0.00022	0.1139	0.0069	-4	1785	4
1605K.1-1	5033	35604	7	0.00	3.03	0.10910	0.00033	0.1070	0.0066	-3	1784	5
1605H.1-1	2377	29574	12	0.10	3.08	0.10879	0.00040	0.1055	0.0065	-2	1779	7
1605J.1-1	2710	35807	13	0.02	2.84	0.10879	0.00074	0.1223	0.0076	-9	1779	12
1605E.1-1	3934	33801	9	0.03	2.90	0.10839	0.00019	0.1138	0.0070	-8	1773	3
1605L.1-1	7749	28315	4	0.01	3.09	0.10839	0.00031	0.1080	0.0068	-2	1773	5
1605A.1-1	3687	31904	9	0.02	2.98	0.10810	0.00045	0.1121	0.0069	-6	1768	8
1606K.1-1	5892	40126	7	0.02	3.03	0.10738	0.00096	0.0963	0.0038	-5	1755	16
1606I.1-1	4447	41661	9	0.08	3.06	0.10725	0.00064	0.0892	0.0034	-4	1753	11
<i>Statistical outlier/younger group</i>												
1606B.1-1	4937	48287	10	0.03	3.09	0.10750	0.00033	0.0850	0.0033	-3	1757	6
1606G.1-1	3212	45634	14	0.04	3.18	0.10641	0.00043	0.0856	0.0033	-1	1739	7
<i>Excluded imprecise 7/6</i>												
1606F.1-1	3015	59191	20	0.08	3.25	0.10497	0.00458	0.0819	0.0065	-1	1714	80
1606C.1-1	5816	55204	9	0.04	3.30	0.10336	0.00502	0.0801	0.0033	-1	1685	90

Grain spot	²³⁸ U (ppm)	²³² Th (ppm)	²³² Th / ²³⁸ U	<i>f</i> ₂₀₆ (%)	²³⁸ U/ ²⁰⁶ Pb* ±1s	²⁰⁷ Pb*/ ²⁰⁶ Pb* ±1s	²⁰⁸ Pb*/ ²³² Th ±1s	Disc (%)	²⁰⁷ Pb*/ ²⁰⁶ Pb* date (Ma) ±1s				
<i>Discordance > 8%</i>													
1605D.1-1	4645	34586	7	0.01	2.99	0.14	0.10529	0.00368	0.1038	0.0072	-8	1719	64
1605J.1-2	3610	35303	10	0.04	3.09	0.23	0.10057	0.00641	0.1099	0.0087	-10	1635	118
1605F.1-1	5006	40882	8	0.00	3.85	0.34	0.10049	0.00433	0.0706	0.0061	9	1633	80

Notes:

Pb* indicates radiogenic Pb (i.e. corrected for common Pb).

*f*₂₀₆, proportion of common ²⁰⁶Pb in measured ²⁰⁶Pb, determined using measured ²⁰⁴Pb/²⁰⁶Pb and contemporaneous common Pb composition (Stacey & Kramers, 1975).

Disc. is apparent discordance, as D (%) = 100 x ([²⁰⁷Pb*/²⁰⁶Pb* date] - [²³⁸U/²⁰⁶Pb* date]) / [²⁰⁷Pb*/²⁰⁶Pb* date].

Analytical uncertainties from the multiple sessions have been applied to the data during data reduction.

Analyses are sorted by descending ²⁰⁷Pb*/²⁰⁶Pb* age for all samples

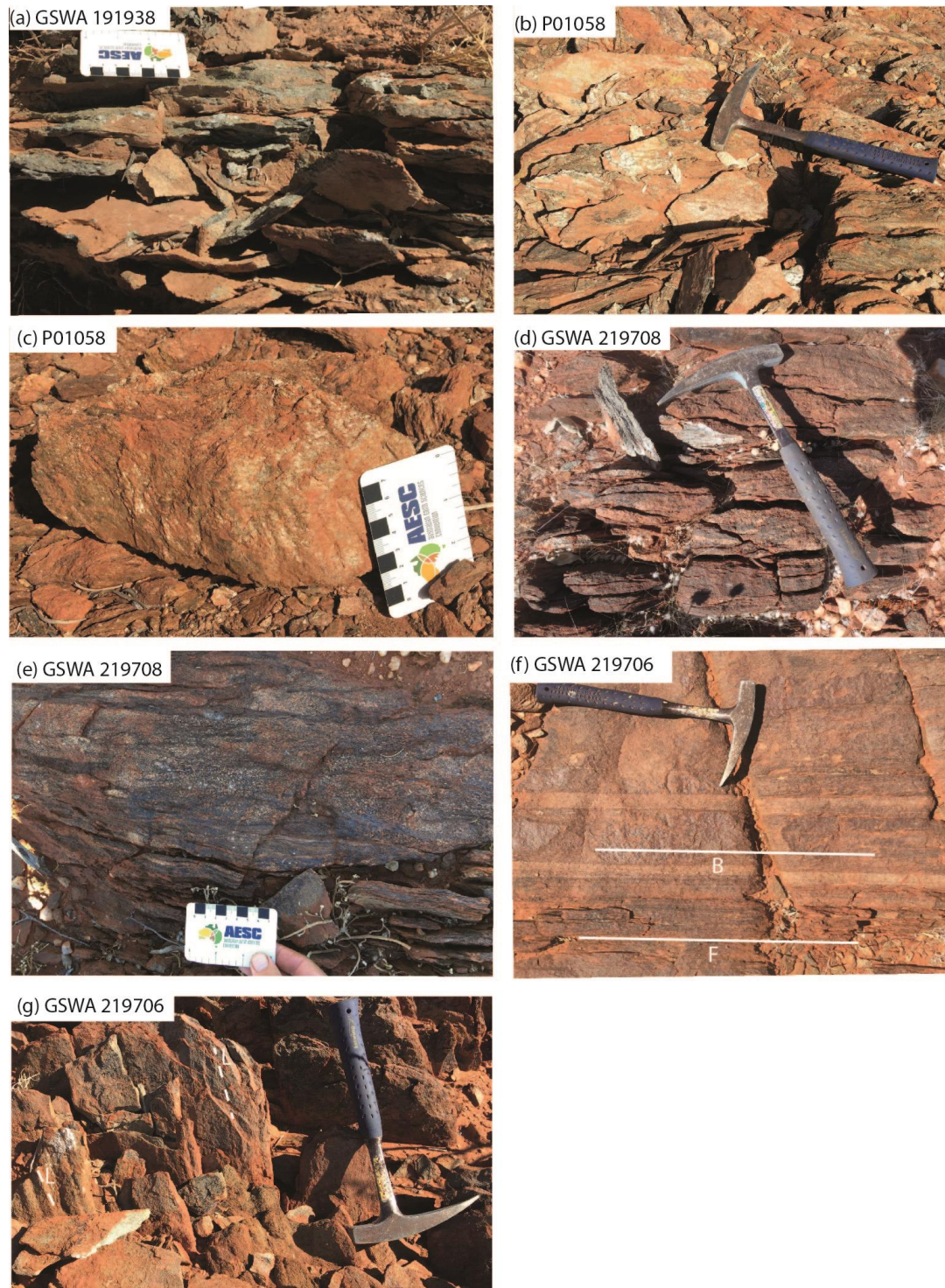


Figure 2.2 Field outcrop photos of selected samples from the northern Gascoyne Province– (a) sample GSWA 191938 quartz–muscovite–chlorite–garnet pelitic schist, Limejuice Zone; (b) sample P01058 quartz–muscovite–biotite–tourmaline schist, Mangaroon Zone; (c) hand sample (P01058) showing crenulation cleavage; (d) sample GSWA 219708 garnet–biotite pelitic gneiss, Boora Boora Zone; (e) granitic intrusions parallel to gneissic fabric sample GSWA 219708; (f) sample GSWA 219706 feldspathic metasandstone, Boora Boora Zone, with bedding parallel to foliation; (g) sample GSWA 219706 lineation subparallel to the foliation.

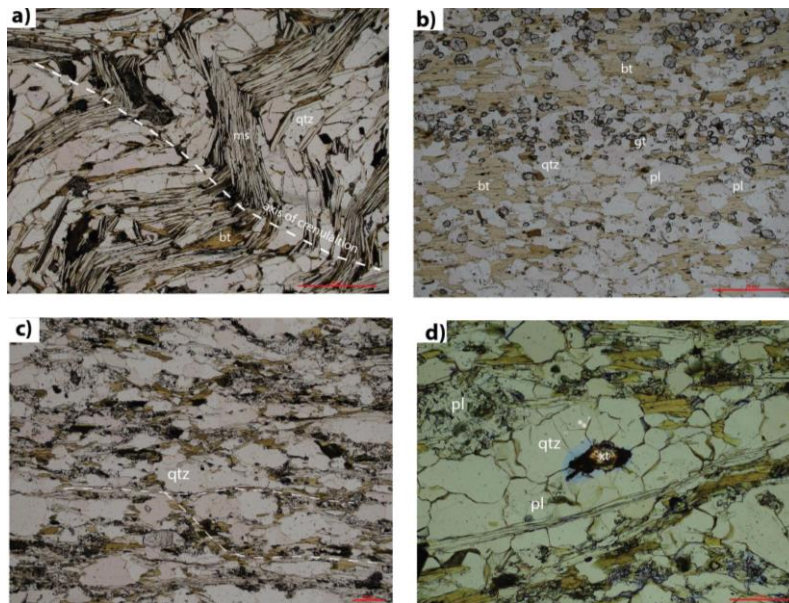


Figure 2.3 Petrographic images – (a) sample P01056 folded crenulation; (b) compositional layering in sample GSWA 219708; (c) sample GSWA 219706 weak crenulation; (d) sample GSWA 219706 quartz-hosted xenotime used for SHRIMP dating.

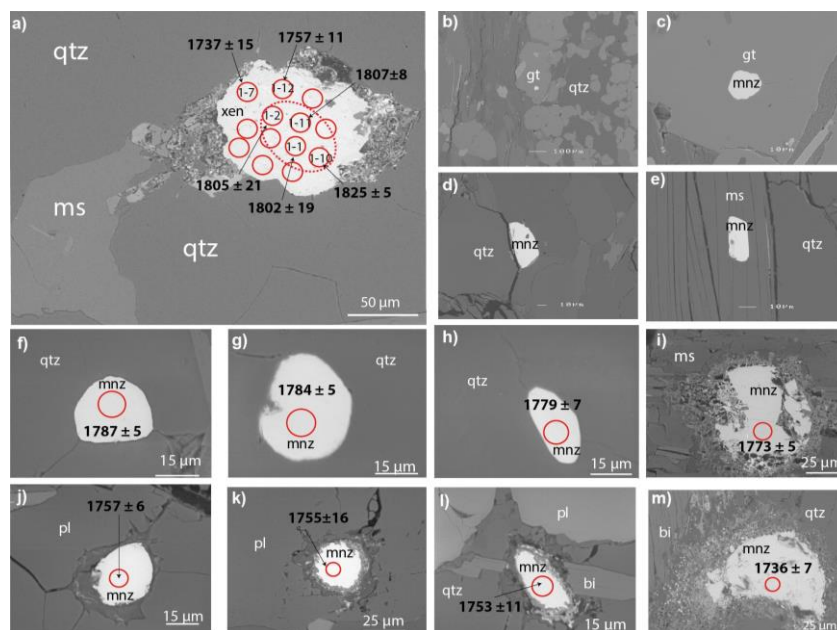


Figure 2.4 Back-scattered electron (BSE) images of representative monazites and xenotime from samples analysed in situ. Solid circles represent SHRIMP pits. (a) sample GSWA 219706 xenotime age data showing a zoning pattern (dashed circle); (b & c) garnet-hosted monazite in sample GSWA 191938; (d & e) aligned monazite with fabric in sample P01058; (f–h) quartz-hosted monazite in sample GSWA 219708; (i) muscovite-hosted monazite sample GSWA 219708; (j–k) plagioclase-hosted monazite with reaction rims; (l) monazite cross-cutting biotite sample GSWA 219708; (m) interstitial monazite sample GSWA 219708. Abbreviations: bi = biotite, gt = garnet, mnz = monazite, ms = muscovite, pl = plagioclase, qtz = quartz, xen = xenotime.

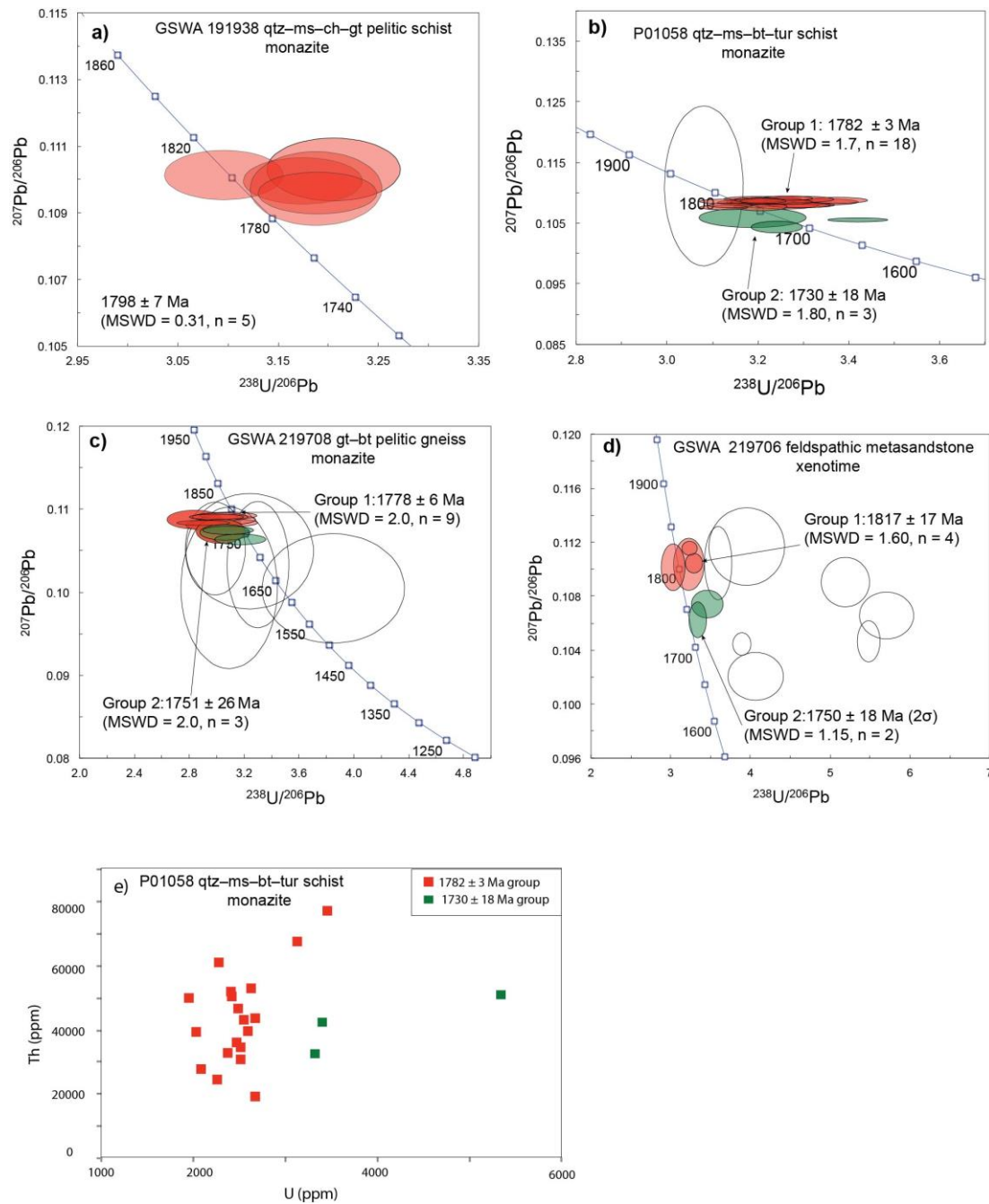


Figure 2.5 U–Pb Concordia diagrams for (a–c) monazite and (d) and xenotime.

(e) Th and U concentration of monazite from sample P01058. Data plotted with 68.3% error ellipses; red and green ellipses indicate analyses used to calculate the age population of the sample, and unfilled ellipses indicate data excluded due to discordance >5%, high common Pb, or as statistical outliers. Weighted mean dates are based on $^{207}\text{Pb}/^{206}\text{Pb}$ ratios and quoted with 95% confidence intervals.

Sample GSWA 219708: garnet–biotite pelitic gneiss

This sample is a pelitic gneiss (Figure 2.2d) locally intruded by metamonzogranite (Figure 2.2e) and pegmatite parallel to the gneissic layering. Garnets make up about 40% of the rock and are subhedral to anhedral and typically <2 mm in diameter. The compositional layering is defined by zones dominated by garnet (+biotite+quartz+feldspar) and zones dominated by biotite (+quartz+feldspar+garnet) (Figure 2.3b). A weak foliation is defined by aligned biotite crystals and flattened quartz (Figure 2.3d).

The monazites are anhedral and range in size from 20 to 80 μm and occur as inclusions within quartz, muscovite and plagioclase, and interstitial to the main silicate phases (Table 2.2). Six thin sections were examined to locate suitable monazite crystals for dating. Seventeen analyses were carried out on 16 monazite crystals (Table 2.2) all of which contain low concentrations of common Pb ($f_{206} < 1\%$). One analysis was excluded from the final age calculation due to >10% discordance. Four analyses showing anomalously large $^{207}\text{Pb}/^{206}\text{Pb}$ uncertainties are also disregarded. Nine analytical spots show a systematic variation in Th concentration with values from 26,000 to 41,000 ppm and a larger spread of U concentrations from 2,000 to 8,000 ppm compared to the younger group. The nine analyses yield $^{207}\text{Pb}^*/^{206}\text{Pb}^*$ dates between 1787 and 1755 Ma with a weighted mean of 1778 ± 6 Ma (MSWD = 2.0), which is interpreted as the timing of monazite growth (Figure 2.5c). Analysis 1753 ± 11 Ma is excluded from the main grouping because the probability of fit of 0.011 indicates the data do not from a single population (Mahon, 1996). Two remaining concordant analyses, from two crystals are excluded from the main grouping due to being greater than three standard deviations from the mean. Therefore, the dates 1757 ± 6 Ma, 1753 ± 11 Ma and 1739 ± 7 Ma could be considered to be part of a younger group with a $^{207}\text{Pb}^*/^{206}\text{Pb}^*$ weighted mean of 1751 ± 26 Ma (MSWD = 2.0) (Figure 2.5c). The younger group shows Th concentration with values from 41,000 to 48,000 ppm and U concentrations from 3,000 to 5,000 ppm.

2.6.2 Xenotime

Sample GSWA 219706: Feldspathic metasandstone

Sample 219706 is a fine- to medium-grained feldspathic metasandstone that has bedding parallel to foliation with the bedding defined by thin (cm-scale) quartz-rich layers (Figure 2.2f). A steeply dipping lineation (70°) is subparallel to the foliation (Figure 2.2g). A weak crenulation cleavage is observed in outcrop and in thin section (Figure 2.3c). In thin section, the muscovite laths are seen to cross-cut the quartz crystals that host the xenotime crystal dated here (Figure 2.3d).

Table 2.3 U–Pb xenotime data for sample GSWA 219706.

Grain .spot	^{238}U (ppm)	^{232}Th (ppm)	^{232}Th $/^{238}\text{U}$	f_{206} (%)	$^{238}\text{U}/^{206}\text{Pb}^*$ $\pm 1\sigma$	$^{207}\text{Pb}^*/^{206}\text{Pb}^*$ $\pm 1\sigma$	$^{208}\text{Pb}^*/^{232}\text{Th}$ $\pm 1\sigma$	Disc (%)	$^{207}\text{Pb}^*/^{206}\text{Pb}^*$ date (Ma) $\pm 1\sigma$
GSWA 219706 feldspathic metasandstone									
<i>older group</i>									
NP1604F.1-10	16273	24313	1.5	0.04	3.22	0.11154	0.0893	0.0095	5 1825
NP1604F.1-11	18270	11668	0.6	0.05	3.28	0.11044	0.0706	0.0095	5 1807
NP1604F.1-2	15447	13979	0.9	0.06	3.22	0.11035	0.0513	0.0097	3 1805
NP1604F.1-1	19290	9747	0.5	0.02	3.02	0.11015	0.0942	0.0102	-2 1802
<i>younger group</i>									
NP1604F.1-7	10767	12101	1.1	0.08	3.45	0.10746	0.0761	0.0093	7 1757
NP1604F.1-12	11570	11832	1.0	0.13	3.33	0.10630	0.0453	0.0098	2 1737
<i>disc. > 5% and $f_{206} > 1\%$</i>									
NP1604F.1-8	21203	16422	0.8	0.00	3.95	0.11166	0.0721	0.0080	20 1827
NP1604F.1-5	18279	8833	0.5	0.03	3.59	0.11045	0.0823	0.0088	12 1807
NP1604F.1-6	28610	26527	0.9	0.09	5.18	0.10906	0.0371	0.0064	36 1784
NP1604F.1-3	11035	15194	1.4	0.35	5.70	0.10662	0.0283	0.0060	40 1742
NP1604F.1-13	11388	16280	1.4	1.48	5.47	0.10473	0.0252	0.0063	37 1710
NP1604F.1-9	9315	11696	1.3	0.07	3.88	0.10453	0.0495	0.0087	13 1706
NP1604F.1-4	18930	10617	0.6	0.01	4.05	0.10216	0.0701	0.0085	15 1664

Notes:

Pb* indicates radiogenic Pb (i.e. corrected for common Pb)

f_{206} , proportion of common ^{206}Pb in measured ^{206}Pb , determined using measured $^{204}\text{Pb}/^{206}\text{Pb}$ and contemporaneous common Pb composition (Stacey and Kramers, 1975)

Disc. is apparent discordance, as $D(\%) = 100 \times ([^{207}\text{Pb}^*/^{206}\text{Pb}^* \text{ date}] - [^{238}\text{U}/^{206}\text{Pb}^* \text{ date}]) / [^{207}\text{Pb}^*/^{206}\text{Pb}^* \text{ date}]$

Analytical uncertainties from the multiple sessions have been applied to the data during data reduction.

Analyses are sorted by descending $^{207}\text{Pb}^*/^{206}\text{Pb}^*$ age for all samples

A single xenotime crystal within a quartz crystal was identified from four thin sections. There was no indication of retrogressed xenotime within the matrix. The xenotime crystal is anhedral and about 100 μm in diameter and occurs within an elongate quartz crystal (Figure 2.4a). No obvious zoning is visible. The xenotime is surrounded by alteration that is replacing the original crystal. Thirteen analyses were carried out on the xenotime crystal (Table 2.3). Seven analyses are excluded from the final age calculation due to high common Pb ($f_{206} > 1\%$) and/or $> 5\%$ discordance. Four analytical spots show Th concentrations ranging from 10,000 to 14,000 ppm (with one analysis at 24,000 ppm) and U concentrations from 15,000 to 19,000 ppm. The four analyses, clustered in the centre of the crystal, yield $^{207}\text{Pb}/^{206}\text{Pb}$ dates between 1825 Ma and 1802 Ma with a $^{207}\text{Pb}^*/^{206}\text{Pb}^*$ weighted mean date of 1817 ± 17 Ma (MSWD = 1.60), which is interpreted as the timing of xenotime growth (Figure 2.5d). The remaining two analyses are considered to be part of a younger group with a $^{207}\text{Pb}^*/^{206}\text{Pb}^*$ weighted mean date of 1750 ± 18 Ma (2σ) (MSWD = 1.15). These two analyses with Th concentrations of 12,000 ppm and U concentrations of 10,000 ppm are from the edge of the xenotime crystal (Figure 2.4a).

2.7 Discussion

The first intraplate reworking event in the Capricorn Orogen occurred at 1820–1770 Ma during the Capricorn Orogeny (Sheppard et al., 2010a). The Capricorn Orogeny has the largest footprint of all the reworking events in the Capricorn Orogen (Figure 2.6), affecting the entire Gascoyne Province, as well as the Yarlalweelor Gneiss Complex, and the Ashburton Basin (Sheppard et al., 2010a; 2010b), and the Bryah, Padbury and Earraheedy basins (Occhipinti et al., 2017). In the southern parts of the Gascoyne Province, including the Mooloo Zone, Paradise Zone and Errabiddy Shear Zone, the Capricorn Orogeny is the only reworking event recognised, although Neoproterozoic fault reactivation affected the Errabiddy Shear Zone and Chalba Shear Zone (Bodorkos and Wingate, 2007; Occhipinti and Reddy, 2009; Piechocka et al., 2018).

In the Mutherbukin Zone and the central Gascoyne Province, Capricorn Orogeny fabrics are overprinted by at least one episode of magmatism associated with the 1680–1620 Ma Mangaroon Orogeny (Sheppard et al., 2010b), and two reworking events: the 1320–1170 Ma Mutherbukin Tectonic Event ($> 650^\circ\text{C}$ and 4.4–7 kbar) (Korhonen et al., 2017) and the 1030–900 Ma Edmondian Orogeny ($500\text{--}550^\circ\text{C}$ and 3–4 kbar) (Piechocka et al., 2017; Sheppard et al., 2007). In the northern Gascoyne Province, the reworking associated with the

1680–1620 Ma Mangaroon Orogeny (with estimated conditions at (<750°C and <6 kbar) (Sheppard et al., 2005) is known from the Mangaroon Zone. This repeated tectonothermal history has made it challenging to directly date the timing of metamorphism associated with the Capricorn Orogeny. However, the new results obtained in this study provide robust new age constraints from the northern parts of the Gascoyne Province.

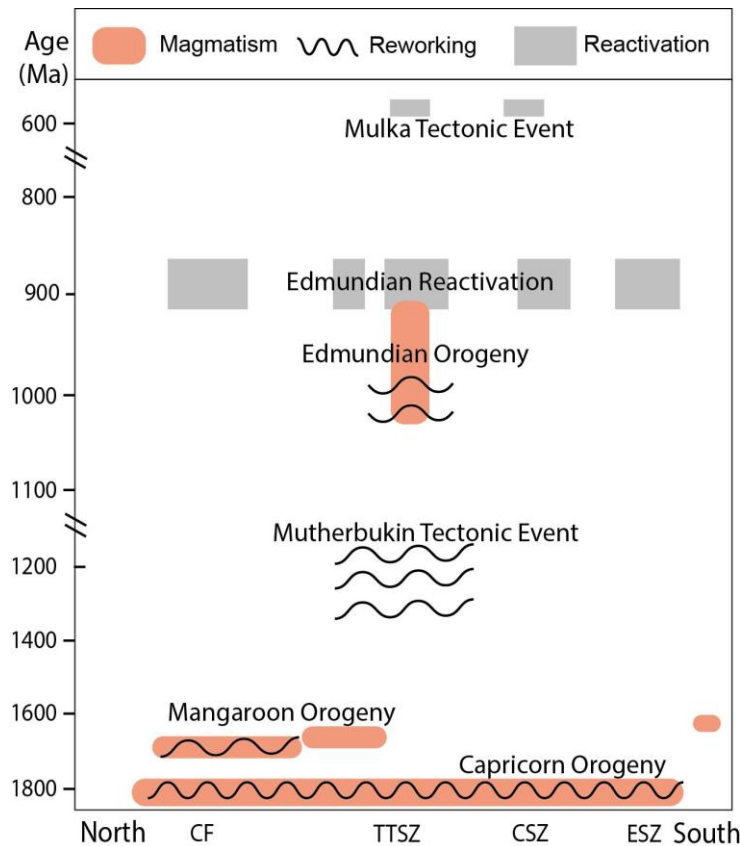


Figure 2.6 Summary diagram of tectonothermal events in the Gascoyne Province highlighting zones of multiple stages of overprinting (adapted from Piechocka et al., 2018).

2.7.1 Previous U–Pb zircon and monazite constraints on Capricorn-aged metamorphism

Scattered U–Pb zircon, monazite and xenotime geochronology data have been reported for Capricorn-aged metamorphism in the Mutherbukin Zone, central Gascoyne Province only as a by-product of attempts to date younger orogenic events.

In the Mutherbukin Zone, Capricorn-aged metamorphism was recorded from four spots on four separate zircon rims in a coarse-grained orthoquartzite that yielded a youngest population at 1772 ± 6 Ma (GSWA 187403: Wingate et al., 2010) interpreted as the timing of metamorphism during D_{3n} (Johnson et al., 2010; Sheppard et al., 2010b).

Also, in the Mutherbukin Zone, both monazite and xenotime from a tourmaline-rich metasomatic schist, adjacent to a pegmatite dyke yielded Capricorn Orogeny dates. Monazite yielded an age grouping at 1780 ± 2 Ma interpreted as the timing of new monazite growth (GSWA 88475: Korhonen et al., 2015). This data set is the most robust with 24 analyses performed on 10 grains. Two younger groups were also recorded from sample GSWA 88475 at 1171 ± 4 Ma and 958 ± 16 Ma (Korhonen et al., 2015), which can be correlated with two younger reworking events: the Mutherbukin Tectonic Event and the Edmondian Orogeny. Xenotime, from the same sample, yielded two age groupings: 1805 ± 9 Ma (four analyses from two spots —includes repeat analyses— on one grain) interpreted as possible new xenotime growth and a single analysis yielded 1725 ± 11 Ma (1σ) interpreted as fine-scale recrystallisation (GSWA 88475: Korhonen et al., 2015). Younger ages were also recorded in this sample ranging from 1725 to 1680 Ma and 1269 to 1182 Ma (Korhonen et al., 2015), which may reflect activity during younger reworking events. Although these samples record Capricorn-age metamorphism the dataset in two instances is small and requires further work to define a more robust age.

2.7.2 New U–Pb monazite and xenotime constraints on the Capricorn Orogeny in the northern Gascoyne Province

Our new U–Pb phosphate geochronology provides the first direct record of metamorphism associated with the 1820–1770 Ma Capricorn Orogeny in the northern Gascoyne Province. Field observations suggested that the Capricorn Orogeny, affected the Limejuice and Boora zones (Sheppard et al., 2010a; 2010b) but no direct dates for metamorphism have previously been obtained. However, in the Mangaroon Zone no prior deformation fabrics or structures could be assigned to the Capricorn Orogeny. Our results have identified two age groupings: 1805–1772 Ma (including uncertainties) and a less robust group at c.1750–1730 Ma.

Monazite from a quartz–muscovite–chlorite–garnet pelitic schist (GSWA 191938) from the northern Limejuice Zone along the northern margin of the Minnie Creek batholith (Figure 2.1) yielded an age grouping at 1798 ± 7 Ma (Table 2.2 and Figure 2.5a), interpreted as the timing of monazite growth during the metamorphic event. Although only five analytical spots were obtained the crystals contain high concentrations of uranium and low common Pb with concordant analyses yielding a low MSWD of 0.31. Therefore, we consider 1798 ± 7 Ma to be a robust age. The monazites occur as inclusions in the garnet, plagioclase quartz and within the matrix and yield the

same age meaning that the monazite probably grew at the same time as the porphyroblast growth. The local metamorphic foliation, which trends $322^{\circ}/72^{\circ}$ (NE) (at sample GSWA 191938 locality) is different from the orientation of the northerly trending D_{2n} faults and folds and an upright foliation (Sheppard et al., 2010b). The current constraints on D_{2n} are 1808–1786 Ma therefore the rocks in this region (represented by sample 191938) may have been affected by the D_{2n} deformation event.

In the Mangaroon Zone, the later 1680–1620 Ma Mangaroon Orogeny has obliterated most of the older Capricorn Orogeny fabrics. In the southeastern parts of the Mangaroon Zone monazite from a crenulated quartz–muscovite–biotite–tourmaline schist (P01058) yielded a main age grouping of 1782 ± 3 Ma, interpreted as timing of new monazite growth during metamorphism. Due to the effect of the overprinting Mangaroon Orogeny, any link to a particular deformation episode associated with the Capricorn Orogeny is difficult to make; however, based on geochronology, the age may correlate with either D_{2n} or D_{3n} .

Further north, in the Boora Boora Zone, monazite from garnet–biotite pelitic gneiss (GSWA 219708) yielded a main age grouping at 1778 ± 6 Ma, interpreted as the timing of monazite growth during metamorphism. The monazites occur as inclusions in quartz and one crystal occurs in muscovite. Also in the Boora Boora Zone, xenotime in a feldspathic metasandstone (GSWA 219706) yielded a main age grouping at 1817 ± 17 Ma, interpreted as the timing of xenotime growth during metamorphism. or the xenotime core could be detrital. The geological mapping suggests the feldspathic metasandstone belongs to the Leake Springs Metamorphics of which the protoliths were deposited between 1842–1807 Ma (Sheppard et al., 2010b). Although no obvious zoning can be observed, the analytical spots show that the older dates came from the centre of the xenotime crystal (Figure 2.4a). The U and Th concentrations of this xenotime crystal (GSWA 219706) fall outside of the fields represented by hydrothermal xenotime but there does appear to be some overlap with the older group and detrital xenotime (Figure 2.8). Therefore, it is possible that the 1817 ± 17 Ma age could indicate the presence of a detrital core and the younger analyses obtained from the rim may reflect timing of growth during a tectonothermal event. If the xenotime core from sample GSWA 219706 were interpreted as detrital in origin, the timing of metamorphism, in the northern Gascoyne Province, occurred between 1805 and 1772 Ma (given the uncertainties quoted for samples GSWA 191938 and 219708).

Magmatism in the Gascoyne Province was characterised by voluminous felsic magmatic stocks, plutons and batholiths of the 1820–1775 Ma Moorarie Supersuite (Figure 2.7) (Sheppard et al., 2010b). The oldest magmatism in the Boora Boora Zone is known to have occurred at 1806 ± 7 Ma (GSWA 169088; Nelson, 2004a) with the youngest recorded at 1784 ± 5 Ma (GSWA 169086; Nelson, 2004b) (Figure 2.7). Magmatism in the Limejuice Zone to the south is constrained at 1807 ± 3 Ma (GSWA 183205; Kirkland et al., 2009) and 1777 ± 5 Ma (GSWA 190634; Wingate et al., 2012b) (Figure 2.7). Our metamorphic ages from samples from the Limejuice, Mangaroon and Boora Boora zones are synchronous with the known magmatism in these areas (Figure 2.7). In the Ashburton Basin, magmatism related to the Moorarie Supersuite, is recorded by the Boolaloo Granodiorite dated at 1786 ± 5 Ma (Krapez and McNaughton 1999) and volcanism coeval with the supersuite has been identified in the June Hill Volcanics at 1799 ± 8 and 1786 ± 11 Ma (Evans et al., 2003) (Figure 2.7).

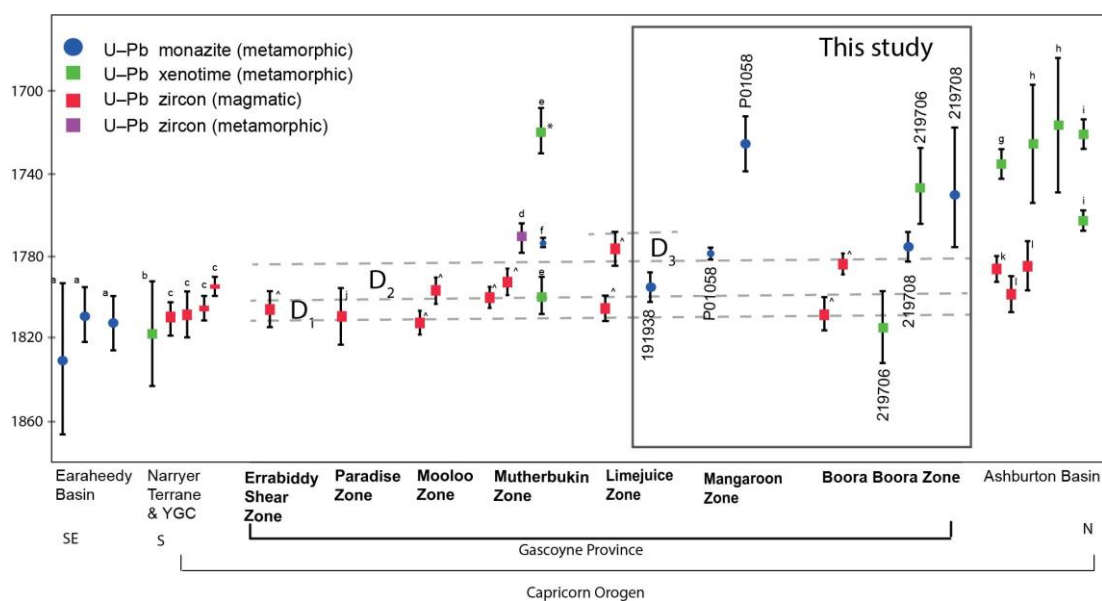


Figure 2.7 Summary diagram of Capricorn aged geochronology from the Western Australian Craton including data from this study and published data. * 1σ date. ^a Muhling et al., 2012; ^b Rasmussen et al., 2010; ^c Occhipinti et al., 1998; ^d Wingate et al., 2010; ^{e,f} Korhonen et al., 2015; ^g Şener et al., 2005; ^h Fielding et al., 2017; ⁱ Fielding et al., 2018; ^j Sheppard et al., 2010b; ^k Krapez and McNaughton, 1999; ^l Evans et al., 2003; [^] GSWA 2016.

Our geochronology results, considering the given uncertainties, overlap with the previously defined episodes of deformation (D_{1n} – D_{3n}). However, the lack of textural and structural evidence preserved in some samples means that it is difficult to correlate our results, with confidence, to a particular deformation episode. However, the magmatism

associated with the Capricorn Orogeny is constrained at 1820–1775 Ma (Sheppard et al., 2010a; 2010b) and our older age grouping at 1805–1772 Ma appears to be synchronous with emplacement of the Moorarie Supersuite in the northern Gascoyne Province (Figure 2.7).

2.7.3 A 1750–1730 Ma tectonothermal event in the northern Capricorn Orogen?

Our results also reveal a potentially younger age grouping in samples P015058, GSWA 219708 and GSWA 219706 at c. 1750–1730 Ma.

Sample (P10158) records a younger age grouping at 1730 ± 18 Ma (MSWD = 1.80) (Figure 2.5b), derived from three concordant analytical spots from two grains. The U and Th concentrations show a distinct grouping between the older and younger age groupings with the younger age grouping consisting of elevated U concentrations and a tighter cluster of Th concentrations (Figure 2.5e).

The younger age grouping in samples GSWA 219708 and 219706 must be treated with more caution. For instance, in sample GSWA 219706 the younger age spots are located in the rim of the large xenotime crystal and together may form a younger age grouping at 1750 ± 18 Ma (2σ). However, the spot closest to the rim yielded the youngest age at 1737 ± 15 Ma (which likely represents new growth) but the second spot in the rim is close to the zone of the older age grouping, so this 1757 ± 11 Ma spot could be considered age mixing.

In sample GSWA 219708, three analyses form a younger age grouping at 1751 ± 26 Ma (MSWD = 2.0). Analyses 1757 ± 6 Ma and 1739 ± 7 Ma spots are greater than three standard deviations from the weighted mean and, therefore, are excluded from the main grouping. Furthermore, age spot 1753 ± 11 Ma was excluded from the main grouping due to a probability of fit of < 0.025 (Mahon, 1996) indicating the dataset does not form a single population. No unequivocal textures can be used to split the data, therefore it is grouped based on statistics. Although age spots 1757 ± 6 Ma and 1739 ± 7 Ma could be considered to reflect Pb loss they do yield precise $^{207}\text{Pb}/^{206}\text{Pb}$ dates compared to the excluded two ages, which are very imprecise likely due to Pb loss. The precise 1757 ± 6 Ma, 1753 ± 11 Ma and 1739 ± 7 Ma dates (sample GSWA 219708) are very similar to the two spots at 1757 ± 11 Ma and 1737 ± 15 Ma from GSWA 219706: therefore it is likely that these dates reflect a younger age group. However, further dating is needed to obtain a more robust age.

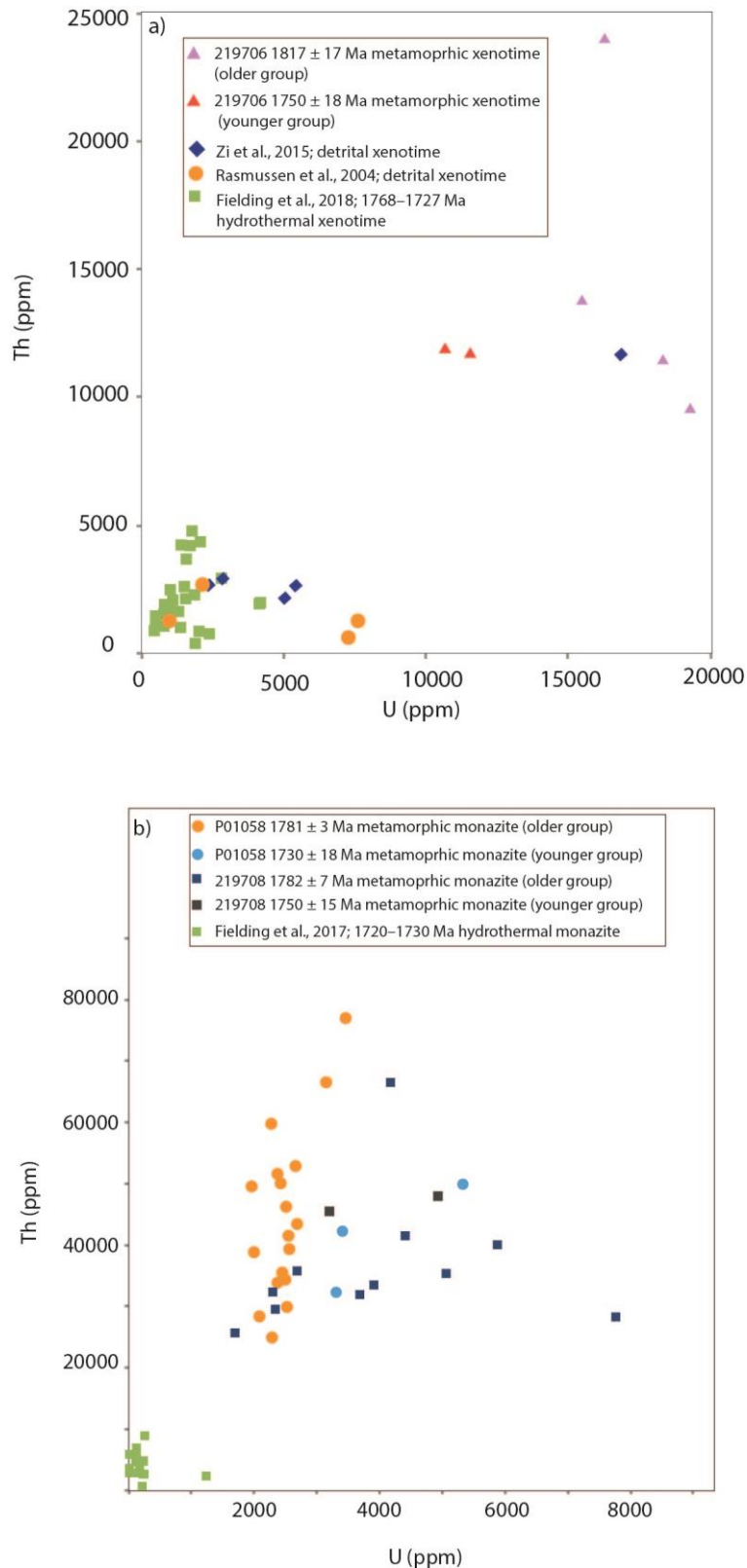


Figure 2.8 Diagram of Th versus U concentrations in xenotime – (a) and monazite (b) from samples analysed in this study compared with published data, from the Capricorn Orogen, representing low-grade hydrothermal monazite and xenotime growth and detrital xenotime.

Despite the uncertainty of the younger age grouping, in two of the samples the consistency of this age recorded across various locations and various rock types could point to a late stage deformation event in the Gascoyne Province and hydrothermal episode in the Ashburton Basin related to fluid migration along crustal-scale faults. However, further analytical work would be required to obtain a more robust dataset for the younger age grouping in the Gascoyne Province.

A comparison of the U and Th concentrations of monazite and xenotime from our samples against low-grade hydrothermal and detrital samples from other studies in the Capricorn Orogen was conducted (Figure 2.8a and b). The results show that our data are distinct from hydrothermal (monazite and xenotime) and detrital (xenotime) U and Th compositions from the other studies in the Capricorn Orogen. This suggests that the younger group may represent a higher-grade of late stage deformation compared to the low-grade effects seen in the Ashburton Basin at the same time around c. 1750–1730 Ma.

2.7.4 Regional correlations

Capricorn-aged tectonic activity is known to have occurred outside of the Gascoyne Province in other parts of the West Australian Craton. In the southeastern parts of the Capricorn Orogen in the Earraheedy Basin authigenic monazite in a sandstone yielded an age of 1811 ± 13 Ma interpreted as timing of fluid flow (Muhling et al., 2012). Furthermore, monazite and xenotime, from sedimentary rocks at the Cano Pb deposit, in the Earraheedy Basin, yielded similar age populations at 1815 ± 13 Ma and 1832 ± 36 Ma interpreted as the timing of mineralisation related to the Capricorn Orogeny (Muhling et al., 2012). In the eastern Capricorn Orogen at the DeGrussa copper–gold–silver, volcanic-hosted massive sulfide deposit Pb–Pb ages between 1820 and 1730 Ma were correlated with the Capricorn Orogeny (Table 4 of Hawke et al., 2015). To the southwest in the Jack Hills area, of the Narryer Terrane, xenotime growth related to hydrothermal fluid flow at 1820 ± 25 Ma was attributed to possible fault reactivation related to the Capricorn Orogeny (Rasmussen et al., 2010). Tectonic activity occurring synchronously with the Capricorn Orogen is also known from the Rudall Province which is situated between the West Australian Craton and North Australian Craton. For instance, 1804–1762 Ma magmatism, known as the Kalkan Supersuite (Gardiner et al., 2018) and magmatism as young as c. 1750 Ma (Tucker et al., 2018) is recorded in the Rudall Province. Our new results can also be linked to several occurrences of gold mineralisation known from within the West Australian Craton. For example, hydrothermal xenotime growth yielded ages of 1738 ± 5 Ma from the Mt Olympus Gold

Mine in the Ashburton Basin (Şener et al., 2005). A recent study from Mt Olympus shows xenotime growth occurred during gold mineralisation at 1769 ± 5 Ma and subsequently at 1727 ± 7 Ma due to hydrothermal alteration (Fielding et al., 2018). Furthermore, xenotime growth associated regional-scale hydrothermal events, related to fault reactivation, yielded 1730 ± 28 Ma and 1721 ± 31 Ma age modes, from the Paulsens orogenic gold deposit (Fielding et al., 2017).

2.7.5 New evidence for the drivers for metamorphism during the Capricorn Orogeny

Many theories existed for the driving forces behind the 1820–1775 Ma Capricorn Orogeny, most of which invoked a subduction-driven model. The model proposed by Tyler and Throne (1990) and Tyler (1990) invoked a continent–continent collision for the orogeny, with the Ashburton Basin developing as a foreland basin during the early stages of the Capricorn Orogeny (Thorne and Seymour, 1991). However, the study by Sheppard et al. (2010a) demonstrated through SHRIMP U–Pb zircon geochronology combined with whole-rock Nd isotopic data for granitic magmatism, that there was no evidence for subduction immediately prior to the Capricorn Orogeny. Rather, a suggested model favoured compressional intraplate reworking of an earlier collisional zone, driven by far-field stresses propagated from active plate boundaries (Occhipinti et al., 2004; Sheppard et al., 2010a).

Due to the absence of both detailed geochronology on the metamorphism and the P – T conditions of the metamorphism associated with the Capricorn Orogeny, no tectonic model has been proposed for the metamorphism during this event. Although the direct P – T conditions remain elusive, this study combined with previous work, has established the following framework that must be explained by any tectonic model: regional low- to medium-grade metamorphic assemblages (except for the Yarlalweelor Gneiss Complex, which shows a higher grade of metamorphism); direct ages for metamorphism at 1805–1772 Ma; geochronological constraints on deformation at 1813–1772 Ma; and regional magmatism at 1820–1775 Ma. The higher-grade rocks exposed in the Yarlalweelor Gneiss Complex could be a result of dextral transpression affecting the Errabiddy Shear Zone during the Capricorn Orogeny, resulting in uplift of deeper crustal rocks (Occhipinti and Reddy, 2004). Any proposed model must be able to explain the synchronicity of magmatism, active deformation and metamorphism during compression. Due to the new results presented in this study, the synchronistic nature of upper amphibolite to granulite

facies metamorphism with magmatism, we propose that the principal driver was possibly emplacement of the Moorarie Supersuite.

The recognition of a younger age population at c. 1750–1730 Ma in the northern Gascoyne Province, post-dating the regional magmatism, could be related to a discrete hydrothermal fluid flow event following the Capricorn Orogeny and coeval hydrothermal activity in the Ashburton Basin (Fielding et al., 2017; 2018). Unlike the older age grouping at 1805–1777 Ma driven by the 1820–1775 Ma magmatism, the causes for the activity at c. 1750–1730 Ma, known from the northern Gascoyne Province, are currently unknown.

2.8 Conclusions

Despite the years of U–Pb geochronology and field work conducted across the Gascoyne Province and the recent advances in constraining the prolonged reworking history of the Capricorn Orogen, the timing and duration of the metamorphism associated with first intraplate reworking, the 1820–1770 Ma Capricorn Orogeny, had not been directly dated. Our new U–Pb monazite and xenotime results from metasedimentary rocks provide robust ages for metamorphism spanning from 1805 to 1777 Ma linking previous published dates from the southern Gascoyne Province with the northern Gascoyne Province. The results presented in this study demonstrate the synchronistic nature of the upper amphibolite to granulite facies metamorphism with magmatism and we propose the principal driver was likely to have been widespread magmatism of the 1820–1775 Ma Moorarie Supersuite. Our results reveal a potential new age grouping at c. 1750–1730 Ma, in the northern Gascoyne Province, which is similar to published ages from orogenic gold deposits in the Ashburton Basin. The regional-scale c. 1750–1730 Ma episode may be either related to the late stages of the Capricorn Orogeny or to a new discrete episode of tectonism.

2.9 Acknowledgements

The authors thank Michael T. D. Wingate for providing constructive comments on the geochronology section. We thank I. C. W. Fitzsimons and S. P. Johnson for their comments on an earlier version. This PhD project was funded through an Australian Research Council (ARC) grant (LP130100922) and the Exploration Incentive Scheme. U–Pb measurements were conducted using the SHRIMP ion microprobes at the John de Laeter Centre at Curtin University.

2.10 References

- Bodorkos, S., & Wingate, M. T. D. (2007). The contribution of geochronology to GSWA's mapping programs: current perspectives and future directions: Geological Survey of Western Australia, Record 2007/2, 10–11.
- Cawood, P. A., & Tyler, I. M. (2004). Assembling and reactivating the Proterozoic Capricorn Orogen: lithotectonic elements, orogenies, and significance. *Precambrian Research*, 128, 201–218.
- Evans, D. A. D., Sircombe, K. N., Wingate, M. T. D., Doyle, M., McCarthy, M., Pidgeon, R. T., & Van Niekerk, H. S. (2003). Revised geochronology of magmatism in the western Capricorn Orogen at 1805–1785 Ma: Diachroneity of the Pilbara-Yilgarn collision. *Australian Journal of Earth Sciences*, 50, 853–864.
- Fielding, I. O. H., Johnson, S. P., Meffre, S., Zi, J.-W., Sheppard, S., Large, R. R., & Rasmussen, B. (2018). Linking gold mineralization to regional-scale drivers of mineral systems using in situ U–Pb geochronology and pyrite LA-ICP-MS. *Geoscience Frontiers*, 10, 89–105.
- Fielding, I. O. H., Johnson, S. P., Zi, J. W., Rasmussen, B., Muhling, J. R., Dunkley, D. J., Sheppard, S., Wingate, M. T. D., & Rogers, J. R. (2017). Using In Situ SHRIMP U-Pb Monazite and Xenotime Geochronology to Determine the Age of Orogenic Gold Mineralization: An Example from the Paulsens Mine, Southern Pilbara Craton. *Economic Geology*, 112, 1205–1230.
- Fletcher, I. R., McNaughton, N. J., Aleinikoff, J. A., Rasmussen, B., & Kamo, S.L. (2004). Improved calibration procedures and new standards for U-Pb and Th-Pb dating of Phanerozoic xenotime by ion microprobe. *Chemical Geology*, 209, 295–314.
- Fletcher, I. R., McNaughton, N. J., Davis, W. J., & Rasmussen, B. (2010). Matrix effects and calibration limitations in ion probe U–Pb and Th–Pb dating of monazite. *Chemical Geology*, 270, 31–44.
- Fletcher, I.R., McNaughton, N.J., & Rasmussen, B. (2000). SHRIMP U–Pb geochronology of authigenic xenotime and its potential for dating sedimentary basins. *Australian Journal of Earth Sciences*, 47, 845–859.
- Foster, G., Kinny, P., Vance, D., Prince, C., and Harris, N. (2000). The significance of monazite U–Th–Pb age data in metamorphic assemblages; a combined study of monazite and garnet chronometry. *Earth and Planetary Science Letters*, 181, 327–340.
- Gardiner, N. J., Maidment, D. W., Kirkland, C. L., Bodorkos, S., Smithies, R. H., & Jeon, H. (2018). Isotopic insight into the Proterozoic crustal evolution of the Rudall Province, Western Australia: *Precambrian Research*, 313, 31–50.

- GSWA (2016). Compilation of geochronology information, 2016 update, digital data product. www.dmp.wa.gov.au/geoview.
- Hand, M., & Buick, I. S. (2001). Tectonic evolution of the Reynolds-Anmatjira Ranges: a case study in terrain reworking from the Arunta Inlier, central Australia, in Continental reactivation and reworking edited by JA Miller, RE Holdsworth, IS Buick and M Hand. Geological Society, London, Special Publications, 184, 237–260.
- Hawke, M. L., Meffre, S., Stein, H., Hilliard, P., Large, R., & Gemmell, J. B. (2015). Geochronology of the DeGrussa volcanic-hosted massive sulphide deposit and associated mineralisation of the Yerrida, Bryah and Padbury Basins, Western Australia. *Precambrian Research*, 267, 250–284.
- Johnson, S. P., Sheppard, S., Rasmussen, B., Wingate, M. T. D., Kirkland, C. L., Muhling, J. R., Fletcher, I. R., & Belousova, E. A. (2011). Two collisions, two sutures: Punctuated pre-1950Ma assembly of the West Australian Craton during the Ophthalmian and Glenburgh Orogenies. *Precambrian Research*, 189, 239–262.
- Johnson, S. P., Sheppard, S., Rasmussen, B., Wingate, M. T. D., Kirkland, C. L., Muhling, J., Fletcher, I. R., & Belousova, E. (2010). The Glenburgh Orogeny as a record of Paleoproterozoic continent-continent collision: Geological Survey of Western Australia, Record 2010/5, p. 54.
- Kirkland, C. L., Wingate, M. T. D., Bodorkos, S & Sheppard, S. (2009). 183205: schistose metatonalite, Mallet Well: Geochronology Record 753: Geological Survey of Western Australia, p.4.
- Krapez, B., & McNaughton, N. J. (1999). SHRIMP zircon U–Pb age and tectonic significance of the Palaeoproterozoic Boolaloo Granodiorite in the Ashburton Province, Western Australia. *Australian Journal of Earth Sciences*, 46, 283–287.
- Korhonen, F. J., Johnson, S. P., Fletcher, I. R., Rasmussen, B., Sheppard, S., Muhling, J. R., Dunkley, D. J., Wingate, M. T. D., Roberts, M. P., & Kirkland, C. L. (2015). Pressure-Temperature-Time evolution of the Mutherbukin Tectonic event, Capricorn Orogen: Geological Survey of Western Australia, Report 146, p. 64.
- Korhonen, F. J., Johnson, S. P., Wingate, M. T. D., Kirkland, C. L., Fletcher, I. R., Dunkley, D. J., Roberts, M. P., Sheppard, S., Muhling, J. R., & Rasmussen, B. (2017). Radiogenic heating and craton-margin plate stresses as drivers for intraplate orogeny. *Journal of Metamorphic Geology*, 35, 631–661.
- Mahon, K. I. (1996). The New “York” regression: application of an improved statistical method to geochemistry. *International Geology Review*, 38, 293–303.
- Ludwig, K.R. (2009). Squid 2.50, A User’s Manual: Berkeley Geochronology Centre Special Publication, p. 95.

- Martin, D. McB, Sheppard, S., & Thorne, A. M. (2005). Geology of the Maroonah, Ullawarra, Capricorn, Mangaroon, Edmund, and Elliot Creek 1: 100 000 sheets: Geological Survey of Western Australia, 1: 100 000 Geological Series Explanatory Notes, p.65.
- Muhling, J. R., Fletcher, I. R., & Rasmussen, B. (2012). Dating fluid flow and Mississippi Valley type base-metal mineralization in the Paleoproterozoic Earahedy Basin, Western Australia. *Precambrian Research* 212–213, 75–90.
- Nelson, D. R. (2004a). 169088: foliated biotite monzogranite, Mundong Well, Geochronology dataset 45; in *Compilation of geochronology data, June 2006 update*: Western Australia Geological Survey, p.4.
- Nelson, D. R. (2004b). 169086: biotite monzogranite, Boora Boora Bore, Geochronology dataset 117; in *Compilation of geochronology data, June 2006 update*: Western Australia Geological Survey, p.4.
- Nelson, D. R. (1998a). 142849: foliated coarse-grained monzogranite, northeast of White Well; in *Compilation of SHRIMP U–Pb zircon geochronology data, 1997*: Western Australia Geological Survey, Record 1998/2, 176–179.
- Nelson, D. R. (1998b). 142851: recrystallised monzogranite, Kerba Pool; Geochronology dataset 367: Geological Survey of Western Australia, p.4.
- Occhipinti, S. A., Hocking, R., Lindsay, M., Aitken, A., Copp, I., Jones, J., Sheppard, S., Pirajno, F., Metelk, V. (2017). Paleoproterozoic basin development on the northern Yilgarn Craton, Western Australia. *Precambrian Research*, 300, 121–140.
- Occhipinti, S. A., & Reddy, S. M. (2009). Neoproterozoic reworking of the Paleoproterozoic Capricorn Orogen of Western Australia and implications for the amalgamation of Rodinia. *Geological Society, London, Special Publications*, 327, 445–456.
- Occhipinti, S., & Reddy, S. (2004). Deformation in a crustal scale shear zone: Errabiddy Shear Zone, Western Australia. In: ALSOP, G. I., Holdsworth, R. E., McCafrey, K. J. W. & Hand, M. (eds) 2004. *Flow processes in Faults and Shear Zones*. Geological Society, London, Special Publication 224, 229–248.
- Occhipinti, S. A., Sheppard, S., Nelson, D., Myers, J., & Tyler, I. (1998). Syntectonic granite in the southern margin of the Paleoproterozoic Capricorn Orogen, Western Australia. *Australian Journal of Earth Sciences*, 45, 509–512.
- Occhipinti, S. A., Sheppard, S., Myers, J. S., Tyler, I. M., & Nelson, D. R. (2001). Archaean and Paleoproterozoic geology of the Narryer Terrane (Yilgarn Craton) and the southern Gascoyne Complex (Capricorn Orogen), Western Australia — a field guide: Western Australia Geological Survey, Record 2001/8, p.70.

- Occhipinti, S. A., Sheppard, S., Passchier, C., Tyler, I. M., & Nelson, D. R. (2004). Paleoproterozoic crustal accretion and collision in the southern Capricorn Orogen: the Glenburgh Orogeny. *Precambrian Research*, 128, 237–255.
- Piechocka, A. M., Gregory, C. J., Zi, J.-W., Sheppard, S., Wingate, M. T. D., & Rasmussen, B. (2017). Monazite trumps zircon: applying SHRIMP U–Pb geochronology to systematically evaluate emplacement ages of leucocratic, low-temperature granites in a complex Precambrian orogen. *Contributions to Mineralogy and Petrology*, 172, 1–17.
- Piechocka, A. M., Sheppard, S., Fitzsimons, I. C. W., Johnson, S. P., Rasmussen, B., & Jourdan, F. (2018). Neoproterozoic $^{40}\text{Ar}/^{39}\text{Ar}$ mica ages mark the termination of a billion years of intraplate reworking in the Capricorn Orogen, Western Australia. *Precambrian Research*, 310, 391–406.
- Rasmussen, B. (2005). Zircon growth in very low grade metasedimentary rocks: evidence for zirconium mobility at $\sim 250^\circ\text{C}$. *Contributions to Mineralogy and Petrology*, 150, 146–155.
- Rasmussen, B., Fletcher, I. R., Muhling, J. R., & Wilde, S. A. (2010). In situ U–Th–Pb geochronology of monazite and xenotime from the Jack Hills belt: Implications for the age of deposition and metamorphism of Hadean zircons. *Precambrian Research*, 180, 26–46.
- Rasmussen, B., Fletcher, I. R., & Sheppard, S. (2005). Isotopic dating of the migration of a low-grade metamorphic front during orogenesis. *Geology*, 33, 773–776.
- Şener, K. A., Young, C., Groves, D. I., Krapez, B., & Fletcher, I. R. (2005). Major orogenic gold episode associated with Cordilleran-style tectonics related to the assembly of Paleoproterozoic Australia? *Geology*, 33, 225–228.
- Sheppard, S., Bodorkos, S., Johnson, S. P., Wingate, M. T. D., & Kirkland, C. L. (2010a). The Paleoproterozoic Capricorn Orogeny: Intracontinental Reworking Not Continent-Continent Collision: Geological Survey of Western Australia, Report 108, p. 33.
- Sheppard, S., Johnson, S. P., Wingate, M. T. D., Kirkland, C. L., & Pirajno, F. (2010b). Explanatory notes for the Gascoyne Province: Geological Survey of Western Australia, 1:100 000 Explanatory Notes, p. 336.
- Sheppard, S., Rasmussen, B., Muhling, J. R., Farrell, T. R., & Fletcher, I. R. (2007). Grenvillian-aged orogenesis in the Paleoproterozoic Gascoyne Complex, Western Australia: 1030–950 Ma reworking of the Proterozoic Capricorn Orogen. *Journal of Metamorphic Geology*, 25, 477–494.

- Sheppard, S., Occhipinti, S. A., & Nelson, D. R. (2005). Intracontinental reworking in the Capricorn Orogen, Western Australia: the 1680–1620 Ma Mangaroon Orogeny. *Australian Journal of Earth Sciences*, 52, 443–460.
- Sheppard, S., Occhipinti, S. A., & Tyler, I. M. (2004). A 2005–1970 Ma Andean-type batholith in the southern Gascoyne Complex, Western Australia. *Precambrian Research*, 128, 257–277.
- Stacey, J.S., & Kramers, J.D. (1975). Approximation of terrestrial lead isotope evolution by a two-stage model. *Earth and Planetary Science Letters*, 26, 207–221.
- Stern, T. A., & Sanborn, N. (1998). Monazite U–Pb and Th–Pb geochronology by high-resolution secondary ion mass spectrometry. *Radiogenic Age and Isotope Studies: Report 11*, Geological Survey of Canada, Current Research 1998-F, 1–18.
- Stern, R. A., & Rainbird, R. H. (2001). Advancements in xenotime U–Pb geochronology by ion microprobe, Eleventh V.I. Goldschmidt Conference Lunar and Planetary Science Institute, Houston.
- Tucker, N. M., Morrissey, L. J., Payne, J. L., & Szpunar, M. (2018). Genesis of the Archean–Paleoproterozoic Tabletop Domain, Rudall Province, and its endemic relationship to the West Australian Craton. *Australian Journal of Earth Sciences*, 65, 1–30.
- Tyler, I. M. (1990). The geology of the Sylvania Inlier and the southeast Hamersley Basin: Geological Survey of Western Australia, Bulletin 138, p.124.
- Tyler, I. M., & Thorne, A. M. (1990) The northern margin of the Capricorn Orogen Western Australia an example of an Early Proterozoic collision zone. *Journal of Structural Geology*, 12, 685–701.
- Thorne, A. M., & Seymour, D. B. (1991). Geology of the Ashburton Basin, Western Australia: Geological Survey of Western Australia, Bulletin 139, p. 141.
- Wingate, M. T. D., Kirkland, C. L., Bodorkos, S., Groenewalk, P. B., & Sheppard, S. (2010). 187403, quartzite, Robinson Bore; Geochronology Record 862: Geological Survey of Western Australia, p. 5.
- Wingate, M. T. D., Kirkland, C. L. & Johnson, S. P. (2011). 190662: gneissic metamonzogranite, Recovery Well; Geochronology Record 1005: Geological Survey of Western Australia, 4p.
- Wingate, M. T. D., Kirkland, C. L., Johnson, S. P., & Sheppard, S. (2012a). 190660: metamonzogranite, Midway Bore; Geochronology Record 1036: Geological Survey of Western Australia, p. 4.

- Wingate, M. T. D., Kirkland, C. L., Johnson, S. P., & Sheppard, S. (2012b). 190634: metamonzogranite, Minierra Well; Geochronology Record 1034: Geological Survey of Western Australia, p. 4.
- Wingate, M. T. D., Kirkland, C. L., Johnson, S. P., & Sheppard, S. (2017). 188974, metamonzogranite, Mount James homestead; Geochronology Record 1362: Geological Survey of Western Australia, p. 4.
- Zi, J.-W., Rasmussen, B., Muhling, J. R., Fletcher, I. R., Thorne, A. M., Johnson, S. P., Cutten, H. N., Dunkley, D. J., & Korhonen, F. J. (2015). In situ U–Pb geochronology of xenotime and monazite from the Abra polymetallic deposit in the Capricorn Orogen, Australia: Dating hydrothermal mineralization and fluid flow in a long-lived crustal structure. *Precambrian Research*, 260, 91–112.

Chapter 3

PAPER 2: The Mangaroon Orogeny: Synchronous c. 1.7 Ga magmatism and low-P, high-T metamorphism in the West Australian Craton

Authors:

Agnieszka M Piechocka^{1*}, Jian-Wei Zi^{2, 3}, Courtney J Gregory¹, Stephen Sheppard^{1,6}, Fawna J Korhonen⁴, Ian CW Fitzsimons¹, T. E. Johnson¹, Birger Rasmussen^{3,5}

¹School of Earth and Planetary Sciences, Curtin University, Kent Street, Bentley, WA 6102, Australia

²John de Laeter Centre, Curtin University, Kent Street, Bentley, WA 6102, Australia

³State Key Laboratory of Geological Processes and Mineral Resources, China University of Geosciences, Wuhan, 430074, China

⁴Geological Survey of Western Australia, 100 Plain Street, East Perth, WA, 6004, Australia

⁵School of Earth Sciences, The University of Western Australia, Nedlands, WA 6009, Australia

⁶Calidus Resources Limited, Suite 12, 11 Ventnor Avenue, West Perth, WA 6005, Australia

Keywords:

intraplate orogeny, U–Pb geochronology, monazite, xenotime, LPHT metamorphism, Proterozoic

3.1 Abstract

The Capricorn Orogen records nearly one billion years of intraplate orogenesis within the West Australian Craton, although the processes responsible for this protracted, punctuated reworking remain unclear. Of the major tectonic events that affected the region, the 1680–1620 Ma Mangaroon Orogeny is one of the least-well understood, mainly due to a lack of direct ages for metamorphism, an absence of pressure (P)–temperature (T) constraints, and uncertainty regarding the duration of granitic magmatism that is spatially and, possibly, temporally associated with deformation. In this study we define the P – T –time (t) conditions associated with the Mangaroon Orogeny based on *in situ* SHRIMP U–Pb monazite and xenotime geochronology and calculated P – T pseudosections. Data from a pelitic migmatite constrain the timing of low- P , high- T metamorphism to 1691 ± 7 Ma at conditions of 665–755 °C and 2.7–4.3 kbar (~175–240 °C/kbar). Data from a garnet-bearing sillimanite–biotite pelitic gneiss suggests higher pressure during the clockwise prograde history at one locality. Furthermore, the onset of the metamorphism coincides with the oldest granites in the region (1695 ± 9 Ma), which constrain the onset of the Mangaroon Orogeny. Our results also show that deposition and burial of the precursor sediments occurred, at most, c. 70 million years before the onset of partial melting at c. 1695 Ma. Therefore, there was no long incubation period before the onset of orogenesis. We conclude that, unlike many of the Proterozoic orogenic events in Australia, the c. 1.7 Ga low- P , high- T metamorphism recorded in the upper crust in the Capricorn Orogen cannot be explained by a thermal lid model, but rather was synchronous with granitic magmatism.

3.2 Introduction

Proterozoic Australia has been subjected to numerous intraplate orogenic events, typically characterised by low-pressure (low- P) and high-temperature (high- T) metamorphism. Several tectonic models have been proposed to explain the causes and characteristics of low- P , high- T metamorphism, including crustal thickening with coeval magmatism (Loosveld and Etheridge, 1990), crustal extension (Wickham and Oxburgh, 1987; Sandiford and Powell, 1986), and regional contact metamorphism (e.g. Barton and Hanson, 1989). A model commonly invoked for many Australian Proterozoic terrains is that of low- P , high- T metamorphism a product of lithospheric weakening owing to high concentrations of heat-producing elements (McLaren et al., 2005), perhaps enhanced by thick sedimentary sequences that provided insulation (Sandiford and Hand, 1998).

In the Capricorn Orogen of Western Australia, intraplate metamorphism and deformation associated with the Mesoproterozoic Mutherbukin Tectonic Event was interpreted to reflect elevated heat production beneath a thick thermal blanket, resulting in elevated temperatures that lasted in excess of 100 million years (Korhonen and Johnson, 2015; Korhonen et al., 2017). Although this model has been proposed for other Proterozoic orogens in Australia (e.g. McLaren et al., 2005; Korhonen et al., 2017; Morrissey et al., 2014), it is unclear as to whether all Proterozoic orogenies reflect such a process.

An alternative model for low- P , high- T metamorphism in Proterozoic Australian orogens, is one which invokes intrusion of voluminous granites or mafic rocks to provide the heat for metamorphism (e.g. Clark et al., 2014; Collins and Vernon, 1991; Oliver and Zakowski, 1995; Glasson et al., 2019). Collins and Vernon (1991) proposed that low- P , high- T metamorphism in the upper crust of the Arunta Orogen was caused by granite magmatism, triggered by a mantle perturbation that induced partial melting of the lower crust. Clark et al. (2014) and Glasson et al. (2019) argued that the drivers for low- P , high- T metamorphism associated with Stage I of the Albany–Fraser Orogeny included elevated heat flow and mafic magmatism during lithospheric extension. Furthermore, it was suggested that low- P , high- T metamorphism in the eastern Mt Lofty Ranges, south Australia, was synchronous with granite magmatism in an extensional setting (Oliver and Zakowski, 1995).

The Capricorn Orogen of Western Australia records a prolonged history of repeated intraplate orogenesis, comprising multiple episodes of predominantly felsic magmatism,

metamorphism and deformation. This study focuses on one of these events—the 1680–1620 Ma Mangaroon Orogeny—which has been proposed as an example of low- P , high- T regional metamorphism, based on diagnostic mineral assemblages and a widespread gneissic textures in rocks of the southern Mangaroon Zone, although local occurrences of contact metamorphism have been recorded (Sheppard et al., 2005). However, no detailed work has been done on the timing of metamorphism and the determination of precise P – T conditions. Therefore, the cause and duration of metamorphism associated with the Mangaroon Orogeny remain unknown.

In this contribution, we use SHRIMP U–Pb monazite and xenotime data, and P – T pseudosections to provide the first robust constraints on the duration and P – T conditions of intraplate low- P , high- T metamorphism associated with the Mangaroon Orogeny. Furthermore, we obtained whole-rock geochemistry to determine the peraluminosity of the granites and calculate zircon saturation temperatures. This study indicates that the thermal lid model, which is favoured for other Proterozoic intraplate tectonic events in Australia, cannot easily explain the anomalous thermal gradients in the crust during the Mangaroon Orogeny. The data are then integrated with studies of low-grade metamorphic and hydrothermally altered rocks across the West Australian Craton to show that the Mangaroon Orogeny has a significantly wider footprint than previously thought. Further, we contend that the metamorphism and magmatism recorded in the Capricorn Orogen may have been responsible for widespread circulation of fluids in the upper crust over much of the craton.

3.3 Regional Geology

The study area is in the Capricorn Orogen of Western Australia (Figure 3.1). The Capricorn Orogen records the two-stage assembly of the West Australian Craton, separating the Archean Pilbara and Yilgarn cratons to the north and south, respectively. Assembly of the West Australian Craton, which was complete by c. 1950 Ma (Johnson et al., 2011; Occhipinti et al., 2004), was followed by five episodes of intraplate reworking and reactivation spanning nearly 1.5 billion years that shaped the current architecture of the orogen (Korhonen et al., 2017; Piechocka et al., 2018; Piechocka et al., 2019; Sheppard et al., 2005, 2007, 2010a). All these tectonic events are recorded in rocks of the Gascoyne Province, a basement complex of magmatic and metamorphic rocks exposed at the western end of the orogen (Figure 3.1).

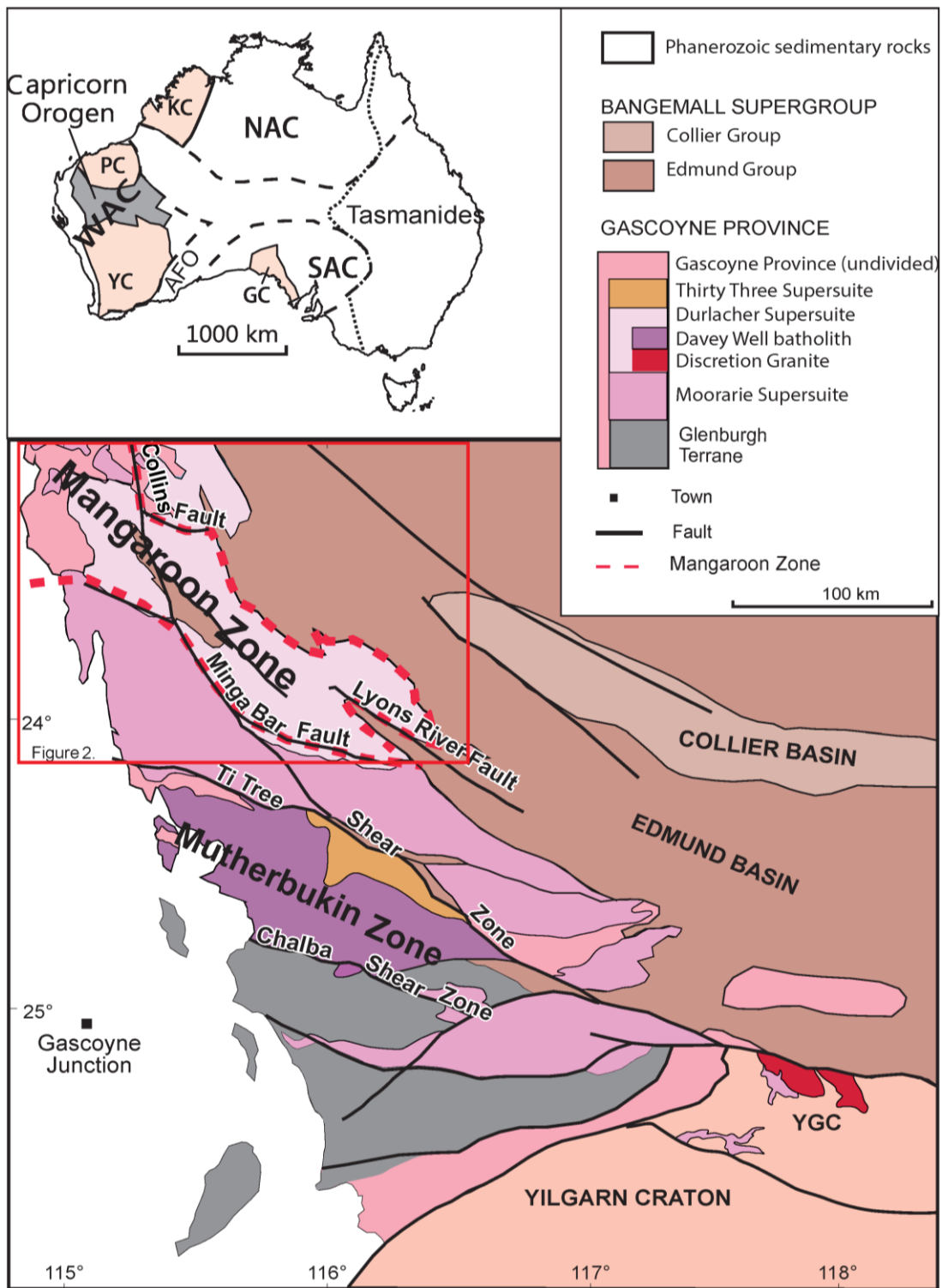


Figure 3.1 Regional geological setting of the Capricorn Orogen in relation to Australia (inset map) and simplified regional geology of the Gascoyne Province showing discrete fault- bounded NW-SE trending domains. PC = Pilbara Craton, YC = Yilgarn Craton, WAC = West Australian Craton, AFO = Albany- Fraser Orogen, GC = Gawler Craton, KC = Kimberley Craton, NAC = North Australian Craton, SAC = South Australian Craton, YGC = Yarlalweelor Gneiss Complex (adapted from Johnson et al. (2017)).

The Gascoyne Province is subdivided into several southeast-trending structural and metamorphic zones, each recording a discrete tectonothermal history. Of the five intraplate events, four record reworking (i.e., pervasive deformation accompanied by metamorphism and/or magmatism; Korhonen et al 2017; Piechocka et al., 2019; Sheppard et al., 2005; Sheppard et al., 2007; Sheppard et al., 2010a), whereas the youngest events, including the later stages of the fourth episode of reworking, reflect reactivation along discrete structures, in which the intervening rocks were largely unaffected (Bodorkos and Wingate, 2007; Piechocka et al., 2018).

The two Paleoproterozoic intraplate events—the 1820–1775 Ma Capricorn Orogeny (Sheppard et al., 2010a; Piechocka et al., 2019) and the 1680–1620 Ma Mangaroon Orogeny (Sheppard et al., 2005)—produced pervasive metamorphism and deformation accompanied by voluminous, granitic magmatism. The Capricorn Orogeny is characterised by extensive compressional deformation (mostly at low to medium metamorphic grade), magmatism and some sedimentation (Sheppard et al., 2010a). A recent U–Pb phosphate geochronology study showed that metamorphism during the Capricorn Orogeny was synchronous with magmatism (Piechocka et al., 2019). Deformation and medium-grade metamorphism (<750 °C and <6 kbar) associated with the Mangaroon Orogeny was preceded by the deposition of siliciclastic sedimentary rocks (the Pooranoo Metamorphics; Sheppard et al., 2005).

During the Meso- to Neoproterozoic the Gascoyne Province was subjected to two additional reworking events and two reactivation events. The driver for the older of the reworking events, the 1320–1170 Ma Mutherbukin Tectonic Event in the central Gascoyne Province, was proposed to be thickening of metasedimentary rocks deposited at 1842–1807 Ma which are enriched in high heat-producing elements. According to Korhonen et al. (2017), these Paleoproterozoic rocks formed a thermal lid that generated radiogenic heat for c. 110 million years prior to the onset of peak metamorphism at >650 °C and 4.4–7.0 kbar.

The second reworking event, the 1030–900 Ma Edmondian Orogeny, is characterised by coeval leucogranite magmatism and metamorphism and deformation at 500–550° C and 3–4 kbar (Piechocka et al., 2017; Sheppard et al., 2007). Although metamorphism had ceased by c. 990 Ma, the leucogranite magmatism persisted for another c. 100 million years (Piechocka et al., 2017). Orogen-scale reactivation of pre-existing shear zones at 920–830 Ma involved dextral strike-slip movement in the northern parts of the province and exhumation of the southern portion (Occhipinti &

Reddy 2009, Piechocka et al., 2018). This widespread reactivation may be attributed to the Edmondian Orogeny. The effects of the youngest reactivation event, the c. 570 Ma Mulka Tectonic Event (Bodorkos and Wingate, 2007), are limited to faulting and dextral shearing on discrete structures.

3.4 Mangaroon Zone

The study area is located in the Mangaroon Zone of the northern Gascoyne Province (Figure 3.1 and Figure 3.2) and comprises metasedimentary rocks of the Pooranoo Metamorphics and voluminous granitic intrusions of the Durlacher Supersuite. The Mangaroon Zone is about 40–70 km wide and is overlain by Phanerozoic sedimentary rocks in the west and by Meso- to Neoproterozoic metasedimentary rocks to the east. It is bounded to the north by the Collins Fault and to the south by the Minga Bar Fault. Figure 3.2 shows the geology of the Mangaroon Zone along with sample locations.

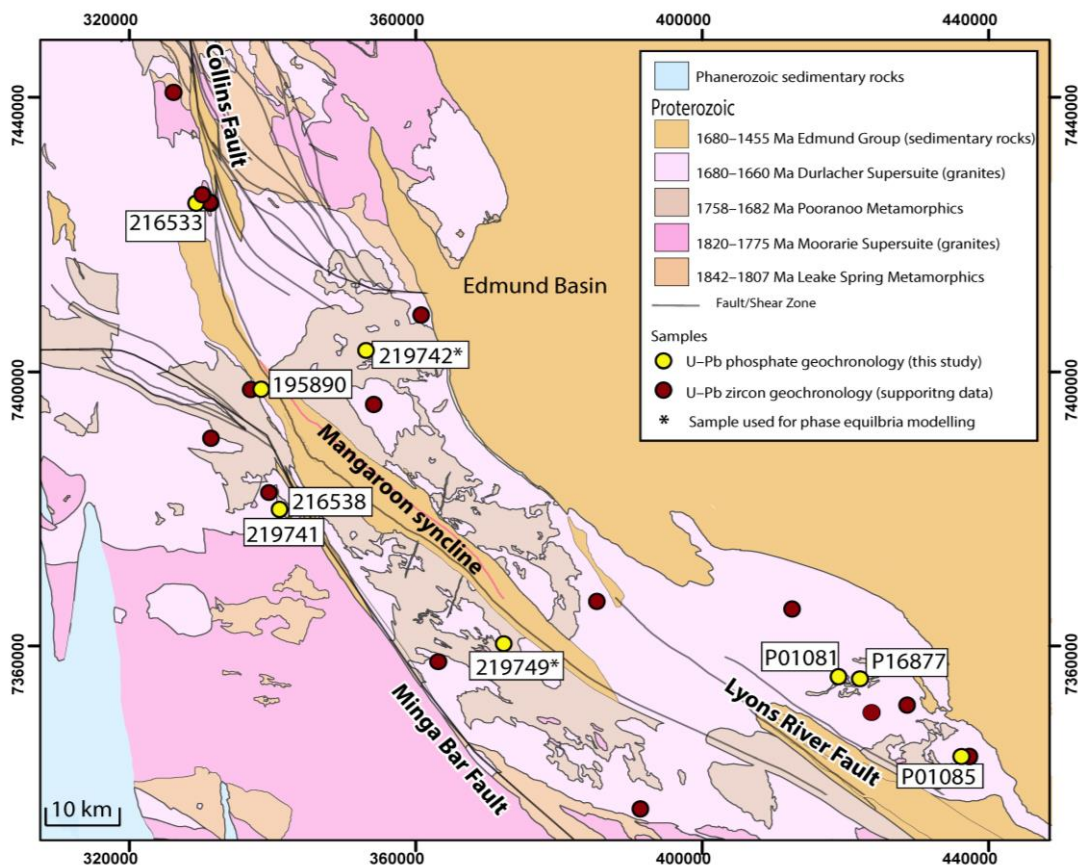


Figure 3.2 Geology of the Mangaroon Zone showing location of samples used in this study and locations of previously dated granitic samples. The Minga Bar Fault, the Collins Fault and the Edmund Basin bound the Mangaroon Zone. Coordinate system is GDA 1994 MGA Zone 50. Geology polygons and linear features were extracted from the 1:500 000 Geological Map of Western Australia (GSWA 2016a).

3.4.1 Pooranoo Metamorphics

The Pooranoo Metamorphics comprise mainly interlayered psammitic schist and feldspathic metasandstone with pelitic rocks and metaconglomerate (Sheppard et al., 2010b). In the Mangaroon Zone, the rocks are commonly schistose, but gneissic and migmatitic metapelitic rocks are known from one locality in the southern Mangaroon Zone. Locally, graded bedding is preserved in the feldspathic metasandstone (Sheppard et al., 2010b). The protoliths to the Pooranoo Metamorphics were deposited as a turbidite sequence in a narrow ~50 km-wide basin, with an unknown thickness. The turbiditic nature of the protoliths suggests a deep-water depositional setting (Sheppard et al., 2005; Sheppard et al., 2010b; Sheppard and Johnson, 2016).

SHRIMP U–Pb zircon geochronology was conducted by the Geological Survey of Western Australia (GSWA) to constrain the maximum and minimum depositional ages of precursors to the Pooranoo Metamorphics. A sample of the Biddenew Formation of the Mt James Subgroup yielded a youngest detrital zircon population at 1758 ± 18 Ma, which is interpreted as the maximum depositional age of the formation (Sheppard and Johnson, 2016; GSWA 183255; Wingate et al., 2009). A minimum depositional age is provided by the oldest granite to intrude the Pooranoo Metamorphics, which has an igneous crystallization age of 1682 ± 4 Ma (GSWA 208318; Wingate et al., 2013). Therefore, sedimentary precursors to the Pooranoo Metamorphics were deposited between c. 1758 and 1682 Ma.

3.4.2 Durlacher Supersuite in the Mangaroon Zone

In the Mangaroon Zone, the Durlacher Supersuite granites were emplaced as voluminous plutons and dykes that intruded the Pooranoo Metamorphics at c. 1680–1660 Ma (Sheppard et al., 2005) and comprise biotite–muscovite monzogranite, granodiorite, syenogranite and minor muscovite–tourmaline monzogranite (Sheppard et al., 2010b). A deep-crustal seismic reflection survey suggests that granites extend to at least 10 km depth (Fig. 10 of Johnson et al., 2013). Durlacher granites are also known from outside the Mangaroon Zone in other parts of the Gascoyne Province: in the Mutherbukin Zone and in the Yarlalweelor Gneiss Complex (Figure 3.1). The current upper and lower age limits of Durlacher Supersuite magmatism are constrained by the oldest monzogranite with an igneous crystallization age of 1682 ± 4 Ma, from the Mangaroon Zone, (Sheppard

and Johnson 2016; GSWA 208318; Wingate et al., 2013) and a porphyritic biotite monzogranite from the Yarlalweelor Gneiss Complex that yielded a crystallisation age of 1619 ± 15 Ma (GSWA 142855: Nelson 1998; Sheppard et al., 2005). However, no granites younger than c. 1660 Ma are known from the Mangaroon Zone. Furthermore, no metamorphic assemblages or deformation fabrics associated with the Mangaroon Orogeny are known outside of the Mangaroon Zone. Recent $^{40}\text{Ar}/^{39}\text{Ar}$ mica geochronology, from a monzogranite in the northern Mangaroon Zone (GSWA 195890), yielded a c. 1640 Ma age, interpreted to record cooling and uplift (Piechocka et al., 2018).

3.4.3 Deformation and metamorphism (D_1/M_1 and D_2/M_2)

In the Mangaroon Zone, of the northern Gascoyne Province, two distinct tectonometamorphic events, D_1/M_1 and D_2/M_2 , have been recognised (Sheppard et al., 2005). D_1/M_1 is characterised by amphibolite facies regionally extensive of the Pooranoo Metamorphics. In the southern Mangaroon Zone, D_1 deformation produced local gneissic fabrics or granofelsic textures, with evidence for partial melting of pelitic and semi-pelitic lithologies at the Star of Mangaroon locality (Sheppard et al., 2005). Also, at the Star of Mangaroon mine local recumbent folds with axial surfaces defined by sillimanite are associated with D_1 (Sheppard et al., 2005). However, some areas preserve a granofelsic texture, which suggests minimal non-coaxial strain. M_1 metamorphic assemblages preserved in pelitic and granofels of biotite–muscovite–quartz–plagioclase–sillimanite, quartz–biotite–cordierite–plagioclase–muscovite(–sillimanite) and plagioclase–biotite–quartz–sillimanite–muscovite–cordierite combined with the general absence of garnet were previously interpreted to record low- P , high- T regional metamorphism (Sheppard et al., 2005). The grade of metamorphism appears to be lower in the northern half of the Mangaroon Zone (Sheppard et al., 2005). Formerly, the upper age constraint on D_1/M_1 , and the lower age constraint on D_2/M_2 , were based on a diatexitic granite with a zircon crystallisation age of c. 1677 Ma (GSWA 178027: Nelson 2005) that cross-cuts an undated gneissic fabric that was presumed to be associated with D_1 (Sheppard et al., 2005). However, recent zircon ages of c. 1808 Ma obtained from the gneissic host that is cross-cut by the diatexite show that it is part of the older 1820–1775 Ma Moorarie Supersuite (Wingate et al., 2013), and unrelated to the Mangaroon Orogeny. Consequently, the previous upper age constraint on D_1/M_1 and lower age constraint on D_2/M_2 , (i.e., 1677 Ma) may not be valid.

The D₂ deformation event produced a pervasive schistosity, metre- to kilometre-scale upright folds, and retrogression of D₁ metamorphic minerals to greenschist facies assemblages (Sheppard et al., 2005; 2010b). M₂ is characterised by sericite (after sillimanite, cordierite, plagioclase and microcline), and chlorite (after cordierite) with a typical M₂ assemblage consisting of sericite–chlorite–quartz–plagioclase–biotite observed in schists (Sheppard et al., 2005). Many granites of the Durlacher Supersuite with crystallization ages of c. 1675 Ma or older were deformed during D₂, providing a maximum age constraint for D₂ (Sheppard et al., 2005; 2010b).

3.5 Sample descriptions and petrography

In total, nine samples of pelitic and granitic rocks were collected from across the Mangaroon Zone for U–Pb geochronology. Monazite was used to determine the crystallisation ages for the granitic rocks (three samples) and monazite and xenotime were selected to date the timing of metamorphism in the pelitic rocks (six samples). Of these pelitic samples, two (GSWA 219742 and 219749) contained a preserved mineral assemblage that was suitable for phase equilibria modelling (GSWA 219742 and GSWA 219749). Locations of all samples used in this study are shown in Figure 3.2. Descriptions of all the granitic and pelitic samples analysed as part of this study are provided below and summarised in Table 3.1. Figure 3.3 shows images of granitic sample sites in outcrop and thin section; Figure 3.4 consists of outcrop photos of pelitic sample locations; and Figure 3.5 consists of photomicrographs of pelitic samples.

Granitic rocks (Durlacher Supersuite)

GSWA 195890: muscovite–biotite metamonzogranite

This rock is a medium-grained, porphyritic muscovite–biotite monzogranite (Figure 3.3a). The monzogranite shows variation in strain across the outcrop with zones of mylonitisation, quartz veining and brecciation and zones with preserved igneous textures. The vertical metamorphic foliation trends 230°. The typical mineral assemblage consists of K-feldspar, quartz, muscovite and plagioclase with ~25% ferromagnesian minerals including biotite and secondary chlorite, along with accessory Fe-oxides, fluorite, zircon and monazite. In places, zones of pervasive mylonitization resulted in almost complete recrystallisation of the rock during the Neoproterozoic (Piechocka et al., 2018) (Figure 3.3c).

Table 3.1 Summary of granitic and pelitic samples from the Mangaroon Zone analysed in this study.

GSWA Sample ^a	Easting	Northing	Sample description	Structure	P-T constraints	Mineral	U-Pb Age (Ma)
<i>Granite samples</i>							
195890	338457	7397374	ms–bt metamonzogranite	230°/90° metamorphic foliation		monazite	1695 ± 9
P01085 ^c	436219	7343766	bt–ms syenogranite			monazite	1682 ± 3
219741	339577	7382285	tur–ms monzogranite			monazite	1659 ± 13
Supporting samples ^d							
208365	326186	7440703	bt metagranodiorite	228°/70° SE metamorphic foliation; D1		zircon	1689 ± 6
195888	331433	7390220	bt monzogranite			zircon	1689 ± 4
216532	331336	7424614	bt metagranodiorite	260/85° SE gneissic layering; D1		zircon	1688 ± 4
195887	341014	7379817	tur–ms monzogranite			zircon	1682 ± 9
216531	331336	7424614	ms–tur monzogranite			zircon	1673 ± 4
<i>Pelitic samples</i>							
219749	372340	7359950	cd–sill pelitic migmatite	147°/85° SE fold axial surface; 230°/70° SE fold axis; D1	665–755°C; 2.7–4.3 kbar	monazite	1691 ± 7
219742	353086	7402982	sill–bt pelitic gneiss			monazite	1685 ± 9
216533	330613	7424503	gt–bt–ep pelitic gneiss	241°/30° SE metamorphic foliation; D1	675–850°C; 4–7.5 kbar	monazite	1683 ± 6
P01081c	419044	7355430	qtz–ms–tour schist			monazite	1681 ± 9
P16877c	422009	7355110	qtz–bt–ms schist			monazite	1680 ± 7
216538	339577	7382285	bt–ms–tur pelitic gneiss			monazite	1680 ± 4
216538	339577	7382285	bt–ms–tur pelitic gneiss			xenotime	1680 ± 4

Notes:

Sample locations quoted in coordinate system MGA 94 Zone 50.

Planar structures are quoted as strike/dip and dip direction.

^a Sample prefix is GSWA unless otherwise stated.

^b Durlacher Supersuite.

^c Samples collected by J. Pearson (Pearson 1996).

^d Published GSWA data. References within text.

^e Pooranoo Metamorphics.

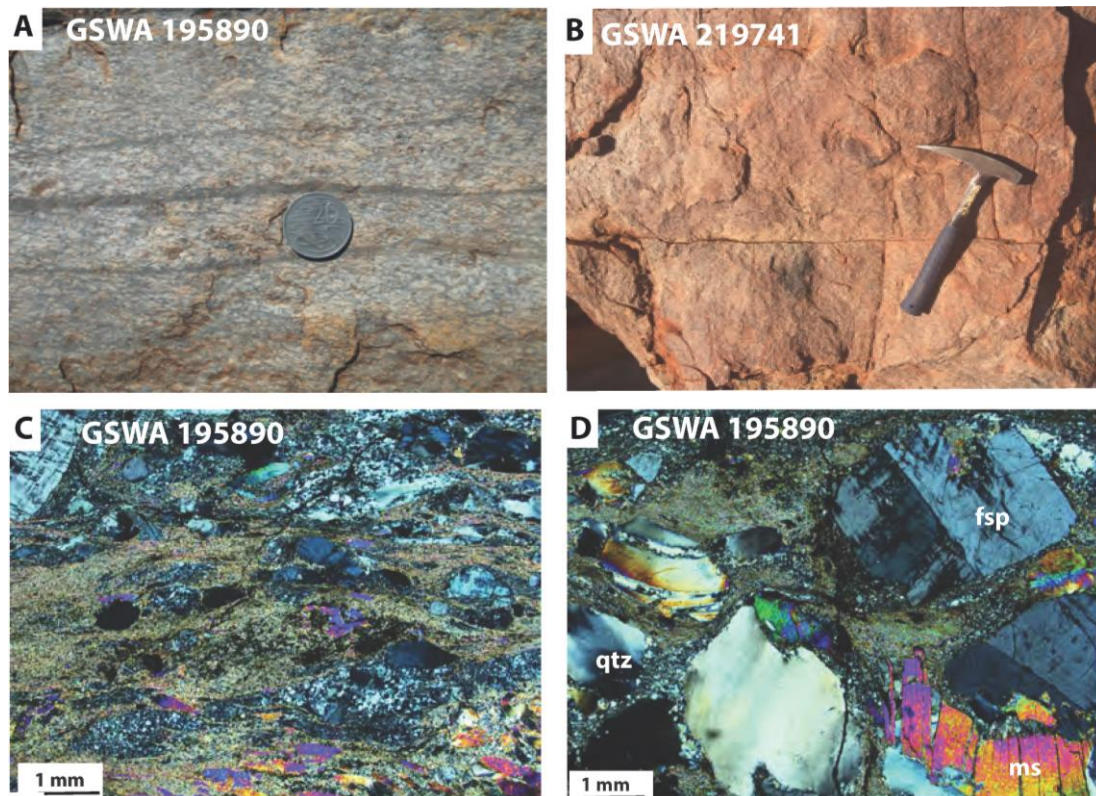


Figure 3.3 Field photos of granites and representative photomicrograph images of granitic sample 195890 in cross-polarised light. analysed in this study.. A. Variably deformed porphyritic muscovite–biotite monzogranite characterised by discrete cm-scale mylonite zones (GSWA 195890). B. Leucocratic undeformed tourmaline–muscovite monzogranite (GSWA 219741). C. Fine-grained biotite matrix with recrystallised quartz and feldspar porphyroblasts showing sigma tails (GSWA 195890). D. A less deformed part of the rock (GSWA 195890) showing feldspar and muscovite porphyroclasts. Abbreviations: fsp = feldspar; ms = muscovite; qtz = quartz.

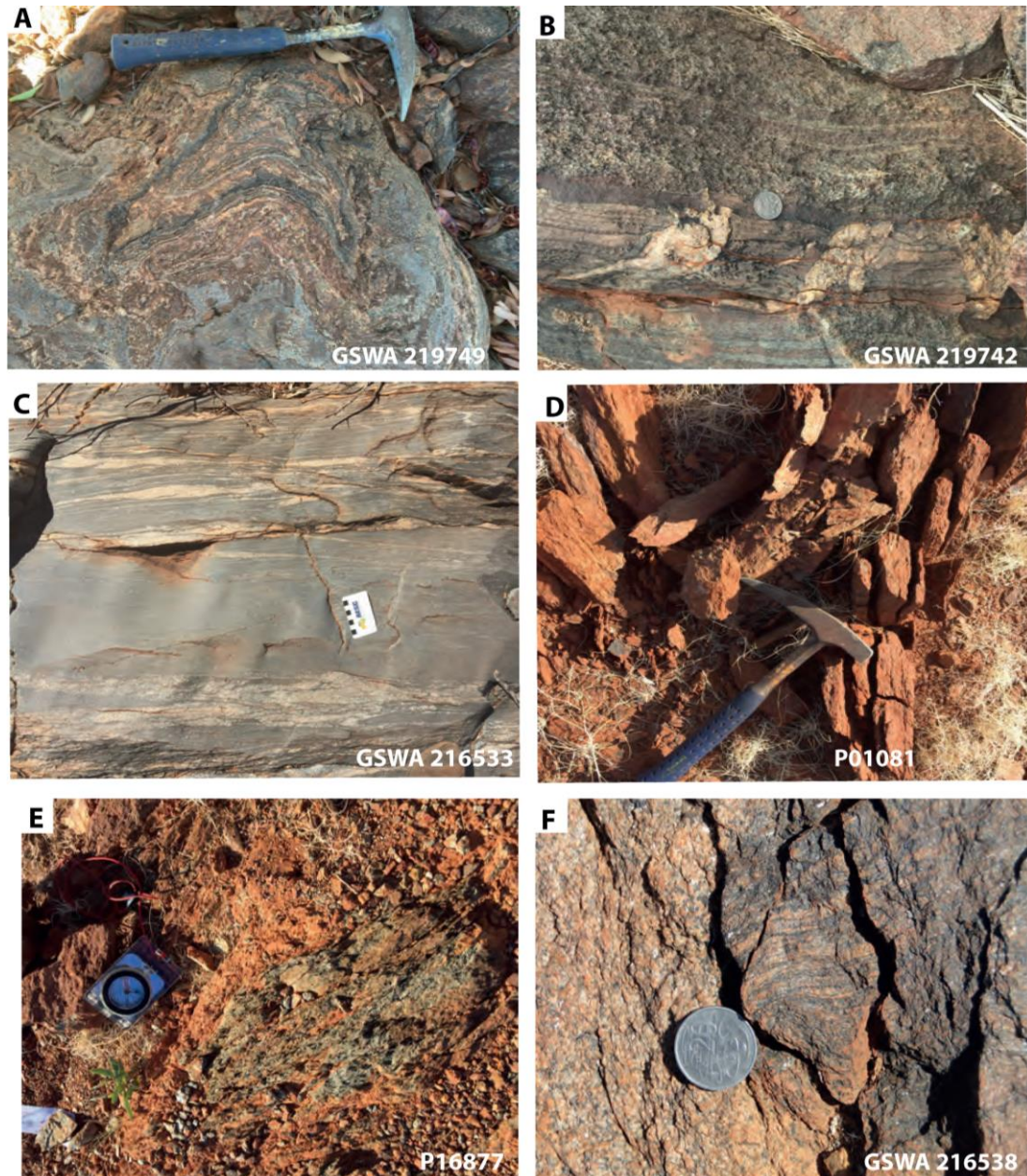


Figure 3.4 Field photos of pelitic samples analysed in this study. A. Stromatic cordierite–sillimanite pelitic migmatite (GSWA 219749). B. Sillimanite–biotite pelitic gneiss that in outcrop appears bedded (GSWA 219742). Local melting observed at several locations across the outcrop. C. Meter-wide biotite-rich zones with leucosomes (GSWA 216533). D. Weathered outcrop of quartz–biotite–tourmaline schist (P01081). E. Sub-crop of deformed muscovite–biotite schist (P16877). F. Inclusion of deformed biotite–muscovite–tourmaline pelitic gneiss (GSWA 216538) enclosed within a relatively undeformed monzogranite (GSWA 219741).

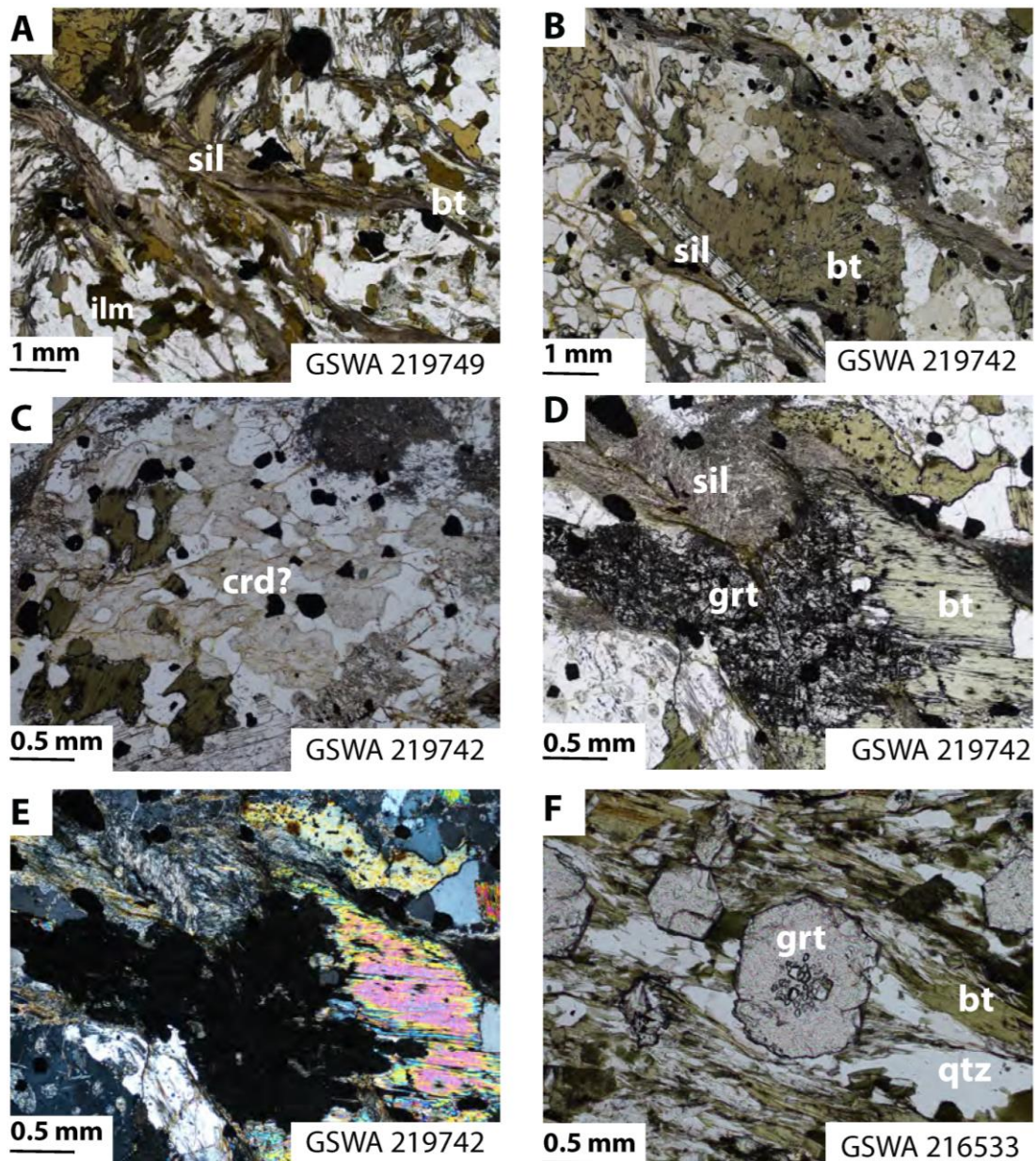


Figure 3.5 Representative photomicrograph images of analysed pelitic samples in plane-polarised light (PPL) and cross-polarised light (XPL). A. Fabric defined by fibrous sillimanite, biotite, quartz and ilmenite in the cordierite–sillimanite pelitic migmatite (GSWA 219749; PPL). B. Sillimanite–biotite pelitic gneiss with tabular and fibrous sillimanite (GSWA 219742; PPL). C. Possible ex-cordierite crystal (GSWA 219742; PPL). D. Anhedronal garnet associated with biotite (GSWA 219742; PPL). E. As per D but in XPL. F. Garnet porphyroblast with pressure shadow and biotite–quartz foliation in the garnet–biotite–epidote pelitic gneiss. Inclusions are restricted to the garnet cores and are randomly oriented (GSWA 216533; PPL). Abbreviations: bt = biotite; crd = cordierite; grt = garnet; ilm = ilmenite; pl = plagioclase; qtz = quartz; sil = sillimanite.

P01085: biotite–muscovite syenogranite

This sample is a porphyritic, biotite–muscovite syenogranite consisting of orthoclase, quartz, plagioclase, and muscovite. Mafic minerals make up around 15% of the rock and include biotite and Fe–Ti oxides. Orthoclase predominantly occurs as anhedral crystals and is perthitic. The largest orthoclase crystals occur as tabular phenocrysts up to 8 mm long by 4 mm wide. Plagioclase shows multiple twinning and quartz shows undulose extinction. Sericite is pervasive throughout the sample.

GSWA 219741: tourmaline–muscovite monzogranite

This sample is a relatively undeformed medium-grained leucocratic monzogranite (Figure 3.3b) consisting of orthoclase, quartz, plagioclase and muscovite. Ferromagnesian minerals make up around 10% of the rock and include tourmaline, biotite, chlorite, and Fe-oxides. Pervasive sericite and recrystallised quartz show a minor post magmatic overprint, although the rock looks relatively undeformed in outcrop.

Pelitic rocks (Pooranoo Metamorphics)*GSWA 219749: sillimanite–cordierite pelitic migmatite*

The outcrop from which this sample was collected is characterised by stromatic migmatites (Figure 3.4a) with leucosomes of feldspar, quartz and biotite and melanosomes of coarse sillimanite and biotite. Seemingly unmigmatized layers of psammite, up to a few meters thick, are cross-cut by a sparse network of leucocratic veins. Folded pelitic and psammitic rocks have axial planar fabrics defined by biotite (D_1) (Martin et al., 2006). At this locality the fold axial surface trends $147^\circ/85^\circ$ (SE) with a fold axis trending $230^\circ/70^\circ$ (SE). In thin section, the foliation (D_1) in the pelitic migmatite is defined by elongate flattened quartz grains that wrap recrystallised quartz, anhedral cordierite porphyroblasts that are altered around their margins (up to 4.5 mm), and magnetite up to 0.5 mm in diameter (Figure 3.5a). Fibrolite defines a lineation. Quartz does not show undulose extinction. Anhedral biotite has brown to orange pleochroism, contains pleochroic halos and is associated with Fe–Ti oxides at its margins. K-feldspar is anhedral and up to 1 mm across. Secondary muscovite cross-cuts biotite crystals, and sericite alteration suggests post-peak alteration. The interpreted peak metamorphic assemblage (M_1) is sillimanite-cordierite-biotite-magnetite-K-feldspar-quartz-plagioclase-ilmenite-melt.

GSWA 219742: sillimanite–biotite pelitic gneiss

This fine- to coarse-grained rock contains conspicuous porphyroblasts of prismatic sillimanite minor patches of leucosome (Figure 3.4b). In outcrop, the rock is not obviously deformed and shows no signs of retrogression. The gneiss is layered (probably reflecting relict bedding) with the sillimanite occurring in the thicker horizons. In thin section this sample contains both fibrolitic and prismatic sillimanite. Fibrolite defines a weak foliation (D_1) that wraps around anhedral biotite porphyroblasts (up to 4 mm) (Figure 3.5b). Prismatic sillimanite cross cuts fibrolite and appears to be randomly oriented. Biotite, muscovite and plagioclase crystals have embayed edges. Fine-grained aggregates of pinitite are interpreted to be pseudomorphs after cordierite (Figure 3.5c). Very rare grains of anhedral garnet occur in association with biotite (Figure 3.5d–e). Equigranular quartz crystals do not appear to be recrystallised and rarely display undulose extinction. Ilmenite crystals are distributed more-or-less evenly throughout the sample. Secondary tourmaline overprints biotite. Large plates of randomly oriented muscovite are interpreted to be secondary, probably replacing K-feldspar. The peak metamorphic assemblage (M_1) is sillimanite–biotite–cordierite–K-feldspar–plagioclase–quartz–ilmenite–melt. Rare anhedral grains of garnet are interpreted to have grown during the prograde evolution.

GSWA 216533: garnet–biotite–epidote pelitic gneiss

In outcrop, the sample is characterised by a gneissic layering and subparallel leucocratic veins (Figure 3.4c). The metamorphic foliation trends $241^\circ/30^\circ$ (SE). In thin section, this sample has a well-developed foliation defined by biotite that wraps garnet porphyroblasts (Figure 3.5f). The gneissic fabric is defined by alternating layers of biotite and elongate recrystallised quartz. The rock mainly comprises biotite, quartz, muscovite and garnet with minor epidote and ilmenite, and trace plagioclase, with accessory monazite. Garnet porphyroblasts (up to 0.5 mm) are euhedral to subhedral, the latter showing embayed edges. Randomly-oriented inclusions within garnet cores consist of quartz, muscovite and biotite whereas epidote inclusions occur in garnet rims. Late alteration to chlorite post-dates the peak metamorphic assemblage (M_1) of garnet–biotite–quartz–epidote–muscovite–plagioclase–ilmenite.

P01081: quartz–muscovite–tourmaline pelitic schist

This sample is a quartz–muscovite–tourmaline pelitic schist (Figure 3.4d). In thin section it consists of quartz and muscovite, with minor tourmaline and plagioclase and

accessory Fe-oxides. Rare plagioclase crystals are subhedral to anhedral, range from 1 to 4 mm in length and are partially sericitised. Muscovite is euhedral to anhedral and up to 4 mm. Quartz crystals are typically ~1mm in size and also occur as smaller recrystallised aggregates; both varieties shows undulose extinction. Quartz and muscovite are intergrown, suggesting they replace K-feldspar. The tourmaline is typically subhedral and is similar in size to the smaller quartz and muscovite crystals.

P16877: quartz–biotite–muscovite pelitic schist

In the field the schist forms a green sub-crop (Figure 3.4e) and consists of muscovite, quartz, biotite and sericite with accessory tourmaline. The schist is a protomylonite with a well-developed S–C fabric (S₁ or S₂).

GSWA 216538: biotite–muscovite–tourmaline pelitic gneiss

This sample is a metre-scale inclusion of deformed pelitic gneiss within a leucocratic monzogranite (GSWA 219741) (Figure 3.4f). This pelitic gneiss has a well-defined biotite foliation (S₁) alternating with layers of elongate and tabular quartz surrounded by a fine-grained groundmass of sericite. Biotite also occurs as relict porphyroblasts up to 4.5 mm long. Deformed muscovite porphyroblasts (up to 8 mm long) are aligned with the fabric. Prismatic tourmaline crystals (up to 4 mm long) are intergrown with quartz and are also aligned with the foliation. Secondary chlorite and sericite indicate some post-peak retrogression.

3.6 Analytical methods

3.6.1 In situ SHRIMP U–Pb monazite and xenotime geochronology

For six pelitic samples (P01081, P16877 and GSWA 216533, 216338, 219742 and 219749) and three granitic samples (P01085 and GSWA 195890, 219741) polished thin sections were imaged using a scanning electron microscope (SEM) in back-scattered electron (BSE) mode fitted with an energy dispersive X-ray spectrometer (EDS) to identify suitable monazite and xenotime crystals for *in situ* SHRIMP geochronology. Monazite and xenotime crystals >10 µm across were drilled out in 3 mm-diameter plugs and cast in a several 25 mm epoxy mounts. In all sessions the reference standards for Pb/U and Pb/Th calibrations and for ²⁰⁷Pb/²⁰⁶Pb fractionation monitoring were in separate mounts, which were cleaned and Au-coated together with the sample mounts to ensure consistent conductivity.

U–Pb analyses of monazite were conducted using a SHRIMP II ion microprobe in the John de Laeter Centre at Curtin University, Perth. Optical and BSE images were used to guide placement of the primary ion beam during analysis. SHRIMP analytical procedures followed established methods for monazite (Fletcher et al., 2010) and xenotime (Fletcher et al., 2000, 2004). During all analytical sessions, an O_2^- primary beam, with a spot size of 10 to 15 μm , was focussed through a 30 to 50 μm Kohler aperture with a beam intensity of 0.18 to 0.45 nA. The secondary ion beam was focused through a 100 μm collector slit onto an electron multiplier to produce mass peaks with flat tops and a mass resolution (1% peak heights) of $>5,200$. A post-collector retardation lens was used to reduce background counts produced from stray ions.

Monazite was analysed with a 13-peak run table as defined by Fletcher et al. (2010), which includes mass stations for the estimation of La, Ce and Nd (REEPO_2^+), and Y (YCeO^+). Monazite data were collected in sets of eight scans with a 5:1 unknown to standard ratio. Count times per scan for ^{204}Pb , background position 204.045, ^{206}Pb , ^{207}Pb , and ^{208}Pb were 10, 10, 10, 30, and 10s, respectively. The primary Pb/U and Pb/Th standard used was MAD 1 (known as FRENCH; Foster et al., 2000). Matrix effects on Pb/U data from U and Th were determined using Z2234 standard (Stern and Sanborn, 1998). Standard Z2908 (provided by Richard Stern) was used to monitor instrumental mass fractionation (IMF) of the instrument.

Some of the analysed monazite grains in this study show distinct alteration corona that indicate fluid-mediated alteration (Finger et al., 1998). However, as the aim of this study was to constrain the timing of peak metamorphism and magmatism rather than the processes of secondary alteration processes, we only analysed primary monazite.

Xenotime was analysed with a nine-peak run table and analytical procedure followed established methods (Fletcher et al., 2000, 2004). The primary Pb/U standard MG-1 (Fletcher et al., 2004) was used for Pb/U, Pb/Th and U abundance calibrations. The secondary standards were z6413 (XENO1: Fletcher et al., 2004; Stern and Rainbird, 2001) used for $^{207}\text{Pb}/^{206}\text{Pb}$ normalisation and used in conjunction with MG-1 for matrix corrections to Pb/U and Pb/Th, and z6410 (XENO2: Fletcher et al., 2004; Stern and Rainbird, 2001) used to monitor matrix effects.

Squid-2.50.11.02.03 software (Ludwig, 2009) was used for initial data reduction, including correction for common Pb. Common Pb corrections were based on individual measured ^{204}Pb abundances, assuming crustal common Pb at the approximate age of the

samples modelled by Stacey and Kramers (1975). Corrections for matrix effects in Pb/U and Pb/Th, from U and Th in xenotime (Fletcher et al., 2004) and from U, Th, Pb, and REE in monazite and for instrumental mass fractionation in $^{207}\text{Pb}/^{206}\text{Pb}$ (Fletcher et al., 2010) were applied to the sample data. Weighted mean dates are reported with 95% confidence limits, whereas individual analyses are presented with 1σ uncertainties.

3.6.2 Whole-rock geochemistry

Whole-rock geochemical analyses of granitic and pelitic samples, including loss on ignition (LOI), were determined by X-ray fluorescence (XRF) spectroscopy at Intertek-Genalysis Australia or at ALS Chemex, Australia by the Geological Survey of Western Australia. All data and additional analytical details are available from the Geological Survey of Western Australia's WACHEM database¹. The data were used to determine zircon saturation temperatures and to determine the alumina saturation index (ASI). Pelitic samples were analysed specifically to constrain bulk compositions for use in phase equilibrium modelling.

The granites display a range of SiO_2 compositions (62.9–74.0% wt %), with 94% having >65 wt% SiO_2 (Table 3.2). The granites are generally peraluminous (i.e., $\text{ASI} = \text{molar Al}_2\text{O}_3/(\text{CaO} + \text{Na}_2\text{O} + \text{K}_2\text{O}) > 1$ (Appendix B, Figure B.1); Chappell, 1999; Scaillet et al., 2016; Zen, 1986)—most have ASI values that cluster tightly between 1.12 and 1.20, but two samples have much higher values of 1.55 and 1.61 (Table 3.2). All but one sample has Zr contents between 70 and 222 ppm—one samples outside this range has 316 ppm Zr (Table 3.2).

3.7 Results

3.7.1 U–Pb monazite and xenotime geochronology

The results are presented as two groups: first granitic rocks and then pelites. The results are discussed in chronological order rather than by the geochronometer used. Figure 3.6 contains SEM images of analysed monazite and xenotime grains; Figure 3.7 consists of U–Pb monazite concordia diagrams for the granitic rocks, Figure 3.8 consists of U–Pb monazite and xenotime concordia diagrams for the pelitic rocks.

¹ (<http://geochem.dmp.wa.gov.au/geochem/>)

Table 3.2 Whole-rock geochemistry data for Mangaroon Zone Durlacher Supersuite granite samples, from this study and published data (GSWA 2016b).

Sample	195890 ^b	195888 ^c	208365 ^c	216532 ^c	88410 ^c	195887 ^c	169092 ^c	178030
Rock Type	<i>Ms–bt meta-onzograniite</i>	<i>Bt porphyritic monzogranite</i>	<i>Bt meta-granodiorite</i>	<i>Bt porphyritic monzogranite</i>	<i>Ms–bt monzogranite</i>	<i>Tur monzogranite</i>	<i>Bt–ms monzogranite</i>	<i>Bt granodiorite</i>
<i>wt%</i>								
SiO ₂	-	67.40	65.09	67.43	73.99	72.90	73.85	62.93
TiO ₂	-	0.58	0.64	0.51	0.14	0.19	0.19	0.81
Al ₂ O ₃	-	16.00	15.26	15.16	13.57	14.85	13.86	16.00
Fe ₂ O ₃ ^T	-	5.72	5.29	4.67	1.60	1.69	1.593	7.232
FeO	-	5.14	3.08	4.20	1.17	1.52	1.08	3.8
MgO	-	1.79	1.74	1.36	0.33	0.39	0.39	2.12
MnO	-	0.07	0.11	0.11	0.06	0.05	0.06	0.17
CaO	-	1.36	3.01	2.31	1.00	0.91	0.81	3.39
Na ₂ O	-	1.79	2.60	2.76	2.60	2.98	2.86	2.35
K ₂ O	-	4.19	3.64	3.97	5.46	5.41	5.21	3.91
P ₂ O ₅	-	0.13	0.22	0.20	0.10	0.20	0.24	0.24
LOI	-	1.50	1.87	1.02	1.03	0.89	0.85	1.03
A/CNK ^a		1.61	1.12	1.16	1.13	1.20	1.17	1.12
<i>ppm</i>								
Zr	-	159.0	181.0	161.0	93.0	95.0	70.0	191.0
Age (Ma)	1695 ± 9 [^]	1689 ± 4 [*]	1689 ± 6 [*]	1688 ± 4 [*]	1688 ± 7 [*]	1682 ± 9 [*]	1681 ± 10 [*]	1678 ± 6 [*]

Sample	178027 ^c	169053 ^c	178029 ^c	178028 ^c	169062 ^c	216531 ^c	169060 ^c	169059 ^c	169055 ^c	219741 ^b
Rock Type	<i>Bt-ms</i> granodiorite	<i>Bt-ms</i> monzogranite	<i>Bt</i> monzogranite	<i>Bt-ms</i> syenogranite dyke	Porphyritic syenogranite	<i>Ms-tur</i> monzogranite	Porphyritic syenogranite	<i>Ms-bt</i> monzogranite	<i>Bt-ms</i> monzogranite	<i>Tur-ms</i> monzogranite
wt%										
SiO ₂	65.38	68.44	70.50	70.89	70.08	72.92	72.18	71.85	72.15	-
TiO ₂	0.69	0.46	0.25	0.38	0.49	0.19	0.37	0.32	0.30	-
Al ₂ O ₃	15.99	15.00	14.44	14.31	14.71	14.29	14.18	14.69	14.13	-
Fe ₂ O ₃ ^T	5.12	4.97	2.123	2.728	2.149	1.67	2.80	1.82	2.15	-
FeO	2.79	2.25	1.43	1.72	1.13	1.50	1.76	0.80	1.26	-
MgO	1.21	1.39	0.48	0.75	0.61	0.39	0.68	0.40	0.41	-
MnO	0.10	0.09	0.07	0.07	0.05	0.05	0.06	0.04	0.06	-
CaO	2.70	1.06	0.80	0.79	1.34	0.87	1.92	0.96	0.94	-
Na ₂ O	2.89	1.84	2.45	1.92	2.35	3.10	3.19	2.55	2.47	-
K ₂ O	3.67	4.36	6.23	6.73	6.25	5.26	3.66	6.08	5.66	-
P ₂ O ₅	0.11	0.14	0.21	0.25	0.30	0.09	0.13	0.26	0.21	-
LOI	2.30	2.36	2.49	1.20	1.02	0.71	0.91	1.00	1.53	-
A/CNK ^a	1.17	1.55	1.18	1.20	1.13	1.15	1.12	1.17	1.19	-
ppm										
Zr	112.0	131.0	147.0	222.0	316.0	126.0	167.0	174.0	140.0	-
Age (Ma)	1677 ± 5*	1677 ± 6#*	1675 ± 11*	1674 ± 8*	1674 ± 8*	1673 ± 4*	1673 ± 15*	1660 ± 9*	1659 ± 10*	1659 ± 13 [^]

Notes:

^a A/CNK = molar Al₂O₃/(CaO+Na₂O+K₂O); ^b this study; ^c = published data (GSWA 2016b);

- = not analysed for whole-rock geochemistry; * = zircon age; ^ = monazite age; # age recalculated from Nelson 2002; Ms = muscovite; bt = biotite; tur = tourmaline.

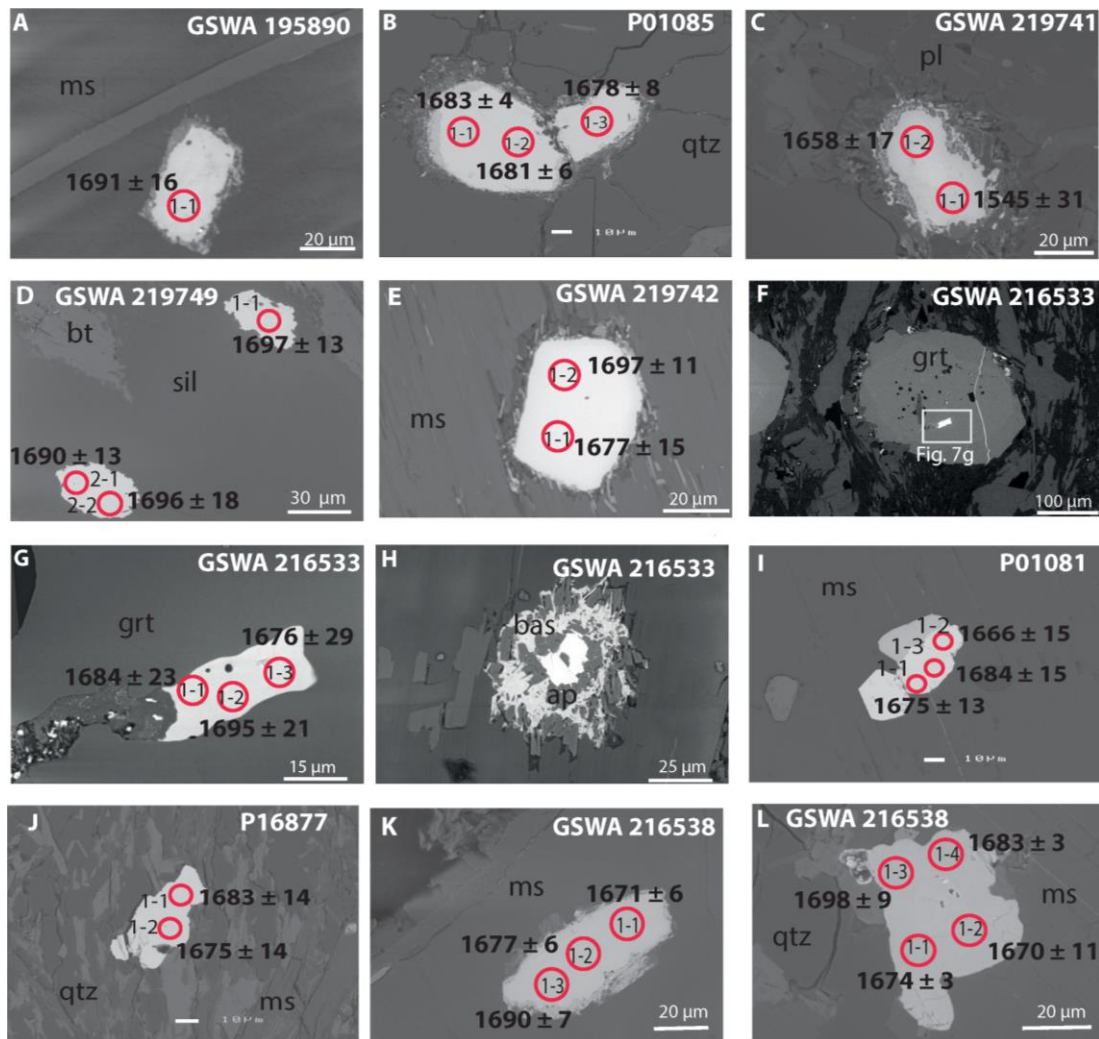


Figure 3.6 Back-scattered electron (BSE) images of representative monazites and xenotime from samples analysed *in situ*. A. GSWA 195890 (muscovite–biotite monzogranite) monazite grain 1612A. B. P01085 (biotite–muscovite syenogranite) monazite crystal C. C. GSWA 219741 (tourmaline–muscovite monzogranite) monazite crystal C. D. GSWA 219749 (cordierite–sillimanite pelitic migmatite) crystals H. E. GSWA 219742 (sillimanite–biotite pelitic gneiss) monazite crystal D. F. GSWA 216533 (garnet–biotite–epidote pelitic gneiss), garnet crystal. G. GSWA 216533 monazite inclusion within garnet crystal, 1503D, showing an alteration pathway to the left. H. GSWA 216533 example of altered monazite surrounded by apatite corona and bastnaesite (bas) rim. I. P01081 (quartz–muscovite–tourmaline schist) monazite crystal G. J. P16877 (quartz–biotite–muscovite schist) monazite crystal A. J. GSWA 216538 (biotite–muscovite–tourmaline pelitic gneiss) monazite crystal D. K. GSWA 216538 xenotime crystal A. Red circles denote SHRIMP spot locations. Ages are indicated in black with errors indicated at 95% confidence level. Analytical data are presented in Appendix B, Table B.1.

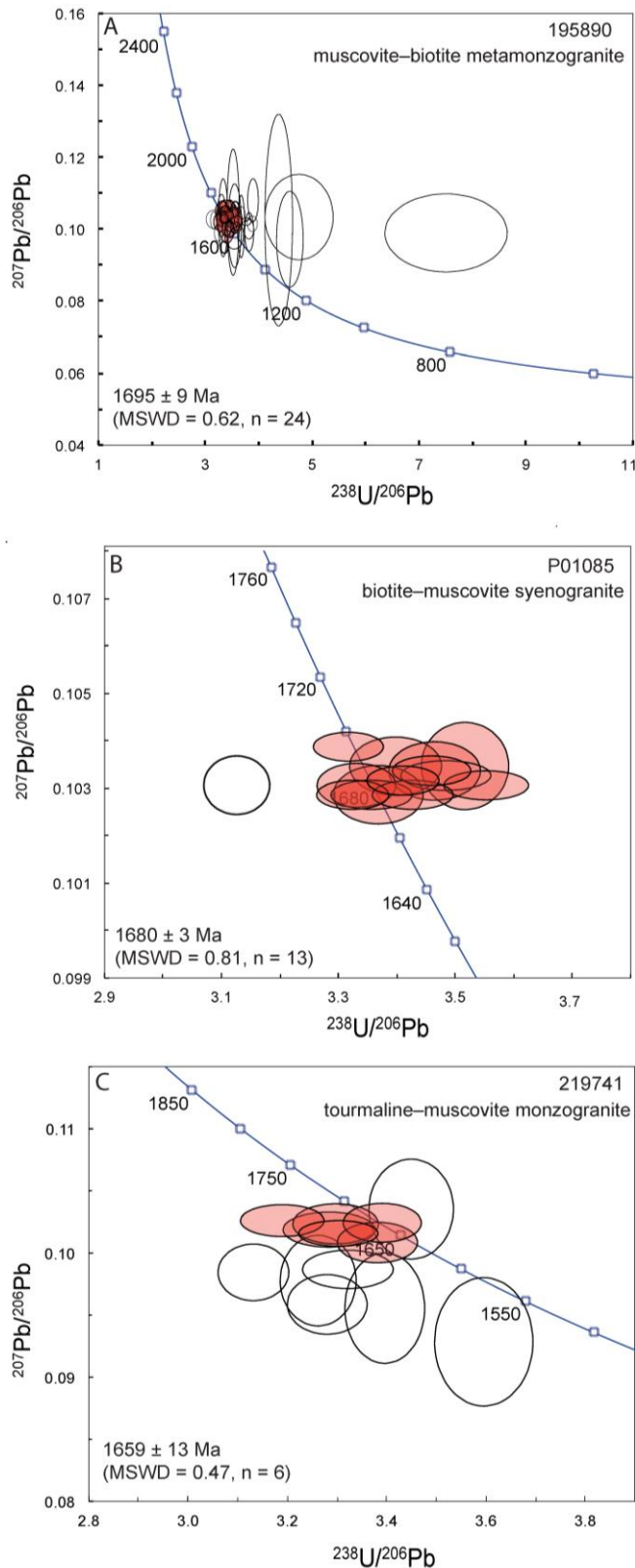


Figure 3.7 U-Pb concordia diagrams for monazite from granitic samples A-C.

Data plotted with 68.3% error ellipses; red ellipses indicate analyses used to calculate the age of the sample, and unfilled ellipses indicate data excluded due to discordance >5%, high common Pb, or as statistical outliers. Weighted mean dates are based on $^{207}\text{Pb}/^{206}\text{Pb}$ ratios and quoted with 95% confidence intervals.

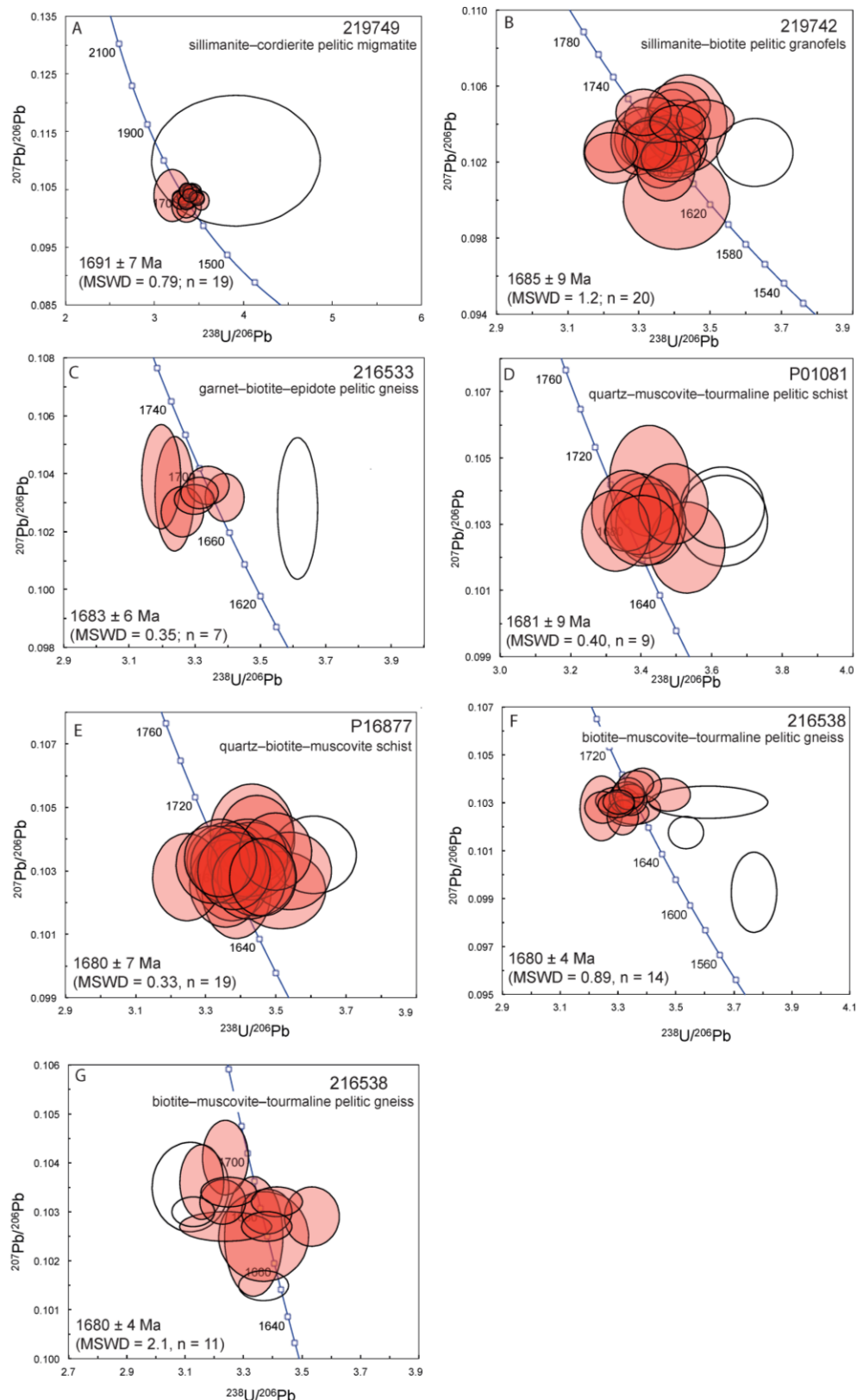


Figure 3.8 U–Pb concordia diagrams for monazite (A–F) and xenotime (G) from pelitic samples. Data plotted with 68.3% error ellipses; red ellipses indicate analyses used to calculate the age of the sample; unfilled ellipses indicate data excluded due to discordance >5% or as statistical outliers. Weighted mean dates are based on $^{207}\text{Pb}/^{206}\text{Pb}$ ratios and quoted with 95% confidence intervals.

Granitic rocks

GSWA 195890: muscovite-biotite metamonzogranite

The monazite grains are anhedral to subhedral with some crystals showing retrograde corona (Figure 3.6a). The crystals range in size from 30 to 80 μm and occur as inclusions in quartz, plagioclase, and muscovite and within the groundmass. Fifty-four analyses were carried out on 29 monazite crystals (Appendix B). Twenty-six analyses are excluded from the final age calculation due to high common ^{206}Pb (>1 wt%) and/or >5% discordance. A further four analyses are statistical outliers (i.e., >2 standard deviations from the mean) and are not considered further. The remaining twenty-four analytical spots show Th concentrations typically ranging from 50,000 to 93,000 ppm with one analysis at 26,000 ppm, whereas U concentrations cluster into three groups: 300–1300 ppm (fourteen analyses), 2000–3000 ppm (eight analyses) and 5000–6000 ppm (two analyses). The Th/U ratios range from 10 to 198. The 24 analyses yield $^{207}\text{Pb}/^{206}\text{Pb}$ dates between 1732 and 1640 Ma with a weighted mean of 1695 ± 9 Ma (MSWD = 0.62), which is interpreted as the crystallisation age of the monzogranite (Figure 3.7a).

P01085: biotite–muscovite syenogranite

The monazite crystals are anhedral to subhedral, and range in size from 30 to 60 μm . Some have secondary apatite and/or retrograde coronas around their margins (Finger et al., 1998; Figure 3.6b). The monazites occur both in the matrix and as inclusions in quartz. Fourteen analyses were conducted on five monazite crystals (Appendix B). Excluded from the age calculations is one analysis >5% discordant that likely represents an overlap between unaltered monazite and the retrograde corona. The remaining 13 analyses have U concentrations of 1100–4600 ppm and tightly-clustered Th contents of 69,000–94,000 ppm, with Th/U ratios from 15 to 72. The 13 analyses yielded $^{207}\text{Pb}/^{206}\text{Pb}$ dates between 1694 Ma and 1676 Ma and a weighted mean of 1680 ± 3 Ma (MSWD = 0.81), which is interpreted as the crystallisation age of the syenogranite (Figure 3.7b).

GSWA 219741 tourmaline–muscovite monzogranite

The monazite grains are typically anhedral, and some have retrograde coronas (Figure 3.6c). The crystals range in size from 25 to 70 μm and occur in the groundmass and as inclusions in quartz, plagioclase, and muscovite. Thirteen analyses were carried out on seven monazite crystals (Appendix B). Two analyses of a single crystal have high common ^{206}Pb contents (>1%) and were not considered in the final age calculation, nor

were a further five analyses >5% discordant. U and Th concentrations of the six remaining analyses are 750–7750 ppm and 13,000–64,500 ppm, respectively, with Th/U ratios of 8–35. The main group of six analyses yielded $^{207}\text{Pb}/^{206}\text{Pb}$ dates between 1671 and 1639 Ma, with a weighted mean of 1659 ± 13 Ma (MSWD = 0.47), which is interpreted as the crystallisation age of the monzogranite (Figure 3.7c).

Pelitic rocks

GSWA 219749: cordierite–sillimanite pelitic migmatite

Monazite crystals in this sample are unzoned, anhedral to subhedral, and range in size from 15 to 50 μm . They occur as inclusions in quartz, sillimanite, muscovite, and biotite and are also interstitial to the main silicate phases (Figure 3.6d). Twenty analyses were carried out on 11 monazite crystals (Appendix B). Excluded from the age calculations is one discordant analysis (>5%) that overlapped an inclusion. The remaining 19 analyses have U concentrations of 1800 to 4100 ppm and consistently high Th concentrations (35,900–54,000 ppm), with Th/U ratios of 11–24. They yielded $^{207}\text{Pb}/^{206}\text{Pb}$ dates between 1710 Ma and 1652 Ma, and a weighted mean of 1691 ± 7 Ma (MSWD = 0.79) interpreted as the timing of monazite growth during migmatisation (Figure 3.8a).

GSWA 219742: sillimanite–biotite pelitic gneiss

Subhedral monazite crystals range from 35 to 60 μm and occur as inclusions in quartz, biotite, plagioclase and muscovite. Fe-oxides commonly occur around the margins of the monazite crystals (Figure 3.6e). Some grains have a corona of apatite (e.g. Finger et al., 1998), for which a smaller spot size was used to avoid these retrograde areas. Twenty-one analyses were carried out on 11 monazite crystals (Appendix B). Th concentrations range from 39,000 to 60,000 ppm, and U concentrations are mostly 550–5000 ppm (17 analyses) with four analyses having much higher concentrations (8000–10,100 ppm). Th/U ratios show a wide range from 4 to 90. One analysis with >5% discordance was excluded from the final age calculation. The 20 analyses yield $^{207}\text{Pb}/^{206}\text{Pb}$ dates between 1713 and 1624 Ma, and a weighted mean of 1685 ± 9 Ma (MSWD = 1.2) interpreted as the timing of monazite growth during metamorphism (Figure 3.8b).

GSWA 216533: garnet–biotite–epidote pelitic gneiss

The monazite crystals range in size from 15 to 40 μm , are anhedral to euhedral, and occur as inclusions in quartz and in garnet cores, and within the matrix (Figure 3.6f–h). Monazite inclusions are unzoned and unaltered. In contrast, monazite crystals in the matrix are highly altered to bastnaesite (Figure 3.6h) and were unsuitable for SHRIMP analysis due to the small size of surviving monazite ($<10 \mu\text{m}$). Eight analyses were carried out on five monazite crystals (Appendix B). Excluded from the age calculations is one discordant analysis ($>5\%$ discordance). The seven remaining analyses have tightly-clustered U and Th concentrations that vary from 1600 to 5000 ppm and 23,000–48,650 ppm, respectively, and Th/U ratios of 8–17. They yield $^{207}\text{Pb}/^{206}\text{Pb}$ dates between 1695 and 1673 Ma, and a weighted mean of $1683 \pm 6 \text{ Ma}$ (MSWD = 0.35) interpreted as the age of monazite growth during metamorphism (Figure 3.8c).

P01081: quartz–biotite tourmaline schist

The monazites are unzoned, mainly subhedral, and range in size from 20 to 70 μm . They occur as inclusions in quartz and muscovite and do not appear to be preferentially aligned with the fabric (Figure 3.6i). Some crystals show secondary corona. Eleven analyses were carried out on five monazite crystals (Appendix B). Excluded from the age calculations are two analyses that are $>5\%$ discordant. The remaining nine analyses show a large spread of U and Th concentrations (700–14,100 ppm and 2400–68,500 ppm, respectively), and Th/U ratios of 1–22. They yield $^{207}\text{Pb}/^{206}\text{Pb}$ dates between 1702 and 1666 Ma and a weighted mean of $1681 \pm 9 \text{ Ma}$ (MSWD = 0.44) interpreted as the timing of monazite growth during metamorphism (Figure 3.8d).

P16877: quartz–muscovite–biotite schist

The monazites are unzoned, mainly anhedral, range in size from 15 to 40 μm , and are hosted in muscovite and quartz (Figure 3.6k). There is no obvious alignment with the enclosing minerals. Twenty analyses were carried out on 13 monazite crystals (Appendix B). One analysis $>5\%$ discordant was excluded from the final age calculation. The remaining 19 analyses indicate U concentrations of 800–7700 ppm, bimodal Th concentrations of 15,000–18,000 ppm and 23,000–45,000 ppm, and Th/U ratios of 2–32. They yield $^{207}\text{Pb}/^{206}\text{Pb}$ dates between 1701 and 1667 Ma, and a weighted mean of $1680 \pm 7 \text{ Ma}$ (MSWD = 0.33) interpreted as the timing of monazite growth during metamorphism (Figure 3.8e).

GSWA 216538: biotite–muscovite–tourmaline pelitic gneiss

Both monazite and xenotime from this sample were analysed. Anhedral to subhedral monazite crystals range from 20 to 80 μm and occur as inclusions in quartz and muscovite, with one matrix grain (Figure 3.6k). Some crystals show resorption around their margins. Seventeen analyses were carried out on 10 monazite crystals (Appendix B). Th concentrations range from 36,500 to 58,500 ppm and U concentrations between 2700 and 8300 ppm, with Th/U ratios of 6–19. Two analyses with >5% discordance were excluded from the final age calculation, as was one young outlier with a $^{207}\text{Pb}/^{206}\text{Pb}$ age of 1656 ± 8 Ma (1602B.1-2). However, this latter outlier may record contact metamorphism associated with the intrusion of the granite host of this gneissic inclusion (sample GSWA 219741). The remaining 14 analyses yield $^{207}\text{Pb}/^{206}\text{Pb}$ dates between 1692 and 1668 Ma, and a weighted mean of 1680 ± 4 Ma (MSWD = 0.89) interpreted as the timing of monazite growth during metamorphism (Figure 3.8f).

Unzoned, unaltered anhedral to subhedral xenotime crystals are 20 to 60 μm in size, and typically occur as inclusions in muscovite and rarely as matrix grains (Figure 3.6l). Fourteen analyses were carried out on six xenotime crystals (Appendix B). Uranium concentrations range from 9700 to 17,800 ppm and Th concentrations between 1500 and 2700 ppm, with Th/U ratios of 0.1–0.3. Two analyses showing >5% discordance were excluded from the final age calculation, as was one young outlier with a $^{207}\text{Pb}/^{206}\text{Pb}$ age of 1653 ± 4 Ma (1604G.1-2). The 11 remaining analyses yield $^{207}\text{Pb}/^{206}\text{Pb}$ dates between 1698 and 1670 Ma, and a weighted mean of 1680 ± 4 Ma (MSWD = 2.1) interpreted as the timing of xenotime growth during metamorphism (Figure 3.8g).

3.8 Phase equilibria modelling

Repeated episodes of reworking and reactivation affected rocks of the Mangaroon Zone, making it challenging to find suitable samples for P – T investigations. However, two samples (GSWA 219749 and 219742) from the Pooranoo Metamorphics (Figure 2.2) preserve low-variance mineral assemblages best suited to constrain P – T conditions. Based on the presence of leucosomes, samples GSWA 219749 (sillimanite–cordierite pelitic migmatite) and GSWA 219742 (sillimanite–biotite pelitic gneiss) are both interpreted to be former melt-bearing rocks and to have equilibrated above the solidus.

Isochemical phase diagrams (pseudosections) were calculated based on the bulk compositions of the two samples (Table 3.3). FeO contents were analysed by titration

and Fe₂O₃ was calculated by difference. The H₂O content assumes all LOI as H₂O. As the rocks are interpreted to have been melt-bearing, and likely lost melt at or near the metamorphic peak, their modelled bulk compositions are only valid for constraining the peak and post-peak evolution of these samples. Phase equilibrium modelling used THERMOCALC 3.40i and the internally consistent dataset of Holland and Powell (2011) (tcds62 generated on 6 February 2012), and were calculated in the system MnO–Na₂O–CaO–K₂O–FeO–MgO–Al₂O₃–SiO₂–H₂O–TiO₂–Fe₂O₃ (MnNCKFMASHTO), using the *a-x* models from White et al. (2014).

Table 3.3 Whole-rock chemistry used to construct *P–T* pseudosections for samples GSWA 219742 and 219749.

Sample	GSWA 219742	GSWA 219749
<i>XRF whole rock compositions (wt%)</i>		
SiO ₂	57.24	58.56
TiO ₂	0.78	0.83
Al ₂ O ₃	21.37	21.81
Fe ₂ O ₃ ^(a)	4.78	1.93
FeO ^(a)	4.78	6.24
MnO	0.23	0.17
MgO	2.72	2.93
CaO	0.61	0.34
Na ₂ O	0.92	0.62
K ₂ O	3.7	4.48
LOI	1.85	0.89
Total	98.98	98.80
<i>Normalised molar proportions used for phase equilibria modelling^(b)</i>		
SiO ₂	63.22	65.59
TiO ₂	0.65	0.70
Al ₂ O ₃	13.91	14.39
O	1.99	0.81
FeO	4.42	5.84
MnO	0.22	0.16
MgO	4.48	4.89
CaO	0.72	0.41
Na ₂ O	0.99	0.67
K ₂ O	2.61	3.20
H ₂ O	6.81	3.32
Total	100.00	100.00

Notes:

^(a) FeO analysed by Fe²⁺ titration; Fe₂O₃ calculated by difference

^(b) final compositions used for P-T pseudosection, based on adjusted FeO:Fe₂O₃

3.8.1 Results

GSWA 219749: sillimanite–cordierite pelitic migmatite

The calculated solidus lies between 670–720°C and 2–8 kbar. The interpreted peak metamorphic assemblage of cordierite–sillimanite–magnetite–biotite–K-feldspar–quartz–plagioclase–ilmenite–melt is stable at 665–755°C and 2.7–4.3 kbar (Figure 3.9a). The presence of sillimanite provides a lower temperature constraint, whereas the absence of garnet bounds the inferred peak assemblage field to higher pressure. The presence of biotite and cordierite provide upper and lower temperature limits, respectively.

GSWA 219742: sillimanite–biotite–pelitic gneiss

The calculated solidus lies between 670–700°C and 2–12 kbar. The interpreted metamorphic assemblage of sillimanite–biotite–cordierite–K-feldspar–plagioclase–quartz–ilmenite–melt is stable in a narrow field that extends from around 4 kbar at ~675°C to around 7.5 kbar at 850°C (Figure 3.9b). Although the modelled bulk composition is not strictly valid for constraining the prograde evolution due to likely melt loss, the presence of rare grains of anhedral, partially resorbed garnet, suggests higher pressures than those recorded at the peak during the prograde history of this sample (Figure 3.9b). This implies a broad clockwise metamorphic P – T path, as illustrated in Figure 3.9b.

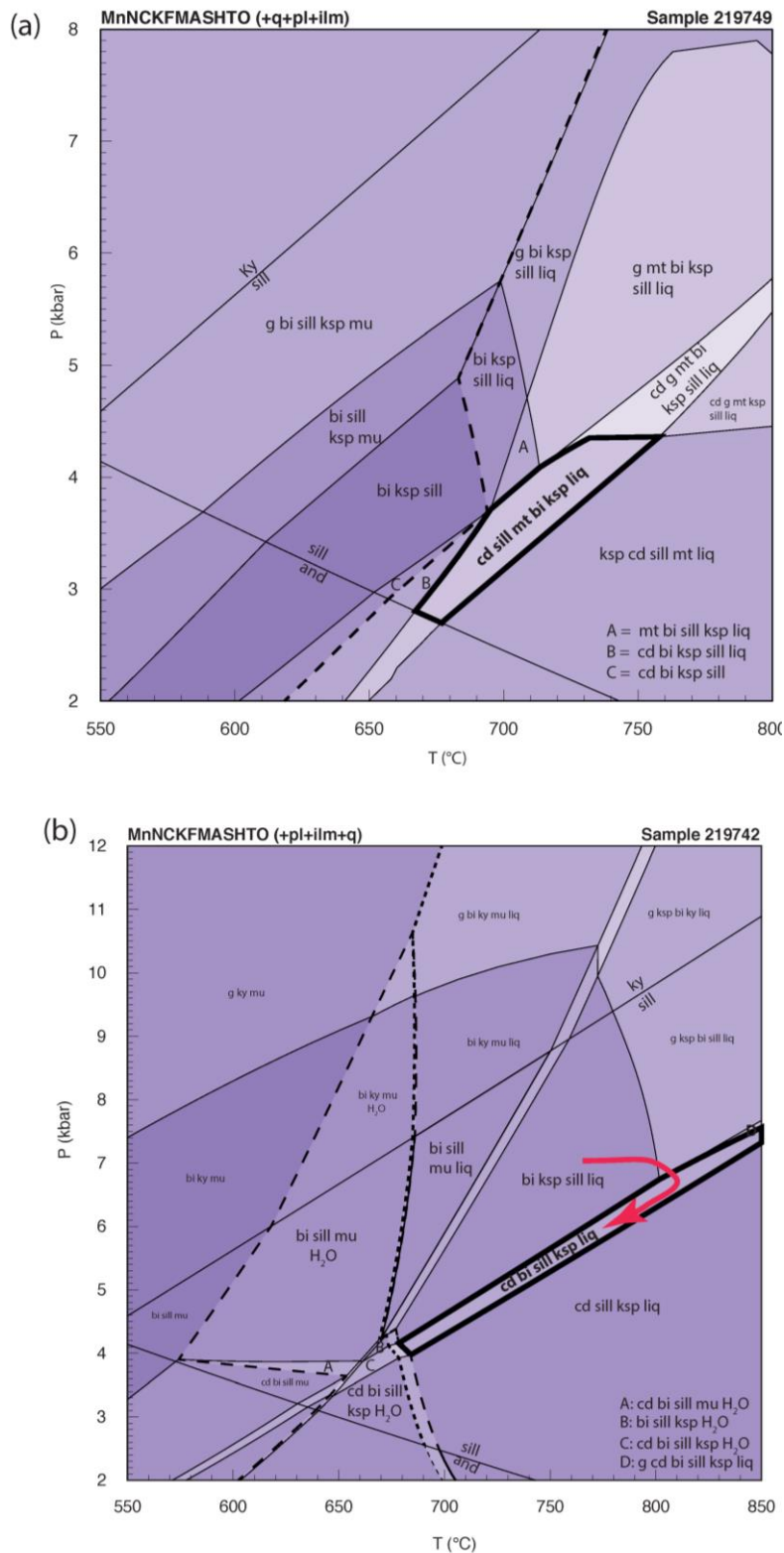


Figure 3.9 *P–T* pseudosections for (a) GSWA 219749 and (b) GSWA 219742. Peak metamorphism field is outlined by thick lines; solidus shown by thick dashed lines; H₂O field shown in (b) by thick dotted line.

Abbreviations used on pseudosections: and, andalusite; bi, biotite; cd, cordierite; g, garnet; H₂O, H₂O; ilm, ilmenite; ksp, K-feldspar; ky, kyanite; mt, magnetite; liq, melt; mu, muscovite; pl, plagioclase; q, quartz; sill, sillimanite.

3.9 Discussion

Prior to the study of Sheppard et al. (2005), the deformation fabrics and magmatism observed in the Mangaroon Zone were attributed to the 1820–1770 Ma Capricorn Orogeny. However, subsequent field mapping and SHRIMP U–Pb zircon geochronology in the southern part of the Mangaroon Zone, revealed an orogenic event at c. 1680–1620 Ma (Sheppard et al., 2005). Although this study defined the approximate timing of the Mangaroon Orogeny, there remains significant uncertainty on the timing and duration of metamorphism and magmatism, and how these processes relate to each other.

3.9.1 Duration of magmatism associated with the Mangaroon Orogeny

Before this study, the age range for the intrusion of the Durlacher Supersuite was 1680–1620 Ma (Sheppard et al., 2005). The monazite geochronology demonstrates that magmatism commenced earlier than previously thought, at 1695 ± 9 Ma (GSWA 195890). Furthermore, recent U–Pb geochronology on zircon from granites yields crystallisation ages of 1689 ± 6 Ma (GSWA 208365: Wingate et al., 2017), 1689 ± 4 Ma (GSWA 195888: Wingate et al., 2018) and 1688 ± 4 Ma (GSWA 216532: Wingate et al., 2019a). Combined, these data confirm that magmatism began earlier than 1680 Ma (Figure 3.10) and place a new age constraint on the minimum depositional age of the protoliths of the Pooranoo Metamorphics of >1695 Ma. Because of Neoproterozoic overprinting (Fig. 11 of Piechocka et al., 2018) at the locality from which sample GSWA 195890 was collected, it is difficult to assign with any certainty an age to the well-developed fabric formed during the Mangaroon Orogeny. Ar–Ar dating of biotite from the mylonite zone yielded a Neoproterozoic age interpreted as the timing of mylonite formation during fault reactivation (Piechocka et al., 2018).

Our new results combined with previously published zircon data (Table 3.2) show that magmatism in the Mangaroon Zone may have occurred in two pulses. The first episode likely occurred at 1695–1673 Ma, overlapping with D₁ deformation, with a second episode younger than 1660 ± 9 Ma (constrained by sample GSWA 169059, Table 3.2) that possibly accompanied D₂ deformation. The only published age for a presumed Durlacher Supersuite granite to lie outside of this 1695–1660 Ma range is the 1620 Ma age for the Discretion Granite (GSWA 142855; Nelson, 1998), located in the southernmost Capricorn Orogen (Figure 3.1). The isolated nature of this body, which intrudes the Yarlalweelor Gneiss Complex, and its anomalously young age, suggests it may be unrelated to the Mangaroon Orogeny. Therefore, magmatism in the Mangaroon

Zone lasted for less than 35 million years (1695–1660 Ma; Figure 3.10). However, recent $^{40}\text{Ar}/^{39}\text{Ar}$ mica geochronology, from a monzogranite yielded a c. 1640 Ma cooling age (Piechocka et al., 2018), and it may be possible that magmatism continued until as late as 1640 Ma.

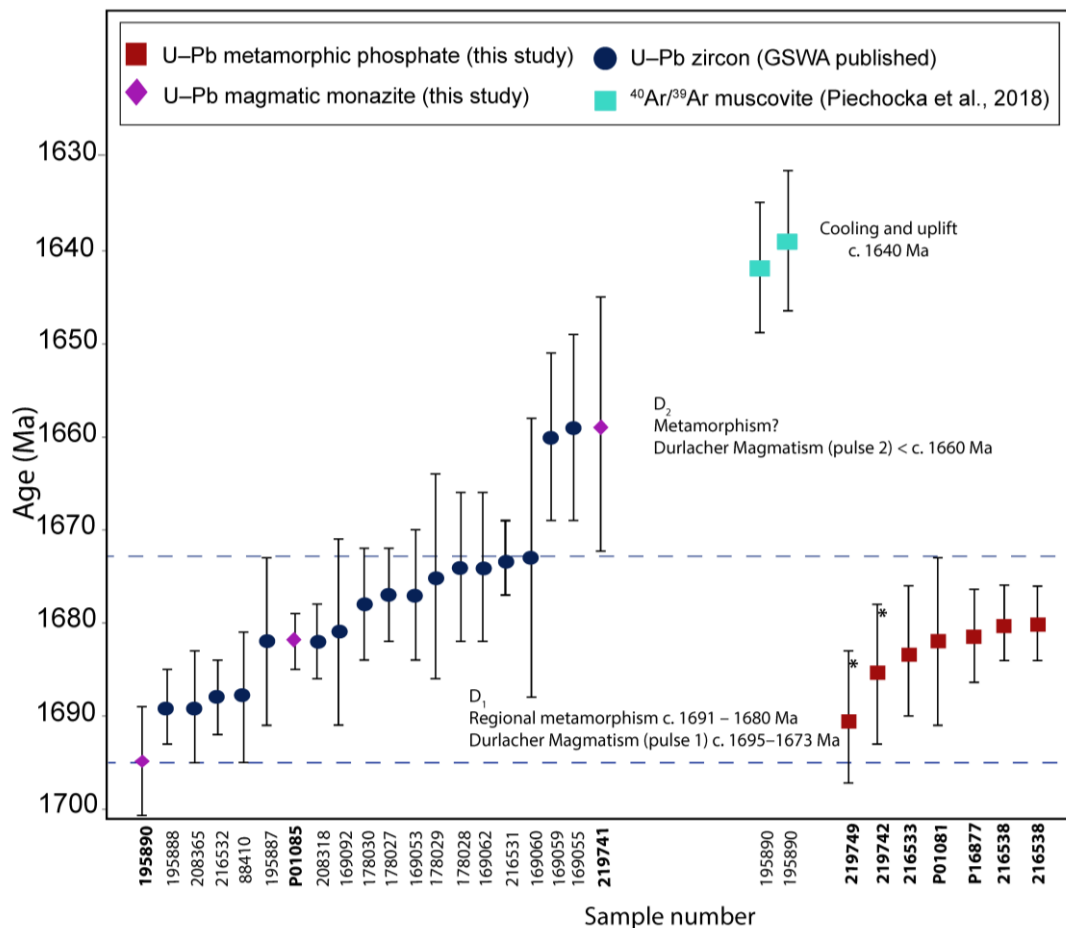


Figure 3.10 Compilation diagram of Mangaroon-age geochronology from the Mangaroon Zone. Includes results from this study and published data (GSWA 2016b). The data show that magmatism was initiated at 1695 Ma followed by upper crustal metamorphism at 1691 Ma. Magmatism continued for an additional 20 million years after peak metamorphism. $^{40}\text{Ar}/^{39}\text{Ar}$ mica ages of c. 1640 Ma are interpreted to indicate the timing of cooling and exhumation of the Mangaroon Zone crust. Sample numbers in bold indicate this study. Asterisks indicates samples used for P – T modelling. Blue dashed lines indicate the geochronology samples used to constrain magmatism associated with D_1 deformation.

3.9.2 P – T – t conditions of early metamorphism

Phase equilibrium modelling indicates low- P , high- T metamorphic conditions (Figure 3.9). In particular, the calculated peak field for sample GSWA 219749, at 665–

755 °C and 2.7–4.3 kbar is relatively well constrained and indicates that metamorphism occurred at relatively shallow crustal levels (<15 km depth) assuming no significant tectonic overpressure. The interpreted peak metamorphic assemblage of sillimanite–biotite–cordierite–K-feldspar–melt in sample GSWA 219742 suggests higher P – T conditions of ~800 °C, 6–7 kbar. The inferred presence of rare prograde garnet is consistent with some near-peak decompression and a clockwise P – T path (Figure 3.9b), although the amount of decompression is unconstrained.

3.9.3 Timing, duration and causes of metamorphism

The new phosphate geochronology from samples across the Mangaroon Zone show that peak metamorphism occurred at c. 1690 ± 7 Ma and continued until at least 1680 ± 4 Ma (Figure 3.10). The absence of younger (<1680 Ma) metamorphic phosphate growth suggests that regional metamorphism may have been relatively short-lived at around 10–20 million years (i.e., 1698–1676 Ma).

The oldest metamorphic monazite age of c. 1691 Ma comes from the cordierite–sillimanite migmatite (GSWA 219749, Figure 3.10). This sample defines an apparent thermal gradient of 175 to 240 °C/kbar (Figure 3.11), compared to an ambient thermal gradient calculated for the Gascoyne Province of ~46 °C/kbar (calculated at 1320 Ma; Fig. 8 of Korhonen and Johnson, 2015). Furthermore, in comparison to typical thermal gradients in the crust (Fig. 1 of Morrissey et al., 2014) the thermal gradient in the Mangaroon Zone can be considered anomalous. High thermal gradients are commonly associated with magmatism and significant extension (e.g., Smithies et al., 2011; Sandiford and Powell, 1986), or rapid exhumation of deep crustal rocks (e.g., Cooke and O’Brien, 2001). Our geochronology shows that metamorphism was coeval with magmatism at c. 1690 Ma.

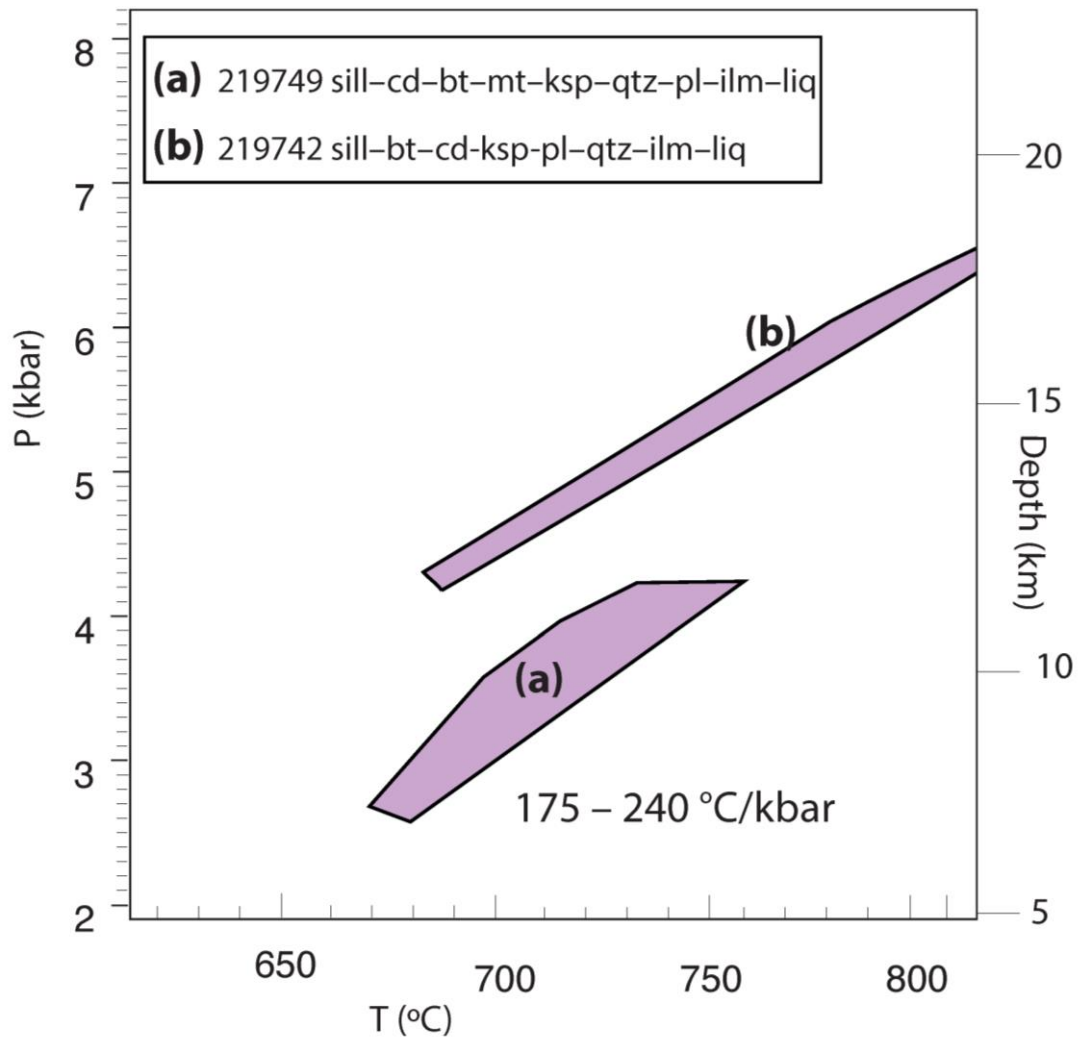


Figure 3.11 Summary diagram showing P - T pseudosections from GSWA 219742 and 219749 plotted in P - T space. Sample (b) indicates a higher prograde temperature than sample (a).

Although the geochronology, in this study, may initially point to short duration metamorphism, the absence of post c. 1680 Ma dates does not mean that metamorphism was not more protracted considering that magmatism continued until 1660 Ma. For example, monazite crystals in the matrix in sample GSWA 216533 (Figure 3.6h) were so altered such that they could not be dated. Thus, the lack of post-1680 Ma metamorphic ages could be due to pervasive retrogression by fluids released from later magmatism (related to D_2) and/or by fluids flowing through crustal-scale fault systems (e.g., Johnson et al., 2013), possibly during the later stages of D_1 or during D_2 . Furthermore, Sheppard et al. (2005) assigned the greenschist-facies schistosity to D_2 deformation, meaning the lower grade mineral assemblages and destruction of monazites in sample 216533 may have been the result of D_2 deformation.

There is some hint of a c. 1660 Ma metamorphic episode recorded in a deformed pelitic gneiss (GSWA 216538) that is intruded by tourmaline–muscovite monzogranite at 1659 ± 13 Ma (GSWA 219741) (Figure 3.4f). Sample GSWA 216538 yielded a single monazite analysis with an age of 1656 ± 8 (1σ) Ma and a single xenotime analysis with an age of 1653 ± 4 (1σ) Ma (GSWA 216538, Appendix B), which may reflect contact metamorphism associated with the intrusion of monzogranite (1659 ± 13 Ma; GSWA 219741), possibly during D2 deformation.

3.9.4 Temperatures and causes of granite emplacement

Zircon saturation temperatures were used to evaluate the emplacement temperatures of Durlacher Supersuite granites in the Mangaroon Zone. Zirconium contents in the analysed granites range from 70 to 316 ppm, with calculated temperatures ranging from 733 to 863 °C (Appendix B, Figure B.2), based on the *M* parameter of Watson and Harrison (1983). These results are also consistent with Miller et al. (2003), who demonstrated that granites with 80–150 ppm Zr record a mean temperature of 766 ± 24 °C and granites with 200–800 ppm Zr record a temperature mean 837 ± 48 °C. Field mapping in the Mangaroon Zone shows that granites account for >50% of the Mangaroon Zone (at surface) (Figure 3.2), and extend to at least 10 km depth (Johnson et al., 2013), but it is unclear whether the older or younger granites make up the greater proportion of the crust. These factors suggest that the heat required for metamorphism was in part derived from the granites.

The Durlacher Supersuite magmatism is characterised by melting and recycling of older crust (i.e., the 1820–1775 Ma Moorarie Supersuite) with no evidence for a significant mantle component (Fig. 4 of Johnson et al., 2017). The peraluminous nature of the Durlacher granites in the Mangaroon Zone suggests they also have a metasedimentary source (Table 3.2) and Johnson et al., (2017) suggested the Durlacher granites are likely to have been derived from partial melting of the Pooranoo Metamorphics, consistent with the age of xenocrystic zircon (Appendix B, Figure B.3).

Heat production values of crustal rocks in the Mangaroon Zone show that the source components are quite radiogenic, with average values of 3.5 and 4 uW/m³ (at 1.7 Ga) for the Pooranoo Metamorphics and the Moorarie Supersuite, respectively (F. J. Korhonen, 2018, personal communication). Thermal modelling of the Mesoproterozoic Gascoyne Province crust showed that it would take c. 140 million years to reach temperatures in excess of 650 °C at depths greater than 15 km (Fig. 8 of Korhonen and Johnson, 2015).

However, it is unclear whether the conditions during the Mesoproterozoic are applicable to the Mangaroon Orogeny. Nevertheless, in the Mangaroon Zone, at c. 1.7 Ga, anatexis of the Pooranoo Metamorphics (protoliths were deposited, buried and melted between c. 1758 and 1695 Ma) to generate the Durlacher Supersuite occurred at depths of less than about 15 km. This time frame (c. 63 million years) suggests there was probably insufficient time for a thermal lid, overlying the Pooranoo Metamorphics, to incubate and heat the crust and cause melting. Therefore, it appears unlikely that radiogenic heating alone was the heat source for crustal melting.

3.9.5 New age constraints on D₁/D₂

Constraining D₁ deformation has been challenging due to a lack of consistent field relationships and structures across the Mangaroon Zone.

The previous upper age constraint on D₁/M₁, from the southern Mangaroon Zone, was c. 1675 Ma (Sheppard et al., 2005), but recent zircon geochronology showed that a deformation fabric previously assigned to the Mangaroon Orogeny formed during an older orogenic event (Wingate et al., 2013). Furthermore, there was a lack of direct constraints on the age of metamorphism and uncertainty about the timing of granite magmatism across the Mangaroon Zone. The geochronology from the northern, central and southern Mangaroon Zone, demonstrate that metamorphism and deformation commenced at 1691 ± 7 Ma, coeval with magmatism at 1695 ± 9 Ma. Therefore, the new lower constraint on the onset of deformation and metamorphism, and coeval magmatism, D₁/M₁ during the Mangaroon Orogeny is c. 1695 Ma. In contrast to the metamorphic assemblages reported by Sheppard et al. (2005), the new interpretation of M₁ assemblage includes the presence of K-feldspar (in GSWA 219749 and 219742) and early garnet in GSWA 219742.

Although the timing of peak metamorphism in sample GSWA 216533 from the northern Mangaroon Zone was constrained at 1683 ± 6 Ma based on data from monazite inclusions in garnet cores and monazite within matrix quartz, the timing of foliation development and the growth of garnet rims could not be dated due to severe retrogression and small size of the matrix monazite. However, recent zircon geochronology from granites in the northern Mangaroon Zone, only ~ 700 m to the west of GSWA 216533, may be used to interpret the timing of foliation development in sample GSWA 216533. There, an undeformed muscovite–tourmaline monzogranite with an age of 1673 ± 4 Ma (GSWA 216531: Wingate et al., 2019b) intrudes a foliated

biotite–metagranodiorite with an age of 1688 ± 4 Ma (GSWA 216532: Wingate et al., 2019a). This relationship indicates that the foliation (D_1) in the garnet–biotite–epidote pelitic gneiss (GSWA 216533) may have developed between 1688 ± 4 and 1673 ± 4 Ma, which overlaps with the timing of D_1 in the central (GSWA 219742) and southern Mangaroon Zone (GSWA 219749) at 1685 ± 9 Ma and 1691 ± 7 Ma, respectively. Although, the timing of D_1 deformation is constrained the lack of megascopic structures across the Mangaroon Zone, typical of compressional or transpressional settings, suggests that D_1 may have occurred in an extensional setting.

Compared to the limited structures associated with D_1 deformation, D_2 deformation produced a pervasive schistosity, metre- to kilometre-scale upright folds, and retrogression of D_1 metamorphic minerals to greenschist facies assemblages (Sheppard et al., 2005; 2010b). The age constraints for granite magmatism in the Mangaroon Zone show that there may have been two pulses of magmatism associated with the Durlacher Supersuite. The first pulse at 1695–1673 Ma, coincides with D_1 deformation and peak metamorphism. The second pulse of magmatism at c. 1660 Ma maybe be linked with D_2 deformation. The existing constraints for D_2 come from deformed granites older than c. 1675 Ma that suggests regional deformation occurred after 1675 Ma. The interpreted crystallisation age of 1659 ± 13 Ma (GSWA 219741), from the undeformed tourmaline–muscovite monzogranite, provides a new minimum age for D_2 , which is constrained to the internal c 1675–1660 Ma.

3.9.6 Geodynamic setting of the Mangaroon Zone

Many models have been invoked for low- P , high- T metamorphism, but the most common one for Proterozoic Australian orogens is the thermal lid model. In this section we will discuss how the commonly applied thermal lid model does not apply to the metamorphism associated with the Mangaroon Orogeny. Any model for the Mangaroon Orogeny must explain the following:

- burial and melting of the protoliths to the Pooranoo Metamorphics took place within c. 63 million years of them being deposited;
- granitic magmatism at c. 1695 Ma was coeval with peak metamorphism at c. 1691 Ma during D_1 deformation (Figure 3.10);

- the Mangaroon Orogeny was associated with an anomalous thermal gradient 175 to 240 °C/kbar (Figure 3.11) compared to an ambient thermal gradient of ~46 °C/kbar for the Gascoyne Province;
- the presence of rare grains of garnet at one locality, suggests higher pressures than those recorded at the peak during the prograde history, implying a broad clockwise metamorphic P – T path (Figure 3.9b);

The thermal lid model requires high concentrations of heat-producing elements in the crust combined with an incubation period typically lasting >100 million years (Korhonen et al., 2015; 2017; Morrissey et al., 2014). Although the crust in the Mangaroon Zone was radiogenic at c. 1.7 Ga, deposition, burial and melting of the Pooranoo Metamorphics (source rocks for the Durlacher Supersuite) occurred within c. 63 million years. Therefore, it is unlikely that there was sufficient time for radiogenic heat build up to cause the upper crustal metamorphism during the Mangaroon Orogeny. If radiogenic heating alone was unlikely the cause of the crustal melting, another heat source is required. For instance, the elevated Moho below the Mangaroon Zone (Johnson et al., 2013) and the anomalous thermal gradient during peak metamorphism, which is commonly associated with magmatism and significant extension (Smithies et al., 2011), suggests lithospheric thinning during the Mangaroon Orogeny.

Mantle upwelling during lithospheric thinning is a common driver proposed for low- P , high- T metamorphism (Collins, 1994; Vilà et al., 2007). In the Mangaroon Zone there is a lack of evidence for mafic magmatism; therefore, it is difficult to say with certainty that there was a mantle contribution.

3.9.7 Mangaroon Orogeny: high-grade core, low-grade halo

Although medium- to high-grade rocks formed during the Mangaroon Orogeny are restricted to the Gascoyne Province, disparate studies in recent years suggest that the effects of the orogeny may be present across much of the West Australian Craton (Figure 3.12). For instance, in the Ashburton Basin at the Paulsens Gold Mine, SHRIMP U–Pb monazite dating yielded an age of 1680 ± 9 Ma and at the nearby Belvedere orebody xenotime yielded an age of c. 1680 Ma, both of which are interpreted as the timing of hydrothermal gold mineralisation as a result of fault reactivation during the Mangaroon Orogeny (Fielding et al., 2017; 2018). Further north in the Pilbara Craton, hydrothermal monazite growth occurred at c. 1650 Ma (Rasmussen et al., 2007a), and in the southern

Pilbara at Mt Tom Price, hydrothermal xenotime growth occurred at c. 1670 Ma (Rasmussen et al., 2007b). Both these SHRIMP U–Pb studies attributed phosphate growth to reactivation of pre-existing crustal-scale structures during the Mangaroon Orogeny. Furthermore, shear zones within the Sylvania Inlier in the Pilbara Craton yielded $^{40}\text{Ar}/^{39}\text{Ar}$ mica ages of c. 1650 Ma (Sheppard et al., 2006). Similarly, a c. 1650 Ma $^{40}\text{Ar}/^{39}\text{Ar}$ mica age, from quartz-mica schist, was identified in the Earraheedy Basin, and was interpreted as the timing of deformation within the Stanley Fold Belt (Pirajno et al., 2009). These scattered low-grade events highlight that what initially appeared to be a very localised high-grade event in the Mangaroon Zone had a significant regional impact across the West Australian Craton.

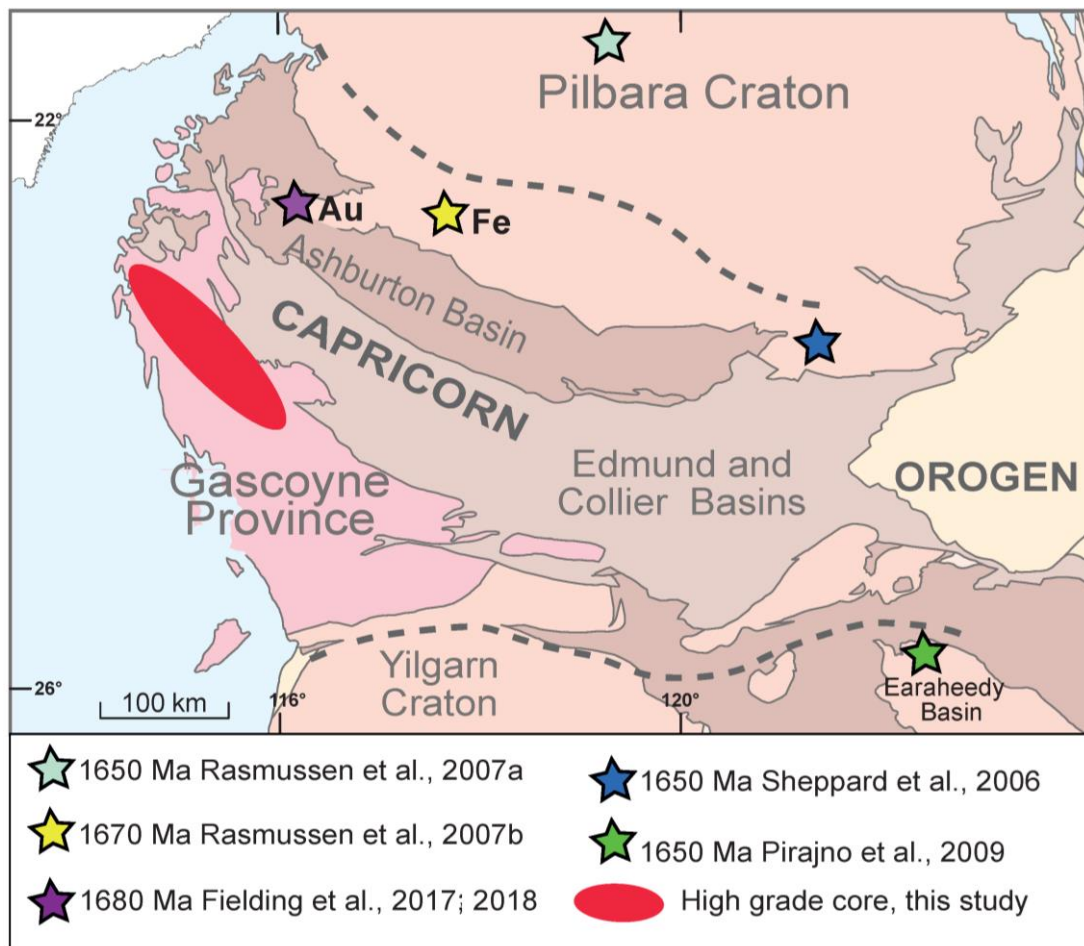


Figure 3.12 The Mangaroon orogeny high-grade core, low-grade halo in the West Australian Craton. The red oval represents the high-grade 1691–1680 Ma metamorphism recorded in the Mangaroon Zone. The stars represent low-grade occurrences of 1680–1650 Ma ages from outside of the Gascoyne Province. The grey dashed lines represent the northern and southern limits of the Capricorn Orogen. These data show that the footprint of the Mangaroon Orogeny extends far beyond the high-grade core.

Tectonic activity occurring synchronously with the Mangaroon Orogeny is also known more widely in western and central Australia. For instance, in the adjacent Albany–Fraser Orogen, two tectonic episodes are known: the 1710–1650 Ma Biranup Orogeny (Spaggiari et al., 2014) and, the c. 1680 Ma high-grade metamorphic Zanthus Event (Kirkland et al., 2011). In the Gawler Craton of the South Australia Craton (Figure 3.1), ultra-high temperature metamorphism at 1690–1650 Ma was the result of initial crustal thinning followed by crustal thickening (Cutts et al., 2013). In the Arunta Inlier of the North Australian Craton (Figure 3.1) the Argilke Event at 1680–1660 Ma involved magmatism, migmatization and metamorphism (Collins and Shaw, 1995; Black and Shaw, 1995) and high temperature metamorphism associated with the 1640–1635 Ma Liebig Orogeny was the result of the accretion of the Warumpi Province onto the North Australian Craton (Scrimgeour et al., 2005). These (presently) separated occurrences of c. 1.7 Ga tectonism in the western, northern and southern parts of Australia suggests that the Mangaroon Orogeny was perhaps part of a continent-scale tectonic event.

3.10 Conclusions

The combined U–Pb geochronology and *P–T* results suggest that upper crustal metamorphism at 1691 ± 7 Ma (665–755 °C and 2.7–4.3 kbar) coincided with the oldest phases of the Durlacher Supersuite coeval at 1695 ± 9 Ma, and continued until 1680 ± 4 Ma, with continued magmatism until c. 1660 Ma, in the Mangaroon Zone. The monazite geochronology shows that magmatism commenced at least 15 million years earlier than previously thought. Although the geochronology suggests a short duration of metamorphism (~22 million years), associated with D_1 , the magmatism continued until c. 1660 Ma. The absence of robust metamorphic dates younger than c. 1680 Ma does not imply that metamorphism ceased. Rather, the absence of dates is likely due to the severe destruction of matrix monazite, possibly related to the continued magmatism. A low-grade schistosity fabric was previously assigned to D_2 deformation; therefore, there is indication of continued metamorphism.

Our new results show that, in the Mangaroon Zone, the Pooranoo Metamorphics were deposited, buried and melted in c. 63 million years (<1758 and >1695 Ma). The new constraints on the ages of sedimentation and magmatism, combined with the elevated thermal gradient immediately following sediment deposition, suggest that upper-crustal granite emplacement likely occurred in an extensional tectonic setting. Unlike other intraplate metamorphic events in Proterozoic Australia, the thermal lid

model is unlikely to explain the metamorphism in the Mangaroon Zone during the Mangaroon Orogeny. Rather, our results show that magmatism was synchronous with upper crustal metamorphism. The low-grade halo of the Mangaroon Orogeny can be traced well outside of the Capricorn Orogen to the northern parts of the Pilbara Craton and the eastern Earraheedy Basin.

3.11 Acknowledgements

The authors thank Natasha Wodicka and an anonymous reviewer for their constructive and insightful comments resulting in a more focused manuscript. Simon Johnson is thanked for his assistance with sample collection and field work. This PhD project was funded through an Australian Research Council (ARC) grant (LP130100922) to BR and the Western Australian government Exploration Incentive Scheme. U–Pb measurements were conducted using the SHRIMP ion microprobes at the John de Laeter Centre at Curtin University. FJK publishes with permission of the Executive Director of the Geological Survey of Western Australia.

3.12 References

- Barton, M. D., & Hanson, R. B. (1989). Magmatism and the development of low-pressure metamorphic belts: Implications from the western United States and thermal modeling. *GSA Bulletin* 101, 1051–1065.
- Black, L. P., & Shaw, R. D. (1995). An assessment, based on U–Pb zircon data, of Rb/Sr dating in the Arunta Inlier, central Australia. *Precambrian Research* 71, 3–15.
- Bodorkos, S., and Wingate, M. T. D. (2007). The contribution of geochronology to GSWA's mapping programs: current perspectives and future directions: *Geological Survey of Western Australia, Record 2007/2*, p. 10–11.
- Chappell, B. W. (1999). Aluminium saturation in I- and S-type granites and the characterization of fractionated haplogranites. *Lithos* 46, 535–551.
- Clark, C., Kirkland, C. L., Spaggiari, C. V., Oorschot, C., Wingate, M. T. D., & Taylor, R. J. (2014). Proterozoic granulite formation driven by mafic magmatism: An example from the Fraser Range Metamorphics, Western Australia. *Precambrian Research* 240, 1–21.
- Collins, W. J. (1994). Upper- and middle-crustal response to delamination: An example from the Lachlan fold belt, eastern Australia. *Geology* 22, 1431–146.
- Collins, W. J., & Shaw, R. D. (1995). Geochronological constraints on orogenic events in the Arunta Inlier: a review. *Precambrian Research* 71, 315–346.
- Collins, W. J., & Vernon, R. H. (1991). Orogeny associated with anticlockwise P–T–t paths: Evidence from low-P, high-T metamorphic terranes in the Arunta inlier, central Australia. *Geology* 19, 835–838.
- Cooke, R. A., & O'Brien, P. J. (2001). Resolving the relationship between high P–T rocks and gneisses in collisional terranes: an example from the Gföhl gneiss–granulite association in the Moldanubian Zone, Austria. *Lithos* 58, 33–54.
- Cutts, K. A., Kelsey, D. E., & Hand, M. (2013). Evidence for late Paleoproterozoic (ca 1690–1665Ma) high- to ultrahigh-temperature metamorphism in southern Australia: Implications for Proterozoic supercontinent models. *Gondwana Research* 23, 617–640.
- Fielding, I. O. H., Johnson, S. P., Zi, J. W., Rasmussen, B., Muhling, J. R., Dunkley, D. J., Sheppard, S., Wingate, M. T. D., & Rogers, J. R. (2017). Using In Situ SHRIMP U–Pb Monazite and Xenotime Geochronology to Determine the Age of Orogenic Gold Mineralization: An Example from the Paulsens Mine, Southern Pilbara Craton. *Economic Geology* 112, 1205–1230.

- Fielding, I. O. H., Johnson, S. P., Zi, J.-W., Sheppard, S., & Rasmussen, B. (2018). Neighbouring orogenic gold deposits may be the products of unrelated mineralizing events. *Ore Geology Reviews* 95, 593–603.
- Finger, F., Broska, I., Roberts, M. P., & Schermaier, A. (1998). Replacement of primary monazite by apatite-allanite-epidote coronas in an amphibolite facies granite gneiss from the eastern Alps. *American Mineralogist* 83, 248–258.
- Fletcher, I. R., McNaughton, N. J., Aleinikoff, J. A., Rasmussen, B., & Kamo, S.L. (2004). Improved calibration procedures and new standards for U-Pb and Th-Pb dating of Phanerozoic xenotime by ion microprobe. *Chemical Geology* 209, 295–314.
- Fletcher, I. R., McNaughton, N. J., Davis, W. J., & Rasmussen, B. (2010). Matrix effects and calibration limitations in ion probe U–Pb and Th–Pb dating of monazite. *Chemical Geology* 270, 31–44.
- Fletcher, I.R., McNaughton, N.J., & Rasmussen, B. (2000). SHRIMP U–Pb geochronology of authigenic xenotime and its potential for dating sedimentary basins. *Australian Journal of Earth Sciences* 47, 845–859.
- Foster, G., Kinny, P., Vance, D., Prince, C., and Harris, N. (2000). The significance of monazite U–Th–Pb age data in metamorphic assemblages; a combined study of monazite and garnet chronometry. *Earth and Planetary Science Letters*, 181, 327–340.
- Glasson, K.J., Johnson, T.E., Kirkland, C.L., Gardiner, N.J., Clark, C., Blereau, E., Hartnady, M.I., Spaggiari, C. and Smithies, H. (2019). A window into an ancient backarc? The magmatic and metamorphic history of the Fraser Zone, Western Australia. *Precambrian Research*, 323, 55–69.
- GSWA. (2016a). 1:500 000 State interpreted bedrock geology of Western Australia, 2016: Geological Survey of Western Australia, digital data layer. www.dmp.wa.gov.au/geoview
- GSWA. (2016b). Compilation of geochronology information, 2016 update, digital data product. www.dmp.wa.gov.au/geoview
- Holland T. J. B., & Powell, R. (2011). An improved and extended internally consistent thermodynamic dataset for phases of petrological interest, involving a new equation of state for solids. *Journal of Metamorphic Geology* 29, 333–383.
- Johnson, S. P., Sheppard, S., Rasmussen, B., Wingate, M. T. D., Kirkland, C. L., Muhling, J. R., Fletcher, I. R., & Belousova, E. A. (2011). Two collisions, two sutures: Punctuated pre-1950Ma assembly of the West Australian Craton during the Ophthalmian and Glenburgh Orogenies. *Precambrian Research* 189, 239–262.

- Johnson, S. P., Korhonen, F. J., Kirkland, C. L., Cliff, J. B., Belousova, E. A., & Sheppard, S. (2017). An isotopic perspective on growth and differentiation of Proterozoic orogenic crust: From subduction magmatism to cratonization. *Lithos* 268, 76–86.
- Johnson, S. P., Thorne, A. M., Tyler, I. M., Korsch, R. J., Kennett, B. L. N., Cutten, H. N., Goodwin, J., Blay, O., Blewett, R. S., Joly, A., Dentith, M. C., Aitken, A. R. A., Holzschuh, J., Salmon, M., Reading, A., Heinson, G., Boren, G., Ross, J., Costelloe, R. D., & Fomin, T. (2013). Crustal architecture of the Capricorn Orogen, Western Australia and associated metallogeny. *Australian Journal of Earth Sciences* 60, 681–705.
- Kirkland, C. L., Spaggiari, C. V., Pawley, M. J., Wingate, M. T. D., Smithies, R. H., Howard, H. M., Tyler, I. M., Belousova, E. A., & Poujol, M. (2011). On the edge: U–Pb, Lu–Hf, and Sm–Nd data suggests reworking of the Yilgarn craton margin during formation of the Albany-Fraser Orogen. *Precambrian Research* 187, 223–247.
- Korhonen, F. J., & Johnson, S. P. (2015). The role of radiogenic heat in prolonged intraplate reworking: The Capricorn Orogen explained?. *Earth and Planetary Science Letters* 428, 22–32.
- Korhonen, F. J., Johnson, S. P., Wingate, M. T. D., Kirkland, C. L., Fletcher, I. R., Dunkley, D. J., Roberts, M. P., Sheppard, S., Muhling, J. R., & Rasmussen, B. (2017). Radiogenic heating and craton-margin plate stresses as drivers for intraplate orogeny. *Journal of Metamorphic Geology* 35, 631–661.
- Loosveld, R. J. H., & Etheridge, M. A. (1990). A model for low-pressure facies metamorphism during crustal thickening. *Journal of Metamorphic Geology* 8, 257–267.
- Ludwig, K.R. (2009). *Squid 2.50, A User's Manual*. Berkeley Geochronology Centre Special Publication, pp. 95.
- Martin, D. M., Sheppard, S., Thorne, A., Farrell, T. R., and Groenewald, P. B. (2006). Proterozoic Geology of the Western Capricorn Orogen - a field guide: Geological Survey of Western Australia, Record 2006/18, p.43.
- McLaren, S., Sandiford, M., & Powell, R. (2005). Contrasting styles of Proterozoic crustal evolution: A hot-plate tectonic model for Australian terranes. *Geology* 33, 673–676.
- Miller, C. F., Meschter McDowell, S., & Mapes, R. W., 2003, Hot and cold granites? Implications of zircon saturation temperatures and preservation of inheritance. *Geology* 31, 529–532.
- Morrissey, L. J., Hand, M., Raimondo, T., and Kelsey, D. E., 2014, Long-lived high-T, low-P granulite facies metamorphism in the Arunta Region, central Australia: *Journal of Metamorphic Geology*, v. 32, no. 1, p. 25-47.

- Nelson, D. R. (1998). 142855: porphyritic monzogranite, Anderson well; in *Compilation of SHRIMP U–Pb zircon geochronology data, 1997*: Western Australia Geological Survey, Record 1998/2, 194–197.
- Nelson, D. R. (2002). 169053: biotite muscovite monzogranite, Fraser Well; in *Compilation of geochronology data, 2001*: Western Australia Geological Survey, Record 2002/2, p. 35–38.
- Nelson, D. R. (2005). 178027: biotite-muscovite granodiorite, Mangaroon Homestead; Geochronology dataset 536; in *Compilation of geochronology data, June 2006 update*; Western Australia Geological Survey.
- Occhipinti, S. A., Sheppard, S., Passchier, C., Tyler, I. M., & Nelson, D. R. (2004). Palaeoproterozoic crustal accretion and collision in the southern Capricorn Orogen: the Glenburgh Orogeny. *Precambrian Research* 128, 237–255.
- Occhipinti, S. A., & Reddy, S. M. (2009). Neoproterozoic reworking of the Palaeoproterozoic Capricorn Orogen of Western Australia and implications for the amalgamation of Rodinia. *Geological Society, London, Special Publications* 327, 445–456.
- Oliver, N. H. S., & Zakowski, S. (1995). Timing and geometry of deformation, low-pressure metamorphism and anatexis in the eastern Mt Lofty Ranges: The possible role of extension. *Australian Journal of Earth Sciences* 42, 501–507.
- Pearson, J. M. (1996). Alkaline rocks of the Gifford Creek Complex, Gascoyne Province, Western Australia — their petrogenetic and tectonic significance: University of Western Australia, Perth, PhD thesis (unpublished).
- Piechocka, A. M., Gregory, C. J., Zi, J.-W., Sheppard, S., Wingate, M. T. D., & Rasmussen, B. (2017). Monazite trumps zircon: applying SHRIMP U–Pb geochronology to systematically evaluate emplacement ages of leucocratic, low-temperature granites in a complex Precambrian orogen. *Contributions to Mineralogy and Petrology* 172, 1–17.
- Piechocka, A. M., Sheppard, S., Fitzsimons, I. C. W., Johnson, S. P., Rasmussen, B., & Jourdan, F. (2018). Neoproterozoic $^{40}\text{Ar}/^{39}\text{Ar}$ mica ages mark the termination of a billion years of intraplate reworking in the Capricorn Orogen, Western Australia. *Precambrian Research* 310, 391–406.
- Piechocka, A. M., Zi, J. W., Gregory, C. J., Sheppard, S., and Rasmussen, B. (2019). SHRIMP U–Pb phosphate dating shows metamorphism was synchronous with magmatism during the Paleoproterozoic Capricorn Orogeny: *Australian Journal of Earth Sciences* 66, 973–990.

- Pirajno, F., Hocking, R. M., Reddy, S. M., & Jones, A. J. (2009). A review of the geology and geodynamic evolution of the Palaeoproterozoic Earaheedy Basin, Western Australia. *Earth-Science Reviews* 94, 39–77.
- Rasmussen, B., Fletcher, I. R., & Muhling, J. R. (2007a). In situ U–Pb dating and element mapping of three generations of monazite: Unravelling cryptic tectonothermal events in low-grade terranes. *Geochimica et Cosmochimica Acta* 71, 670–690.
- Rasmussen, B., Fletcher, I. R., Muhling, J. R., Thorne, W. S., & Broadbent, G. C. (2007b). Prolonged history of episodic fluid flow in giant hematite ore bodies: Evidence from in situ U–Pb geochronology of hydrothermal xenotime. *Earth and Planetary Science Letters* 258, 249–259.
- Sandiford, M., & Hand, M. (1998). Controls on the locus of intraplate deformation in central Australia. *Earth and Planetary Science Letters* 162, 97–110.
- Sandiford, M., & Powell, R. (1986). Deep crustal metamorphism during continental extension: modern and ancient examples. *Earth and Planetary Science Letters* 79, 151–158.
- Scaillet, B., Holtz, F., & Pichavant, M. (2016). Experimental Constraints on the Formation of Silicic Magmas. *Elements* 12, 109–114.
- Scrimgeour, I. R., Kinny, P. D., Close, D. F., & Edgoose, C. J. (2005). High-T granulites and polymetamorphism in the southern Arunta Region, central Australia. Evidence for a 1.64 Ga accretional event. *Precambrian Research* 142, 1–27.
- Sheppard, S., Bodorkos, S., Johnson, S. P., Wingate, M. T. D., & Kirkland, C. L. (2010a). The Paleoproterozoic Capricorn Orogeny: Intracontinental Reworking Not Continent-Continent Collision: Geological Survey of Western Australia, Report 108, p. 33.
- Sheppard, S., Farrell, T. R., Bodorkos, S., Hollingsworth, D., Tyler I., M., & Pirajno, F. (2006). Late Paleoproterozoic (1680–1620) sedimentation, magmatism, and tectonism in the Capricorn Orogen, *in* GSWA 2006 extended abstracts: promoting the prospectivity of Western Australia: Geological Survey of Western Australia, Record 2006/3, p. 11–12.
- Sheppard, S., & Johnson, S. P. (2016). Pooranoo Metamorphics (P_₁-PO-md): Geological Survey of Western Australia, WA Geology Online, Explanatory Notes extract, viewed 20 November 2017, www.dmp.wa.gov.au/ens.
- Sheppard, S., Johnson, S. P., Wingate, M. T. D., Kirkland, C. L., & Pirajno, F. (2010b). Explanatory notes for the Gascoyne Province: Geological Survey of Western Australia, 1:100 000 Explanatory Notes, p. 336.

- Sheppard, S., Occhipinti, S. A., & Nelson, D. R. (2005). Intracontinental reworking in the Capricorn Orogen, Western Australia: the 1680–1620 Ma Mangaroon Orogeny. *Australian Journal of Earth Sciences* 52, 443–460.
- Sheppard, S., Rasmussen, B., Muhling, J. R., Farrell, T. R., and Fletcher, I. R. (2007). Grenvillian-aged orogenesis in the Palaeoproterozoic Gascoyne Complex, Western Australia: 1030–950 Ma reworking of the Proterozoic Capricorn Orogen. *Journal of Metamorphic Geology* 25, 477–494.
- Smithies, R. H., Howard, H. M., Evins, P. M., Kirkland, C. L., Kelsey, D. E., Hand, M., Wingate, M. T. D., Collins, A. S., & Belousova, E. (2011). High-Temperature Granite Magmatism, Crust–Mantle Interaction and the Mesoproterozoic Intracontinental Evolution of the Musgrave Province, Central Australia. *Journal of Petrology* 52, 931–958.
- Spaggiari, C. V., Kirkland, C. L., Smithies, R. H., & Wingate, M. T. D. (2014). Tectonic links between Proterozoic sedimentary cycles, basin formation and magmatism in the Albany-Fraser Orogen: Geological Survey of Western Australia, Report 133.
- Stacey, J.S., & Kramers, J.D. (1975). Approximation of terrestrial lead isotope evolution by a two-stage model. *Earth and Planetary Science Letters* 26, 207–221.
- Stern, R. A., & Rainbird, R. H. (2001). Advancements in xenotime U–Pb geochronology by ion microprobe, Eleventh V.I. Goldschmidt Conference Lunar and Planetary Science Institute, Houston.
- Stern, T. A., & Sanborn, N. (1998). Monazite U–Pb and Th–Pb geochronology by high-resolution secondary ion mass spectrometry. *Radiogenic Age and Isotope Studies: Report 11, Geological Survey of Canada, Current Research 1998-F*, 1–18.
- Vilà, M., Pin, C., Liesa, M., & Enrique, P. (2007). LPHT metamorphism in a late orogenic transpressional setting, Albera Massif, NE Iberia: implications for the geodynamic evolution of the Variscan Pyrenees. *Journal of Metamorphic Geology* 25, 321–347.
- Watson, E. B., & Harrison, T. M. (1983). Zircon saturation revisited: temperature and composition effects in a variety of crustal magma types. *Earth and Planetary Science Letters* 64, 295–304.
- White, R. W., Powell, R., & Johnson, T. E. (2014). The effect of Mn on mineral stability in pelites revisited: new a–x relations for manganese-bearing minerals. *Journal of Metamorphic Geology* 32, 809–828.

- Wickham, S. M., & Oxburgh, F. R. S. (1987). Low-pressure regional metamorphism in the Pyrenees and its implications for the thermal evolution of rifted continental crust. *Philosophical Transactions of the Royal Society of London. Series A, Mathematical and Physical Sciences* 321, 219–242.
- Wingate, M. T. D., Kirkland, C. L., & Korhonen F. J. (2013). 208318: metagranite, Brown Well; *Geochronology Record* 1174: Geological Survey of Western Australia, 4p.
- Wingate, M. T. D., Kirkland, C. L., Bodorkos, S., S, Sheppard, & Farrell, T. R. (2009). 183255: metasandstone, Mount Samuel; *Geochronology Record* 772: Geological Survey of Western Australia, 5p.
- Wingate, M. T. D., Lu, Y., Korhonen, F. J., & Johnson, S. P. (2019a). 216532: granodiorite gneiss, Mountain Creek; *Geochronology Record* 1559: Geological Survey of Western Australia, 4p.
- Wingate, M. T. D., Lu, Y., Korhonen, F. J., & Johnson, S. P. (2019b). 216531: muscovite monzogranite, Mountain Creek; *Geochronology Record* 1558: Geological Survey of Western Australia, 4p.
- Wingate, M. T. D., Lu, Y., Korhonen, F. J., & Johnson, S. P. (2018). 195888: metamonzogranite, Brown Well; *Geochronology Record* 1552: Geological Survey of Western Australia, 6p.
- Wingate, M. T. D., Lu, Y., Korhonen, F. J., & Johnson, S. P. (2017). 208365: biotite metagranodiorite, Kimbers well; *Geochronology Record* 1356: Geological Survey of Western Australia, 4p.
- Zen, E. (1986). Aluminum Enrichment in Silicate Melts by Fractional Crystallization: Some Mineralogic and Petrographic Constraints. *Journal of Petrology* 27, 1095–1117.

Chapter 4

PAPER 3: Monazite trumps zircon: applying SHRIMP U-Pb geochronology to systematically evaluate emplacement ages of leucocratic, low-temperature granites in a complex Precambrian orogen

Authors:

Agnieszka M Piechocka^{a*}, Courtney J Gregory^a, Jian-Wei Zi^a, Stephen Sheppard^a, Michael TD Wingate^b, Birger Rasmussen^a

^aDepartment of Applied Geology, Curtin University, Kent Street, Bentley, WA 6102, Australia

^bGeological Survey of Western Australia, 100 Plain Street, East Perth, WA 6004, Australia

Email addresses:

*Corresponding author nishka.piechocka@postgrad.curtin.edu.au

courtneyjaynegregory@gmail.com

j.zi@curtin.edu.au

stephen.sheppard@curtin.edu.au

Michael.WINGATE@dmp.wa.gov.au

B.Rasmussen@curtin.edu.au

Keywords:

monazite; SHRIMP geochronology; leucocratic granite; pegmatite; Proterozoic; Capricorn Orogen

4.1 Abstract

Although zircon is the most widely used geochronometer to determine the crystallisation ages of granites, it can be unreliable for low-temperature melts because they may not crystallise new zircon. For leucocratic granites U–Pb zircon dates, therefore, may reflect the ages of the source rocks rather than the igneous crystallisation age. In the Proterozoic Capricorn Orogen of Western Australia, leucocratic granites are associated with several pulses of intracontinental magmatism spanning ~ 800 million years. In several instances, SHRIMP U–Pb zircon dating of these leucocratic granites either yielded ages that were inconclusive (e.g., multiple concordant ages) or incompatible with other geochronological data. To overcome this we used SHRIMP U–Th–Pb monazite geochronology to obtain igneous crystallisation ages that are consistent with the geological and geochronological framework of the orogen. The U–Th–Pb monazite geochronology has resolved the time interval over which two granitic supersuites were emplaced; a Paleoproterozoic supersuite thought to span ~ 80 million years was emplaced in less than half that time (1688–1659 Ma) and a small Meso– to Neoproterozoic supersuite considered to have been intruded over ~ 70 million years was instead assembled over ~ 130 million years and outlasted associated regional metamorphism by ~ 100 million years. Both findings have consequences for the duration of associated orogenic events and any estimates for magma generation rates. The monazite geochronology has contributed to a more reliable tectonic history for a complex, long-lived orogen. Our results emphasise the benefit of monazite as a geochronometer for leucocratic granites derived by low-temperature crustal melting, and are relevant to other orogens worldwide.

4.2 Introduction

Leucocratic granites are peraluminous (i.e., alumina saturation index [ASI] = molar $\text{Al}_2\text{O}_3/(\text{CaO}+\text{Na}_2\text{O}+\text{K}_2\text{O}) > 1$; Scaillet et al. 2016; Zen 1986) rocks containing < 5 vol. % mafic minerals (Le Maitre 1989). They are typically derived from low-temperature (< 750 °C; Ayres et al. 1997; Scaillet et al. 1995) partial melting of crustal sources without direct mass input from the mantle (Gao et al. 2017; Patiño and Harris 1998). Leucocratic granites are common in intracontinental and collisional settings and typically account for a small proportion of all granites in orogenic belts (Gilotti and McClelland 2005; Harrison et al. 1999; Kemp and Hawkesworth 2003). However, they are important for determining the tectonic history of orogenic belts (Crowley et al. 2008) as they commonly form during periods of crustal thickening (Brown 1994). Kemp and Hawkesworth (2003) divided leucocratic granites into two types on the basis of their Sr concentrations: a low-Sr (< 200 ppm Sr) type formed by melting in the upper continental crust (e.g., leucogranites of the Himalayan Orogen), and the less common high-Sr (250–450 ppm) types related to deeper crustal sources (e.g., Glenelg River Complex, southeastern Australia).

Dating leucocratic, low-temperature granites (*sensu lato*) using U-Pb zircon geochronology can be challenging due to the zircon population being dominated by inherited grains (Bea et al. 2007; Harrison et al. 1987; Miller et al. 2003; Schärer 1986). Experimental studies have shown that zircon solubility is mainly governed by temperature and melt composition, and for typical peraluminous melts zircon solubility ranges from ~ 100 ppm dissolved at 750 °C to 1300 ppm at 1020 °C (Boehnke et al. 2013; Watson and Harrison 1983). This means that the low solubility of Zr in low-temperature (< 800 °C) crustal melts limits the amount of zircon that can dissolve during partial melting and re-precipitate during crystallisation. These findings are consistent with observations that low-temperature granites (mean 766 ± 24 °C) with abundant inherited zircon typically have lower Zr concentrations (80–150 ppm) compared with high-temperature granites (200–800 ppm, mean 837 ± 48 °C) with minimal inheritance (Miller et al. 2003).

Although zircon is most widely used to constrain crystallisation ages of granites, monazite geochronology has been employed sporadically to date the crystallisation age of granites (e.g., Grosse et al. 2009; Harrison et al. 1999; Kusiak et al., 2014; Miller and Mittlefehldt 1982; Parrish and Tirrul 1989; Townsend et al. 2001; Williams et al. 1983). However, there has been little attempt to systematically evaluate the suitability of monazite for geochronology of leucocratic granites types even though monazite appears

to be common in a range of granites, including leucocratic granites (Bea 1996; Montel 1993; Rapp and Watson 1986). The stability of monazite is considered to be dependent on pressure, temperature, bulk rock chemistry and interacting fluid chemistry (Budzyń et al. 2011; Poitrasson et al. 1996). It has been suggested that monazite is stable in host compositions that are low in Ca (< 0.7%) in contrast to higher Ca (> 1.8%) which favour allanite growth (Lee and Dodge 1964; Montel 1993; Parrish 1990), although monazite and allanite do coexist in peraluminous granites (Broska et al. 2000). Furthermore, although not widespread, instances of monazite inheritance in granites have been documented (Copeland et al. 1988; Parrish 1990).

Leucocratic granites are widespread in the Proterozoic Gascoyne Province, Capricorn Orogen of Western Australia, and apparently formed during several episodes of magmatism (Sheppard et al. 2010b). The crystallization ages of several leucocratic granites are not well defined by U–Pb zircon geochronology, which has created uncertainty about the duration and distribution of some of the granite supersuites and related orogenic events in the province. In this paper we use SHRIMP U–Th–Pb monazite geochronology to re-evaluate the emplacement ages of these granites in order to obtain reliable igneous crystallisation ages consistent with the existing geological framework. In turn, this provides better constraints on the duration of granitic magmatism and magma production rates and allows for a more complete magmatic and tectonothermal history of the orogen to be established.

4.3 Regional Geology

The study area is located in the Capricorn Orogen in Western Australia (Figure 4.1), which records the Paleoproterozoic assembly of the West Australian Craton by c. 1950 Ma (Johnson et al. 2011; Occhipinti et al. 2004). Five subsequent, episodic intracontinental reworking and reactivation events spanning nearly 1.5 billion years has shaped the current architecture of this orogen (Korhonen et al. 2015; Sheppard et al. 2010a). All of these tectonic events are known from the Gascoyne Province, at the presently exposed western end of the orogen (Figure 4.1). Of the five intracontinental reworking events in the Gascoyne Province, two are accompanied by voluminous, mainly high-temperature granitic magmatism (i.e., the Capricorn Orogeny being associated with the 1820–1775 Ma Moorarie Supersuite, and the Mangaroon Orogeny with the 1680–1620 Ma Durlacher Supersuite), whereas a third, spatially restricted event (the Edmundian Orogeny) was accompanied solely by leucocratic granitic magmatism (995–955 Ma Thirty Three Supersuite) (Sheppard et al. 2010b).

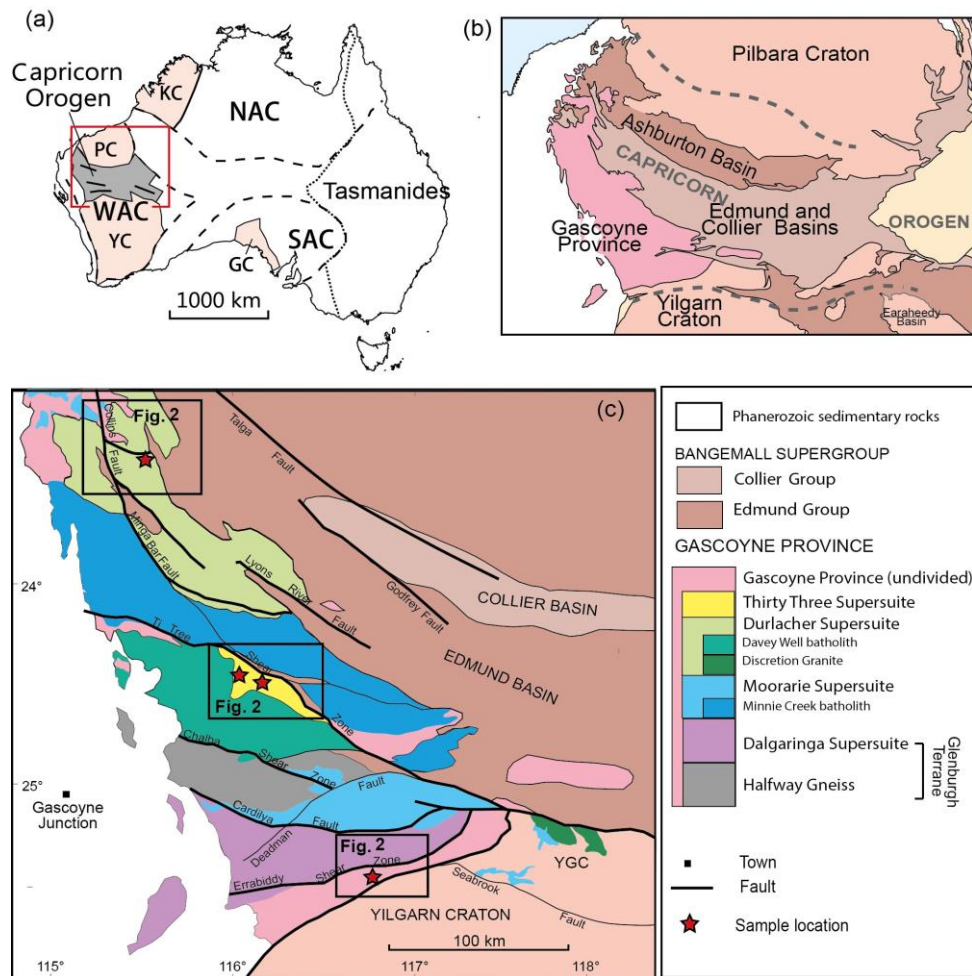


Figure 4.1 Regional geological setting of the Capricorn Orogen in relation to Australia (a) and (b) and simplified regional geology of the Gascoyne Province showing discrete fault- bounded E-W trending domains (c). Outlines of study areas are presented in more detail in Figure 4.2. PC = Pilbara Craton, YC = Yilgarn Craton, WAC = West Australian Craton, GC = Gawler Craton, NAC = North Australian Craton, SAC = South Australian Craton YGC = Yarlalweelor Gneiss Complex (adapted from Johnson et al. (2017) and Zi et al. (2015)).

The 1820–1775 Ma Moorarie Supersuite was emplaced during the Capricorn Orogeny (Sheppard et al. 2010a; Sheppard et al. 2010b), and comprises batholiths and plutons of weakly peraluminous, biotite-bearing monzogranite and granodiorite, with minor syenogranite, tonalite, and quartz diorite, although, biotite (–muscovite–tourmaline)-bearing monzogranite is common in the southern Gascoyne Province. Most granites of the Moorarie Supersuite contain little or no xenocrystic zircon, so that their igneous crystallisation ages are well constrained. A number of undated plutons have also been assigned to the supersuite on the basis of their field relationships, including a pluton of leucocratic granodiorite 12 km long by 5 km wide in the Errabiddy Shear Zone, which marks the boundary between the Yilgarn Craton and Gascoyne Province (Figure 4.1, Figure 4.2a).

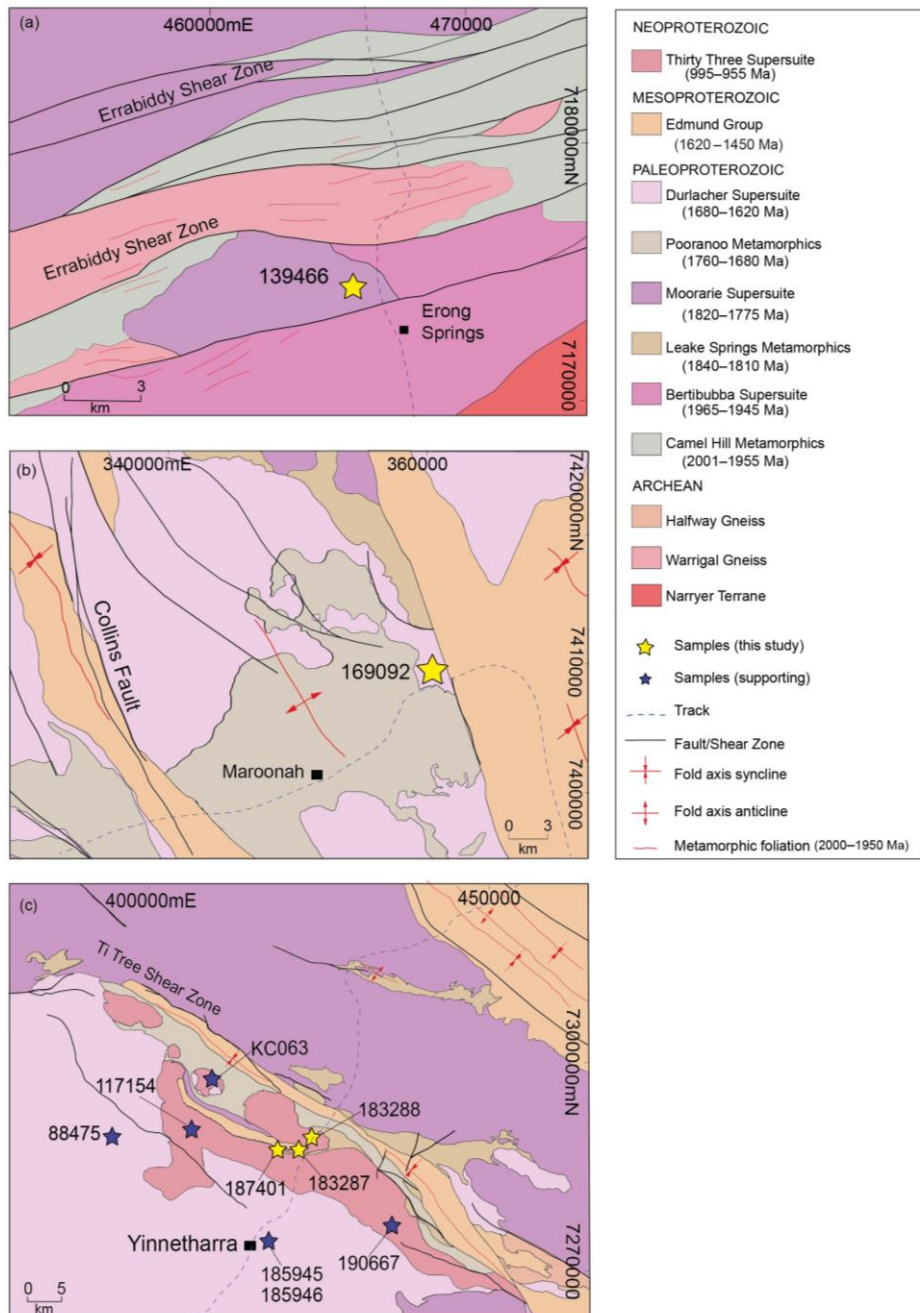


Figure 4.2 Local geology of sample areas: (a) the Errabiddy Shear Zone with penetrative deformation fabrics in the older granites and metasedimentary rocks; the star indicates Erong Granite sample GSWA 139466; (b) the northern Gascoyne Province is dominated by Proterozoic granites and folded metasedimentary rocks of the Edmund Group; the star shows the location of Red Rock Bore granite sample GSWA 169092; (c) The area south of the Ti Tree Shear Zone hosts the only occurrence of Thirty Three Supersuite, in the Gascoyne Province; yellow stars indicate granite samples GSWA 183287, 183288, and 187401. Blue stars indicate supporting samples mentioned throughout the text. The ages for the metamorphic packages are depositional ages. Coordinate system in GDA 1994 MGA Zone 50. Geology polygons and linear features were extracted from the 1:500 000 Geological Map of Western Australia (GSWA 2016a).

The pluton, referred to as the Erong Granite, cuts across Paleoproterozoic (c. 1950 Ma) migmatitic structures in surrounding metamorphic rocks (Occhipinti et al. 2001). However, previous SHRIMP U–Pb zircon dating of the granodiorite (GSWA 139466) only yielded an Archean maximum crystallization age (Nelson 2000).

The 1680–1620 Ma Durlacher Supersuite comprises peraluminous biotite–muscovite monzogranite, granodiorite, and syenogranite, and some leucocratic muscovite–tourmaline (–biotite) monzogranite (Sheppard et al. 2005; Sheppard et al. 2010b). Crystallisation ages of the Durlacher Supersuite granites are well constrained by U–Pb zircon geochronology and most granites are older than c. 1659 Ma (Sheppard et al. 2010b) with two main exceptions: the c. 1620 Ma Discretion Granite (Nelson 1998) and one leucocratic sample (Figure 4.2b) from the northern Gascoyne Province (GSWA 169092). This leucocratic granite (GSWA 169092) yielded two concordant ages 60 million years apart, none of which could be interpreted unequivocally as the crystallisation age. The younger age component is within error of the igneous crystallisation age of c. 1620 Ma for a batholith (Discretion Granite) about 250 km to the southeast (Figure 4.1), and both samples were used to provide a minimum age for the Mangaroon Orogeny (Sheppard et al., 2005).

Intrusion of the 995–955 Ma Thirty Three Supersuite (Figure 4.2c) coincided with deformation and metamorphism of the Edmondian Orogeny within a narrow structural corridor in the centre of the Gascoyne Province (Sheppard et al. 2007). The supersuite crops out over an area 70 km long by 10 km wide, and is structurally bound to the north by the Ti Tree Shear Zone (Figure 4.2c). The Thirty Three Supersuite comprises muscovite (–tourmaline) metamonzogranite, biotite–muscovite (–tourmaline) monzogranite and granodiorite, and a belt of muscovite–tourmaline and rare-element bearing pegmatites (Sheppard et al. 2010b). Crystallisation ages for Thirty Three Supersuite granites have proven difficult to resolve via U–Pb zircon geochronology due to the presence of copious xenocrystic zircon. Early indications were that the granites belonged to the Paleoproterozoic Durlacher Supersuite (Culver 2001). This appeared to be consistent with the fact that the leucocratic granites and pegmatites do not intrude Mesoproterozoic sedimentary rocks of the Bangemall Supergroup within the Ti Tree Shear Zone (Figure 4.2c). However, later in situ monazite geochronology showed that the granites cut metamorphic fabrics formed at 1030–990 Ma (Sheppard et al. 2007).

4.4 Sample descriptions and previous zircon geochronology

Leucocratic granite samples analysed previously using U-Pb zircon geochronology were re-analysed in this study using U-Th-Pb monazite geochronology. Presented below are the original zircon geochronology results for selected peraluminous, leucocratic samples from three generations of Proterozoic magmatism (Table 4.1). The corresponding monazite geochronology is discussed in the subsequent results section.

GSWA 139466

This sample is a medium-grained, equigranular biotite–muscovite granodiorite that grades into coarser grained granite and pegmatite (Occhipinti et al. 2001). The sample contains minor muscovite and approximately 5% total mafic minerals (biotite, garnet and epidote) (Figure 4.3a).

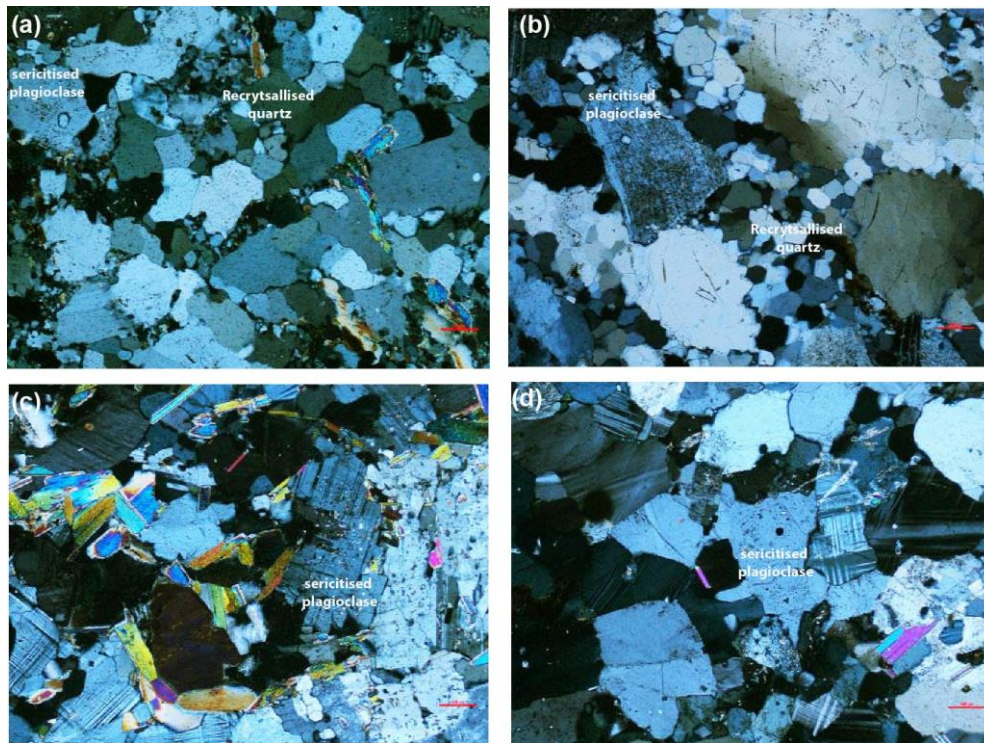


Figure 4.3 Representative photomicrograph images (cross polarised light)

highlighting a weak post-magmatic overprint observed in the leucocratic samples (a) 139466: medium-grained equigranular biotite–muscovite granodiorite showing minor sericitisation and quartz recrystallization; (b) 169092: massive, medium-grained biotite–muscovite monzogranite, showing minor sericite, quartz recrystallisation and undulose extinction in the quartz; (c) 183287: medium- to coarse-grained, equigranular muscovite–tourmaline granodiorite with partly sericitised plagioclase and recrystallised quartz; (d) 187401: fine to medium-grained equigranular tourmaline–muscovite monzogranite showing recrystallised quartz and minor sericitisation.

Minor sericitisation, quartz recrystallisation and biotite replacement by chlorite is evidence of a weak metamorphic overprint. The zircon crystals are equant to elongate and euhedral pale green to black, 30–250 μm long and 25–80 μm wide, with only a few grains showing subtle internal zoning (Nelson 2000). U-Pb zircon geochronology yielded a date of 2621 ± 9 Ma (all ages in this paper are quoted with 95% uncertainties, unless indicated otherwise) (Nelson 2000). This age is interpreted to represent the age of a xenocrystic population because the pluton intruded 1965–1945 Ma granitic rocks and 2001–1955 Ma metasedimentary rocks (Sheppard et al. 2010b) and crosscuts deformation fabrics related to the 2005–1950 Ma Glenburgh Orogeny (Figure 4.2a and Figure 4.3a). The granodiorite is overprinted by Neoproterozoic (c. 900 Ma) mylonite zones (Occhipinti and Reddy 2009), but this is the only minimum constraint on its age. The low whole-rock Zr content (60 ppm; Table 4.1) is characteristic of a rock dominated by inherited zircons (Miller et al. 2003), and the combination of high Sr (369 ppm) and low Rb are consistent with the granite having formed by fluid-fluxed melting of muscovite during crustal anatexis (Gao et al. 2017). The rare-earth elements (La, Ce and Nd) are abundant in the whole rock composition (Table 4.1).

GSWA 169092

This sample is from a leucocratic granite unit located in the northern Gascoyne Province where it intrudes 1840–1810 Ma and 1760–1680 Ma metasedimentary rocks, and is overlain by 1620–1450 Ma siliciclastic rocks (Sheppard et al. 2010b) (Figure 4.2b). It is a massive, medium-grained biotite–muscovite monzogranite (Figure 4.3b and Figure 4.4b) with minor muscovite and 5% mafic minerals (chlorite, epidote, tourmaline and garnet). Biotite is partly replaced by chlorite, and minor sericite and undulose extinction in the quartz and recrystallised quartz are indicative of a weak metamorphic overprint. The zircon crystals are euhedral to anhedral, 100–250 μm long and 40–180 μm wide, pale brown, dark brown or black, with only a minority of grains displaying subtle zoning (Nelson 2004). Zircon geochronology yielded two age components, one at 1810 ± 22 and 1681 ± 10 Ma, and one concordant analysis at 1619 ± 15 Ma (1 \square) which, at the time, was interpreted as the maximum crystallisation age (Nelson 2004) and used by Sheppard et al (2005) to constrain the younger limits of the 1680–1620 Ma Mangaroon Orogeny. Although, a recent re-interpretation has concluded the younger analysis to represent Pb loss (M. Wingate pers. comm., March 14, 2016) it remained unclear as to whether the 1681 ± 10 Ma population should be interpreted as the crystallization age or a maximum for crystallization. Whole-rock geochemistry of the

geochronology sample (Table 4.1) indicates that it has low Zr (70 ppm) and low Sr (63 ppm) contents and elevated rare-earth element contents ((La, Ce and Nd).

Table 4.1 Selected whole-rock geochemistry data for leucocratic granite samples.

	139466	169092	183287	183288	187401
	<i>Biotite- muscovite granodiorite</i>	<i>Biotite- muscovite monzogranite</i>	<i>Muscovite- tourmaline granodiorite</i>	<i>Biotite- muscovite- tourmaline monzogranite</i>	<i>Tourmaline- muscovite monzogranite</i>
<i>(wt %)</i>					
SiO ₂	76.84	73.85	75.51	73.24	73.19
TiO ₂	0.09	0.18	0.05	0.21	0.14
Al ₂ O ₃	13.61	13.86	13.16	13.27	13.83
Fe ₂ O ₃ ^{Total}	0.70	1.59	0.94	1.87	1.21
MnO	0.02	0.06	0.04	0.08	0.02
CaO	1.36	0.81	0.58	0.86	0.77
Na ₂ O	4.91	2.86	2.96	2.77	3.41
K ₂ O	2.20	5.20	4.75	5.24	5.69
P ₂ O ₅	0.05	0.23	0.22	0.15	0.10
LOI	-0.01	0.85	1.57	1.84	1.31
A/CNK [*]	1.05	1.17	1.19	1.13	1.05
<i>(ppm)</i>					
Rb	56	376	687	492	346
Sr	369	63	18	48	59
Th	6	16	8	22	26
U	1	8	14	12	8
Zr	60	70	38	122	113
La	21	21	7	32	40
Ce	42	41	23	70	84
Nd	13	17	12	31	31

Notes:

*A/CNK = molar Al₂O₃/(CaO+Na₂O+K₂O)

GSWA 183287, 183288, and 187401

Sample GSWA 183287 is a medium- to coarse-grained, equigranular muscovite–tourmaline granodiorite with 5% tourmaline and garnet (Figure 4.3c and Figure 4.4c). The presence of partly sericitised plagioclase, recrystallised quartz, and minor myrmekitic textures suggest a thermal overprint. The zircons are typically anhedral, up to 150 µm long, ranging from colourless to brown and most grains have idiomorphic zoning (Kirkland et al. 2009). Zircons from this sample yielded a range of dates between

2085 and 1309 Ma, interpreted as the ages of xenocrystic zircon (Kirkland et al. 2009) because the granite cross-cuts Neoproterozoic metamorphic fabrics in surrounding metasedimentary rocks (Sheppard et al. 2007). GSWA 183288 is a strongly porphyritic medium-grained, biotite-muscovite–tourmaline monzogranite. It contains about 15% biotite, and ~2% muscovite and tourmaline combined. Plagioclase is partially sericitised, quartz is recrystallised, minor myrmekite is developed, and biotite is partially replaced by chlorite. Zircons from this sample yielded a dominant age component at 1648 ± 5 Ma (MSWD = 1.1, $n = 39/41$) with one older analysis at 1755 ± 25 Ma (Wingate et al. in press). This monzogranite also cuts Neoproterozoic metamorphic fabrics, so the dominant zircon population must represent the age of the main source component. In both instances, zircon geochronology was unable to constrain the emplacement age.

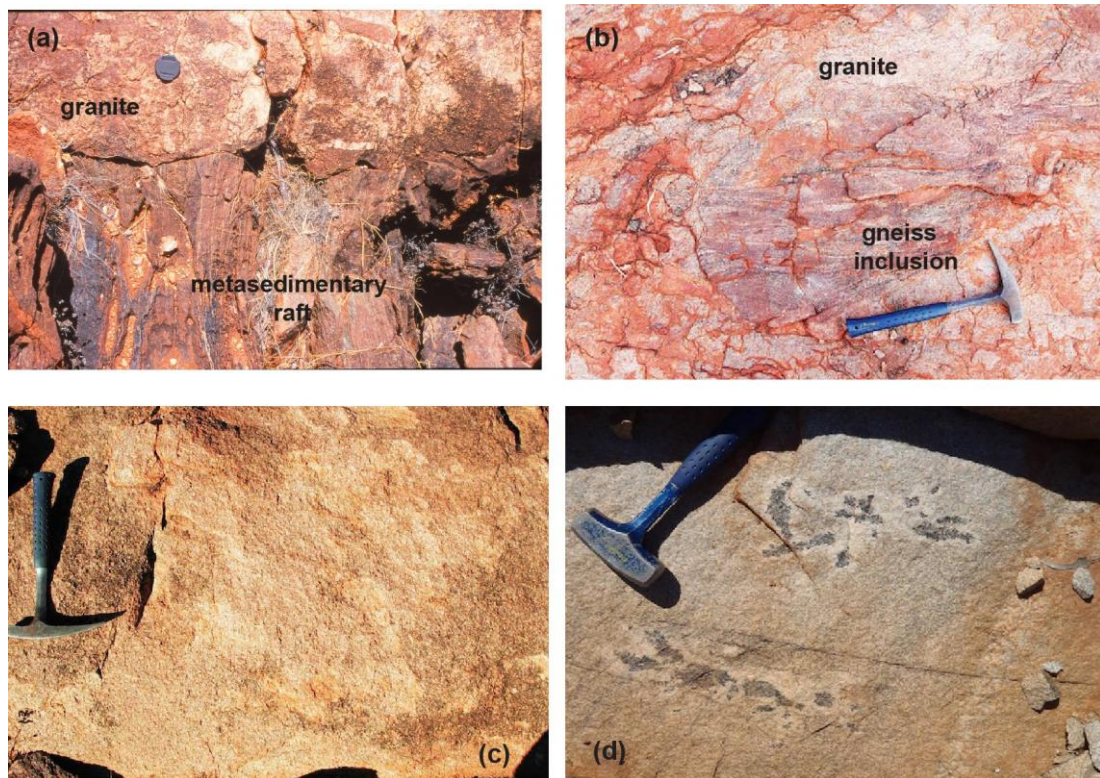


Figure 4.4 Field photos (~ 7 cm camera cover in (a) and ~ 30 cm long hammer in (b-d) for scale: (a) an undeformed coarse-grained granite dyke of the Erong Granite cutting the deformation fabrics in metasedimentary gneiss; (b) gneiss inclusion in the Durlacher Granite about 1 km from the Red Rock Bore granite locality; (c) sample 183287: a medium- to coarse-grained, equigranular muscovite–tourmaline granodiorite of the Thirty Three Supersuite; (d) sample 187401: coarse-grained equigranular tourmaline–muscovite monzogranite of the Thirty Three Supersuite with distinct tourmaline nodules.

Sample GSWA 187401 is a fine- to medium-grained, equigranular tourmaline–muscovite monzogranite that was sampled by GSWA for zircon geochronology, but was not analysed. It contains tourmaline nodules with leucocratic halos (Figure 4.4d). The monzogranite contains muscovite, and roughly 5% ferromagnesian minerals (biotite, tourmaline, epidote, and titanite). Recrystallised quartz, minor sericitisation, and mymerkite are indicative of minor post-magmatic deformation (Figure 4.3d).

The three samples (183287, 183288 and 187401) have relatively low whole-rock Zr and Sr concentrations (Table 4.1). Of the three samples 183287 shows significantly lower abundances of Th, La, Ce and Nd.

4.5 Analytical methods

Monazite from three leucocratic granite samples (GSWA 139466, 169092 and 183287) were separated using standard mineral separation methods (Wingate and Lu 2016), and cast in 25-mm-diameter epoxy mounts which were then polished to expose the interiors of the crystals. No monazite grains were found in sample GSWA 183288. For sample GSWA 187401, polished thin sections were imaged using a scanning electron microscope (SEM) in back-scattered electron (BSE) mode fitted with an energy dispersive X-ray spectrometer (EDS) to identify suitable monazite grains for *in situ* SHRIMP geochronology. Monazite grains >10 μm across were drilled out in 3 mm-diameter plugs and cast in a single 25 mm epoxy mount. Monazite reference materials FRENCH, Z2908, Z2234 and PD95 were in a separate mount that was cleaned and Au-coated with the sample mounts prior to analysis. Monazite reference OX1 was located on the same mount as the unknowns (183287).

U–Th–Pb analyses of monazite were conducted using a SHRIMP II ion microprobe in the John de Laeter Centre at Curtin University, Perth. Optical and BSE images were used to guide placement of the primary ion beam during SHRIMP analysis. The SHRIMP instrument set-up and operating protocols followed the established procedure for small spot analysis of monazite (Fletcher et al. 2010). A total of six sessions were conducted to obtain the U–Th–Pb data presented here. During all sessions, an O^{2-} primary beam focused through a 30 μm Kohler aperture to produce a spot size $\sim 10 \mu\text{m}$, with a beam intensity of 0.2 – 0.4 nA. The secondary ion system was focused through a 100 μm collector slit onto an electron multiplier to produce mass peaks with flat tops and a mass resolution ($M/\Delta M$ at 1% peak height) of > 5000 in all sessions. Post-collector retardation lens was activated to reduce stray ions. Squid-2.50.11.02.03 software (Ludwig 2009) was used for initial

data reduction, including correction for common Pb. Corrections for matrix effects in $^{206}\text{Pb}/^{238}\text{U}$ and $^{208}\text{Pb}/^{232}\text{Th}$, and for instrumental mass fractionation in $^{207}\text{Pb}/^{206}\text{Pb}$, were applied to monazite data (Fletcher et al. 2010). To adjust for analytical bias the respective 1 sigma calibration uncertainty was applied in quadrature to $^{238}\text{U}/^{206}\text{Pb}$ and $^{232}\text{Th}/^{208}\text{Pb}$ individual analyses (samples 187401 and 183287) prior to the calculation of the weighted mean. Weighted mean dates are reported with 95% confidence limits, whereas individual analyses are presented with 1sigma uncertainties. Because our samples span almost a billion years, from the Paleoproterozoic to Neoproterozoic, the choice of isotopic system ($^{207}\text{Pb}/^{206}\text{Pb}$, $^{238}\text{U}/^{206}\text{Pb}$, and $^{232}\text{Th}/^{208}\text{Pb}$) is sample dependent (e.g. Kirkland and Wingate 2012). For Paleoproterozoic and older samples the $^{207}\text{Pb}/^{206}\text{Pb}$ analysis are typically the most precise and preferred for weighted mean calculation. However, from late Mesoproterozoic $^{238}\text{U}/^{206}\text{Pb}$ or $^{232}\text{Th}/^{208}\text{Pb}$ ratios provide the most reliable age estimates. The precisions of ^{238}U and ^{232}Th abundances measured by SHRIMP are typically 5-10 %.

4.6 Monazite geochronology results

SHRIMP U–Th–Pb monazite data are presented in Appendix D and are summarised in Table 4.2, which also includes U-Pb zircon data from previous work for comparison.

Sample 139466: biotite–muscovite granodiorite

Monazite crystals from this sample are yellow, transparent and unzoned. They are subhedral to predominantly anhedral and range in size from 50 to >100 μm . Monazite occurs primarily as inclusions in quartz, but is also hosted in plagioclase. Thirteen analyses were carried out on eight monazite grains (Appendix D). Excluded from age calculations are a single concordant analysis that indicates high common Pb ($f_{206} > 1\%$) and another that is >10% discordant. The remaining 11 analyses are <5% discordant and indicate low common Pb. Ten of the 11 analyses indicate well-grouped, measured U and Th concentrations that vary from 350–500 ppm and 21,400–37,500 ppm, respectively, with Th/U ratios from 54–88. They yielded $^{207}\text{Pb}/^{206}\text{Pb}$ dates between 1868 and 1787 Ma, with a weighted mean of 1830 ± 19 Ma (MSWD = 2.8). Despite the large MSWD, rejection of additional analyses is not warranted given the uniformity of these monazites in morphology and U-Th composition. Therefore, 1830 ± 19 Ma (Figure 4.5a) is considered the best estimate of the timing of monazite growth during magma crystallisation. An old outlier yielded a $^{207}\text{Pb}/^{206}\text{Pb}$ date of 1933 ± 7 Ma (1σ), and is interpreted to be a xenocryst.

Table 4.2 Summary of field data, U–Pb zircon and U–Th–Pb monazite geochronology for leucocratic granite samples.

Sample ID	Easting	Northing	Rock type	Stratigraphic Unit	Zircon $^{207}\text{Pb}^*/^{206}\text{Pb}$ age (Ma)	Monazite age (Ma)	Isotopic system used for monazite
GSWA 139466	465700	174600	Biotite- muscovite granodiorite	Moorarie Supersuite	2621 ± 9	1830 ± 19	$^{207}\text{Pb}^*/^{206}\text{Pb}^*$
GSWA 169092	361420	7409000	Biotite-muscovite monzogranite	Durlacher Supersuite	1681 ± 10, 1619 ± 15	1682 ± 3	$^{207}\text{Pb}^*/^{206}\text{Pb}^*$
GSWA 187401	418385	7286232	Tourmaline-muscovite monzogranite	Thirty Three Supersuite	-	1006 ± 14	$^{238}\text{U}/^{206}\text{Pb}^*$
GSWA 183287	422561	7287407	Muscovite-tourmaline granodiorite	Thirty Three Supersuite	2085–1309	899 ± 10	$^{232}\text{Th}/^{208}\text{Pb}^*$
GSWA 183288	423293	7288459	Biotite-muscovite- tourmaline monzogranite	Thirty Three Supersuite	1648 ± 5	-	

Notes:

Pb* indicates radiogenic Pb (i.e. corrected for common Pb)

The choice of isotopic system used to calculate the weighted mean for monazite data is discussed in the text.

- Not analysed. Monazite was not found in sample 183288. Sample 187401 was not submitted for routine zircon geochronology due to leucocratic nature. Sample locations quoted in coordinate system MGA 1994 GDA Zone 50.

Sample 169092: biotite–muscovite monzogranite

Monazite is widespread in this rock, and occurs as inclusion in quartz, plagioclase, undeformed muscovite, and in biotite. Monazite crystals are >100 µm in size, yellow and transparent, and mainly subhedral and unzoned. Thorium concentrations range from 42,700 to 73,800 ppm, whereas U concentrations are bimodal: 1000–1900 ppm (four analyses) and 3500–7900 ppm (13 analyses). The Th/U ratios range from 8 to 70. Twenty-five analyses were obtained from 14 monazite grains; seven analyses that show >5% discordance are disregarded. A single analysis yielding a date of 1663 ± 2 Ma (1σ) is considered an outlier due to its significantly higher U (17,600 ppm) and lower Th (34,700 ppm), and resultant much lower Th/U (2 vs. 8–70) compared with the range seen in the main population (Appendix D). The remaining 17 analyses of 14 monazite grains yielded a weighted mean $^{207}\text{Pb}/^{206}\text{Pb}$ date of 1682 ± 3 Ma (MSWD = 0.99) (Figure 4.5b), interpreted as the age of igneous crystallisation, consistent with the main age component of the initial zircon age.

Sample 187401: tourmaline–muscovite monzogranite

Monazite crystals in this sample show two different morphologies: i) subhedral crystals 30 to 60 µm in size, and, ii) larger (>100 µm) anhedral crystals. The anhedral types are typically associated with secondary apatite and show retrogression coronas (e.g., Finger et al. 1998). However, the effect of post-magmatic alteration is not evident from the concordant age data, which ranges from 1058 to 970 Ma ($^{238}\text{U}/^{206}\text{Pb}$) across the monazite grains. The subhedral monazite crystals are typically hosted in plagioclase and quartz or are interstitial to the main silicate minerals (Figure 4.6). The monazites from this sample have high Th contents, similar to sample 169092, ranging from 39,900 to 80,200 ppm, and with uniformly moderate U, from 1050 to 1900 ppm, consistent with other samples in this study (Appendix D). Corresponding Th/U values range from 30 to 70. Nineteen analyses were obtained from nine monazite grains (Appendix D). Six analyses are >5% discordant and/or indicate high common ^{206}Pb (>1%) and, therefore, are not considered in the age calculation. Thirteen analyses of nine monazite grains yielded a single age component with a weighted mean $^{238}\text{U}/^{206}\text{Pb}$ date of 1006 ± 14 Ma (MSWD = 2.6) (Figure 4.5c). The same group of analyses were also used to calculate a weighted mean $^{207}\text{Pb}/^{206}\text{Pb}$ date of 1018 ± 16 (MSWD = 1.5). Excluding an analysis that yielded an imprecise $^{232}\text{Th}/^{208}\text{Pb}$ date, 18 analyses give a weighted mean $^{232}\text{Th}/^{208}\text{Pb}$ age of 1047 ± 20 (MSWD = 1.5). The weighted mean dates derived from the $^{207}\text{Pb}/^{206}\text{Pb}$ and

$^{238}\text{U}/^{206}\text{Pb}$ decays systems agree within uncertainty and because this sample falls within the Mesoproterozoic-Neoproterozoic boundary either the $^{207}\text{Pb}/^{206}\text{Pb}$ or $^{238}\text{U}/^{206}\text{Pb}$ could be used to represent the age of crystallisation. However, the individual $^{238}\text{U}/^{206}\text{Pb}$ analyses are more precise with uncertainties two to three times lower than for $^{207}\text{Pb}/^{206}\text{Pb}$, therefore, the $^{238}\text{U}/^{206}\text{Pb}$ date of 1006 ± 14 Ma is taken as the most reliable estimate of the crystallisation age.

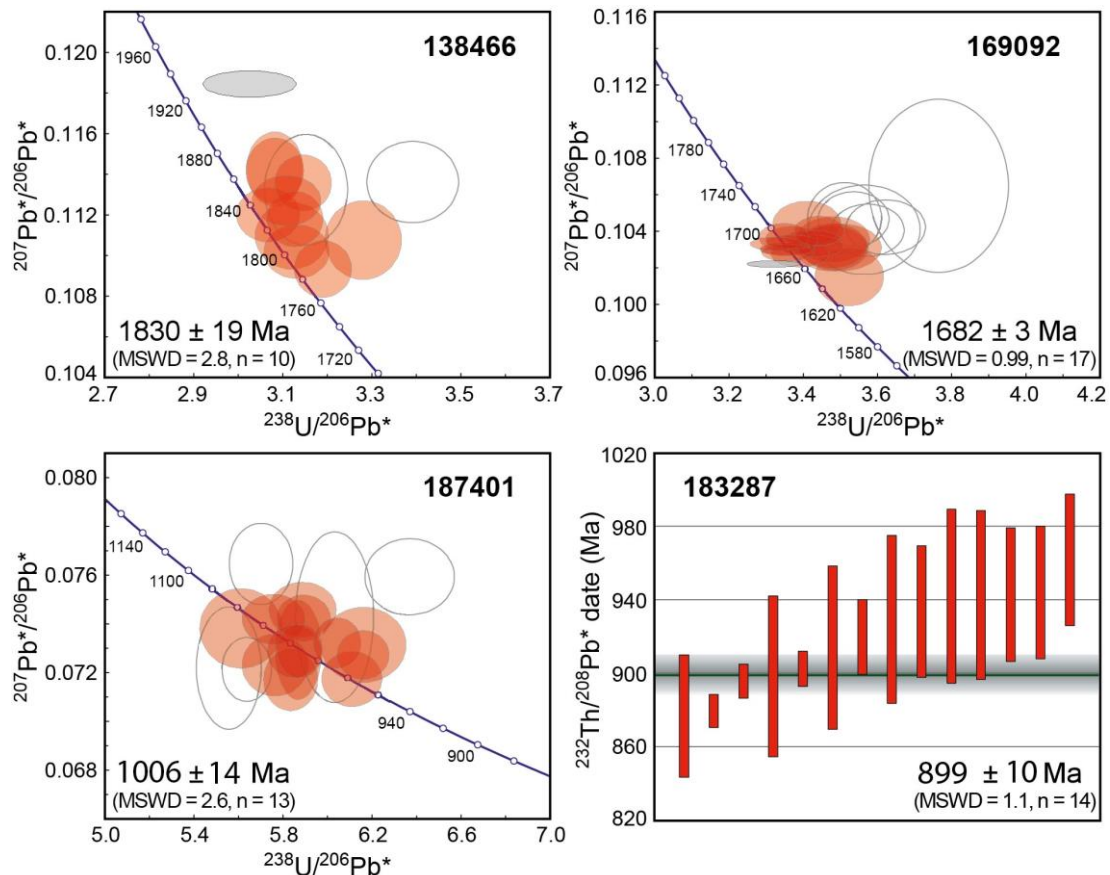


Figure 4.5 SHRIMP U–Th–Pb analytical results for monazite from leucocratic granites in the Gascoyne Province. Ellipses in the concordia diagrams (d-f) correspond to analyses with 1σ uncertainties; red ellipses represent the main group of analyses; grey ellipses denote analyses with high common Pb, and open ellipse indicate discordance >5%. Weighted mean dates are $^{207}\text{Pb}/^{206}\text{Pb}$ (a-b) and $^{206}\text{Pb}/^{238}\text{U}$ (c). (a) Erong Granite sample GSWA 139466; (b) leucocratic granite sample GSWA 169092; (c) Thirty Three Supersuite sample GSWA 187401; (d) Thirty Three Supersuite sample GSWA 183287 weighted mean $^{232}\text{Th}/^{208}\text{Pb}$ plot. Mean ages are quoted with 95% confidence intervals.

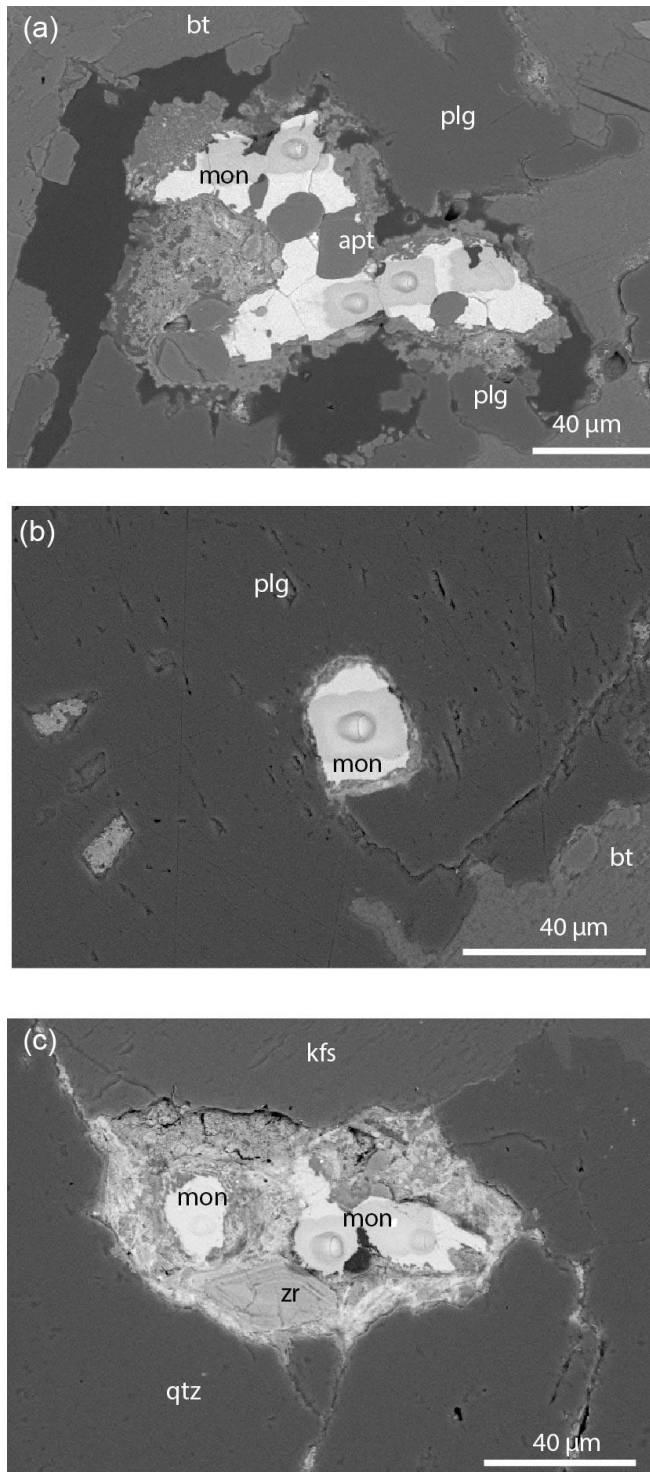


Figure 4.6 Back-scattered electron (BSE) images of representative *in situ* monazite from sample GSWA 187401 (a-c). SHRIMP pits shown by the circles and the haloes around the SHRIMP spots show the effect of the raster. (a) Monazite growth associated with secondary apatite; (b) subhedral monazite within plagioclase feldspar; (c) multiple anhedral monazites in between quartz and K-feldspar (Fe alteration around the monazite). (bt = biotite, plg = plagioclase feldspar, mon = monazite, apt = apatite, kfs = K-feldspar, qtz = quartz, zr = zircon). Dark circles are SHRIMP pits with a raster halo.

Sample 183287: biotite-muscovite–tourmaline monzogranite

Monazite crystals from this sample are subhedral to anhedral, and yellow and transparent, with an average size of 60 μm (Figure 4.7). The crystals occur as inclusions in quartz and plagioclase. Compared with those from sample 187401, monazites from this sample contain significantly lower U and Th concentrations ranging from 250 to 750 ppm and from 14,800 to 40,500 ppm, respectively, but with more uniform and elevated Th/U ratios (52–61, with an average of 54). Sixteen analyses were obtained from seven monazite grains (Appendix D). For this sample, dates determined from $^{207}\text{Pb}/^{206}\text{Pb}$ or $^{238}\text{U}/^{206}\text{Pb}$ ratios are significantly more dispersed and discordant than those based on $^{232}\text{Th}/^{208}\text{Pb}$ ratios, and several analyses indicate high common ^{206}Pb , whereas common ^{208}Pb (f_{208} in Appendix D) is, with one exception, $<1\%$. Excluding the single analysis with high common ^{208}Pb ($>1\%$), and one old outlier, 14 analyses of six monazites yielded a weighted mean $^{232}\text{Th}/^{208}\text{Pb}$ date of 899 ± 10 Ma (MSWD = 1.1) (Appendix D). Weighted mean dates calculated using $^{207}\text{Pb}/^{206}\text{Pb}$ and $^{238}\text{U}/^{206}\text{Pb}$ ratios, applying the discordance and common Pb criteria as above (cut-off value at 1% for f_{206} and $\pm 5\%$ for discordance), are 907 ± 24 ($n = 6$, MSWD = 1.3) and 917 ± 25 ($n = 6$, MSWD = 2.0), respectively. The results show that the $^{238}\text{U}/^{206}\text{Pb}$, $^{207}\text{Pb}/^{206}\text{Pb}$ and $^{232}\text{Th}/^{208}\text{Pb}$ weighted mean ages are indistinguishable within uncertainty; however, the overall weighted mean is most precise for the $^{232}\text{Th}/^{208}\text{Pb}$ system, therefore, for this Neoproterozoic sample, we consider the $^{232}\text{Th}/^{208}\text{Pb}$ age of 899 ± 10 Ma to be the best estimate of the age of igneous crystallisation (Figure 4.5d).

4.7 Discussion

Igneous crystallisation ages for some leucocratic granites are difficult to determine using U–Pb zircon geochronology because these low-temperature crustal melts commonly contain a significant proportion of inherited zircon (e.g. Crowley et al. 2008; Harrison et al. 1999; Scott et al. 2011). The samples in this study contain Zr contents < 150 ppm, which according to Miller et al (2003), is a criterion for potential zircon inheritance in a melt. Due to the historic issue of xenocrystic zircons in the leucocratic granites in the Gascoyne Province, an alternative was required to determine the crystallisation age of these granites. Monazite is a common accessory mineral in a wide variety of granitic rocks, and, in particular, is commonly found as primary monazite in peraluminous leucogranites. Magmatic monazite is distinguished from metamorphic monazite by observing the textural context of the crystals and noticing any effects of post magmatic deformation experienced by the rock. Here we show how obtaining reliable crystallization ages is important to determine the duration and extent of major granitic events and associated orogenic activity

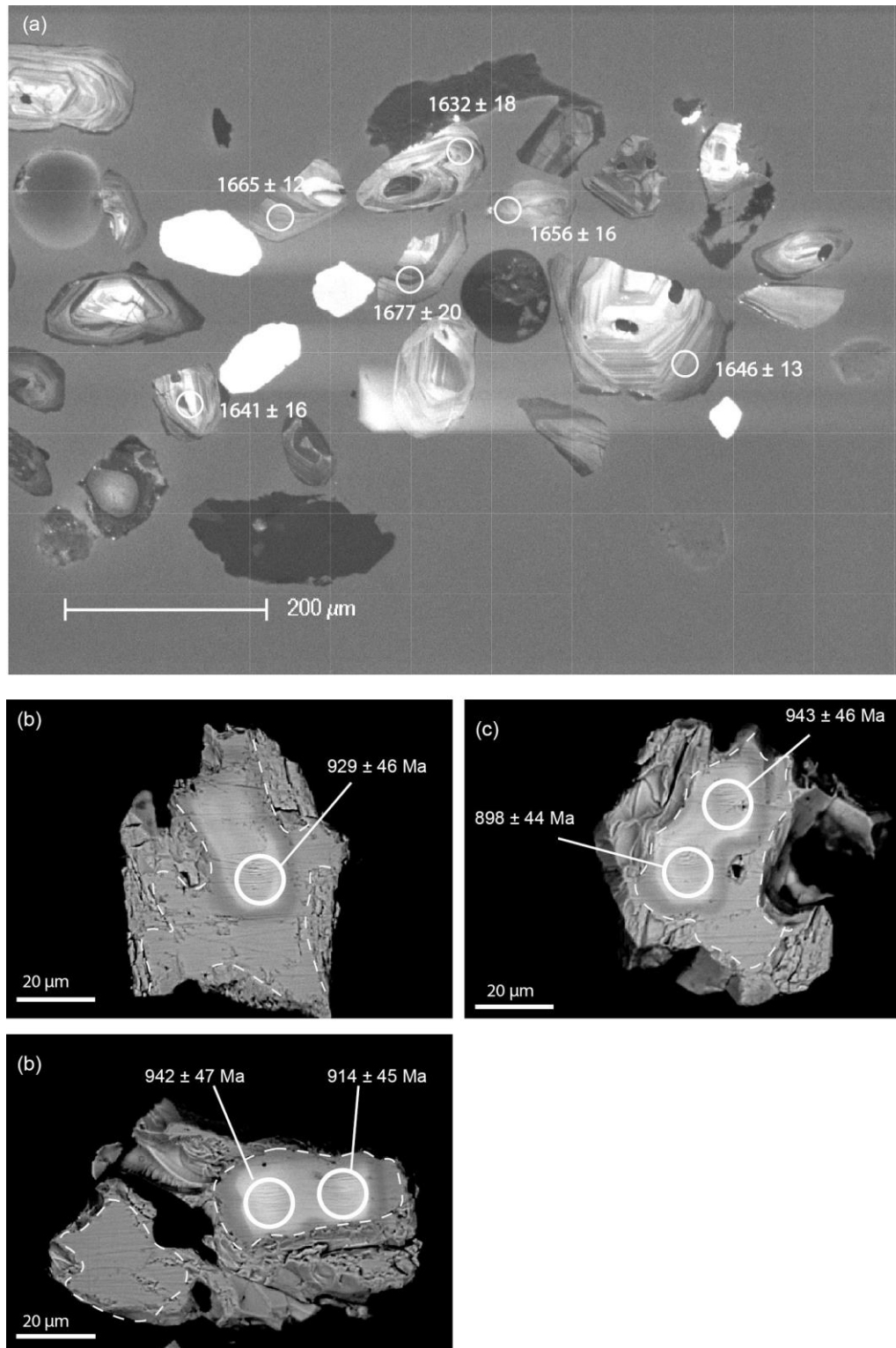


Figure 4.7 Cathodoluminescence image of representative zircon grains from **sample 183287** showing the original xenocrystic zircon ages (Kirkland et al. 2009) (a). Back-scattered electron (BSE) images of representative separated monazite grains from 183287 plus SHRIMP pits and corresponding ages from sample GSWA 183287 (b-d) subhedral to anhedral uniform monazite grains typically around 60 μm in size. Zoning indicated by dashed outline. SHRIMP pits are shown by the circles and the haloes around the SHRIMP spots show the effect of the raster.

4.7.1 Assessment of magmatic monazite

Igneous monazite may become unstable during low- to medium grade regional metamorphism (Townsend et al. 2001) resulting in secondary apatite-allanite coronas (Finger et al. 1998). The *in situ* monazite crystals in the tourmaline–muscovite monzogranite sample (GSWA 18740) are accompanied by secondary apatite and display some reaction coronas (Figure 4.6). Although some monazite crystals in sample 187401 show secondary alteration rims, both monazite inclusions in plagioclase and interstitial monazite yielded similar ages. Although magmatic monazites typically show zoning (Bea 1996; Broska et al. 2000; Crowley et al. 2008; Montel 1996; Townsend et al. 2001), we found that only monazite in the muscovite–tourmaline granodiorite (GSWA 183287) shows zoning (Figure 4.7); despite this, small-spot analysis enabled the primary monazite to be targeted and the results show consistent dates across the grains (Appendix D).

In sample 187401 the monazite crystals hosted in quartz and plagioclase suggest that monazite crystallised with the melt in contrast to inclusions in biotite that may contain inherited monazite (Rapp and Watson 1986). For the grain mounted samples (139466, 169092 and 183287), monazite is found as inclusions in quartz and plagioclase and, more rarely, in biotite and muscovite or as an interstitial mineral. The results in Copeland et al. (1988) suggested that monazite inheritance is common in Tertiary S-types granites. Although the original location of the analysed monazite crystals is not known, our data contain only one analysis of inherited monazite (sample 139466) across four granite samples. This confirms the suggestion by Parish (1990) that monazite inheritance is less common than zircon in granites and, in particular, Precambrian granites.

Typically magmatic monazite shows a consistent pattern of elevated Th and moderate U concentrations. In Figure 4.8, the Th and U concentrations of monazite analysed in this study are compared with monazite from other granites. The plot shows that our monazites are consistent with the Th and U signature of igneous monazites presented in other studies. Lower U and Th concentrations distinguish magmatic monazite from hydrothermal monazite and monazite grown during low-temperature metamorphism or mineralisation from the southern Pilbara margin (Rasmussen et al. 2005) and the Abra deposit in the Capricorn Orogen (Zi et al. 2015) (Figure 4.8). However, monazite related to medium-grade metamorphism may yield similar Th and U concentrations to magmatic monazite (e.g., U ranges from 1100 to 6700 ppm and Th from 1200 to 104,800 ppm, Sheppard et al. 2007). Although the rocks in this study show signs of minor recrystallisation related to low-grade metamorphic overprints the absence

of multiple age populations in individual samples suggest that the post-magmatic effects are minimal. Additionally, the two samples that display minor alteration of monazite (183287 and 187401) the analytical small spot allowed for careful targeting of monazite. The leucocratic granites lack any evidence of a medium-grade metamorphic overprint (Figure 4.3) and demonstrably post-date regional metamorphic fabrics. Therefore, considering the textural context of the monazites and the observed minimal post-magmatic alteration we conclude that the monazites analysed are magmatic in origin.

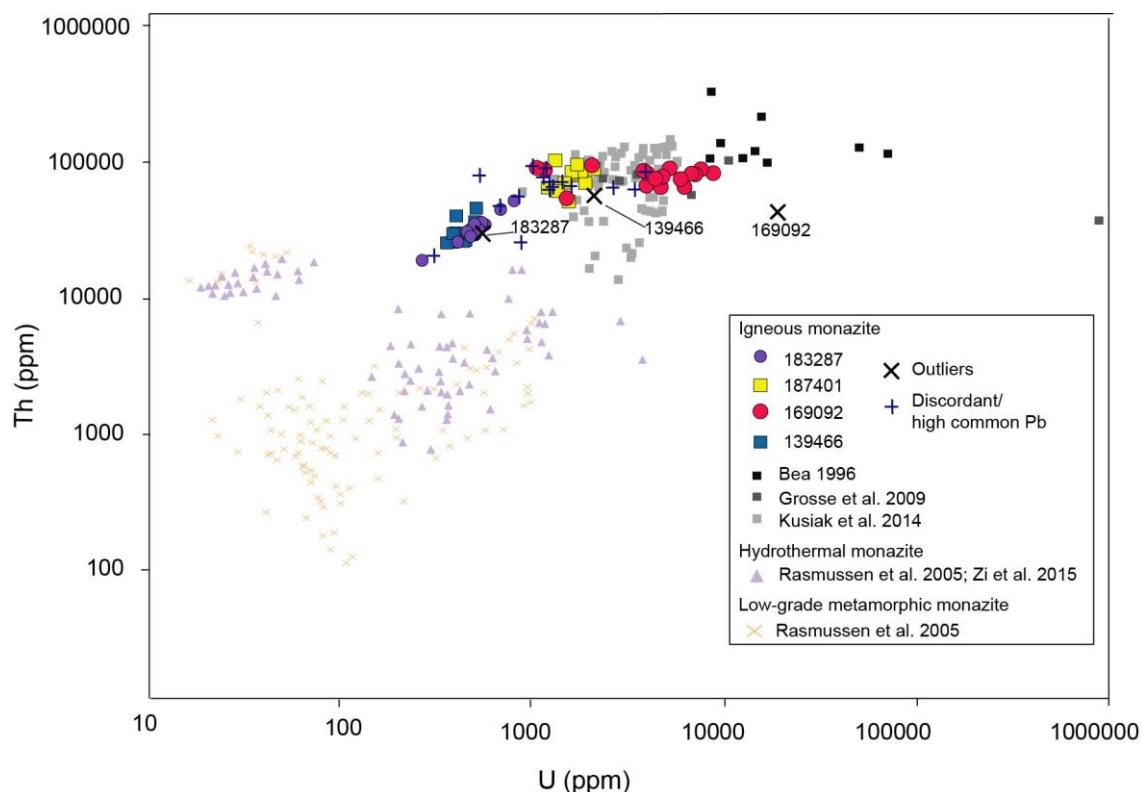


Figure 4.8 Diagram of Th versus U concentrations in monazite from leucocratic granites analysed in this study, and published data (Bea 1996; Grosse et al. 2009; Kusiak et al. 2014), relative to the field for hydrothermal monazites (Zi et al. 2015), and low grade metamorphism and mineralisation (Rasmussen et al. 2005) and medium grade metamorphism (Sheppard et al. 2007) from study areas in the Capricorn Orogen. The plot shows a clear distinction between igneous monazite and hydrothermal and low-grade metamorphism.

4.7.2 Implications of the monazite geochronology

Correctly dating the timing and duration of magmatism is essential both for reconstructing reliable tectonic histories in complex intracratonic orogenic belts and for addressing the thermal history of orogens. Below we examine the wider implications of our new geochronology results.

The life-span of an orogeny

Many Precambrian orogenic belts dominated by low- to medium-grade metamorphic rocks lack direct metamorphic ages (and when biostratigraphy is not available), the ages of granitic supersuites have been used as a proxy for the duration of orogenic events (e.g., the 1680–1620 Ma Durlacher Supersuite, Sheppard et al., 2005). The biotite-muscovite monzogranite (GSWA 169092) in the far north of the province yielded zircon results that were inconclusive and allowed for two possible interpretations of the igneous crystallisation age. However, our monazite geochronology provides an unambiguous igneous crystallisation age of 1682 ± 3 Ma for sample 169092, indicating that it was emplaced during the main stage of magmatism (1688–1659 Ma). There is a lack of evidence for granites younger than c. 1659 Ma in the Durlacher Supersuite in the northern Gascoyne Province suggesting that magma emplacement occurred over a shorter interval (Figure 4.9) than previously thought by Sheppard et al. (2005). In turn, new data imply a higher flux of felsic magma generation during intracontinental reworking and that the reworking was of shorter duration than previously supposed.

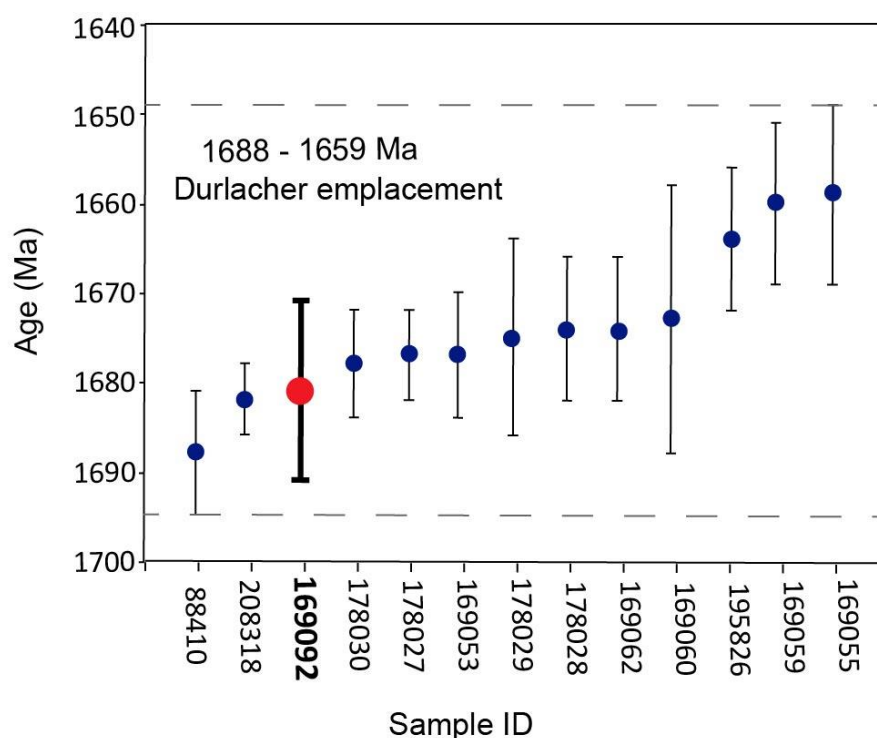


Figure 4.9 Zircon dates from Durlacher Supersuite granites in the northern Gascoyne Province (GSWA 2016b). The data indicate that magmatism in the northern Gascoyne spanned c. 30 million years and ceased by c. 1659 Ma. Error bars indicate 95% confidence intervals.

Sample GSWA 169092 and the c. 1620 Ma Discretion Granite were used to provide a younger limit to the Durlacher Supersuite and tectonothermal activity during the Mangaroon Orogeny (Sheppard et al., 2005). However, the Discretion Granite (Figure 4.1c) appears to be an episode of felsic magmatism isolated in space and time, and may either belong to a discrete tectonothermal event or be related to a flare-up of intracratonic reworking far to the southeast.

A slow-burning supersuite

The Thirty Three Supersuite (995–955 Ma) comprises ~ 420 km² of leucocratic granite plutons and pegmatites restricted to the central part of the Gascoyne Province. Volumetrically, the supersuite is by far the smallest of the four supersuites in the province. Despite being emplaced in a narrow structural corridor, the timing of the Thirty Three Supersuite has proven difficult to constrain. The initial zircon geochronology and our new monazite results are discussed below.

4.7.3 Zircon geochronology

Initial U-Pb zircon geochronology for one pluton of the Thirty Three Supersuite yielded a date of 1652 ± 5 Ma, interpreted as the crystallisation age (sample KC063, a biotite-muscovite-tourmaline monzogranite; Culver 2001). At that time this age appeared to be consistent with the field relationships for two reasons: (1) tectonic fabrics in surrounding metasedimentary rocks cut by the plutons were considered to be Paleoproterozoic, and (2) the leucocratic granites do not intrude the unconformably overlying 1620–1450 Ma metasediments (Figure 4.2c). However, later monazite geochronology established that the metamorphic assemblages are actually related to the 1030–950 Ma Edmundian Orogeny, and that a large rare-earth-element-bearing pegmatite considered to be associated with the leucocratic granites has an igneous crystallisation age of 954 ± 12 Ma (Sample 117154, Sheppard et al. 2007). Further U-Pb zircon geochronology of the leucocratic granites yielded zircon dates that were interpreted as representing the ages of xenocrystic zircon. A biotite-muscovite-tourmaline monzogranite (183287) yielded zircon populations between 2085 and 1309 Ma (Kirkland et al. 2009), and secondly, a muscovite-tourmaline monzogranite (183288) yielded a single age population 1648 ± 5 Ma (Wingate et al. in press).

4.7.4 Pegmatites

Additional zircon geochronology on pegmatites (samples GSWA 185946, 185945 and 190667) in the area established igneous crystallisation ages, respectively, of 1030 ± 6 Ma, 1000 ± 8 Ma, and 939 ± 5 Ma (Wingate et al. 2011; Wingate et al. 2010a; Wingate et al. 2010b) better aligned with the field relationships and existing phosphate geochronology. Furthermore, monazite from a tourmaline-rich schist which is part of a metasomatic halo around a tourmaline-bearing pegmatite dyke yielded a date of 958 ± 16 Ma (Sample GSWA 88475 Figure 4.2c, Korhonen et al. 2015).

4.7.5 Monazite geochronology

Our monazite data from two leucocratic samples, of the Thirty Three Supersuite, yielded Neoproterozoic ages consistent with the metamorphic fabrics in the adjacent rocks. Sample 187401, a tourmaline–muscovite monzogranite, yielded an age of 1006 ± 14 Ma representing the initial stages of magmatism. Furthermore, our results highlight that magmatism continued until c. 899 Ma (sample 183287: biotite–muscovite–tourmaline monzogranite).

The combined monazite and zircon data suggests that magmatism of the Thirty Three Supersuite spanned about 130 million years (c. 1030–899 Ma) and that leucocratic magmatism outlasted the regional metamorphism in the same structural corridor by c. 100 million years (Figure 4.10). Furthermore, given the small area (and likely small volume) of the supersuite, the geochronology implies exceptionally low magma production rates. The monazite and zircon geochronology confirm that the Thirty Three Supersuite is much younger than c. 1620–1465 Ma metasedimentary rocks of the Edmund Group, despite the absence of pegmatite and leucocratic granite in the Edmund Group in the Ti Tree Shear Zone immediately to the north. Therefore, reworking and magmatism must have been funnelled into a narrow structural corridor south of the shear zone from c. 1030 Ma onwards. This work further highlights the problem of attempting to correlate events across major structures within a complex orogen.

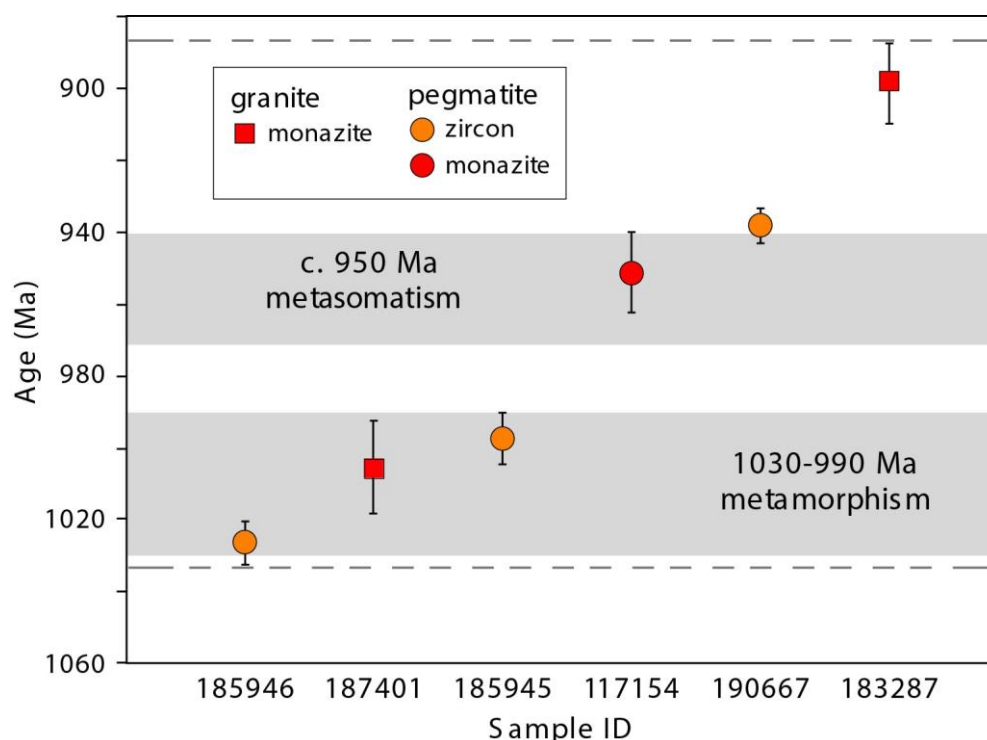


Figure 4.10 Monazite and zircon ages for leucocratic granites and pegmatites of the Thirty Three Supersuite. Two stages of granite and pegmatite are suggested by the combined monazite and zircon geochronology. The first stage corresponds with metamorphism and deformation during the Edmondian Orogeny, whereas the younger pulse may be associated with periodic reactivation of the Ti Tree Shear Zone. Error bars indicate 95% confidence intervals.

4.7.6 An isolated granite

Sample GSWA 139466 was taken from a pluton of biotite-muscovite granodiorite pluton that intruded a crustal-scale shear zone (the Errabiddy Shear Zone). The existing geochronological constraints allowed the pluton to have been emplaced at any time over a c. 1000 million-year interval. Our U-Th-Pb monazite geochronology yielded a date of 1830 ± 19 Ma, interpreted as the age of igneous crystallisation and is consistent with field relationships that show the Erong Granite cutting deformation fabrics formed during the 2005–1950 Ma Glenburgh Orogeny. The new monazite data indicates that the pluton is part of the voluminous Moorarie Supersuite associated with reworking during the Paleoproterozoic Capricorn Orogeny. This study shows that even for an area shaped by multiple episodes of reworking and reactivation monazite is a powerful geochronometer for constructing a more reliable tectonic and magmatic history of a major shear zone.

4.8 Conclusions

Our study has highlighted the benefits of using U-Th-Pb monazite geochronology for dating peraluminous leucocratic, low-temperature granites. This study has demonstrated that U-Th-Pb monazite geochronology is preferable for determining the crystallisation ages of Precambrian low-temperature, peraluminous leucocratic granites for the following reasons: (1) new monazite growth occurs readily at a range of P-T conditions remaining robust over time with a closure temperature of 720–750° C (Copeland et al 1988); (2) monazite contains high U and Th and incorporates minor common Pb (Townsend et al. 2001); (3) monazite, unlike zircon, generally does not contain inherited cores and is immune from radiogenic Pb loss at low temperatures (Grosse et al. 2009); (4) occurrences of inherited monazite, although common in Tertiary S-type granites (Copeland et al. 1988), are uncommon in Precambrian rocks (Parrish 1990); and (5) magmatic monazite is one of the most common accessory mineral in granites and is abundant in peraluminous compositions (Bea 1996; Montel 1993; Rapp and Watson 1986). Our study has also resolved the duration of two generations of magmatism: in one instance emplacement occurred over a much shorter time interval (~ 30 million years) implying a higher rate of magma production than previously thought, and secondly, whereas purely leucocratic granites and pegmatites of the Thirty Three Supersuite span a remarkably long duration of c. 130 million years implying a very low rate of magma generation. Finally, the use of monazite geochronology was able to narrow the possible window of magmatism to a discrete reworking event significantly reducing the time span previously thought.

4.9 Acknowledgements

We thank Simon Johnson and Ian Fitzsimons for their critical and insightful reviews. Zedenka Martelli kindly provided assistance with monazite identification and picking. This manuscript was significantly improved by valuable comments received from an anonymous reviewer. U-Th-Pb measurements were conducted using the SHRIMP ion microprobes at the John de Laeter Centre at Curtin University. Michael Wingate publishes with permission of the Director of the Geological Survey of Western Australia. Australian Research Council Linkage Grant LP130100922 and the Geological Survey of Western Australia (through the Exploration Incentive Scheme) funded this PhD project.

4.10 References

- Ayres, M., Harris, N., & Vance, D. (1997). Possible constraints on anatectic melt residence times from accessory mineral dissolution rates; an example from Himalayan leucogranites. *Mineralogical Magazine*, 61, 29–36.
- Bea, F. (1996). Residence of REE, Y, Th and U in Granites and Crustal Protoliths; Implications for the Chemistry of Crustal Melts. *Journal of Petrology*, 37, 521–552.
- Bea, F., Montero, P., González-Lodeiro, F., Talavera, C. (2007). Zircon Inheritance Reveals Exceptionally Fast Crustal Magma Generation Processes in Central Iberia during the Cambro-Ordovician. *Journal of Petrology*, 48, 2327–2339.
- Bodorkos, S., & Wingate, M. T. D. (2007). The contribution of geochronology to GSWA's mapping programs: current perspectives and future directions. *Geological Survey of Western Australia, Record 2007/2*, 10–11.
- Boehnke, P., Watson, E. B., Trail, D., Harrison, T. M., & Schmitt, A. K. (2013). Zircon saturation re-revisited. *Chemical Geology*, 351, 324–334.
- Broska, I., Petrik, I., & Williams, C. T. (2000). Coexisting monazite and allanite in peraluminous granitoids of the Tribeč Mountains, Western Carpathians. *American Mineralogist*, 85, 22–32.
- Brown, M. (1994). The generation, segregation, ascent and emplacement of granite magma: the migmatite-to-crustally-derived granite connection in thickened orogens. *Earth-Science Reviews*, 36, 83–130.
- Budzyń, B., Harlov, D. E., Williams, M. L., & Jercinovic, M. J. (2011). Experimental determination of stability relations between monazite, fluorapatite, allanite, and REE-epidote as a function of pressure, temperature, and fluid composition. *American Mineralogist*, 96, 1547–1567.
- Copeland, P., Parrish, R. R., & Harrison, T. M. (1988). Identification of inherited radiogenic Pb in monazite and its implications for U-Pb systematics. *Nature*, 333, 760–763.
- Crowley, J. L., Brown, R. L., Gervais, F., & Gibson, H. D. (2008). Assessing Inheritance of Zircon and Monazite in Granitic Rocks from the Monashee Complex, Canadian Cordillera. *Journal of Petrology*, 49, 1915–1929.
- Culver, K. E. (2001). Structure, metamorphism and geochronology of the northern margin of the Gurun Gutta Granite, central Gascoyne Complex, Western Australia. Curtin University of Technology, Perth BSc. (Hons) thesis (unpublished).

- Finger, F., Broska, I., Roberts, M. P., & Schermaier, A. (1998). Replacement of primary monazite by apatite-allanite-epidote coronas in an amphibolite facies granite gneiss from the eastern Alps. *American Mineralogist*, 83, 248–258.
- Fletcher, I. R., McNaughton, N. J., Davis, W. J., & Rasmussen, B. (2010). Matrix effects and calibration limitations in ion probe U–Pb and Th–Pb dating of monazite. *Chemical Geology*, 270, 31–44.
- Gao, L-E., Zeng, L., & Asimow, P. D. (2017). Contrasting geochemical signatures of fluid-absent versus fluid-fluxed melting of muscovite in metasedimentary sources: The Himalayan leucogranites. *Geology*, 45, 39–42.
- Gilotti, J. A., & McClelland, W. C. (2005). Leucogranites and the Time of Extension in the East Greenland Caledonides. *The Journal of Geology*, 113, 399–417.
- Grosse, P., Söllner, F., Báez, M. A., Toselli, A. J., Rossi, J. N., de la Rosa, J. D. (2009). Lower Carboniferous post-orogenic granites in central-eastern Sierra de Velasco, Sierras Pampeanas, Argentina: U–Pb monazite geochronology, geochemistry and Sr–Nd isotopes. *International Journal of Earth Sciences*, 98, 1001–1025.
- GSWA. (2016a). 1:500 000 State interpreted bedrock geology of Western Australia, 2016: Geological Survey of Western Australia, digital data layer. www.dmp.wa.gov.au/geoview.
- GSWA. (2016b). Compilation of geochronology information, 2016 update, digital data product. www.dmp.wa.gov.au/geoview.
- Harrison, M. T., Grove, M., McKeegan, K.D., Coath, C.D., Lovera, O.M., & Fort, P. L. (1999). Origin and Episodic Emplacement of the Manaslu Intrusive Complex, Central Himalaya. *Journal of Petrology*, 40, 3–19.
- Johnson, S. P., Sheppard, S., Rasmussen, B., Wingate, M. T. D., Kirkland, C. L., Muhling, J. R., Fletcher, I. R., & Belousova, E. A. (2011). Two collisions, two sutures: Punctuated pre-1950Ma assembly of the West Australian Craton during the Ophthalmian and Glenburgh Orogenies. *Precambrian Research*, 189, 239–262.
- Johnson, S. P., Korhonen, F. J., Kirkland, C. L., Cliff, J. A., Belousova, E.A., & Sheppard, S. (2017). An isotopic perspective on growth and differentiation of Proterozoic orogenic crust: from subduction magmatism to cratonization. *Lithos*, 268, 76–86.
- Kemp, A. I. S., & Hawkesworth, C. J. (2003). 3.11 - Granitic Perspectives on the Generation and Secular Evolution of the Continental Crust A2 - Holland, Heinrich D. In: Turekian KK (ed) *Treatise on Geochemistry*. Pergamon, Oxford, p. 349–410.
- Kirkland, C. L., Wingate, M. T. D. (2012). Reading Deep Time: Radiogenic Isotopic Geochronology. Geological Survey of Western Australia, Record 2012/15, p.10.

- Kirkland, C.L., Wingate, M. T. D., Bodorkos, S., & Sheppard, S. (2009). 183287: granite, Perseverance Well; Geochronology Record 756. Geological Survey of Western Australia, p. 4.
- Korhonen, F. J., Johnson, S. P., Fletcher, I. R., Rasmussen, B., Sheppard, S., Muhling, J. R., Dunkley, D. J., Wingate, M. T. D., Roberts, M. P., & Kirkland, C. L. (2015). Pressure-Temperature-Time evolution of the Mutherbukin Tectonic event, Capricorn Orogen: Geological Survey of Western Australia, Report 146, p.64.
- Kusiak, M. A., Williams, I. S., Dunkley, D. J., Konečný, P., Słaby, E., & Martin, H. (2014). Monazite to the rescue: U–Th–Pb dating of the intrusive history of the composite Karkonosze pluton, Bohemian Massif. *Chemical Geology*, 364, 76–92.
- Le Maitre, R. W. (1989). *A Classification of the Igneous Rocks and Glossary of Terms*. Blackwell, Oxford, p. 193.
- Lee, D. E., & Dodge, F. C. W. (1964). Accessory minerals in some granitic rocks in California and Nevada as a function of calcium content. *American Mineralogist* 49, 1660–1669.
- Ludwig, K.R. (2009). *Squid 2.50, A User's Manual* Berkeley Geochronology Centre Special Publication, p. 95.
- Miller, C.F., Meschter McDowell, S., & Mapes, R. W. (2003). Hot and cold granites? Implications of zircon saturation temperatures and preservation of inheritance. *Geology*, 31, 529–532.
- Miller, C. F., Mittlefehldt, D. W. (1982). Depletion of light rare-earth elements in felsic magmas. *Geology*, 10, 129–133.
- Montel, J-M. (1993). A model for monazite/melt equilibrium and application to the generation of granitic magmas. *Chemical Geology*, 110, 127–146.
- Nelson, D. R. (1998). 142855: porphyritic monzogranite, Anderson Well; Geochronology Record 371: Geological Survey of Western Australia, p.4.
- Nelson, D. R. (2000). 139466: foliated biotite-muscovite-garnet granodiorite, Erong Homestead; Geochronology Record 427: Geological Survey of Western Australia, p. 4.
- Nelson, D. R. (2004). 169092: biotite-muscovite monzogranite, Red Rock Bore; Geochronology Record 103: Geological Survey of Western Australia, p. 5.
- Occhipinti, S. A., & Reddy, S. M. (2009). Neoproterozoic reworking of the Palaeoproterozoic Capricorn Orogen of Western Australia and implications for the amalgamation of Rodinia. *Geological Society, London, Special Publications*, 327, 445–456.

- Occhipinti, S. A., Sheppard, S., Myers, J. S., Tyler, I. M., & Nelson, D. R. (2001). Archaean and Palaeoproterozoic geology of the Narryer Terrane (Yilgarn Craton) and the southern Gascoyne Complex (Capricorn Orogen), Western Australia — a field guide. Geological Survey of Western Australia, Record 2001/8, p. 70.
- Occhipinti, S. A., Sheppard, S., Passchier, C., Tyler, I.M., & Nelson, D. R. (2004). Palaeoproterozoic crustal accretion and collision in the southern Capricorn Orogen: the Glenburgh Orogeny. *Precambrian Research*, 128, 237–255.
- Parrish, R. R. (1990). U–Pb dating of monazite and its application to geological problems Canadian. *Journal of Earth Sciences*, 27, 1431–1450.
- Parrish, R. R., & Tirrul, R. (1989). U-Pb age of the Baltoro granite, northwest Himalaya, and implications for monazite U-Pb systematics. *Geology*, 17, 1076–1079.
- Patiño Douce, A. E., & Harris, N. (1998). Experimental Constraints on Himalayan Anatexis. *Journal of Petrology*, 39, 689–710.
- Poitrasson, F., Chenery, S., & Bland, D. J. (1996). Contrasted monazite hydrothermal alteration mechanisms and their geochemical implications. *Earth and Planetary Science Letters*, 145, 79–96.
- Rapp, R. P., & Watson, E. B. (1986). Monazite solubility and dissolution kinetics: implications for the thorium and light rare earth chemistry of felsic magmas. *Contributions to Mineralogy and Petrology*, 94, 304–316.
- Rasmussen, B., Fletcher, I. R., & Sheppard, S. (2005). Isotopic dating of the migration of a low-grade metamorphic front during orogenesis. *Geology*, 33, 773–776.
- Scaillet, B., Holtz, F., & Pichavant, M. (2016). Experimental Constraints on the Formation of Silicic Magmas. *Elements*, 12, 109–114.
- Scaillet, B., Pichavant, M., & Roux, J. (1995). Experimental Crystallization of Leucogranite Magmas. *Journal of Petrology*, 36, 663–705.
- Schärer, U., Xu, R. H., & Allègre, C. J. (1986). U-(Th)-Pb systematics and ages of Himalayan leucogranites, South Tibet. *Earth and Planetary Science Letters*, 77, 35–48.
- Scott, J. M., Palin, J. M., Cooper, A. F., Sagar, M. W., Allibone, A. H., & Tulloch, A. J. (2011). From richer to poorer: zircon inheritance in Pomona Island Granite, New Zealand. *Contributions to Mineralogy and Petrology*, 161, 667–681.
- Sheppard S, Occhipinti, S. A., & Nelson, D. R. (2005). Intracontinental reworking in the Capricorn Orogen, Western Australia: the 1680–1620 Ma Mangaroon Orogeny. *Australian Journal of Earth Sciences*, 52, 443–460.

- Sheppard, S., Rasmussen, B., Muhling, J. R., Farrell, T. R., & Fletcher, I. R. (2007). Grenvillian-aged orogenesis in the Palaeoproterozoic Gascoyne Complex, Western Australia: 1030–950 Ma reworking of the Proterozoic Capricorn Orogen. *Journal of Metamorphic Geology*, 25, 477–494.
- Sheppard, S., Bodorkos, S., Johnson, S. P., Wingate, M. T. D., & Kirkland, C. L. (2010a). The Paleoproterozoic Capricorn Orogeny: Intracontinental Reworking Not Continent-Continent Collision: Geological Survey of Western Australia, Report 108, p. 33.
- Sheppard, S., Johnson, S. P., Wingate, M. T. D., Kirkland, C. L., & Pirajno, F. (2010b). Explanatory notes for the Gascoyne Province: Geological Survey of Western Australia, 1:100 000 Explanatory Notes, p. 336.
- Townsend, K. J., Miller, C.F., D'Andrea, J.L., Ayers, J.C., Harrison, T. M., & Coath, C. D. (2001). Low temperature replacement of monazite in the Ireteba granite, Southern Nevada: geochronological implications. *Chemical Geology*, 172, 95–112.
- Watson, E. B., & Harrison, T. M. (1983). Zircon saturation revisited: temperature and composition effects in a variety of crustal magma types. *Earth and Planetary Science Letters*, 64, 295–304.
- Williams, I. S., Compston, W., & Chappell, B. W. (1983). Zircon and monazite U–Pb systems and the histories of I-type magmas, Berridale Batholith, Australia. *Journal of Petrology*, 24, 76–97.
- Wingate, M., & Lu, Y. (2016). Introduction to geochronology information released in 2014: Geological Survey of Western Australia, p. 5.
- Wingate, M., Kirkland, C., Sheppard, S., & Johnson, S. (2010a). 185945: pegmatite lenses in metamonzogranite, Yinnetharra Homestead; Geochronology Record 901: Geological Survey of Western Australia, p. 5.
- Wingate, M., Kirkland, C., Sheppard, S., & Johnson, S. (2010b). 185946: pegmatite dyke, Yinnetharra Homestead; Geochronology Record 902: Geological Survey of Western Australia, p. 4.
- Wingate, M. T. D., Lu, Y., & Johnson, S. P. (in press). 183288: biotite–tourmaline monzogranite, Perseverance Well; Geochronology Record 1352: Geological Survey of Western Australia, p. 5.
- Zen, E. (1986). Aluminum Enrichment in Silicate Melts by Fractional Crystallization: Some Mineralogical and Petrographic Constraints. *Journal of Petrology*, 27, 1095–1117.
- Zi, J.-W., Rasmussen, B., Muhling, J. R., Fletcher, I. R., Thorne, A. M., Johnson, S. P., Cutten, H. N., Dunkley, D. J., & Korhonen, F. J. (2015). In situ U–Pb geochronology of xenotime and monazite from the Abra polymetallic deposit in the Capricorn Orogen, Australia: Dating hydrothermal mineralization and fluid flow in a long-lived crustal structure. *Precambrian Research*, 260, 91–112.

Chapter 5

PAPER 4: Neoproterozoic $^{40}\text{Ar}/^{39}\text{Ar}$ mica ages mark the termination of a billion years of intraplate reworking in the Capricorn Orogen, Western Australia

Authors:

Agnieszka M. Piechocka¹, Stephen Sheppard^{1,2}, Ian C. W. Fitzsimons¹, Simon P. Johnson³, Birger Rasmussen⁴, and Fred Jourdan¹

¹School of Earth and Planetary Sciences, Curtin University, Kent Street, Bentley, WA 6102, Australia

²Prime Geological Mapping, PO Box 3014, Carlisle South, WA, 6101, Australia

³Geological Survey of Western Australia, 100 Plain Street, East Perth, WA 6004, Australia

⁴School of Earth Sciences, The University of Western Australia, Nedlands, WA 6009, Australia

Keywords:

intraplate orogeny, $^{40}\text{Ar}/^{39}\text{Ar}$ geochronology, U–Pb xenotime geochronology, Neoproterozoic, Capricorn Orogen, West Australian Craton

5.1 Abstract

The tectonic history of the Proterozoic Capricorn Orogen, Western Australia, records complex intraplate reworking lasting nearly one billion years. Although the Paleo–Mesoproterozoic reworking history is well defined in the crystalline basement of the Gascoyne Province, at the western end of the orogen, the younger reactivation history remains unclear. Four reworking events affected the orogen at 1820–1770 Ma, 1680–1620 Ma, 1320–1170 Ma, and 1030–900 Ma. These events were succeeded by a breakout in predominantly dextral strike-slip reactivation of major shear zones across the Gascoyne Province. Currently, the age of this reactivation is constrained by only one date of c. 570 Ma from a single shear zone, but field relationships imply that some of the shear zones must be older than a suite of c. 755 Ma dolerite dykes. In order to constrain the age of fault and shear zone reactivation we obtained new $^{40}\text{Ar}/^{39}\text{Ar}$ dates for mica and *in situ* SHRIMP U–Pb dates for xenotime within shear zones. Our results when combined with previously published data, show that reactivation occurred between 920 and 830 Ma. These dates overlap with the youngest reworking event, the 1030–900 Ma Edmundian Orogeny. Furthermore, Neoproterozoic U–Pb phosphate ages are known from the bounding cratons and faulting within the adjacent Mesoproterozoic sedimentary basins suggest this event is of regional significance. In contrast to previous suggestions that this Neoproterozoic reactivation was the result of a collision from the west, we propose that it reflects north-south compression that caused dextral strike-slip fault reactivation in the north and exhumation of the southern part of the orogen.

5.2 Introduction

Intraplate orogens are less common than orogens at plate margins but their significance in tectonics is increasingly recognized (e.g., Aitken et al., 2009; Raimondo et al., 2010; Raimondo et al., 2014). Intraplate orogens are highly susceptible to repeated tectonic activity which is commonly considered to be a far-field response to events at plate margins (e.g., Aitken et al., 2013; Raimondo et al., 2014; Dyksterhuis and Müller, 2008). The Petermann and Alice Springs orogenies in central Australia and the Tien Shan orogen in central Asia are regarded as archetypal examples of compressional intraplate tectonics, all being characterised by thickening and substantial exhumation (Aitken et al., 2009; Raimondo et al., 2014). However, it is unlikely that these orogenies reflect the full range of behaviour in intraplate settings.

The Capricorn Orogen is a zone ~1000 km long and 500 km wide that comprises the deformed margins of two Archean cratons (the Pilbara Craton in the north and Yilgarn Craton in the south) and intervening Proterozoic granitic and metasedimentary rocks of the Gascoyne Province, overlain by variably deformed Paleo- to Mesoproterozoic sedimentary basins (Cawood and Tyler, 2004) (Figure 5.1). These rocks record the two-stage assembly of the Pilbara and Yilgarn cratons to form the larger West Australian Craton. First, the Pilbara Craton collided with the Glenburgh Terrane during the c. 2200 Ma Ophthalmian Orogeny, which was followed by the subsequent collision of the Pilbara Craton–Glenburgh Terrane with the Yilgarn Craton at c. 1950 Ma during the Glenburgh Orogeny (Cawood and Tyler, 2004; Johnson et al., 2011; Occhipinti et al., 2004). After assembly, the orogen remained susceptible to reworking and reactivation, recording a prolonged tectonothermal history spanning over one billion years. The protracted tectonic history involved four episodes of tectonothermal reworking (Korhonen et al., 2017; Sheppard et al., 2005; 2007; Sheppard et al., 2010b), followed by one or more poorly constrained reactivation events, all of which are best recorded in the Gascoyne Province at the western end of the orogen. The youngest elements of the orogen are very low-grade metasedimentary rocks of the 1680–1465 Ma Edmund Basin and the 1170–1070 Ma Collier Basin.

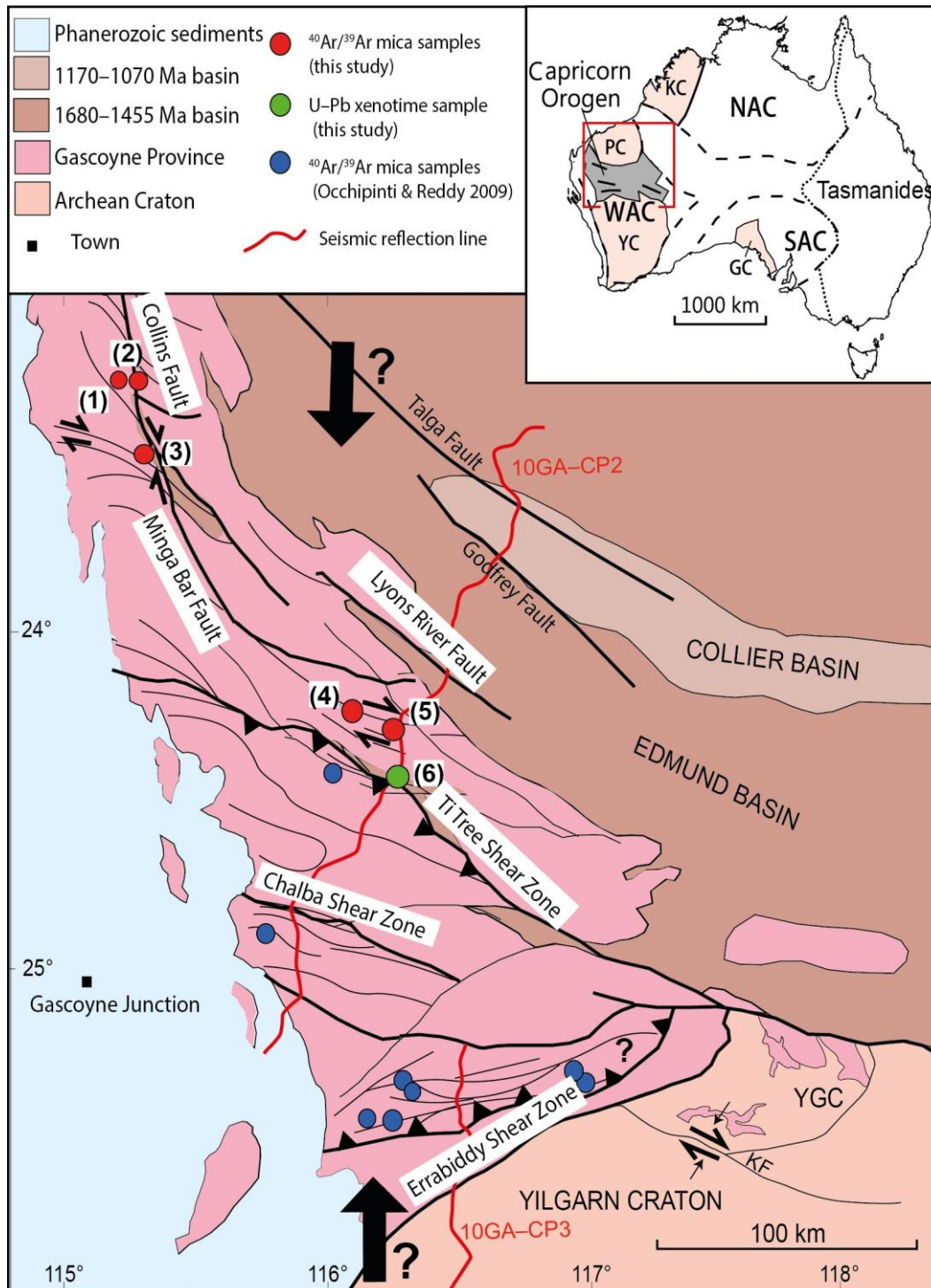


Figure 5.1 Regional geological map of the Gascoyne Province, Capricorn Orogen. The large black arrows indicate the suggested north–south compression. Numbers in brackets relate to sample localities detailed in Table 5.1. (1) GSWA 216533; (2) GSWA 216540B; (3) GSWA 195890B and D–E; (4) GSWA 183294; (5) GSWA 183295; (6) GSWA 149009 & 149010. KF—Kerba Fault (Reddy and Occhipinti, 2004), YGC—Yilgarn Gneiss Complex, YC—Yilgarn Craton, PC—Pilbara Craton, WAC—West Australian Craton, KC—Kimberley Craton, NAC—North Australian Craton, GC—Gawler Craton, SAC—South Australian Craton. (Modified after Johnson et al., 2017).

The Gascoyne Province comprises several southeast-trending structural and metamorphic zones each recording a unique history of reworking (Sheppard et al., 2010b). Although the Paleo–Mesoproterozoic reworking history is well constrained (Korhonen et al., 2017; Sheppard et al., 2005; 2007; Sheppard et al., 2010b) the history of Neoproterozoic reactivation and uplift is almost entirely unknown. Poorly constrained total fusion $^{40}\text{Ar}/^{39}\text{Ar}$ mica dates of c. 920–860 Ma, obtained from the southern Errabiddy Shear Zone, were interpreted to represent cooling after a regional greenschist reworking event (Occhipinti and Reddy, 2009). The youngest known reactivation event, the c. 570 Ma Mulka Tectonic Event (Bodorkos and Wingate, 2007) identified by *in situ* $^{40}\text{Ar}/^{39}\text{Ar}$ mica dating, is known from one shear zone in the southern province, the Chalba Shear Zone (Figure 5.1). The Chalba Shear Zone is characterised by dextral strike-slip kinematics and cross cuts c. 755 Ma dykes of the Mundine Well Dolerite Suite (Wingate and Giddings, 2000). Other undated shear zones in the area show the same kinematics and offset the c. 755 Ma dolerites suggesting that they also belong to the Mulka Tectonic Event. However, field relationships show that some shear zones are cut by the c. 755 Ma dolerite dykes suggesting that there was also an older reactivation event. In the northern half of the orogen, numerous shear zones with dextral kinematics cut metasedimentary rocks of the 1680–1465 Ma Edmund Group and probably the 1170–1070 Ma Collier Group, but the age of this faulting and shear zone reactivation event is unknown.

The focus of this study is to determine the age and cause of the low-temperature reactivation of shear zones in the northern Capricorn Orogen by integrating $^{40}\text{Ar}/^{39}\text{Ar}$ mica and U–Pb xenotime geochronology. Dating low-grade hydrothermal fluid flow within major faults may be achieved by U–Pb phosphate geochronology (e.g., Rasmussen et al., 2007; 2010) but preliminary dating of one major shear zone, in the northern Gascoyne Province, using monazite yielded a Paleoproterozoic age (unpublished data) which is likely to date the host rock rather than the reactivation. Although, no datable xenotime was identified in the northern shear zones we were able to date a central shear zone using U–Pb xenotime geochronology. Therefore we turned to $^{40}\text{Ar}/^{39}\text{Ar}$ mica geochronology to date the low-grade fault reactivation in the Gascoyne Province. Our study also demonstrates that the reactivation event dated here does not involve substantial crustal thickening or exhumation, unlike other key examples of compressional intraplate orogens.

5.3 Intraplate reworking and reactivation in the Gascoyne Province

5.3.1 Reworking

The earliest episode of reworking occurred at 1820–1770 Ma during the Capricorn Orogeny and is marked by the emplacement of voluminous felsic magmatic rocks and extensive deformation, mostly at low to medium metamorphic grade (Sheppard et al., 2010a). This event has the largest metamorphic and magmatic footprint of all the intraplate reworking events to have affected the orogen; igneous rocks, metamorphic assemblages and structures attributed to the Capricorn Orogeny span the entire orogen, from the Errabiddy Shear Zone in the south to north of the Collins Fault (Figure 5.1). The Capricorn Orogeny was followed by the 1680–1620 Ma Mangaroon Orogeny, which is characterised by voluminous felsic magmatism and complex deformation and medium- to high-grade metamorphism (<750°C and <6 kbar; Sheppard et al., 2005). The Mangaroon Orogeny reworked a smaller portion of the Gascoyne Province with only the central and northern parts affected (i.e., from the Chalba Shear Zone to the Collins Fault). The next event was the Mutherbukin Tectonic Event at 1320–1170 Ma, which comprised deformation and metamorphism at >650°C and 4.4–7 kbar (Korhonen et al., 2017), but without magmatism, affecting the central parts of the orogen only (i.e., between the Ti Tree Shear Zone and Chalba Shear Zone). The youngest reworking event, the Meso–Neoproterozoic Edmundian Orogeny 1030–950 Ma (Sheppard et al., 2007), is restricted to a 20 km-wide structural corridor south of the Ti Tree Shear Zone (Figure 5.1). This orogeny was characterised by local deformation and greenschist to amphibolite facies metamorphism (500–550°C and 3–4 kbar) from 1030–990 Ma and leucocratic magmatism at 950 Ma (Sheppard et al., 2007). The age of leucocratic magmatism was further constrained by Piechocka et al. (2017) from 1006–899 Ma, showing that magmatism persisted for c. 90 million years and providing a new minimum age constraint for the Edmundian Orogeny at 900 Ma.

5.3.2 Reactivation

The youngest known events in the Capricorn Orogen involve the reactivation of a series of major, sub-parallel, predominantly low-grade shear zones and faults (Figure 5.1), many of which are crustal-scale structures related to the assembly of the West Australian Craton (Johnson et al., 2013). However, the timing of this reactivation is poorly constrained. The youngest known reactivation event was identified by a c. 570 Ma

$^{40}\text{Ar}/^{39}\text{Ar}$ mica date from a dextral shear zone in the central part of the Gascoyne Province that cross-cuts and offsets dolerite dykes of the c. 755 Ma Mundine Well Dolerite Suite (Bodorkos and Wingate, 2007; Wingate and Giddings, 2000). However, other cross-cutting relationships imply that most of the reactivation is older because shear zones and faults that affect Mesoproterozoic sedimentary rocks of the Edmund Basin and, possibly the Collier Basin (Cutten et al., 2016) are themselves cut by c. 755 Ma dolerite dykes (Wingate and Giddings, 2000). These field relationships suggest the presence of another reactivation event between c. 1465 and 755 Ma in the Capricorn Orogen.

5.4 Characteristics of fault and shear zone reactivation and sample details

In the Gascoyne Province the major faults and shear zones, as well as their ancillary structures, are sub-vertical at surface and some carry a shallow-plunging (0–30°) stretching lineation (sub-horizontal in the north and plunging up to 30° in the central parts of the province), implying dominantly strike-slip deformation with a minor component of uplift in the centre of the province (Table 5.1). Regional-scale map patterns of anastomosing faults, as well as local shear sense indicators (sigma and delta porphyroclasts, S–C fabrics and asymmetric extensional shear bands; Figure 5.2A–C; Hanmer and Passchier, 1991), imply an overall dextral sense of shear, although the style of deformation varies across the province.

5.4.1 The northern Gascoyne Province (Collins Fault)

In the northern part of the Gascoyne Province (i.e., Collins Fault) deformation is partitioned mainly into discrete, 1–50 mm-wide, anastomosing zones of mylonite within medium- to coarse-grained granitic rocks (Figure 5.3A). The mylonite zones commonly show millimetre- to centimetre-scale offsets, with the production of early ductile S–C fabrics that are overprinted by brittle cataclastic textures. Samples GSWA 216540B and 195890B and D–E, which are representative of these thin mylonites, were collected from two different localities (Figure 5.1; Table 5.1) showing different levels of strain (Figure 5.2A and C) for $^{40}\text{Ar}/^{39}\text{Ar}$ mica dating. Horizontal lineations (Figure 5.2D) and shear sense indicators at the GSWA 195890 sample locality (Table 5.1) suggest dextral strike-slip movement.

Table 5.1 Summary of field data and sample details from the Gascoyne Province, Capricorn Orogen.

Sample ID	Latitude (N)	Longitude (E)	Rock type	Structures	Shear Zone	⁴⁰ Ar/ ³⁹ Ar age (Ma)	²⁰⁷ Pb*/ ²⁰⁶ Pb* (Ma)
GSWA 216533 (1)	-23° 16' 48.42	115° 20' 37.93	Garnet–biotite gneiss	1680–1620 Ma Metamorphic foliation 151°/30° WSW	0.8 km west of the Collins Fault	908 ± 3	
GSWA 216533 (1)	-23° 16' 48.42	115° 20' 37.93	Garnet–biotite gneiss	1680–1620 Ma Metamorphic foliation 151°/30° WSW	0.8 km west of the Collins Fault	918 ± 3	
GSWA 216540B (2)	-23° 16' 47.97	115° 21' 06.19	Leucocratic muscovite–biotite metamonzogranite	Vertical mylonites trend at 160° 1680–1620 Ma Metamorphic foliation 190°/90°	Collins Fault	898 ± 3*	
GSWA 195890B (3)	-23° 31' 33.13	115° 25' 03.46	Porphyritic muscovite–biotite monzogranite	Lineation 0°/140° and 0°/160° Vertical mylonite sets at 140° and 160° 1680–1620 Ma Metamorphic foliation 140°/85° WSW	2 km west of Collins Fault	862 ± 4*	
GSWA 195890D (3)	-23° 31' 33.13	115° 25' 03.46	Porphyritic muscovite–biotite metamonzogranite	Lineation 0°/140° and 0°/160° Vertical mylonite sets at 140° and 160° 1680–1620 Ma Metamorphic foliation 140°/85° WSW	2 km west of Collins Fault	1642 ± 7	
GSWA 195890E (3)	-23° 31' 33.13	115° 25' 03.46	Porphyritic muscovite–biotite metamonzogranite	Lineation 0°/140° and 0°/160° Vertical mylonite sets at 140° and 160° 1680–1620 Ma Metamorphic foliation 140°/85° WSW	2 km west of Collins Fault	1639 ± 8	
GSWA 183294 (4)	-24° 20' 27.81	116° 17' 24.73	Quartz–muscovite mylonite	Lineation 25°/141° 1820–1770 Ma Metamorphic foliation 141°/85° WSW	Shears within the Minnie Creek Batholith	882 ± 3	
GSWA 183295 (5)	-24° 19' 25.22	116° 08' 42.01	Quartz–muscovite mylonite	Lineation 30°/112° 1820–1770 Ma Metamorphic foliation 304°/87° NE	Shears within the Minnie Creek Batholith	882 ± 3	
GSWA 149009 (6)	-24° 22' 12.91	116° 04' 04.03	Laminated siltstone	Bedding 305°/76° NE (35°)	Ti Tree Shear Zone		891 ± 26 (1σ)
GSWA 149010 (6)	-24° 21' 59.33	116° 04' 01.36	Silicified mudstone	Cleavage 106°/80° SW (196°)	Ti Tree Shear Zone		893 ± 25

Notes:

Numbers in brackets, in sample ID column, refer to locations in Figure 1.

Planar structures are quoted as strike/dip

Pb* indicates radiogenic Pb (i.e. corrected for common Pb)

²⁰⁷Pb*/²⁰⁶Pb* xenotime weighted mean dates are reported with 95% confidence limits unless otherwise specified.

⁴⁰Ar/³⁹Ar weighted means reported at 2 sigma level.

* Indicates a mini plateau age.

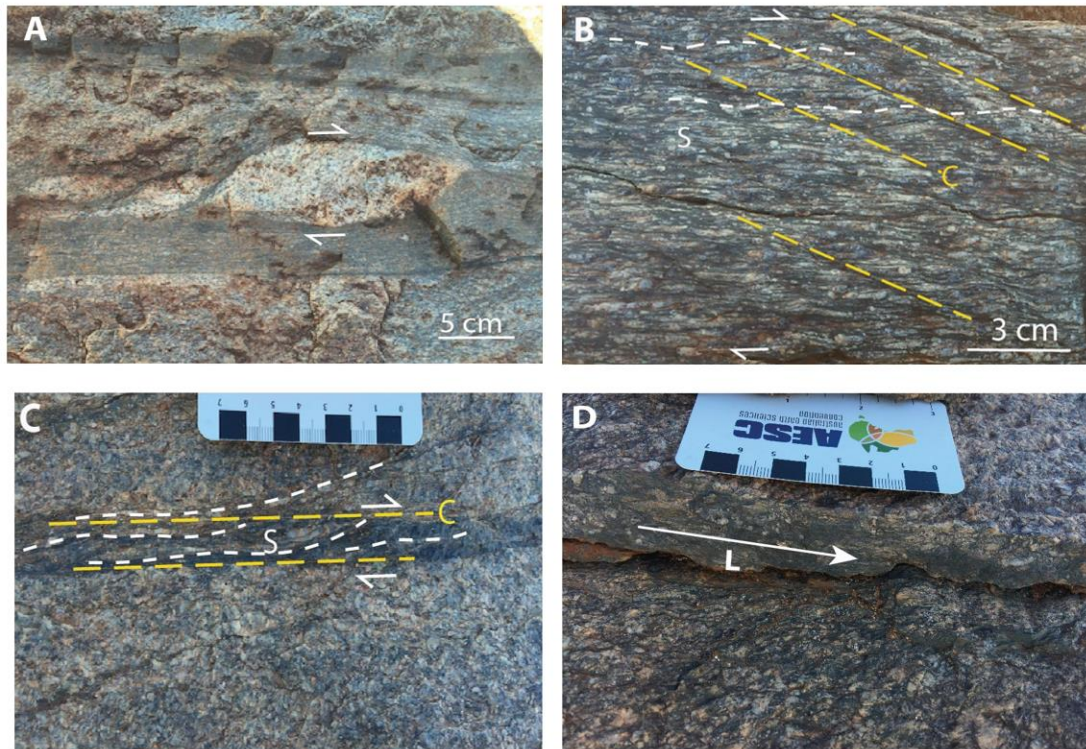


Figure 5.2 **Sample Detail A:** Granitic clast (composed of feldspar and quartz) with dextral sigma tails within a ~15 cm-wide mylonite zone (Collins Fault, locality 2, GSWA 216540B). B: Extensional crenulation cleavage defined by recrystallised biotite and feldspar augen within a porphyritic biotite rich monzogranite, locality within 80 m of sample GSWA 216540B (Collins Fault, locality 2). C: Well-developed C-S fabric in the porphyritic muscovite-biotite monzogranite showing a lower strain rate and less deformation away from the major Collins Fault (Locality 3 and GSWA 195890). D: Subhorizontal lineation within a mylonite zone at Locality 3. For localities refer to Figure 5.1.

Sample GSWA 216540B is a deformed muscovite–biotite metamonzogranite comprising K-feldspar, quartz, plagioclase and muscovite with 5% mafic minerals biotite, chlorite (2%) and accessory zircon and monazite. The quartz is recrystallised and shows undulose extinction. The well-defined foliation is characterised by aligned recrystallised quartz and elongate muscovite crystals. Zones of mylonitisation are characterised by fine-grained recrystallised muscovite, with the occasional larger primary muscovite (Figure 5.3E–F). Feldspar porphyroclasts are elongate and show sigma tails with a dextral sense of shear. There is minimal preservation of primary igneous textures (in contrast to GSWA195890 below) with sparse relatively undeformed K-feldspar phenocrysts. Sericite and perthite are indicative of post magmatic alteration.

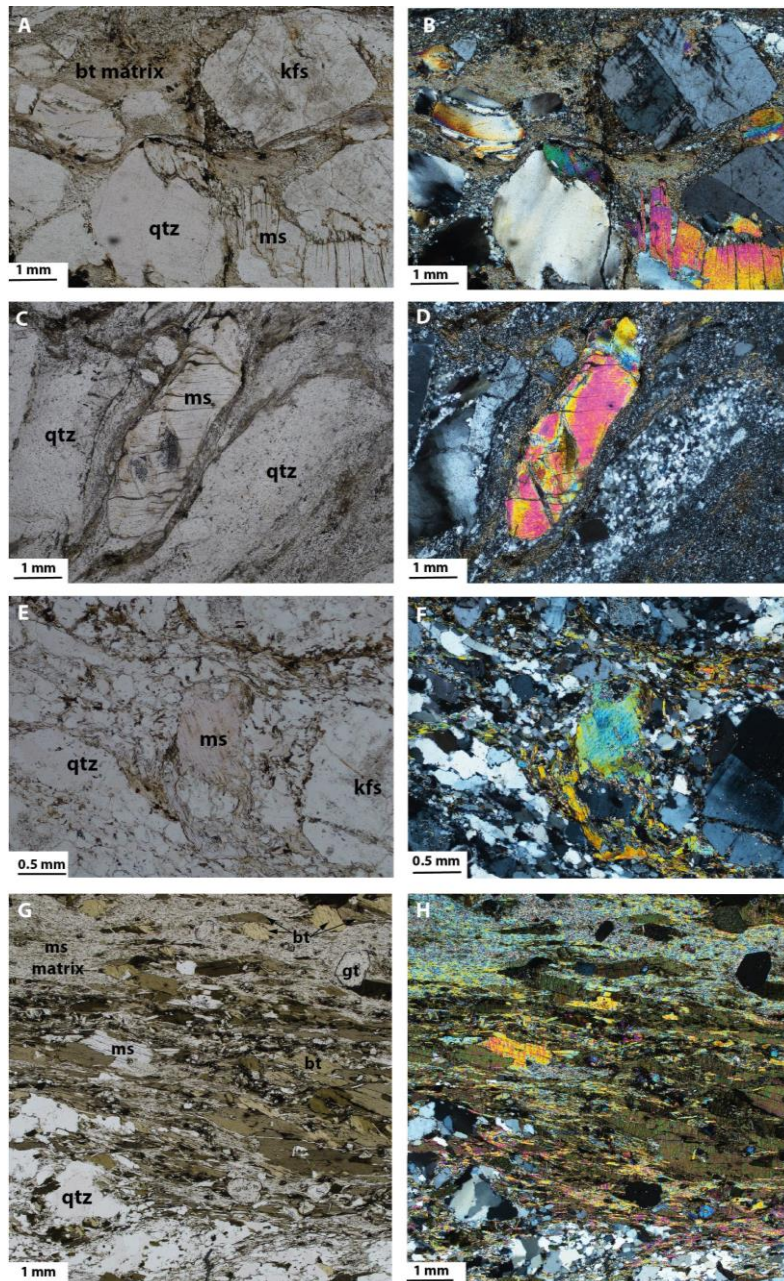


Figure 5.3 Plane polarized light and crossed polar photomicrographs of typical mica crystals from the host granites and mylonite zones in the Collins Fault area. All samples yielded a Neoproterozoic age with the exception of GSWA 195890D (images C–D) which yielded a Paleoproterozoic age. A–D. Sample GSWA195890B (A–B) and 195890D (C–D) (3) a porphyritic muscovite–biotite metamazonz granite shows well preserved primary igneous muscovite surrounded by a finer grained matrix of biotite and quartz. E–F. Sample GSWA 216540B (2) a deformed metamazonz granite shows minimal preservation of primary igneous textures with recrystallised muscovite defining the main foliation. G–H. Sample GSWA 216533 (1) a garnet–biotite gneiss defined by alternating layers of recrystallised quartz, tabular biotite and muscovite and recrystallised muscovite. ms = muscovite, bt = biotite, kfs = K-feldspar, qtz = quartz, gt = garnet. Numbers in brackets refer to locations in Figure 5.1.

Sample GSWA 195890 (B and D–E) is a medium-grained muscovite–biotite metamonzogranite that in parts contains a well-developed S–C fabric. The metamonzogranite shows variation in strain across the outcrop with zones of mylonitisation (biotite), quartz veining and brecciation and zones with preserved igneous textures. The typical mineral assemblage consists of K-feldspar, quartz, muscovite and plagioclase with mafic minerals making up around 25% and includes biotite, chlorite (10–15%) iron oxides with accessory fluorite, zircon and monazite. The preserved igneous muscovite (as mildly deformed porphyroclasts) occur as large crystals up to ~ 4 mm in length and the biotite forms the very fine-grained matrix (Figure 5.3A–D).

Deformation is also partitioned into laterally discontinuous, compositionally weaker zones 0.3–10 m wide. One sample from a ~30 cm-wide zone of strongly deformed, biotite–garnet gneiss (sample GSWA 216533) with 1–5 cm-wide, discontinuous leucocratic veins (Figure 5.4B) was collected for $^{40}\text{Ar}/^{39}\text{Ar}$ mica dating.

Sample GSWA 216533 is defined by a well-developed gneissic fabric comprised of alternating domains of elongate biotite with minor elongate muscovite; recrystallised quartz; and, recrystallised very-fine grained muscovite. The mineral assemblage is garnet (15%), biotite (25%), quartz (20%), muscovite (20%), chlorite (9%), epidote (8%), opaques (2%), and plagioclase (1%). The inclusions in the garnet cores consist of quartz, muscovite and biotite, with epidote in the garnet rims. The biotite ranges in pleochroism from light tan colour to a medium green–brown colour. The biotite porphyroblasts that occur within the very fine-grained muscovite layer typically show two internal fabrics (Figure 5.3G–H). The fabric shows either an oblique orientation to the main foliation or is parallel to the foliation. Muscovite occurs as millimeter-sized tabular crystals intergrown with the biotite. Recrystallized muscovite forms the very fine-grained matrix. Some of the quartz and biotite show sigma tails with dextral kinematics. Late chlorite alteration post-dates the peak metamorphic assemblage.

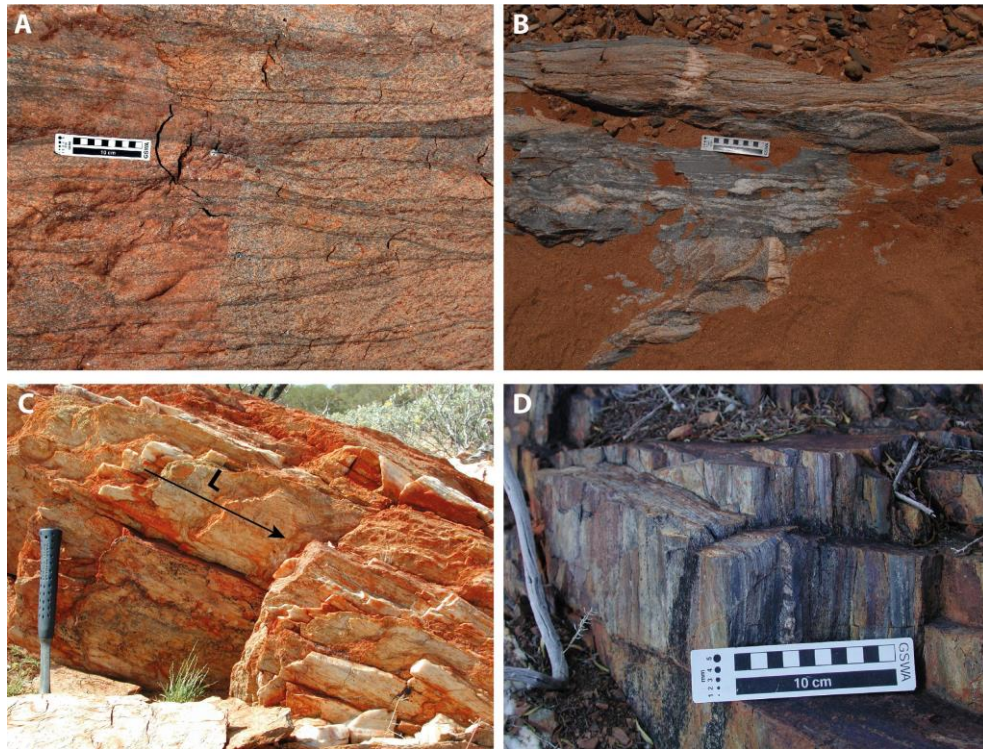


Figure 5.4 Outcrop photos of sample localities. A. Collins Fault outcrop showing anastomosing zones of 1–50 mm-wide mylonite within medium- to coarse-grained granitic rocks, GSWA 21654 (2). B. Compositionally weaker biotite–garnet schist (1) enclave within medium- to coarse-grained granitic rocks ~0.8 km west of the Collins Fault, GSWA 216533. C. ~ 5 m quartz mylonites (4) developed in granites with shallow plunging lineations from the central Gascoyne Province, GSWA 183294. D. Outcrop of a strongly foliated mudstone tending to chert (Edmund Group) (6) at the Ti Tree Shear Zone, GSWA 149010. Numbers in brackets refer to locations in Figure 5.1 in the main body text.

5.4.2 The central Gascoyne Province (Ti Tree Shear Zone)

In the central part of the province (north of the Ti Tree Shear Zone) discrete, discontinuous zones of quartz–muscovite mylonite up to 5 m wide are developed in coarse-grained granitic rocks (Figure 5.4C). These mylonites are associated with ancillary structures related to major faults. The quartz mylonites are steeply dipping with shallowly-plunging east–southeast stretching lineations and locally contain well-developed S–C fabrics that indicate dextral strike-slip movement. Two samples (GSWA 183284 and 183285) were collected for $^{40}\text{Ar}/^{39}\text{Ar}$ mica dating from typical quartz–muscovite mylonite zones. Shallowly plunging lineations (Figure 5.4C) within the quartz–muscovite mylonite zones (Table 5.1) indicate predominantly strike-slip movement with minor uplift of the southern side.

The Ti Tree Shear Zone is interpreted to be a major crustal structure (Johnson et al., 2013) with evidence for multiple Proterozoic movements (Korhonen et al., 2017). At the southeastern end of the shear zone phyllites of the Edmund Group have been strongly silicified (Figure 5.4D) and contain a steeply dipping cleavage and steeply plunging intrafolial folds with axial surfaces parallel to the cleavage. Two quartz phyllite samples (GSWA 149009 and 149010, ~ 400m apart) were collected for U–Pb xenotime geochronology.

A summary of all samples used in this study and location details is provided in Table 5.1.

5.5 Geochronology methodology

5.5.1 $^{40}\text{Ar}/^{39}\text{Ar}$ mica geochronology

$^{40}\text{Ar}/^{39}\text{Ar}$ geochronology was carried out on single mica crystals from mineral separates of seven samples; muscovite was dated from six of these samples (GSWA 183294, 183295, 195890D–E, 216533 and 216540B) and biotite from two of them (samples GSWA 195890B and 216533). Muscovite and biotite crystals, ranging from 355–125 μm size fractions, were washed and dried and then hand-picked under a binocular stereomicroscope. Only unaltered and transparent grains were chosen. The best looking grains were selected and were irradiated for 40 hours in the Oregon State University nuclear reactor in central position during two separate irradiations (I22 in April–July 2016 and I23 in November 2016–February 2017). For both irradiations the best grains (i.e., transparent with pearly lustre) were loaded in two separate discs that were Cd-shielded (to minimize undesirable nuclear interference reactions). I23 included a fully calibrated Fish Canyon sanidine (FCs) standard, for which an age of 28.294 Ma ($\pm 0.13\%$; Renne et al., 2011) was used and I22 included a fully calibrated WA1ms standard, which has an age of 2613 Ma ($\pm 0.09\%$; Jourdan et al., 2014). The detailed analytical methodology is provided in Appendix A.

The mean J-value (irradiation parameter) computed from standard grains within the small pits was 0.01055740 ± 00000792 ($\pm 0.075\%$ 1 sigma) for the samples in irradiation I22 and 0.01085900 ± 00001466 ($\pm 0.135\%$ 1 sigma) for the samples in irradiation I23. Mass discrimination was monitored regularly through the analysis using an automated air pipette and provided a mean value of 1.00431 ($\pm 0.04\%$) per dalton (atomic mass unit) relative to an air ratio of 298.56 ± 0.31 (Lee et al., 2006) for I22 and 1.003996 ($\pm 0.06\%$) per dalton (atomic mass unit) relative to an air ratio of 298.56 ± 0.31 (Lee et al., 2006) for

I23. The correction factors for interfering isotopes were $(^{39}\text{Ar}/^{37}\text{Ar})_{\text{Ca}} = 7.0 \times 10^{-4}$ ($\pm 1.2\%$), $(^{36}\text{Ar}/^{37}\text{Ar})_{\text{Ca}} = 2.6 \times 10^{-4}$ ($\pm 0.4\%$) and $(^{40}\text{Ar}/^{39}\text{Ar})_{\text{K}} = 7.3 \times 10^{-4}$ ($\pm 12.4\%$).

The criteria for the determination of plateaus are as follows: a plateau must include at least 70% of ^{39}Ar and the plateau should be distributed over a minimum of three consecutive steps agreeing at 95% confidence level and satisfying a probability of fit, or P-value, (P) of at least 0.05 (e.g., Jourdan et al., 2005). Mini-plateaus follow the same criteria except that they include between 50% and 70% of released ^{39}Ar and, as a consequence, are considered less reliable. Uncertainties include analytical and J-value errors. Plateau and mini-plateau ages from step-heated single-grain aliquots are reported with 2 sigma uncertainties.

5.5.2 SHRIMP U–Pb xenotime geochronology

Two samples were analysed using *in situ* U–Pb xenotime geochronology. Optical microscopy and scanning electron microscopy were used to identify suitable xenotime crystals ($>15 \mu\text{m}$ in diameter) for analysis by Sensitive High Resolution Ion Microprobe (SHRIMP). Xenotime grains $>15 \mu\text{m}$ across were drilled out in 3 mm-diameter plugs and cast in a single 25 mm epoxy mount. Xenotime reference materials were in a separate mount that was cleaned and Au-coated with the sample mounts prior to analysis.

The U–Pb data were obtained during two SHRIMP analytical sessions on the 13th and 20th October 2008. An O^{-2} primary beam, with a spot size of 10 to 15 μm , was focussed through a 30 μm Kohler aperture with a beam intensity of 0.22 to 0.28 nA. The secondary ion beam was focused through a 100- μm collector slit onto an electron multiplier to produce mass peaks with flat tops and a mass resolution (1% peak heights) of >5000 . A post-collector retardation lens was used to reduce stray ion produced from background counts. Xenotime was analysed with a 9-peak run table, and analytical procedures followed established methodologies (Fletcher et al., 2000, 2004). The primary Pb/U standard MG-1 ($^{206}\text{Pb}/^{238}\text{U}$ age of 490 Ma, $^{207}\text{Pb}/^{206}\text{Pb}$ age of 491.8 Ma, and U concentration of 1,050 ppm) (Fletcher et al., 2004) was used for Pb/U, Pb/Th, and U and Th abundance calibrations. The secondary standards were z6413 (XENO1 of Stern and Rainbird, 2001) and BS-1 (Fletcher et al., 2004) used in conjunction with MG-1 for matrix corrections to Pb/U and Pb/Th. Z6413 was also used to monitor (and if necessary to correct) instrumental mass fractionation in $^{207}\text{Pb}/^{206}\text{Pb}$.

Squid-2.50.11.02.03 software (Ludwig, 2009) was used for initial data reduction, including correction for common Pb. Common Pb corrections were based on individual measured ^{204}Pb abundances and assuming crustal common Pb at the approximate age of the samples modelled by Stacey and Kramers (1975). Corrections for matrix effects in Pb/U and Pb/Th, and for instrumental mass fractionation in $^{207}\text{Pb}/^{206}\text{Pb}$, were carried out following established protocols as described by Fletcher et al. (2004). Weighted mean dates are reported with 95% confidence limits, whereas individual analyses are presented with 1 sigma uncertainties.

5.6 Geochronology Results

5.6.1 $^{40}\text{Ar}/^{39}\text{Ar}$ mica age data

Single-grain muscovite from a mylonite sample at the Collins Fault (GSWA 216540B) yielded a plateau age of 898 ± 3 Ma (mini-plateau) (mean square weighted deviation (MSWD) = 1.07, $P = 0.38$). Single-grain muscovite and biotite from a biotite–garnet gneiss (GSWA 216533), ~0.8 km west of the Collins Fault, yielded plateau ages of, respectively, 918 ± 3 Ma (MSWD = 1.44, $P = 0.13$) and 908 ± 3 Ma (MSWD = 1.35, $P = 0.24$). Single-grain biotite from a mylonite ~2 km west of the Collins Fault (GSWA 195890B), yielded a plateau age of 862 ± 4 Ma (mini-plateau) (MSWD = 0.68, $P = 0.64$). However, muscovite from the same variably deformed outcrop sample yielded plateau ages of 1642 ± 7 Ma (MSWD = 1.72, $P = 0.08$) (GSWA 195890D) and 1639 ± 8 Ma (MSWD = 1.67, $P = 0.08$) (GSWA 195890E). Two quartz-mylonite samples from the centre of the orogen yielded muscovite plateau ages of 882 ± 3 Ma (MSWD = 1.19, $P = 0.27$) (183294) and 882 ± 3 Ma (MSWD = 0.67, $P = 0.77$) (GSWA 183295).

In summary, six plateau ages were calculated from our samples with >70% ^{39}Ar released, and two ‘mini-plateau’ ages were calculated with >50% ^{39}Ar (Figure 5.5, Figure 5.6 and Table 5.2). The typical mica crystals seen in thin section from samples GSWA 195890B and D, 216533 and 216540B are shown in Figure 5.3. However, since the analyses were completed on single grains from mineral separates it is not known whether the typical grains shown are the ones that were analysed.

5.6.2 U–Pb xenotime age data

Two xenotime crystals with distinct morphologies were identified in phyllite sample GSWA 149009 from the Ti Tree Shear Zone: a 50×80 μm , anhedral crystal wrapped by the main foliation and a subhedral crystal (~20 μm across) (Figure 5.7A–B). Four analyses of the anhedral crystal yielded a weighted mean $^{207}\text{Pb}^*/^{206}\text{Pb}^*$ date of c. 1275

Ma and a single analysis on the subhedral crystal yielded a date of 891 ± 26 Ma (1σ) (Table 5.3). The second phyllite sample (GSWA 149010) contained elongate or subhedral xenotime crystals from ~ 30 to 90 μm in diameter (Figure 5.7C–E). Seven analyses were carried out on five xenotime crystals (Table 5.3). Three statistical outliers (>2 standard deviations from the mean) were excluded from the main group. The remaining four analyses yielded a weighted mean $^{207}\text{Pb}^*/^{206}\text{Pb}^*$ date of 887 ± 17 Ma (MSWD = 1.3) indistinguishable from the single analysis of 891 ± 26 Ma in the first sample. Combining the five analyses from the two samples yields a weighted mean $^{207}\text{Pb}^*/^{206}\text{Pb}^*$ date of 887 ± 9 Ma (MSWD = 0.96, $n = 5$) (Figure 5.7F) interpreted as the age of hydrothermal xenotime growth.

Table 5.2 $^{40}\text{Ar}/^{39}\text{Ar}$ muscovite and biotite results from the Gascoyne Province, Capricorn Orogen.

Sample ID	Mineral	Optical properties	Size Fraction (μm)	Plateau Age (Ma, $\pm 2\sigma$)	^{39}Ar (%)	MSWD	P	n
GSWA 183294	Muscovite	aggregates of mica, yellowish color	< 355 > 212	882 \pm 3	90.02	1.19	0.27	15
GSWA 183295	Muscovite	sericitized, opaque and translucent	< 212 > 125	882 \pm 3	85.49	0.67	0.77	12
GSWA 195890B	Biotite	Mostly unaltered and fresh	< 250 > 125	862 \pm 4*	52.40	0.68	0.64	6
GSWA 216540B	Muscovite	Transparent, pearly luster	< 355 > 212	898 \pm 3*	54.28	1.07	0.38	7
GSWA 216533	Biotite	Unaltered and fresh	< 355 > 212	908 \pm 3	81.55	1.35	0.24	6
GSWA 216533	Muscovite	Transparent, pearly luster	< 355 > 212	918 \pm 3	82.01	1.44	0.13	14
GSWA 195890D	Muscovite	Transparent, pearly luster	< 355 > 212	1642 \pm 7	70.93	1.72	0.08	10
GSWA 195890E	Muscovite	Transparent, pearly luster	< 212 > 125	1639 \pm 8	95.60	1.67	0.08	11

Notes:

* indicates mini-plateau age determination (weighted mean age includes 50–70% of total ^{39}Ar . MSWD, mean squared weighted deviation; P, P-value; n, number of steps used in plateau.

Table 5.3 SHRIMP U–Pb xenotime data from phyllite samples central Gascoyne Province, Capricorn Orogen.

Grain spot	Sample	^{238}U (ppm)	^{232}Th (ppm)	$^{232}\text{Th}/^{238}\text{U}$	f_{206} (%)	$^{238}\text{U}/^{206}\text{Pb}^*$ $\pm 1\sigma$	$^{207}\text{Pb}^*/^{206}\text{Pb}^*$ $\pm 1\sigma$	$^{208}\text{Pb}^*/^{232}\text{Th}$ $\pm 1\sigma$	Disc (%)	$^{238}\text{U}/^{206}\text{Pb}^*$ date (Ma) $\pm 1\sigma$	$^{207}\text{Pb}^*/^{206}\text{Pb}^*$ date (Ma) $\pm 1\sigma$					
older group																
0812E.1-3	149009	3878	2469	0.6	0.0103	4.8242	0.1156	0.0838	0.0628	0.0094	0.0002	6	1214	26	1289	5
0812E.1-1	149009	4058	2882	0.7	0.0058	4.9006	0.1176	0.0834	0.0624	0.0094	0.0002	6	1197	26	1278	6
0812E.1-2	149009	3668	1633	0.4	0.0114	4.9355	0.1177	0.0832	0.0619	0.0093	0.0002	7	1189	26	1273	6
0812E.1-4	149009	4340	3205	0.7	0.0077	5.1491	0.1244	0.0828	0.0591	0.0091	0.0002	9	1144	25	1264	4
main group																
0729G.1-1	149010	3135	1356	0.4	0.0327	6.8584	0.2335	0.0695	0.0476	0.0096	0.0006	4	877	28	914	17
0729E.1-1	149009	2144	1423	0.7	0.1163	7.3884	0.2262	0.0688	0.0425	0.0092	0.0009	8	818	23	891	26
0812J.1-2	149010	3810	1077	0.3	0.0087	7.0170	0.1664	0.0687	0.0455	0.0097	0.0002	3	859	19	890	7
0812K.1-1	149010	2862	842	0.3	0.0219	7.3555	0.1742	0.0684	0.0409	0.0093	0.0003	7	822	18	881	8
0729G.1-2	149010	2910	771	0.3	0.0320	21.3637	4.5330	0.0682	0.0468	0.0099	0.0006	1	868	24	874	17
statistical outliers																
0812J.1-1	149010	1275	1117	0.9	0.2765	6.1914	0.1481	0.0724	0.0521	0.0097	0.0011	3	965	21	998	31
0812D.1-1	149010	1232	405	0.3	0.0553	21.0674	4.3294	0.0705	0.0475	0.0098	0.0005	2	920	21	943	14
0812B.1-1	149010	1850	808	0.4	0.0618	6.5059	0.1568	0.0702	0.0476	0.0099	0.0004	1	922	21	935	13

Notes:

[^] Indicates measured ^{238}U and ^{232}Th levels. The precisions of ^{238}U and ^{232}Th abundances measured by SHRIMP are typically 5–10 %.

Pb^* indicates radiogenic Pb (i.e. corrected for common Pb)

f_{206} , proportion of common ^{206}Pb in measured ^{206}Pb , determined using measured $^{204}\text{Pb}/^{206}\text{Pb}$ and contemporaneous common Pb composition (Stacey and Kramers, 1975)

Disc. is apparent discordance, as $D (\%) = 100 \times ([^{207}\text{Pb}^*/^{206}\text{Pb}^* \text{ date}] - [^{238}\text{U}/^{206}\text{Pb}^* \text{ date}]) / [^{207}\text{Pb}^*/^{206}\text{Pb}^* \text{ date}]$

Analyses are sorted by descending $^{207}\text{Pb}^*/^{206}\text{Pb}^*$

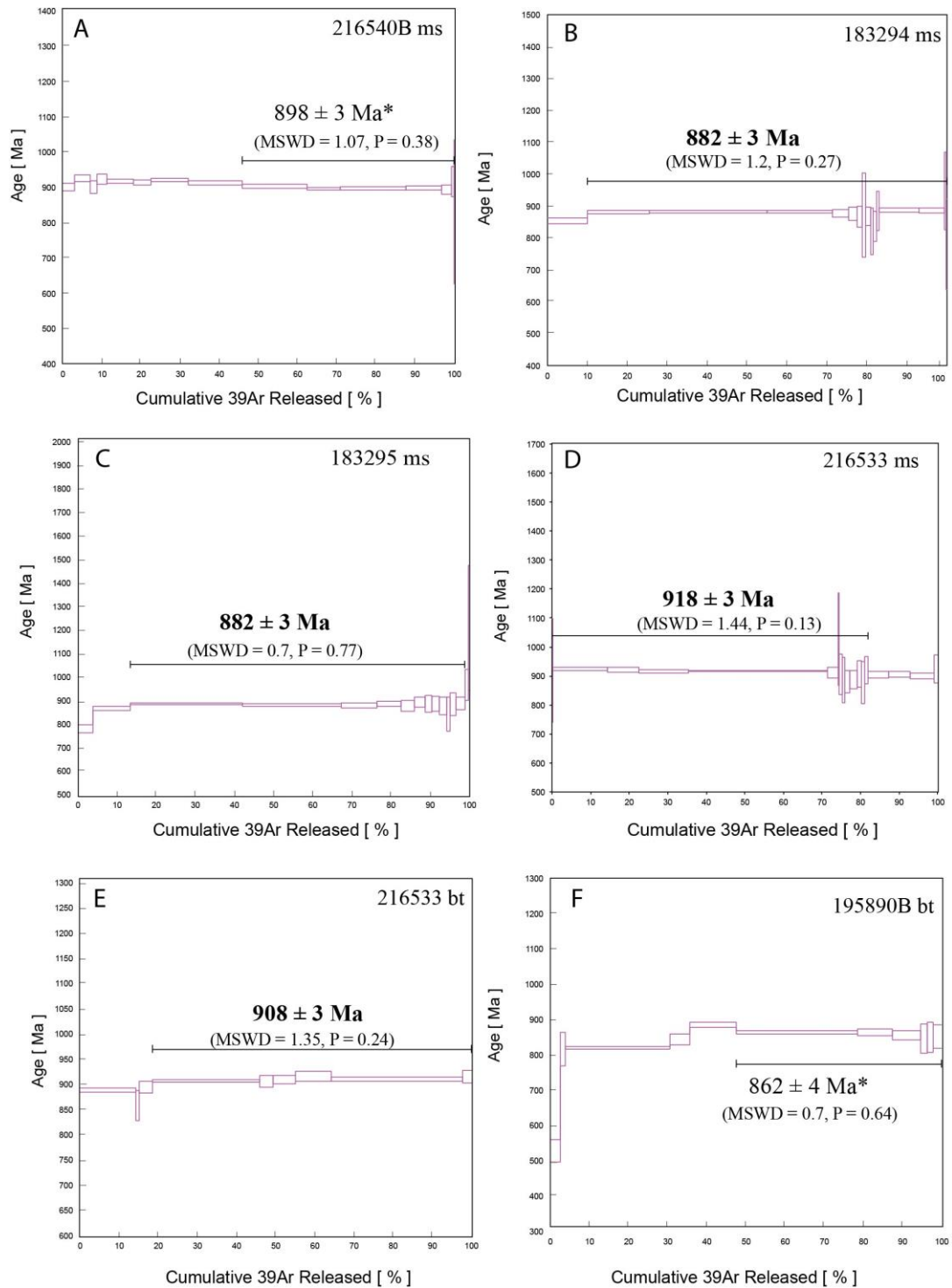


Figure 5.5 A–F: $^{40}\text{Ar}/^{39}\text{Ar}$ age plateaus from mylonites within metagranites and quartz mylonites and a biotite schist from the Gascoyne Province. Asterisk indicates mini-plateau age determination. Mean ages are reported with 2 sigma uncertainty. ms = muscovite; bt = biotite.

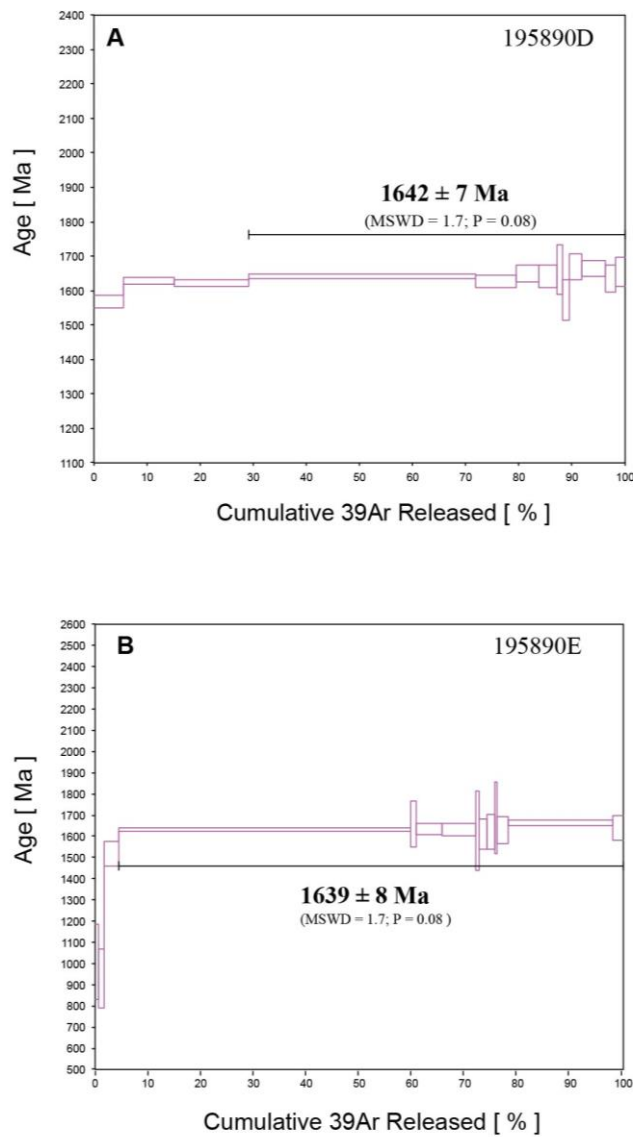


Figure 5.6 A–B: $^{40}\text{Ar}/^{39}\text{Ar}$ muscovite age plateaus from a Paleoproterozoic metagranite from the Gascoyne Province. Mean ages are reported with 2σ uncertainty

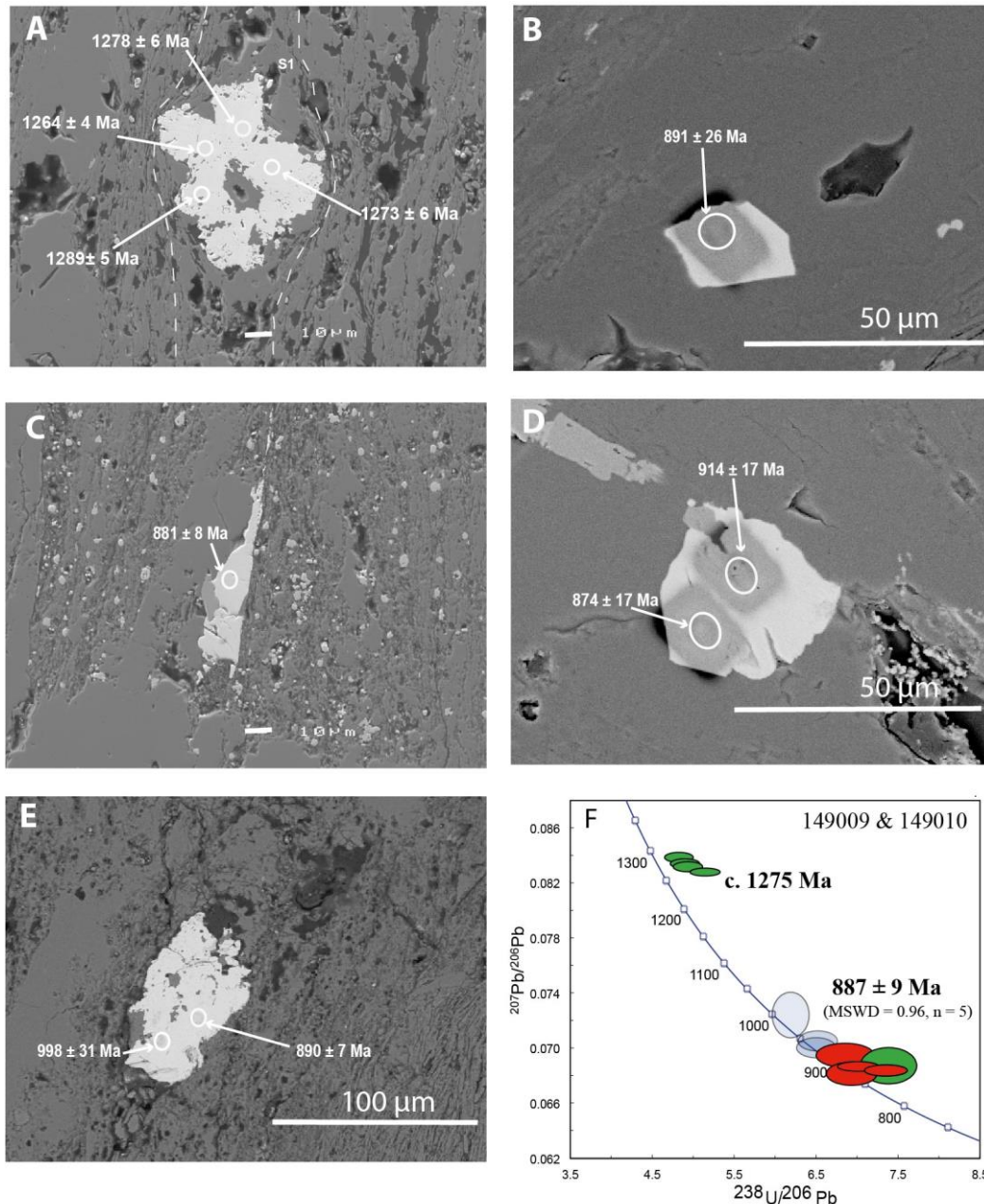


Figure 5.7 A–E: Representative backscattered electron images of xenotime from siltstone/mudstone samples. A: Anhedral crystal wrapped by the 1.3–1.2 Ga quartz tectonic fabric (sample 149009). B: euhedral 25 µm xenotime crystal in quartz (Sample 149009). C: Euhedral to subhedral elongate and tabular xenotime crystal growing parallel to the adjacent quartz crystal (sample 149010) with intergrown Fe-oxide. D–E: Subhedral xenotime crystals with intergrowths and/or inclusions of Fe-oxides. F: Combined SHRIMP U-Pb xenotime results from samples 149009 and 149010. Green ellipses denote analyses from sample 149009, red ellipses denote analyses from sample 149010, and transparent blue ellipses indicate statistical outliers excluded from the final weighted mean age calculation. Mean ages are quoted with 95% uncertainty intervals.

5.7 Discussion

Our $^{40}\text{Ar}/^{39}\text{Ar}$ mica and U–Pb xenotime results of 918–862 Ma overlap with previously published total fusion $^{40}\text{Ar}/^{39}\text{Ar}$ mica dates of 960–820 Ma obtained from the Errabiddy Shear Zone in the southern Capricorn Orogen (Occhipinti and Reddy, 2009). In that study the authors interpreted their results as cooling ages related to the Edmondian Orogeny. Because mica argon dates in metamorphic terrains can either be interpreted as cooling ages (Scibioriski et al., 2015) or deformation ages (Hansama et al., 2016) we discuss the possibility of our data in terms of a new growth phase or cooling process. To assist with the interpretation we conducted diffusion modelling of muscovite. We integrate our new results with previously published geochronology to show that fault and shear zone reactivation spans not only the Gascoyne Province but the bounding Archean cratons.

5.7.1 $^{40}\text{Ar}/^{39}\text{Ar}$ diffusion modelling of muscovite from the northern Gascoyne Province

Here we test whether the c. 900 Ma plateau ages are the result of complete thermal resetting of old muscovite (c. 1600 Ma) by regional thermal metamorphism or if they arose from the shear zone reactivation at c. 900 Ma. In the northern Capricorn Orogen, the observed crystal sizes in the shear zone are around 500 μm compared to the 4 mm c. 1640 Ma muscovite crystals (Figure 5.3). Since the closure temperature of muscovite is proportional to the crystal (or more accurately domain) size, it is possible that the smaller crystals within the shear zone were reset by a regional Neoproterozoic thermal event whereas the larger crystals from the country rocks remained unaffected (e.g., Dunlap et al., 1991). Therefore, we carried out diffusion simulations on the effect of regional metamorphism on synthetic $^{40}\text{Ar}/^{39}\text{Ar}$ spectra using the ArArDiff algorithm (Jourdan and Eroglu, 2017). The modelling parameters included the selection of three grain sizes (in radius): 125 μm , 500 μm and 1000 μm (Table 5.4), each assumed to have resided in the same crustal volume at c. 900 Ma with an identical P–T history during the Neoproterozoic thermal event. The crystallisation age of the host rock was set at 1650 Ma, the known age of granitic rocks in the area (Sheppard et al., 2010b). It was assumed that the temperatures were $\sim 150^\circ\text{C}$ either side of the Neoproterozoic thermal event period (they must have dropped below the muscovite closure temperature soon after igneous crystallisation since we obtained c. 1640 Ma plateau ages). The modelling comprised three time periods. Period 1 (920–880 Ma) involved heating from 150°C up to an assumed peak of 420°C , the minimum temperature needed to fully reset the small muscovite crystals for the duration used. Period 2 (880–860 Ma) involved cooling from the peak back to 150°C . Period 3 (860–0 Ma) represents slow cooling as the rock was exhumed to its present-day location at the surface. The parameters used for the muscovite and the thermal events are listed in Table 5.4.

Table 5.4 Diffusion parameters and time-temperature history used in the ArArDiff models (Jourdan and Eroglu, 2017) to generate synthetic age spectra for muscovite.

Diffusion parameters	Mixed phases					
	D_0 (cm ² /s)	E_a (J/mol)	Radius (μ m)	Modal composition	%K ₂ O for each mineral	K ₂ O contribution (mixed phase)
Muscovite	2.30E+00	264000	125	1%	0.5%	33%
Muscovite	2.30E+00	264000	500	44%	0.01%	33%
Muscovite	2.30E+00	264000	1000	45%	0.01%	34%

Thermal history*	Start (Ma)	End (Ma)	Duration (Ma)	Starting temp. (°C)	Ending temp. (°C)	Cooling rate (°C/Ma)
Period 1	920	880	40	150	470	-8
Period 2	880	860	20	470	150	16
Period 3	860	0	860	150	0	0
Period 4	0	0	0	0	0	0

Notes:

*Crystallization age = 1650 (Ma)

The diffusion modelling results show that the conditions needed to fully reset the smallest muscovite crystals (125 μm) at 920–860 Ma (100% ^{40}Ar loss) would also substantially affect the largest muscovite crystals. Muscovite with 500 μm and 1000 μm radius in our models have lost 52% and 26% of their $^{40}\text{Ar}^*$ (relative to their Ar contents at 920 Ma immediately before the thermal event), effectively preventing these crystals from yielding plateau or even mini-plateau ages (Figure 5.8). Because our $^{40}\text{Ar}/^{39}\text{Ar}$ analyses show that the larger muscovite crystals from the surrounding country rocks do not display strong diffusion patterns but rather yield well-defined plateau ages (Figure 5.6), we conclude that it is unlikely that there was a regional thermal event at c. 900 Ma exceeding the muscovite closure temperature. Alternatively, it could be that the processes responsible for the c. 900 Ma muscovite ages were restricted to within the shear zones (i.e., sample 216540B which yielded 898 ± 3 Ma) whereas muscovite in the host granite was largely unaffected by this Neoproterozoic event (i.e., samples GSWA195890D and E which yielded 1642 ± 7 Ma and 1639 ± 8 Ma, respectively). As a consequence, our results suggest that either conditions within the shear zone (Collins Fault) were above the closure temperature ($\sim 450^\circ\text{C}$) at c. 900 Ma but were much lower temperature away from the shear zone, or that regional temperatures were below the closure temperature across the entire northern Capricorn Orogen during Neoproterozoic reactivation, and the c. 900 Ma muscovite in the shear zone either grew or recrystallised at this time.

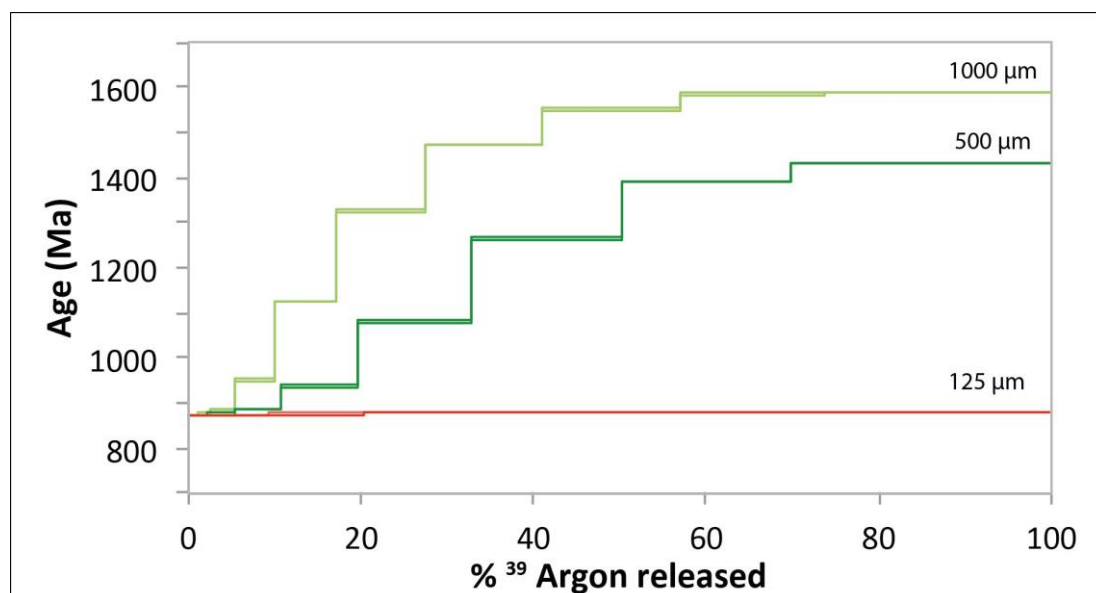


Figure 5.8 Modelled $^{40}\text{Ar}/^{39}\text{Ar}$ age spectra for 125 μm , 500 μm and 1000 μm radius muscovite grains with an initial age of 1650 Ma that were later affected by a thermal overprint at 920–860 Ma that attained a maximum temperature of 460°C (details of diffusion parameters and thermal history given in Table 5.4).

5.7.2 Ages of mica growth or cooling?

Current estimates of the closure temperature for muscovite and biotite are, respectively, $\sim 425 \pm 70^\circ\text{C}$ and $\sim 365 \pm 35^\circ\text{C}$ (Harrison et al., 1985; Harrison et al., 2009; recalculated by Scibiorski et al., 2015). However, there are caveats on closure temperatures which include the following variables: grain size (a reduction in grain size typically causes a reduction in closure temperature: Dodson, 1973); the rate of cooling (faster cooling rates yield higher closure temperatures: Reddy & Potts 1999) and; temperature of deformation (in particular, greenschist facies deformation commonly causes a reduction in grain size: Dunlap et al., 1991).

Our new $^{40}\text{Ar}/^{39}\text{Ar}$ results from low-grade mylonite zones could be interpreted as ages of mica neocrystallisation or recrystallisation (i.e., reduction in grain size). Determining whether the dates represent neocrystallisation ages can be difficult to ascertain, mainly because our study involve whole-grain analysis of mineral separates, which means the ages obtained cannot be readily linked to any microstructural observations or compositional data, unlike studies that use *in situ* laser argon analysis (e.g., Mulch & Cosca, 2004; Reddy et al., 1997). However, several mica $^{40}\text{Ar}/^{39}\text{Ar}$ studies on low-grade greenschist facies mylonite zones have demonstrated mica dates as neocrystallisation ages rather than cooling ages (e.g., Kirschner et al., 1996; Dunlap 1997).

Aggregates of muscovite within the mylonite zone at the Collins Fault (e.g., GSWA 216540B), form a well-defined foliation (Figure 5.3E–F). In contrast, the Paleoproterozoic host rock sample away from the Collins Fault (GSWA 195890) consists of preserved igneous muscovite (as deformed porphyroclasts) and a foliation defined by very fine-grained biotite (Figure 5.3A–D). The sizes of muscovite crystals in the shear zone have been significantly reduced compared with the large igneous muscovite crystals preserved in the host granite. The reduction in size is likely associated with low-grade deformation localised within the shear zone (Dunlap et al., 1991). In contrast, there appears to have been no new muscovite growth in the host rock away from the shear zone (sample GSWA 195890) as the muscovite yielded a Paleoproterozoic age.

Alternatively, our $^{40}\text{Ar}/^{39}\text{Ar}$ dates could be interpreted as cooling ages, an interpretation that would be consistent with that of Occhipinti & Reddy (2009), who regarded their 960–820 Ma dates from the southern Errabiddy Shear Zone to represent

cooling and uplift after the 1030–900 Ma Edmondian Orogeny. In particular, our mica (882 Ma) and xenotime (887 Ma) ages from the central parts of the province closely follow the end stages of reworking (c. 900 Ma) related to the Edmondian Orogeny. The xenotime interpreted as hydrothermal growth possibly formed during exhumation along the Ti Tree Shear Zone. Therefore, our mica dates from the quartz mylonites, immediately north of the Ti Tree Shear Zone, could also be related to the post-Edmondian cooling and exhumation. Here the lineations plunge at $\sim 30^\circ$ which indicates there was a component of dip-slip movement in addition to the predominant dextral strike-slip component.

In addition to our $^{40}\text{Ar}/^{39}\text{Ar}$ dates, there are four occurrences of 920–800 Ma U–Pb phosphate ages from faults zones within the Gascoyne Province and from the bounding Archean cratons: a xenotime date of 887 ± 9 Ma (this study) interpreted to represent new growth aided by hydrothermal fluids moving along the shear zone; monazite and xenotime dates at c. 920 Ma from the Chalba Shear Zone (Meadows et al., 2017) and; c. 850 Ma and c. 800 Ma phosphate dates, interpreted as growth from hydrothermal fluids moving along faults, from the adjacent Archean cratons (Rasmussen et al., 2007; 2010) (Figure 5.9). The U–Pb phosphate ages demonstrate that there were fluids moving along pre-existing faults not only in the Gascoyne Province but within the bounding Archean cratons.

Our $^{40}\text{Ar}/^{39}\text{Ar}$ dates of 920–860 Ma could be interpreted as cooling ages, neocrystallization or recrystallization ages. However, the diffusion modeling and the petrographic evidence from the northern samples suggests that the 918–898 Ma ages represent mica growth. In contrast, interpretation of the younger muscovite dates (882 Ma), as either growth or cooling, from immediately north of the Ti Tree Shear Zone remains equivocal.

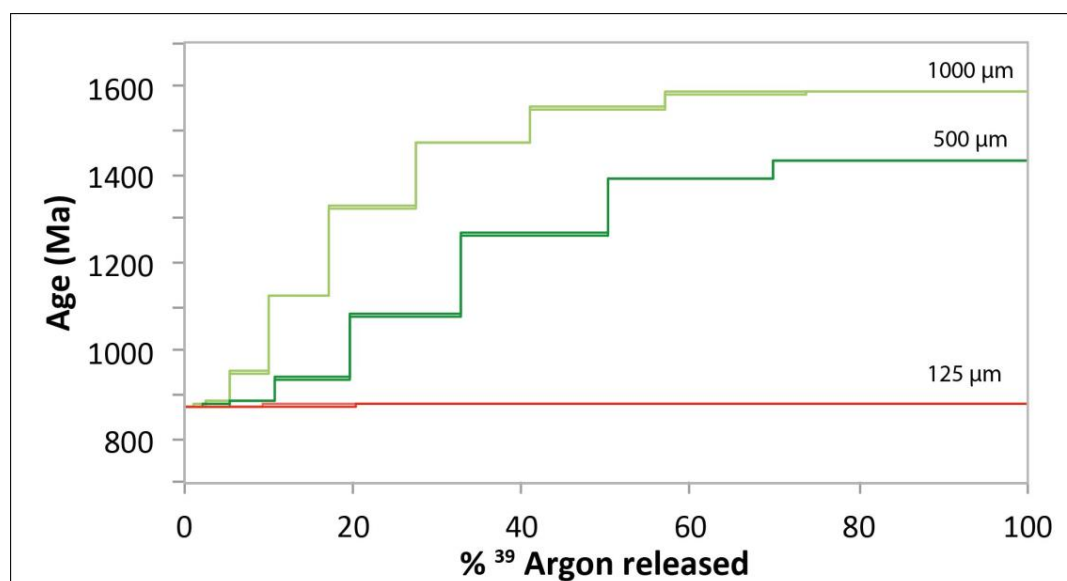


Figure 5.9 Summary diagram illustrating the spread of ages defined by $^{40}\text{Ar}/^{39}\text{Ar}$ mica and SHRIMP U–Pb xenotime geochronology from major structures across the Gascoyne Province (this study) in comparison to published geochronology data in the province and from adjacent Archean Cratons. Only representative data from Occhipinti and Reddy (2009) are plotted. * Mini-plateau. (1) GSWA 216533; (2) GSWA 216540B; (3) GSWA 195890B; (4) GSWA 183294; (5) GSWA 183295; (6) GSWA 149009 & 149101. ESZ—Errabiddy Shear Zone; CSZ—Chalba Shear Zone; —Ti Tree Shear Zone; CF—Collins Fault.

5.7.3 The extent of the Neoproterozoic reactivation

Muscovite and biotite from greenschist facies mylonites and shear zones in c. 1680 Ma granitic rocks from the Collins Fault in the northern part of the Gascoyne Province yielded $^{40}\text{Ar}/^{39}\text{Ar}$ dates of 918 ± 3 Ma (muscovite, GSWA 216533), 908 ± 3 Ma (biotite, GSWA 216533) and 898 ± 3 Ma (muscovite mini-plateau age, GSWA 216540B). The muscovite dates are likely to be recording a growth phase for the reasons addressed above. Therefore, the estimated temperature during the reactivation must have been below $\sim 425 \pm 70$ °C (the muscovite closure temperature, Scibiorski et al., 2015). Preliminary U–Pb monazite dating of samples GSWA 216533 and GSWA 216540B yielded c. 1680 Ma ages (unpublished data). However, muscovite from mylonites in c. 1680 Ma granite ~ 2 km west of the Collins Fault, yielded dates of 1642 ± 7 Ma (GSWA 195890D) and 1639 ± 8 Ma (GSWA 195890E) and are interpreted as cooling ages of igneous muscovite that was unaffected by the Neoproterozoic reactivation event. However, biotite from the same rock (GSWA 195890 B), forming the very fine-grained foliation, yielded a date of 862 ± 4 Ma (mini-plateau). This suggests that the temperature

away from the main shear zone was either below or above $365 \pm 35^\circ\text{C}$ (biotite closure temperature) but below $425 \pm 70^\circ\text{C}$ (muscovite closure temperature).

Muscovite from two quartz–muscovite mylonites (GSWA 183294 and 183295) 14 km apart in c. 1800 Ma granitic rocks (Minnie Creek batholith) farther south in the central part of the province, immediately north of the Ti Tree Shear Zone, both yielded $^{40}\text{Ar}/^{39}\text{Ar}$ dates of 882 ± 3 Ma. These shear zones also show dextral kinematics as seen in the north. This area north of the Ti Tree Shear Zone also was likely to have been uplifted at c. 1640 Ma because of the unconformable relationship between the 1680–1465 Ma Edmund Group sediments and the Minnie Creek batholith (Sheppard et al., 2010b). In contrast to the subhorizontal lineations in the northern part of the province here lineations plunge at $25\text{--}30^\circ$ to the east–southeast which suggests there was some vertical component of movement in addition to the predominant dextral strike-slip component.

In contrast to the northern part of the province that displays consistent dextral movement along faults, the kinematics south of the Ti Tree Shear Zone are ambiguous. Our U–Pb xenotime age of 887 ± 9 Ma from the Ti Tree Shear Zone is interpreted to date hydrothermal fluids flow along the shear zone. This age overlaps with the youngest granite magmatism in this area at 899 ± 10 Ma (Piechocka et al., 2017) related to the Edmondian Orogeny. Our xenotime age may reflect growth during the uplift and exhumation during the later stages of the Edmondian Orogeny.

Our new dates overlap with poorly defined, total fusion $^{40}\text{Ar}/^{39}\text{Ar}$ mica error-dates of 925–820 Ma from the Errabiddy Shear Zone at the southern end of the Gascoyne Province (Occhipinti and Reddy, 2009). These dates were interpreted as approximate cooling ages related to a regional low-grade tectonic event associated with the Edmondian Orogeny (Occhipinti and Reddy, 2009). A single concordant plateau age of 832 ± 1.6 Ma came from a sample south of the Ti Tree Shear Zone (Figure 5.1; Occhipinti and Reddy, 2009). Although many of their step-heated samples show signs of disturbance, the dataset does suggest that the Errabiddy Shear Zone was reactivated during the 920–860 Ma tectonism we have dated here. Furthermore, new U–Pb phosphate dates as young as c. 920 Ma suggest that Neoproterozoic activity also affected the Chalba Shear Zone (Meadows et al., 2017) (Figure 5.9). Cutten et al. (2016) note that the 1680–1465 Ma Edmund and 1170–1070 Ma Collier Basins, present north of the Ti Tree Shear Zone are weakly metamorphosed. The Edmund Group may have been deformed either during the earlier 1320–1170 Ma Mutherbukin Tectonic Event or the

Edmundian Orogeny whereas the younger Collier Group must have been affected during the Edmundian Orogeny or sometime later.

Outside of the core of the Capricorn Orogen, SHRIMP U–Pb *in situ* phosphate dates of c. 850 from the southern Pilbara Craton and 800 Ma from the northern Yilgarn Craton have been interpreted as precipitation from hydrothermal fluid flow along faults (Rasmussen et al., 2007; 2010). Their regional significance was unclear, but they could be related to discrete faulting and shearing in the margins of the bounding Archean cratons in response to the reactivation of faults in the Gascoyne Province dated here at 920–860 Ma (or 920–830 Ma if the single concordant plateau age of Occhipinti and Reddy (2009) is included as part of the same event). It is also likely that at least some faults in the 1170–1070 Ma Collier Basin formed at this time. This Neoproterozoic reactivation appears to overlap with and follow on directly from the 1030–900 Ma Edmundian Orogeny as previously defined. It seems unlikely that events spanning 1030–830 Ma would represent a tectonic continuum, but there are insufficient data at present to subdivide this history into a sequence of discrete tectonic events.

5.7.4 Implications of reactivation of pre-existing crustal sutures and faults

Our results, combined with existing data, show that Neoproterozoic reactivation affected the two former suture zones in the Capricorn Orogen: the 2200 Ma Collins Fault/Lyons River Fault and the 1950 Ma Errabiddy Shear Zone/Cardilya Fault (Occhipinti et al., 2004; Selway et al., 2009; Johnson et al., 2013), as well as other major crustal structures including the Ti Tree Shear Zone and the Chalba Shear Zone (Figure 5.10). The Ti Tree Shear Zone is thought to have originated during Mesoproterozoic tectonism (Sheppard et al., 2010b) with recent evidence showing that the Ti Tree Shear Zone was active during the 1320–1170 Ma Mutherbukin Tectonic Event (Korhonen et al., 2017). The Neoproterozoic reactivation is best preserved within discrete structures whereas the adjacent low-grade greenschist rocks lack any distinct Neoproterozoic deformation fabrics (Sheppard et al., 2010b). This suggests that tectonism at this time was focussed within pre-existing structures.

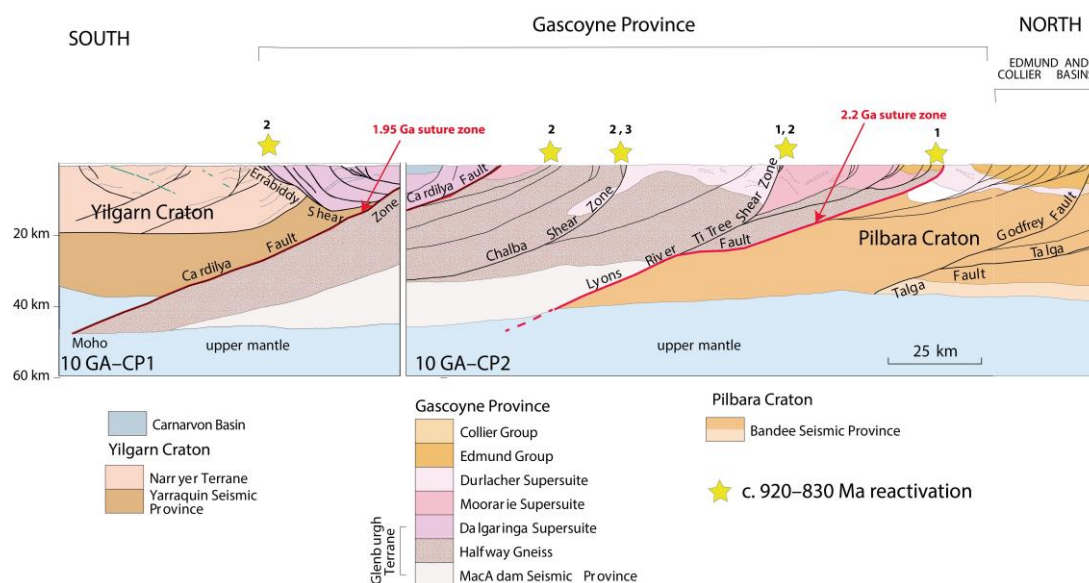


Figure 5.10 Interpreted crustal geology from the seismic lines 10GA-CP3 and 10GA-CP3 (Johnson et al., 2013) highlighting the crustal architecture dominated by south dipping mantle tapping faults and shear zones that were reactivated during the 920–830 Ma Neoproterozoic event. Refer to Figure 5.1 for location of seismic line. (Modified from Johnson et al., 2013). 1: Reactivation dated in this study; 2: reactivation dated by Occhipinti & Reddy (2009); 3: reactivation dated by Meadows et al., (2017).

Unlike the Petermann and Alice Springs orogenies in central Australia (Aitken et al., 2009) and the Tien Shan Orogen in central Asia (Raimondo et al., 2014), the lack of significant metamorphic discontinuities across Neoproterozoic shear zones in the Gascoyne Province and their preservation of subhorizontal lineations (at least in the north), suggest very little exhumation or crustal thickening during reactivation. However, we do see evidence for exhumation in the central parts of the province south of the Ti Tree Shear Zone with the juxtaposition of medium-grade rocks (formed during the Edmundian Orogeny) against low-grade metasedimentary rocks of the Edmund Group (Sheppard et al., 2010b).

In this study we have presented evidence for mica growth in the northern parts of the orogen related to dextral strike-slip reactivation. The interpretation of mica ages from the quartz–muscovite mylonites immediately north of the Ti Tree Shear Zone remains equivocal, but our U–Pb xenotime age from the Ti Tree Shear Zone could reflect phosphate growth during exhumation. This interpretation would be consistent with the cooling interpreted by Occhipinti and Reddy (2009). However, our field observations do not support the earlier interpretation of regional uplift of the orogen. Occhipinti and Reddy (2009) interpreted cooling ages of mica from the Gascoyne Province, together

with Gascoyne-aged detrital zircon populations in Neoproterozoic Officer Basin to the east, to infer uplift and erosion of the western Capricorn Orogen. They suggested the cause of uplift to be collision of either Greater India or the Kalahari Craton with the West Australian Craton. However, our new geochronology data tied to dextral strike-slip kinematics of shear zones, in the northern parts of the province, along with the general lack of juxtaposition of rocks of substantially differing metamorphic grade, suggest there was no uplift in the northern part of the province. The structural interpretation of the deep seismic survey (Johnson et al., 2013) (Figure 5.10) shows the boundary of the Pilbara Craton to extend at depth to the Ti Tree Shear Zone. Therefore, during north-south compression the southern part of the province may have been squeezed between the more rigid northern block and the Yilgarn Craton, which resulted in strike slip dextral faulting in the northern block and exhumation of the southern part of the orogen.

5.7.5 From reworking to reactivation on an orogen scale

An interesting finding of our study is that our $^{40}\text{Ar}/^{39}\text{Ar}$ mica and U–Pb xenotime dates from major shear zones and faults are only slightly younger than the youngest reworking event in the province (the 1030–900 Ma Edmondian Orogeny, Piechocka et al., 2017; Sheppard et al., 2007). The Edmondian Orogeny is largely restricted to a 20 km-wide zone in the central part of the province and is marked by greenschist to mid-amphibolite facies metamorphism and deformation. The intrusion of leucocratic granitic plutons and pegmatites in the centre of the orogen however post-dates the medium-grade reworking, which ceased at 990 Ma with magmatism having continued until 899 ± 10 Ma (Piechocka et al., 2017). The age for this youngest granitic rock is similar to our $^{207}\text{Pb}^*/^{206}\text{Pb}^*$ date of 887 ± 9 Ma for xenotime, interpreted as hydrothermal growth, from phyllites within the nearby Ti Tree Shear Zone, and to $^{40}\text{Ar}/^{39}\text{Ar}$ dates from across the Gascoyne Province recording reactivation. Therefore, from our new results and those of Piechocka et al. (2017), we show that while crustal reworking finished at 899 ± 10 Ma in the centre of the orogen (the youngest leucocratic magmatism) reactivation was occurring in the northern province at 918 ± 3 Ma. This records the transition from the final crustal reworking event in Capricorn Orogen to reactivation of crustal- and lithospheric-scale structures across the entire Gascoyne Province. Furthermore, the reworking history shows a pattern of progressive narrowing of (medium and high-grade) reworking toward the centre of the orogen (Figure 5.11) as the crust became more dehydrated and refractory (Korhonen and Johnson, 2015; Johnson et al., 2017).

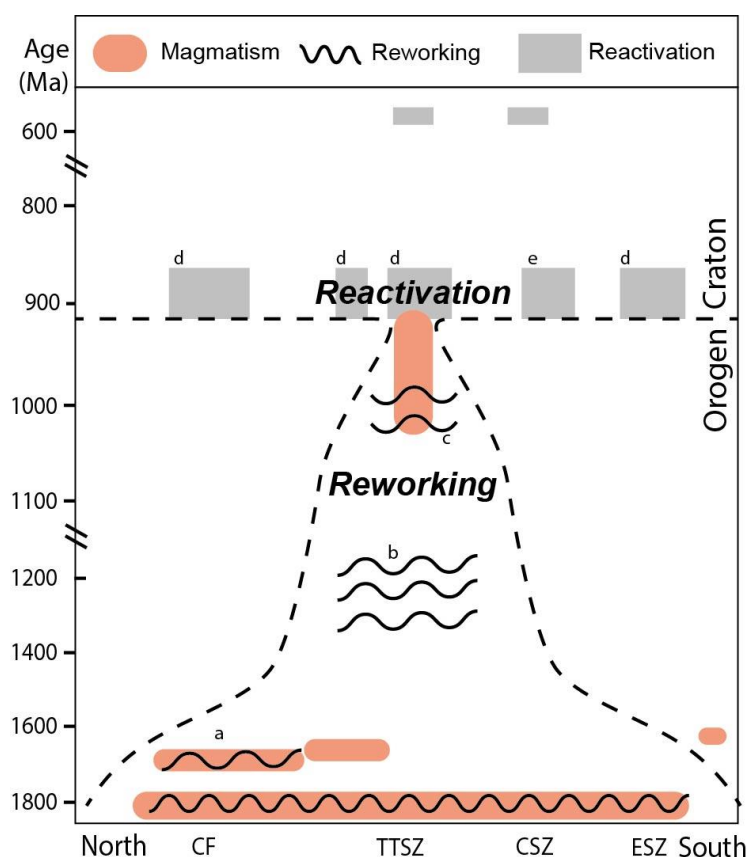


Figure 5.11 Simplified time-space plot showing the distribution of reworking and reactivation events spanning the Gascoyne Province. ^a < 750°C, >6 kbar (Sheppard et al., 2005); ^b < 650°C, 4.4–7 kbar (Korhonen et al., 2015); ^c 500–550°C, 3–4 kbar (Sheppard et al., 2007); ^d < 350°C (Occhipinti and Reddy 2009; this study), ^e > 640°C, 3–4 kbar (Meadows et al., 2017). ESZ—Errabiddy Shear Zone; CSZ—Chalba Shear Zone; TTSZ—Ti Tree Shear Zone; CF—Collins Fault.

Our results, which combine multi-mineral geochronology techniques and field observations, demonstrate how a long-lived orogen with a complex and protracted reworking history saw a breakout in fault reactivation across the Gascoyne Province at 920–860 Ma. The footprint of the c. 920–820 Ma Neoproterozoic activity (including the one concordant plateau age from Occhipinti and Reddy (2009)) extends across much of the West Australian Craton suggesting that the far-field forces responsible reflected tectonism on a much larger scale.

5.8 Conclusions

Our geochronology has identified Neoproterozoic mica dates of 918–862 Ma from shear zones in the northern Gascoyne Province. In the centre of the province we obtained mica dates of 882 Ma and a U–Pb xenotime age of 887 Ma. Argon diffusion modelling and field observations suggest the muscovite ages in the north reflect growth

(neocrystallisation or crystallisation) ages during dextral strike-slip reactivation related to the Edmondian Orogeny. We find no evidence of exhumation of the northern parts of the province, but our interpretation of exhumation in the south is consistent with that of Occhipinti and Reddy (2009). However, rather than uplift due to a collision from the west, tectonism may have been caused by north-south compression resulting in a rigid northern block squeezing a less competent piece of crust between the Pilbara and Yilgarn Cratons. Our results suggest that the crustal architecture of the Capricorn Orogen was effectively frozen at c. 900 Ma, with only minor localised subsequent fault-related activity recorded. The lack of evidence for any younger significant regional tectonic events suggests that the structural architecture established during the Neoproterozoic reactivation event has essentially remained unchanged since then. Nevertheless, some of the structures that were active in the Neoproterozoic continue to be the focus of present-day seismicity (the Middalya and Mount Clere clusters in figure 2 of Revets et al., 2009; Keep et al., 2012).

5.9 Acknowledgements

The authors thank R. Parrish for constructive comments which have resulted in a more focussed and improved manuscript. C. Mayers of WAAIF is thanked for assistance during sample preparation. $^{40}\text{Ar}/^{39}\text{Ar}$ measurements were conducted at the Western Australian Argo Facility (WAAIF) and U–Th–Pb measurements were conducted using the SHRIMP ion microprobes, at the John de Laeter Centre at Curtin University. Simon Johnson publishes with permission of the Director of the Geological Survey of Western Australia. This PhD project was funded through an Australian Research Council (ARC) grant (LP130100922) and the Exploration Incentive Scheme.

5.10 References

- Aitken, A.R.A., Betts, P.G., & Ailleres, L. (2009). The architecture, kinematics, and lithospheric processes of a compressional intraplate orogen occurring under Gondwana assembly: The Petermann orogeny, central Australia. *Lithosphere*, 6, 343–357.
- Aitken, A.R.A., Raimondo, T., & Capitanio, F.A. (2013). The intraplate character of supercontinent tectonics. *Gondwana Research*, 24, 807–814.
- Bodorkos, S., & Wingate M. T. D. (2007). The contribution of geochronology to GSWA's mapping programs: current perspectives and future directions. *Geological Survey of Western Australia, Record 2007/2*, p.11.
- Cawood, P. A., & Tyler, I. M. (2004). Assembling and reactivating the Proterozoic Capricorn Orogen: lithotectonic elements, orogenies, and significance. *Precambrian Research*, 128, 201–218.
- Cutten, H. N., Johnson, S. P., Thorne, A.M., Wingate, M.T.D., Kirkland, C.L., Belousova, E.A., Blay, O. A., & Zwingmann, H. (2016). Deposition, provenance, inversion history and mineralization of the Proterozoic Edmund and Collier Basins, Capricorn Orogen. *Geological Survey of Western Australia, Report 127*, p.80.
- Dodson, M. H. (1973). Closure temperature in cooling geochronological and petrological systems. *Contributions to Mineralogy and Petrology*, 40, 259–274.
- Dunlap, W. J. (1997). Neocrystallization or cooling? $^{40}\text{Ar}/^{39}\text{Ar}$ ages of white micas from low-grade mylonites. *Chemical Geology*, 143, 181–203.
- Dunlap, W., Teyssier, C., McDougall, I., & Baldwin, S. (1991). Ages of deformation from K/Ar and $^{40}\text{Ar}/^{39}\text{Ar}$ dating of white micas. *Geology*, 19, 1213–1216.
- Dyksterhuis, S., & Müller, R.D. (2008). Cause and evolution of intraplate orogeny in Australia. *Geology*, 36, 495–498.
- Fletcher, I.R., McNaughton, N.J., Aleinikoff, J.A., Rasmussen, B., & Kamo, S.L. (2004). Improved calibration procedures and new standards for U-Pb and Th-Pb dating of Phanerozoic xenotime by ion microprobe. *Chemical Geology*, 209, 295–314.
- Fletcher, I.R., McNaughton, N.J., & Rasmussen, B. (2000). SHRIMP U-Pb geochronology of authigenic xenotime and its potential for dating sedimentary basins. *Australian Journal of Earth Sciences*, 47, 845–859.
- Hanmer, S., & Passchier, C.W. (1991). Shear sense indicators: a review. *Geological Survey of Canada* 90, p.70.

- Hansma, J., Tohver, E., Schrank, C., Jourdan, F., & Adams, D. (2016). The timing of the Cape Orogeny: New $^{40}\text{Ar}/^{39}\text{Ar}$ age constraints on deformation and cooling of the Cape Fold Belt, South Africa. *Gondwana Research*, 32, 122–137.
- Harrison, T.M., C  lerier, J., Aikman, A.B., Hermann, J., & Heizler, M.T. (2009). Diffusion of ^{40}Ar in muscovite. *Geochimica et Cosmochimica Acta*, 73, 1039–1051.
- Harrison, T.M., Duncan, I., & McDougall, I. (1985). Diffusion of ^{40}Ar in biotite: Temperature, pressure and compositional effects. *Geochimica et Cosmochimica Acta*, 49, 2461–2468.
- Johnson, S. P., Korhonen, F. J., Kirkland, C. L., Cliff, J. B., Belousova, E. A., & Sheppard, S. (2017). An isotopic perspective on growth and differentiation of Proterozoic orogenic crust: From subduction magmatism to cratonization. *Lithos*, 268, 76–86.
- Johnson, S.P., Sheppard, S., Rasmussen, B., Wingate, M. T. D., Kirkland, C. L., Muhling, J. R., Fletcher, I. R., & Belousova, E. A. (2011). Two collisions, two sutures: Punctuated pre-1950 Ma assembly of the West Australian Craton during the Ophthalmian and Glenburgh Orogenies. *Precambrian Research*, 189, 239–262.
- Johnson, S. P., Thorne, A. M., Tyler, I. M., Korsch, R. J., Kennett, B. L. N., Cutten, H. N., Goodwin, J., Blay, O., Blewett, R. S., Joly, A., Dentith, M. C., Aitken, A. R. A., Holzschuh, J., Salmon, M., Reading, A., Heinson, G., Boren, G., Ross, J., Costelloe, R. D., & Fomin, T. (2013). Crustal architecture of the Capricorn Orogen, Western Australia and associated metallogeny. *Australian Journal of Earth Sciences*, 60, 681–705.
- Jourdan, F. & Eroglu, E. $^{40}\text{Ar}/^{39}\text{Ar}$ and (U-Th)/He model age signatures of elusive mercurian and venusian meteorites: *Meteoritics & Planetary Science*, in press. (2017).
- Jourdan F., Feraud, G., Bertrand, A.B., Kampunzu, G., Tshoso, M. K., & Watkeys, B. (2005). Karoo large igneous province; brevity, origin, and relation to mass extinction questioned by new $^{40}\text{Ar}/^{39}\text{Ar}$ age data: *Geology*, 33, 745–748.
- Jourdan, F., Frew, A., Joly, A., Mayers, C., & Evans, N. J. (2014). WA1ms: A ~ 2.61 Ga muscovite standard for $^{40}\text{Ar}/^{39}\text{Ar}$ dating. *Geochimica et Cosmochimica Acta*, 141, 113–126.
- Keep, M., Hengesh, J., & Whitney, B. (2012). Natural seismicity and tectonic geomorphology reveal regional transpressive strain in northwestern Australia. *Australian Journal of Earth Sciences*, 59, 341–354.
- Kirschner, D. I., Cosca, M. A., Masson, H., & Hunziker, C. (1996). Staircase $^{40}\text{Ar}/^{39}\text{Ar}$ spectra of fine-grained white mica: Timing and duration of deformation and empirical constraints on argon diffusion. *Geology*, 24, 747–750.

- Koppers, A. A. P. (2002). ArArCalc—Software for $^{40}\text{Ar}/^{39}\text{Ar}$ age calculations. *Computers & Geoscience*, 48, 605–619.
- Korhonen, F.J., & Johnson, S.P. (2015). The role of radiogenic heat in prolonged intraplate reworking: The Capricorn Orogen explained?. *Earth and Planetary Science Letters*, 428, 22–32.
- Korhonen, F.J., Johnson, S.P., Wingate, M.T.D., Kirkland, C.L., Fletcher, I.R., Dunkley, D.J., Roberts, M.P., Sheppard, S., Muhling, J.R., & Rasmussen, B. (2017). Radiogenic heating and craton-margin plate stresses as drivers for intraplate orogeny. *Journal of Metamorphic Geology* 35, 631–661.
- Lee, Y.J., Marti, K., Severinghaus, J.P., Kawamura, K., Yoo, H.S., Lee, J.B., Kim, J.S. (2006). A redetermination of the isotopic abundances of atmospheric Ar. *Geochimica et Cosmochimica Acta* 70, 4507–4512.
- Ludwig, K.R. (2009). *Squid 2.50, A User's Manual*. Berkeley Geochronology Centre Special Publication, p. 95.
- Meadows, H.R., Reddy, S.M., Clark, C., Plavsa, D., & Johnson, T. (2017). Localisation of high strain and high temperature into the Chalba Shear Zone, Gascoyne Province. Specialist Group in Tectonics and Structural Geology, Conference Abstract.
- Mulch, A., & Cosca, M. A. (2004). Recrystallization or cooling ages: *in situ* UV-laser $^{40}\text{Ar}/^{39}\text{Ar}$ geochronology of muscovite in mylonitic rocks. *Journal of the Geological Society*, 161, 573–582.
- Occhipinti, S.A., & Reddy, S.M. (2009). Neoproterozoic reworking of the Paleoproterozoic Capricorn Orogen of Western Australia and implications for the amalgamation of Rodinia. *Geological Society, London, Special Publications*, 327, 445–456.
- Occhipinti, S.A., Sheppard, S., Passchier, C., Tyler, I.M., & Nelson, D.R. (2004). Paleoproterozoic crustal accretion and collision in the southern Capricorn Orogen: the Glenburgh Orogeny. *Precambrian Research* 128, 237–255.
- Piechocka, A.M., Gregory, C.J., Zi, J., Sheppard, S., Wingate, M.T.D., & Rasmussen, B. (2017). Monazite trumps zircon: applying SHRIMP U-Pb geochronology to systematically evaluate emplacement ages of leucocratic, low-temperature granites in a complex Precambrian orogen. *Contributions to Mineralogy and Petrology*, 172, 1–17.
- Raimondo, T., Hand, M., & Collins, M. J. (2014). Compressional intracontinental orogens: Ancient and modern perspectives. *Earth-Science Reviews*, 130, 128–153.

- Raimondo, T., Collins, A. S., Hand, M., Walker-Hallam, A., Smithies, R. H., Evins, P. M., & Howard, H. M. (2010). The anatomy of a deep intracontinental orogen. *Tectonics*, 29, 1–31.
- Rasmussen, B., Fletcher, I.R., Muhling, J.R., Thorne, W.S., & Broadbent, G.C. (2007). Prolonged history of episodic fluid flow in giant hematite ore bodies: Evidence from *in situ* U–Pb geochronology of hydrothermal xenotime. *Earth and Planetary Science Letters*, 258, 249–259.
- Rasmussen, B., Fletcher, I.R., Muhling, J.R., & Wilde, A.W. (2010). *In situ* U–Th–Pb geochronology of monazite and xenotime from the Jack Hills belt: Implications for the age of deposition and metamorphism of Hadean zircons. *Precambrian Research* 180, 26–46.
- Reddy, S. M., Kelley, S. P., & Magennis, L. (1997). A microstructural and argon laserprobe study of shear zone development at the western margin of the Nanga Parbat–Haramosh Massif, western Himalaya. *Contributions to Mineralogy and Petrology*, 128, 16–29.
- Reddy, S.M., & Occhipinti, S.A. (2004). High-strain zone deformation in the southern Capricorn Orogen, Western Australia: kinematics and age constraints. *Precambrian Research*, 128, 295–314.
- Reddy, S. M., & Potts, G. J. (1999). Constraining absolute deformation ages: the relationship between deformation mechanisms and isotope systematics. *Journal of Structural Geology*, 21, 1255–1265.
- Renne, P.R., G.Balco, K.R. Ludwig, R. Mundil, & K. Min. (2011). Response to the comment by W.H. Schwarz et al. on “Joint determination of 40K decay constants and $^{40}\text{Ar}/^{40}\text{K}$ for the Fish Canyon sanidine standard, and improved accuracy for $^{40}\text{Ar}/^{39}\text{Ar}$ geochronology” by P. R. Renne et al. (2010). *Geochim. Cosmochim. Acta*, 75, 5097–5100.
- Revels, S.A., Keep, M., & Kennett, B.L.N. (2009). NW Australian intraplate seismicity and stress regime. *Journal of Geophysical Research*, 114, 1–10.
- Scibiorski, E., Tohver, E., & Jourdan, F. (2015). Rapid cooling and exhumation in the western part of the Mesoproterozoic Albany-Fraser Orogen, Western Australia. *Precambrian Research*, 265, 232–248.
- Selway, K., Sheppard, S., Thorne, A.M., Johnson, S.P., & Groenewald, P.B. (2009). Identifying the lithospheric structure of a Precambrian orogen using magnetotellurics: The Capricorn Orogen, Western Australia. *Precambrian Research*, 168, 185–196.

- Sheppard, S., Bodorkos S., Johnson S.P., Wingate M.T.D, & Kirkland, C.L. (2010a). The Paleoproterozoic Capricorn Orogeny: Intracontinental Reworking Not Continent-Continent Collision: Geological Survey of Western Australia, Report, 108, p.33.
- Sheppard, S., Johnson, S.P., Wingate, M.T.D., Kirkland, C.L., & Pirajno, F. (2010b). Explanatory notes for the Gascoyne Province. Geological Survey of Western Australia 1:100 000 Explanatory Notes, p.336.
- Sheppard, S., Occhipinti, S.A., & Nelson, D.R. (2005). Intracontinental reworking in the Capricorn Orogen, Western Australia: the 1680–1620 Ma Mangaroon Orogeny. *Australian Journal of Earth Sciences*, 52, 443–460.
- Sheppard, S., Rasmussen, B., Muhling, J.R., Farrell, T.R., & Fletcher, I.R. (2007). Grenvillian-aged orogenesis in the Palaeoproterozoic Gascoyne Complex, Western Australia: 1030–950 Ma reworking of the Proterozoic Capricorn Orogen. *Journal of Metamorphic Geology*, 25, 477–494.
- Stacey, J.S., & Kramers, J.D. (1975). Approximation of terrestrial lead isotope evolution by a two-stage model. *Earth and Planetary Science Letters*, 26, 207–221.
- Stern, R.A., & Rainbird, R.H. (2001). Advancements in xenotime U–Pb geochronology by ion microprobe. Eleventh V.I. Goldschmidt Conference Lunar and Planetary Science Institute, Houston.
- Wingate, M.T.D., & Giddings, J.W. (2000). Age and palaeomagnetism of the Mundine Well dyke swarm, Western Australia: implications for an Australia-Laurentia connection at 755 Ma. *Precambrian Research*, 100, 335–357.

Chapter 6

Conclusion

In many instances worldwide the ages of orogenic events are either defined by radiometric dates on associated felsic magmatism or bracketed by radiometric dates on pre- and post-orogenic igneous rocks, rather than by direct dates on minerals that grew during metamorphism. A lack of direct dating means that the duration of the metamorphism and the temporal relationship to associated igneous rocks remains unknown. Therefore, the drivers for metamorphism can also remain poorly understood. This PhD research highlights the benefits of using SHRIMP U–Th–Pb monazite and xenotime to date low to high-temperature geological processes, such as metamorphism and magmatism, during intraplate reworking of the Proterozoic Capricorn Orogen. Integrating robust geochronology data with P – T pseudosections allows for P – T – t paths to be determined and provides clues as to the drivers for orogenesis. Where monazite and xenotime are severely retrogressed and unsuitable for U–Pb dating, $^{40}\text{Ar}/^{39}\text{Ar}$ mica geochronology is used to date late fault reactivation in the Capricorn Orogen. The results of this thesis, presented as major findings from Chapters 2–5, are discussed below.

Previous work utilised U–Pb zircon geochronology to constrain the timing of magmatism associated with the Capricorn Orogeny at 1820–1775 Ma. Despite the extensive studies on the magmatism associated with the Capricorn Orogeny the timing and duration of metamorphism and the relationship of the metamorphism to magmatism have remained unknown. New SHRIMP U–Pb phosphate geochronology provide direct ages for metamorphism, from the central and northern parts of the Gascoyne province, showing that the regional low- to medium-grade metamorphism (with a localised occurrence of higher grade metamorphism) occurred at 1817–1777 Ma (Chapter 2). This age span shows that metamorphism was synchronous with regional 1820–1775 Ma magmatism and 1813–1772 Ma compressional deformation. Based on the new results it is proposed that the regional intraplate metamorphism was probably driven by the emplacement of the regional magmatism associated with the Moorarie Supersuite. This magmatic model for metamorphism is in contrast to the more common idea that a thermal lid model best accounts for metamorphism in many Proterozoic orogenic settings. This study also identified a second group of ages, not previously known from the Gascoyne Province, at 1750–1730 Ma, restricted to the northern parts of the province. This episode of activity post-dates the regional magmatism and likely reflects a late stage deformation (i.e., hydrothermal) event following the peak metamorphism associated with the Capricorn Orogeny.

Although magmatism and deformation associated with the 1680–1620 Ma Mangaroon Orogeny had been previously identified the P – T – t information remained elusive. Without the direct ages for metamorphism and P – T conditions the duration and drivers for metamorphism remained unknown. Chapter 3 outlines how the use of SHRIMP U–Pb monazite and xenotime geochronology in conjunction with the construction of P – T pseudosections provided new P – T – t data associated with the Mangaroon Orogeny in the northern Gascoyne Province. SHRIMP U–Pb monazite geochronology shows that magmatism in the northern Gascoyne Province commenced 15 million years earlier than originally thought. The new results indicate that magmatism commenced at 1695 Ma and was closely followed by peak metamorphism of 665–755 °C and 2.7–4.3 kbar (~175–240 °C/kbar) at 1691 Ma, as recorded in a pelitic migmatite. Data from a garnet bearing sillimanite–biotite pelitic gneiss suggests higher pressures during a clockwise prograde history at one locality. The results demonstrate that the anomalous thermal gradient was related to regional low- P , high- T regional metamorphism. The results also show that the precursor sediments to the Pooranoo Metamorphics were deposited, buried and melted in c. 63 million years; therefore, it is unlikely there was sufficient time for radiogenic heat to build up to cause the upper crustal metamorphism. Unlike the model proposed for many Proterozoic orogens, i.e., the thermal lid model, this study showed that a magmatism was synchronous with upper crustal metamorphism.

Chapter 4 discusses the benefit of using SHRIMP U–Pb monazite geochronology to measure the crystallisation age of low-temperature leucocratic granites. Temperature conditions < 750° C have shown to limit new zircon growth in the magma resulting in an abundance of inherited zircon in the crystallised granites. Therefore, zircon geochronology often records the age of the source material rather than the timing of igneous crystallisation. Chapter 4 shows how monazite was used to date the crystallisation of leucocratic granites in the Gascoyne Province. Existing zircon geochronology for a pluton associated with the 1030–950 Ma Edmondian Orogeny yielded a Paleoproterozoic age which also contradicted dated metamorphic fabrics that were cross-cut by the Supersuite. The monazite results showed that the leucocratic magmatism was emplaced between 1005–900 Ma. The results showed that the low-volume, structurally controlled leucocratic supersuite was emplaced over a c. 100 million year interval, compared to the adjacent higher volume Paleoproterozoic batholiths which were emplaced over a more reasonable duration of 15–30 million years. Furthermore, the leucocratic magmatism post-dated the known metamorphism providing new constraints on the Edmondian Orogeny at 1030–900 Ma. This study shows that

using monazite in combination with zircon can deliver a robust and less ambiguous history of low-temperature leucocratic magmatism. The results have implications for constructing reliable magmatic histories in orogens with low-temperature granites, as well as the duration of leucocratic magmatic events and magma generation rates.

Reactivation of recent and ancient intraplate orogens is commonly accompanied by substantial crustal thickening and exhumation as indicated by, for example, numerous studies on the Neoproterozoic to Paleozoic orogenies in central Australia and the Tian Shan orogen; however, it is unclear whether these tectonic events reflect the full range of behavior in intraplate orogens. In Chapter 5 the timing of regional Neoproterozoic fault reactivation of major shear zones in the Gascoyne Province was resolved using $^{40}\text{Ar}/^{39}\text{Ar}$ mica geochronology. Although previous geochronology from a shear zone in the southern parts of the province yielded a single age of c 570 Ma it was uncertain whether other faults in the province were reactivated at this time. For instance, field observations in the northern parts of the province show faults displacing 1680–1465 Ma sedimentary basins, and the faults are then cut by c. 755 Ma dolerite dykes. Therefore, fault reactivation in the north was older than c. 755 Ma but younger than 1465 Ma. The $^{40}\text{Ar}/^{39}\text{Ar}$ mica geochronology, collected from shear zones in the north and central Gascoyne Province, revealed a widespread reactivation at 920–830 Ma. The geochronology combined with structural observations showed that there was dextral strike slip of the northern Gascoyne Province and exhumation of the central and southern parts of the province. The late fault reactivation, probably involved lateral extrusion of Paleoproterozoic crust from between two Archean cratons without significant crustal thickening, unlike archetypal compressional intraplate orogenic events. This interpretation differs from an earlier tectonic model suggesting that Neoproterozoic tectonism was the result of a collision with a craton to the west during the assembly of Rodinia. The widespread breakout in reactivation, which established the present crustal architecture, immediately followed the final reworking associated with the 1030–900 Ma Edmondian Orogeny. Since there is no evidence of younger reworking events in the orogen post c. 900 Ma the Neoproterozoic reactivation, across the Capricorn Orogen, also symbolises a change in crustal behaviour to a more rigid state.

This thesis demonstrates the versatility and robust nature of using SHRIMP U–Pb monazite and xenotime geochronology to date low- to high-grade geological processes in complex Proterozoic orogens. Furthermore, when U–Pb monazite and xenotime geochronology is combined with other techniques such as P – T pseudosection construction or $^{40}\text{Ar}/^{39}\text{Ar}$ mica geochronology a more detailed understanding of the drivers for orogenesis can be achieved.

Bibliography

- Aitken, A.R.A., Betts, P.G., & Ailleres, L. (2009). The architecture, kinematics, and lithospheric processes of a compressional intraplate orogen occurring under Gondwana assembly: The Petermann orogeny, central Australia. *Lithosphere*, 6, 343–357.
- Aitken, A.R.A., Raimondo, T., & Capitanio, F.A. (2013). The intraplate character of supercontinent tectonics. *Gondwana Research*, 24, 807–814.
- Ayres, M., Harris, N., & Vance, D. (1997). Possible constraints on anatectic melt residence times from accessory mineral dissolution rates; an example from Himalayan leucogranites. *Mineralogical Magazine*, 61, 29–36.
- Barton, M. D., & Hanson, R. B. (1989). Magmatism and the development of low-pressure metamorphic belts: Implications from the western United States and thermal modeling. *GSA Bulletin* 101, 1051–1065.
- Bea, F. (1996). Residence of REE, Y, Th and U in Granites and Crustal Protoliths; Implications for the Chemistry of Crustal Melts. *Journal of Petrology*, 37, 521–552.
- Bea, F., Montero, P., González-Lodeiro, F., Talavera, C. (2007). Zircon Inheritance Reveals Exceptionally Fast Crustal Magma Generation Processes in Central Iberia during the Cambro-Ordovician. *Journal of Petrology*, 48, 2327–2339.
- Black, L. P., Kamo, S. L., Allen, C. M., Davis, D. W., Aleinikoff, J. N., Valley, J. W., Mundil, R., Campbell, I. H., Korsch, R. J., Williams, I. S., & Foudoulis, C. (2004). Improved $^{206}\text{Pb}/^{238}\text{U}$ microprobe geochronology by the monitoring of a trace-element-related matrix effect; SHRIMP, ID-TIMS, ELA-ICP-MS and oxygen isotope documentation for a series of zircon standards. *Chemical Geology* 205, 115–140.
- Black, L. P., & Shaw, R. D. (1995). An assessment, based on U–Pb zircon data, of Rb/Sr dating in the Arunta Inlier, central Australia. *Precambrian Research* 71, 3–15.
- Bodorkos, S., & Wingate, M. T. D. (2007). The contribution of geochronology to GSWA's mapping programs: current perspectives and future directions: Geological Survey of Western Australia, Record 2007/2, 10–11.
- Boehnke, P., Watson, E. B., Trail, D., Harrison, T. M., & Schmitt, A. K. (2013). Zircon saturation re-revisited. *Chemical Geology*, 351, 324–334.
- Broska, I., Petrik, I., & Williams, C. T. (2000). Coexisting monazite and allanite in peraluminous granitoids of the Tribeč Mountains, Western Carpathians. *American Mineralogist*, 85, 22–32.

- Brown, M. (1994). The generation, segregation, ascent and emplacement of granite magma: the migmatite-to-crustally-derived granite connection in thickened orogens. *Earth-Science Reviews*, 36, 83–130.
- Budzyń, B., Harlov, D. E., Williams, M. L., & Jercinovic, M. J. (2011). Experimental determination of stability relations between monazite, fluorapatite, allanite, and REE-epidote as a function of pressure, temperature, and fluid composition. *American Mineralogist*, 96, 1547–1567.
- Cawood, P. A., & Tyler, I. M. (2004). Assembling and reactivating the Proterozoic Capricorn Orogen: lithotectonic elements, orogenies, and significance. *Precambrian Research*, 128, 201–218.
- Chappell, B. W. (1999). Aluminium saturation in I- and S-type granites and the characterization of fractionated haplogranites. *Lithos* 46, 535–551.
- Cherniak, D. J., & Watson, E. B. (2001). Pb diffusion in zircon: *Chemical Geology* 172, 5–24.
- Cherniak, D. J., Watson, E. B., Grove, M., & Harrison, T. M. (2004). Pb diffusion in monazite: a combined RBS/SIMS study: *Geochimica et Cosmochimica Acta* 68, 829–840.
- Clark, C., Fitzsimons, I. C. W., Healy, D., & Harley, S. L. (2011). How does the continental crust get really hot?. *Elements* 7, 235–240.
- Clark, C., Kirkland, C. L., Spaggiari, C. V., Oorschot, C., Wingate, M. T. D., & Taylor, R. J. (2014). Proterozoic granulite formation driven by mafic magmatism: An example from the Fraser Range Metamorphics, Western Australia. *Precambrian Research* 240, 1–21.
- Collins, W. J. (1994). Upper- and middle-crustal response to delamination: An example from the Lachlan fold belt, eastern Australia. *Geology* 22, 143–146.
- Collins, W. J., & Shaw, R. D. (1995). Geochronological constraints on orogenic events in the Arunta Inlier: a review. *Precambrian Research* 71, 315–346.
- Collins, W. J., & Vernon, R. H. (1991). Orogeny associated with anticlockwise P-T-t paths: Evidence from low-P, high-T metamorphic terranes in the Arunta inlier, central Australia. *Geology* 19, 835–838.
- Cooke, R. A., & O'Brien, P. J. (2001). Resolving the relationship between high P-T rocks and gneisses in collisional terranes: an example from the Gföhl gneiss-granulite association in the Moldanubian Zone, Austria. *Lithos* 58, 33–54.
- Copeland, P., Parrish, R. R., & Harrison, T. M. (1988). Identification of inherited radiogenic Pb in monazite and its implications for U-Pb systematics. *Nature*, 333, 760–763.

- Crowley, J. L., Brown, R. L., Gervais, F., & Gibson, H. D. (2008). Assessing Inheritance of Zircon and Monazite in Granitic Rocks from the Monashee Complex, Canadian Cordillera. *Journal of Petrology*, 49, 1915–1929.
- Crowley, J. L., & Parrish, R. R. (1999). U–Pb isotopic constraints on diachronous metamorphism in the northern Monashee complex, southern Canadian Cordillera: *Journal of Metamorphic Geology* 17, 483–502.
- Culver, K. E. (2001). Structure, metamorphism and geochronology of the northern margin of the Gurun Gutta Granite, central Gascoyne Complex, Western Australia. Curtin University of Technology, Perth BSc. (Hons) thesis (unpublished).
- Cutten, H. N., Johnson, S. P., Thorne, A.M., Wingate, M.T.D., Kirkland, C.L., Belousova, E.A., Blay, O. A., & Zwingmann, H. (2016). Deposition, provenance, inversion history and mineralization of the Proterozoic Edmund and Collier Basins, Capricorn Orogen: Geological Survey of Western Australia Report 127, p.80.
- Cutts, K. A., Kelsey, D. E., & Hand, M. (2013). Evidence for late Paleoproterozoic (ca 1690–1665Ma) high- to ultrahigh-temperature metamorphism in southern Australia: Implications for Proterozoic supercontinent models. *Gondwana Research* 23, 617–640.
- Dodson, M. H. (1973). Closure temperature in cooling geochronological and petrological systems. *Contributions to Mineralogy and Petrology*, 40, 259–274.
- Dunlap, W. J. (1997). Neocrystallization or cooling? $^{40}\text{Ar}/^{39}\text{Ar}$ ages of white micas from low-grade mylonites. *Chemical Geology*, 143, 181–203.
- Dunlap, W., Teyssier, C., McDougall, I., & Baldwin, S. (1991). Ages of deformation from K/Ar and $^{40}\text{Ar}/^{39}\text{Ar}$ dating of white micas. *Geology*, 19, 1213–1216.
- Dyksterhuis, S., & Müller, R.D. (2008). Cause and evolution of intraplate orogeny in Australia. *Geology*, 36, 495–498.
- Evans, D. A. D., Sircombe, K. N., Wingate, M. T. D., Doyle, M., McCarthy, M., Pidgeon, R. T., & Van Niekerk, H. S. (2003). Revised geochronology of magmatism in the western Capricorn Orogen at 1805–1785 Ma: Diachroneity of the Pilbara-Yilgarn collision. *Australian Journal of Earth Sciences*, 50, 853–864.
- Fielding, I. O. H., Johnson, S. P., Meffre, S., Zi, J.-W., Sheppard, S., Large, R. R., & Rasmussen, B. (2018). Linking gold mineralization to regional-scale drivers of mineral systems using in situ U–Pb geochronology and pyrite LA-ICP-MS. *Geoscience Frontiers*, 1–17.

- Fielding, I. O. H., Johnson, S. P., Zi, J. W., Rasmussen, B., Muhling, J. R., Dunkley, D. J., Sheppard, S., Wingate, M. T. D., & Rogers, J. R. (2017). Using In Situ SHRIMP U-Pb Monazite and Xenotime Geochronology to Determine the Age of Orogenic Gold Mineralization: An Example from the Paulsens Mine, Southern Pilbara Craton. *Economic Geology*, 112, 1205–1230.
- Fielding, I. O. H., Johnson, S. P., Zi, J.-W., Sheppard, S., & Rasmussen, B. (2018). Neighbouring orogenic gold deposits may be the products of unrelated mineralizing events: *Ore Geology Reviews* 95, 593–603.
- Finger, F., Broska, I., Roberts, M. P., & Schermaier, A. (1998). Replacement of primary monazite by apatite-allanite-epidote coronas in an amphibolite facies granite gneiss from the eastern Alps. *American Mineralogist* 83, 248–258.
- Fletcher, I. R., McNaughton, N. J., Aleinikoff, J. A., Rasmussen, B., & Kamo, S.L. (2004). Improved calibration procedures and new standards for U-Pb and Th-Pb dating of Phanerozoic xenotime by ion microprobe. *Chemical Geology*, 209, 295–314.
- Fletcher, I. R., McNaughton, N. J., Davis, W. J., & Rasmussen, B. (2010.). Matrix effects and calibration limitations in ion probe U-Pb and Th-Pb dating of monazite. *Chemical Geology*, 270, 31–44.
- Fletcher, I.R., McNaughton, N.J., & Rasmussen, B. (2000). SHRIMP U-Pb geochronology of authigenic xenotime and its potential for dating sedimentary basins. *Australian Journal of Earth Sciences*, 47, 845–859.
- Foster, G., Kinny, P., Vance, D., Prince, C., and Harris, N. (2000). The significance of monazite U-Th-Pb age data in metamorphic assemblages; a combined study of monazite and garnet chronometry. *Earth and Planetary Science Letters*, 181, 327–340.
- Glasson, K. J., Johnson, T. E., Kirkland, C. L., Gardiner, N. J., Clark, C., Blereau, E., Hartnady, M. I., Spaggiari, C., & Smithies, H. (2019). A window into an ancient backarc? The magmatic and metamorphic history of the Fraser Zone, Western Australia. *Precambrian Research*, 323, 55–69.
- Gao, L-E., Zeng, L., & Asimow, P. D. (2017). Contrasting geochemical signatures of fluid-absent versus fluid-fluxed melting of muscovite in metasedimentary sources: The Himalayan leucogranites. *Geology*, 45, 39–42.
- Gardiner, N. J., Maidment, D. W., Kirkland, C. L., Bodorkos, S., Smithies, R. H., & Jeon, H. (2018). Isotopic insight into the Proterozoic crustal evolution of the Rudall Province, Western Australia: *Precambrian Research*, 313, 31–50
- Gee, R. D. (1979). Structure and tectonic style of the Western Australian Shield: *Tectonophysics* 58, 327–369.

- Gilotti, J. A., & McClelland, W. C. (2005). Leucogranites and the Time of Extension in the East Greenland Caledonides. *The Journal of Geology*, 113, 399–417.
- Grosse, P., Söllner, F., Báez, M. A., Toselli, A. J., Rossi, J. N., de la Rosa, J. D. (2009). Lower Carboniferous post-orogenic granites in central-eastern Sierra de Velasco, Sierras Pampeanas, Argentina: U–Pb monazite geochronology, geochemistry and Sr–Nd isotopes. *International Journal of Earth Sciences*, 98, 1001–1025.
- GSWA. (2016). Compilation of geochronology information, 2016 update, digital data product. www.dmp.wa.gov.au/geoview.
- GSWA. (2016). 1:500 000 State interpreted bedrock geology of Western Australia, 2016: Geological Survey of Western Australia, digital data layer. www.dmp.wa.gov.au/geoview
- Hacker, B. R., Ratschbacher, L., Webb, L., Ireland, T., Walker, D., & Shuwen, D. (1998). U–Pb zircon ages constrain the architecture of the ultrahigh-pressure Qinling–Dabie Orogen, China: *Earth and Planetary Science Letters* 161, 215–230.
- Hand, M., & Buick, I. S. (2001). Tectonic evolution of the Reynolds-Anmatjira Ranges: a case study in terrain reworking from the Arunta Inlier, central Australia, in *Continental reactivation and reworking* edited by JA Miller, RE Holdsworth, IS Buick and M Hand. Geological Society, London, Special Publications, 184, 237–260.
- Hanmer, S., & Passchier, C.W. (1991). Shear sense indicators: a review. *Geological Survey of Canada* 90, p.70.
- Hansma, J., Tohver, E., Schrank, C., Jourdan, F., & Adams, D. (2016). The timing of the Cape Orogeny: New $^{40}\text{Ar}/^{39}\text{Ar}$ age constraints on deformation and cooling of the Cape Fold Belt, South Africa: *Gondwana Research* 32, 122–137.
- Hanson, R. B., & Barton, M. D. (1989). Thermal development of low-pressure metamorphic belts: Results from two-dimensional numerical models: *Journal of Geophysical Research. Solid Earth* 94, 10363–10377.
- Harig, C., Molnar, P., & Houseman, G. A. (2010). Lithospheric thinning and localization of deformation during rayleigh-taylor instability with nonlinear rheology and implications for intracontinental magmatism. *Journal of Geophysical Research. Solid Earth* 115, 1–11.
- Harrison, T.M., Célérier, J., Aikman, A.B., Hermann, J., & Heizler, M.T. (2009). Diffusion of ^{40}Ar in muscovite. *Geochimica et Cosmochimica Acta*, 73, 1039–1051.
- Harrison, T.M., Duncan, I., & McDougall, I. (1985). Diffusion of ^{40}Ar in biotite: Temperature, pressure and compositional effects. *Geochimica et Cosmochimica Acta*, 49, 2461–2468.

- Harrison, M. T., Grove, M., McKeegan, K.D., Coath, C.D., Lovera, O.M., & Fort, P. L. (1999). Origin and Episodic Emplacement of the Manaslu Intrusive Complex, Central Himalaya. *Journal of Petrology*, 40, 3–19.
- Hawke, M. L., Meffre, S., Stein, H., Hilliard, P., Large, R., & Gemmell, J. B. (2015). Geochronology of the DeGrussa volcanic-hosted massive sulphide deposit and associated mineralisation of the Yerrida, Bryah and Padbury Basins, Western Australia. *Precambrian Research*, 267, 250–284.
- Heaman, L., and Parrish, R. (1991). U–Pb geochronology of accessory minerals. In: Heaman, L. Ludden, J. N. (Eds.), *Applications of radiogenic isotope systems to problems in geology: Short Course Handbook-Mineralogical Association of Canada* 19, 59–102.
- Holland T. J. B., & Powell, R. (2011). An improved and extended internally consistent thermodynamic dataset for phases of petrological interest, involving a new equation of state for solids. *Journal of Metamorphic Geology* 29, 333–383.
- Jourdan, F. & Eroglu, E. $^{40}\text{Ar}/^{39}\text{Ar}$ and (U-Th)/He model age signatures of elusive mercurian and venusian meteorites: *Meteoritics & Planetary Science*, in press. (2017).
- Jourdan F., Feraud, G., Bertrand, A.B., Kampunzu, G., Tshoso, M. K., & Watkeys, B. (2005). Karoo large igneous province; brevity, origin, and relation to mass extinction questioned by new $^{40}\text{Ar}/^{39}\text{Ar}$ age data: *Geology*, 33, 745–748.
- Jourdan, F., Frew, A., Joly, A., Mayers, C., & Evans, N. J. (2014). WA1ms: A ~ 2.61 Ga muscovite standard for $^{40}\text{Ar}/^{39}\text{Ar}$ dating. *Geochimica et Cosmochimica Acta*, 141, 113–126.
- Johnson, S. P., Korhonen, F. J., Kirkland, C. L., Cliff, J. B., Belousova, E. A., & Sheppard, S. (2017). An isotopic perspective on growth and differentiation of Proterozoic orogenic crust: From subduction magmatism to cratonization. *Lithos* 268, 76–86.
- Johnson, S. P., & Sheppard, S. (2018). Mount James Subgroup (P_-POJ-md): Geological Survey of Western Australia, WA Geology Online, Explanatory Notes extract, viewed 21 November 2018, www.dmp.wa.gov.au/ens.
- Johnson, S. P., Sheppard, S., Rasmussen, B., Wingate, M. T. D., Kirkland, C. L., Muhling, J. R., Fletcher, I. R., & Belousova, E. A. (2011). Two collisions, two sutures: Punctuated pre-1950Ma assembly of the West Australian Craton during the Ophthalmian and Glenburgh Orogenies. *Precambrian Research*, 189, 239–262.

- Johnson, S. P., Sheppard, S., Rasmussen, B., Wingate, M. T. D., Kirkland, C. L., Muhling, J., Fletcher, I. R., & Belousova, E. (2010). The Glenburgh Orogeny as a record of Paleoproterozoic continent-continent collision: Geological Survey of Western Australia, Record 2010/5, p. 54.
- Johnson, S. P., Thorne, A. M., Tyler, I. M., Korsch, R. J., Kennett, B. L. N., Cutten, H. N., Goodwin, J., Blay, O., Blewett, R. S., Joly, A., Dentith, M. C., Aitken, A. R. A., Holzschuh, J., Salmon, M., Reading, A., Heinson, G., Boren, G., Ross, J., Costelloe, R. D., & Fomin, T. (2013). Crustal architecture of the Capricorn Orogen, Western Australia and associated metallogeny. *Australian Journal of Earth Sciences*, 60, 681–705.
- Kay, R. W., & Mahlburg Kay, S. (1993). Delamination and delamination Magmatism. *Tectonophysics* 219, 177–189.
- Keep, M., Hengesh, J., & Whitney, B. (2012). Natural seismicity and tectonic geomorphology reveal regional transpressive strain in northwestern Australia. *Australian Journal of Earth Sciences*, 59, 341–354.
- Kemp, A. I. S., & Hawkesworth, C. J. (2003). 3.11 - Granitic Perspectives on the Generation and Secular Evolution of the Continental Crust A2 - Holland, Heinrich D. In: Turekian KK (ed) *Treatise on Geochemistry*. Pergamon, Oxford, p. 349–410.
- Kirschner, D. I., Cosca, M. A., Masson, H., & Hunziker, C. (1996). Staircase $^{40}\text{Ar}/^{39}\text{Ar}$ spectra of fine-grained white mica: Timing and duration of deformation and empirical constraints on argon diffusion. *Geology*, 24, 747–750.
- Koppers, A. A. P. (2002). ArArCalc—Software for $^{40}\text{Ar}/^{39}\text{Ar}$ age calculations. *Computers & Geoscience*, 48, 605–619.
- Kirkland, C. L., Spaggiari, C. V., Pawley, M. J., Wingate, M. T. D., Smithies, R. H., Howard, H. M., Tyler, I. M., Belousova, E. A., & Poujol, M. (2011). On the edge: U–Pb, Lu–Hf, and Sm–Nd data suggests reworking of the Yilgarn craton margin during formation of the Albany-Fraser Orogen. *Precambrian Research* 187, 223–247.
- Kirkland, C. L., Wingate, M. T. D. (2012). Reading Deep Time: Radiogenic Isotopic Geochronology. Geological Survey of Western Australia, Record 2012/15, p.10.
- Kirkland, C.L., Wingate, M. T. D., Bodorkos, S., & Sheppard, S. (2009). 183287: granite, Perseverance Well; Geochronology Record 756. Geological Survey of Western Australia, p. 4.
- Kirkland, C. L., Wingate, M. T. D., Bodorkos, S & Sheppard, S. (2009). 183205: schistose metatonalite, Mallet Well: Geochronology Record 753: Geological Survey of Western Australia, p.4.

- Korhonen, F. J., Johnson, S. P., Fletcher, I. R., Rasmussen, B., Sheppard, S., Muhling, J. R., Dunkley, D. J., Wingate, M. T. D., Roberts, M. P., & Kirkland, C. L. (2015). Pressure-Temperature-Time evolution of the Mutherbukin Tectonic event, Capricorn Orogen: Geological Survey of Western Australia, Report 146, p. 64.
- Korhonen, F. J., & Johnson, S. P. (2015). The role of radiogenic heat in prolonged intraplate reworking: The Capricorn Orogen explained?. *Earth and Planetary Science Letters* 428, 22–32.
- Korhonen, F. J., Johnson, S. P., Wingate, M. T. D., Kirkland, C. L., Fletcher, I. R., Dunkley, D. J., Roberts, M. P., Sheppard, S., Muhling, J. R., & Rasmussen, B. (2017). Radiogenic heating and craton-margin plate stresses as drivers for intraplate orogeny. *Journal of Metamorphic Geology* 35, 631–661.
- Kusiak, M. A., Williams, I. S., Dunkley, D. J., Konečný, P., Słaby, E., & Martin, H. (2014). Monazite to the rescue: U–Th–Pb dating of the intrusive history of the composite Karkonosze pluton, Bohemian Massif. *Chemical Geology*, 364, 76–92.
- Krapez, B., & McNaughton, N. J. (1999). SHRIMP zircon U–Pb age and tectonic significance of the Palaeoproterozoic Boolaloo Granodiorite in the Ashburton Province, Western Australia. *Australian Journal of Earth Sciences*, 46, 283–287.
- Le Maitre, R. W. (1989). *A Classification of the Igneous Rocks and Glossary of Terms*. Blackwell, Oxford, p. 193.
- Lee, D. E., & Dodge, F. C. W. (1964). Accessory minerals in some granitic rocks in California and Nevada as a function of calcium content. *American Mineralogist* 49, 1660–1669.
- Lee, Y.J., Marti, K., Severinghaus, J.P., Kawamura, K., Yoo, H.S., Lee, J.B., Kim, J.S. (2006). A redetermination of the isotopic abundances of atmospheric Ar. *Geochimica et Cosmochimica Acta* 70, 4507–4512.
- Lee, J. K. W., Williams, I. S., & Ellis, D. J. (1997). Pb, U and Th diffusion in natural zircon: *Nature* 390, 159–162.
- Loosveld, R. J. H., & Etheridge, M. A. (1990). A model for low-pressure facies metamorphism during crustal thickening. *Journal of Metamorphic Geology* 8, 257–267.
- Ludwig, K.R. (2009). *Squid 2.50, A User's Manual: Berkeley Geochronology Centre Special Publication*, p. 95.
- Mahon, K. I. (1996). The New “York” regression: application of an improved statistical method to geochemistry. *International Geology Review*, 38, 293–303.

- Martin, D. McB., & Morris, P. A. (2010). Tectonic setting and regional implications of ca 2.2 Ga mafic magmatism in the southern Hamersley Province, Western Australia. *Australian Journal of Earth Sciences*, 57, 911–931.
- Martin, D. McB, Sheppard, S., & Thorne, A. M. (2005). Geology of the Maroonah, Ullawarra, Capricorn, Mangaroon, Edmund, and Elliot Creek 1: 100 000 sheets: Geological Survey of Western Australia, 1: 100 000 Geological Series Explanatory Notes, p.65.
- McLaren, S., Sandiford, M., & Powell, R. (2005). Contrasting styles of Proterozoic crustal evolution: A hot-plate tectonic model for Australian terranes. *Geology* 33, 673–676.
- Meadows, H.R., Reddy, S.M., Clark, C., Plavsa, D., & Johnson, T. (2017). Localisation of high strain and high temperature into the Chalba Shear Zone, Gascoyne Province. Specialist Group in Tectonics and Structural Geology, Conference Abstract.
- Miller, C. F., Meschter McDowell, S., & Mapes, R. W. (2003). Hot and cold granites? Implications of zircon saturation temperatures and preservation of inheritance. *Geology* 31, 529–532.
- Miller, C. F., Mittlefehldt, D. W. (1982). Depletion of light rare-earth elements in felsic magmas. *Geology*, 10, 129–133.
- Montel, J-M. (1993). A model for monazite/melt equilibrium and application to the generation of granitic magmas. *Chemical Geology*, 110, 127–146.
- Morrissey, L.J, Hand, M., Raimondo, T., & Kelsey, D. E. (2014) Long-lived high-T, low-P granulite facies metamorphism in the Arunta Region, central Australia: *Journal of Metamorphic Geology*, 32, 25–47.
- Mulch, A., & Cosca, M. A. (2004). Recrystallization or cooling ages: *in situ* UV-laser $^{40}\text{Ar}/^{39}\text{Ar}$ geochronology of muscovite in mylonitic rocks. *Journal of the Geological Society*, 161, 573–582.
- Muhling, J. R., Fletcher, I. R., & Rasmussen, B. (2012). Dating fluid flow and Mississippi Valley type base-metal mineralization in the Paleoproterozoic Earahedy Basin, Western Australia. *Precambrian Research* 212–213, 75–90.
- Nelson, D. R. (2005). 178027: biotite-muscovite granodiorite, Mangaroon Homestead; Geochronology dataset 536; in *Compilation of geochronology data, June 2006 update*; Western Australia Geological Survey.
- Nelson, D. R. (2004). 169094: quartz-plagioclase-biotite-sillimanite gneiss, Woorkailjia Pool; Geochronology dataset 88; in *Compilation of geochronology data, June 2006 update*; Western Australia Geological Survey.

- Nelson, D. R. (2004). 169092: biotite-muscovite monzogranite, Red Rock Bore; Geochronology Record 103: Geological Survey of Western Australia, p. 5.
- Nelson, D. R. (2004). 169086: biotite monzogranite, Boora Boora Bore, Geochronology dataset 117; in *Compilation of geochronology data, June 2006 update*: Western Australia Geological Survey, p.4.
- Nelson, D. R. (2004). 169088: foliated biotite monzogranite, Mundong Well, Geochronology dataset 45; in *Compilation of geochronology data, June 2006 update*: Western Australia Geological Survey, p.4.
- Nelson, D. R. (2002). 169053: biotite muscovite monzogranite, Fraser Well; in *Compilation of geochronology data, 2001*: Western Australia Geological Survey, Record 2002/2, p. 35–38.
- Nelson, D. R. (2000). 139466: foliated biotite-muscovite-garnet granodiorite, Erong Homestead; Geochronology Record 427: Geological Survey of Western Australia, p. 4.
- Nelson, D. R. (1998). 142849: foliated coarse-grained monzogranite, northeast of White Well; Geochronology dataset 365; in *Compilation of geochronology data, June 2006 update*: Western Australia Geological Survey.
- Nelson, D. R. (1998). 142851: recrystallised monzogranite, Kerba Pool; Geochronology dataset 367: Geological Survey of Western Australia, p.4.
- Nelson, D. R. (1998). 142855: porphyritic monzogranite, Anderson well; in *Compilation of SHRIMP U–Pb zircon geochronology data, 1997*: Western Australia Geological Survey, Record 1998/2, 194–197.
- Occhipinti, S. A., Hocking, R., Lindsay, M., Aitken, A., Copp, I., Jones, J., Sheppard, S., Pirajno, F., & Metelk, V. (2017). Paleoproterozoic basin development on the northern Yilgarn Craton, Western Australia. *Precambrian Research*, 300, 121–140
- Occhipinti, S. A., & Reddy, S. M. (2009). Neoproterozoic reworking of the Palaeoproterozoic Capricorn Orogen of Western Australia and implications for the amalgamation of Rodinia. *Geological Society, London, Special Publications* 327, 445–456.
- Occhipinti, S., & Reddy, S. (2004). Deformation in a crustal scale shear zone: Errabiddy Shear Zone, Western Australia. In: ALSOP, G. I., Holdsworth, R. E., McCafrey, K. J. W. & Hand, M. (eds) 2004. *Flow processes in Faults and Shear Zones*. Geological Society, London, Special Publication 224, 229–248.

- Occhipinti, S. A., Sheppard, S., Myers, J. S., Tyler, I. M., & Nelson, D. R. (2001). Archaean and Paleoproterozoic geology of the Narryer Terrane (Yilgarn Craton) and the southern Gascoyne Complex (Capricorn Orogen), Western Australia — a field guide: Western Australia Geological Survey, Record 2001/8, p. 70.
- Occhipinti, S. A., Sheppard, S., Nelson, D., Myers, J., & Tyler, I. (1998). Syntectonic granite in the southern margin of the Paleoproterozoic Capricorn Orogen, Western Australia. *Australian Journal of Earth Sciences*, 45, 509–512.
- Occhipinti, S. A., Sheppard, S., Passchier, C., Tyler, I. M., & Nelson, D. R. (2004). Paleoproterozoic crustal accretion and collision in the southern Capricorn Orogen: the Glenburgh Orogeny. *Precambrian Research*, 128, 237–255.
- Oliver, N. H. S., & Zakowski, S. (1995). Timing and geometry of deformation, low-pressure metamorphism and anatexis in the eastern Mt Lofty Ranges: The possible role of extension. *Australian Journal of Earth Sciences* 42, 501–507.
- Parrish, R. R. (1990). U–Pb dating of monazite and its application to geological problems Canadian. *Journal of Earth Sciences*, 27, 1431–1450.
- Parrish, R. R., & Tirrul, R. (1989). U-Pb age of the Baltoro granite, northwest Himalaya, and implications for monazite U-Pb systematics. *Geology*, 17, 1076–1079.
- Patiño Douce, A. E., & Harris, N. (1998). Experimental Constraints on Himalayan Anatexis. *Journal of Petrology*, 39, 689–710.
- Pearson, J. M. (1996). Alkaline rocks of the Gifford Creek Complex, Gascoyne Province, Western Australia — their petrogenetic and tectonic significance: University of Western Australia, Perth, PhD thesis (unpublished).
- Piechocka, A. M., Gregory, C. J., Zi, J.-W., Sheppard, S., Wingate, M. T. D., & Rasmussen, B. (2017). Monazite trumps zircon: applying SHRIMP U–Pb geochronology to systematically evaluate emplacement ages of leucocratic, low-temperature granites in a complex Precambrian orogen. *Contributions to Mineralogy and Petrology*, 172, 1–17.
- Piechocka, A. M., Sheppard, S., Fitzsimons, I. C. W., Johnson, S. P., Rasmussen, B., & Jourdan, F. (2018). Neoproterozoic $^{40}\text{Ar}/^{39}\text{Ar}$ mica ages mark the termination of a billion years of intraplate reworking in the Capricorn Orogen, Western Australia. *Precambrian Research*, 310, 391–406.
- Piechocka, A.M., Zi, J. W., Gregory, C. J., Sheppard, S., & Rasmussen, B. (2019). SHRIMP U–Pb phosphate dating shows metamorphism was synchronous with magmatism during the Paleoproterozoic Capricorn Orogeny. *Australian Journal of Earth Sciences*, 66, 973–990.

- Pirajno, F., Hocking, R. M., Reddy, S. M., & Jones, A. J. (2009). A review of the geology and geodynamic evolution of the Palaeoproterozoic Earaheedy Basin, Western Australia. *Earth-Science Reviews* 94, 39–77.
- Poitrasson, F., Chenery, S., & Bland, D. J. (1996). Contrasted monazite hydrothermal alteration mechanisms and their geochemical implications. *Earth and Planetary Science Letters*, 145, 79–96.
- Raimondo, T., Hand, M., & Collins, M. J. (2014). Compressional intracontinental orogens: Ancient and modern perspectives. *Earth-Science Reviews*, 130, 128–153.
- Raimondo, T., Collins, A. S., Hand, M., Walker-Hallam, A., Smithies, R. H., Evins, P. M., & Howard, H. M. (2010). The anatomy of a deep intracontinental orogen. *Tectonics*, 29, 1–31.
- Rapp, R. P., & Watson, E. B. (1986). Monazite solubility and dissolution kinetics: implications for the thorium and light rare earth chemistry of felsic magmas. *Contributions to Mineralogy and Petrology*, 94, 304–316.
- Rasmussen, B. (2005). Zircon growth in very low grade metasedimentary rocks: evidence for zirconium mobility at ~250°C. *Contributions to Mineralogy and Petrology*, 150, 146–155.
- Rasmussen, B. (2005). Radiometric dating of sedimentary rocks: the application of diagenetic xenotime geochronology. *Earth-Science Reviews* 68, 197–243.
- Rasmussen, B., Fletcher, I. R., and Muhling, J. R. (2007). In situ U–Pb dating and element mapping of three generations of monazite: Unraveling cryptic tectonothermal events in low-grade terranes. *Geochimica et Cosmochimica Acta*, 71, 670–690.
- Rasmussen, B., Fletcher, I. R., Muhling, J. R., Thorne, W. S., & Broadbent, G. C. (2007). Prolonged history of episodic fluid flow in giant hematite ore bodies: Evidence from in situ U–Pb geochronology of hydrothermal xenotime. *Earth and Planetary Science Letters* 258, 249–259.
- Rasmussen, B., Fletcher, I. R., Muhling, J. R., & Wilde, S. A. (2010). In situ U–Th–Pb geochronology of monazite and xenotime from the Jack Hills belt: Implications for the age of deposition and metamorphism of Hadean zircons. *Precambrian Research*, 180, 26–46.
- Rasmussen, B., Fletcher, I. R., & Sheppard, S. (2005). Isotopic dating of the migration of a low-grade metamorphic front during orogenesis. *Geology*, 33, 773–776.
- Reddy, S.M., & Occhipinti, S.A. (2004). High-strain zone deformation in the southern Capricorn Orogen, Western Australia: kinematics and age constraints. *Precambrian Research*, 128, 295–314.

- Reddy, S. M., & Potts, G. J. (1999). Constraining absolute deformation ages: the relationship between deformation mechanisms and isotope systematics. *Journal of Structural Geology*, 21, 1255–1265.
- Renne, P.R., G.Balco, K.R. Ludwig, R. Mundil, & K. Min. (2011). Response to the comment by W.H. Schwarz et al. on “Joint determination of ^{40}K decay constants and $^{40}\text{Ar}/^{40}\text{K}$ for the Fish Canyon sanidine standard, and improved accuracy for $^{40}\text{Ar}/^{39}\text{Ar}$ geochronology” by P. R. Renne et al. (2010). *Geochim. Cosmochim. Acta*, 75, 5097–5100.
- Revels, S.A., Keep, M., & Kennett, B.L.N. (2009). NW Australian intraplate seismicity and stress regime. *Journal of Geophysical Research*, 114, 1–10.
- Rowley, D. B., Xue, F., Tucker, R. D., Peng, Z. X., Baker, J., & Davis, A. (1997). Ages of ultrahigh pressure metamorphism and protolith orthogneisses from the eastern Dabie Shan: U/Pb zircon geochronology: *Earth and Planetary Science Letters* 151, 191–203.
- Sandiford, M., & Hand, M. (1998). Controls on the locus of intraplate deformation in central Australia. *Earth and Planetary Science Letters* 162, 97–110.
- Sandiford, M., & Powell, R. (1986). Deep crustal metamorphism during continental extension: modern and ancient examples. *Earth and Planetary Science Letters* 79, 151–158.
- Scaillet, B., Holtz, F., & Pichavant, M. (2016). Experimental Constraints on the Formation of Silicic Magmas. *Elements* 12, 109–114.
- Scaillet, B., Pichavant, M., & Roux, J. (1995). Experimental Crystallization of Leucogranite Magmas. *Journal of Petrology*, 36, 663–705.
- Schärer, U., Xu, R. H., & Allègre, C. J. (1986). U-(Th)-Pb systematics and ages of Himalayan leucogranites, South Tibet. *Earth and Planetary Science Letters*, 77, 35–48.
- Scibiorski, E., Tohver, E., & Jourdan, F. (2015). Rapid cooling and exhumation in the western part of the Mesoproterozoic Albany-Fraser Orogen, Western Australia: *Precambrian Research* 265, 232–248.
- Scott, J. M., Palin, J. M., Cooper, A. F., Sagar, M. W., Allibone, A. H., & Tulloch, A. J. (2011). From richer to poorer: zircon inheritance in Pomona Island Granite, New Zealand. *Contributions to Mineralogy and Petrology*, 161, 667–681.
- Scrimgeour, I. R. (2003). Developing a revised framework for the Arunta Region, in *Annual Geoscience Exploration Seminar (AGES) 2003: Northern Territory Geological Survey, Record 2003-001*, p. 1–3.

- Scrimgeour, I. R., Kinny, P. D., Close, D. F., & Edgoose, C. J. (2005). High-T granulites and polymetamorphism in the southern Arunta Region, central Australia. Evidence for a 1.64 Ga accretional event. *Precambrian Research* 142, 1–27.
- Selway, K., Sheppard, S., Thorne, A.M., Johnson, S.P., & Groenewald, P.B. (2009). Identifying the lithospheric structure of a Precambrian orogen using magnetotellurics: The Capricorn Orogen, Western Australia. *Precambrian Research*, 168, 185–196.
- Şener, K. A., Young, C., Groves, D. I., Krapez, B., & Fletcher, I. R. (2005). Major orogenic gold episode associated with Cordilleran-style tectonics related to the assembly of Paleoproterozoic Australia? *Geology*, 33, 225–228.
- Sheppard, S., Bodorkos, S., Johnson, S. P., Wingate, M. T. D., & Kirkland, C. L. (2010). The Paleoproterozoic Capricorn Orogeny: Intracontinental Reworking Not Continent-Continent Collision: Geological Survey of Western Australia, Report 108, p. 33.
- Sheppard, S., Farrell, T. R., Bodorkos, S., Hollingsworth, D., Tyler I., M., & Pirajno, F. (2006). Late Paleoproterozoic (1680–1620) sedimentation, magmatism, and tectonism in the Capricorn Orogen, in GSWA 2006 extended abstracts: promoting the prospectivity of Western Australia: Geological Survey of Western Australia, Record 2006/3, p. 11–12.
- Sheppard, S., & Johnson, S. P. (2016). Pooranoo Metamorphics (P_-PO-md): Geological Survey of Western Australia, WA Geology Online, Explanatory Notes extract, viewed 20 November 2017, www.dmp.wa.gov.au/ens.
- Sheppard, S., Johnson, S. P., Wingate, M. T. D., Kirkland, C. L., & Pirajno, F. (2010). Explanatory notes for the Gascoyne Province: Geological Survey of Western Australia, 1:100 000 Explanatory Notes, p. 336.
- Sheppard, S., Occhipinti, S. A., & Nelson, D. R. (2005). Intracontinental reworking in the Capricorn Orogen, Western Australia: the 1680–1620 Ma Mangaroon Orogeny. *Australian Journal of Earth Sciences*, 52, 443–460.
- Sheppard, S., Occhipinti, S. A., & Tyler, I. M. (2004). A 2005–1970 Ma Andean-type batholith in the southern Gascoyne Complex, Western Australia. *Precambrian Research*, 128, 257–277.
- Sheppard, S., Rasmussen, B., Muhling, J. R., Farrell, T. R., & Fletcher, I. R. (2007). Grenvillian-aged orogenesis in the Paleoproterozoic Gascoyne Complex, Western Australia: 1030–950 Ma reworking of the Proterozoic Capricorn Orogen. *Journal of Metamorphic Geology*, 25, 477–494.

- Smithies, R. H., Howard, H. M., Evins, P. M., Kirkland, C. L., Kelsey, D. E., Hand, M., Wingate, M. T. D., Collins, A. S., & Belousova, E. (2011). High-Temperature Granite Magmatism, Crust–Mantle Interaction and the Mesoproterozoic Intracontinental Evolution of the Musgrave Province, Central Australia. *Journal of Petrology* 52, 931–958.
- Spaggiari, C. V., Kirkland, C. L., Smithies, R. H., & Wingate, M. T. D. (2014). Tectonic links between Proterozoic sedimentary cycles, basin formation and magmatism in the Albany-Fraser Orogen: Geological Survey of Western Australia, Report 133.
- Stacey, J.S., & Kramers, J.D. (1975). Approximation of terrestrial lead isotope evolution by a two-stage model. *Earth and Planetary Science Letters*, 26, 207–221.
- Steiger, R. H., & Jäger, E. (1977). Subcommittee on geochronology: Convention on the use of decay constants in geo- and cosmochronology. *Earth and Planetary Science Letters* 36, 359–362.
- Stern R. A., Bodorkos, S., Kamo, S. L., Hickman, A. H., & Corfu, F. (2009). Measurement of SIMS Instrumental Mass Fractionation of Pb Isotopes During Zircon Dating. *Geostandards and Geoanalytical Research* 33, 145–168.
- Stern, R. A. (2001). A new isotopic and trace-element standard for the ion microprobe: preliminary thermal ionization mass spectrometry (TIMS) U–Pb and electron-microprobe data; Radiogenic Age and Isotopic Studies: Report 14, Geological Survey of Canada, Current Research 2001-F1, 11p.
- Stern, R. A., & Rainbird, R. H. (2001). Advancements in xenotime U–Pb geochronology by ion microprobe, Eleventh V.I. Goldschmidt Conference Lunar and Planetary Science Institute, Houston.
- Stern, T. A., & Sanborn, N. (1998). Monazite U–Pb and Th–Pb geochronology by high-resolution secondary ion mass spectrometry. Radiogenic Age and Isotope Studies: Report 11, Geological Survey of Canada, Current Research 1998-F, 1–18.
- Thorne, A. M. (2015). Bresnahan Group (P₋BR-s): Geological Survey of Western Australia, WA Geology Online, Explanatory Notes extract, viewed 21 November 2018, www.dmp.wa.gov.au/ens.
- Thorne, A. M., & Seymour, D. B. (1991). Geology of the Ashburton Basin, Western Australia: Geological Survey of Western Australia, Bulletin 139, p. 141.
- Townsend, K. J., Miller, C.F., D'Andrea, J.L., Ayers, J.C., Harrison, T. M., & Coath, C. D. (2001). Low temperature replacement of monazite in the Ireteba granite, Southern Nevada: geochronological implications. *Chemical Geology*, 172, 95–112.

- Tucker, N. M., Morrissey, L. J., Payne, J. L., & Szpunar, M. (2018). Genesis of the Archean–Paleoproterozoic Tabletop Domain, Rudall Province, and its endemic relationship to the West Australian Craton. *Australian Journal of Earth Sciences*, 65, 1–30.
- Tyler, I. M. (1990). The geology of the Sylvania Inlier and the southeast Hamersley Basin: Geological Survey of Western Australia, Bulletin 138, p.124.
- Tyler, I. M., & Thorne, A. M. (1990) The northern margin of the Capricorn Orogen Western Australia an example of an Early Proterozoic collision zone. *Journal of Structural Geology*, 12, 685–701.
- Vilà, M., Pin, C., Liesa, M., & Enrique, P. (2007). LPHT metamorphism in a late orogenic transpressional setting, Albera Massif, NE Iberia: implications for the geodynamic evolution of the Variscan Pyrenees. *Journal of Metamorphic Geology* 25, 321–347.
- Viete, D. R., & Lister, G. S. (2016). On the significance of short-duration regional Metamorphism. *Journal of the Geological Society* 174, 377–392.
- Vernon, R. H., & Clarke, G. L. (2008). Principles of metamorphic petrology. New York, USA: Cambridge Press University.
- Watson, E. B., & Harrison, T. M. (1983). Zircon saturation revisited: temperature and composition effects in a variety of crustal magma types. *Earth and Planetary Science Letters* 64, 295–304.
- White, R. W., Powell, R., & Johnson, T. E. (2014). The effect of Mn on mineral stability in metapelites revisited: new a–x relations for manganese-bearing minerals. *Journal of Metamorphic Geology* 32, 809–828.
- Wickham, S. M., & Oxburgh, F. R. S. (1987). Low-pressure regional metamorphism in the Pyrenees and its implications for the thermal evolution of rifted continental crust. *Philosophical Transactions of the Royal Society of London. Series A, Mathematical and Physical Sciences* 321, 219–242.
- Williams, S. J. (1986). Geology of the Gascoyne Province, western Australia: Geological Survey of Western Australia, Report 15, p. 85.
- Williams, I. S., Compston, W., & Chappell, B. W. (1983). Zircon and monazite U–Pb systems and the histories of I-type magmas, Berridale Batholith, Australia. *Journal of Petrology*, 24, 76–97.
- Wingate, M. T. D., & Giddings, J. W. (2000). Age and palaeomagnetism of the Mundine Well dyke swarm, Western Australia: implications for an Australia-Laurentia connection at 755 Ma: *Precambrian Research* 100, 335–357.

- Wingate, M. T. D., Kirkland, C. L., Bodorkos, S., Groenewalk, P. B., & Sheppard, S. (2010). 187403, quartzite, Robinson Bore; Geochronology Record 862: Geological Survey of Western Australia, p. 5.
- Wingate, M. T. D., Kirkland, C. L., Bodorkos, S., S, Sheppard, & Farrell, T. R. (2009). 183255: metasandstone, Mount Samuel; Geochronology Record 772: Geological Survey of Western Australia, 5p.
- Wingate, M. T. D., Kirkland, C. L., & Korhonen F. J. (2013). 208318: metagranite, Brown Well; Geochronology Record 1174: Geological Survey of Western Australia, 4p.
- Wingate, M. T. D., Kirkland, C. L & Johnson, S. P. (2011). 190662: gneissic metamonzogranite, Recovery Well; Geochronology Record 1005: Geological Survey of Western Australia, 4p.
- Wingate, M. T. D., Kirkland, C. L., Johnson, S. P., & Sheppard, S. (2017). 188974, metamonzogranite, Mount James homestead; Geochronology Record 1362: Geological Survey of Western Australia, p. 4.
- Wingate, M. T. D., Kirkland, C. L., Johnson, S. P., & Sheppard, S. (2012). 190634: metamonzogranite, Minierra Well; Geochronology Record 1034: Geological Survey of Western Australia, p. 4.
- Wingate, M. T. D., Kirkland, C. L., Johnson, S. P., & Sheppard, S. (2012). 190660: metamonzogranite, Midway Bore; Geochronology Record 1036: Geological Survey of Western Australia, p. 4.
- Wingate, M. T. D., Kirkland, C., Sheppard, S., & Johnson, S. (2010). 185945: pegmatite lenses in metamonzogranite, Yinnetharra Homestead; Geochronology Record 901: Geological Survey of Western Australia, p. 5.
- Wingate, M. T. D., Kirkland, C., Sheppard, S., & Johnson, S. (2010). 185946: pegmatite dyke, Yinnetharra Homestead; Geochronology Record 902: Geological Survey of Western Australia, p. 4.
- Wingate, M. T. D, & Lu, Y. (2016). Introduction to geochronology information released in 2014: Geological Survey of Western Australia, 5p.
- Wingate, M. T. D., Lu, Y., & Johnson, S. P. (in press). 183288: biotite–tourmaline monzogranite, Perseverance Well; Geochronology Record 1352: Geological Survey of Western Australia, p. 5.
- Zen, E. (1986). Aluminum Enrichment in Silicate Melts by Fractional Crystallization: Some Mineralogic and Petrographic Constraints. *Journal of Petrology*, 27, 1095–1117.

Zhou, M.-F., Yan, D.-P., Kennedy, A. K., Li, Y., & Ding, J. (2002). SHRIMP U–Pb zircon geochronological and geochemical evidence for Neoproterozoic arc-magmatism along the western margin of the Yangtze Block, South China: Earth and Planetary Science Letters 196, 51–67.

Zi, J.-W., Rasmussen, B., Muhling, J. R., Fletcher, I. R., Thorne, A. M., Johnson, S. P., Cutten, H. N., Dunkley, D. J., & Korhonen, F. J. (2015). In situ U–Pb geochronology of xenotime and monazite from the Abra polymetallic deposit in the Capricorn Orogen, Australia: Dating hydrothermal mineralization and fluid flow in a long-lived crustal structure. Precambrian Research, 260, 91–112.

Every reasonable attempt has been made to acknowledge the owners of copyright material. I would be pleased to hear from any copyright owner who has been omitted or incorrectly acknowledged.

APPENDICES

Appendix A

First Author Journal Publications

This appendix presents the published papers reprinted with permission from Springer (Contributions to Mineralogy and Petrology), Elsevier (Precambrian Research) and Taylor & Francis (Australian Journal of Earth Sciences):

- Piechocka, A. M., Gregory, C. J., Zi, J.-W., Sheppard, S., Wingate, M. T. D., & Rasmussen, B. (2017). *Monazite trumps zircon: applying SHRIMP U–Pb geochronology to systematically evaluate emplacement ages of leucocratic, low-temperature granites in a complex Precambrian orogen*. Contributions to Mineralogy and Petrology, 172, 1–17.
- Piechocka, A. M., Sheppard, S., Fitzsimons, I. C. W., Johnson, S. P., Rasmussen, B., & Jourdan, F. (2018). *Neoproterozoic $^{40}\text{Ar}/^{39}\text{Ar}$ mica ages mark the termination of a billion years of intraplate reworking in the Capricorn Orogen, Western Australia*. Precambrian Research, 310, 391–406.
- Piechocka, A. M., Zi, J.-W., Gregory, C. J., Sheppard, S., and Rasmussen, B. (2019). *SHRIMP U–Pb phosphate dating shows metamorphism was synchronous with magmatism during the Paleoproterozoic Capricorn Orogeny*. Australian Journal of Earth Sciences, 66, 973–990.
- Piechocka, A. M., Zi, J.-W., Wingate, M. T. D., Gregory, C. J., Sheppard, S., Korhonen, F. J., Fitzsimons, I. C. W., Johnson, T. E., and Rasmussen, B. (2019). *The Mangaroon Orogeny: Synchronous c. 1.7 Ga magmatism and low-*P*, high-*T* metamorphism in the West Australian Craton*. Precambrian Research, 333, 105425.

Furthermore, the Appendix presents all Statements of Authorship forms for published papers.

A.1 Paper 1 (published)

Statement of Authorship

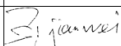
Title of Paper	SHRIMP U–Pb phosphate dating shows metamorphism was synchronous with magmatism of the Paleoproterozoic Capricorn Orogeny
Publication Status	Published
Publication Details	Piechocka, A. M., Zi, J.-W., Gregory, C. J., Sheppard, & Rasmussen, B. (2019). SHRIMP U–Pb phosphate dating shows metamorphism was synchronous with magmatism of the Paleoproterozoic Capricorn Orogeny. <i>Australian Journal of Earth Sciences</i> 66 , 973–990.

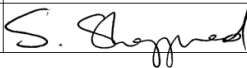
Author Contributions

By signing the Statement of Authorship, each author certifies that their stated contribution to the publication is accurate and that permission is granted for the publication to be included in the candidate's thesis.

Name of Principal Author (Candidate)	Agnieszka M. Piechocka		
Contribution to the Paper	Conducted geological field work (mapping and sampling), prepared samples for SHRIMP U–Pb monazite analysis, conducted the analysis. Data interpretation and wrote the manuscript.		
Signature		Date	13/11/2018

Name of Co-Author	Courtney J. Gregory		
Contribution to the Paper	Provided SHRIMP U–Pb monazite data for one sample to be incorporated in the study.		
Signature		Date	18/03/2019

Name of Co-Author (Supervisor)	Jian-Wei Zi		
Contribution to the Paper	Assisted with SHRIMP set-up and data processing for the additional analysis. Reviewed the geochronology section of the manuscript.		
Signature		Date	16/03/2019

Name of Co-Author (Supervisor)	Stephen Sheppard		
Contribution to the Paper	Supervised work, assisted with data interpretation and manuscript revision.		
Signature		Date	31/10/2018

Name of Co-Author (Supervisor)	Birger Rasmussen		
Contribution to the Paper	Provided data for one U–Pb xenotime sample used in the study. Reviewed the final manuscript.		
Signature		Date	19/03/2019

License Agreement

This is a licence agreement under which you, the author, retain copyright in your article, and grant the Geological Society of Australia, Suite 8, Level 2, 141 Peats Ferry Road, Hornsby, NSW 2077 Australia (hereinafter 'the Society') to allow us and our publisher Informa UK Limited registered in England under no. 1072954 trading as Taylor & Francis Group, Registered Office: Mortimer House, 37–41 Mortimer Street, London W1T 3JH (hereinafter 'Taylor & Francis') a non-exclusive licence to publish your article, including abstract, tables, figures, data, and supplemental material hosted by our publisher, as the Version of Record in the Journal on an Open Access basis under a Creative Commons Attribution-NonCommercial-NoDerivatives License (CC BY-NC-ND) <https://creativecommons.org/licenses/by-nc-nd/4.0/> subject to the Terms & Conditions set out below.

ARTICLE TITLE ('Article):	SHRIMP U-Pb phosphate dating shows metamorphism was synchronous with magmatism during the Paleoproterozoic Capricorn Orogeny
ARTICLE DOI:	10.1080/08120099.2019.1587644
AUTHOR(S):	Agnieszka Piechocka, Jian-Wei Zi, Courtney Jayne Gregory, Stephen Sheppard, Birger Rasmussen
JOURNAL TITLE ('Journal):	Australian Journal of Earth Sciences
JOURNAL ISSN:	1440-0952
APC Quote ID (if applicable):	

In consideration of the publication of the Article, you hereby grant with full title guarantee all rights of copyright and related rights in the above specified Article as the Version of Scholarly Record which is intended for publication in all forms and all media (whether known at this time or developed at any time in the future) throughout the world, in all languages, for the full term of copyright, to take effect if and when the Article is accepted for publication in the Journal.

- I confirm that I have read and accept the full terms of the Journal's Article Publishing Agreement including the Terms & Conditions.
- I confirm the article will be made available under the following access and use licence. I have read and understood the terms of this licence: Creative Commons Attribution-NonCommercial-NoDerivatives License (CC BY-NC-ND) <https://creativecommons.org/licenses/by-nc-nd/4.0/>.
- I confirm that I agree to assume responsibility for any applicable payment of the Article Publishing Charge.
- I confirm I grant the Society the rights to publish my article on an Open Access basis, in all forms and all media (whether known at this time or developed at any time in the future) throughout the world, including the right to translate the article into other languages, create adaptations, summaries or extracts of the article or other derivative works based on the article and the right to sub-license all such rights to others subject to the Terms & Conditions set out below, to take effect if and when the article is accepted for publication. If a statement of government or corporate ownership appears above, that statement modifies this assignment as described.
- I confirm that I have read and accept my author warranties.
- I confirm that I have read and agree to comply with Taylor & Francis' [policy on publishing ethics](#)

GRANT OF PUBLISHING RIGHTS

Signed and dated: Agnieszka Piechocka, 15 March 2019

Geological Society of Australia, 15 March 2019

Copyright Information



Copyright Clearance Center

RightsLink®

Home

Create Account

Help

✉



Title: The Mangaroon Orogeny: Synchronous c. 1.7 Ga magmatism and low-P, high-T metamorphism in the West Australian Craton

Author: Agnieszka M. Piechocka, Jian-Wei Zi, Courtney J. Gregory, Stephen Sheppard, Fawna J. Korhonen, Ian C.W. Fitzsimons, T.E. Johnson, Birger Rasmussen

Publication: Precambrian Research

Publisher: Elsevier

Date: 1 October 2019

© 2019 Elsevier B.V. All rights reserved.

LOGIN

If you're a **copyright.com** user, you can login to RightsLink using your copyright.com credentials. Already a **RightsLink** user or want to [learn more?](#)

Please note that, as the author of this Elsevier article, you retain the right to include it in a thesis or dissertation, provided it is not published commercially. Permission is not required, but please ensure that you reference the journal as the original source. For more information on this and on your other retained rights, please visit: <https://www.elsevier.com/about/our-business/policies/copyright#Author-rights>

BACK

CLOSE WINDOW

Copyright © 2019 [Copyright Clearance Center, Inc.](#) All Rights Reserved. [Privacy statement.](#) [Terms and Conditions.](#) Comments? We would like to hear from you. E-mail us at customer@copyright.com

Reprint of Paper

AUSTRALIAN JOURNAL OF EARTH SCIENCES
<https://doi.org/10.1080/08120099.2019.1587644>



OPEN ACCESS Check for updates

SHRIMP U–Pb phosphate dating shows metamorphism was synchronous with magmatism during the Paleoproterozoic Capricorn Orogeny

A. M. Piechocka^a , J.-W. Zi^{b,c}, C. J. Gregory^a, S. Sheppard^d and B. Rasmussen^{c,e}

^aSchool of Earth and Planetary Sciences, Curtin University, Bentley, WA, Australia; ^bJohn de Laeter Centre, Curtin University, Bentley, WA, Australia; ^cState Key Laboratory of Geological Processes and Mineral Resources, China University of Geosciences, Wuhan, PR China; ^dCalidus Resources Ltd, West Perth, WA, Australia; ^eSchool of Earth Sciences, The University of Western Australia, Nedlands, WA, Australia

ABSTRACT

Unlike many Phanerozoic orogens, where the primary effects of orogenic events can be easily determined, Precambrian orogens are commonly characterised by repeated tectonothermal events making it challenging to decipher the geological history. The Capricorn Orogen is a complex Precambrian intraplate orogen located within the West Australian Craton that has been subjected to four separate reworking tectonic events between 1820 and 900 Ma. Although direct U–Pb ages for metamorphism have been obtained for the younger events, there is only limited geochronological data for the oldest event, the 1820–1770 Ma Capricorn Orogeny. This is primarily because of multiple episodes of deformation and metamorphism overprinting and obscuring the original tectonic fabrics and destroying metamorphic chronometers. In this study, we use *in situ* U–Pb monazite and xenotime geochronology, from a feldspathic metasandstone, a quartz–muscovite–chlorite–garnet pelitic schist, a quartz–muscovite–tourmaline schist and a garnet–biotite–plagioclase pelitic gneiss, to obtain the first direct age constraints for metamorphism during the Capricorn Orogeny in the northern Gascoyne Province. Metamorphism was synchronous with the 1820–1775 Ma magmatism in the northern part, and possibly in the southern part, of the Gascoyne Province. Furthermore, our results hint at a late stage hydrothermal fluid event at ca 1750–1730 Ma, post-dating the magmatism in the northern Gascoyne Province.

ARTICLE HISTORY

Received 14 October 2018
 Accepted 24 January 2019

KEYWORDS

intraplate orogeny; U–Pb geochronology; monazite; xenotime; Proterozoic; Capricorn Orogen

Introduction

Determining the timing of geological processes in Proterozoic intraplate orogens can be challenging, especially in cases where the orogen has been subjected to a prolonged history of tectonic reworking and reactivation (e.g. Hand & Buick, 2001). The Proterozoic Capricorn Orogen of Western Australia is an orogen that records nearly a billion years of intraplate reworking (Korhonen *et al.*, 2017; Occhipinti, Sheppard, Myers, Tyler, & Nelson, 2001; Piechocka *et al.*, 2017; Sheppard, Occhipinti, & Nelson, 2005; Sheppard, Rasmussen, Muhling, Farrell, & Fletcher, 2007; Sheppard, Bodorkos, Johnson, Wingate, & Kirkland, 2010). The Capricorn Orogen is at least 1000 km long and 500 km wide and includes the southern margin of the Pilbara Craton and the northern edge of the Yilgarn Craton (Figure 1). It is divided into several tectonic units that include the Gascoyne Province, Glenburgh Terrane, Narryer Terrane, Errabiddy Shear Zone, and numerous Paleoproterozoic basins with sedimentary ± volcanic fill (Cawood & Tyler, 2004).

Early studies suggested that the fabrics and metamorphic assemblages in the Gascoyne Province and Paleoproterozoic

basins were the product of a single protracted Capricorn Orogeny (Tyler & Thorne, 1990). Furthermore, it was thought that the Capricorn Orogeny spanned roughly 400 million years from 2000 to 1600 Ma (Tyler & Thorne, 1990). Subsequent U–Pb zircon geochronology suggested that many fabrics and metamorphic assemblages in the Capricorn Orogen belonged to two earlier collisional events: a collision between the Pilbara Craton and the Glenburgh Terrane during the 2.2 Ga Ophthalmia Orogeny (Rasmussen, Fletcher, & Sheppard, 2005) and a second collision between the combined Pilbara–Glenburgh Terrane with the northern Yilgarn Craton during the 1.95 Ga Glenburgh Orogeny (Johnson *et al.*, 2011; Occhipinti, Sheppard, Passchier, Tyler, & Nelson, 2004; Sheppard, Occhipinti, & Tyler, 2004), thus forming the West Australian Craton. Further U–Pb zircon geochronology identified two reworking events: the Capricorn and Mangaroon orogenies.

The 1820–1770 Ma Capricorn Orogeny was constrained through a combination of detailed field mapping and dating of granites across the Gascoyne Province (Sheppard, Bodorkos, *et al.*, 2010; Sheppard, Johnson, Wingate, Kirkland, & Pirajno, 2010). Although scattered dates for

CONTACT A. M. Piechocka nishka.piechocka@postgrad.curtin.edu.au

© 2019 The Author(s). Published with license by Taylor & Francis Group, LLC

This is an Open Access article distributed under the terms of the Creative Commons Attribution-NonCommercial-NoDerivatives License (<http://creativecommons.org/licenses/by-nc-nd/4.0/>), which permits non-commercial re-use, distribution, and reproduction in any medium, provided the original work is properly cited, and is not altered, transformed, or built upon in any way.

2 A. M. PIECHOCKA ET AL.

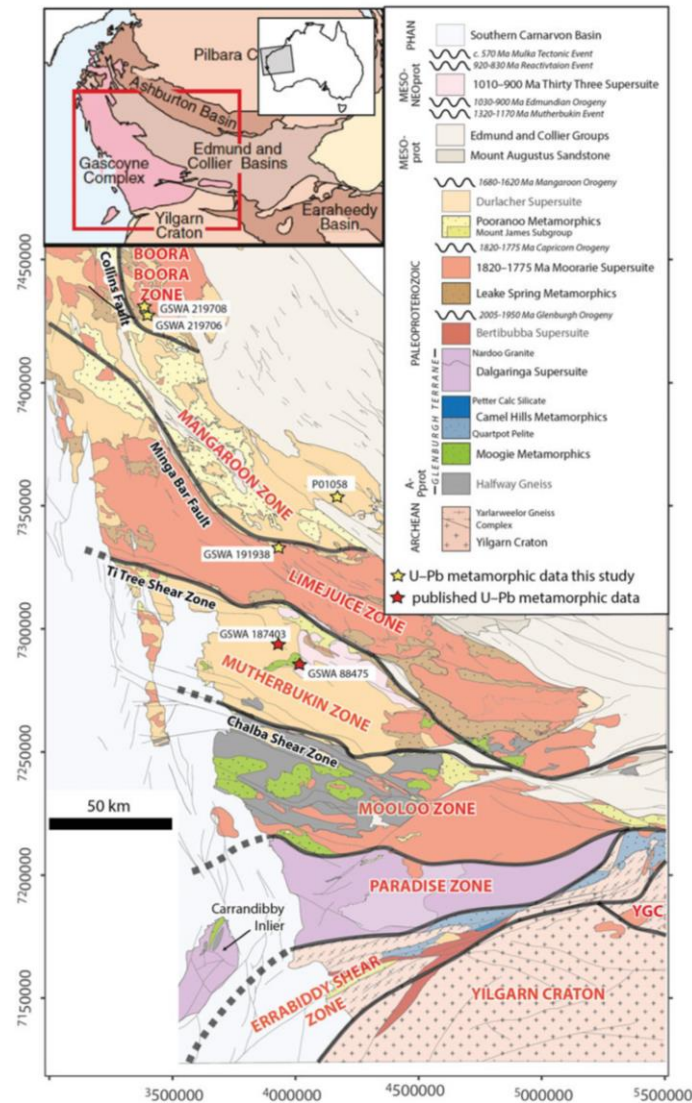


Figure 1. Regional geology map of the Gascoyne Province, Capricorn Orogen, showing the distinct structural-metamorphic zones and sample locations related to this study and published supporting samples (adapted from Sheppard, Johnson, *et al.*, 2010). YGC, Yarlarweelor Gneiss Complex. Coordinate system is GDA 1994 MGA Zone 50.

metamorphism associated with the Capricorn Orogeny have been captured (Korhonen *et al.*, 2015; Wingate, Kirkland, Bodorkos, Groenewalk, & Sheppard, 2010), there remains a lack of robust and systematic dating of the regional metamorphism. Similarly, the 1680–1620 Ma Mangaroon Orogeny was identified by routine SHRIMP U–Pb zircon dating of granites across the Gascoyne

Province combined with regional field mapping in the Mangaroon Zone (Sheppard *et al.*, 2005).

U–Pb monazite and xenotime geochronology identified a further two reworking events at 1321–1171 Ma and 1030–900 Ma (Korhonen *et al.*, 2017; Piechocka *et al.*, 2017; Sheppard *et al.*, 2007). SHRIMP U–Pb monazite and xenotime geochronology combined with field mapping and *P–T*

pseudosections constrained the P - T - t evolution of the 1320–1170 Ma Mutherbukin Tectonic Event (Korhonen *et al.*, 2017). Similarly, field mapping combined with SHRIMP U–Pb monazite and xenotime geochronology used to directly date metamorphism and magmatism identified the 1030–900 Ma Edmondian Orogeny (Piechocka *et al.*, 2017; Sheppard *et al.*, 2007). This reworking was followed by two reactivation episodes at 920–830 Ma (Piechocka *et al.*, 2018) and ca 570 Ma (Bodorkos & Wingate 2007).

The 1820–1770 Ma Capricorn Orogeny has the biggest geographic footprint of the orogenic events, extending outside the Gascoyne Province to other parts of the Capricorn Orogen, including the Ashburton Basin and the Yarlalweelor Gneiss Complex (Occhipinti *et al.*, 2001; Sheppard, Bodorkos, *et al.*, 2010; Sheppard, Johnson, *et al.*, 2010). SHRIMP U–Pb zircon dating has shown that 1820–1775 Ma magmatism is both widespread and voluminous, and bracketing relationships indicate that magmatism was accompanied by deformation and metamorphism associated with the Capricorn Orogeny (Occhipinti *et al.*, 2001; Sheppard, Bodorkos, *et al.*, 2010; Sheppard, Johnson, *et al.*, 2010). Despite all the SHRIMP U–Pb zircon and phosphate dating, direct ages for metamorphism have remained elusive and hindered our understanding of the duration and likely causes of the metamorphism associated with the 1820–1770 Ma Capricorn Orogeny.

Here we present the first reliable *in situ* U–Pb monazite and xenotime geochronology for the metamorphism associated with the Capricorn Orogeny in the northern Gascoyne Province, providing new insights into the duration and regional extent of this Paleoproterozoic tectonothermal event. Although the P - T conditions remain unknown, we propose that magmatism was the likely cause of the regional metamorphism. A secondary outcome of this study is the suggestion of a younger age grouping that could reflect a late-stage deformation and hydrothermal fluid flow event linked to recently published ages from orogenic gold deposits in the Ashburton Basin to the north.

Regional geology

Of all the lithotectonic units of the Capricorn Orogen, the Gascoyne Province records the most complex and protracted tectonothermal history. The province is characterised by fault-bounded structural and metamorphic zones (Sheppard, Bodorkos, *et al.*, 2010) (Figure 1), each recording distinct deformation fabrics and mineral assemblages. The Gascoyne Province includes the Errabiddy Shear Zone, Paradise Zone, Mooloo Zone, Mutherbukin Zone, Mangaroon Zone and the Boora Boora Zone (Figure 1). Three episodes of deformation associated with the 1820–1770 Ma Capricorn Orogeny have been recognised and are referred to as D_{1n} , D_{2n} and D_{3n} (Sheppard, Bodorkos, *et al.*, 2010; Sheppard, Johnson, *et al.*, 2010). The maximum age constraint comes from the age of the oldest igneous intrusion of the Moorarie Supersuite at ca

1820 Ma while the minimum age constraint is derived from metamorphic zircon rims dated at ca 1770 Ma (Sheppard, Johnson, *et al.*, 2010). The timing of these events has been constrained by SHRIMP U–Pb zircon dating of felsic igneous rocks that were overprinted by, or cut, the individual events. D_{1n} and D_{2n} are known to have affected the entire Gascoyne Province and D_{3n} is known only from the Limejuice Zone (Sheppard, Johnson, *et al.*, 2010). The metamorphic grade ranges from greenschist to upper amphibolite facies (Sheppard, Johnson, *et al.*, 2010). Although deformation and metamorphism associated with D_{1n} – D_{3n} are thought to have been broadly coeval with the emplacement of 1820–1775 Ma granites (Sheppard, Johnson, *et al.*, 2010), there are no direct constraints on the start or end of metamorphism.

In this paper, the northern Gascoyne Province refers to the Mangaroon Zone and the Boora Boora Zone. While the northern Capricorn Orogen refers to the Boora Boora Zone, Ashburton Basin and the southern margin of the Pilbara Craton. The central Capricorn Orogen consists of the Mutherbukin and Limejuice zones. The southern Capricorn Orogen refers to the Yarlalweelor Gneiss Complex, Errabiddy Shear Zone, Paradise Zone and Mooloo Zone.

Southern Capricorn Orogen

In the southern Capricorn Orogen, the Capricorn Orogeny overprints the earlier metamorphism and deformation associated with the 1950 Ma Glenburgh Orogeny (Johnson *et al.*, 2010). In the Yarlalweelor Gneiss Complex in the southern part of the Capricorn Orogen, gneissic fabrics, upright folds and metamorphic assemblages up to amphibolite facies, accompanied by magmatism record deformation and metamorphism associated with the Capricorn Orogeny (Sheppard, Bodorkos, *et al.*, 2010). In the Errabiddy Shear Zone, the southernmost zone of the Gascoyne Province, 1950 Ma structures are overprinted by greenschist-facies metamorphic assemblages, upright folds and anastomosing shear zones considered to be an extension of the Capricorn Orogeny (Sheppard, Bodorkos, *et al.*, 2010). The upper amphibolite to granulite facies metamorphism associated with the 1950 Ma Glenburgh Orogeny affected the Paradise Zone (Johnson *et al.*, 2010), however, retrogression fabrics in the Paradise Zone may be related to the Capricorn Orogeny (Sheppard, Bodorkos, *et al.*, 2010).

The geochronological constraints on D_{1n} in the Yarlalweelor Gneiss Complex come from the youngest deformed intrusions dated at 1813 ± 8 Ma (GSWA 142849; Nelson, 1998a) and the oldest undeformed granites dated at 1808 ± 6 Ma (GSWA 142851; Nelson, 1998b; Sheppard, Johnson, *et al.*, 2010). In the Glenburgh Terrane, foliated granodiorite dated at 1811 ± 6 Ma, 1810 ± 9 Ma, and 1804 ± 5 Ma, is intruded by an undeformed granite dated at 1800 ± 7 Ma (Sheppard, Johnson, *et al.*, 2010). Therefore, the first recognisable event, D_{1n} , occurred between ca 1813 and 1800 Ma.

The Yarlarweelor Gneiss Complex also provides a geochronological constraint on D_{2n} . The youngest granite (Kerba Granite) determined from field relationships is dated at 1808 ± 6 Ma (GSWA 142849; Nelson, 1998a) and is cut by D_{2n} structures, providing a maximum age for the deformation (Sheppard, Johnson, *et al.*, 2010). The minimum age constraint for D_{2n} and the deformation and metamorphism associated with D_{3n} are known from the central Gascoyne Province in the Limejuice Zone (see below).

Central Capricorn Orogen

In the central part of the Gascoyne Province, greenschist-facies retrogression of garnet to chloritoid, and sillimanite to sericite, with abundant chloritoid across the Mooloo Zone (Figure 1) indicate that peak P - T associated with Capricorn metamorphism was 425 – 500 °C and <4 kbar (Sheppard, Bodorkos, *et al.*, 2010). The timing of deformation is constrained by deformed granite dated at 1810 Ma and undeformed granite dated at 1800 Ma (Sheppard, Bodorkos, *et al.*, 2010).

Capricorn-aged metamorphism, in the Mutherbukin Zone, is recorded by U–Pb zircon dating from a single quartzite sample (GSWA 187403), and U–Pb monazite and xenotime geochronology from a metasomatic schist (GSWA 88475) (see Figure 1 for locations). Metamorphic zircon rims on detrital grains from the quartzite yielded 1772 ± 6 Ma (GSWA 187403; Wingate *et al.*, 2010). The zircons in sample GSWA 187403 are anhedral to subhedral, and clear and colourless to dark brown. Concentric growth zoning in the zircon cores is truncated at grain boundaries (Wingate *et al.*, 2010, figure 1). The 1772 ± 6 Ma age from the zircon rims could be related to D_{3n} (Johnson *et al.*, 2010; Sheppard, Bodorkos, *et al.*, 2010). More recently, monazite from a metasomatic schist from the Mutherbukin Zone (Figure 1), yielded a U–Pb date of 1780 ± 2 Ma interpreted as the timing of new monazite growth. Xenotime from the same sample yielded two age groupings: 1805 ± 9 Ma (four analyses from two spots on one grain), interpreted as possible new xenotime growth, and a single analysis at 1725 ± 11 Ma (1 σ), interpreted as fine-scale recrystallisation (GSWA 88475; Korhonen *et al.*, 2015). The link between the recent phosphate results and the tectonic fabrics and mineral assemblages associated with the Capricorn Orogeny is unclear.

Deformation fabrics associated with D_{3n} are currently only known from the Limejuice Zone, north of the Mutherbukin Zone, and consist of a low-grade crenulation, and a mineral assemblage of muscovite–chlorite–quartz in pelitic rocks and quartz–muscovite in psammitic rocks (Sheppard, Johnson, *et al.*, 2010), suggesting greenschist-facies metamorphism. If the zircons in sample GSWA 187403 (discussed above) had grown under low-grade metamorphic conditions they would typically display zircon outgrowths surrounding the zircon crystal (*e.g.* Rasmussen, 2005, figure 3). Therefore, it is likely that the zircons in GSWA 187403, in the Mutherbukin Zone,

formed under higher than greenschist-facies temperatures as seen in the Limejuice Zone.

In the Limejuice Zone, field observations show granites with a gneissic fabric parallel to the fabric in the metasedimentary rocks are intruded by undeformed granites (Sheppard, Johnson, *et al.*, 2010). For instance, a deformed granite with crystallisation age of 1788 ± 7 Ma (GSWA 190662; Wingate, Kirkland, & Johnson, 2011) is intruded by undeformed granite dated at 1791 ± 4 Ma and 1786 ± 6 Ma (Sheppard, Johnson, *et al.*, 2010; GSWA 190660; Wingate, Kirkland, Johnson, & Sheppard, 2012a; GSWA 188974; Wingate, Kirkland, Johnson, & Sheppard, 2017). Therefore, D_{2n} is constrained between 1808 Ma (the maximum age for D_{2n} as defined in the Yarlarweelor Gneiss Complex) and 1786 Ma. Owing to the presence of relict peak assemblages of andalusite–cordierite–biotite–muscovite–plagioclase in amphibolites and pelitic gneisses the P - T conditions were assumed to be of high-temperature and low-pressure (Sheppard, Bodorkos, *et al.*, 2010).

Although deformation associated with the Capricorn Orogeny has been constrained by U–Pb zircon dates that bracket deformed and undeformed granites, there remains a lack of direct ages for metamorphism associated with the orogeny.

Northern Capricorn Orogen

Two episodes of deformation in the northern Capricorn Orogen are recognised as D_{1a} and D_{2a} (Krapez & McNaughton, 1999; Martin, Sheppard, & Thorne, 2005; Sheppard, Bodorkos, *et al.*, 2010; Thorne & Seymour, 1991; Tyler & Thorne, 1990). The age of D_{1a} is constrained between *ca* 1805 and *ca* 1790 Ma (Martin *et al.*, 2005, p. 14). The age of D_{2a} is loosely defined at between *ca* 1790 and *ca* 1620 Ma with the younger age limit is possibly related to the 1680–1620 Ma Mangaroon Orogeny rather than the Capricorn Orogeny (Sheppard, Bodorkos, *et al.*, 2010). Considering that the geochronological constraints in the Boora Boora Zone and Ashburton Basin are similar in age to D_{1n} and D_{2n} fabrics in other parts of the Gascoyne Province, D_{1a} and D_{2a} may be related to the Capricorn Orogeny (Krapez & McNaughton, 1999; Sheppard, Bodorkos, *et al.*, 2010; Sheppard, Johnson, *et al.*, 2010).

Sample details

Earlier work focused in the southern Gascoyne Province revealed that the Capricorn Orogeny appeared to be associated with the retrogression of medium- to high-grade assemblages of the older Glenburgh Orogeny (Johnson *et al.*, 2010). The effect of this retrogression was the destruction of metamorphic monazite and xenotime, rendering them unsuitable for SHRIMP dating. However, the northern Gascoyne Province has provided the ideal location to date the timing of Capricorn-age metamorphism owing to the preservation of monazite and xenotime in the samples.

Table 1. Summary table of samples from the northern Gascoyne Province, Capricorn Orogen.

Sample ID	Easting ^c	Northing	Rock type	Location	Structure	Mineral	²⁰⁷ Pb*/ ²⁰⁶ Pb* age (Ma) ^a
GSWA 219706	342310	7427355	Feldspathic metasandstone	Boora Boora Zone	Lineation: 70°/350° Metamorphic foliation: 140°/90	Xenotime	1817 ± 17 and 1750 ± 18 ^b
GSWA 191938	393576	7333031	Quartz–muscovite–chlorite–garnet pelitic schist	Northern Gascoyne (northern Minnie Creek Batholith)	Metamorphic foliation: 322°/72° (NE)	Monazite	1798 ± 7
P01058	413508	7355209	Quartz–muscovite–biotite–tourmaline schist	Mangaroon Zone	Axis of crenulation: 35°/315°	Monazite	1782 ± 3 and 1730 ± 18
GSWA 219708	342168	7429822	Garnet–biotite pelitic gneiss	Boora Boora Zone	Metamorphic foliation 325°/85° (NE)	Monazite	1778 ± 6 and 1751 ± 26

^a ²⁰⁷Pb*/²⁰⁶Pb* ages quoted at 95% confidence unless otherwise stated.

^b Quoted as 2σ.

^c Sample locations quoted in coordinate system MGA GDA 1994 Zone 50.

The sampling strategy for this study was to collect samples for U–Pb phosphate geochronology from the northern Gascoyne Province to test whether Capricorn-aged metamorphism is preserved in the Limejuice, Mangaroon and Boora Boora zones (Figure 1). In particular, the Mangaroon Zone is characterised by fabrics and metamorphism associated with the 1680–1620 Ma Mangaroon Orogeny (Sheppard *et al.*, 2005), and is the only zone where Capricorn-aged deformation or metamorphism has not been previously recorded (Sheppard, Bodorkos, *et al.*, 2010; Sheppard, Johnson, *et al.*, 2010). A quartz–muscovite–biotite–tourmaline schist (sample P01058) was collected from the Mangaroon Zone. Three further samples were collected from either side of the Mangaroon Zone: a quartz–muscovite–chlorite–garnet pelitic schist (GSWA 191938) was collected from the Limejuice Zone and two samples (GSWA 219708: garnet–biotite pelitic gneiss and GSWA 219706: feldspathic metasandstone) were collected from the Boora Boora Zone (Figure 1). Outcrop and petrographic descriptions of the samples (Table 1) are provided in the Results section.

Analytical methods

Four samples were collected from the northern Gascoyne Province for SHRIMP U–Pb monazite and xenotime geochronology. For samples P01058 and GSWA 191938, 219708 and 219706, typically several polished thin-sections were imaged using a scanning electron microscope in back-scattered electron (BSE) mode fitted with an energy-dispersive X-ray spectrometer to identify suitable monazite and xenotime grains for *in situ* SHRIMP geochronology. Monazite and xenotime grains >10 μm across were drilled out in 3 mm-diameter plugs and cast in a single 25 mm epoxy mount. In all sessions the reference standards for Pb/U and Pb/Th calibrations and for ²⁰⁷Pb/²⁰⁶Pb fractionation monitoring were in separate mounts that were cleaned and Au-coated with the sample mounts prior to analysis.

U–Pb analyses of monazite were conducted using a SHRIMP II ion microprobe in the John de Laeter Centre at

Curtin University, Perth. Optical and BSE images were used to guide placement of the primary ion beam during SHRIMP analysis. The SHRIMP analytical procedures followed established methodologies for monazite (Fletcher, McNaughton, Davis, & Rasmussen, 2010) and xenotime (Fletcher, McNaughton, & Rasmussen, 2000; Fletcher, McNaughton, Aleinikoff, Rasmussen, & Kamo, 2004). During all analytical sessions, an O₂⁻ primary beam, with a spot size of 10–15 μm, was focused through a 30–50 μm Kohler aperture with a beam intensity of 0.18–0.45 nA. The secondary ion beam was focused through a 100-μm collector slit onto an electron multiplier to produce mass peaks with flat tops and a mass resolution (1% peak heights) of >5200. A post-collector retardation lens was used to reduce background counts produced from stray ions.

Monazite was analysed with a 13-peak run table as defined by Fletcher *et al.* (2010), which includes mass stations for the estimation of La, Ce and Nd (REEPO₂⁺), and Y (YCeO⁺). Count times per scan for Pb isotopes 204, background position 204.045, 206, 207 and 208 were 10, 10, 10, 30 and 10 s, respectively. The primary Pb/U and Th/Pb standard used was French (known as MAD 1; Foster, Kinny, Vance, Prince, & Harris, 2000). Matrix effects on Pb/U data from U and Th were determined using Z2234 standard (Stern & Sanborn, 1998). Standard Z2908 (moderate U and Th contents; provided by Richard Stern) was used to monitor ²⁰⁷Pb/²⁰⁶Pb fractionation of the SHRIMP II instrument.

Xenotime was analysed with a 9-peak run table. The primary Pb/U standard MG-1 (Fletcher *et al.*, 2004) was used for Pb/U, Pb/Th and U, Th and Pb abundance calibrations. The secondary standards were XENO1 (Stern & Rainbird, 2001) used for ²⁰⁷Pb/²⁰⁶Pb normalisation and used in conjunction with MG-1 for matrix corrections to Pb/U and Pb/Th, and XENO2 (Stern & Rainbird, 2001) used to monitor matrix effects.

Squid-2.50.11.02.03 software (Ludwig, 2009) was used for initial data reduction, including correction for common Pb. Common Pb corrections were based on individual measured ²⁰⁴Pb abundances and assuming crustal common Pb at the approximate age of the samples modelled by Stacey and Kramers (1975). Corrections for matrix effects in Pb/U and Pb/Th, from U and Th in xenotime

6  A. M. PIECHOCKA ET AL.

(Fletcher *et al.*, 2004) and from U, Th, Pb, and REE in monazite and for instrumental mass fractionation in $^{207}\text{Pb}/^{206}\text{Pb}$ (Fletcher *et al.*, 2010) were applied to the sample data. Weighted mean dates are reported with 95% confidence limits, unless otherwise stated, whereas individual analyses are presented with 1σ uncertainties.

Results

In situ U–Pb monazite and xenotime geochronology results

Monazite

Sample GSWA 191938 is a strongly foliated quartz–muscovite–chlorite–garnet schist (Figure 2a). In thin-section, the foliation is defined by laths of muscovite and chlorite. The monazites are subhedral and anhedral, and range in size from 15 to 30 μm occurring as inclusions in quartz, plagioclase, garnet (Figure 4b, c) and within the matrix. One thin-section was examined to locate suitable monazite crystals for dating. Five analyses were carried out on three monazite crystals (Table 2), all showing low discordance (<5%) and low common Pb ($f_{206} < 1\%$). The five analytical spots show Th concentrations typically ranging from 46 000 to 130 000 ppm and U concentrations from 3000 to 4000 ppm. The five analyses yield $^{207}\text{Pb}^*/^{206}\text{Pb}^*$ dates between 1805 and 1793 Ma with a weighted mean of 1798 ± 7 Ma (MSWD = 0.31), which is interpreted as the timing of monazite growth (Figure 5a).

Sample P01058 is a strongly crenulated quartz–muscovite–biotite–tourmaline schist (Figures 2b, c and 3a). The monazite crystals are typically subhedral and range in size from 10 to 50 μm and are aligned with quartz and within muscovite (Figure 4d, e). One thin-section was examined to locate suitable monazite crystals for dating. Twenty-three analyses were carried out on nine monazite crystals (Table 2). One analysis is excluded from the final age calculation owing to high common Pb ($f_{206} > 1\%$). A further one analysis is excluded as it is deemed to be a statistical outlier (*i.e.* it is greater than 2.5 times from the mean). Eighteen analytical spots from 16 crystals, show Th concentrations typically ranging from 25 000 to 80 000 ppm and U concentrations from 2000 to 3000 ppm. The 18 analyses yield $^{207}\text{Pb}^*/^{206}\text{Pb}^*$ dates between 1792 and 1769 Ma with a weighted mean of 1782 ± 3 Ma (MSWD = 1.7), which is interpreted as the timing of monazite growth (Figure 5b). The remaining three analyses of two crystals yielded a $^{207}\text{Pb}^*/^{206}\text{Pb}^*$ weighted mean of 1730 ± 18 Ma (MSWD = 1.8) (Figure 5b). The Th and U concentrations of this group form a distinct population (Figure 5e).

Sample GSWA 219708 is a garnet–biotite pelitic gneiss (Figure 2d) locally intruded by metamonzogranite (Figure 2e) and pegmatite parallel to the gneissic layering. Garnets make up around 40% of the rock and are subhedral to anhedral and typically <2 mm in diameter. The

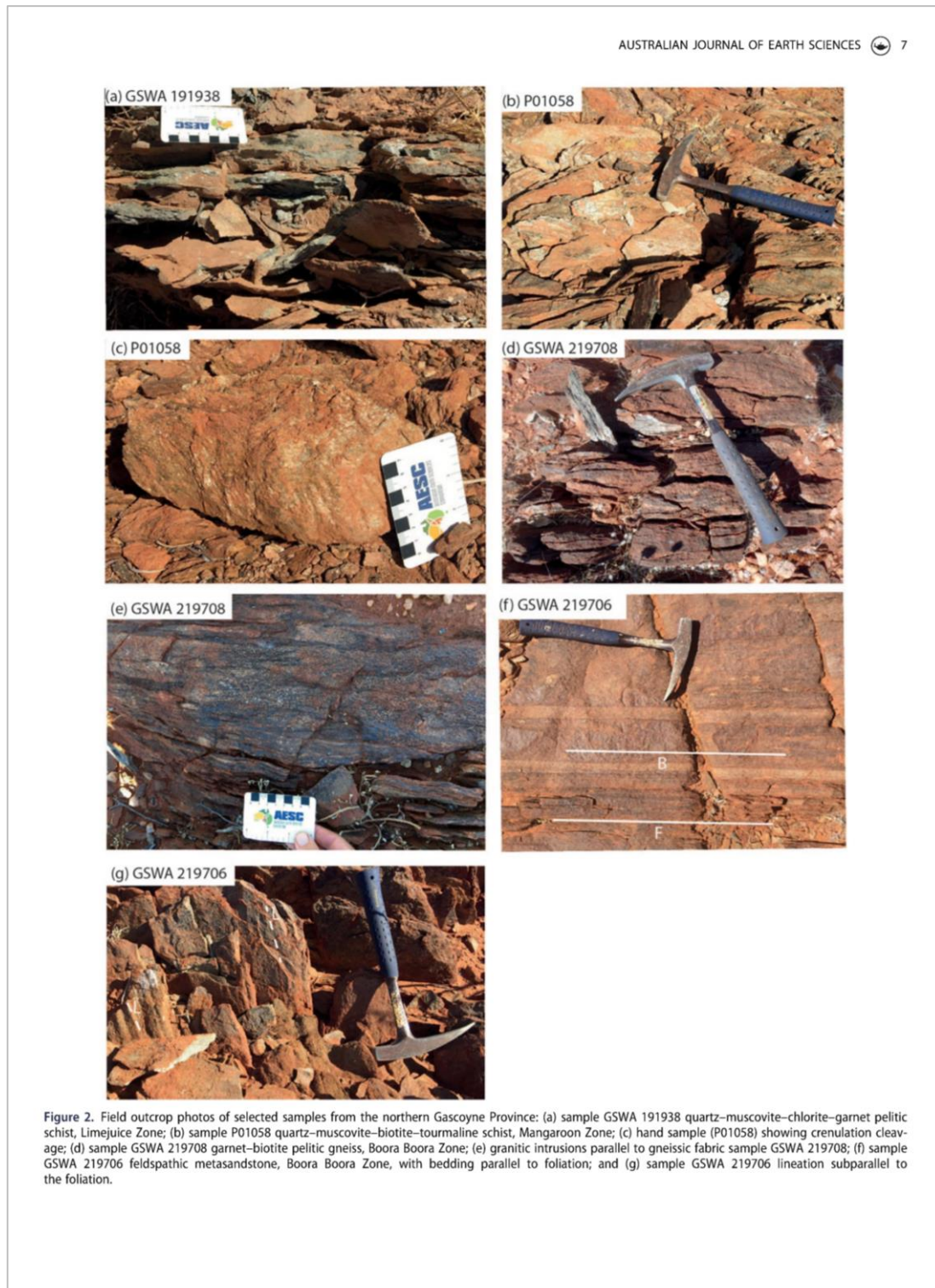
compositional layering is defined by zones dominated by garnet (+ biotite + quartz + feldspar) and zones dominated by biotite (+ quartz + feldspar + garnet) (Figure 3b). A weak foliation is defined by aligned biotite crystals and flattened quartz (Figure 3d).

The monazites are anhedral and range in size from 20 to 80 μm and occur as inclusions within quartz, muscovite and plagioclase, and interstitial to the main silicate phases (Figure 4f–m). Six thin-sections were examined to locate suitable monazite crystals for dating. Seventeen analyses were carried out on 16 monazite crystals (Table 2) all of which contain low concentrations of common Pb ($f_{206} < 1\%$). One analysis was excluded from the final age calculation owing to >10% discordance. Four analyses showing anomalously large $^{207}\text{Pb}/^{206}\text{Pb}$ uncertainties are also disregarded. Nine analytical spots show a systematic variation in Th concentration with values from 26 000 to 41 000 ppm and a larger spread of U concentrations from 2000 to 8000 ppm compared with the younger group. The nine analyses yield $^{207}\text{Pb}^*/^{206}\text{Pb}^*$ dates between 1787 and 1755 Ma with a weighted mean of 1778 ± 6 Ma (MSWD = 2.0), which is interpreted as the timing of monazite growth (Figure 5c). Analysis 1753 ± 11 Ma is excluded from the main grouping because the probability of fit of 0.011 indicates the data do not form a single population (Mahon, 1996). Two remaining concordant analyses, from two crystals are excluded from the main grouping owing to being greater than three standard deviations from the mean. Therefore, the dates 1757 ± 6 Ma, 1753 ± 11 Ma and 1739 ± 7 Ma could be considered to be part of a younger group with a $^{207}\text{Pb}^*/^{206}\text{Pb}^*$ weighted mean of 1751 ± 26 Ma (MSWD = 2) (Figure 5c). The younger group shows Th concentration with values from 41 000 to 48 000 ppm and U concentrations from 3000 to 5000 ppm.

Xenotime

Sample GSWA 219706 is a fine- to medium-grained feldspathic metasandstone that has bedding parallel to foliation with the bedding defined by thin (cm-scale) quartz-rich layers (Figure 2f). A steeply dipping lineation (70°) is subparallel to the foliation (Figure 2g). A weak crenulation cleavage is observed in outcrop and in thin-section (Figure 3c). In thin-section, the muscovite laths are seen to cross-cut the quartz crystals that host the xenotime crystal dated here (Figure 3d).

A single xenotime crystal within a quartz crystal was identified from four thin-sections. There was no indication of retrogressed xenotime within the matrix. The xenotime crystal is anhedral and about 100 μm in diameter and occurs within an elongate quartz crystal (Figure 4a). No obvious zoning is visible. The xenotime is surrounded by alteration that is replacing the original crystal. Thirteen analyses were carried out on the xenotime crystal (Table 3). Seven analyses are excluded from the final age calculation owing to high common Pb ($f_{206} > 1\%$) and/or >5% discordance. Four analytical spots show Th



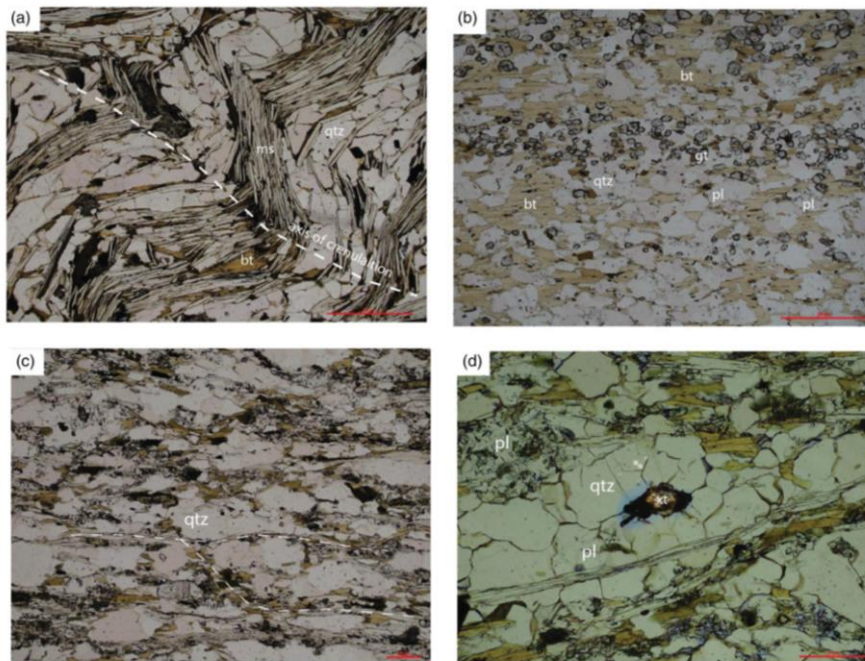
8  A. M. PIECHOCKA ET AL.

Figure 3. Petrographic images: (a) sample P01056 folded crenulation; (b) compositional layering in sample GSWA 219708; (c) sample GSWA 219706 weak crenulation; and (d) sample GSWA 219706 quartz-hosted xenotime used for SHRIMP dating.

concentrations ranging from 10 000 to 14 000 ppm (with one analysis at 24 000 ppm) and U concentrations from 15 000 to 19 000 ppm. The four analyses, clustered in the centre of the crystal, yield $^{207}\text{Pb}/^{206}\text{Pb}$ dates between 1825 and 1802 Ma with a $^{207}\text{Pb}^*/^{206}\text{Pb}^*$ weighted mean of 1817 ± 17 Ma (MSWD = 1.60), which is interpreted as the timing of xenotime growth (Figure 5d). The remaining two analyses are considered to be part of a younger group with a $^{207}\text{Pb}^*/^{206}\text{Pb}^*$ weighted mean of 1750 ± 18 Ma (2σ) (MSWD = 1.15). These two analyses showing Th concentrations at 12 000 ppm and U concentrations at 10 000 ppm are from the edge of the xenotime crystal (Figure 4a).

Discussion

The first intraplate reworking event in the Capricorn Orogen occurred at 1820–1770 Ma during the Capricorn Orogeny (Sheppard, Bodorkos, *et al.*, 2010). The Capricorn Orogeny has the largest footprint of all the reworking events in the Capricorn Orogen (Figure 6), affecting the entire Gascoyne Province, as well as the Yarlalweelor Gneiss Complex, and the Ashburton Basin (Sheppard, Bodorkos, *et al.*, 2010; Sheppard, Johnson, *et al.*, 2010), and the Bryah, Padbury and Earaheedy basins (Occhipinti *et al.*, 2017). In the southern parts of the Gascoyne Province, including the Mooloo Zone, Paradise Zone and Errabiddy Shear Zone, the Capricorn Orogeny is the

only reworking event recognised, although Neoproterozoic fault reactivation affected the Errabiddy Shear Zone and Chalba Shear Zone (Bodorkos & Wingate, 2007; Occhipinti & Reddy, 2009; Piechocka *et al.*, 2018).

In the Mutherbukin Zone and the central Gascoyne Province, Capricorn Orogeny fabrics are overprinted by at least one episode of magmatism associated with the 1680–1620 Ma Mangaroon Orogeny (Sheppard, Johnson, *et al.*, 2010), and two reworking events: the 1320–1170 Ma Mutherbukin Tectonic Event ($>650^\circ\text{C}$ and 4.4–7 kbar) (Korhonen *et al.*, 2017) and the 1030–900 Ma Edmundian Orogeny ($500\text{--}550^\circ\text{C}$ and 3–4 kbar) (Piechocka *et al.*, 2017; Sheppard *et al.*, 2007). In the northern Gascoyne Province, the reworking associated with the 1680–1620 Ma Mangaroon Orogeny (with estimated conditions at $<750^\circ\text{C}$ and <6 kbar) (Sheppard *et al.*, 2005) is known from the Mangaroon Zone. This repeated tectonothermal history has made it challenging to directly date the timing of metamorphism associated with the Capricorn Orogeny. However, the new results obtained in this study provide robust new age constraints from the northern parts of the Gascoyne Province.

Previous U–Pb zircon and monazite constraints on Capricorn-aged metamorphism

Scattered U–Pb zircon, monazite and xenotime geochronology data have been reported for Capricorn-aged

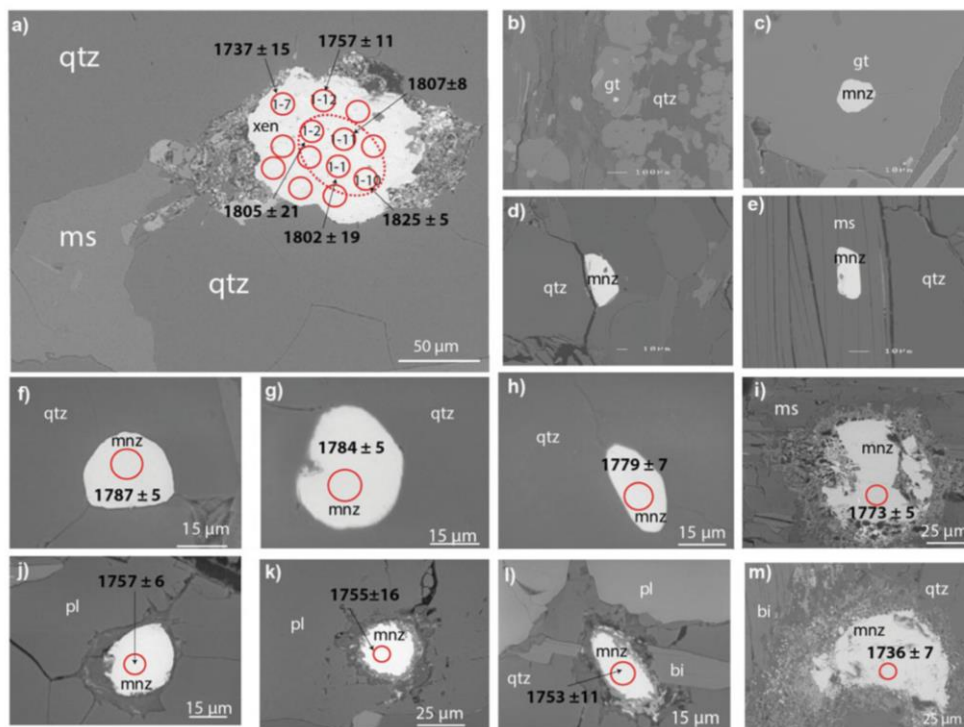


Figure 4. Back-scattered electron (BSE) images of representative monazites and xenotime from samples analysed *in situ*. Solid circles represent SHRIMP pits. (a) Sample GSWA 219706 xenotime age data showing a zoning pattern (dashed circle); (b, c) garnet-hosted monazite in sample GSWA 191938; (d, e) aligned monazite with fabric in sample P01058; (f–h) quartz-hosted monazite in sample GSWA 219708; (i) muscovite-hosted monazite sample GSWA 219708; (j, k) plagioclase-hosted monazite with reaction rims; (l) monazite cross-cutting biotite sample 219708; and (m) interstitial monazite sample GSWA 219708. Abbreviations: bi, biotite; gt, garnet; mnz, monazite; ms, muscovite; pl, plagioclase; qtz, quartz; xen, xenotime.

metamorphism in the Mutherbukin Zone, central Gascoyne Province only as a by-product of younger orogenic events.

In the Mutherbukin Zone, Capricorn-aged metamorphism was recorded from four spots on four separate zircon rims in a coarse-grained orthoquartzite that yielded a youngest population at 1772 ± 6 Ma (GSWA 187403: Wingate *et al.*, 2010) interpreted as the timing of metamorphism during D_{3n} (Johnson *et al.*, 2010; Sheppard, Johnson, *et al.*, 2010). Also, in the Mutherbukin Zone, both monazite and xenotime from a tourmaline-rich metasomatic schist, adjacent to a pegmatite dyke yielded Capricorn Orogeny dates. Monazite yielded an age grouping at 1780 ± 2 Ma interpreted as the timing of new monazite growth (GSWA 88475: Korhonen *et al.*, 2015). This data set is the most robust with 24 analyses performed on 10 grains. Two younger groups were also recorded from sample GSWA 88475 at 1171 ± 4 Ma and 958 ± 16 Ma (Korhonen *et al.*, 2015), which can be correlated with two younger reworking events: the Mutherbukin Tectonic Event and the Edmundian Orogeny. Xenotime, from the same sample, yielded two age groupings: 1805 ± 9 Ma (four analyses from two spots—includes repeat

analyses—on one grain) interpreted as possible new xenotime growth and a single analysis yielded 1725 ± 11 Ma (1σ) interpreted as fine-scale recrystallisation (GSWA 88475: Korhonen *et al.*, 2015). Younger ages were also recorded in this sample ranging from 1725 to 1680 Ma and 1269 to 1182 Ma (Korhonen *et al.*, 2015), which may reflect activity during younger reworking events. Although these samples record Capricorn-age metamorphism, the dataset in two instances is small and requires further work to define a more robust age.

New U–Pb monazite and xenotime constraints on the Capricorn Orogeny in the northern Gascoyne Province

Our new U–Pb phosphate geochronology provides the first direct record of metamorphism associated with the 1820–1770 Ma Capricorn Orogeny in the northern Gascoyne Province. Field observations suggested that the Capricorn Orogeny affected the Limejuice and Boora zones (Sheppard, Bodorkos, *et al.*, 2010; Sheppard, Johnson, *et al.*, 2010) but no

Table 2. U–Pb monazite data for samples GSWA 191938, P01085 and GSWA 219708.

Grain spot	²³⁸ U (ppm)	²³² Th / ²³⁸ U	²³² Th / ²³⁸ U	<i>f</i> ₉₆ (%)	²³⁸ U/ ²⁰⁶ Pb* ± 1σ	²⁰⁷ Pb*/ ²⁰⁶ Pb* ± 1σ	²⁰⁸ Pb*/ ²³² Th ± 1σ	Disc (%)	²⁰⁷ Pb*/ ²⁰⁶ Pb* date (Ma) ± 1σ
GSWA 191938 quartz–muscovite–chlorite–garnet pelitic schist									
Main group									
0673G-1-1	3217	70 730	22	0.09	3.20	0.11031	0.0880	0.0019	1805
0673G-2-1	2884	75 870	26	0.06	3.10	0.11014	0.0937	0.0020	1802
0673H-1-1	2967	53 354	18	0.18	3.17	0.10997	0.00045	0.0020	1799
0673A-1-1	2008	130 250	65	0.02	3.19	0.10975	0.09072	0.0020	1795
0673B-1-1	4608	46 518	10	0.06	3.19	0.10961	0.00041	0.0019	1793
P01058 quartz–muscovite–biotite–tourmaline schist									
Older group									
1005H-2-2	2289	60 040	26	0.04	3.27	0.10955	0.00026	0.0013	1792
1005I-4-2	2108	28 215	13	0.06	3.21	0.10942	0.00028	0.0013	1790
1005E-2-1	2012	38 879	19	0.05	3.30	0.10936	0.00033	0.0016	1789
1005I-3-1	2403	51 326	21	0.02	3.20	0.10923	0.00027	0.0014	1787
1005D-1-1	3471	77 110	22	0.05	3.38	0.10922	0.00033	0.0015	1786
1005C-3-1	2424	50 106	21	0.03	3.22	0.10911	0.00029	0.0014	1785
1005I-1-1	3119	66 705	21	0.05	3.13	0.10901	0.00024	0.0014	1783
1005C-3-2	1984	49 871	25	0.09	3.35	0.10895	0.00033	0.0015	1782
1005B-1-1	2259	25 137	11	0.01	3.23	0.10891	0.00028	0.0014	1781
1005H-2-1	2427	33 935	14	0.03	3.27	0.10890	0.00029	0.0015	1781
1005I-1-1	2489	34 382	14	0.03	3.21	0.10890	0.00046	0.0015	1781
1005G-1-1	2474	35 373	14	0.03	3.20	0.10889	0.00027	0.0013	1781
1005C-2-1	2572	41 842	16	0.03	3.17	0.10884	0.00026	0.0016	1780
1005F-2-1	2634	52 995	20	0.06	3.26	0.10853	0.00051	0.0014	1775
1005E-1-1	2673	43 606	16	0.04	3.30	0.10844	0.00028	0.0013	1775
1005C-1-1	2573	39 549	15	0.03	3.30	0.10841	0.00026	0.0017	1773
1005I-4-1	2509	30 378	12	0.04	3.14	0.10838	0.00026	0.0013	1772
1005F-1-1	2496	46 880	19	0.05	3.21	0.10816	0.00043	0.0014	1769
Statistical outlier/Pb loss									
1005I-2-1	2683	19 222	7	0.03	3.13	0.10804	0.00025	0.0013	1767
Younger group									
1005I-1-2	3338	32 650	10	0.06	3.19	0.10637	0.00106	0.0013	1738
1005I-1-2	5336	50 274	9	0.04	3.42	0.10598	0.00019	0.0012	1731
1005J-2-1	3407	42 682	13	0.11	3.25	0.10480	0.00060	0.0015	1711
GSWA 219708 garnet–biotite pelitic gneiss									
Older group									
1605G-1-1	1710	25 773	15	0.02	3.09	0.10924	0.00027	0.0067	1787
1605B-1-1	2310	32 351	14	0.03	3.00	0.10911	0.00022	0.0069	1785
1605K-1-1	5033	35 604	7	0.00	3.03	0.10910	0.00033	0.0066	1784
1605H-1-1	2377	29 574	12	0.10	3.08	0.10879	0.00040	0.0055	1779
1605J-1-1	2710	35 807	13	0.02	2.84	0.10879	0.00074	0.0076	1779
1605E-1-1	3934	33 801	9	0.03	2.90	0.10839	0.00019	0.0070	1773
1605L-1-1	7749	28 315	4	0.01	3.09	0.10831	0.00031	0.0068	1773
1605A-1-1	3687	31 904	9	0.02	2.98	0.10810	0.00045	0.0069	1768
1606K-1-1	5892	40 126	7	0.02	3.03	0.10738	0.00096	0.0038	1755
1606I-1-1	4447	41 661	9	0.08	3.06	0.10725	0.00064	0.0034	1753

(Continued)

Table 2. (Continued).

Statistical outlier/younger group	4937	48 287	10	0.03	3.09	0.12	0.10750	0.00033	0.0850	0.0033	-3	1757	6
1606B.1-1	3212	45 634	14	0.04	3.18	0.12	0.10641	0.00043	0.0856	0.0033	-1	1739	7
Excluded imprecise 7/6	3015	59 191	20	0.08	3.25	0.31	0.10497	0.00458	0.0819	0.0065	-1	1714	80
1606F.1-1	5816	55 204	9	0.04	3.30	0.15	0.10336	0.00502	0.0801	0.0033	-1	1685	90
1606C.1-1													
Discordance > 8%	4645	34 586	7	0.01	2.99	0.14	0.10529	0.00368	0.1038	0.0072	-8	1719	64
1605D.1-1	3610	35 303	10	0.04	3.09	0.23	0.10057	0.00641	0.1099	0.0087	10	1635	118
1605J.1-2	5006	40 882	8	0.00	3.85	0.34	0.10049	0.00433	0.0706	0.0061	9	1633	80
1605F.1-1													

Pb* indicates radiogenic Pb (i.e. corrected for common Pb). f_{206} , proportion of common ^{206}Pb in measured ^{206}Pb , determined using measured ^{206}Pb and contemporaneous common Pb composition (Stacey & Kramers, 1975). f_{208} , proportion of common ^{208}Pb in measured ^{208}Pb , determined using measured ^{208}Pb and contemporaneous common Pb composition (Stacey & Kramers, 1975). Disc. is apparent discordance, as D (%) = $100 \times ((^{207}\text{Pb}/^{206}\text{Pb}^* \text{ date}) - (^{238}\text{U}/^{206}\text{Pb}^* \text{ date})) / ((^{207}\text{Pb}/^{206}\text{Pb}^* \text{ date}))$. Analytical uncertainties from the multiple sessions have been applied to the data during data reduction. Analyses are sorted by descending $^{207}\text{Pb}/^{206}\text{Pb}^*$ age for all samples.

direct dates for metamorphism have previously been obtained. However, in the Mangaroon Zone no prior deformation fabrics or structures could be assigned to the Capricorn Orogeny owing to the effects of younger tectonic events. Our results have identified two age groupings: 1805–1772 Ma (including uncertainties) and a less robust group at ca 1750–1730 Ma.

Monazite from a quartz–muscovite–chlorite–garnet pelitic schist (GSWA 191938) from the northern Limejuice Zone along the northern margin of the Minnie Creek batholith (Figure 1) yielded an age grouping at 1798 ± 7 Ma (Table 2; Figure 5a), interpreted as the timing of monazite growth during the metamorphic event. Although only five analytical spots were obtained, the crystals contain high concentrations of uranium and low common Pb with concordant analyses yielding a low MSWD of 0.31. Therefore, we consider 1798 ± 7 Ma to be a robust age. The monazites occur as inclusions in the garnet, plagioclase, quartz and within the matrix and yield the same age meaning that the monazite growth likely grew during the porphyroblast growth. The local metamorphic foliation, which trends $322^\circ/72^\circ$ (NE) (at sample GSWA 191938 locality), is different to the orientation of the northerly trending D_{2n} faults and folds and an upright foliation (Sheppard, Johnson, *et al.*, 2010). The current constraints on D_{2n} are 1808–1786 Ma therefore the rocks in this region (represented by sample GSWA 191938) may have been affected by the D_{2n} deformation event.

In the Mangaroon Zone, the later 1680–1620 Ma Mangaroon Orogeny has obliterated most of the older Capricorn Orogeny fabrics. In the southeastern parts of the Mangaroon Zone monazite from a crenulated quartz–muscovite–biotite–tourmaline schist (P01058) yielded a main age grouping of 1782 ± 3 Ma, interpreted as timing of new monazite growth during metamorphism. Owing to the effect of the overprinting Mangaroon Orogeny, any link to a particular deformation episode associated with the Capricorn Orogeny is difficult to make; however, based on geochronology, the age may correlate with either D_{2n} or D_{3n} .

Further north, in the Boora Boora Zone, monazite from garnet–biotite pelitic gneiss (GSWA 219708) yielded a main age grouping at 1778 ± 6 Ma, interpreted as the timing of monazite growth during metamorphism. The monazites occur as inclusions in quartz and one crystal occurs in muscovite. Also, in the Boora Boora Zone, xenotime in a feldspathic metasandstone (GSWA 219706) yielded a main age grouping at 1817 ± 17 Ma, interpreted as the timing of xenotime growth during metamorphism or the xenotime core could be detrital. The geological mapping suggests the feldspathic metasandstone belongs to the Leake Springs Metamorphics of which the protoliths were deposited between 1842–1807 Ma (Sheppard, Johnson, *et al.*, 2010). Although no obvious zoning can be observed, the analytical spots show that the older dates came from the centre of the xenotime crystal (Figure 4a). The U and Th concentrations of this xenotime crystal (GSWA 219706) fall

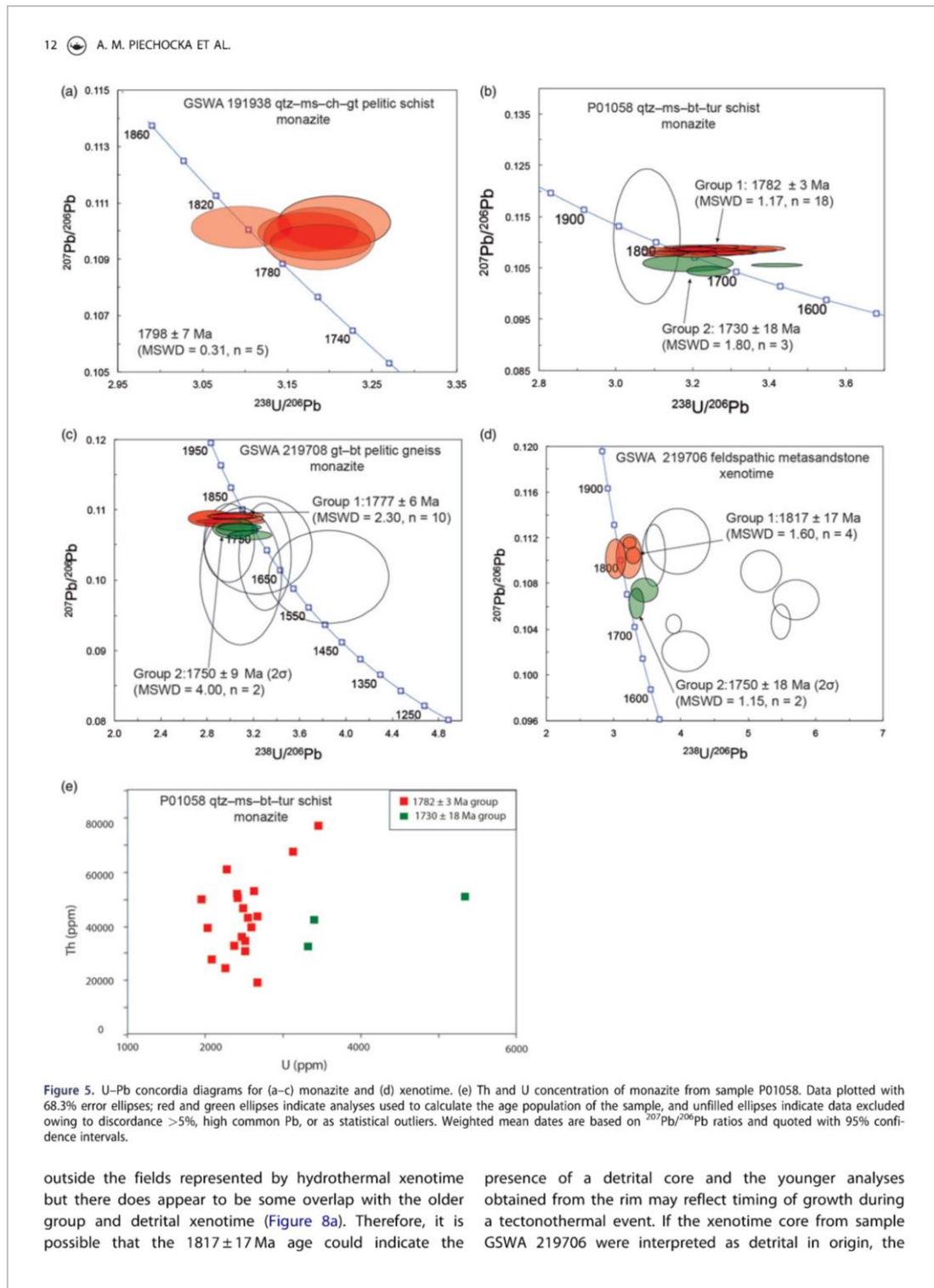


Figure 5. U–Pb concordia diagrams for (a–c) monazite and (d) xenotime. (e) Th and U concentration of monazite from sample P01058. Data plotted with 68.3% error ellipses; red and green ellipses indicate analyses used to calculate the age population of the sample, and unfilled ellipses indicate data excluded owing to discordance >5%, high common Pb, or as statistical outliers. Weighted mean dates are based on $^{207}\text{Pb}/^{206}\text{Pb}$ ratios and quoted with 95% confidence intervals.

outside the fields represented by hydrothermal xenotime but there does appear to be some overlap with the older group and detrital xenotime (Figure 8a). Therefore, it is possible that the 1817 ± 17 Ma age could indicate the

presence of a detrital core and the younger analyses obtained from the rim may reflect timing of growth during a tectonothermal event. If the xenotime core from sample GSWA 219706 were interpreted as detrital in origin, the

AUSTRALIAN JOURNAL OF EARTH SCIENCES 13

Table 3. U–Pb xenotime data for sample GSWA 219706.

Grain.spot	²³⁸ U (ppm)	²³² Th (ppm)	²³² Th / ²³⁸ U	f ₂₀₆ (%)	²³⁸ U/ ²⁰⁶ Pb*		²⁰⁷ Pb*/ ²⁰⁶ Pb*		²⁰⁶ Pb*/ ²³² Th		Disc (%)	date (Ma) ± 1σ
					± 1σ	± 1σ	± 1σ	± 1σ				
GSWA 219706 feldspathic metasediment												
Older group												
NP1604F-1-10	16 273	24 313	1.5	0.04	3.22	0.06	0.11154	0.00034	0.0893	0.0095	5	1825
NP1604F-1-11	18 270	11 668	0.6	0.05	3.28	0.07	0.11044	0.00047	0.0706	0.0095	5	1807
NP1604F-1-2	15 447	13 979	0.9	0.06	3.22	0.13	0.11035	0.00125	0.0513	0.0097	3	1805
NP1604F-1-1	19 290	9747	0.5	0.02	3.02	0.10	0.11015	0.00113	0.0942	0.0102	-2	1802
Younger group												
NP1604F-1-7	10 767	12 101	1.1	0.08	3.45	0.13	0.10746	0.00067	0.0761	0.0093	7	1757
NP1604F-1-12	11 570	11 832	1.0	0.13	3.33	0.07	0.10630	0.00086	0.0453	0.0098	2	1737
Disc. >5% and f ₂₀₆ > 1%												
NP1604F-1-8	21 203	16 422	0.8	0.00	3.95	0.31	0.11166	0.00187	0.0721	0.0080	20	1827
NP1604F-1-5	18 279	8833	0.5	0.03	3.59	0.11	0.11045	0.00177	0.0823	0.0088	12	1807
NP1604F-1-6	28 610	26 527	0.9	0.09	5.18	0.20	0.10906	0.00120	0.0371	0.0064	36	1784
NP1604F-1-3	11 035	15 194	1.4	0.35	5.70	0.23	0.10662	0.00113	0.0283	0.0060	40	1742
NP1604F-1-13	11 388	16 280	1.4	1.48	5.47	0.09	0.10473	0.00100	0.0252	0.0063	37	1710
NP1604F-1-9	9315	11 696	1.3	0.07	3.88	0.08	0.10453	0.00055	0.0495	0.0087	13	1706
NP1604F-1-4	18 930	10 617	0.6	0.01	4.05	0.23	0.10216	0.00115	0.0701	0.0085	15	1664

Pb* indicates radiogenic Pb (i.e. corrected for common Pb). f₂₀₆, proportion of common ²⁰⁶Pb in measured ²⁰⁶Pb, determined using measured ²⁰⁶Pb and contemporaneous common Pb composition (Stacey & Kramers, 1975). f₂₀₆, proportion of common ²⁰⁶Pb in measured ²⁰⁶Pb, determined using measured isotope ratios and contemporaneous common Pb composition (Stacey & Kramers, 1975). Disc. is apparent discordance, as D (%) = 100 × ((²⁰⁷Pb*/²⁰⁶Pb* date) - (²³⁸U/²⁰⁶Pb* date)) / ((²⁰⁷Pb*/²⁰⁶Pb* date)). Analytical uncertainties from the multiple sessions have been applied to the data during data reduction. Analyses are sorted by descending ²⁰⁷Pb*/²⁰⁶Pb* age for all samples.

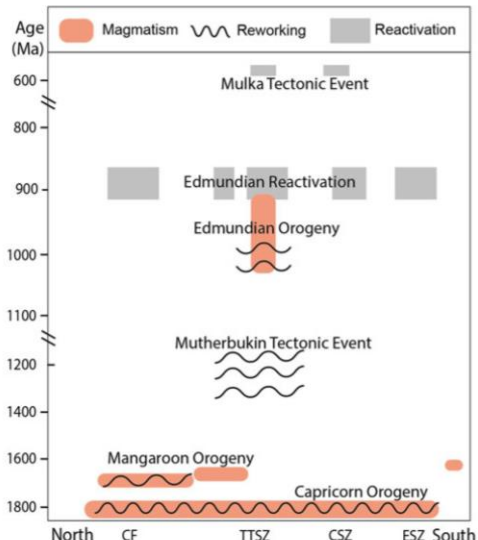
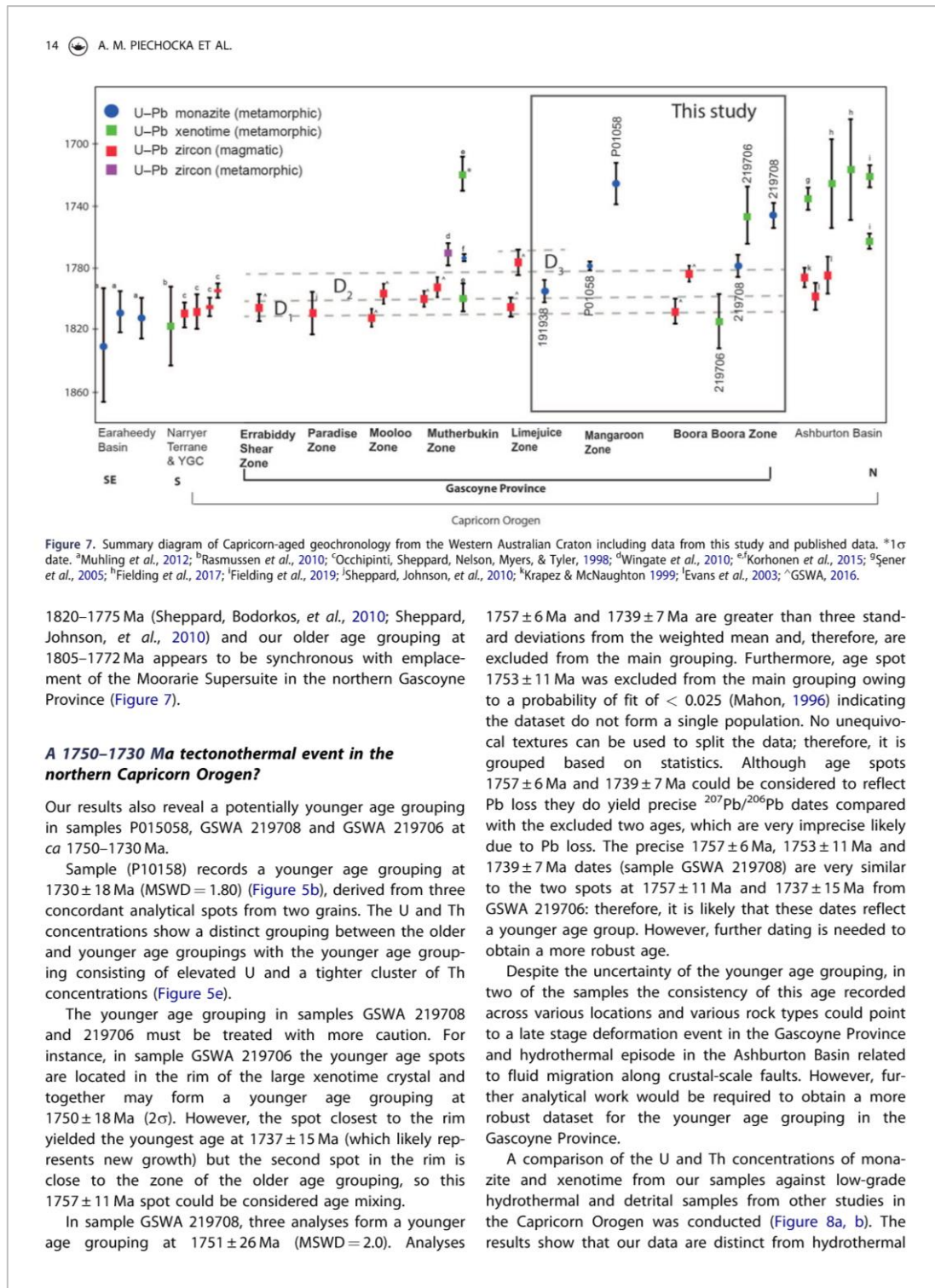


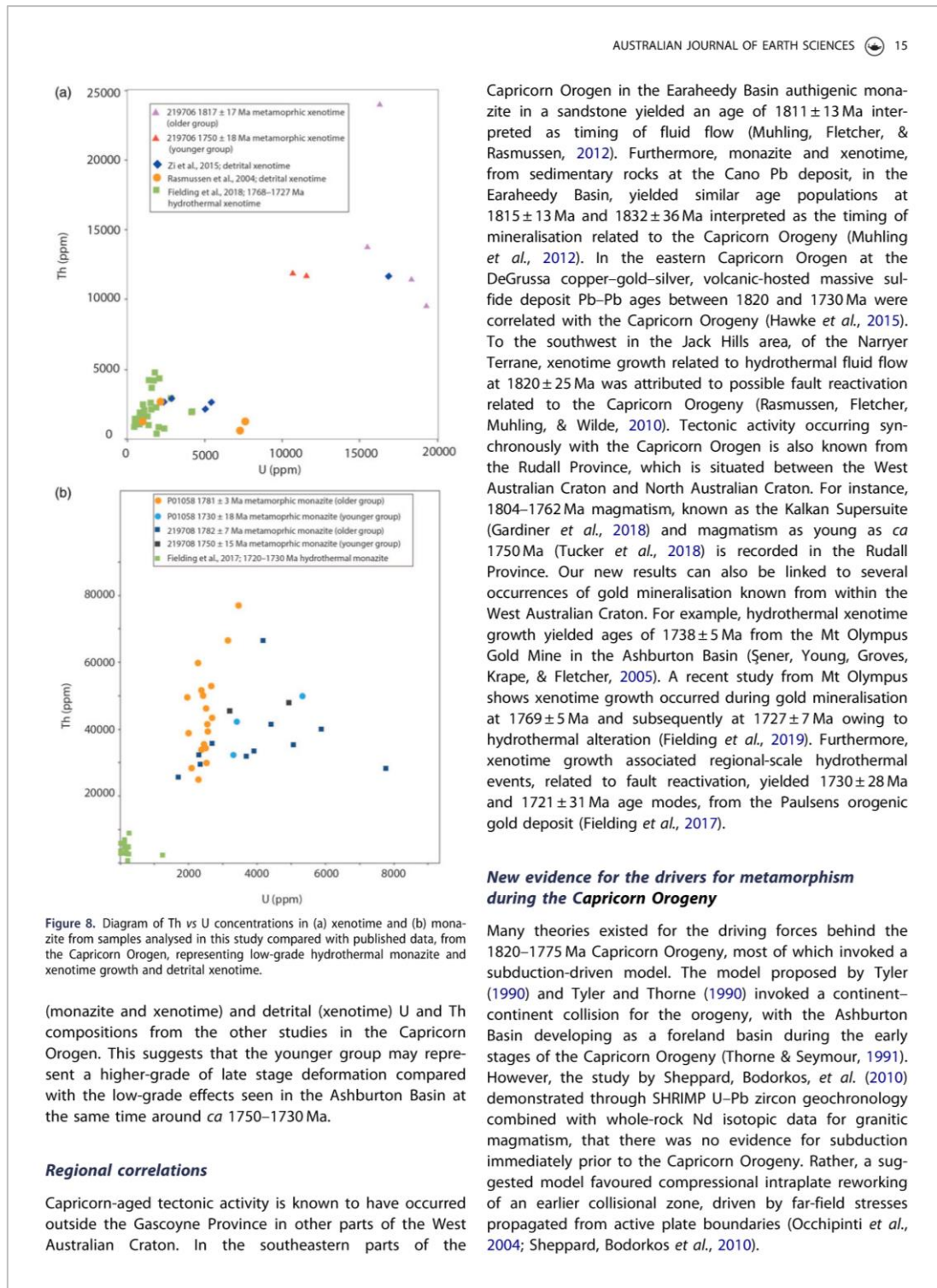
Figure 6. Summary diagram of tectonothermal events in the Gascoyne Province highlighting zones of multiple stages of overprinting (adapted from Piechocka *et al.*, 2018).

timing of metamorphism in the northern Gascoyne Province occurred between 1805 and 1772 Ma (given the uncertainties quoted for samples GSWA 191938 and 219706).

Magmatism in the Gascoyne Province was characterised by voluminous felsic magmatic stocks, plutons and batholiths of the 1820–1775 Ma Moorarie Supersuite (Figure 7) (Sheppard, Johnson, *et al.*, 2010). The oldest magmatism in the Boora Boora Zone is known to have occurred at 1806 ± 7 Ma (GSWA 169088; Nelson, 2004a) with the youngest recorded at 1784 ± 5 Ma (GSWA 169086; Nelson, 2004b) (Figure 7). Magmatism in the Limejuice Zone to the south is constrained at 1807 ± 3 Ma (GSWA 183205; Kirkland, Wingate, Bodorkos, & Sheppard, 2009) and 1777 ± 5 Ma (GSWA 190634; Wingate, Kirkland, Johnson & Sheppard, 2012b) (Figure 7). Our metamorphic ages from samples from the Limejuice, Mangaroon and Boora Boora zones are synchronous with the known magmatism in these areas (Figure 7). In the Ashburton Basin, magmatism related to the Moorarie Supersuite, is recorded by the Boolaloo Granodiorite dated at 1786 ± 5 Ma (Krapez & McNaughton 1999) and volcanism coeval with the supersuite has been identified in the June Hill Volcanics at 1799 ± 8 and 1786 ± 11 Ma (Evans *et al.*, 2003) (Figure 7).

Our geochronology results, considering the given uncertainties, overlap with the previously defined episodes of deformation (D_{1n}–D_{3n}). However, the lack of textural and structural evidence preserved in some samples means that it is difficult to correlate our results, with confidence, to a particular deformation episode. However, the magmatism associated with the Capricorn Orogeny is constrained at





16  A. M. PIECHOCKA ET AL.

Owing to the absence of both detailed geochronology on the metamorphism and the P – T conditions of the metamorphism associated with the Capricorn Orogeny, no tectonic model has been proposed for the metamorphism during this event. Although the direct P – T conditions remain elusive, this study combined with previous work, has established the following framework that must be explained by any tectonic model: regional low- to medium-grade metamorphic assemblages (except for the Yarlalweelor Gneiss Complex, which shows a higher grade of metamorphism); direct ages for metamorphism at 1805–1772 Ma; geochronological constraints on deformation at 1813–1772 Ma; and regional magmatism at 1820–1775 Ma. The higher-grade rocks exposed in the Yarlalweelor Gneiss Complex could be a result of dextral transpression affecting the Errabiddy Shear Zone during the Capricorn Orogeny, resulting in uplift of deeper crustal rocks (Occhipinti & Reddy, 2004). Any proposed model must be able to explain the synchronicity of magmatism, active deformation and metamorphism during compression. Owing to the new results presented in this study, the synchronistic nature of upper amphibolite to granulite facies metamorphism with magmatism, we propose that the principal driver was possibly emplacement of the Moorarie Supersuite.

The recognition of a younger age population at ca 1750–1730 Ma in the northern Gascoyne Province, post-dating the regional magmatism, could be related to a discrete hydrothermal fluid flow event following the Capricorn Orogeny and coeval hydrothermal activity in the Ashburton Basin (Fielding *et al.*, 2017, 2019). Unlike the older age grouping at 1805–1772 Ma driven by the 1820–1775 Ma magmatism, the causes for the activity at ca 1750–1730 Ma, known from the northern Gascoyne Province, are currently unknown.

Conclusions

Despite years of U–Pb geochronology and fieldwork conducted across the Gascoyne Province and the recent advances in constraining the prolonged reworking history of the Capricorn Orogen, the timing and duration of the metamorphism associated with first intraplate reworking, the 1820–1770 Ma Capricorn Orogeny, had not been directly dated. Our new U–Pb monazite and xenotime results from metasedimentary rocks provide robust ages for metamorphism spanning from 1805–1772 Ma linking previous published dates from the southern Gascoyne Province with the northern Gascoyne Province. The results presented in this study demonstrate the synchronistic nature of the upper amphibolite to granulite facies metamorphism with magmatism and we propose the principal driver was likely to have been widespread magmatism of the 1820–1775 Ma Moorarie Supersuite. Our results reveal a potential new age grouping at ca 1750–1730 Ma, in the northern Gascoyne Province, which is similar to published ages from orogenic

gold deposits in the Ashburton Basin. The regional-scale ca 1750–1730 Ma episode may be related either to the late stages of the Capricorn Orogeny or to a new discrete episode of tectonism.

Acknowledgements

The authors thank Michael T. D. Wingate for providing constructive comments on the geochronology section. We thank I. C. W. Fitzsimons and S. P. Johnson for their comments on an earlier version. U–Pb measurements were conducted using the SHRIMP ion microprobes at the John de Laeter Centre at Curtin University.

Disclosure statement

No potential conflict of interest was reported by the authors.

Funding

This PhD project was funded through an Australian Research Council (ARC) grant (LP130100922) and the Exploration Incentive Scheme.

ORCID

A. M. Piechocka  <http://orcid.org/0000-0003-0124-7171>
S. Sheppard  <https://orcid.org/0000-0002-2517-5574>
B. Rasmussen  <https://orcid.org/0000-0001-5052-6797>

References

- Bodorkos, S., & Wingate, M. T. D. (2007). *The contribution of geochronology to GSWA's mapping programs: Current perspectives and future directions*. Perth, WA: Geological Survey of Western Australia, Record 2007/2, 10–11.
- Cawood, P. A., & Tyler, I. M. (2004). Assembling and reactivating the Proterozoic Capricorn Orogen: Lithotectonic elements, orogenies, and significance. *Precambrian Research*, 128(3–4), 201–218. doi:10.1016/j.precamres.2003.09.001
- Evans, D. A. D., Sircombe, K. N., Wingate, M. T. D., Doyle, M., McCarthy, M., Pidgeon, R. T., & Van Niekerk, H. S. (2003). Revised geochronology of magmatism in the western Capricorn Orogen at 1805–1785 Ma: Diachroneity of the Pilbara–Yilgarn collision. *Australian Journal of Earth Sciences*, 50(6), 853–864. doi:10.1111/j.1400-0952.2003.01031.x
- Fielding, I. O. H., Johnson, S. P., Zi, J.-W., Rasmussen, B., Muhling, J. R., Dunkley, D. J., ... Rogers, J. R. (2017). Using *in situ* SHRIMP U–Pb monazite and xenotime geochronology to determine the age of orogenic gold mineralization: An example from the Paulsens Mine, Southern Pilbara Craton. *Economic Geology*, 112(5), 1205–1230. doi:10.5382/econgeo.2017.4507
- Fielding, I. O. H., Johnson, S. P., Meffre, S., Zi, J.-W., Sheppard, S., Large, R. R., & Rasmussen, B. (2019). Linking gold mineralization to regional-scale drivers of mineral systems using *in situ* U–Pb geochronology and pyrite LA-ICP-MS. *Geoscience Frontiers*, 10(1), 89–105. doi:10.1016/j.gsf.2018.06.005
- Fletcher, I. R., McNaughton, N. J., Aleinikoff, J. A., Rasmussen, B., & Kamo, S. L. (2004). Improved calibration procedures and new standards for U–Pb and Th–Pb dating of Phanerozoic xenotime by ion microprobe. *Chemical Geology*, 209(3–4), 295–314. doi:10.1016/j.chemgeo.2004.06.015

- Fletcher, I. R., McNaughton, N. J., Davis, W. J., & Rasmussen, B. (2010). Matrix effects and calibration limitations in ion probe U–Pb and Th–Pb dating of monazite. *Chemical Geology*, 270(1–4), 31–44. doi:10.1016/j.chemgeo.2009.11.003
- Fletcher, I. R., McNaughton, N. J., & Rasmussen, B. (2000). SHRIMP U–Pb geochronology of authigenic xenotime and its potential for dating sedimentary basins. *Australian Journal of Earth Sciences*, 47(5), 845–859. doi:10.1046/j.1440-0952.2000.00819.x
- Foster, G., Kinny, P., Vance, D., Prince, C., & Harris, N. (2000). The significance of monazite U–Th–Pb age data in metamorphic assemblages; a combined study of monazite and garnet chronometry. *Earth and Planetary Science Letters*, 181(3), 327–340. doi:10.1016/S0012-821X(00)00212-0
- Gardiner, N. J., Maidment, D. W., Kirkland, C. L., Bodorkos, S., Smithies, R. H., & Jeon, H. (2018). Isotopic insight into the Proterozoic crustal evolution of the Rudall Province, Western Australia. *Precambrian Research*, 313, 31–50. doi:10.1016/j.precamres.2018.05.003
- GSWA (2016). Compilation of geochronology information, 2016 update, digital data product. Retrieved from www.dmp.wa.gov.au/geoview.
- Hand, M., & Buick, I. S. (2001). Tectonic evolution of the Reynolds-Anmatjira Ranges: A case study in terrain reworking from the Arunta Inlier, central Australia. In J. A. Miller, R. E. Holdsworth, I. S. Buick & M. Hand (Eds.), *Continental reactivation and reworking* (pp. 237–260). London, UK: Geological Society, London, Special Publication, 184.
- Hawke, M. L., Meffre, S., Stein, H., Hilliard, P., Large, R., & Gemmill, J. B. (2015). Geochronology of the DeGrussa volcanic-hosted massive sulphide deposit and associated mineralisation of the Yerrida, Bryah and Padbury Basins, Western Australia. *Precambrian Research*, 267, 250–284. doi:10.1016/j.precamres.2015.06.011
- Johnson, S. P., Sheppard, S., Rasmussen, B., Wingate, M. T. D., Kirkland, C. L., Muhling, J. R., ... Belousova, E. A. (2011). Two collisions, two sutures: Punctuated pre-1950 Ma assembly of the West Australian Craton during the Ophthalmian and Glenburgh Orogenies. *Precambrian Research*, 189(3–4), 239–262. doi:10.1016/j.precamres.2011.07.011
- Johnson, S. P., Sheppard, S., Rasmussen, B., Wingate, M. T. D., Kirkland, C. L., Muhling, J., ... Belousova, E. (2010). *The Glenburgh Orogeny as a record of Paleoproterozoic continent-continent collision*. Perth, WA: Geological Survey of Western Australia, Record 2010/5, 54 p.
- Kirkland, C. L., Wingate, M. T. D., Bodorkos, S., & Sheppard, S. (2009). 183205: Schistose metatonalite, Mallet Well. *Geochronology Record* 753. Perth WA: Geological Survey of Western Australia, 4 p.
- Krapez, B., & McNaughton, N. J. (1999). SHRIMP zircon U–Pb age and tectonic significance of the Palaeoproterozoic Boolaloo Granodiorite in the Ashburton Province, Western Australia. *Australian Journal of Earth Sciences*, 46(2), 283–287. doi:10.1046/j.1440-0952.1999.00698.x
- Korhonen, F. J., Johnson, S. P., Fletcher, I. R., Rasmussen, B., Sheppard, S., Muhling, J. R., ... Kirkland, C. L. (2015). *Pressure-Temperature-Time evolution of the Mutherbukin Tectonic event, Capricorn Orogen*. Perth, WA: Geological Survey of Western Australia, Report 146, 64 p.
- Korhonen, F. J., Johnson, S. P., Wingate, M. T. D., Kirkland, C. L., Fletcher, I. R., Dunkley, D. J., ... Rasmussen, B. (2017). Radiogenic heating and craton-margin plate stresses as drivers for intraplate orogeny. *Journal of Metamorphic Geology*, 35(6), 631–661. doi:10.1111/jmg.12249
- Ludwig, K. R. (2009). *Squid 2.50, A User's Manual*: Berkeley Geochronology Centre Special Publication, p. 95.
- Mahon, K. I. (1996). The New "York" regression: Application of an improved statistical method to geochemistry. *International Geology Review*, 38(4), 293–303. doi:10.1080/08120099.2018.1479307
- Martin, D. McB., Sheppard, S., & Thorne, A. M. (2005). *Geology of the Maroonah, Ullawarra, Capricorn, Mangaroon, Edmund, and Elliot Creek 1: 100 000 sheets*. Perth WA: Geological Survey of Western Australia, 1: 100 000 Geological Series Explanatory Notes, 65 p.
- Muhling, J. R., Fletcher, I. R., & Rasmussen, B. (2012). Dating fluid flow and Mississippi Valley type base-metal mineralization in the Paleoproterozoic Earaheedy Basin, Western Australia. *Precambrian Research*, 212–213, 75–90. doi:10.1016/j.precamres.2012.04.016
- Nelson, D. R. (1998a). 142849: *Foliated coarse-grained monzogranite, northeast of White Well; in Compilation of SHRIMP U–Pb zircon geochronology data, 1997* (pp. 176–179). Perth WA: Western Australia Geological Survey, Record 1998/2.
- Nelson, D. R. (1998b). 142851: *Recrystallised monzogranite, Kerba Pool; Geochronology dataset 367*. Perth WA: Geological Survey of Western Australia, 4 p.
- Nelson, D. R. (2004a). 169088: *Foliated biotite monzogranite, Mundong Well, Geochronology dataset 45; in Compilation of geochronology data, June 2006 update*. Perth WA: Western Australia Geological Survey, 4 p.
- Nelson, D. R. (2004b). 169086: *Biotite monzogranite, Boora Boora Bore, Geochronology dataset 117; in Compilation of geochronology data, June 2006 update*. Perth WA: Western Australia Geological Survey, 4 p.
- Occhipinti, S. A., Hocking, R., Lindsay, M., Aitken, A., Copp, I., Jones, J., ... Metelk, V. (2017). Paleoproterozoic basin development on the northern Yilgarn Craton, Western Australia. *Precambrian Research*, 300, 121–140. doi:10.1016/j.precamres.2017.08.003
- Occhipinti, S., & Reddy, S. (2004). Deformation in a crustal scale shear zone: Errabiddy Shear Zone, Western Australia. In G. I. Alsop, R. E. Holdsworth, K. J. W. McCafrey & M. Hand (Eds.), *Flow processes in Faults and Shear Zones* (pp. 229–248). London UK: Geological Society, London, Special Publication 224. doi:10.1144/GSL.SP.2004.224.01.15
- Occhipinti, S. A., & Reddy, S. M. (2009). Neoproterozoic reworking of the Paleoproterozoic Capricorn Orogen of Western Australia and implications for the amalgamation of Rodinia. In J. B. Murphy, J. D. Keppie & A. J. Hynes (Eds.), *Ancient Orogens and modern analogues* (pp. 445–456). London UK: Geological Society, London, Special Publications, 327.
- Occhipinti, S. A., Sheppard, S., Nelson, D., Myers, J., & Tyler, I. (1998). Syntectonic granite in the southern margin of the Paleoproterozoic Capricorn Orogen, Western Australia. *Australian Journal of Earth Sciences*, 45(4), 509–512. doi:10.1080/08120099808728408
- Occhipinti, S. A., Sheppard, S., Myers, J. S., Tyler, I. M., & Nelson, D. R. (2001). *Archaean and Paleoproterozoic geology of the Narryer Terrane (Yilgarn Craton) and the southern Gascoyne Complex (Capricorn Orogen), Western Australia — a field guide*. Perth WA: Western Australia Geological Survey, Record 2001/8, 70 p.
- Occhipinti, S. A., Sheppard, S., Passchier, C., Tyler, I. M., & Nelson, D. R. (2004). Paleoproterozoic crustal accretion and collision in the southern Capricorn Orogen: the Glenburgh Orogeny. *Precambrian Research*, 128(3–4), 237–255. doi:10.1016/j.precamres.2003.09.002
- Piechocka, A. M., Gregory, C. J., Zi, J.-W., Sheppard, S., Wingate, M. T. D., & Rasmussen, B. (2017). Monazite trumps zircon: Applying SHRIMP U–Pb geochronology to systematically evaluate emplacement ages of leucocratic, low-temperature granites in a complex Precambrian Orogen. *Contributions to Mineralogy and Petrology*, 172, 1–117. doi:10.1007/s00410-017-1386-5
- Piechocka, A. M., Sheppard, S., Fitzsimons, I. C. W., Johnson, S. P., Rasmussen, B., & Jourdan, F. (2018). Neoproterozoic ⁴⁰Ar/³⁹Ar mica ages mark the termination of a billion years of intraplate reworking in the Capricorn Orogen, Western Australia. *Precambrian Research*, 310, 391–406. doi:10.1016/j.precamres.2018.04.006
- Rasmussen, B. (2005). Zircon growth in very low grade metasedimentary rocks: Evidence for zirconium mobility at ~250°C. *Contributions to Mineralogy and Petrology*, 150(2), 146–155. doi:10.1007/s00410-005-0006-y
- Rasmussen, B., Fletcher, I. R., & Sheppard, S. (2005). Isotopic dating of the migration of a low-grade metamorphic front during orogenesis. *Geology*, 33(10), 773–776. doi:10.1130/G21666.1
- Rasmussen, B., Fletcher, I. R., Muhling, J. R., & Wilde, S. A. (2010). *In situ* U–Th–Pb geochronology of monazite and xenotime from the Jack

18  A. M. PIECHOCKA ET AL.

- Hills belt: Implications for the age of deposition and metamorphism of Hadean zircons. *Precambrian Research*, 180(1–2), 26–46. doi:10.1016/j.precamres.2010.03.004
- Şener, A. K., Young, C., Groves, D. I., Krape, B., & Fletcher, I. R. (2005). Major orogenic gold episode associated with Cordilleran-style tectonics related to the assembly of Paleoproterozoic Australia? *Geology*, 33(3), 225–228. doi:10.1130/G21017.1
- Sheppard, S., Bodorkos, S., Johnson, S. P., Wingate, M. T. D., & Kirkland, C. L. (2010). *The Paleoproterozoic Capricorn Orogeny: Intracontinental reworking not continent-continent collision*. Perth, WA: Geological Survey of Western Australia, Report 108, 33 p.
- Sheppard, S., Johnson, S. P., Wingate, M. T. D., Kirkland, C. L., & Pirajno, F. (2010). *Explanatory notes for the Gascoyne Province, 1:100 000 sheet*. Perth WA: Geological Survey of Western Australia, 336 p.
- Sheppard, S., Occhipinti, S. A., & Tyler, I. M. (2004). A 2005–1970 Ma Andean-type batholith in the southern Gascoyne Complex, Western Australia. *Precambrian Research*, 128(3–4), 257–277. doi:10.1016/j.precamres.2003.09.003
- Sheppard, S., Occhipinti, S. A., & Nelson, D. R. (2005). Intracontinental reworking in the Capricorn Orogen, Western Australia: The 1680–1620 Ma Mangaroon Orogeny. *Australian Journal of Earth Sciences*, 52(3), 443–460. doi:10.1080/08120090500134589
- Sheppard, S., Rasmussen, B., Muhling, J. R., Farrell, T. R., & Fletcher, I. R. (2007). Grenvillian-aged orogenesis in the Paleoproterozoic Gascoyne Complex, Western Australia: 1030–950 Ma reworking of the Proterozoic Capricorn Orogen. *Journal of Metamorphic Geology*, 25(4), 477–494. doi:10.1111/j.1525-1314.2007.00708.x
- Stacey, J. S., & Kramers, J. D. (1975). Approximation of terrestrial lead isotope evolution by a two-stage model. *Earth and Planetary Science Letters*, 26(2), 207–221. doi:10.1016/0012-821X(75)90088-6
- Stern, T. A., & Sanborn, N. (1998). Monazite U–Pb and Th–Pb geochronology by high-resolution secondary ion mass spectrometry. Radiogenic Age and Isotope Studies: Report 11, Geological Survey of Canada, Current Research 1998-F, 1–18.
- Stern, R. A., & Rainbird, R. H. (2001). Advancements in xenotime U–Pb geochronology by ion microprobe, Eleventh V. I. Goldschmidt Conference Lunar and Planetary Science Institute, Houston.
- Thorne, A. M., & Seymour, D. B. (1991). *Geology of the Ashburton Basin, Western Australia*. Perth WA: Geological Survey of Western Australia, Bulletin 139, 141 p.
- Tucker, N. M., Morrissey, L. J., Payne, J. L., & Szpunar, M. (2018). Genesis of the Archean–Paleoproterozoic Tabletop Domain, Rudall Province, and its endemic relationship to the West Australian Craton. *Australian Journal of Earth Sciences*, 65, 1–30. doi:10.1080/08120099.2018.1479307
- Tyler, I. M. (1990). *The geology of the Sylvania Inlier and the southeast Hamersley Basin*. Perth WA: Geological Survey of Western Australia, Bulletin 138, 124 p.
- Tyler, I. M., & Thorne, A. M. (1990). The northern margin of the Capricorn Orogen Western Australia an example of an Early Proterozoic collision zone. *Journal of Structural Geology*, 12(5–6), 685–701. doi:10.1016/0191-8141(90)90082-A
- Wingate, M. T. D., Kirkland, C. L., Bodorkos, S., Groenewalk, P. B., & Sheppard, S. (2010). 187403, quartzite, Robinson Bore; *Geochronology Record 862*. Perth WA: Geological Survey of Western Australia, 5 p.
- Wingate, M. T. D., Kirkland, C. L., & Johnson, S. P. (2011). 190662: Gneissic metamonzogranite, Recovery Well; *Geochronology Record 1005*. Perth WA: Geological Survey of Western Australia, 4p.
- Wingate, M. T. D., Kirkland, C. L., Johnson, S. P., & Sheppard, S. (2012a). 190660: Metamonzogranite, Midway Bore; *Geochronology Record 1036*. Perth WA: Geological Survey of Western Australia, 4 p.
- Wingate, M. T. D., Kirkland, C. L., Johnson, S. P., & Sheppard, S. (2012b). 190634: Metamonzogranite, Minierra Well; *Geochronology Record 1034*. Perth WA: Geological Survey of Western Australia, 4 p.
- Wingate, M. T. D., Kirkland, C. L., Johnson, S. P., & Sheppard, S. (2017). 188974, Metamonzogranite, Mount James homestead; *Geochronology Record 1362*. Perth WA: Geological Survey of Western Australia, 4 p.

A.2 Paper 2 (published)

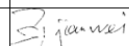
Statement of Authorship

Title of Paper	The Mangaroon Orogeny: Synchronous c. 1.7 Ga magmatism and low- <i>P</i> , high- <i>T</i> metamorphism in the West Australian Craton
Publication Status	Published
Publication Details	Piechocka, A. M., Zi, J.-W, Gregory, C. J., Sheppard, S., F. J. Korhonen, I. C. W. Fitzsimons, T. E. Johnson, and Rasmussen, B. (2019). The Mangaroon Orogeny: Synchronous c. 1.7 Ga magmatism and low- <i>P</i> , high- <i>T</i> metamorphism in the West Australian Craton. <i>Precambrian Research</i> , 333, 105425.

Author Contributions

By signing the Statement of Authorship, each author certifies that their stated contribution to the publication is accurate and that permission is granted for the publication to be included in the candidate's thesis.

Name of Principal Author (Candidate)	Agnieszka M. Piechocka		
Contribution to the Paper	Conducted geological field work (mapping and sampling), prepared samples for SHRIMP U–Pb monazite and xenotime analysis, conducted the analysis. Constructed P–T pseudosections. Data interpretation and wrote the manuscript.		
Signature		Date	13/11/2018

Name of Co-Author (Supervisor)	Jian-Wei Zi		
Contribution to the Paper	Jian-Wei assisted with SHRIMP set-up and data processing for the additional analysis. Reviewed the geochronology section of the manuscript.		
Signature		Date	16/03/2019

Name of Co-Author	Courtney J. Gregory		
Contribution to the Paper	Provided SHRIMP U–Pb monazite data to be incorporated in the paper.		
Signature		Date	18/03/2019

Name of Co-Author (Supervisor)	Stephen Sheppard		
Contribution to the Paper	Supervised work, assisted with data interpretation and manuscript revision.		
Signature		Date	31/10/2018

Name of Co-Author	Fawna J. Korhonen		
Contribution to the Paper	Assisted with the construction of the P–T pseudosections and interpretation of the results. Assisted with writing the manuscript.		
Signature		Date	23/10/2018

Name of Co-Author	Ian C. W. Fitzsimons		
Contribution to the Paper	Reviewed manuscript.		
Signature		Date	22/10/2018

Name of Co-Author (Supervisor)	Tim E. Johnson		
Contribution to the Paper	Assisted with interpretation of the metamorphic evolution.		
Signature		Date	31/10/2019

Name of Co-Author (Supervisor)	Birger Rasmussen		
Contribution to the Paper	Reviewed manuscript.		
Signature		Date	19/03/2019

Reprint of Paper

Precambrian Research 333 (2019) 105425



Contents lists available at ScienceDirect

Precambrian Research

journal homepage: www.elsevier.com/locate/precamres

The Mangaroon Orogeny: Synchronous c. 1.7 Ga magmatism and low-*P*, high-*T* metamorphism in the West Australian Craton

Agnieszka M. Piechocka^{a,*}, Jian-Wei Zi^{b,c}, Courtney J. Gregory^a, Stephen Sheppard^{a,f},
Fawna J. Korhonen^d, Ian C.W. Fitzsimons^a, T.E. Johnson^a, Birger Rasmussen^{c,e}

^a School of Earth and Planetary Sciences, Curtin University, Kent Street, Bentley, WA 6102, Australia

^b John de Laeter Centre, Curtin University, Kent Street, Bentley, WA 6102, Australia

^c State Key Laboratory of Geological Processes and Mineral Resources, China University of Geosciences, Wuhan 430074, China

^d Geological Survey of Western Australia, 100 Plain Street, East Perth, WA 6004, Australia

^e School of Earth Sciences, The University of Western Australia, Nedlands, WA 6009, Australia

^f Calidus Resources Limited, Suite 12, 11 Ventnor Avenue, West Perth, WA 6005, Australia



ARTICLE INFO

Keywords:

Intraplate orogeny
U–Pb geochronology
Monazite
Xenotime
LPHT metamorphism
Proterozoic

ABSTRACT

The Capricorn Orogen records nearly one billion years of intraplate orogenesis within the West Australian Craton, although the processes responsible for this protracted, punctuated reworking remain unclear. Of the major tectonic events that affected the region, the 1680–1620 Ma Mangaroon Orogeny is one of the least-well understood, mainly due to a lack of direct ages for metamorphism, an absence of pressure (*P*)–temperature (*T*) constraints, and uncertainty regarding the duration of granitic magmatism that is spatially and, possibly, temporally associated with deformation. In this study we define the *P*–*T*–time (*t*) conditions associated with the Mangaroon Orogeny based on *in situ* SHRIMP U–Pb monazite and xenotime geochronology and calculated *P*–*T* pseudosections. Data from a pelitic migmatite constrain the timing of low-*P*, high-*T* metamorphism to 1691 ± 7 Ma at conditions of 665–755 °C and 2.7–4.3 kbar (–175–240 °C/kbar). Data from a garnet-bearing sillimanite–biotite pelitic gneiss suggests higher pressure during the clockwise prograde history at one locality. Furthermore, the onset of the metamorphism coincides with the oldest granites in the region (1695 ± 9 Ma), which constrain the onset of the Mangaroon Orogeny. Our results also show that deposition and burial of the precursor sediments occurred, at most, c. 70 million years before the onset of partial melting at c. 1695 Ma. Therefore, there was no long incubation period before the onset of orogenesis. We conclude that, unlike many of the Proterozoic orogenic events in Australia, the c. 1.7 Ga low-*P*, high-*T* metamorphism recorded in the upper crust in the Capricorn Orogen cannot be explained by a thermal lid model, but rather was synchronous with granitic magmatism.

1. Introduction

Proterozoic Australia has been subjected to numerous intraplate orogenic events, typically characterised by low-pressure (low-*P*) and high-temperature (high-*T*) metamorphism. Several tectonic models have been proposed to explain the causes and characteristics of low-*P*, high-*T* metamorphism, including crustal thickening with coeval magmatism (Loosveld and Etheridge, 1990), crustal extension (Wickham and Oxburgh, 1987; Sandiford and Powell, 1986), and regional contact metamorphism (e.g. Barton and Hanson, 1989). A model commonly invoked for many Australian Proterozoic terrains is that of low-*P*, high-*T* metamorphism a product of lithospheric weakening owing to high concentrations of heat-producing elements (McLaren et al., 2005), perhaps enhanced by thick sedimentary sequences that provided insulation (Sandiford and Hand, 1998).

In the Capricorn Orogen of Western Australia, intraplate metamorphism and deformation associated with the Mesoproterozoic Matherbukin Tectonic Event was interpreted to reflect elevated heat production beneath a thick thermal blanket, resulting in elevated temperatures that lasted in excess of 100 million years (Korhonen and Johnson, 2015; Korhonen et al., 2017). Although this model has been proposed for other Proterozoic orogens in Australia (e.g. McLaren et al., 2005; Korhonen et al., 2017; Morrissey et al., 2014), it is unclear as to whether all Proterozoic orogenies reflect such a process.

An alternative model for low-*P*, high-*T* metamorphism in Proterozoic Australian orogens, is one which invokes intrusion of voluminous granites or mafic rocks to provide the heat for metamorphism (e.g. Clark et al., 2014; Collins and Vernon, 1991; Oliver and Zakowski, 1995; Glasson et al., 2019). Collins and Vernon (1991) proposed that

* Corresponding author.

E-mail address: nishka.piechocka@postgrad.curtin.edu.au (A.M. Piechocka).

<https://doi.org/10.1016/j.precamres.2019.105425>

Received 13 June 2018; Received in revised form 17 August 2019; Accepted 19 August 2019

Available online 21 August 2019

0301-9268/© 2019 Elsevier B.V. All rights reserved.

low-*P*, high-*T* metamorphism in the upper crust of the Arunta Orogen was caused by granite magmatism, triggered by a mantle perturbation that induced partial melting of the lower crust. Clark et al. (2014) and Glasson et al. (2019) argued that the drivers for low-*P*, high-*T* metamorphism associated with Stage I of the Albany–Fraser Orogeny included elevated heat flow and mafic magmatism during lithospheric extension. Furthermore, it was suggested that low-*P*, high-*T* metamorphism in the eastern Mt Lofty Ranges, south Australia, was synchronous with granite magmatism in an extensional setting (Oliver and Zakowski, 1995).

The Capricorn Orogen of Western Australia records a prolonged history of repeated intraplate orogenesis, comprising multiple episodes of predominantly felsic magmatism, metamorphism and deformation. This study focuses on one of these events—the 1680–1620 Ma Mangaroon Orogeny—which has been proposed as an example of low-*P*, high-*T* regional metamorphism, based on diagnostic mineral assemblages and a widespread gneissic textures in rocks of the southern Mangaroon Zone, although local occurrences of contact metamorphism have been recorded (Sheppard et al., 2005). However, no detailed work has been done on the timing of metamorphism and the determination of precise *P*–*T* conditions. Therefore, the cause and duration of metamorphism associated with the Mangaroon Orogeny remain unknown.

In this contribution, we use SHRIMP U–Pb monazite and xenotime data, and *P*–*T* pseudosections to provide the first robust constraints on the duration and *P*–*T* conditions of intraplate low-*P*, high-*T* metamorphism associated with the Mangaroon Orogeny. Furthermore, we obtained whole-rock geochemistry to determine the peraluminosity of the granites and calculate zircon saturation temperatures. This study indicates that the thermal lid model, which is favoured for other Proterozoic intraplate tectonic events in Australia, cannot easily explain the anomalous thermal gradients in the crust during the Mangaroon Orogeny. The data are then integrated with studies of low-grade metamorphic and hydrothermally altered rocks across the West Australian Craton to show that the Mangaroon Orogeny has a significantly wider footprint than previously thought. Further, we contend that the metamorphism and magmatism recorded in the Capricorn Orogen may have been responsible for widespread circulation of fluids in the upper crust over much of the craton.

2. Regional geology

The study area is in the Capricorn Orogen of Western Australia (Fig. 1). The Capricorn Orogen records the two-stage assembly of the West Australian Craton, separating the Archean Pilbara and Yilgarn cratons to the north and south, respectively. Assembly of the West Australian Craton, which was complete by c. 1950 Ma (Johnson et al., 2011; Occhipinti et al., 2004), was followed by five episodes of intraplate reworking and reactivation spanning nearly 1.5 billion years that shaped the current architecture of the orogen (Korhonen et al., 2017; Piechocka et al., 2018; Piechocka et al., 2019; Sheppard et al., 2005, 2007, 2010a). All these tectonic events are recorded in rocks of the Gascoyne Province, a basement complex of magmatic and metamorphic rocks exposed at the western end of the orogen (Fig. 1). The Gascoyne Province is subdivided into several southeast-trending structural and metamorphic zones, each recording a discrete tectonothermal history. Of the five intraplate events, four record reworking (i.e., pervasive deformation accompanied by metamorphism and/or magmatism; Korhonen et al. 2017; Piechocka et al., 2019; Sheppard et al., 2005; Sheppard et al., 2007; Sheppard et al., 2010a), whereas the youngest events, including the later stages of the fourth episode of reworking, reflect reactivation along discrete structures, in which the intervening rocks were largely unaffected (Bodorkos and Wingate, 2007; Piechocka et al., 2018).

The two Paleoproterozoic intraplate events—the 1820–1775 Ma Capricorn Orogeny (Sheppard et al., 2010a; Piechocka et al., 2019) and the 1680–1620 Ma Mangaroon Orogeny (Sheppard et al., 2005)—produced pervasive metamorphism and deformation accompanied by

voluminous, granitic magmatism. The Capricorn Orogeny is characterised by extensive compressional deformation (mostly at low to medium metamorphic grade), magmatism and some sedimentation (Sheppard et al., 2010a). A recent U–Pb phosphate geochronology study showed that metamorphism during the Capricorn Orogeny was synchronous with magmatism (Piechocka et al., 2019). Deformation and medium-grade metamorphism (< 750 °C and < 6 kbar) associated with the Mangaroon Orogeny was preceded by the deposition of siliciclastic sedimentary rocks (the Pooranoo Metamorphics; Sheppard et al., 2005).

During the Meso- to Neoproterozoic the Gascoyne Province was subjected to two additional reworking events and two reactivation events. The driver for the older of the reworking events, the 1320–1170 Ma Mutherbukin Tectonic Event in the central Gascoyne Province, was proposed to be thickening of metasedimentary rocks deposited at 1842–1807 Ma which are enriched in high heat-producing elements. According to Korhonen et al. (2017), these Paleoproterozoic rocks formed a thermal lid that generated radiogenic heat for c. 110 million years prior to the onset of peak metamorphism at > 650 °C and 4.4–7.0 kbar.

The second reworking event, the 1030–900 Ma Edmondian Orogeny, is characterised by coeval leucogranite magmatism and metamorphism and deformation at 500–550 °C and 3–4 kbar (Piechocka et al., 2017; Sheppard et al., 2007). Although metamorphism had ceased by c. 990 Ma, the leucogranite magmatism persisted for another c. 100 million years (Piechocka et al., 2017). Orogen-scale reactivation of pre-existing shear zones at 920–830 Ma involved dextral strike-slip movement in the northern parts of the province and exhumation of the southern portion (Occhipinti & Reddy 2009, Piechocka et al., 2018). This widespread reactivation may be attributed to the Edmondian Orogeny. The effects of the youngest reactivation event, the c. 570 Ma Mulka Tectonic Event (Bodorkos and Wingate, 2007), are limited to faulting and dextral shearing on discrete structures.

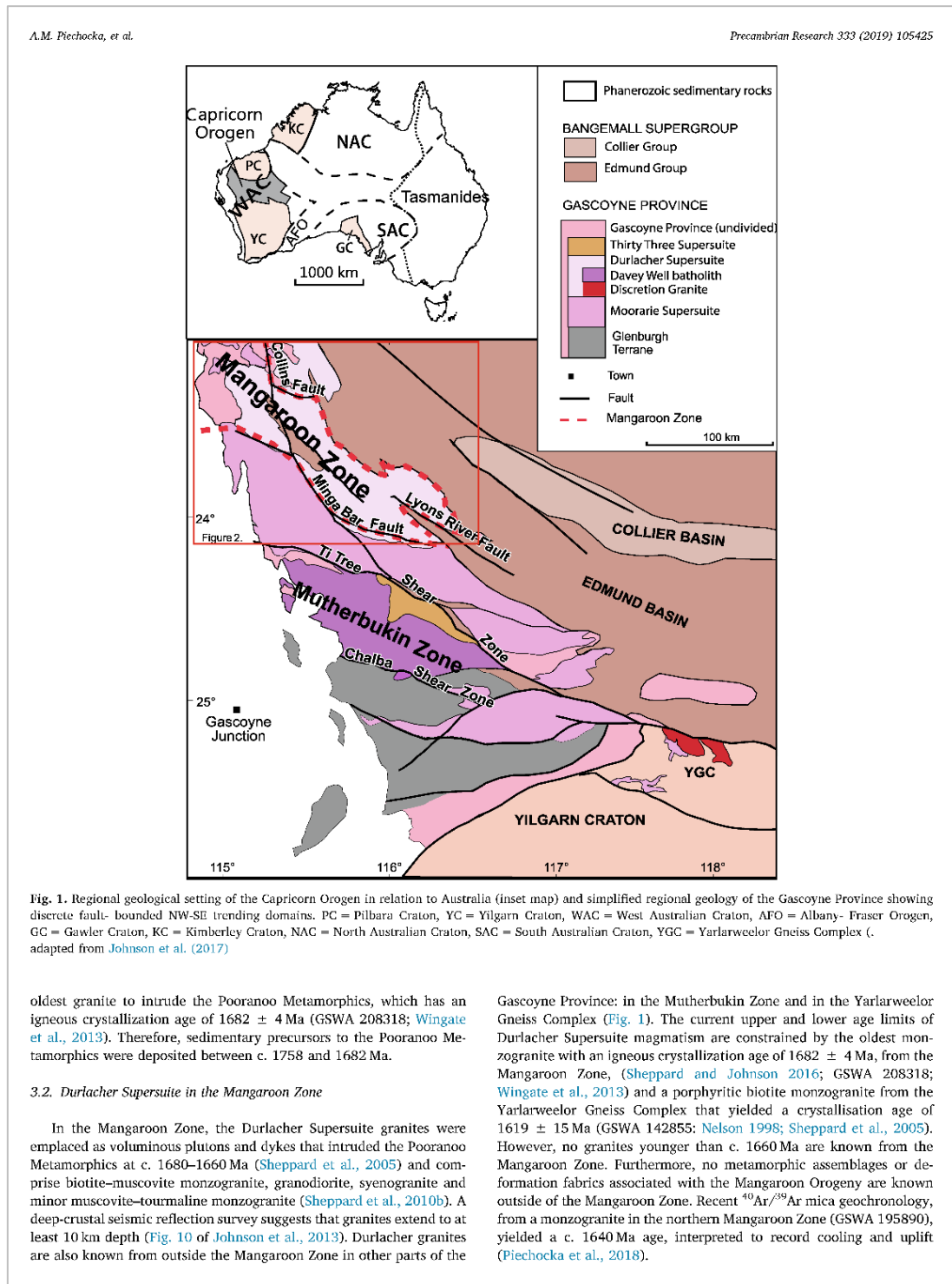
3. Mangaroon Zone

The study area is located in the Mangaroon Zone of the northern Gascoyne Province (Figs. 1 and 2) and comprises metasedimentary rocks of the Pooranoo Metamorphics and voluminous granitic intrusions of the Durlacher Supersuite. The Mangaroon Zone is about 40–70 km wide and is overlain by Phanerozoic sedimentary rocks in the west and by Meso- to Neoproterozoic metasedimentary rocks to the east. It is bounded to the north by the Collins Fault and to the south by the Minga Bar Fault. Fig. 2 shows the geology of the Mangaroon Zone along with sample locations.

3.1. Pooranoo Metamorphics

The Pooranoo Metamorphics comprise mainly interlayered psammitic schist and feldspathic metasediments with pelitic rocks and metaconglomerate (Sheppard et al., 2010b). In the Mangaroon Zone, the rocks are commonly schistose, but gneissic and migmatitic metapelitic rocks are known from one locality in the southern Mangaroon Zone. Locally, graded bedding is preserved in the feldspathic metasediments (Sheppard et al., 2010b). The protoliths to the Pooranoo Metamorphics were deposited as a turbidite sequence in a narrow ~50 km-wide basin, with an unknown thickness. The turbiditic nature of the protoliths suggests a deep-water depositional setting (Sheppard et al., 2005; Sheppard et al., 2010b; Sheppard and Johnson, 2016).

SHRIMP U–Pb zircon geochronology was conducted by the Geological Survey of Western Australia (GSWA) to constrain the maximum and minimum depositional ages of precursors to the Pooranoo Metamorphics. A sample of the Biddenew Formation of the Mt James Subgroup yielded a youngest detrital zircon population at 1758 ± 18 Ma, which is interpreted as the maximum depositional age of the formation (Sheppard and Johnson, 2016; GSWA 183255; Wingate et al., 2009). A minimum depositional age is provided by the



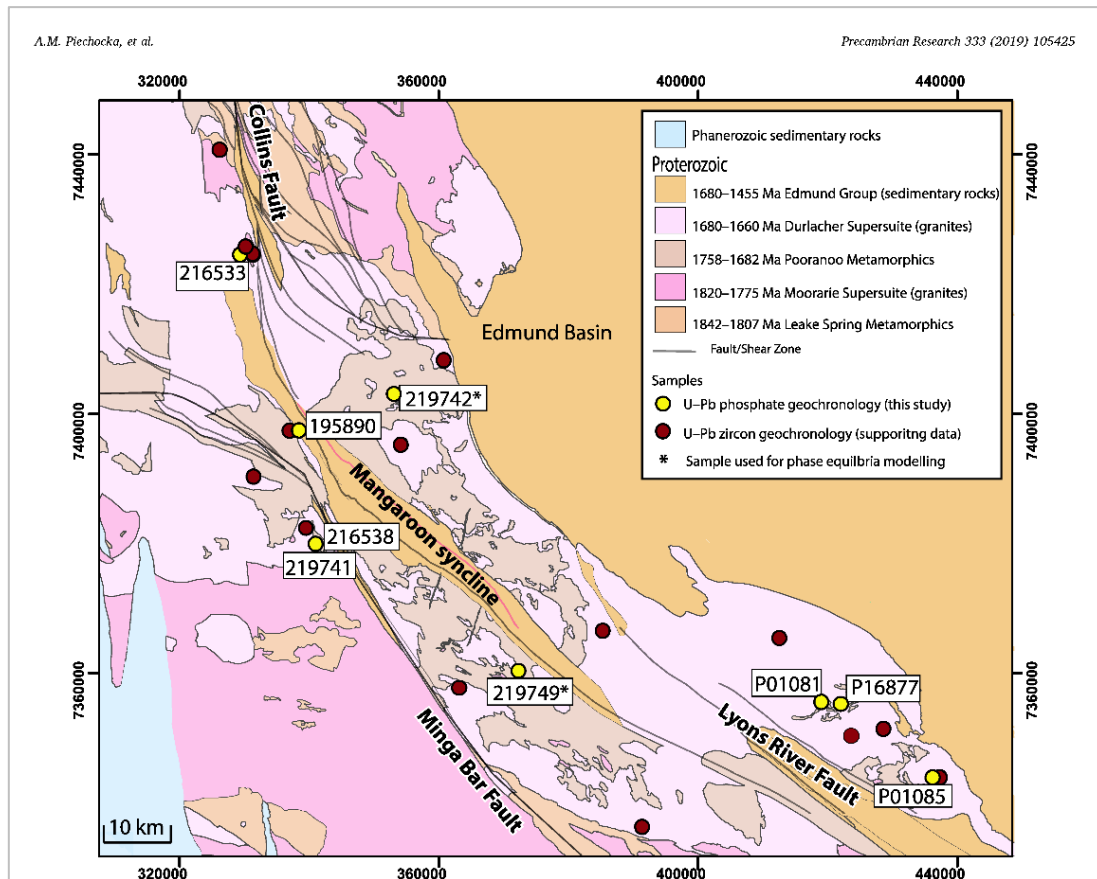


Fig. 2. Geology of the Mangaroon Zone showing location of samples used in this study and locations of previously dated granitic samples. The Minga Bar Fault, the Collins Fault and the Edmund Basin bound the Mangaroon Zone. Coordinate system is GDA 1994 MGA Zone 50. Geology polygons and linear features were extracted from the 1:500 000 Geological Map of Western Australia (GSWA 2016a).

3.3. Deformation and metamorphism (D_1/M_1 and D_2/M_2)

In the Mangaroon Zone, of the northern Gascoyne Province, two distinct tectonometamorphic events, D_1/M_1 and D_2/M_2 , have been recognised (Sheppard et al., 2005). D_1/M_1 is characterised by amphibolite facies regionally extensive of the Pooranoo Metamorphics. In the southern Mangaroon Zone, D_1 deformation produced local gneissic fabrics or granofelsic textures, with evidence for partial melting of pelitic and semi-pelitic lithologies at the Star of Mangaroon locality (Sheppard et al., 2005). Also, at the Star of Mangaroon mine local recumbent folds with axial surfaces defined by sillimanite are associated with D_1 (Sheppard et al., 2005). However, some areas preserve a granofelsic texture, which suggests minimal non-coaxial strain. M_1 metamorphic assemblages preserved in pelitic and granofelsic of biotite–muscovite–quartz–plagioclase–sillimanite, quartz–biotite–cordierite–plagioclase–muscovite(–sillimanite) and plagioclase–biotite–quartz–sillimanite–muscovite–cordierite combined with the general absence of garnet were previously interpreted to record low- P , high- T regional metamorphism (Sheppard et al., 2005). The grade of metamorphism appears to be lower in the northern half of the Mangaroon Zone (Sheppard et al., 2005). Formerly, the upper age constraint on D_1/M_1 , and the lower age constraint on D_2/M_2 , were based on a diatexitic granite with a zircon crystallisation age of c. 1677 Ma (GSWA 178027; Nelson 2005) that cross-cuts an undated gneissic fabric that was presumed

to be associated with D_1 (Sheppard et al., 2005). However, recent zircon ages of c. 1808 Ma obtained from the gneissic host that is cross-cut by the diatexite show that it is part of the older 1820–1775 Ma Moorarie Supersuite (Wingate et al., 2013), and unrelated to the Mangaroon Orogeny. Consequently, the previous upper age constraint on D_1/M_1 and lower age constraint on D_2/M_2 (i.e., 1677 Ma) may not be valid.

The D_2 deformation event produced a pervasive schistosity, metre- to kilometre-scale upright folds, and retrogression of D_1 metamorphic minerals to greenschist facies assemblages (Sheppard et al., 2005; 2010b). M_2 is characterised by sericite (after sillimanite, cordierite, plagioclase and microcline), and chlorite (after cordierite) with a typical M_2 assemblage consisting of sericite–chlorite–quartz–plagioclase–biotite observed in schists (Sheppard et al., 2005). Many granites of the Durlacher Supersuite with crystallization ages of c. 1675 Ma or older were deformed during D_2 , providing a maximum age constraint for D_2 (Sheppard et al., 2005; 2010b).

4. Sample descriptions and petrography

In total, nine samples of pelitic and granitic rocks were collected from across the Mangaroon Zone for U–Pb geochronology. Monazite was used to determine the crystallisation ages for the granitic rocks (three samples) and monazite and xenotime were selected to date the

A.M. Piechocka, et al.

Precambrian Research 333 (2019) 105425

Table 1
Summary of pelitic and granitic samples from the Mangaroo Zone analysed in this study.

GSWA Sample ^a	Easting	Northing	Sample description	Structure	P–T constraints	Mineral	U–Pb Age (Ma)
<i>Granite samples^b</i>							
195,890	338,457	7,397,374	ms–bt metamonzogranite	230°/90° metamorphic foliation		monazite	1695 ± 9
P01085 ^c	436,219	7,343,766	bt–ms syenogranite			monazite	1682 ± 3
219,741	339,577	7,382,285	tur–ms monzogranite			monazite	1659 ± 13
<i>Supporting samples^d</i>							
208,365	326,186	7,440,703	bt metagranodiorite	228°/70° SE metamorphic foliation; D ₁		zircon	1689 ± 6
195,888	331,433	7,390,220	bt monzogranite			zircon	1689 ± 4
216,532	331,336	7,424,614	bt metagranodiorite	260°/85° SE gneissic layering; D ₁		zircon	1688 ± 4
195,887	341,014	7,379,817	tur–ms monzogranite			zircon	1682 ± 9
216,531	331,336	7,424,614	ms–tur monzogranite			zircon	1673 ± 4
<i>Pelitic samples^e</i>							
219,749	372,340	7,359,950	cd–sill pelitic migmatite	147°/85° SE fold axial surface; 230°/70° SE fold axis; D ₁	665–755 °C; 2.7–4.3 kbar	monazite	1691 ± 7
219,742	353,086	7,402,982	sill–bt pelitic gneiss			monazite	1685 ± 9
	675–850 °C; 4–7.5 kbar						
216,533	330,613	7,424,503	gt–bt–ep pelitic gneiss	241°/30° SE metamorphic foliation; D ₁		monazite	1683 ± 6
P01081 ^c	419,044	7,355,430	qtz–ms–lour schist			monazite	1681 ± 9
P16877 ^c	422,009	7,355,110	qtz–bt–ms schist			monazite	1680 ± 7
216,538	339,577	7,382,285	bt–ms–tur pelitic gneiss			monazite	1680 ± 4
216,538	339,577	7,382,285	bt–ms–tur pelitic gneiss			xenotime	1680 ± 4

Sample locations quoted in coordinate system MGA 94 Zone 50.

Planar structures are quoted as strike/dip and dip direction.

^a Sample prefix is GSWA unless otherwise stated.

^b Durlacher Supersuite.

^c Samples collected by J. Pearson (Pearson 1996).

^d Published GSWA data. References within text.

^e Pooranoo Metamorphics.

timing of metamorphism in the pelitic rocks (six samples). Of these pelitic samples, two (GSWA 219,742 and 219749) contained a preserved mineral assemblage that was suitable for phase equilibria modelling (GSWA 219,742 and GSWA 219749). Locations of all samples used in this study are shown in Fig. 2. Descriptions of all the granitic and pelitic samples analysed as part of this study are provided below and summarised in Table 1. Fig. 3 shows images of granitic sample sites in outcrop and thin section; Fig. 4 consists of outcrop photos of pelitic sample locations; and Fig. 5 consists of photographs of pelitic samples.

4.1. Granitic rocks (Durlacher Supersuite)

4.1.1. GSWA 195890: muscovite–biotite metamonzogranite

This rock is a medium-grained, porphyritic muscovite–biotite monzogranite (Fig. 3a). The monzogranite shows variation in strain across the outcrop with zones of mylonitisation, quartz veining and brecciation and zones with preserved igneous textures. The vertical metamorphic foliation trends 230°. The typical mineral assemblage consists of K-feldspar, quartz, muscovite and plagioclase with ~25% ferromagnesian minerals including biotite and secondary chlorite, along with accessory Fe-oxides, fluorite, zircon and monazite. In places, zones of pervasive mylonitization resulted in almost complete recrystallisation of the rock during the Neoproterozoic (Piechocka et al., 2018) (Fig. 3c).

4.1.2. P01085: biotite–muscovite syenogranite

This sample is a porphyritic, biotite–muscovite syenogranite consisting of orthoclase, quartz, plagioclase, and muscovite. Mafic minerals make up around 15% of the rock and include biotite and Fe–Ti oxides. Orthoclase predominantly occurs as anhedral crystals and is perthitic. The largest orthoclase crystals occur as tabular phenocrysts up to 8 mm long by 4 mm wide. Plagioclase shows multiple twinning and quartz shows undulose extinction. Sericite is pervasive throughout the sample.

4.1.3. GSWA 219741: tourmaline–muscovite monzogranite

This sample is a relatively undeformed medium-grained leucocratic monzogranite (Fig. 3b) consisting of orthoclase, quartz, plagioclase and muscovite. Ferromagnesian minerals make up around 10% of the rock and include tourmaline, biotite, chlorite, and Fe-oxides. Pervasive sericite and recrystallised quartz show a minor post magmatic overprint, although the rock looks relatively undeformed in outcrop.

4.2. Pelitic rocks (Pooranoo Metamorphics)

4.2.1. GSWA 219749: sillimanite–cordierite pelitic migmatite

The outcrop from which this sample was collected is characterised by stromatic migmatites (Fig. 4a) with leucosomes of feldspar, quartz and biotite and melanosomes of coarse sillimanite and biotite. Seemingly unmigmatized layers of psammite, up to a few meters thick, are cross-cut by a sparse network of leucocratic veins. Folded pelitic and psammitic rocks have axial planar fabrics defined by biotite (D₁) (Martin et al., 2006). At this locality the fold axial surface trends 147°/85° (SF) with a fold axis trending 230°/70° (SF). In thin section, the foliation (D₁) in the pelitic migmatite is defined by elongate flattened quartz grains that wrap recrystallised quartz, anhedral cordierite porphyroblasts that are altered around their margins (up to 4.5 mm), and magnetite up to 0.5 mm in diameter (Fig. 5a). Fibrolite defines a lineation. Quartz does not show undulose extinction. Anhedral biotite has brown to orange pleochroism, contains pleochroic halos and is associated with Fe–Ti oxides at its margins. K-feldspar is anhedral and up to 1 mm across. Secondary muscovite cross-cuts biotite crystals, and sericite alteration suggests post-peak alteration. The interpreted peak metamorphic assemblage (M₁) is sillimanite–cordierite–biotite–magnetite–K-feldspar–quartz–plagioclase–ilmenite–melt.

4.2.2. GSWA 219742: sillimanite–biotite pelitic gneiss

This fine- to coarse-grained rock contains conspicuous porphyroblasts of prismatic sillimanite minor patches of leucosome (Fig. 4b). In outcrop, the rock is not obviously deformed and shows no signs of retrogression. The gneiss is layered (probably reflecting relict bedding)

A.M. Piechocka, et al.

Precambrian Research 333 (2019) 105425

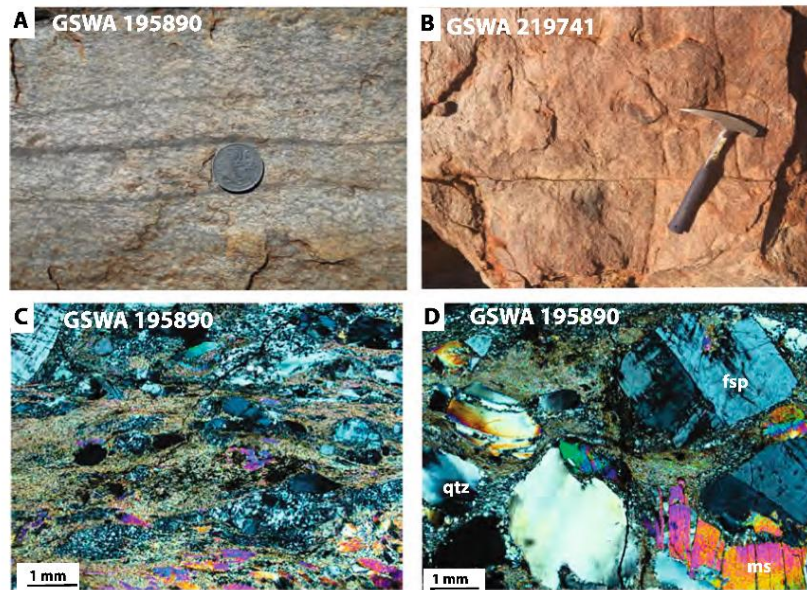


Fig. 3. Field photos of granites and representative photomicrograph images of granitic sample 195,890 in cross-polarised light, analysed in this study. A. Variably deformed porphyritic muscovite–biotite monzogranite characterised by discrete cm-scale mylonite zones (GSWA 195890). B. Leucocratic undeformed tourmaline–muscovite monzogranite (GSWA 219741). C. Fine-grained biotite matrix with recrystallised quartz and feldspar porphyroblasts showing sigma tails (GSWA 195890). D. A less deformed part of the rock (GSWA 195890) showing feldspar and muscovite porphyroclasts. Abbreviations: fsp = feldspar; ms = muscovite; qtz = quartz.

with the sillimanite occurring in the thicker horizons. In thin section this sample contains both fibrolitic and prismatic sillimanite. Fibrolite defines a weak foliation (D_1) that wraps around anhedral biotite porphyroblasts (up to 4 mm) (Fig. 5b). Prismatic sillimanite cross cuts fibrolite and appears to be randomly oriented. Biotite, muscovite and plagioclase crystals have embayed edges. Fine-grained aggregates of pinite are interpreted to be pseudomorphs after cordierite (Fig. 5c). Very rare grains of anhedral garnet occur in association with biotite (Fig. 5d–e). Equigranular quartz crystals do not appear to be recrystallised and rarely display undulose extinction. Ilmenite crystals are distributed more-or-less evenly throughout the sample. Secondary tourmaline overprints biotite. Large plates of randomly oriented muscovite are interpreted to be secondary, probably replacing K-feldspar. The peak metamorphic assemblage (M_1) is sillimanite–biotite–cordierite–K-feldspar–plagioclase–quartz–ilmenite–melt. Rare anhedral grains of garnet are interpreted to have grown during the prograde evolution.

4.2.3. GSWA 216533: garnet–biotite–epidote pelitic gneiss

In outcrop, the sample is characterised by a gneissic layering and subparallel leucocratic veins (Fig. 4c). The metamorphic foliation trends $241^\circ/30^\circ$ (SE). In thin section, this sample has a well-developed foliation defined by biotite that wraps garnet porphyroblasts (Fig. 5f). The gneissic fabric is defined by alternating layers of biotite and elongate recrystallised quartz. The rock mainly comprises biotite, quartz, muscovite and garnet with minor epidote and ilmenite, and trace plagioclase, with accessory monazite. Garnet porphyroblasts (up to 0.5 mm) are euhedral to subhedral, the latter showing embayed edges. Randomly-oriented inclusions within garnet cores consist of quartz, muscovite and biotite whereas epidote inclusions occur in garnet rims. Late alteration to chlorite post-dates the peak metamorphic assemblage (M_1) of garnet–biotite–quartz–epidote–muscovite–plagioclase–ilmenite.

4.2.4. P01081: quartz–muscovite–tourmaline pelitic schist

This sample is a quartz–muscovite–tourmaline pelitic schist (Fig. 4d). In thin section it consists of quartz and muscovite, with minor tourmaline and plagioclase and accessory Fe-oxides. Rare plagioclase crystals are subhedral to anhedral, range from 1 to 4 mm in length and are partially sericitised. Muscovite is euhedral to anhedral and up to 4 mm. Quartz crystals are typically ~1 mm in size and also occur as smaller recrystallised aggregates; both varieties shows undulose extinction. Quartz and muscovite are intergrown, suggesting they replace K-feldspar. The tourmaline is typically subhedral and is similar in size to the smaller quartz and muscovite crystals.

4.2.5. P16877: quartz–biotite–muscovite pelitic schist

In the field the schist forms a green sub-crop (Fig. 4c) and consists of muscovite, quartz, biotite and sericite with accessory tourmaline. The schist is a protomylonite with a well-developed S–C fabric (S_1 or S_2).

4.2.6. GSWA 216538: biotite–muscovite–tourmaline pelitic gneiss

This sample is a metre-scale inclusion of deformed pelitic gneiss within a leucocratic monzogranite (GSWA 219741) (Fig. 4f). This pelitic gneiss has a well-defined biotite foliation (S_1) alternating with layers of elongate and tabular quartz surrounded by a fine-grained groundmass of sericite. Biotite also occurs as relict porphyroblasts up to 4.5 mm long. Deformed muscovite porphyroblasts (up to 8 mm long) are aligned with the fabric. Prismatic tourmaline crystals (up to 4 mm long) are intergrown with quartz and are also aligned with the foliation. Secondary chlorite and sericite indicate some post-peak retrogression.

A.M. Piechocka, et al.

Precambrian Research 333 (2019) 105425

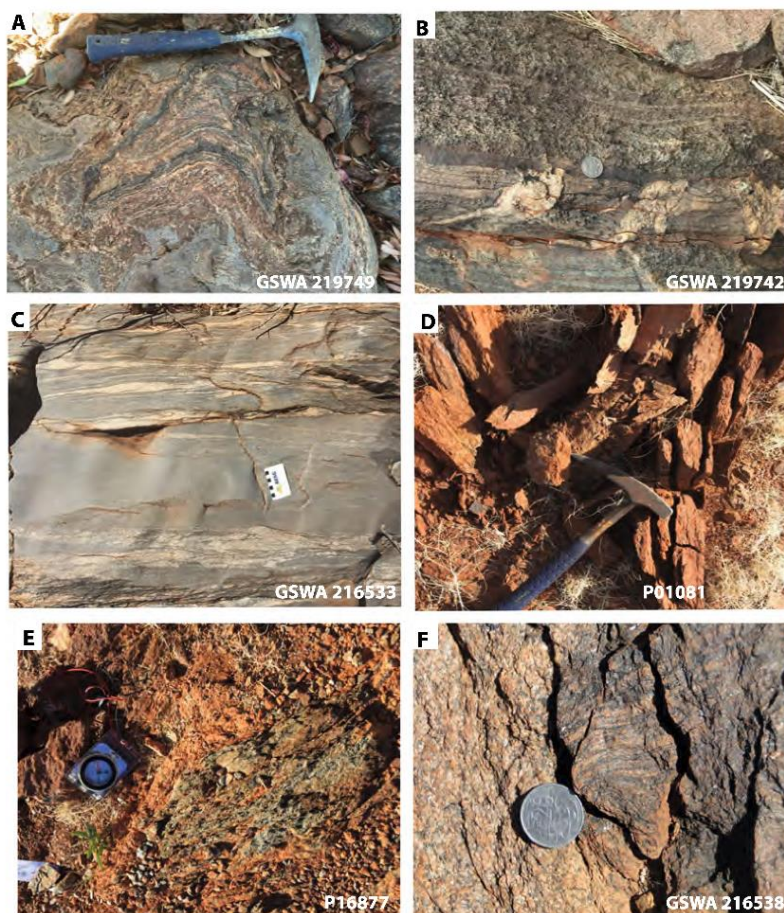


Fig. 4. Field photos of pelitic samples analysed in this study. A. Stromatic cordierite-sillimanite pelitic migmatite (GSWA 219749). B. Sillimanite-biotite pelitic gneiss that in outcrop appears bedded (GSWA 219742). Local melting observed at several locations across the outcrop. C. Meter-wide biotite-rich zones with leucosomes (GSWA 216533). D. Weathered outcrop of quartz-biotite-tourmaline schist (P01081). E. Sub-crop of deformed muscovite-biotite schist (P16877). F. Inclusion of deformed biotite-muscovite-tourmaline pelitic gneiss (GSWA 216538) enclosed within a relatively undeformed monzogranite (GSWA 219741).

5. Analytical methods

5.1. *In situ* SHRIMP U-Pb monazite and xenotime geochronology

For six pelitic samples (P01081, P16877 and GSWA 216533, 216338, 219742 and 219749) and three granitic samples (P01085 and GSWA 195890, 219741) polished thin sections were imaged using a scanning electron microscope (SEM) in back-scattered electron (BSE) mode fitted with an energy dispersive X-ray spectrometer (EDS) to identify suitable monazite and xenotime crystals for *in situ* SHRIMP geochronology. Monazite and xenotime crystals > 10 μm across were drilled out in 3 mm-diameter plugs and cast in a several 25 mm epoxy mounts. In all sessions the reference standards for Pb/U and Pb/Th calibrations and for $^{207}\text{Pb}/^{206}\text{Pb}$ fractionation monitoring were in separate mounts, which were cleaned and Au-coated together with the sample mounts to ensure consistent conductivity.

U-Pb analyses of monazite were conducted using a SHRIMP II ion microprobe in the John de Laeter Centre at Curtin University, Perth. Optical and BSE images were used to guide placement of the primary ion beam during analysis. SHRIMP analytical procedures followed established methods for monazite (Fletcher et al., 2010) and xenotime (Fletcher et al., 2000, 2004). During all analytical sessions, an O_2^+ primary beam, with a spot size of 10 to 15 μm , was focussed through a 30 to 50 μm Kohler aperture with a beam intensity of 0.18 to 0.45 nA. The secondary ion beam was focused through a 100 μm collector slit onto an electron multiplier to produce mass peaks with flat tops and a mass resolution (1% peak heights) of > 5,200. A post-collector retardation lens was used to reduce background counts produced from stray ions.

Monazite was analysed with a 13-peak run table as defined by Fletcher et al. (2010), which includes mass stations for the estimation of La, Ce and Nd (REPO_2^+), and Y (YCeO^-). Monazite data were collected in sets of eight scans with a 5:1 unknown to standard ratio. Count

A.M. Piechocka, et al.

Precambrian Research 333 (2019) 105425

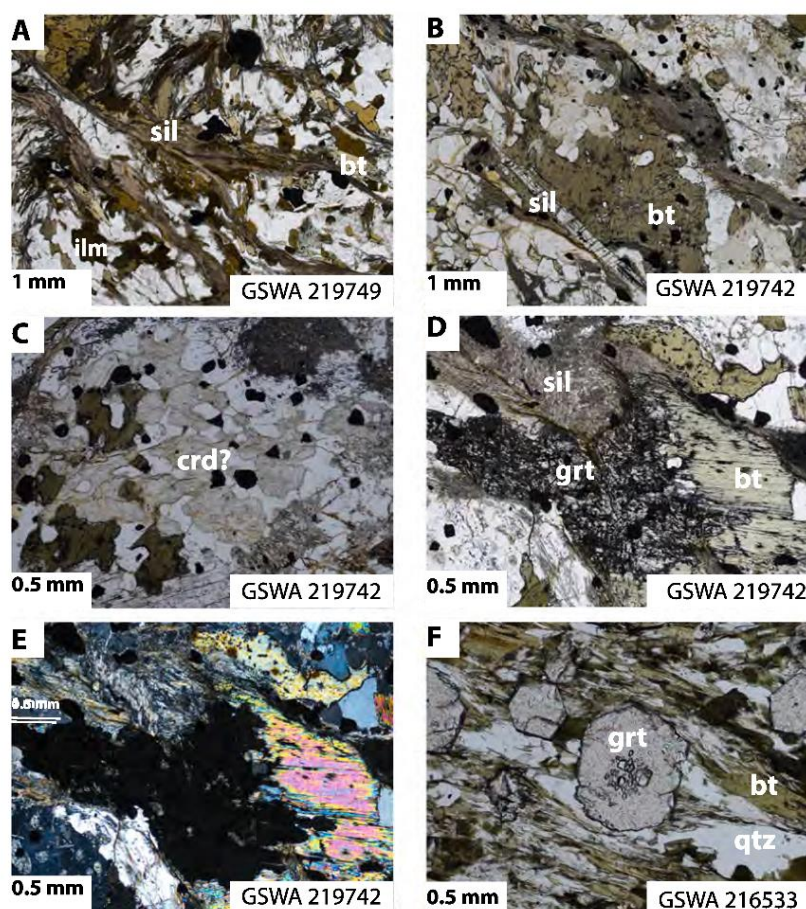


Fig. 5. Representative photomicrograph images of analysed pelitic samples in plane-polarised light (PPL) and cross-polarised light (XPL). A. Fabric defined by fibrous sillimanite, biotite, quartz and ilmenite in the cordierite-sillimanite pelitic migmatite (GSWA 219749; PPL). B. Sillimanite-biotite pelitic gneiss with tabular and fibrous sillimanite (GSWA 219742; PPL). C. Possible ex-cordierite crystal (GSWA 219742; PPL). D. Anhedronal garnet associated with biotite (GSWA 219742; PPL). E. As per D but in XPL. F. Garnet porphyroblast with pressure shadow and biotite-quartz foliation in the garnet-biotite-epidote pelitic gneiss. Inclusions are restricted to the garnet cores and are randomly oriented (GSWA 216533; PPL). Abbreviations: bt = biotite; crd = cordierite; grt = garnet; ilm = ilmenite; pl = plagioclase; qtz = quartz; sil = sillimanite.

times per scan for ^{204}Pb , background position 204.045, ^{206}Pb , ^{207}Pb , and ^{208}Pb were 10, 10, 10, 30, and 10 s, respectively. The primary Pb/U and Pb/Th standard used was MAD 1 (known as FRENCH; Foster et al., 2000). Matrix effects on Pb/U data from U and Th were determined using Z2234 standard (Stern and Sanborn, 1998). Standard Z2908 (provided by Richard Stern) was used to monitor instrumental mass fractionation (IMF) of the instrument.

Some of the analysed monazite grains in this study show distinct alteration corona that indicate fluid-mediated alteration (Finger et al., 1998). However, as the aim of this study was to constrain the timing of peak metamorphism and magmatism rather than the processes of secondary alteration processes, we only analysed primary monazite.

Xenotime was analysed with a nine-peak run table and analytical procedure followed established methods (Fletcher et al., 2000, 2004). The primary Pb/U standard MG-1 (Fletcher et al., 2004) was used for

Pb/U, Pb/Th and U abundance calibrations. The secondary standards were z6413 (XENO1; Fletcher et al., 2004; Stern and Rainbird, 2001) used for $^{207}\text{Pb}/^{206}\text{Pb}$ normalisation and used in conjunction with MG-1 for matrix corrections to Pb/U and Pb/Th, and z6410 (XENO2; Fletcher et al., 2004; Stern and Rainbird, 2001) used to monitor matrix effects.

Squid-2.50.11.02.03 software (Ludwig, 2009) was used for initial data reduction, including correction for common Pb. Common Pb corrections were based on individual measured ^{201}Pb abundances, assuming crustal common Pb at the approximate age of the samples modelled by Stacey and Kramers (1975). Corrections for matrix effects in Pb/U and Pb/Th, from U and Th in xenotime (Fletcher et al., 2004) and from U, Th, Pb, and REE in monazite and for instrumental mass fractionation in $^{207}\text{Pb}/^{206}\text{Pb}$ (Fletcher et al., 2010) were applied to the sample data. Weighted mean dates are reported with 95% confidence limits, whereas individual analyses are presented with 1 σ uncertainties.

5.2. Whole-rock geochemistry

Whole-rock geochemical analyses of granitic and pelitic samples, including loss on ignition (LOI), were determined by X-ray fluorescence (XRF) spectroscopy at Intertek-Genalysis Australia or at ALS Chemex, Australia by the Geological Survey of Western Australia. All data and additional analytical details are available from the Geological Survey of Western Australia's WACHEM database (<http://geochem.dmp.wa.gov.au/geochem/>). The data were used to determine zircon saturation temperatures and to determine the alumina saturation index (ASI). Pelitic samples were analysed specifically to constrain bulk compositions for use in phase equilibrium modelling.

The granites display a range of SiO₂ compositions (62.9–74.0% wt %), with 94% having > 65 wt% SiO₂ (Table 2). The granites are generally peraluminous (i.e., ASI = molar Al₂O₃/(CaO + Na₂O + K₂O) > 1 (Supp. Fig. 1); Chappell, 1999; Scaillet et al., 2016; Zcn, 1986)—most have ASI values that cluster tightly between 1.12 and 1.20, but two samples have much higher values of 1.55 and 1.61 (Table 2). All but one sample has Zr contents between 70 and 222 ppm—one sample outside this range has 316 ppm Zr (Table 2).

6. Results

6.1. U–Pb monazite and xenotime geochronology

The results are presented as two groups: first granitic rocks and then

pelites. The results are discussed in chronological order rather than by the geochronometer used. Fig. 6 contains SEM images of analysed monazite and xenotime grains; Fig. 7 consists of U–Pb monazite concordia diagrams for the granitic rocks, Fig. 8 consists of U–Pb monazite and xenotime concordia diagrams for the pelitic rocks.

6.2. Granitic rocks

6.2.1. GSWA 195890: muscovite-biotite metamonzogranite

The monazite grains are anhedral to subhedral with some crystals showing retrograde corona (Fig. 6a). The crystals range in size from 30 to 80 μm and occur as inclusions in quartz, plagioclase, and muscovite and within the groundmass. Fifty-four analyses were carried out on 29 monazite crystals (Supp. Table 1). Twenty-six analyses are excluded from the final age calculation due to high common ²⁰⁶Pb (> 1 wt%) and/or > 5% discordance. A further four analyses are statistical outliers (i.e., > 2 standard deviations from the mean) and are not considered further. The remaining twenty-four analytical spots show Th concentrations typically ranging from 50,000 to 93,000 ppm with one analysis at 26,000 ppm, whereas U concentrations cluster into three groups: 300–1300 ppm (fourteen analyses), 2000–3000 ppm (eight analyses) and 5000–6000 ppm (two analyses). The Th/U ratios range from 10 to 198. The 24 analyses yield ²⁰⁷Pb/²⁰⁶Pb dates between 1732 and 1640 Ma with a weighted mean of 1695 ± 9 Ma (MSWD = 0.62), which is interpreted as the crystallisation age of the monzogranite (Fig. 7a).

Table 2

Whole-rock geochemistry data for Mangaroon Zone Durlacher Supersuite granite samples, from this study and published data (GSWA 2016b).

Sample	195890 ^b	195888 ^c	208365 ^c	216532 ^c	88410 ^c	195887 ^c	169092 ^d	178030		
Rock Type	Ms-bt metamonzogranite	Bt porphyritic monzogranite	Bt metagranodiorite	Bt porphyritic monzogranite	Ms-bt monzogranite	Tur monzogranite	Bt-ms monzogranite	Bt granodiorite		
wt%										
SiO ₂	–	67.40	65.09	67.43	73.99	72.90	73.85	62.93		
TiO ₂	–	0.58	0.64	0.51	0.14	0.19	0.19	0.81		
Al ₂ O ₃	–	16.00	15.26	15.16	13.57	14.85	13.86	16.00		
Fe ₂ O ₃ ^T	–	5.72	5.29	4.67	1.60	1.69	1.593	7.232		
FeO	–	5.14	3.08	4.20	1.17	1.52	1.08	3.8		
MgO	–	1.79	1.74	1.36	0.33	0.39	0.39	2.12		
MnO	–	0.07	0.11	0.11	0.06	0.05	0.06	0.17		
CaO	–	1.36	3.01	2.31	1.00	0.91	0.81	3.39		
Na ₂ O	–	1.79	2.60	2.76	2.60	2.98	2.86	2.35		
K ₂ O	–	4.19	3.64	3.97	5.46	5.41	5.21	3.91		
P ₂ O ₅	–	0.13	0.22	0.20	0.10	0.20	0.24	0.24		
LOI	–	1.50	1.87	1.02	1.03	0.89	0.85	1.03		
A/CNK ^a	–	1.61	1.12	1.16	1.13	1.20	1.17	1.12		
ppm										
Zr	–	159.0	181.0	161.0	93.0	95.0	70.0	191.0		
Age (Ma)	1695 ± 9 ^c	1689 ± 4 [*]	1689 ± 6 [*]	1688 ± 4 [*]	1688 ± 7 [*]	1682 ± 9 [*]	1681 ± 10 [*]	1678 ± 6 [*]		
Sample	178027 ^c	169053 ^c	178029 ^c	178028 ^c	169062 ^c	216531 ^c	169060 ^c	169059 ^c	169055 ^c	219741 ^b
Rock type	Bt-ms granodiorite	Bt-ms monzogranite	Bt monzogranite	Bt-ms syenogranite dyke	Porphyritic syenogranite	Ms-tur monzogranite	Porphyritic syenogranite	Ms-bt monzogranite	Bt-ms monzogranite	Tur-ms monzogranite
wt%										
SiO ₂	65.38	68.44	70.50	70.89	70.08	72.92	72.18	71.85	72.15	–
TiO ₂	0.69	0.46	0.25	0.38	0.49	0.19	0.37	0.32	0.30	–
Al ₂ O ₃	15.99	15.00	14.44	14.31	14.71	14.29	14.18	14.69	14.13	–
Fe ₂ O ₃ ^T	5.12	4.97	2.123	2.728	2.149	1.67	2.80	1.82	2.15	–
FeO	2.79	2.25	1.43	1.72	1.13	1.50	1.76	0.80	1.26	–
MgO	1.21	1.39	0.48	0.75	0.61	0.39	0.68	0.40	0.41	–
MnO	0.10	0.09	0.07	0.07	0.05	0.05	0.06	0.04	0.06	–
CaO	2.70	1.06	0.80	0.79	1.34	0.87	1.92	0.96	0.94	–
Na ₂ O	2.89	1.84	2.45	1.92	2.35	3.10	3.19	2.55	2.47	–
K ₂ O	3.67	4.36	6.23	6.73	6.25	5.26	3.66	6.08	5.66	–
P ₂ O ₅	0.11	0.14	0.21	0.25	0.30	0.09	0.13	0.26	0.21	–
LOI	2.30	2.36	2.49	1.02	1.02	0.71	0.91	1.00	1.53	–
A/CNK ^a	1.17	1.55	1.18	1.20	1.13	1.15	1.12	1.17	1.19	–
ppm										
Zr	112.0	131.0	147.0	222.0	316.0	126.0	167.0	174.0	140.0	–
Age (Ma)	1677 ± 5 ^c	1677 ± 6 ^{**}	1675 ± 11 [*]	1674 ± 8 [*]	1674 ± 8 [*]	1673 ± 4 [*]	1673 ± 15 [*]	1660 ± 9 [*]	1659 ± 10 [*]	1659 ± 13 [*]

^a A/CNK = molar Al₂O₃/(CaO + Na₂O + K₂O); ^b this study; ^c = published data (GSWA 2016b); – = not analysed for whole-rock geochemistry; * = zircon age; ^ = monazite age; # = age recalculated from Nelson 2002; Ms = muscovite; bt = biotite, tur = tourmaline.

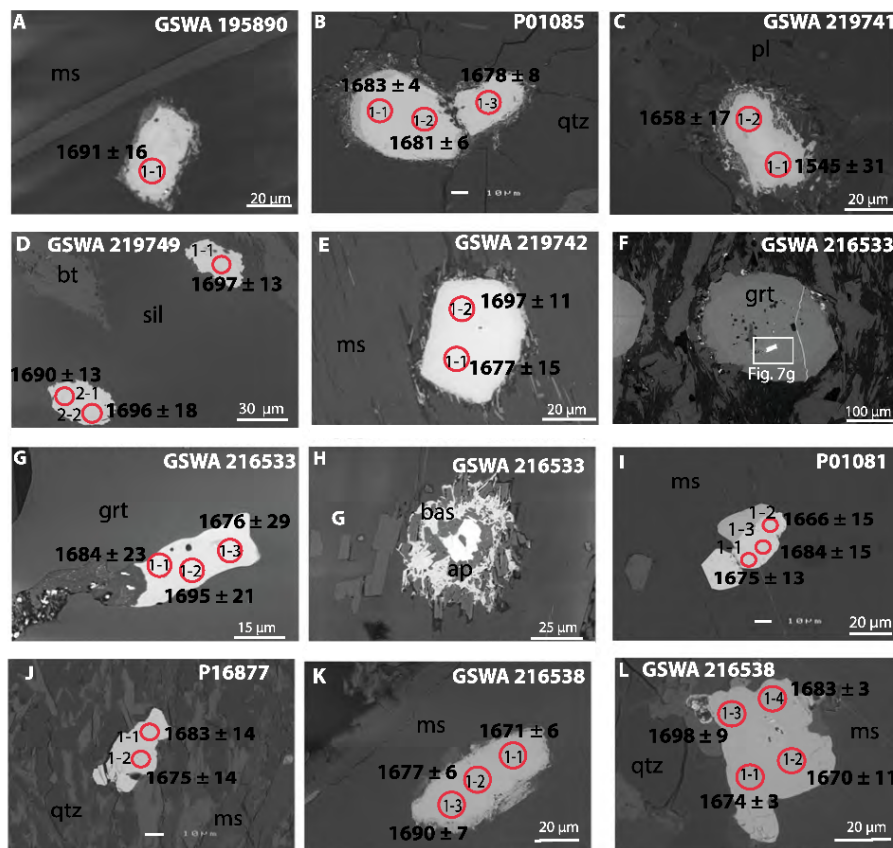


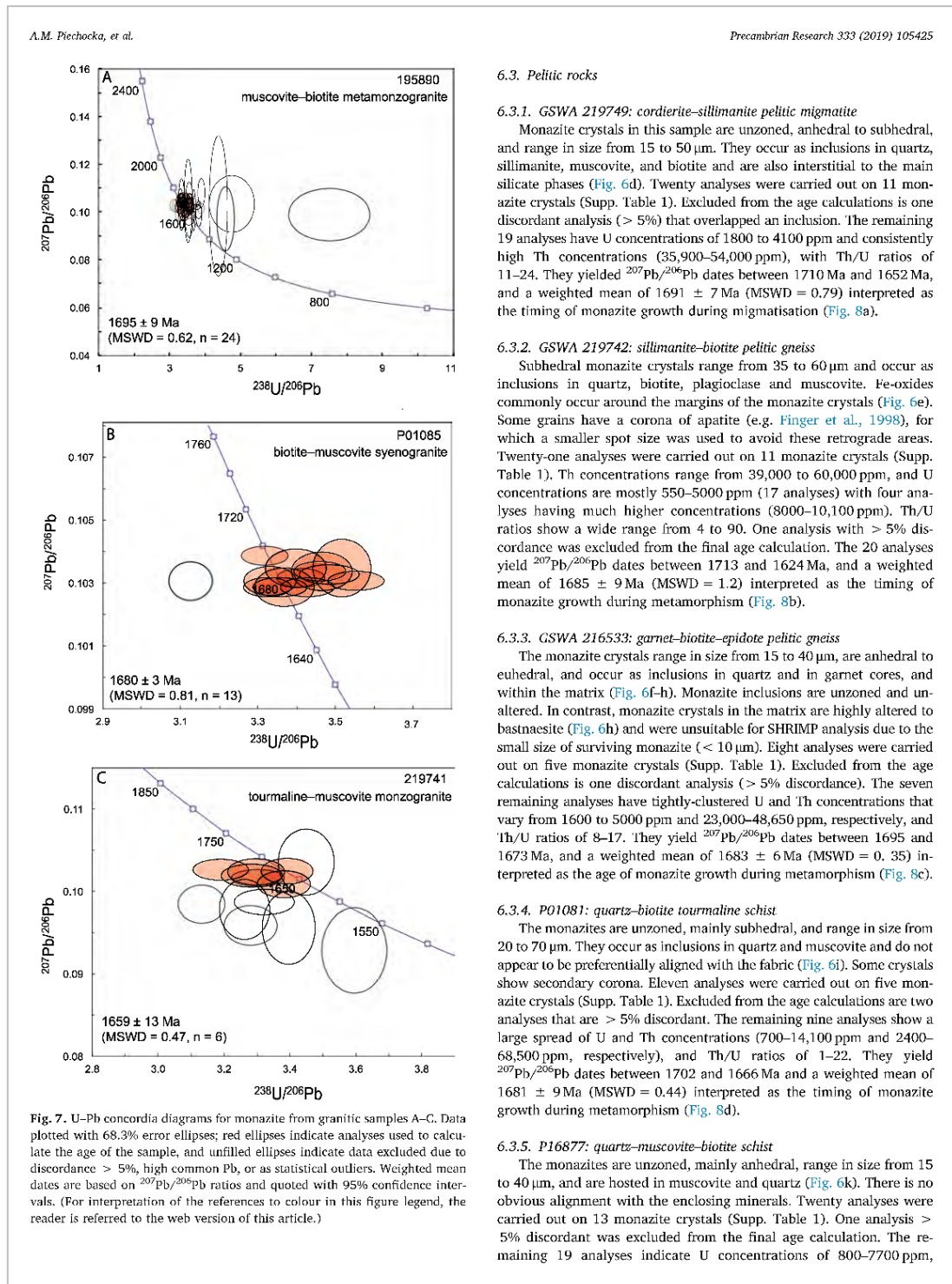
Fig. 6. Back-scattered electron (BSE) images of representative monazites and xenotime from samples analysed *in situ*. A. GSWA 195,890 (muscovite–biotite monzogranite) monazite grain 1612A. B. P01085 (biotite–muscovite syenogranite) monazite crystal C. C. GSWA 219,741 (tourmaline–muscovite monzogranite) monazite crystal D. D. GSWA 219,749 (cordierite–sillimanite pelitic migmatite) crystals H. E. GSWA 219,742 (sillimanite–biotite pelitic gneiss) monazite crystal D. F. GSWA 216,533 (garnet–biotite–epidote pelitic gneiss), garnet crystal. G. GSWA 216,533 monazite inclusion within garnet crystal, 1503D, showing an alteration pathway to the left. H. GSWA 216,533 example of altered monazite surrounded by apatite corona and bastnaesite (bas) rim. I. P01081 (quartz–muscovite–tourmaline schist) monazite crystal G. J. P16877 (quartz–biotite–muscovite schist) monazite crystal A. J. GSWA 216,538 (biotite–muscovite–tourmaline pelitic gneiss) monazite crystal D. K. GSWA 216,538 xenotime crystal A. Red circles denote SHRIMP spot locations. Ages are indicated in black with errors indicated at 95% confidence level. Analytical data are presented in Supplementary Table 1. (For interpretation of the references to colour in this figure legend, the reader is referred to the web version of this article.)

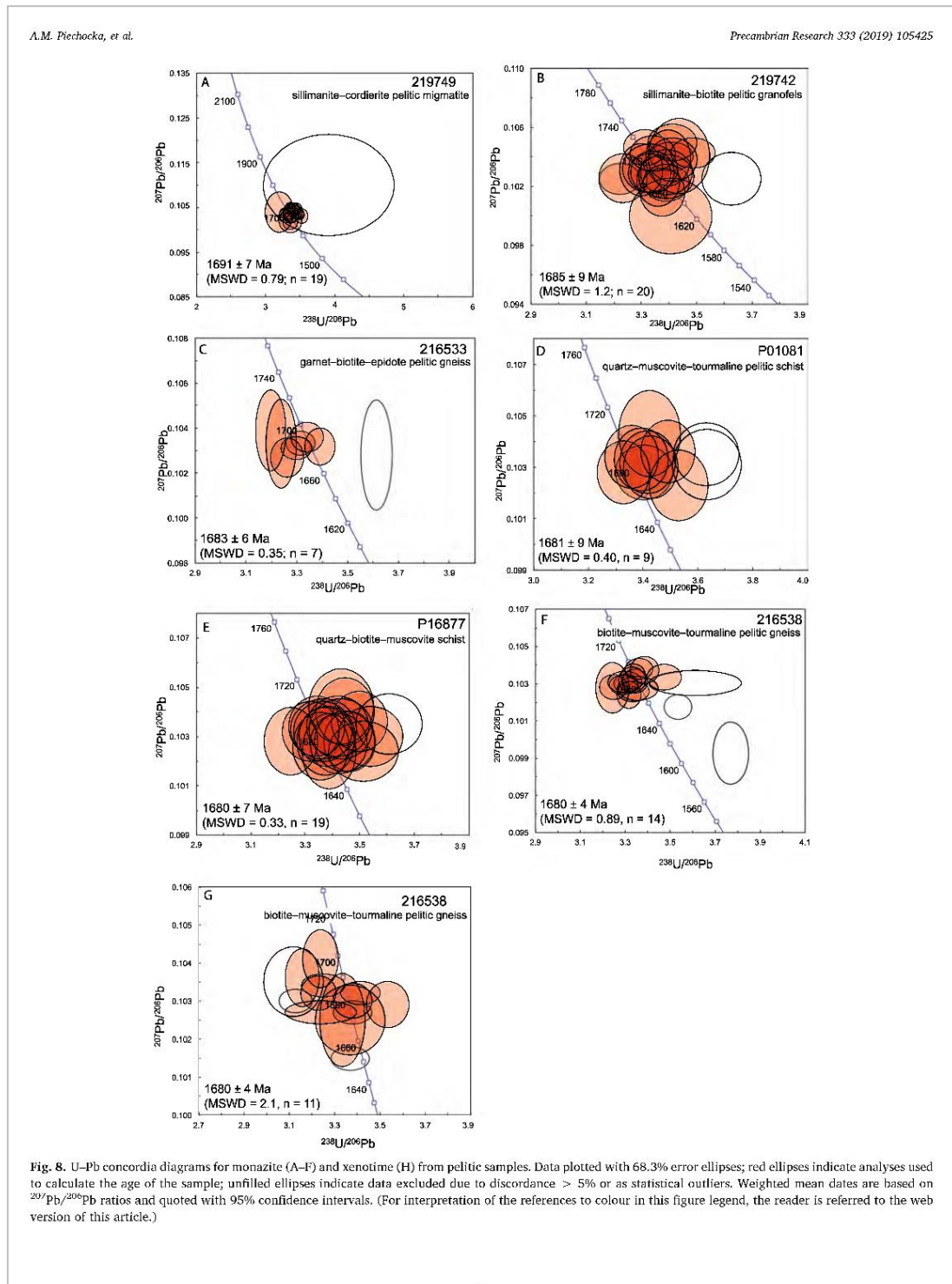
6.2.2. P01085: biotite–muscovite syenogranite

The monazite crystals are anhedral to subhedral, and range in size from 30 to 60 μm . Some have secondary apatite and/or retrograde coronas around their margins (Finger et al., 1998; Fig. 6b). The monazites occur both in the matrix and as inclusions in quartz. Fourteen analyses were conducted on five monazite crystals (Supp. Table 1). Excluded from the age calculations is one analysis > 5% discordant that likely represents an overlap between unaltered monazite and the retrograde corona. The remaining 13 analyses have U concentrations of 1100–4600 ppm and tightly-clustered Th contents of 69,000–94,000 ppm, with Th/U ratios from 15 to 72. The 13 analyses yielded $^{207}\text{Pb}/^{206}\text{Pb}$ dates between 1694 Ma and 1676 Ma and a weighted mean of 1680 ± 3 Ma (MSWD = 0.81), which is interpreted as the crystallisation age of the syenogranite (Fig. 7b).

6.2.3. GSWA 219741 tourmaline–muscovite monzogranite

The monazite grains are typically anhedral, and some have retrograde coronas (Fig. 6c). The crystals range in size from 25 to 70 μm and occur in the groundmass and as inclusions in quartz, plagioclase, and muscovite. Thirteen analyses were carried out on seven monazite crystals (Supp. Table 1). Two analyses of a single crystal have high common ^{206}Pb contents (> 1%) and were not considered in the final age calculation, nor were a further five analyses > 5% discordant. U and Th concentrations of the six remaining analyses are 750–7750 ppm and 13,000–64,500 ppm, respectively, with Th/U ratios of 8–35. The main group of six analyses yielded $^{207}\text{Pb}/^{206}\text{Pb}$ dates between 1671 and 1639 Ma, with a weighted mean of 1659 ± 13 Ma (MSWD = 0.47), which is interpreted as the crystallisation age of the monzogranite (Fig. 7c).





A.M. Piechocka, et al.

Precambrian Research 333 (2019) 105425

Table 3
Whole-rock chemistry used to construct *P–T* pseudosections for samples GSWA 219742 and 219749.

Sample	GSWA 219742	GSWA 219749
<i>XRF whole rock compositions (wt%)</i>		
SiO ₂	57.24	58.56
TiO ₂	0.78	0.83
Al ₂ O ₃	21.37	21.81
Fe ₂ O ₃ ^(a)	4.78	1.93
FeO ^(a)	4.78	6.24
MnO	0.23	0.17
MgO	2.72	2.93
CaO	0.61	0.34
Na ₂ O	0.92	0.62
K ₂ O	3.7	4.48
LOI	1.85	0.89
Total	98.98	98.80
<i>Normalised molar proportions used for phase equilibria modelling^(b)</i>		
SiO ₂	63.22	65.59
TiO ₂	0.65	0.70
Al ₂ O ₃	13.91	14.39
O	1.99	0.81
FeO	4.42	5.84
MnO	0.22	0.16
MgO	4.48	4.89
CaO	0.72	0.41
Na ₂ O	0.99	0.67
K ₂ O	2.61	3.20
H ₂ O	6.81	3.32
Total	100.00	100.00

^(a)FeO analysed by Fe²⁺ titration; Fe₂O₃ calculated by difference

^(b) final compositions used for *P–T* pseudosection, based on adjusted FeO:Fe₂O₃

bimodal Th concentrations of 15,000–18,000 ppm and 23,000–45,000 ppm, and Th/U ratios of 2–32. They yield ²⁰⁷Pb/²⁰⁶Pb dates between 1701 and 1667 Ma, and a weighted mean of 1680 ± 7 Ma (MSWD = 0.33) interpreted as the timing of monazite growth during metamorphism (Fig. 8c).

6.3.6. GSWA 216538: biotite–muscovite–tourmaline pelitic gneiss

Both monazite and xenotime from this sample were analysed. Anhedral to subhedral monazite crystals range from 20 to 80 µm and occur as inclusions in quartz and muscovite, with one matrix grain (Fig. 6k). Some crystals show resorption around their margins. Seventeen analyses were carried out on 10 monazite crystals (Supp. Table 1). Th concentrations range from 36,500 to 58,500 ppm and U concentrations between 2700 and 8300 ppm, with Th/U ratios of 6–19. Two analyses with > 5% discordance were excluded from the final age calculation, as was one young outlier with a ²⁰⁷Pb/²⁰⁶Pb age of 1656 ± 8 Ma (1602B.1–2). However, this latter outlier may record contact metamorphism associated with the intrusion of the granitic host of this gneissic inclusion (sample GSWA 219741). The remaining 14 analyses yield ²⁰⁷Pb/²⁰⁶Pb dates between 1692 and 1668 Ma, and a weighted mean of 1680 ± 4 Ma (MSWD = 0.89) interpreted as the timing of monazite growth during metamorphism (Fig. 8f).

Unzoned, unaltered anhedral to subhedral xenotime crystals are 20 to 60 µm in size, and typically occur as inclusions in muscovite and rarely as matrix grains (Fig. 6l). Fourteen analyses were carried out on six xenotime crystals (Supp. Table 1). Uranium concentrations range from 9700 to 17,800 ppm and Th concentrations between 1500 and 2700 ppm, with Th/U ratios of 0.1–0.3. Two analyses showing > 5% discordance were excluded from the final age calculation, as was one young outlier with a ²⁰⁷Pb/²⁰⁶Pb age of 1653 ± 4 Ma (1604G.1–2). The 11 remaining analyses yield ²⁰⁷Pb/²⁰⁶Pb dates between 1698 and 1670 Ma, and a weighted mean of 1680 ± 4 Ma (MSWD = 2.1) interpreted as the timing of xenotime growth during metamorphism (Fig. 8g).

7. Phase equilibria modelling

Repeated episodes of reworking and reactivation affected rocks of the Mangaroon Zone, making it challenging to find suitable samples for *P–T* investigations. However, two samples (GSWA 219749 and 219742) from the Pooranoo Metamorphics (Fig. 2) preserve low-variance mineral assemblages best suited to constrain *P–T* conditions. Based on the presence of leucosomes, samples GSWA 219,749 (sillimanite–cordierite pelitic migmatite) and GSWA 219,742 (sillimanite–biotite pelitic gneiss) are both interpreted to be former melt-bearing rocks and to have equilibrated above the solidus.

Isochemical phase diagrams (pseudosections) were calculated based on the bulk compositions of the two samples (Table 3). FeO contents were analysed by titration and Fe₂O₃ was calculated by difference. The H₂O content assumes all LOI as H₂O. As the rocks are interpreted to have been melt-bearing, and likely lost melt at or near the metamorphic peak, their modelled bulk compositions are only valid for constraining the peak and post-peak evolution of these samples. Phase equilibrium modelling used THERMOCALC 3.40i and the internally consistent dataset of Holland and Powell (2011) (tds62 generated on 6 February 2012), and were calculated in the system MnO–Na₂O–CaO–K₂O–FeO–MgO–Al₂O₃–SiO₂–H₂O–TiO₂–Fe₂O₃ (MnNCKFMASHITO), using the *a–x* models from White et al. (2014).

8. Results

8.1. GSWA 219749: sillimanite–cordierite pelitic migmatite

The calculated solidus lies between 670 and 720 °C and 2–8 kbar. The interpreted peak metamorphic assemblage of cordierite–sillimanite–magnetite–biotite–K-feldspar–quartz–plagioclase–ilmenite–melt is stable at 665–755 °C and 2.7–4.3 kbar (Fig. 9a). The presence of sillimanite provides a lower temperature constraint, whereas the absence of garnet bounds the inferred peak assemblage field to higher pressure. The presence of biotite and cordierite provide upper and lower temperature limits, respectively.

8.2. GSWA 219742: sillimanite–biotite–pelitic gneiss

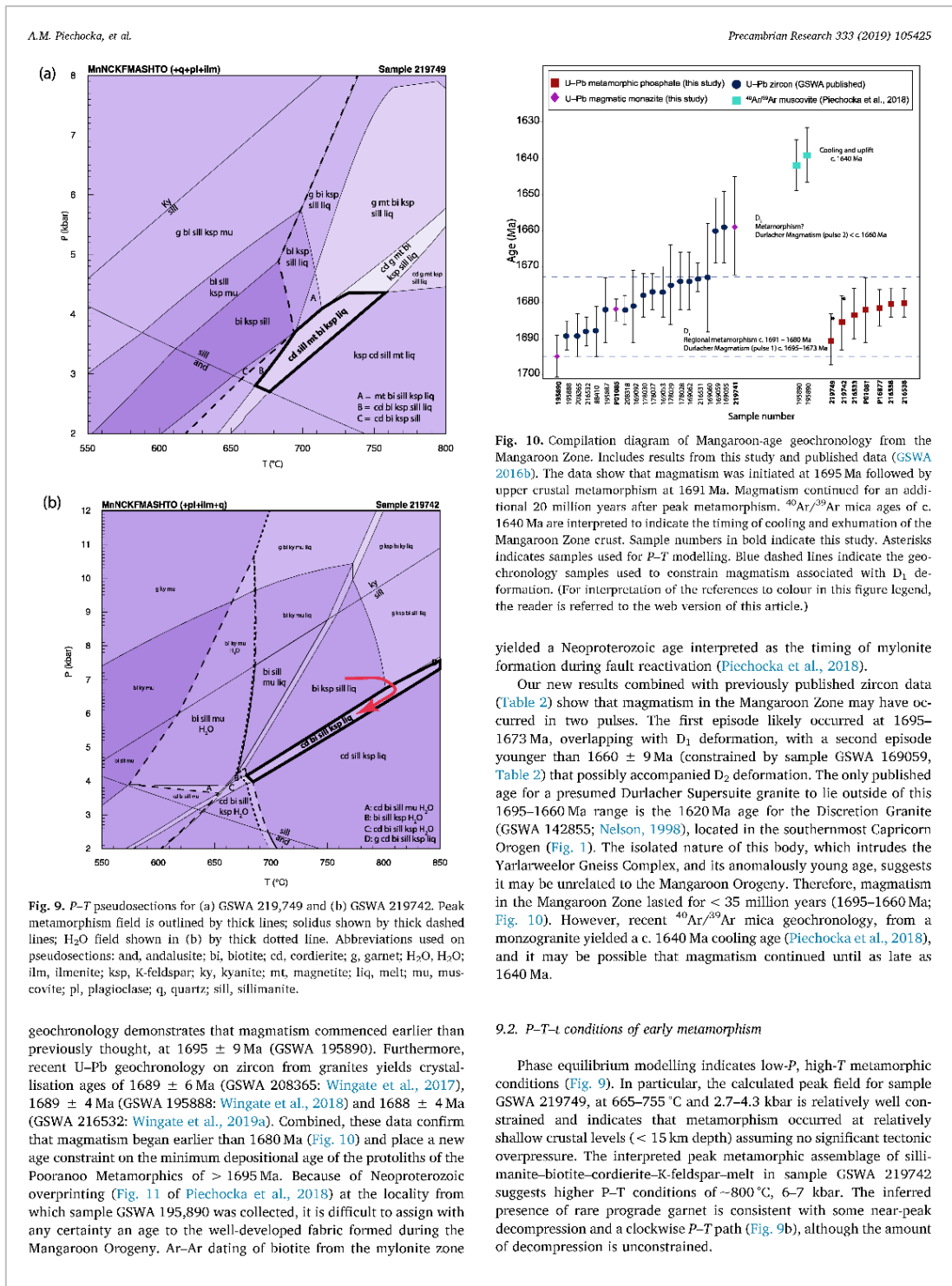
The calculated solidus lies between 670 and 700 °C and 2–12 kbar. The interpreted metamorphic assemblage of sillimanite–biotite–cordierite–K-feldspar–plagioclase–quartz–ilmenite–melt is stable in a narrow field that extends from around 4 kbar at ~675 °C to around 7.5 kbar at 850 °C (Fig. 9b). Although the modelled bulk composition is not strictly valid for constraining the prograde evolution due to likely melt loss, the presence of rare grains of anhedral, partially resorbed garnet, suggests higher pressures than those recorded at the peak during the prograde history of this sample (Fig. 9b). This implies a broad clockwise metamorphic *P–T* path, as illustrated in Fig. 9b.

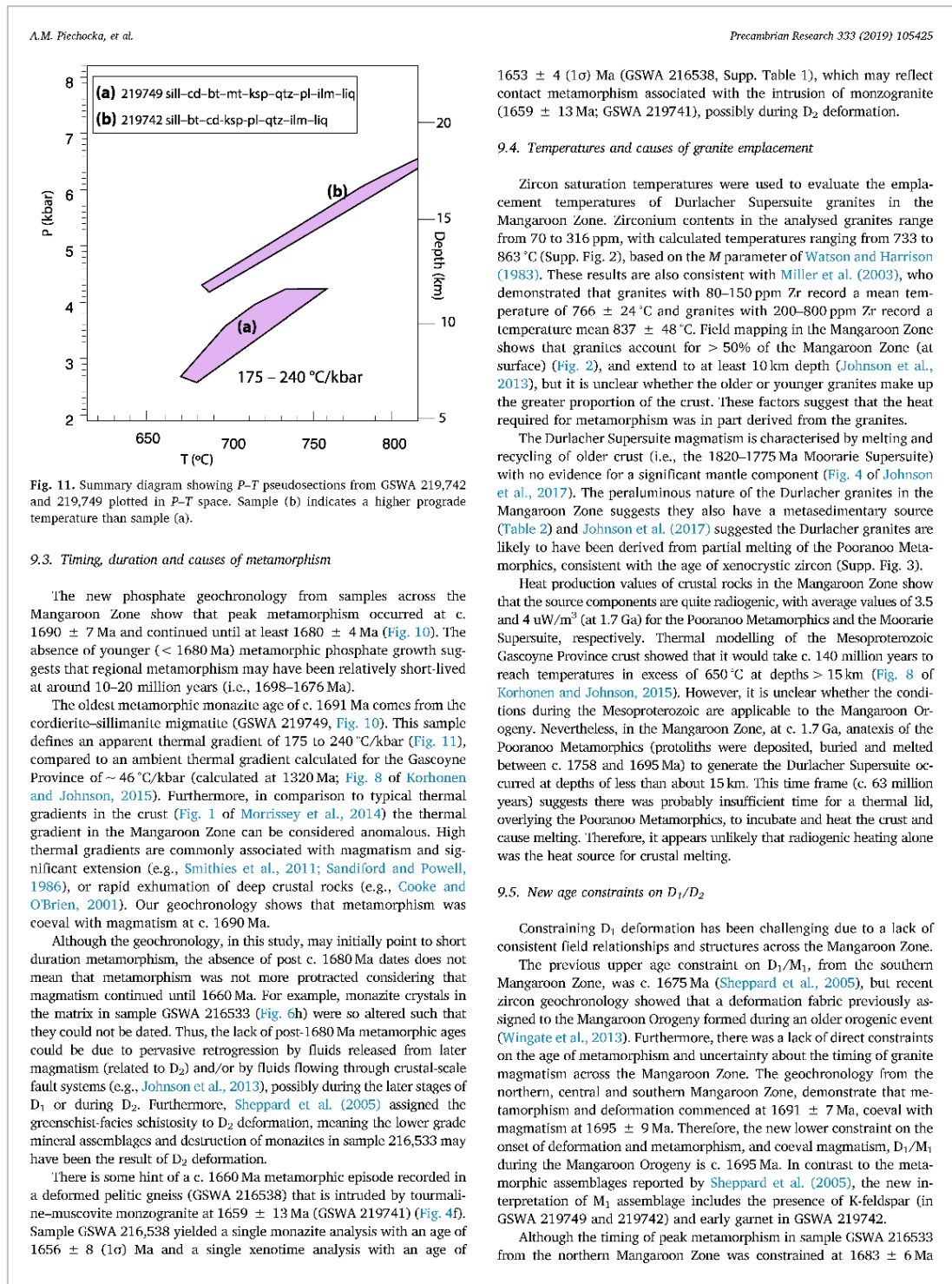
9. Discussion

Prior to the study of Sheppard et al. (2005), the deformation fabrics and magmatism observed in the Mangaroon Zone were attributed to the 1820–1770 Ma Capricorn Orogeny. However, subsequent field mapping and SHRIMP U–Pb zircon geochronology in the southern part of the Mangaroon Zone, revealed an orogenic event at c. 1680–1620 Ma (Sheppard et al., 2005). Although this study defined the approximate timing of the Mangaroon Orogeny, there remains significant uncertainty on the timing and duration of metamorphism and magmatism, and how these processes relate to each other.

9.1. Duration of magmatism associated with the Mangaroon Orogeny

Before this study, the age range for the intrusion of the Durlacher Supersuite was 1680–1620 Ma (Sheppard et al., 2005). The monazite





based on data from monazite inclusions in garnet cores and monazite within matrix quartz, the timing of foliation development and the growth of garnet rims could not be dated due to severe retrogression and small size of the matrix monazite. However, recent zircon geochronology from granites in the northern Mangaroon Zone, only ~700 m to the west of GSWA 216533, may be used to interpret the timing of foliation development in sample GSWA 216533. There, an undeformed muscovite–tourmaline monzogranite with an age of 1673 ± 4 Ma (GSWA 216531; Wingate et al., 2019b) intrudes a foliated biotite–metagranodiorite with an age of 1688 ± 4 Ma (GSWA 216532; Wingate et al., 2019a). This relationship indicates that the foliation (D_1) in the garnet–biotite–epidote pelitic gneiss (GSWA 216533) may have developed between 1688 ± 4 and 1673 ± 4 Ma, which overlaps with the timing of D_1 in the central (GSWA 219742) and southern Mangaroon Zone (GSWA 219749) at 1685 ± 9 Ma and 1691 ± 7 Ma, respectively. Although, the timing of D_1 deformation is constrained the lack of megascopic structures across the Mangaroon Zone, typical of compressional or transpressional settings, suggests that D_1 may have occurred in an extensional setting.

Compared to the limited structures associated with D_1 deformation, D_2 deformation produced a pervasive schistosity, metre- to kilometre-scale upright folds, and retrogression of D_1 metamorphic minerals to greenschist facies assemblages (Sheppard et al., 2005; 2010b). The age constraints for granite magmatism in the Mangaroon Zone show that there may have been two pulses of magmatism associated with the Durlacher Supersuite. The first pulse at 1695–1673 Ma, coincides with D_1 deformation and peak metamorphism. The second pulse of magmatism at c. 1660 Ma may be linked with D_2 deformation. The existing constraints for D_2 come from deformed granites older than c. 1675 Ma that suggests regional deformation occurred after 1675 Ma. The interpreted crystallisation age of 1659 ± 13 Ma (GSWA 219741), from the undeformed tourmaline–muscovite monzogranite, provides a new minimum age for D_2 , which is constrained to the interval c. 1675–1660 Ma.

9.6. Geodynamic setting of the Mangaroon Zone

Many models have been invoked for low- P , high- T metamorphism, but the most common one for Proterozoic Australian orogens is the thermal lid model. In this section we will discuss how the commonly applied thermal lid model does not apply to the metamorphism associated with the Mangaroon Orogeny. Any model for the Mangaroon Orogeny must explain the following:

- burial and melting of the protoliths to the Pooranoo Metamorphics took place within c. 63 million years of them being deposited;
- granitic magmatism at c. 1695 Ma was coeval with peak metamorphism at c. 1691 Ma during D_1 deformation (Fig. 10);
- the Mangaroon Orogeny was associated with an anomalous thermal gradient 175 to 240 °C/kbar (Fig. 11) compared to an ambient thermal gradient of ~46 °C/kbar for the Gascoyne Province;
- the presence of rare grains of garnet at one locality, suggests higher pressures than those recorded at the peak during the prograde history, implying a broad clockwise metamorphic P – T path (Fig. 9b);

The thermal lid model requires high concentrations of heat-producing elements in the crust combined with an incubation period typically lasting > 100 million years (Korhonen et al., 2015, 2017; Morrissey et al., 2014). Although the crust in the Mangaroon Zone was radiogenic at c. 1.7 Ga, deposition, burial and melting of the Pooranoo Metamorphics (source rocks for the Durlacher Supersuite) occurred within c. 63 million years. Therefore, it is unlikely that there was sufficient time for radiogenic heat build up to cause the upper crustal metamorphism during the Mangaroon Orogeny. If radiogenic heating alone was unlikely the cause of the crustal melting, another heat source is required. For instance, the elevated Moho below the Mangaroon Zone (Johnson et al., 2013) and the anomalous thermal gradient during peak metamorphism, which is commonly associated with magmatism and significant extension (Smithies et al.,

2011), suggests lithospheric thinning during the Mangaroon Orogeny.

Mantle upwelling during lithospheric thinning is a common driver proposed for low- P , high- T metamorphism (Collins, 1994; Vilà et al., 2007). In the Mangaroon Zone there is a lack of evidence for mafic magmatism; therefore, it is difficult to say with certainty that there was a mantle contribution.

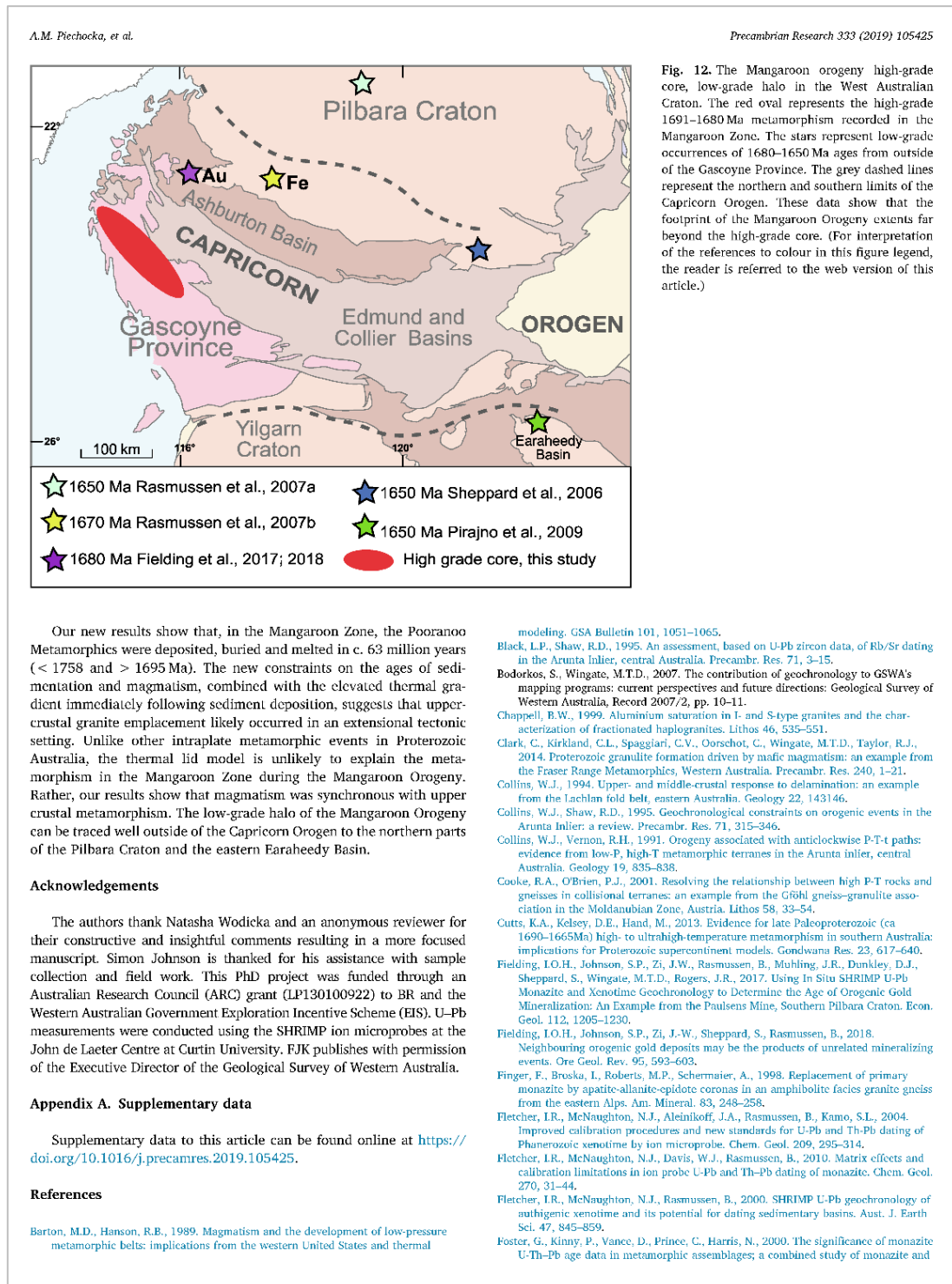
9.7. Mangaroon Orogeny: high-grade core, low-grade halo

Although medium- to high-grade rocks formed during the Mangaroon Orogeny are restricted to the Gascoyne Province, disparate studies in recent years suggest that the effects of the orogeny may be present across much of the West Australian Craton (Fig. 12). For instance, in the Ashburton Basin at the Paulsens Gold Mine, SHRIMP U–Pb monazite dating yielded an age of 1680 ± 9 Ma and at the nearby Belvedere orebody xenotime yielded an age of c. 1680 Ma, both of which are interpreted as the timing of hydrothermal gold mineralisation as a result of fault reactivation during the Mangaroon Orogeny (Fielding et al., 2017, 2018). Further north in the Pilbara Craton, hydrothermal monazite growth occurred at c. 1650 Ma (Rasmussen et al., 2007a), and in the southern Pilbara at Mt Tom Price, hydrothermal xenotime growth occurred at c. 1670 Ma (Rasmussen et al., 2007b). Both these SHRIMP U–Pb studies attributed phosphate growth to reactivation of pre-existing crustal-scale structures during the Mangaroon Orogeny. Furthermore, shear zones within the Sylvania Inlier in the Pilbara Craton yielded $^{40}\text{Ar}/^{39}\text{Ar}$ mica ages of c. 1650 Ma (Sheppard et al., 2006). Similarly, a c. 1650 Ma $^{40}\text{Ar}/^{39}\text{Ar}$ mica age, from quartz–mica schist, was identified in the Earraheedy Basin, and was interpreted as the timing of deformation within the Stanley Fold Belt (Pirajno et al., 2009). These scattered low-grade events highlight that what initially appeared to be a very localised high-grade event in the Mangaroon Zone had a significant regional impact across the West Australian Craton.

Tectonic activity occurring synchronously with the Mangaroon Orogeny is also known more widely in western and central Australia. For instance, in the adjacent Albany–Fraser Orogen, two tectonic episodes are known: the 1710–1650 Ma Biranup Orogeny (Spaggiari et al., 2014) and, the c. 1680 Ma high-grade metamorphic Zanthus Event (Kirkland et al., 2011). In the Gawler Craton of the South Australia Craton (Fig. 1), ultra-high temperature metamorphism at 1690–1650 Ma was the result of initial crustal thinning followed by crustal thickening (Cutts et al., 2013). In the Arunta Inlier of the North Australian Craton (Fig. 1) the Argilke Event at 1680–1660 Ma involved magmatism, migmatitisation and metamorphism (Collins and Shaw, 1995; Black and Shaw, 1995) and high temperature metamorphism associated with the 1640–1635 Ma Liebig Orogeny was the result of the accretion of the Warumpi Province onto the North Australian Craton (Scrimgeour et al., 2005). These (presently) separated occurrences of c. 1.7 Ga tectonism in the western, northern and southern parts of Australia suggests that the Mangaroon Orogeny was perhaps part of a continent-scale tectonic event.

10. Conclusions

The combined U–Pb geochronology and P – T results suggest that upper crustal metamorphism at 1691 ± 7 Ma (665–755 °C and 2.7–4.3 kbar) coincided with the oldest phases of the Durlacher Supersuite coeval at 1695 ± 9 Ma, and continued until 1680 ± 4 Ma, with continued magmatism until c. 1660 Ma, in the Mangaroon Zone. The monazite geochronology shows that magmatism commenced at least 15 million years earlier than previously thought. Although the geochronology suggests a short duration of metamorphism (~22 million years), associated with D_1 , the magmatism continued until c. 1660 Ma. The absence of robust metamorphic dates younger than c. 1680 Ma does not imply that metamorphism ceased. Rather, the absence of dates is likely due to the severe destruction of matrix monazite, possibly related to the continued magmatism. A low-grade schistosity fabric was previously assigned to D_2 deformation; therefore, there is indication of continued metamorphism.



A.M. Piechocka, et al.

Precambrian Research 333 (2019) 105425

- garnet chronometry. *Earth Planet. Sci. Lett.* 181, 327–340.
- Glasson, K.J., Johnson, T.E., Kirkland, C.L., Gardiner, N.J., Clark, C., Blereau, E., Hartnady, M.L., Spaggiari, C., Smithies, H., 2019. A window into an ancient backarc? The magmatic and metamorphic history of the Fraser Zone, Western Australia. *Precamb. Res.* 323, 55–69.
- GSWA, 2016a. 1500 000 State interpreted bedrock geology of Western Australia, 2016: Geological Survey of Western Australia, digital data layer. www.dmp.wa.gov.au/geoview.
- GSWA, 2016b. Compilation of geochronology information, 2016 update, digital data product. www.dmp.wa.gov.au/geoview.
- Holland, T.J.B., Powell, R., 2011. An improved and extended internally consistent thermodynamic dataset for phases of petrological interest, involving a new equation of state for solids. *J. Metamorph. Geol.* 29, 333–383.
- Johnson, S.P., Sheppard, S., Rasmussen, B., Wingate, M.T.D., Kirkland, C.L., Muhling, J.R., Fletcher, I.R., Belousova, E.A., 2011. Two collisions, two sutures: punctuated pre-1950Ma assembly of the West Australian Craton during the Ophthalmanian and Glenburgh Orogenies. *Precamb. Res.* 189, 239–262.
- Johnson, S.P., Korhonen, F.J., Kirkland, C.L., Cliff, J.B., Belousova, E.A., Sheppard, S., 2017. An isotopic perspective on growth and differentiation of Proterozoic orogenic crust: From subduction magmatism to cratonization. *Lithos* 268, 76–86.
- Johnson, S.P., Thorne, A.M., Tyler, I.M., Korsch, R.J., Kennett, B.L.N., Cutten, H.N., Goodwin, J., Blay, O., Blowett, R.S., Joly, A., Dentith, M.C., Aitken, A.R.A., Holzschuh, J., Salmon, M., Reading, A., Heinson, G., Boren, G., Ross, J., Costelloe, R.D., Fomin, T., 2013. Crustal architecture of the Capricorn Orogen, Western Australia and associated metallogeny. *Aust. J. Earth Sci.* 60, 681–705.
- Kirkland, C.L., Spaggiari, C.V., Pawley, M.J., Wingate, M.T.D., Smithies, R.H., Howard, H.M., Tyler, I.M., Belousova, E.A., Poujol, M., 2011. On the edge: U–Pb, Lu–Hf, and Sm–Nd data suggests reworking of the Yilgarn craton margin during formation of the Albany–Fraser Orogen. *Precamb. Res.* 187, 223–247.
- Korhonen, F.J., Johnson, S.P., 2015. The role of radiogenic heat in prolonged intraplate reworking: the Capricorn Orogen explained? *Earth Planet. Sci. Lett.* 428, 22–32.
- Korhonen, F.J., Johnson, S.P., Wingate, M.T.D., Kirkland, C.L., Fletcher, I.R., Dunkley, D.J., Roberts, I.M., Sheppard, S., Muhling, J.R., Rasmussen, B., 2017. Radiogenic heating and craton-margin plate stresses as drivers for intraplate orogeny. *J. Metamorph. Geol.* 35, 631–661.
- Loosveld, R.J.H., Etheridge, M.A., 1990. A model for low-pressure facies metamorphism during crustal thickening. *J. Metamorph. Geol.* 8, 257–267.
- Ludwig, K.R., 2009. *Squid 2.50, A User's Manual*. Berkeley Geochronology Centre Special Publication 95.
- Martin, D.M., Sheppard, S., Thorne, A., Farrell, T.R., Groenewald, P.B., 2006. Proterozoic Geology of the Western Capricorn Orogen - a field guide: Geological Survey of Western Australia, Record 2006/18, p. 43.
- McLaren, S., Sandiford, M., Powell, R., 2005. Contrasting styles of Proterozoic crustal evolution: a hot-plate tectonic model for Australian terranes. *Geology* 33, 673–676.
- Miller, C.F., Meschier McDowell, S., Mapes, R.W., 2003. Hot and cold granites? Implications of zircon saturation temperatures and preservation of inheritance. *Geology* 31, 529–532.
- Morrissey, L.J., Hand, M., Raimondo, T., Kelsey, D.E., 2014. Long-lived high-T, low-P granulite facies metamorphism in the Arunta Region, central Australia. *J. Metamorph. Geol.* 32 (1), 25–47.
- Nelson, D.R., 1998. 142855: porphyritic monzogranite, Anderson well; in *Compilation of SHRIMP U–Pb zircon geochronology data, 1997: Western Australia Geological Survey, Record 1998/2*, 194–197.
- Nelson, D.R., 2002. 169053: biotite muscovite monzogranite, Fraser Well; in *Compilation of geochronology data, 2001: Western Australia Geological Survey, Record 2002/2*, p. 35–38.
- Nelson, D.R., 2005. 178027: biotite-muscovite granodiorite, Mangaroon Homestead; *Geochronology dataset 536; in Compilation of geochronology data, June 2006 update; Western Australia Geological Survey*.
- Occhipinti, S.A., Sheppard, S., Passchier, C., Tyler, I.M., Nelson, D.R., 2004. Palaeoproterozoic crustal accretion and collision in the southern Capricorn Orogen: the Glenburgh Orogeny. *Precamb. Res.* 128, 237–255.
- Occhipinti, S.A., Reddy, S.M., 2009. Neoproterozoic reworking of the Palaeoproterozoic Capricorn Orogen of Western Australia and implications for the amalgamation of Rodinia. *Geological Society, London, Special Publications* 327, 445–456.
- Oliver, N.J.S., Zakowski, S., 1995. Timing and geometry of deformation, low-pressure metamorphism and anatexis in the eastern Mt Lofty Ranges: the possible role of extension. *Aust. J. Earth Sci.* 42, 501–507.
- Pearson, J.M., 1996. Alkaline rocks of the Gifford Creek Complex, Gascoyne Province, Western Australia — their petrogenetic and tectonic significance. PhD thesis (unpublished). University of Western Australia, Perth.
- Piechocka, A.M., Gregory, C.J., Zi, J.-W., Sheppard, S., Wingate, M.T.D., Rasmussen, B., 2017. Monazite trumps zircon: applying SHRIMP U–Pb geochronology to systematically evaluate emplacement ages of leucocratic, low-temperature granites in a complex Precambrian orogen. *Contrib. Miner. Petrol.* 172, 1–17.
- Piechocka, A.M., Sheppard, S., Fitzsimons, I.C.W., Johnson, S.P., Rasmussen, B., Jourdan, F., 2018. Neoproterozoic ⁴⁰Ar/³⁹Ar mica ages mark the termination of a billion years of intraplate reworking in the Capricorn Orogen, Western Australia. *Precamb. Res.* 310, 391–406.
- Piechocka, A.M., Zi, J.W., Gregory, C.J., Sheppard, S., Rasmussen, B., 2019. SHRIMP U–Pb phosphate dating shows metamorphism was synchronous with magmatism during the Palaeoproterozoic Capricorn Orogeny. *Aust. J. Earth Sci.* 66, 973–990.
- Pirajno, F., Hocking, R.M., Reddy, S.M., Jones, A.J., 2009. A review of the geology and geodynamic evolution of the Palaeoproterozoic Eoraheedy Basin, Western Australia. *Earth Sci. Rev.* 94, 39–77.
- Rasmussen, B., Fletcher, I.R., Muhling, J.R., 2007a. In situ U–Pb dating and element mapping of three generations of monazite: unravelling cryptic tectonothermal events in low-grade terranes. *Geochim. Cosmochim. Acta* 71, 670–690.
- Rasmussen, B., Fletcher, I.R., Muhling, J.R., Thorne, W.S., Broadbent, G.C., 2007b. Prolonged history of episodic fluid flow in giant hematite ore bodies: evidence from in situ U–Pb geochronology of hydrothermal xenotime. *Earth Planet. Sci. Lett.* 258, 249–259.
- Sandiford, M., Hand, M., 1998. Controls on the locus of intraplate deformation in central Australia. *Earth Planet. Sci. Lett.* 162, 97–110.
- Sandiford, M., Powell, R., 1986. Deep crustal metamorphism during continental extension: modern and ancient examples. *Earth Planet. Sci. Lett.* 79, 151–158.
- Scaillet, B., Holtz, F., Pichavant, M., 2016. Experimental Constraints on the Formation of Silicic Magmas. *Elements* 12, 109–114.
- Serlingour, L.R., Kinny, P.D., Close, D.F., Edgoose, C.J., 2005. High-T granulites and polymetamorphism in the southern Arunta Region, central Australia. Evidence for a 1.64 Ga accretional event. *Precamb. Res.* 142, 1–27.
- Sheppard, S., Bodorkos, S., Johnson, S.P., Wingate, M.T.D., Kirkland, C.L., 2010a. The Palaeoproterozoic Capricorn Orogeny: Intracontinental Reworking Not Continent–Continent Collision: Geological Survey of Western Australia, Report 108, p. 33.
- Sheppard, S., Farrell, T.R., Bodorkos, S., Hollingsworth, D., Tyler I.M., Pirajno, F., 2006. Late Palaeoproterozoic (1680–1620) sedimentation, magmatism, and tectonism in the Capricorn Orogen. In: GSWA 2006 extended abstracts: promoting the prospectivity of Western Australia: Geological Survey of Western Australia, Record 2006/3, pp. 11–12.
- Sheppard, S., Johnson, S.P., 2016. Pooranoo Metamorphics (P-PO-md): Geological Survey of Western Australia, WA Geology Online, Explanatory Notes extract, viewed 20 November 2017. www.dmp.wa.gov.au/ens.
- Sheppard, S., Johnson, S.P., Wingate, M.T.D., Kirkland, C.L., Pirajno, F., 2010b. Explanatory notes for the Gascoyne Province: Geological Survey of Western Australia, 1:100 000 Explanatory Notes, p. 336.
- Sheppard, S., Occhipinti, S.A., Nelson, D.R., 2005. Intracontinental reworking in the Capricorn Orogen, Western Australia: the 1680–1620 Ma Mangaroon Orogeny. *Aust. J. Earth Sci.* 52, 443–460.
- Sheppard, S., Rasmussen, B., Muhling, J.R., Farrell, T.R., Fletcher, I.R., 2007. Grenvillian-aged orogenesis in the Palaeoproterozoic Gascoyne Complex, Western Australia: 1030–950 Ma reworking of the Proterozoic Capricorn Orogen. *J. Metamorph. Geol.* 25, 477–494.
- Smithies, R.H., Howard, H.M., Evins, P.M., Kirkland, C.L., Kelsey, D.E., Hand, M., Wingate, M.T.D., Collins, A.S., Belousova, E., 2011. High-Temperature Granite Magmatism, Crust–Mantle Interaction and the Mesoproterozoic Intracontinental Evolution of the Musgrave Province, Central Australia. *J. Petrol.* 52, 931–958.
- Spaggiari, C.V., Kirkland, C.L., Smithies, R.H., Wingate, M.T.D., 2014. Tectonic links between Proterozoic sedimentary cycles, basin formation and magmatism in the Albany–Fraser Orogen: Geological Survey of Western Australia, Report 133.
- Stacey, J.S., Kramers, J.D., 1975. Approximation of terrestrial lead isotope evolution by a two-stage model. *Earth Planet. Sci. Lett.* 26, 207–221.
- Stern, R.A., Rainbird, R.H., 2001. Advancements in xenotime U–Pb geochronology by ion microprobe. *Eleventh V.I. Goldschmidt Conference Lunar and Planetary Science Institute, Houston*.
- Stern, T.A., Sanborn, N., 1998. Monazite U–Pb and Th–Pb geochronology by high-resolution secondary ion mass spectrometry. *Radiogenic Age and Isotope Studies: Report 11, Geological Survey of Canada, Current Research 1998-F*, 1–18.
- Vilá, M., Pin, C., Liesa, M., Enrique, P., 2007. LPHT metamorphism in a late orogenic transpressional setting, Albará Massif, NE Iberia: implications for the geodynamic evolution of the Variscan Pyrenees. *J. Metamorph. Geol.* 25, 321–347.
- Watson, E.B., Harrison, T.M., 1983. Zircon saturation revisited: temperature and composition effects in a variety of crustal magma types. *Earth Planet. Sci. Lett.* 64, 295–304.
- White, R.W., Powell, R., Johnson, T.E., 2014. The effect of Mn on mineral stability in pelites revisited: new a–x relations for manganese-bearing minerals. *J. Metamorph. Geol.* 32, 809–828.
- Wickham, S.M., Oxburgh, E.R.S., 1987. Low-pressure regional metamorphism in the Pyrenees and its implications for the thermal evolution of rifted continental crust. *Philosophical Transactions of the Royal Society of London. Series A, Mathematical and Physical Sciences* 321, 219–242.
- Wingate, M.T.D., Kirkland, C.L., Korhonen, F.J., 2013. 208318: metagranite, Brown Well; *Geochronology Record 1174: Geological Survey of Western Australia*, p. 4.
- Wingate, M.T.D., Kirkland, C.L., Bodorkos, S., S., Sheppard, Farrell, T.R., 2009. 183255: metasandstone, Mount Samuel; *Geochronology Record 772: Geological Survey of Western Australia*, p. 5.
- Wingate, M.T.D., Lu, Y., Korhonen, F.J., Johnson, S.P., 2019a. 216532: granodiorite gneiss, Mountain Creek; *Geochronology Record 1559: Geological Survey of Western Australia*, p. 4.
- Wingate, M.T.D., Lu, Y., Korhonen, F.J., Johnson, S.P., 2019b. 216531: muscovite monzogranite, Mountain Creek; *Geochronology Record 1558: Geological Survey of Western Australia*, p. 4.
- Wingate, M.T.D., Lu, Y., Korhonen, F.J., Johnson, S.P., 2018. 195888: metanzogranite, Brown Well; *Geochronology Record 1552: Geological Survey of Western Australia*, p. 6.
- Wingate, M.T.D., Lu, Y., Korhonen, F.J., Johnson, S.P., 2017. 208365: biotite metagranodiorite, Kimbers well; *Geochronology Record 1356: Geological Survey of Western Australia*, p. 4.
- Zen, E., 1986. Aluminum Enrichment in Silicate Melts by Fractional Crystallization: Some Mineralogical and Petrographic Constraints. *J. Petrol.* 27, 1095–1117.

A.3 Paper 3 (published)

Statement of Authorship

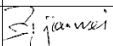
Title of Paper	Monazite trumps zircon: applying SHRIMP U–Pb geochronology to systematically evaluate emplacement ages of leucocratic, low-temperature granites in a complex Precambrian orogen
Publication Status	Published
Publication Details	Piechocka, A. M., Gregory, C. J., Zi, J.-W., Sheppard, S., Wingate, M. T. D., and Rasmussen, B., 2017, Monazite trumps zircon: applying SHRIMP U–Pb geochronology to systematically evaluate emplacement ages of leucocratic, low-temperature granites in a complex Precambrian orogen: Contributions to Mineralogy and Petrology 172, 1–17

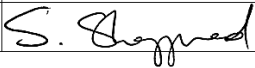
Author Contributions

By signing the Statement of Authorship, each author certifies that their stated contribution to the publication is accurate and that permission is granted for the publication to be included in the candidate's thesis.

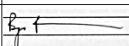
Name of Principal Author (Candidate)	Agnieszka M. Piechocka		
Contribution to the Paper	Conducted geological field work (mapping and sampling), prepared samples for SHRIMP U–Pb monazite analysis, conducted the analysis. Data interpretation and wrote the manuscript.		
Signature		Date	13/11/2018

Name of Co-Author	Courtney J. Gregory		
Contribution to the Paper	Provided SHRIMP U–Pb monazite data to be incorporated in the paper. Manuscript review.		
Signature		Date	18/03/2019

Name of Co-Author (Supervisor)	Jian-Wei Zi		
Contribution to the Paper	Jian-Wei assisted with SHRIMP set-up and data processing for the additional analysis. Reviewed the geochronology section of the manuscript.		
Signature		Date	16/03/2019

Name of Co-Author (Supervisor)	Stephen Sheppard		
Contribution to the Paper	Initiated the study and the data interpretation for this paper. Assisted with the drafting of the paper.		
Signature		Date	31/10/2018

Name of Co-Author	Michael T. Wingate		
Contribution to the Paper	Provided the U–Pb zircon geochronology data and interpretation of geochronology results. Assisted with manuscript review.		
Signature		Date	31/10/2018

Name of Co-Author (Supervisor)	Birger Rasmussen		
Contribution to the Paper	Final manuscript revision.		
Signature		Date	19/03/2019

Copyright Information

The information below is linked to the original published article in Contributions to Mineralogy and Petrology:

<https://link.springer.com/article/10.1007/s00410-017-1386-5#copyrightInformation>

Copyright information

© The Author(s) 2017

Open Access

This article is distributed under the terms of the Creative Commons Attribution 4.0 International License (<http://creativecommons.org/licenses/by/4.0/>), which permits unrestricted use, distribution, and reproduction in any medium, provided you give appropriate credit to the original author(s) and the source, provide a link to the Creative Commons license, and indicate if changes were made.

Letter of authority to reprint

RE: {SrvReqNo:[8001359073]} FW: Permission to publish article in PhD thesis

Journalpermissions <journalpermissions@springernature.com>

Mon 1/10/2018 7:17 PM

To: Nishka Piechocka <nishka.piechocka@postgrad.curtin.edu.au>;

Cc: onlineserviceSAP <onlineservice@springernature.com>;

Dear Nishka,

Thank you for your email. This work is licensed under a Creative Commons Attribution 4.0 International License, which permits unrestricted use, distribution, and reproduction in any medium, provided you give appropriate credit to the original author(s) and the source, provide a link to the Creative Commons license, and indicate if changes were made. **You are not required to obtain permission to reuse this article.** The images or other third party material in this article are included in the article's Creative Commons license, unless indicated otherwise in the credit line; if the material is not included under the Creative Commons license, users will need to obtain permission from the license holder to reproduce the material. To view a copy of this license, visit <http://creativecommons.org/licenses/by/4.0/>.

You do not need a license to reuse this material J

Best wishes,
Oda

Oda Siqveland
Permissions Assistant

SpringerNature
The Campus, 4 Crinan Street, London N1 9XW,
United Kingdom
T +44 (0) 207 014 6851

<http://www.nature.com>
<http://www.springer.com>
<http://www.palgrave.com>

Reprint of Paper

Contrib Mineral Petrol (2017) 172:63
DOI 10.1007/s00410-017-1386-5



ORIGINAL PAPER

Monazite trumps zircon: applying SHRIMP U–Pb geochronology to systematically evaluate emplacement ages of leucocratic, low-temperature granites in a complex Precambrian orogen

Agnieszka M. Piechocka¹ · Courtney J. Gregory¹ · Jian-Wei Zi¹ · Stephen Sheppard¹ · Michael T. D. Wingate² · Birger Rasmussen¹

Received: 13 January 2017 / Accepted: 24 June 2017 / Published online: 7 July 2017
© The Author(s) 2017. This article is an open access publication

Abstract Although zircon is the most widely used geochronometer to determine the crystallisation ages of granites, it can be unreliable for low-temperature melts because they may not crystallise new zircon. For leucocratic granites U–Pb zircon dates, therefore, may reflect the ages of the source rocks rather than the igneous crystallisation age. In the Proterozoic Capricorn Orogen of Western Australia, leucocratic granites are associated with several pulses of intracontinental magmatism spanning ~800 million years. In several instances, SHRIMP

U–Pb zircon dating of these leucocratic granites either yielded ages that were inconclusive (e.g., multiple concordant ages) or incompatible with other geochronological data. To overcome this we used SHRIMP U–Th–Pb monazite geochronology to obtain igneous crystallisation ages that are consistent with the geological and geochronological framework of the orogen. The U–Th–Pb monazite geochronology has resolved the time interval over which two granitic supersuites were emplaced; a Paleoproterozoic supersuite thought to span ~80 million years was emplaced in less than half that time (1688–1659 Ma) and a small Meso- to Neoproterozoic supersuite considered to have been intruded over ~70 million years was instead assembled over ~130 million years and outlasted associated regional metamorphism by ~100 million years. Both findings have consequences for the duration of associated orogenic events and any estimates for magma generation rates. The monazite geochronology has contributed to a more reliable tectonic history for a complex, long-lived orogen. Our results emphasise the benefit of monazite as a geochronometer for leucocratic granites derived by low-temperature crustal melting and are relevant to other orogens worldwide.

Communicated by Franck Poitrasson.

The original version of this article was revised: Figures 1 and 2 were incorrect and they have been corrected.

Electronic supplementary material The online version of this article (doi:10.1007/s00410-017-1386-5) contains supplementary material, which is available to authorized users.

✉ Agnieszka M. Piechocka
nishka.piechocka@postgrad.curtin.edu.au

Courtney J. Gregory
courtneyjaynegregory@gmail.com

Jian-Wei Zi
j.zi@curtin.edu.au

Stephen Sheppard
stephen.sheppard@curtin.edu.au

Michael T. D. Wingate
michael.wingate@dmp.wa.gov.au

Birger Rasmussen
b.rasmussen@curtin.edu.au

¹ Department of Applied Geology, Curtin University, Kent Street, Bentley, WA 6102, Australia

² Geological Survey of Western Australia, 100 Plain Street, East Perth, WA 6004, Australia

Keywords Monazite · SHRIMP geochronology · Leucocratic granite · Pegmatite · Proterozoic · Capricorn Orogen

Introduction

Leucocratic granites are peraluminous [i.e., alumina saturation index (ASI) = molar $Al_2O_3/(CaO + Na_2O + K_2O) > 1$; Scaillet et al. 2016; Zen 1986] rocks containing <5 vol.% mafic minerals (Le Maitre 1989). They are typically derived from low-temperature (<750 °C; Ayres et al. 1997; Scaillet et al. 1995) partial melting of crustal sources without direct

mass input from the mantle (Gao et al. 2017; Patiño and Harris 1998). Leucocratic granites are common in intracontinental and collisional settings and typically account for a small proportion of all granites in orogenic belts (Gilotti and McClelland 2005; Harrison et al. 1999; Kemp and Hawkesworth 2003). However, they are important for determining the tectonic history of orogenic belts (Crowley et al. 2008) as they commonly form during periods of crustal thickening (Brown 1994). Kemp and Hawkesworth (2003) divided leucocratic granites into two types on the basis of their Sr concentrations: a low-Sr (<200 ppm Sr) type formed by melting in the upper continental crust (e.g., leucogranites of the Himalayan Orogen), and the less common high-Sr (250–450 ppm) types related to deeper crustal sources (e.g., Glenelg River Complex, southeastern Australia).

Dating leucocratic, low-temperature granites (*sensu lato*) using U–Pb zircon geochronology can be challenging due to the zircon population being dominated by inherited grains (Bea et al. 2007; Harrison et al. 1999; Miller et al. 2003; Schärer et al. 1986). Experimental studies have shown that zircon solubility is mainly governed by temperature and melt composition, and for typical peraluminous melts zircon solubility ranges from ~100 ppm dissolved at 750 °C to 1300 ppm at 1020 °C (Boehnke et al. 2013; Watson and Harrison 1983). This means that the low solubility of Zr in low-temperature (<800 °C) crustal melts limits the amount of zircon that can dissolve during partial melting and re-precipitate during crystallisation. These findings are consistent with observations that low-temperature granites (mean 766 ± 24 °C) with abundant inherited zircon typically have lower Zr concentrations (80–150 ppm) compared with high-temperature granites (200–800 ppm, mean 837 ± 48 °C) with minimal inheritance (Miller et al. 2003).

Although zircon is most widely used to constrain crystallisation ages of granites, monazite geochronology has been employed sporadically to date the crystallisation age of granites (e.g., Grosse et al. 2009; Harrison et al. 1999; Kusiak et al. 2014; Miller and Mittlefehldt 1982; Parrish and Tirrul 1989; Townsend et al. 2001; Williams et al. 1983). However, there has been little attempt to systematically evaluate the suitability of monazite for geochronology of leucocratic granite types even though monazite appears to be common in a range of granites (Bea 1996; Montel 1993; Rapp and Watson 1986). The stability of monazite is considered to be dependent on pressure, temperature, bulk rock chemistry and interacting fluid chemistry (Budzyń et al. 2011; Poitrasson et al. 1996). It has been suggested that monazite is stable in host compositions that are low in Ca (<0.7%) in contrast to higher Ca (>1.8%) which favour allanite growth (Lee and Dodge 1964; Montel 1993; Parrish 1990), although monazite and allanite do coexist in peraluminous granites (Broska et al. 2000). Furthermore, although not widespread, instances of monazite inheritance

in granites have been documented (Copeland et al. 1988; Parrish 1990).

Leucocratic granites are widespread in the Proterozoic Gascoyne Province, Capricorn Orogen of Western Australia, and apparently formed during several episodes of magmatism (Sheppard et al. 2010b). The crystallisation ages of several leucocratic granites are not well defined by U–Pb zircon geochronology, which has created uncertainty about the duration and distribution of some of the granite supersuites and related orogenic events in the province. In this paper we use SHRIMP U–Th–Pb monazite geochronology to re-evaluate the emplacement ages of these granites in order to obtain reliable igneous crystallisation ages consistent with the existing geological framework. In turn, this provides better constraints on the duration of granitic magmatism and magma production rates and allows for a more complete magmatic and tectonothermal history of the orogen to be established.

Regional geology

The study area is located in the Capricorn Orogen in Western Australia (Fig. 1), which records the Paleoproterozoic assembly of the West Australian Craton by c. 1950 Ma (Johnson et al. 2011; Occhipinti et al. 2004). Five subsequent, episodic intracontinental reworking and reactivation events spanning nearly 1.5 billion years have shaped the current architecture of this orogen (Bodorkos and Wingate 2007; Korhonen et al. 2015; Sheppard et al. 2005, 2007, 2010a). All of these tectonic events are known from the Gascoyne Province, at the presently exposed western end of the orogen (Fig. 1). Of the five intracontinental reworking events in the Gascoyne Province, two are accompanied by voluminous, mainly high-temperature granitic magmatism (i.e., the Capricorn Orogeny being associated with the 1820–1775 Ma Moorarie Supersuite, and the Mangaroon Orogeny with the 1680–1620 Ma Durlacher Supersuite), whereas a third, spatially restricted event (the Edmondian Orogeny) was accompanied solely by leucocratic granitic magmatism (995–955 Ma Thirty-Three Supersuite) (Sheppard et al. 2010b).

The 1820–1775 Ma Moorarie Supersuite was emplaced during the Capricorn Orogeny (Sheppard et al. 2010a, b) and comprises batholiths and plutons of weakly peraluminous, biotite-bearing monzogranite and granodiorite, with minor syenogranite, tonalite and quartz diorite, although, biotite (–muscovite–tourmaline)-bearing monzogranite is common in the southern Gascoyne Province. Most granites of the Moorarie Supersuite contain little or no xenocrystic zircon so that their igneous crystallisation ages are well constrained. A number of undated plutons have also been assigned to the supersuite on the basis of their field

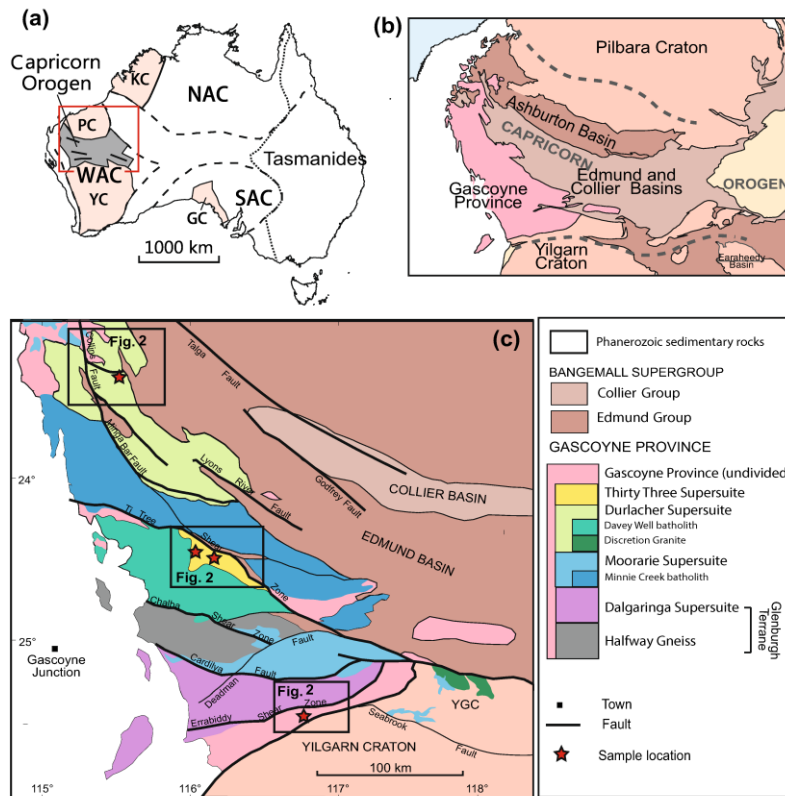


Fig. 1 Regional geological setting of the Capricorn Orogen in relation to Australia (a) and (b) and simplified regional geology of the Gascoyne Province showing discrete fault- bounded E-W trending domains (c). Outlines of study areas are presented in more detail in

Fig. 2. PC Pilbara Craton, YC Yilgarn Craton, WAC West Australian Craton, GC Gawler Craton, NAC North Australian Craton, SAC South Australian Craton, YGC Yarlarveelor Gneiss Complex (adapted from Johnson et al. (2017) and Zi et al. (2015))

relationships, including a pluton of leucocratic granodiorite 12 km long by 5 km wide in the Errabiddy Shear Zone, which marks the boundary between the Yilgarn Craton and Gascoyne Province (Figs. 1, 2a). The pluton, referred to as the Erong Granite, cuts across Paleoproterozoic (c. 1950 Ma) migmatitic structures in surrounding metamorphic rocks (Ocechipinti et al. 2001). However, previous SHRIMP U–Pb zircon dating of the granodiorite (GSWA 139466) only yielded an Archean maximum crystallisation age (Nelson 2000).

The 1680–1620 Ma Durlacher Supersuite comprises peraluminous biotite–muscovite monzogranite, granodiorite,

and syenogranite and some leucocratic muscovite–tourmaline (–biotite) monzogranite (Sheppard et al. 2005, 2010b). Crystallisation ages of the Durlacher Supersuite granites are well constrained by U–Pb zircon geochronology and most granites are older than c. 1659 Ma (Sheppard et al. 2010b) with two main exceptions: the c. 1620 Ma Discretion Granite (Nelson 1998) and one leucocratic sample (Fig. 2b) from the northern Gascoyne Province (GSWA 169092). This leucocratic granite (GSWA 169092) yielded two concordant ages 60 million years apart, none of which could be interpreted unequivocally as the crystallisation age. The younger age component is within error of the

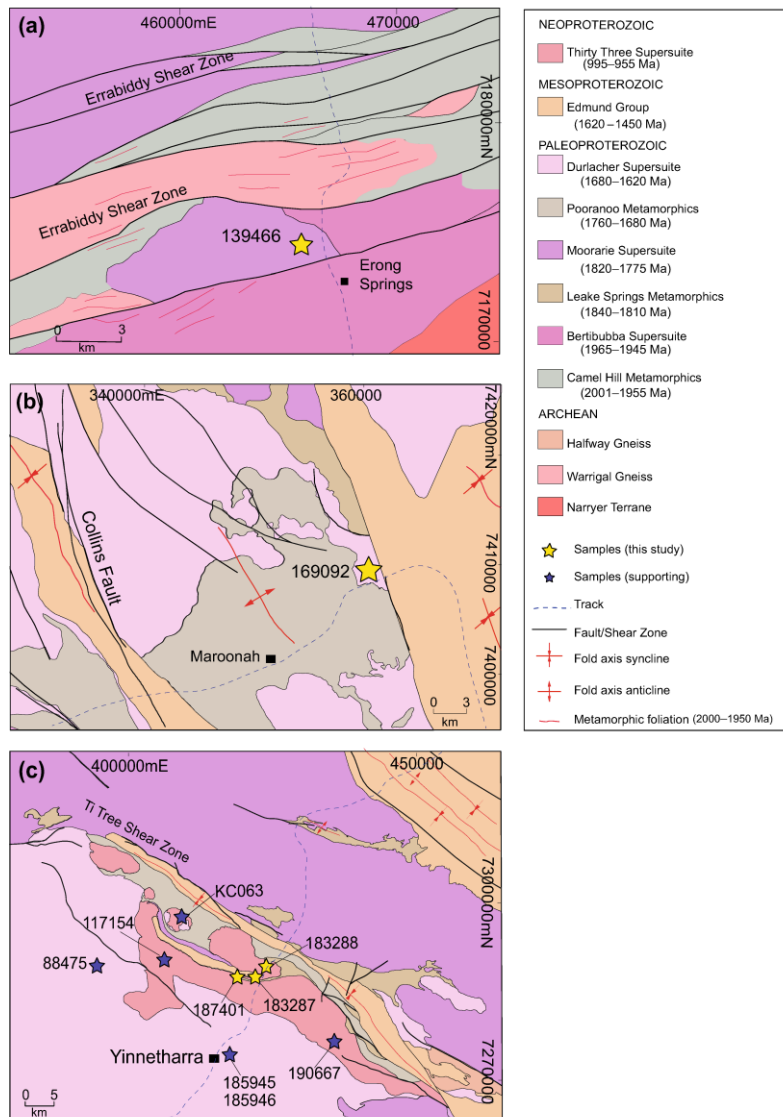


Fig. 2 Local geology of sample areas: **a** the Errabiddy Shear Zone with penetrative deformation fabrics in the older granites and metasedimentary rocks; the star indicates Erong Granite sample GSWA 139466; **b** the northern Gascoyne Province is dominated by Proterozoic granites and folded metasedimentary rocks of the Edmund Group; the star shows the location of Red Rock Bore granite sample GSWA 169092; **c** The area south of the Ti Tree Shear Zone hosts the only occurrence of Thirty-Three Supersuite, in the Gascoyne Province; yellow stars indicate granite samples GSWA 183287, 183288, and 187401. Blue stars indicate supporting samples mentioned throughout the text. The ages for the metamorphic packages are depositional ages. Coordinate system in GDA 1994 MGA Zone 50. Geology polygons and linear features were extracted from the 1:500 000 Geological Map of Western Australia (GSWA 2016a)

igneous crystallisation age of c. 1620 Ma for a batholith (Discretion Granite) about 250 km to the southeast (Fig. 1), and both samples were used to provide a minimum age for the Mangaroon Orogeny (Sheppard et al. 2005).

Intrusion of the 995–955 Ma Thirty-Three Supersuite (Fig. 2c) coincided with deformation and metamorphism of the Edmundian Orogeny within a narrow structural corridor in the centre of the Gascoyne Province (Sheppard et al. 2007). The supersuite crops out over an area 70 km long by 10 km wide and is structurally bound to the north by the Ti Tree Shear Zone (Fig. 2c). The Thirty-Three Supersuite comprises muscovite (–tourmaline) metamonzogranite, biotite–muscovite (–tourmaline) monzogranite and granodiorite and a belt of muscovite–tourmaline and rare-element bearing pegmatites (Sheppard et al. 2010b). Crystallisation ages for Thirty-Three Supersuite granites have proven difficult to resolve via U–Pb zircon geochronology due to the presence of copious xenocrystic zircon. Early indications were that the granites belonged to the Paleoproterozoic Durlacher Supersuite (Culver 2001). This appeared to be consistent with the fact that the leucocratic granites and pegmatites do not intrude Mesoproterozoic sedimentary rocks of the Bangemall Supergroup within the Ti Tree Shear Zone (Fig. 2c). However, later in situ monazite geochronology showed that the granites cut metamorphic fabrics formed at 1030–990 Ma (Sheppard et al. 2007).

Sample descriptions and previous zircon geochronology

Leucocratic granite samples analysed previously using U–Pb zircon geochronology were re-analysed in this study using U–Th–Pb monazite geochronology. Presented below are the original zircon geochronology results for selected peraluminous, leucocratic samples from three generations of Proterozoic magmatism (Table 1). The corresponding monazite geochronology is discussed in the subsequent results section.

GSWA 139466

This sample is a medium-grained, equigranular biotite–muscovite granodiorite that grades into coarser grained granite and pegmatite (Occhipinti et al. 2001). The sample contains minor muscovite and approximately 5% total mafic minerals (biotite, garnet and epidote) (Fig. 3a). Minor sericitisation, quartz recrystallisation and biotite replacement by chlorite is evidence of a weak metamorphic overprint. The zircon crystals are equant to elongate and euhedral pale green to black, 30–250 μm long and 25–80 μm wide, with only a few grains showing subtle internal zoning (Nelson 2000). U–Pb zircon geochronology yielded a date of 2621 ± 9 Ma (all ages in this paper are quoted with 95% uncertainties, unless indicated otherwise) (Nelson 2000). This age is interpreted to represent the age of a xenocrystic population because the pluton intruded 1965–1945 Ma granitic rocks and 2001–1955 Ma metasedimentary rocks (Sheppard et al. 2010b) and crosscuts deformation fabrics related to the 2005–1950 Ma Glenburgh Orogeny (Figs. 2a, 3a). The granodiorite is overprinted by Neoproterozoic (c. 900 Ma) mylonite zones (Occhipinti and Reddy 2009), but this is the only minimum constraint on its age. The low whole-rock Zr content (60 ppm; Table 1) is characteristic of a rock dominated by inherited zircons (Miller et al. 2003), and the combination of high Sr (369 ppm) and low Rb is consistent with the granite having formed by fluid-fluxed melting of muscovite during crustal anatexis (Gao et al. 2017). The rare-earth elements (La, Ce and Nd) are abundant in the whole rock composition (Table 1).

GSWA 169092

This sample is from a leucocratic granite unit located in the northern Gascoyne Province where it intrudes 1840–1810 and 1760–1680 Ma metasedimentary rocks and is overlain by 1620–1450 Ma siliciclastic rocks (Sheppard et al. 2010b) (Fig. 2b). It is a massive, medium-grained biotite–muscovite monzogranite (Figs. 3b, 4b) with minor muscovite and 5% mafic minerals (chlorite, epidote, tourmaline and garnet). Biotite is partly replaced by chlorite, and minor sericite and undulose extinction in the quartz and recrystallised quartz are indicative of a weak metamorphic overprint. The zircon crystals are euhedral to anhedral, 100–250 μm long and 40–180 μm wide, pale brown, dark brown or black, with only a minority of grains displaying subtle zoning (Nelson 2004). Zircon geochronology yielded two age components, one at 1810 ± 22 and 1681 ± 10 Ma, and one concordant analysis at 1619 ± 15 Ma (1σ) which, at the time, was interpreted as the maximum crystallisation age (Nelson 2004) and used by Sheppard et al. (2005) to constrain the younger limits of the 1680–1620 Ma Mangaroon Orogeny. Although a recent

Table 1 Selected whole-rock geochemistry data for leucocratic granite samples

	139466 Biotite-muscovite grano- diorite	169092 Biotite-muscovite mon- zogranite	183287 Muscovite-tourmaline granodiorite	183288 Biotite-muscovite-tour- maline monzogranite	187401 Tourmaline-muscovite monzogranite
(wt%)					
SiO ₂	76.84	73.85	75.51	73.24	73.19
TiO ₂	0.09	0.18	0.05	0.21	0.14
Al ₂ O ₃	13.61	13.86	13.16	13.27	13.83
Fe ₂ O ₃ ^{Total}	0.70	1.59	0.94	1.87	1.21
MnO	0.02	0.06	0.04	0.08	0.02
MgO	0.22	0.38	0.08	0.32	0.20
CaO	1.36	0.81	0.58	0.86	0.77
Na ₂ O	4.91	2.86	2.96	2.77	3.41
K ₂ O	2.20	5.20	4.75	5.24	5.69
P ₂ O ₅	0.05	0.23	0.22	0.15	0.10
LOI	-0.01	0.85	1.57	1.84	1.31
A/CNK ^a	1.05	1.17	1.19	1.13	1.05
(ppm)					
Rb	56	376	687	492	346
Sr	369	63	18	48	59
Th	6	16	8	22	26
U	1	8	14	12	8
Zr	60	70	38	122	113
La	21	21	7	32	40
Ce	42	41	23	70	84
Nd	13	17	12	31	31

^a A/CNK = molar Al₂O₃/(CaO + Na₂O + K₂O)

re-interpretation has concluded the younger analysis to represent Pb loss (M. Wingate pers. comm., March 14, 2016), it remained unclear as to whether the 1681 ± 10 Ma population should be interpreted as the crystallization age or a maximum for crystallization. Whole-rock geochemistry of the geochronology sample (Table 1) indicates that it has low Zr (70 ppm) and low Sr (63 ppm) contents and elevated rare-earth element contents ((La, Ce and Nd).

GSWA 183287, 183288, and 187401

Sample GSWA 183287 is a medium- to coarse-grained, equigranular muscovite–tourmaline granodiorite with 5% tourmaline and garnet (Figs. 3c, 4c). The presence of partly sericitised plagioclase, recrystallised quartz, and minor myrmekitic textures suggest a thermal overprint. The zircons are typically anhedral, up to 150 μ m long, ranging from colourless to brown and most grains have idiomorphic zoning (Kirkland et al. 2009). Zircons from this sample yielded a range of dates between 2085 and 1309 Ma, interpreted as the ages of xenocrystic zircon (Kirkland et al. 2009) because the granite cross-cuts Neoproterozoic metamorphic fabrics in surrounding metasedimentary

rocks (Sheppard et al. 2007). GSWA 183288 is a strongly porphyritic medium-grained, biotite-muscovite–tourmaline monzogranite. It contains about 15% biotite and ~2% muscovite and tourmaline combined. Plagioclase is partially sericitised, quartz is recrystallised, minor myrmekite is developed, and biotite is partially replaced by chlorite. Zircons from this sample yielded a dominant age component at 1648 ± 5 Ma (MSWD = 1.1, $n = 39/41$) with one older analysis at 1755 ± 25 Ma (Wingate et al. in press). This monzogranite also cuts Neoproterozoic metamorphic fabrics, so the dominant zircon population must represent the age of the main source component. In both instances, zircon geochronology was unable to constrain the emplacement age.

Sample GSWA 187401 is a fine- to medium-grained, equigranular tourmaline–muscovite monzogranite that was sampled by GSWA for zircon geochronology, but was not analysed. It contains tourmaline nodules with leucocratic halos (Fig. 4d). The monzogranite contains muscovite, and roughly 5% ferromagnesian minerals (biotite, tourmaline, epidote, and titanite). Recrystallised quartz, minor sericitisation, and myrmekite are indicative of minor post-magmatic deformation (Fig. 3d).

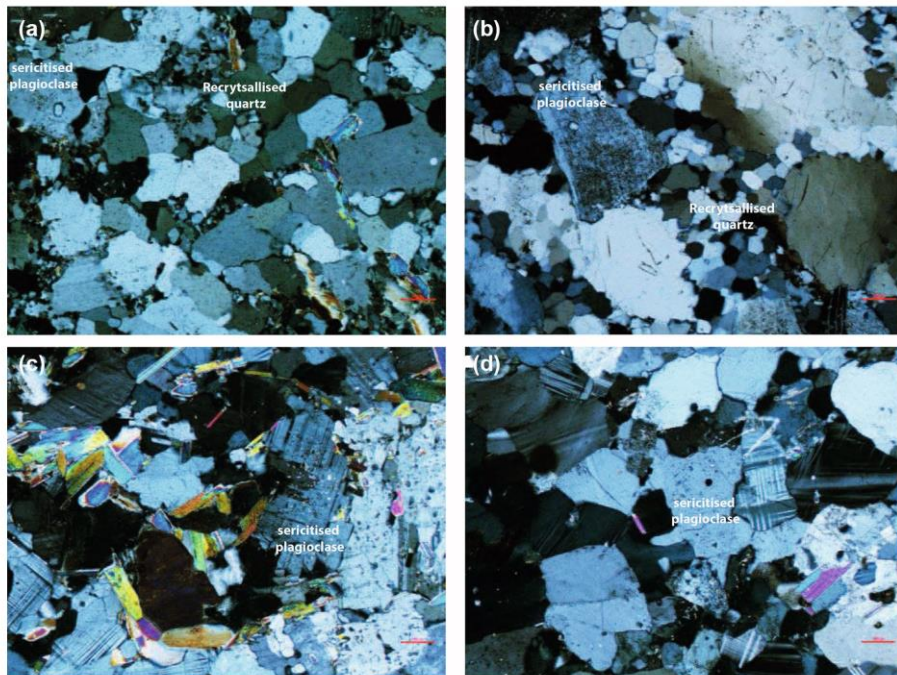


Fig. 3 Representative photomicrograph images (cross polarised light) highlighting a weak post-magmatic overprint observed in the leucogranites samples **a** 139466: medium-grained equigranular biotite–muscovite granodiorite showing minor sericitisation and quartz recrystallization; **b** 169092: massive, medium-grained biotite–muscovite monzogranite, showing minor sericite, quartz recrystallisation

and undulose extinction in the quartz; **c** 183287: medium- to coarse-grained, equigranular muscovite–tourmaline granodiorite with partly sericitised plagioclase and recrystallised quartz; **d** 187401: fine to medium-grained equigranular tourmaline–muscovite monzogranite showing recrystallised quartz and minor sericitisation

The three samples (183287, 183288 and 187401) have relatively low whole-rock Zr and Sr concentrations (Table 1). Of the three samples, 183287 shows significantly lower abundances of Th, La, Ce, and Nd.

Analytical methods

Monazite from three leucocratic granite samples (GSWA 139466, 169092 and 183287) were separated using standard mineral separation methods (Wingate and Lu 2016), and cast in 25-mm-diameter epoxy mounts which were then polished to expose the interiors of the crystals. No monazite grains were found in sample GSWA 183288. For sample GSWA 187401, polished thin sections were imaged using a scanning electron microscope (SEM) in

back-scattered electron (BSE) mode fitted with an energy dispersive X-ray spectrometer (EDS) to identify suitable monazite grains for in situ SHRIMP geochronology. Monazite grains $>10\ \mu\text{m}$ across were drilled out in 3-mm-diameter plugs and cast in a single 25-mm epoxy mount. Monazite reference materials FRENCH, Z2908, Z2234, and PD95 were in a separate mount that was cleaned and Au-coated with the sample mounts prior to analysis. Monazite reference OX1 was located on the same mount as the unknowns (183287).

U–Th–Pb analyses of monazite were conducted using a SHRIMP II ion microprobe in the John de Laeter Centre at Curtin University, Perth. Optical and BSE images were used to guide placement of the primary ion beam during SHRIMP analysis. The SHRIMP instrument set-up and operating protocols followed the established

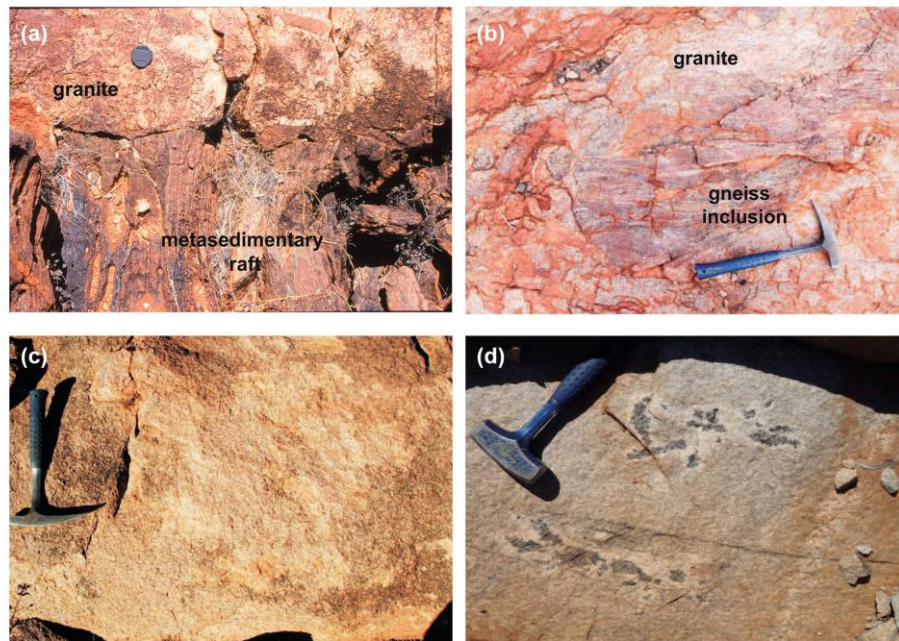


Fig. 4 Field photos (~7 cm camera cover in (a) and ~30 cm long hammer in (b–d) for scale: **a** an undeformed coarse-grained granite dyke of the Erong Granite cutting the deformation fabrics in metasedimentary gneiss; **b** gneiss inclusion in the Durlacher Granite about 1 km from the Red Rock Bore granite locality; **c** sample 183287; **a**

medium- to coarse-grained, equigranular muscovite–tourmaline granodiorite of the Thirty-Three Supersuite; **d** sample 187401: coarse-grained equigranular tourmaline–muscovite monzogranite of the Thirty-Three Supersuite with distinct tourmaline nodules

procedure for small spot analysis of monazite (Fletcher et al. 2010). A total of six sessions were conducted to obtain the U–Th–Pb data presented here. During all sessions, an O^{2-} primary beam focused through a 30- μm Kohler aperture to produce a spot size ~10 μm , with a beam intensity of 0.2–0.4 nA. The secondary ion system was focused through a 100- μm collector slit onto an electron multiplier to produce mass peaks with flat tops and a mass resolution ($M/\Delta M$ at 1% peak height) of >5000 in all sessions. Post-collector retardation lens was activated to reduce stray ions. Squid-2.50.11.02.03 software (Ludwig 2009) was used for initial data reduction, including correction for common Pb. Corrections for matrix effects in $^{206}\text{Pb}/^{238}\text{U}$ and $^{208}\text{Pb}/^{232}\text{Th}$, and for instrumental mass fractionation in $^{207}\text{Pb}/^{206}\text{Pb}$, were applied to monazite data (Fletcher et al. 2010). To adjust for analytical

bias the respective 1 sigma calibration uncertainty was applied in quadrature to $^{238}\text{U}/^{206}\text{Pb}$ and $^{232}\text{Th}/^{208}\text{Pb}$ individual analyses (samples 187401 and 183287) prior to the calculation of the weighted mean. Weighted mean dates are reported with 95% confidence limits, whereas individual analyses are presented with 1σ uncertainties. Because our samples span almost a billion years, from the Paleoproterozoic to Neoproterozoic, the choice of isotopic system ($^{207}\text{Pb}/^{206}\text{Pb}$, $^{238}\text{U}/^{206}\text{Pb}$, and $^{232}\text{Th}/^{208}\text{Pb}$) is sample dependent (e.g., Kirkland and Wingate 2012). For Paleoproterozoic and older samples the $^{207}\text{Pb}/^{206}\text{Pb}$ analysis is typically the most precise and preferred for weighted mean calculation. However, from late Mesoproterozoic $^{238}\text{U}/^{206}\text{Pb}$ or $^{232}\text{Th}/^{208}\text{Pb}$ ratios provide the most reliable age estimates. The precisions of ^{238}U and ^{232}Th abundances measured by SHRIMP are typically 5–10%.

Monazite geochronology results

SHRIMP U–Th–Pb monazite data are presented in Supplementary Table 3 and are summarised in Table 2, which also includes U–Pb zircon data from previous work for comparison.

Sample 139466: biotite–muscovite granodiorite

Monazite crystals from this sample are yellow, transparent, and unzoned. They are subhedral to predominantly anhedral and range in size from 50 to >100 μm . Monazite occurs primarily as inclusions in quartz, but is also hosted in plagioclase. Thirteen analyses were carried out on eight monazite grains (Supplementary Table 3). Excluded from age calculations are a single concordant analysis that indicates high common Pb ($f_{206} > 1\%$) and another that is >10% discordant. The remaining 11 analyses are <5% discordant and indicate low common Pb. Ten of the 11 analyses indicate well-grouped, measured U and Th concentrations that vary from 350 to 500 ppm and 21,400 to 37,500 ppm, respectively, with Th/U ratios from 54 to 88. They yielded $^{207}\text{Pb}/^{206}\text{Pb}$ dates between 1868 and 1787 Ma, with a weighted mean of 1830 ± 19 Ma (MSWD = 2.8). Despite the large MSWD, rejection of additional analyses is not warranted given the uniformity of these monazites in morphology and U–Th composition. Therefore, 1830 ± 19 Ma (Fig. 5a) is considered the best estimate of the timing of monazite growth during magma crystallisation. An old outlier yielded a $^{207}\text{Pb}/^{206}\text{Pb}$ date of 1933 ± 7 Ma (1σ), and is interpreted to be a xenocryst.

Sample 169092: biotite–muscovite monzogranite

Monazite is widespread in this rock and occurs as inclusion in quartz, plagioclase, undeformed muscovite, and in biotite. Monazites crystals are >100 μm in size, yellow and transparent, and mainly subhedral and unzoned. Thorium concentrations range from 42,700 to 73,800 ppm, whereas U concentrations are bimodal: 1000–1900 ppm (four analyses) and 3500–7900 ppm (13 analyses). The Th/U ratios range from 8 to 70. Twenty-five analyses were obtained from 14 monazite grains; seven analyses that show >5% discordance are disregarded. A single analysis yielding a date of 1663 ± 2 Ma (1σ) is considered an outlier due to its significantly higher U (17,600 ppm) and lower Th (34,700 ppm) and resultant much lower Th/U (2 vs. 8–70) compared with the range seen in the main population (Supplementary Table 3). The remaining 17 analyses of 14 monazite grains yielded a weighted mean $^{207}\text{Pb}/^{206}\text{Pb}$ date of 1682 ± 3 Ma (MSWD = 0.99) (Fig. 5b), interpreted as the age of igneous crystallisation, consistent with the main age component of the initial zircon age.

Sample 187401: tourmaline–muscovite monzogranite

Monazite crystals in this sample show two different morphologies: (i) subhedral crystals 30–60 μm in size, and (ii) larger (>100 μm) anhedral crystals. The anhedral types are typically associated with secondary apatite and show retrogression coronas (e.g., Finger et al. 1998). However, the effect of post-magmatic alteration is not evident from the concordant age data, which ranges from 1058 to 970 Ma ($^{238}\text{U}/^{206}\text{Pb}$) across the monazite grains. The

Table 2 Summary of field data, U–Pb zircon and U–Th–Pb monazite geochronology for leucocratic granite samples

Sample ID	Easting	Northing	Rock type	Stratigraphic unit	Zircon $^{207}\text{Pb}/^{206}\text{Pb}$ age (Ma)	Monazite age (Ma)	Isotopic system used for monazite
GSWA 139466	465700	7174600	Biotite–muscovite granodiorite	Moorarie Supersuite	2621 ± 9	1830 ± 19	$^{207}\text{Pb}/^{206}\text{Pb}^*$
GSWA 169092	361420	7409000	Biotite–muscovite monzogranite	Durlacher Supersuite	1681 ± 10 , 1619 ± 15	1682 ± 3	$^{207}\text{Pb}/^{206}\text{Pb}^*$
GSWA 187401	418385	7286232	Tourmaline–muscovite monzogranite	Thirty-Three Supersuite	–	1006 ± 14	$^{238}\text{U}/^{206}\text{Pb}^*$
GSWA 183287	422561	7287407	Muscovite–tourmaline granodiorite	Thirty-Three Supersuite	2085–1309	899 ± 10	$^{232}\text{Th}/^{208}\text{Pb}^*$
GSWA 183288	423293	7288459	Biotite–muscovite–tourmaline monzogranite	Thirty-Three Supersuite	1648 ± 5	–	

Pb* indicates radiogenic Pb (i.e., corrected for common Pb)

The choice of isotopic system used to calculate the weighted mean for monazite data is discussed in the text

Sample locations quoted in coordinate system MGA 1994 GDA Zone 50

– Not analysed. Monazite was not found in sample 183288. Sample 187401 was not submitted for routine zircon geochronology due to leucocratic nature

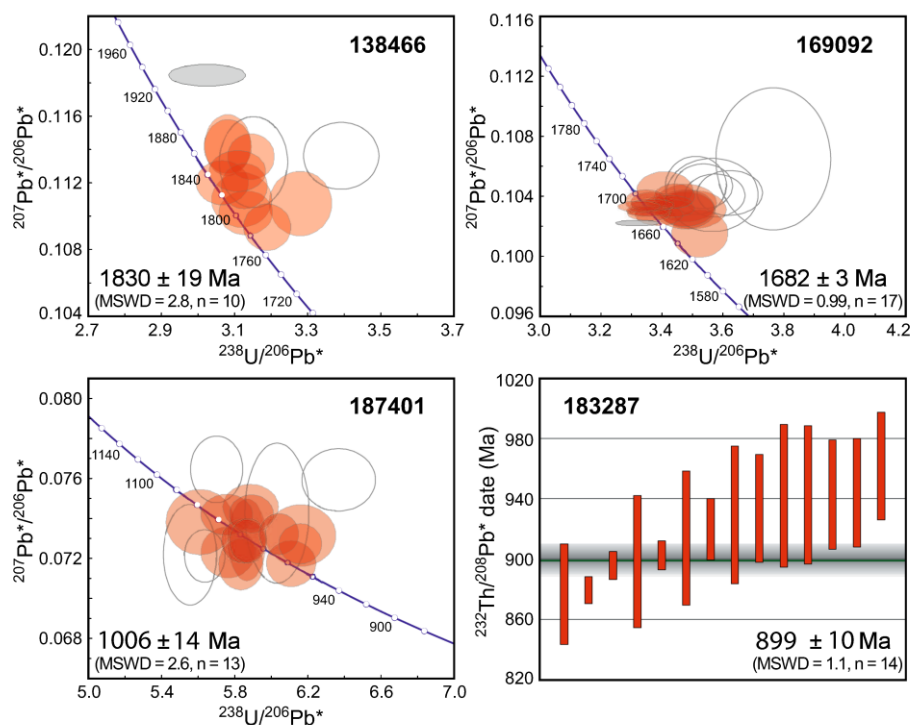


Fig. 5 SHRIMP U–Th–Pb analytical results for monazite from leucocratic granites in the Gascoyne Province. Ellipses in the concordia diagrams (a–c) correspond to analyses with 1σ uncertainties; red ellipses represent the main group of analyses; grey ellipses denote analyses with high common Pb, and open ellipse indicate discordance

>5%. Weighted mean dates are $^{207}\text{Pb}/^{206}\text{Pb}$ (a–b) and $^{206}\text{Pb}/^{238}\text{U}$ (c). a Erong Granite sample GSWA 139466; b leucocratic granite sample GSWA 169092; c Thirty-Three Supersuite sample GSWA 187401; d Thirty-Three Supersuite sample GSWA 183287 weighted mean $^{232}\text{Th}/^{208}\text{Pb}$ plot. Mean ages are quoted with 95% confidence intervals

subhedral monazite crystals are typically hosted in plagioclase and quartz or are interstitial to the main silicate minerals (Fig. 6). The monazites from this sample have high Th contents, similar to sample 169092, ranging from 39,900 to 80,200 ppm, and with uniformly moderate U, from 1050 to 1900 ppm, consistent with other samples in this study (Supplementary Table 3). Corresponding Th/U values range from 30 to 70. Nineteen analyses were obtained from nine monazite grains (Supplementary Table 3). Six analyses are >5% discordant and/or indicate high common ^{206}Pb (>1%) and, therefore, are not considered in the age calculation. Thirteen analyses of nine monazite grains yielded a single age component with a weighted mean $^{238}\text{U}/^{206}\text{Pb}$ date of 1006 ± 14 Ma (MSWD = 2.6) (Fig. 5c). The same

group of analyses was also used to calculate a weighted mean $^{207}\text{Pb}/^{206}\text{Pb}$ date of 1018 ± 16 (MSWD = 1.5). Excluding an analysis that yielded an imprecise $^{232}\text{Th}/^{208}\text{Pb}$ date, 18 analyses give a weighted mean $^{232}\text{Th}/^{208}\text{Pb}$ age of 1047 ± 20 (MSWD = 1.5). The weighted mean dates derived from the $^{207}\text{Pb}/^{206}\text{Pb}$ and $^{238}\text{U}/^{206}\text{Pb}$ decay systems agree within uncertainty and because this sample falls within the Mesoproterozoic–Neoproterozoic boundary either the $^{207}\text{Pb}/^{206}\text{Pb}$ or $^{238}\text{U}/^{206}\text{Pb}$ could be used to represent the age of crystallisation. However, the individual $^{238}\text{U}/^{206}\text{Pb}$ analyses are more precise with uncertainties two to three times lower than for $^{207}\text{Pb}/^{206}\text{Pb}$; therefore, the $^{238}\text{U}/^{206}\text{Pb}$ date of 1006 ± 14 Ma is taken as the most reliable estimate of the crystallisation age.

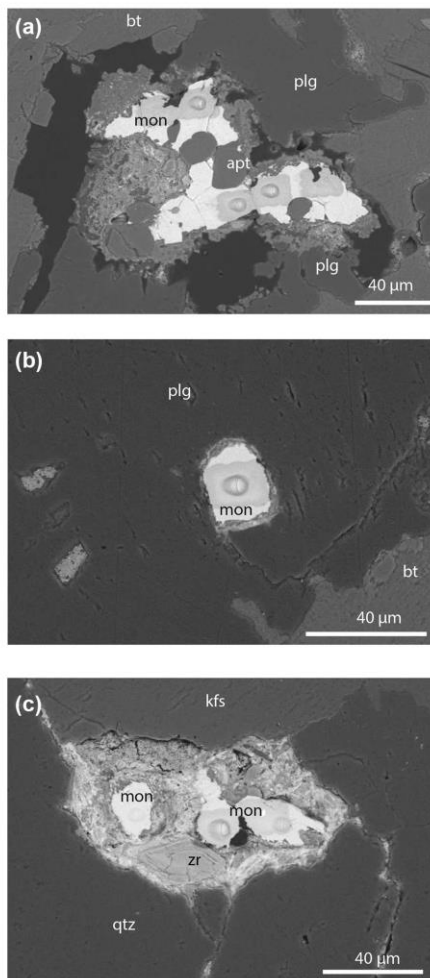


Fig. 6 Back-scattered electron (BSE) images of representative in situ monazite from sample GSWA 187401 (a–c). SHRIMP pits shown by the circles and the haloes around the SHRIMP spots show the effect of the raster. **a** Monazite growth associated with secondary apatite; **b** subhedral monazite within plagioclase feldspar; **c** multiple anhedral monazites in between quartz and K-feldspar (Fe alteration around the monazite). (bt biotite, plg plagioclase feldspar, mon monazite, apt apatite, kfs K-feldspar, qtz quartz, zr zircon). Dark circles are SHRIMP pits with a raster halo

Sample 183287: biotite-muscovite–tourmaline monzogranite

Monazite crystals from this sample are subhedral to anhedral, and yellow and transparent, with an average size of 60 μm (Fig. 7). The crystals occur as inclusions in quartz and plagioclase. Compared with those from sample 187401, monazites from this sample contain significantly lower U and Th concentrations ranging from 250 to 750 ppm and from 14,800 to 40,500 ppm, respectively, but with more uniform and elevated Th/U ratios (52–61, with an average of 54). Sixteen analyses were obtained from seven monazite grains (Supplementary Table 3). For this sample, dates determined from $^{207}\text{Pb}/^{206}\text{Pb}$ or $^{238}\text{U}/^{206}\text{Pb}$ ratios are significantly more dispersed and discordant than those based on $^{232}\text{Th}/^{208}\text{Pb}$ ratios, and several analyses indicate high common ^{206}Pb , whereas common ^{208}Pb (f_{208} in Supplementary Table 3) is, with one exception, <1%. Excluding the single analysis with high common ^{208}Pb (>1%), and one old outlier, 14 analyses of six monazites yielded a weighted mean $^{232}\text{Th}/^{208}\text{Pb}$ date of 899 ± 10 Ma (MSWD = 1.1) (Supplementary Table 3). Weighted mean dates calculated using $^{207}\text{Pb}/^{206}\text{Pb}$ and $^{238}\text{U}/^{206}\text{Pb}$ ratios, applying the discordance and common Pb criteria as above (cut-off value at 1% for f_{206} and $\pm 5\%$ for discordance), are 907 ± 24 ($n = 6$, MSWD = 1.3) and 917 ± 25 ($n = 6$, MSWD = 2.0), respectively. The results show that the $^{238}\text{U}/^{206}\text{Pb}$, $^{207}\text{Pb}/^{206}\text{Pb}$ and $^{232}\text{Th}/^{208}\text{Pb}$ weighted mean ages are indistinguishable within uncertainty; however, the overall weighted mean is most precise for the $^{232}\text{Th}/^{208}\text{Pb}$ system; therefore, for this Neoproterozoic sample, we consider the $^{232}\text{Th}/^{208}\text{Pb}$ age of 899 ± 10 Ma to be the best estimate of the age of igneous crystallisation (Fig. 5d).

Discussion

Igneous crystallisation ages for some leucocratic granites are difficult to determine using U–Pb zircon geochronology because these low-temperature crustal melts commonly contain a significant proportion of inherited zircon (e.g., Crowley et al. 2008; Harrison et al. 1999; Scott et al. 2011). The samples in this study contain Zr contents <150 ppm, which according to Miller et al. (2003) is a criterion for potential zircon inheritance in a melt. Due to the historic issue of xenocrystic zircons in the leucocratic granites in the Gascoyne Province, an alternative was required to determine the crystallisation age of these granites. Monazite is a common accessory mineral in a wide variety of granitic rocks, and, in particular, is commonly found as primary monazite in peraluminous leucogranites. Magmatic

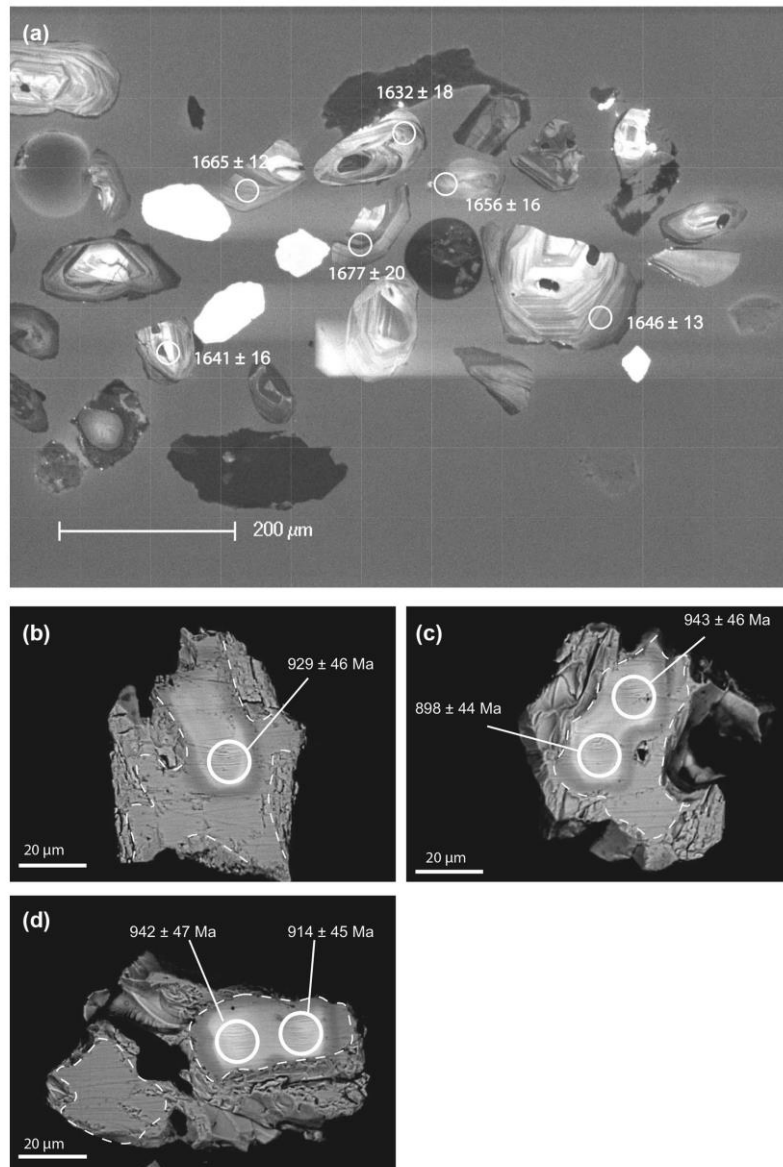


Fig. 7 Cathodoluminescence image of representative zircon grains from sample 183287 showing the original xenocrystic zircon ages (Kirkland et al. 2009) (a). Back-scattered electron (BSE) images of representative separated monazite grains from 183287 plus SHRIMP pits and corresponding ages from sample GSWA 183287 (b–d) sub-hedral to anhedral monazite grains typically around 60 μm in size. Zoning indicated by dashed outline. SHRIMP pits are shown by the circles and the haloes around the SHRIMP spots show the effect of the raster

monazite is distinguished from metamorphic monazite by observing the textural context of the crystals and noticing any effects of post magmatic deformation experienced by the rock. Here we show how obtaining reliable crystallization ages is important to determine the duration and extent of major granitic events and associated orogenic activity.

Assessment of magmatic monazite

Igneous monazite may become unstable during low- to medium-grade regional metamorphism (Townsend et al. 2001) resulting in secondary apatite–allanite coronas (Finger et al. 1998). The in situ monazite crystals in the tourmaline–muscovite monzogranite sample (GSWA 18740) are accompanied by secondary apatite and display some reaction coronas (Fig. 6). Although some monazite crystals in sample 187401 show secondary alteration rims, both monazite inclusions in plagioclase and interstitial monazite yielded similar ages. Although magmatic monazites typically show zoning (Bea 1996; Broska et al. 2000; Crowley et al. 2008; Montel 1993; Townsend et al. 2001), we found that only monazite in the muscovite–tourmaline granodiorite (GSWA 183287) shows zoning (Fig. 7); despite this, small-spot analysis enabled the primary monazite to be targeted and the results show consistent dates across the grains (Supplementary Table 3).

In sample 187401 the monazite crystals hosted in quartz and plagioclase suggest that monazite crystallised with the melt in contrast to inclusions in biotite that may contain inherited monazite (Rapp and Watson 1986). For the grain-mounted samples (139466, 169092 and 183287), monazite is found as inclusions in quartz and plagioclase and, more rarely, in biotite and muscovite or as an interstitial mineral. The results in Copeland et al. (1988) suggested that monazite inheritance is common in Tertiary S-types granites. Although the original location of the analysed monazite crystals is not known, our data contain only one analysis of inherited monazite (sample 139466) across four granite samples. This confirms the suggestion by Parish (1990) that monazite inheritance is less common than zircon in granites and, in particular, Precambrian granites.

Typically magmatic monazite shows a consistent pattern of elevated Th and moderate U concentrations. In Fig. 8, the Th and U concentrations of monazite analysed in this

study are compared with monazite from other granites. The plot shows that our monazites are consistent with the Th and U signature of igneous monazites presented in other studies. Lower U and Th concentrations distinguish magmatic monazite from hydrothermal monazite and monazite grown during low-temperature metamorphism or mineralisation from the southern Pilbara margin (Rasmussen et al. 2005) and the Abra deposit in the Capricorn Orogen (Zi et al. 2015) (Fig. 8). However, monazite related to medium-grade metamorphism may yield similar Th and U concentrations to magmatic monazite (e.g., U ranges from 1100 to 6700 ppm and Th from 1200 to 104,800 ppm, Sheppard et al. 2007). Although the rocks in this study show signs of minor recrystallisation related to low-grade metamorphic overprints the absence of multiple age populations in individual samples suggest that the post-magmatic effects are minimal. Additionally, the two samples that display minor alteration of monazite (183287 and 187401), these zones could be avoided due to careful placement of the analytical spot. The leucocratic granites lack any evidence of a medium-grade metamorphic overprint (Fig. 3) and demonstrably post-date regional metamorphic fabrics. Therefore, considering the textural context of the monazites and the observed minimal post-magmatic alteration we conclude that the monazites analysed are magmatic in origin.

Implications of the monazite geochronology

Correctly dating the timing and duration of magmatism is essential both for reconstructing reliable tectonic histories in complex intracratonic orogenic belts and for addressing the thermal history of orogens. Below we examine the wider implications of our new geochronology results.

The life-span of an orogeny

Many Precambrian orogenic belts dominated by low- to medium-grade metamorphic rocks lack direct metamorphic ages (and when biostratigraphy is not available); the ages of granitic supersuites have been used as a proxy for the duration of orogenic events (e.g., the 1680–1620 Ma Durlacher Supersuite, Sheppard et al. 2005). The biotite–muscovite monzogranite (GSWA 169092) in the far north of the province yielded zircon results that were inconclusive and allowed for two possible interpretations of the igneous crystallisation age. However, our monazite geochronology provides an unambiguous igneous crystallisation age of 1682 ± 3 Ma for sample 169092, indicating that it was emplaced during the main stage of magmatism (1688–1659 Ma). There is a lack of evidence for granites younger than c. 1659 Ma in the Durlacher Supersuite in the northern Gascoyne Province suggesting that magma emplacement occurred over a shorter interval (Fig. 9) than

by the plutons were considered to be Paleoproterozoic, and (2) the leucocratic granites do not intrude the unconformably overlying 1620–1450 Ma metasediments (Fig. 2c). However, later monazite geochronology established that the metamorphic assemblages are actually related to the 1030–950 Ma Edmondian Orogeny and that a large rare-earth-element-bearing pegmatite considered to be associated with the leucocratic granites has an igneous crystallisation age of 954 ± 12 Ma (Sample 117154, Sheppard et al. 2007). Further U–Pb zircon geochronology of the leucocratic granites yielded zircon dates that were interpreted as representing the ages of xenocrystic zircon. A biotite–muscovite–tourmaline monzogranite (183287) yielded zircon populations between 2085 and 1309 Ma (Kirkland et al. 2009), and secondly, a muscovite–tourmaline monzogranite (183288) yielded a single age population 1648 ± 5 Ma (Wingate et al. in press).

Pegmatites Additional zircon geochronology on pegmatites (samples GSWA 185946, 185945 and 190667) in the area established igneous crystallisation ages, respectively, of 1030 ± 6 , 1000 ± 8 , and 939 ± 5 Ma (Wingate et al. 2011, 2010a, b) better aligned with the field relationships and existing phosphate geochronology. Furthermore, monazite from a tourmaline-rich schist which is part of a metasomatic halo around a tourmaline-bearing pegmatite dyke yielded a date of 958 ± 16 Ma (Sample GSWA 88475 Fig. 2c; Korhonen et al. 2015).

Monazite geochronology Our monazite data from two leucocratic samples, of the Thirty-Three Supersuite, yielded Neoproterozoic ages consistent with the metamorphic fabrics in the adjacent rocks. Sample 187401, a tourmaline–muscovite monzogranite, yielded an age of 1006 ± 14 Ma representing the initial stages of magmatism. Furthermore, our results highlight that magmatism continued until c. 899 Ma (sample 183287: biotite–muscovite–tourmaline monzogranite).

The combined monazite and zircon data suggest that magmatism of the Thirty-Three Supersuite spanned about 130 million years (c. 1030–899 Ma) and that leucocratic magmatism outlasted the regional metamorphism in the same structural corridor by c. 100 million years (Fig. 10). Furthermore, given the small area (and likely small volume) of the supersuite, the geochronology implies exceptionally low magma production rates. The monazite and zircon geochronology confirm that the Thirty-Three Supersuite is much younger than c. 1620–1465 Ma metasedimentary rocks of the Edmund Group, despite the absence of pegmatite and leucocratic granite in the Edmund Group in the Ti Tree Shear Zone immediately to the north. Therefore, reworking and magmatism must have been funnelled into a narrow structural corridor south of the shear zone from c. 1030 Ma onwards. This work further highlights

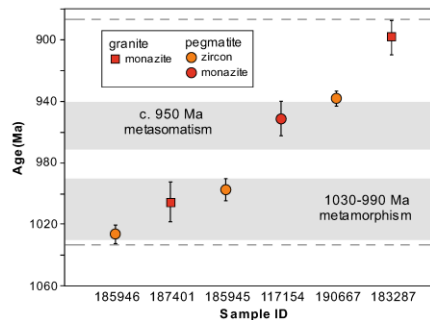


Fig. 10 Monazite and zircon ages for leucocratic granites and pegmatites of the Thirty-Three Supersuite. Two stages of granite and pegmatite are suggested by the combined monazite and zircon geochronology. The first stage corresponds with metamorphism and deformation during the Edmondian Orogeny, whereas the younger pulse may be associated with periodic reactivation of the Ti Tree Shear Zone. Error bars indicate 95% confidence intervals

the problem of attempting to correlate events across major structures within a complex orogen.

An isolated granite

Sample GSWA 139466 was taken from a biotite–muscovite granodiorite pluton that intruded a crustal-scale shear zone (the Errabiddy Shear Zone). The existing geochronological constraints allowed the pluton to have been emplaced at any time over a c. 1000 million-year interval. Our U–Th–Pb monazite geochronology yielded a date of 1830 ± 19 Ma, interpreted as the age of igneous crystallisation and is consistent with field relationships that show the Erong Granite cutting deformation fabrics formed during the 2005–1950 Ma Glenburgh Orogeny. The new monazite data indicate that the pluton is part of the voluminous Moorarie Supersuite associated with reworking during the Paleoproterozoic Capricorn Orogeny. This study shows that even for an area shaped by multiple episodes of reworking and reactivation monazite is a powerful geochronometer for constructing a more reliable tectonic and magmatic history of a major shear zone.

Conclusions

Our study has highlighted the benefits of using U–Th–Pb monazite geochronology for dating peraluminous leucocratic, low-temperature granites. This study has demonstrated that U–Th–Pb monazite geochronology is preferable for determining the crystallisation ages of Precambrian

low-temperature, peraluminous leucocratic granites for the following reasons: (1) new monazite growth occurs readily at a range of P–T conditions remaining robust over time with a closure temperature of 720–750 °C (Copeland et al. 1988); (2) monazite contains high U and Th and incorporates minor common Pb (Townsend et al. 2001); (3) monazite, unlike zircon, generally does not contain inherited cores and is immune from radiogenic Pb loss at low temperatures (Grosse et al. 2009); (4) occurrences of inherited monazite, although common in Tertiary S-type granites (Copeland et al. 1988), are uncommon in Precambrian rocks (Parrish 1990); and (5) magmatic monazite is one of the most common accessory mineral in granites and is abundant in peraluminous compositions (Bea 1996; Montel 1993; Rapp and Watson 1986). Our study has also resolved the duration of two generations of magmatism: in one instance emplacement occurred over a much shorter time interval (~30 million years) implying a higher rate of magma production than previously thought, and second, whereas purely leucocratic granites and pegmatites of the Thirty-Three Supersuite span a remarkably long duration of c. 130 million years implying a very low rate of magma generation. Finally, the use of monazite geochronology was able to narrow the possible window of magmatism to a discrete reworking event significantly reducing the time span previously thought.

Acknowledgements We thank Simon Johnson and Ian Fitzsimons for their critical and insightful reviews. Zdenka Martelli kindly provided assistance with monazite identification and picking. This manuscript was significantly improved by valuable comments received from an anonymous reviewer. U–Th–Pb measurements were conducted using the SHRIMP ion microprobes at the John de Laeter Centre at Curtin University. Michael Wingate publishes with permission of the Director of the Geological Survey of Western Australia. Australian Research Council Linkage Grant LP130100922 and the Geological Survey of Western Australia (through the Exploration Incentive Scheme) funded this PhD Project.

Open Access This article is distributed under the terms of the Creative Commons Attribution 4.0 International License (<http://creativecommons.org/licenses/by/4.0/>), which permits unrestricted use, distribution, and reproduction in any medium, provided you give appropriate credit to the original author(s) and the source, provide a link to the Creative Commons license, and indicate if changes were made.

References

- Ayres M, Harris N, Vance D (1997) Possible constraints on anatectic melt residence times from accessory mineral dissolution rates: an example from Himalayan leucogranites. *Miner Mag* 61:29–36
- Bea F (1996) Residence of REE, Y, Th and U in granites and crustal protoliths: implications for the chemistry of crustal melts. *J Petrol* 37:521–552
- Bea F, Montero P, González-Lodeiro F, Talavera C (2007) Zircon inheritance reveals exceptionally fast crustal magma generation processes in Central Iberia during the Cambro-Ordovician. *J Petrol* 48:2327–2339
- Bodorkos S, Wingate MTD (2007) The contribution of geochronology to GSWA's mapping programs: current perspectives and future directions. *Geol Surv West Aust* 2:10–11
- Boehnke P, Watson EB, Trail D, Harrison TM, Schmitt AK (2013) Zircon saturation re-visited. *Chem Geol* 351:324–334
- Broska I, Petrik I, Williams CT (2000) Coexisting monazite and allanite in peraluminous granitoids of the Tribeč Mountains, Western Carpathians. *Am Miner* 85:22–32
- Brown M (1994) The generation, segregation, ascent and emplacement of granite magma: the migmatite-to-crustally-derived granite connection in thickened orogens. *Earth Sci Rev* 36:83–130
- Budzyń B, Harlov DE, Williams ML, Jercinovic MJ (2011) Experimental determination of stability relations between monazite, fluorapatite, allanite, and REE-epidote as a function of pressure, temperature, and fluid composition. *Am Miner* 96:1547–1567
- Copeland P, Parrish RR, Harrison TM (1988) Identification of inherited radiogenic Pb in monazite and its implications for U–Pb systematics. *Nature* 333:760–763
- Crowley JL, Brown RL, Gervais F, Gibson HD (2008) Assessing Inheritance of Zircon and Monazite in Granitic Rocks from the Monashee Complex, Canadian Cordillera. *J Petrol* 49:1915–1929
- Culver KE (2001) Structure, metamorphism and geochronology of the northern margin of the Gurnee Granite, Central Gascoyne Complex, Western Australia. Curtin University of Technology, Perth BSc. (Hons) thesis (unpublished)
- Finger F, Broska I, Roberts MP, Schermaier A (1998) Replacement of primary monazite by apatite-allanite-epidote coronas in an amphibolite facies granite gneiss from the eastern Alps. *Am Miner* 83:248–258
- Fletcher IR, McNaughton NJ, Davis WJ, Rasmussen B (2010) Matrix effects and calibration limitations in ion probe U–Pb and Th–Pb dating of monazite. *Chem Geol* 270:31–44
- Gao L-E, Zeng L, Asimow PD (2017) Contrasting geochemical signatures of fluid-absent versus fluid-fluxed melting of muscovite in metasedimentary sources: the Himalayan leucogranites. *Geology* 45:39–42
- Gilotti JA, McClelland WC (2005) Leucogranites and the time of extension in the East Greenland Caledonides. *J Geol* 113:399–417
- Grosse P, Söllner F, Báez MA, Toselli AJ, Rossi JN, de la Rosa JD (2009) Lower Carboniferous post-orogenic granites in central-eastern Sierra de Velasco, Sierras Pampeanas, Argentina: U–Pb monazite geochronology, geochemistry and Sr–Nd isotopes. *Int J Earth Sci* 98:1001–1025
- GSWA (2016a) 1:500 000 State interpreted bedrock geology of Western Australia, 2016: Geological Survey of Western Australia, digital data layer. www.dmp.wa.gov.au/geoview
- GSWA (2016b) Compilation of geochronology information, 2016 update, digital data product. www.dmp.wa.gov.au/geoview
- Harrison MT, Grove M, McKeegan KD, Coath CD, Lovera OM, Fort PL (1999) Origin and episodic emplacement of the Manaslu intrusive complex, central Himalaya. *J Petrol* 40:3–19
- Johnson SP et al (2011) Two collisions, two sutures: punctuated pre-1950Ma assembly of the West Australian Craton during the Ophthalmian and Glenburgh Orogenies. *Precamb Res* 189:239–262
- Johnson SP, Korhonen FJ, Kirkland CL, Cliff JA, Belousova EA, Sheppard S (2017) An isotopic perspective on growth and differentiation of Proterozoic orogenic crust: from subduction magmatism to cratonization. *Lithos* 268–271:76–86
- Kemp AIS, Hawkesworth CJ (2003) 3.11—granitic perspectives on the generation and secular evolution of the continental crust A2—Holland, Heinrich D. In: Turekian KK (ed) *Treatise on geochemistry*. Pergamon, Oxford, pp 349–410

- Kirkland CL, Wingate MTD (2012) Reading deep time: radiogenic isotopic geochronology. Geological Survey of Western Australia 2012, 15
- Kirkland CL, Wingate MTD, Bodorkos S, Sheppard S (2009) 183287: Granite, Perseverance Well; Geochronology Record 756. Geological Survey of Western Australia
- Korhonen FJ et al. (2015) Pressure-temperature-time evolution of the Mutherbukin Tectonic event, Capricorn Orogen. Geological Survey of Western Australia 146
- Kusiak MA, Williams IS, Dunkley DJ, Konečný P, Slaby E, Martin H (2014) Monazite to the rescue: U-Th-Pb dating of the intrusive rocks of the composite Karkonosze pluton, Bohemian Massif. Chem Geol 364:76–92
- Le Maitre RW (1989) A classification of the igneous rocks and glossary of terms. Blackwell, Oxford, p 193
- Lee DE, Dodge FCW (1964) Accessory minerals in some granitic rocks in California and Nevada as a function of calcium content. Am Miner 49:1660–1669
- Ludwig KR (2009) Squid 2.50, a user's manual Berkeley geochronology centre special publication
- Miller CF, Mittlefehldt DW (1982) Depletion of light rare-earth elements in felsic magmas. Geology 10:129–133
- Miller CF, Meschter McDowell S, Mapes RW (2003) Hot and cold granites? Implications of zircon saturation temperatures and preservation of inheritance. Geology (Boulder) 31:529–532
- Montel J-M (1993) A model for monazite/melt equilibrium and application to the generation of granitic magmas. Chem Geol 110:127–146
- Nelson DR (1998) 142855: porphyritic monzogranite, Anderson Well; Geochronology Record 371; Geological Survey of Western Australia
- Nelson DR (2000) 139466: foliated biotite-muscovite-garnet granulite, Erong Homestead; Geochronology Record 427; Geological Survey of Western Australia
- Nelson DR (2004) 169092: biotite-muscovite monzogranite, Red Rock Bore; Geochronology Record 103; Geological Survey of Western Australia
- Occhipinti SA, Reddy SM (2009) Neoproterozoic reworking of the Palaeoproterozoic Capricorn Orogen of Western Australia and implications for the amalgamation of Rodinia. Geol Soc Lond Spec Publ 327:445–456
- Occhipinti SA, Sheppard S, Myers JS, Tyler IM, Nelson DR (2001) Archaean and Palaeoproterozoic geology of the Narryer Terrane (Yilgarn Craton) and the southern Gascoyne Complex (Capricorn Orogen), Western Australia—a field guide. Geological Survey of Western Australia 2001, 8
- Occhipinti SA, Sheppard S, Passchier C, Tyler IM, Nelson DR (2004) Palaeoproterozoic crustal accretion and collision in the southern Capricorn Orogen: the Glenburgh Orogeny. Precamb Res 128:237–255
- Parrish RR (1990) U-Pb dating of monazite and its application to geological problems Canadian. J Earth Sci 27:1431–1450
- Parrish RR, Tirrul R (1989) U-Pb age of the Baltoro granite, north-west Himalaya, and implications for monazite U-Pb systematics. Geology 17:1076–1079
- Patiño Douce AE, Harris N (1998) Experimental constraints on Himalayan anatexis. J Petrol 39:689–710
- Poitrasson F, Chenery S, Bland DJ (1996) Contrasted monazite hydrothermal alteration mechanisms and their geochemical implications. Earth Planet Sci Lett 145:79–96
- Rapp RP, Watson EB (1986) Monazite solubility and dissolution kinetics: implications for the thorium and light rare earth chemistry of felsic magmas. Contrib Miner Petrol 94:304–316
- Rasmussen B, Fletcher IR, Sheppard S (2005) Isotopic dating of the migration of a low-grade metamorphic front during orogenesis. Geology 33:773–776
- Scaillot B, Pichavant M, Roux J (1995) Experimental crystallization of leucogranite magmas. J Petrol 36:663–705
- Scaillot B, Holtz F, Pichavant M (2016) Experimental constraints on the formation of silicic magmas. Elements 12:109–114
- Schärer U, Xu RH, Allègre CJ (1986) U-(Th)-Pb systematics and ages of Himalayan leucogranites, South Tibet. Earth Planet Sci Lett 77:35–48
- Scott JM, Palin JM, Cooper AF, Sagar MW, Allibone AH, Tulloch AJ (2011) From richer to poorer: zircon inheritance in Pomona Island Granite, New Zealand. Contrib Miner Petrol 161:667–681
- Sheppard S, Occhipinti SA, Nelson DR (2005) Intracontinental reworking in the Capricorn Orogen, Western Australia: the 1680–1620 Ma Mangaroon Orogeny. Aust J Earth Sci 52:443–460
- Sheppard S, Rasmussen B, Muhling JR, Farrell TR, Fletcher IR (2007) Grenvillian-aged orogenesis in the Palaeoproterozoic Gascoyne Complex, Western Australia: 1030–950 Ma reworking of the Proterozoic Capricorn Orogen. J Metamorph Geol 25:477–494
- Sheppard S, Bodorkos S, Johnson SP, Wingate MTD, Kirkland CL (2010a) The paleoproterozoic capricorn orogeny: intracontinental reworking not continent-continent collision. Geological Survey of Western Australia 108
- Sheppard S, Johnson SP, Wingate MTD, Kirkland CL, Pirajno F (2010b) Explanatory notes for the Gascoyne Province. Geological Survey of Western Australia 1:100 000 Explanatory Notes
- Townsend KJ, Miller CF, D'Andrea JL, Ayers JC, Harrison TM, Coath CD (2001) Low temperature replacement of monazite in the Ireteba granite, Southern Nevada: geochronological implications. Chem Geol 172:95–112
- Watson EB, Harrison TM (1983) Zircon saturation revisited: temperature and composition effects in a variety of crustal magma types. Earth Planet Sci Lett 64:295–304
- Williams IS, Compston W, Chappell BW (1983) Zircon and Monazite U-Pb Systems and the Histories of I-Type Magmas, Berridale Batholith, Australia. J Petrology 24(1):76–97
- Wingate M, Lu Y (2016) Introduction to geochronology information released in 2014. Geological Survey of Western Australia
- Wingate M, Kirkland C, Sheppard S, Johnson S (2010a) 185945: pegmatite lenses in metamonzogranite, Yinnetharra Homestead; Geochronology Record 901. Geological Survey of Western Australia
- Wingate M, Kirkland C, Sheppard S, Johnson S (2010b) 185946: pegmatite dyke, Yinnetharra Homestead; Geochronology Record 902. Geological Survey of Western Australia
- Wingate M, Kirkland C, Johnson S (2011) 190667: granite pegmatite, Camel Hill; Geochronology Record 1003. Geological Survey of Western Australia
- Wingate MTD, Lu Y, Johnson SP (in press) 183288: biotite-tourmaline monzogranite, Perseverance Well; Geochronology Record 1352. Geological Survey of Western Australia
- Zen E (1986) Aluminum enrichment in silicate melts by fractional crystallization: some mineralogic and petrographic constraints. J Petrol 27:1095–1117
- Zi J-W et al (2015) In situ U-Pb geochronology of xenotime and monazite from the Abra polymetallic deposit in the Capricorn Orogen, Australia: dating hydrothermal mineralization and fluid flow in a long-lived crustal structure. Precamb Res 260:91–112

A.4 Paper 4 (published)

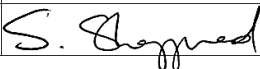
Statement of Authorship

Title of Paper	Neoproterozoic $^{40}\text{Ar}/^{39}\text{Ar}$ mica ages mark the termination of a billion years of intraplate reworking in the Capricorn Orogen, Western Australia
Publication Status	Published
Publication Details	Piechocka, A. M., Sheppard, S., Fitzsimons, I. C. W., Johnson, S. P., Rasmussen, B., and Jourdan, F., 2018, Neoproterozoic $^{40}\text{Ar}/^{39}\text{Ar}$ mica ages mark the termination of a billion years of intraplate reworking in the Capricorn Orogen, Western Australia: Precambrian Research 310, 391–406.

Author Contributions

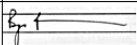
By signing the Statement of Authorship, each author certifies that their stated contribution to the publication is accurate and that permission is granted for the publication to be included in the candidate's thesis.

Name of Principal Author (Candidate)	Agnieszka M. Piechocka		
Contribution to the Paper	Conducted geological field work (mapping and sampling), prepared samples for $^{40}\text{Ar}/^{39}\text{Ar}$ analysis. Data interpretation and wrote the manuscript.		
Signature		Date	13/11/2018

Name of Co-Author (Supervisor)	Stephen Sheppard		
Contribution to the Paper	Supervised work, assisted with data interpretation and manuscript revision.		
Signature		Date	31/10/2018

Name of Co-Author (Supervisor)	Ian C. W. Fitzsimons		
Contribution to the Paper	Assisted with the interpretation of the $^{40}\text{Ar}/^{39}\text{Ar}$ mica results and assisted with writing parts of the manuscript.		
Signature		Date	7/11/19

Name of Co-Author	Simon P. Johnson		
Contribution to the Paper	Assisted with the regional geology and structural sections and writing of the manuscript.		
Signature		Date	22/10/2018

Name of Co-Author (Supervisor)	Birger Rasmussen		
Contribution to the Paper	Provided the U–Pb xenotime data and reviewed the final manuscript.		
Signature		Date	18/03/2019

Name of Co-Author	Fred Jourdan		
Contribution to the Paper	Fred conducted the argon analysis and processing of the data. Provided the diffusion modelling data. Assisted with writing the argon results section.		
Signature		Date	19/03/2019

Copyright Information

The information below is linked to the original published article in Precambrian Research:

<https://creativecommons.org/licenses/by/4.0/>



Attribution 4.0 International (CC BY 4.0)

This is a human-readable summary of (and not a substitute for) the [license](#). [Disclaimer](#).

You are free to:

Share — copy and redistribute the material in any medium or format

Adapt — remix, transform, and build upon the material for any purpose, even commercially.

The licensor cannot revoke these freedoms as long as you follow the license terms.



Under the following terms:



Attribution — You must give [appropriate credit](#), provide a link to the license, and [indicate if changes were made](#). You may do so in any reasonable manner, but not in any way that suggests the licensor endorses you or your use.

No additional restrictions — You may not apply legal terms or [technological measures](#) that legally restrict others from doing anything the license permits.

Notices:

You do not have to comply with the license for elements of the material in the public domain or where your use is permitted by an applicable [exception or limitation](#).

No warranties are given. The license may not give you all of the permissions necessary for your intended use. For example, other rights such as [publicity, privacy, or moral rights](#) may limit how you use the material.

Letter of authority to reprint

RE: Permission to publish article in PhD thesis

Permissions Helpdesk <permissionshelpdesk@elsevier.com>

Mon 1/10/2018 9:11 PM

To: Nishka Piechocka <nishka.piechocka@postgrad.curtin.edu.au>;

Dear Nishka,

As an Elsevier journal author, you retain the right to Include the article in a thesis or dissertation (provided that this is not to be published commercially) whether in full or in part, subject to proper acknowledgment; see <https://www.elsevier.com/about/our-business/policies/copyright/personal-use> for more information. As this is a retained right, no written permission from Elsevier is necessary.

If I may be of further assistance, please let me know.

Best of luck with your thesis and best regards,
Laura

Laura Stingelin

Permissions Helpdesk Associate
ELSEVIER | Global E-Operations Books
+1 215-239-3867 office

l.stingelin@elsevier.com

Contact the Permissions Helpdesk

+1 800-523-4069 x3808 | permissionshelpdesk@elsevier.com

Reprint of Paper

Precambrian Research 310 (2018) 391–406



Contents lists available at ScienceDirect

Precambrian Research

journal homepage: www.elsevier.com/locate/precamres

Neoproterozoic $^{40}\text{Ar}/^{39}\text{Ar}$ mica ages mark the termination of a billion years of intraplate reworking in the Capricorn Orogen, Western Australia



Agnieszka M. Piechocka^{a,*}, Stephen Sheppard^{a,b}, Ian C.W. Fitzsimons^a, Simon P. Johnson^c, Birger Rasmussen^d, Fred Jourdan^a

^a School of Earth and Planetary Sciences, Curtin University, Kent Street, Bentley, WA 6102, Australia

^b Prime Geological Mapping, PO Box 3014, Carlisle South, WA 6101, Australia

^c Geological Survey of Western Australia, 100 Plain Street, East Perth, WA 6004, Australia

^d School of Earth Sciences, The University of Western Australia, Nedlands, WA 6009, Australia

ARTICLE INFO

Keywords:

Intraplate orogeny
 $^{40}\text{Ar}/^{39}\text{Ar}$ geochronology
 U–Pb xenotime geochronology
 Neoproterozoic
 Capricorn orogen
 West Australian Craton

ABSTRACT

The tectonic history of the Proterozoic Capricorn Orogen, Western Australia, records complex intraplate reworking lasting nearly one billion years. Although the Paleo–Mesoproterozoic reworking history is well defined in the crystalline basement of the Gascoyne Province, at the western end of the orogen, the younger reactivation history remains unclear. Four reworking events affected the orogen at 1820–1770 Ma, 1680–1620 Ma, 1320–1170 Ma, and 1030–900 Ma. These events were succeeded by a breakout in predominantly dextral strike-slip reactivation of major shear zones across the Gascoyne Province. Currently, the age of this reactivation is constrained by only one date of c. 570 Ma from a single shear zone, but field relationships imply that some of the shear zones must be older than a suite of c. 755 Ma dolerite dykes. In order to constrain the age of fault and shear zone reactivation we obtained new $^{40}\text{Ar}/^{39}\text{Ar}$ dates for mica and *in situ* SHRIMP U–Pb dates for xenotime within shear zones. Our results when combined with previously published data, show that reactivation occurred between 920 and 830 Ma. These dates overlap with the youngest reworking event, the 1030–900 Ma Edmondian Orogeny. Furthermore, Neoproterozoic U–Pb phosphate ages are known from the bounding cratons and faulting within the adjacent Mesoproterozoic sedimentary basins suggest this event is of regional significance. In contrast to previous suggestions that this Neoproterozoic reactivation was the result of a collision from the west, we propose that it reflects north–south compression that caused dextral strike-slip fault reactivation in the north and exhumation of the southern part of the orogen.

1. Introduction

Intraplate orogens are less common than orogens at plate margins but their significance in tectonics is increasingly recognized (e.g., Aitken et al., 2009; Raimondo et al., 2010, 2014). Intraplate orogens are highly susceptible to repeated tectonic activity which is commonly considered to be a far-field response to events at plate margins (e.g., Aitken et al., 2013; Raimondo et al., 2014; Dyksterhuis and Müller, 2008). The Petermann and Alice Springs orogenies in central Australia and the Tien Shan orogen in central Asia are regarded as archetypal examples of compressional intraplate tectonics, all being characterised by thickening and substantial exhumation (Aitken et al., 2009; Raimondo et al., 2014). However, it is unlikely that these orogenies reflect the full range of behaviour in intraplate settings.

The Capricorn Orogen is a zone ~1000 km long and 500 km wide that comprises the deformed margins of two Archean cratons (the

Pilbara Craton in the north and Yilgarn Craton in the south) and intervening Proterozoic granitic and metasedimentary rocks of the Gascoyne Province, overlain by variably deformed Paleo- to Mesoproterozoic sedimentary basins (Cawood and Tyler, 2004) (Fig. 1). These rocks record the two-stage assembly of the Pilbara and Yilgarn cratons to form the larger West Australian Craton. First, the Pilbara Craton collided with the Glenburgh Terrane during the c. 2200 Ma Ophthalmian Orogeny, which was followed by the subsequent collision of the Pilbara Craton–Glenburgh Terrane with the Yilgarn Craton at c. 1950 Ma during the Glenburgh Orogeny (Cawood and Tyler, 2004; Johnson et al., 2011; Occhipinti et al., 2004). After assembly, the orogen remained susceptible to reworking and reactivation, recording a prolonged tectonothermal history spanning over one billion years. The protracted tectonic history involved four episodes of tectonothermal reworking (Korhonen et al., 2017; Sheppard et al., 2005, 2007, 2010b), followed by one or more poorly constrained reactivation events, all of

* Corresponding author.

E-mail address: nishka.piechocka@postgrad.curtin.edu.au (A.M. Piechocka).

<https://doi.org/10.1016/j.precamres.2018.04.006>

Received 16 February 2018; Received in revised form 16 March 2018; Accepted 5 April 2018

Available online 06 April 2018

0301-9268/ Crown Copyright © 2018 Published by Elsevier B.V. This is an open access article under the CC BY license (<http://creativecommons.org/licenses/by/4.0/>).

A.M. Piechocka et al.

Precambrian Research 310 (2018) 391–406

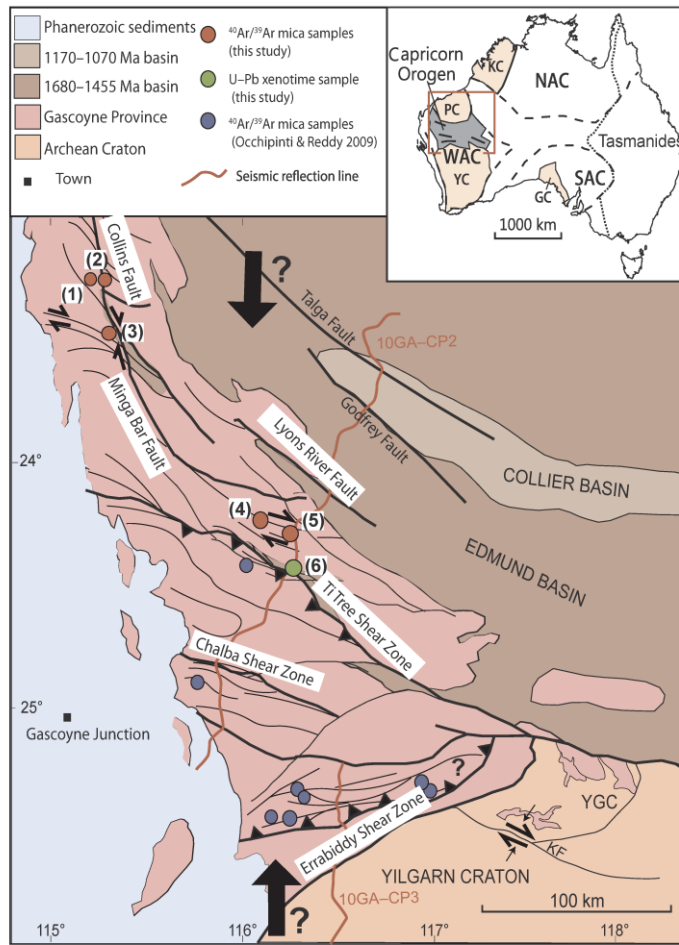


Fig. 1. Regional geological map of the Gascoyne Province, Capricorn Orogen. The large black arrows indicate the suggested north-south compression. Numbers in brackets relate to sample localities detailed in Table 1. (1) GSWA 216533; (2) GSWA 216540B; (3) GSWA 195890B and D and E; (4) GSWA 183294; (5) GSWA 183295; (6) GSWA 149,009 & 149010. KF—Kerba Fault (Reddy and Occhipinti, 2004), YGC—Yilgarn Gneiss Complex, YC—Yilgarn Craton, PC—Pilbara Craton, WAC—West Australian Craton, KC—Kimberley Craton, NAC—North Australian Craton, GC—Gawler Craton, SAC—South Australian Craton. (Modified after Johnson et al., 2017).

which are best recorded in the Gascoyne Province at the western end of the orogen. The youngest elements of the orogen are very low-grade metasedimentary rocks of the 1680–1465 Ma Edmund Basin and the 1170–1070 Ma Collier Basin.

The Gascoyne Province comprises several southeast-trending structural and metamorphic zones each recording a unique history of reworking (Sheppard et al., 2010b). Although the Paleo-Mesoproterozoic reworking history is well constrained (Korhonen et al., 2017; Sheppard et al., 2005, 2007, 2010b) the history of Neoproterozoic reactivation and uplift is almost entirely unknown. Poorly constrained total fusion $^{40}\text{Ar}/^{39}\text{Ar}$ mica dates of c. 920–860 Ma, obtained from the southern Errabiddy Shear Zone, were interpreted to represent cooling after a regional greenschist reworking event (Occhipinti and Reddy, 2009). The youngest known reactivation event, the c. 570 Ma Mulka Tectonic Event (Bodorkos and Wingate, 2007) identified by *in situ*

$^{40}\text{Ar}/^{39}\text{Ar}$ mica dating, is known from one shear zone in the southern province, the Chalba Shear Zone (Fig. 1). The Chalba Shear Zone is characterised by dextral strike-slip kinematics and cross cuts c. 755 Ma dykes of the Mundine Well Dolerite Suite (Wingate and Giddings, 2000). Other undated shear zones in the area show the same kinematics and offset the c. 755 Ma dolerites suggesting that they also belong to the Mulka Tectonic Event. However, field relationships show that some shear zones are cut by the c. 755 Ma dolerite dykes suggesting that there was also an older reactivation event. In the northern half of the orogen, numerous shear zones with dextral kinematics cut metasedimentary rocks of the 1680–1465 Ma Edmund Group and probably the 1170–1070 Ma Collier Group, but the age of this faulting and shear zone reactivation event is unknown.

The focus of this study is to determine the age and cause of the low-temperature reactivation of shear zones in the northern Capricorn

Table 1
Summary of field data and sample details from the Gascoyne Province, Capricorn Orogen.

Sample ID	Latitude (N)	Longitude (E)	Rock type	Structures	Shear Zone	$^{40}\text{Ar}/^{39}\text{Ar}$ age (Ma)	$^{207}\text{Pb}/^{206}\text{Pb}$ (Ma)
GSWA 149,009 (6)	–24° 22' 12.91	116° 04' 04.03	Laminated siltstone	Bedding 305°/76° NE (35°)	T1 Tree Shear Zone	891 ± 26	10
GSWA 149,010 (6)	–24° 21' 59.33	116° 04' 01.36	Silicified mudstone	Cleavage 106°/80° SW (196°)	T1 Tree Shear Zone	882 ± 3	25
GSWA 183,294 (4)	–24° 20' 27.81	116° 17' 24.73	Quartz-muscovite mylonite	Lineation 25°/41°	Shears within the Minnie Creek batholith	882 ± 3	
GSWA 183,295 (5)	–24° 19' 25.22	116° 08' 42.01	Quartz-muscovite mylonite	1520–1770 Ma Metamorphic foliation 141°/85° WSW	Shears within the Minnie Creek batholith	862 ± 4*	
GSWA 195890E (3)	–23° 31' 33.13	115° 25' 03.46	Porphyritic muscovite-biotite monzogranite	Lineation 30°/112° 1520–1770 Ma Metamorphic foliation 304°/87° NE Lineation 0°/140° and 0°/160° Vertical mylonite sets at 140° and 160° 1680–1620 Ma Metamorphic foliation 140°/85° WSW	2 km west of Collins Fault		
GSWA 216540B (2)	–23° 16' 47.97	115° 21' 06.19	Leucocratic muscovite-biotite monzogranite	Vertical mylonites trend at 160°	Collins Fault	898 ± 3*	
GSWA 216,533 (1)	–23° 16' 48.42	115° 20' 37.93	Biotite-garnet schist	1680–1620 Ma Metamorphic foliation 190°/90°	0.8 km west of the Collins Fault	908 ± 3	
GSWA 216,533 (1)	–23° 16' 48.42	115° 20' 37.93	Biotite-garnet schist	1680–1620 Ma Metamorphic foliation 151°/30° WSW	0.8 km west of the Collins Fault	918 ± 3	
GSWA 195890D (3)	–23° 31' 33.13	115° 25' 03.46	Porphyritic muscovite-biotite monzogranite	1680–1620 Ma Metamorphic foliation 151°/30° WSW	2 km west of Collins Fault	1642 ± 7	
GSWA 195890E (3)	–23° 31' 33.13	115° 25' 03.46	Porphyritic muscovite-biotite monzogranite	Lineation 0°/140° and 0°/160° Vertical mylonite sets at 140° and 160° 1680–1620 Ma Metamorphic foliation 140°/85° WSW	2 km west of Collins Fault	1639 ± 8	

Notes: Numbers in brackets, in sample ID column, refer to locations in Fig. 1 in the main body text.

Planar structures are quoted as strike/dip.

Pb* indicates radiogenic Pb (i.e. corrected for common Pb).

$^{207}\text{Pb}/^{206}\text{Pb}$ xenotime weighted mean dates are reported with 95% confidence limits unless otherwise specified.

$^{40}\text{Ar}/^{39}\text{Ar}$ weighted means reported at 2 sigma level.

*Indicates a mini plateau age.

A.M. Piechocka et al.

Precambrian Research 310 (2018) 391–406

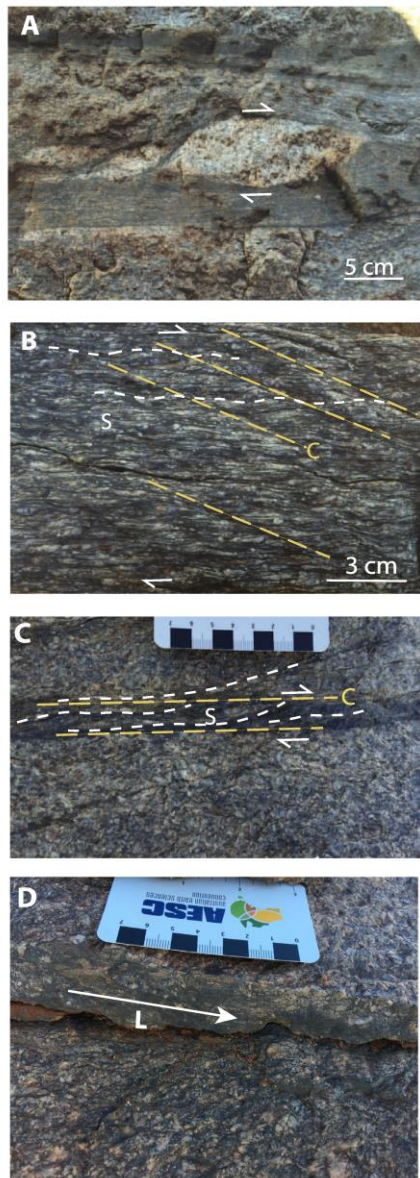


Fig. 2. A: Granitic clast (composed of feldspar and quartz) with dextral sigma tails within a ~15 cm-wide mylonite zone (Collins Fault, locality 2, GSWA 216540B). B: Extensional crenulation cleavage defined by recrystallised biotite and feldspar augen within a porphyritic biotite rich monzogranite, locality within 80 m of sample GSWA 216540B (Collins Fault, locality 2). C: Well-developed C-S fabric in the porphyritic muscovite-biotite monzogranite showing a lower strain rate and less deformation away from the major Collins Fault (Locality 3 and GSWA 195890). D: Subhorizontal lineation within a mylonite zone at Locality 3. For localities refer to Fig. 1.

Orogen by integrating $^{40}\text{Ar}/^{39}\text{Ar}$ mica and U-Pb xenotime geochronology. Dating low-grade hydrothermal fluid flow within major faults may be achieved by U-Pb phosphate geochronology (e.g., Rasmussen et al., 2007, 2010) but preliminary dating of one major shear zone, in the northern Gascoyne Province, using monazite yielded a Paleoproterozoic age (unpublished data) which is likely to date the host rock rather than the reactivation. Although, no datable xenotime was identified in the northern shear zones we were able to date a central shear zone using U-Pb xenotime geochronology. Therefore we turned to $^{40}\text{Ar}/^{39}\text{Ar}$ mica geochronology to date the low-grade fault reactivation in the Gascoyne Province. Our study also demonstrates that the reactivation event dated here does not involve substantial crustal thickening or exhumation, unlike other key examples of compressional intraplate orogens.

2. Intraplate reworking and reactivation in the Gascoyne Province

2.1. Reworking

The earliest episode of reworking occurred at 1820–1770 Ma during the Capricorn Orogeny and is marked by the emplacement of voluminous felsic magmatic rocks and extensive deformation, mostly at low to medium metamorphic grade (Sheppard et al., 2010a). This event has the largest metamorphic and magmatic footprint of all the intraplate reworking events to have affected the orogen; igneous rocks, metamorphic assemblages and structures attributed to the Capricorn Orogeny span the entire orogen, from the Errabiddy Shear Zone in the south to north of the Collins Fault (Fig. 1). The Capricorn Orogeny was followed by the 1680–1620 Ma Mangaroon Orogeny, which is characterised by voluminous felsic magmatism and complex deformation and medium- to high-grade metamorphism (< 750 °C and < 6 kbar; Sheppard et al., 2005). The Mangaroon Orogeny reworked a smaller portion of the Gascoyne Province with only the central and northern parts affected (i.e., from the Chalba Shear Zone to the Collins Fault). The next event was the Mutherbukin Tectonic Event at 1320–1170 Ma, which comprised deformation and metamorphism at > 650 °C and 4.4–7 kbar (Korhonen et al., 2017), but without magmatism, affecting the central parts of the orogen only (i.e., between the Ti Tree Shear Zone and Chalba Shear Zone). The youngest reworking event, the Mesoproterozoic Edmondian Orogeny 1030–950 Ma (Sheppard et al., 2007), is restricted to a 20 km-wide structural corridor south of the Ti Tree Shear Zone (Fig. 1). This orogeny was characterised by local deformation and greenschist to amphibolite facies metamorphism (500–550 °C and 3–4 kbar) from 1030 to 990 Ma and leucocratic magmatism at 950 Ma (Sheppard et al., 2007). The age of leucocratic magmatism was further constrained by Piechocka et al. (2017) from 1006 to 899 Ma, showing that magmatism persisted for c. 90 million years and providing a new minimum age constraint for the Edmondian Orogeny at 900 Ma.

2.2. Reactivation

The youngest known events in the Capricorn Orogen involve the reactivation of a series of major, sub-parallel, predominantly low-grade shear zones and faults (Fig. 1), many of which are crustal-scale structures related to the assembly of the West Australian Craton (Johnson

A.M. Piechocka et al.

Precambrian Research 310 (2018) 391–406

et al., 2013). However, the timing of this reactivation is poorly constrained. The youngest known reactivation event was identified by a c. 570 Ma $^{40}\text{Ar}/^{39}\text{Ar}$ mica date from a dextral shear zone in the central part of the Gascoyne Province that cross-cuts and offsets dolerite dykes of the c. 755 Ma Mundine Well Dolerite Suite (Bodorkos and Wingate, 2007; Wingate and Giddings, 2000). However, other cross-cutting relationships imply that most of the reactivation is older because shear zones and faults that affect Mesoproterozoic sedimentary rocks of the Edmund Basin and, possibly the Collier Basin (Cutten et al., 2016) are themselves cut by c. 755 Ma dolerite dykes (Wingate and Giddings, 2000). These field relationships suggest the presence of another reactivation event between c. 1465 and 755 Ma in the Capricorn Orogen.

3. Characteristics of fault and shear zone reactivation and sample details

In the Gascoyne Province the major faults and shear zones, as well as their ancillary structures, are sub-vertical at surface and some carry a shallow-plunging (0–30°) stretching lineation (sub-horizontal in the north and plunging up to 30° in the central parts of the province), implying dominantly strike-slip deformation with a minor component of uplift in the centre of the province (Table 1). Regional-scale map patterns of anastomosing faults, as well as local shear sense indicators (sigma and delta porphyroclasts, S–C fabrics and asymmetric extensional shear bands; Fig. 2A–C; Hanmer and Passchier, 1991), imply an overall dextral sense of shear, although the style of deformation varies across the province.

3.1. The northern Gascoyne Province (Collins Fault)

In the northern part of the Gascoyne Province (i.e., Collins Fault) deformation is partitioned mainly into discrete, 1–50 mm-wide, anastomosing zones of mylonite within medium- to coarse-grained granitic rocks (Fig. 3A). The mylonite zones commonly show millimetre- to centimetre-scale offsets, with the production of early ductile S–C fabrics that are overprinted by brittle cataclastic textures. Samples GSWA 216540B and 195890B and D–E, which are representative of these thin mylonites, were collected from two different localities (Fig. 1; Table 1) showing different levels of strain (Fig. 2A and C) for $^{40}\text{Ar}/^{39}\text{Ar}$ mica dating. Horizontal lineations (Fig. 2D) and shear sense indicators at the GSWA 195890 sample locality (Table 1) suggest dextral strike-slip movement.

Sample GSWA 216540B is a deformed muscovite–biotite metamonzogranite comprising K-feldspar, quartz, plagioclase and muscovite with 5% mafic minerals biotite, chlorite (2%) and accessory zircon and monazite. The quartz is recrystallised and shows undulose extinction. The well-defined foliation is characterised by aligned recrystallised quartz and elongate muscovite crystals. Zones of mylonitisation are characterised by fine-grained recrystallised muscovite, with the occasional larger primary muscovite (Fig. 3E and F). Feldspar porphyroclasts are elongate and show sigma tails with a dextral sense of shear. There is minimal preservation of primary igneous textures (in contrast to GSWA195890 below) with sparse relatively undeformed K-feldspar phenocrysts. Sericite and perthite are indicative of post magmatic alteration.

Sample GSWA 195890 (B and D–E) is a medium-grained muscovite–biotite metamonzogranite that in parts contains a well-developed S–C fabric. The metamonzogranite shows variation in strain across the outcrop with zones of mylonitisation (biotite), quartz veining and brecciation and zones with preserved igneous textures. The typical mineral assemblage consists of K-feldspar, quartz, muscovite and plagioclase with mafic minerals making up around 25% and includes biotite, chlorite (10–15%) iron oxides with accessory fluorite, zircon and monazite. The preserved igneous muscovite (as mildly deformed porphyroclasts) occur as large crystals up to ~4 mm in length and the biotite forms the very fine-grained matrix (Fig. 3A–D).

Deformation is also partitioned into laterally discontinuous, compositionally weaker zones 0.3–10 m wide. One sample from a ~30 cm-wide zone of strongly deformed, biotite–garnet gneiss (sample GSWA 216533) with 1–5 cm-wide, discontinuous leucocratic veins (Fig. 4B) was collected for $^{40}\text{Ar}/^{39}\text{Ar}$ mica dating. Sample GSWA 216533 is defined by a well-developed gneissic fabric comprised of alternating domains of elongate biotite with minor elongate muscovite; recrystallised quartz; and, recrystallised very-fine grained muscovite. The mineral assemblage is garnet (15%), biotite (25%), quartz (20%), muscovite (20%), chlorite (9%), epidote (8%), opaques (2%), and plagioclase (1%). The inclusions in the garnet cores consist of quartz, muscovite and biotite, with epidote in the garnet rims. The biotite ranges in pleochroism from light tan colour to a medium green-brown colour. The biotite porphyroblasts that occur within the very fine-grained muscovite layer typically show two internal fabrics (Fig. 3G and H). The fabric shows either an oblique orientation to the main foliation or is parallel to the foliation. Muscovite occurs as millimetre-sized tabular crystals intergrown with the biotite. Recrystallised muscovite forms the very fine-grained matrix. Some of the quartz and biotite show sigma tails with dextral kinematics. Late chlorite alteration post-dates the peak metamorphic assemblage.

3.2. The central Gascoyne Province (Ti Tree shear Zone)

In the central part of the province (north of the Ti Tree Shear Zone) discrete, discontinuous zones of quartz–muscovite mylonite up to 5 m wide are developed in coarse-grained granitic rocks (Fig. 4C). These mylonites are associated with ancillary structures related to major faults. The quartz mylonites are steeply dipping with shallowly-plunging east–southeast stretching lineations and locally contain well-developed S–C fabrics that indicate dextral strike-slip movement. Two samples (GSWA 183284 and 183285) were collected for $^{40}\text{Ar}/^{39}\text{Ar}$ mica dating from typical quartz–muscovite mylonite zones. Shallowly plunging lineations (Fig. 4C) within the quartz–muscovite mylonite zones (Table 1) indicate predominantly strike-slip movement with minor uplift of the southern side.

The Ti Tree Shear Zone is interpreted to be a major crustal structure (Johnson et al., 2013) with evidence for multiple Proterozoic movements (Korhonen et al., 2017). At the southeastern end of the shear zone phyllites of the Edmund Group have been strongly silicified (Fig. 4D) and contain a steeply dipping cleavage and steeply plunging intrafolial folds with axial surfaces parallel to the cleavage. Two quartz phyllite samples (GSWA 149009 and 149010, ~400 m apart) were collected for U–Pb xenotime geochronology.

A summary of all samples used in this study and location details are provided in Table 1.

4. Geochronology methodology

4.1. $^{40}\text{Ar}/^{39}\text{Ar}$ Ar mica geochronology

$^{40}\text{Ar}/^{39}\text{Ar}$ geochronology was carried out on single mica crystals from mineral separates of seven samples; muscovite was dated from six of these samples (GSWA 183294, 183295, 195890D–E, 216533 and 216540B) and biotite from two of them (samples GSWA 195890B and 216533). Muscovite and biotite crystals, ranging from 355 to 125 μm size fractions, were washed and dried and then hand-picked under a binocular stereomicroscope. Only unaltered and transparent grains were chosen. The best looking grains were selected and were irradiated for 40 h in the Oregon State University nuclear reactor in central position during two separate irradiations (I22 in April–July 2016 and I23 in November 2016–February 2017). For both irradiations the best grains (i.e., transparent with pearly lustre) were loaded in two separate discs that were Cd-shielded (to minimize undesirable nuclear interference reactions). I23 included a fully calibrated Fish Canyon sanidine (FCs) standard, for which an age of 28.294 Ma ($\pm 0.13\%$; Renne et al.,

A.M. Piechocka et al.

Precambrian Research 310 (2018) 391–406

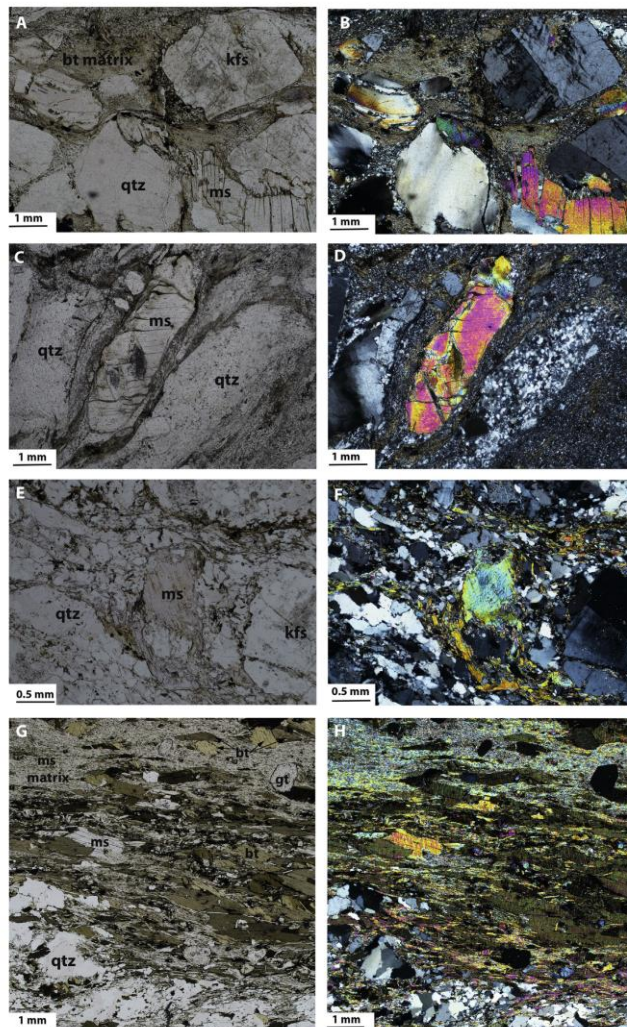


Fig. 3. Plane polarized light and crossed polar photomicrographs of typical mica crystals from the host granites and mylonite zones in the Collins Fault area. All samples yielded a Neoproterozoic age with the exception of GSWA 195890D (images C and D) which yielded a Paleoproterozoic age. A–D. Sample GSWA195890B (A and B) and 195890D (C and D) (3) a porphyritic muscovite–biotite metazonogranite shows well preserved primary igneous muscovite surrounded by a finer grained matrix of biotite and quartz. E and F. Sample GSWA 216540B (2) a deformed metazonogranite shows minimal preservation of primary igneous textures with recrystallised muscovite defining the main foliation. G–H. Sample GSWA 216,533 (1) a garnet–biotite gneiss defined by alternating layers of recrystallised quartz, tabular biotite and muscovite and recrystallised muscovite. ms = muscovite, bt = biotite, kfs = K-feldspar, qtz = quartz, gt = garnet. Numbers in brackets refer to locations in Fig. 1.

2011) was used and I22 included a fully calibrated WA1ms standard, which has an age of 2613 Ma ($\pm 0.09\%$; Jourdan et al., 2014). The detailed analytical methodology is provided in Appendix A.

The mean J-value (irradiation parameter) computed from standard grains within the small pits was 0.01055740 ± 00000792 ($\pm 0.075\%$ 1 sigma) for the samples in irradiation I22 and 0.01085900 ± 00001466 ($\pm 0.135\%$ 1 sigma) for the samples in irradiation I23. Mass discrimination was monitored regularly through the analysis using an automated air pipette and provided a mean value of 1.00431 ($\pm 0.04\%$) per dalton (atomic mass unit) relative to an air

ratio of 298.56 ± 0.31 (Lee et al., 2006) for I22 and 1.003996 ($\pm 0.06\%$) per dalton (atomic mass unit) relative to an air ratio of 298.56 ± 0.31 (Lee et al., 2006) for I23. The correction factors for interfering isotopes were $(^{39}\text{Ar}/^{37}\text{Ar})_{\text{Ca}} = 7.0 \times 10^{-4}$ ($\pm 1.2\%$), $(^{36}\text{Ar}/^{37}\text{Ar})_{\text{Ca}} = 2.6 \times 10^{-4}$ ($\pm 0.4\%$) and $(^{40}\text{Ar}/^{39}\text{Ar})_{\text{K}} = 7.3 \times 10^{-4}$ ($\pm 12.4\%$).

The criteria for the determination of plateaus are as follows: a plateau must include at least 70% of ^{39}Ar and the plateau should be distributed over a minimum of three consecutive steps agreeing at 95% confidence level and satisfying a probability of fit, or P-value, (P) of at

A.M. Piechocka et al.

Precambrian Research 310 (2018) 391–406

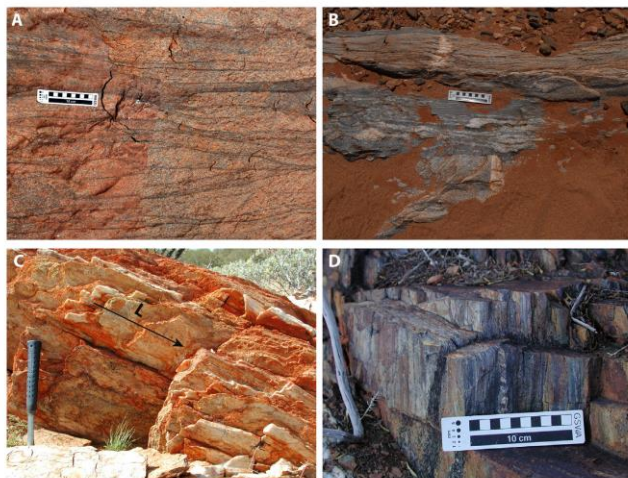


Fig. 4. A. Collins Fault outcrop showing anastomosing zones of 1–50 mm-wide mylonite within medium- to coarse-grained granitic rocks, GSWA 216540B (2). B. Compositionally weaker biotite–garnet schist (1) enclaves within medium- to coarse-grained granitic rocks ~0.8 km west of the Collins Fault, GSWA 216533. C. ~5 m quartz mylonites (4) developed in granites with shallow plunging lineations from the central Gascoyne Province, GSWA 183294. D. Outcrop of a strongly foliated mudstone tending to chert (Edmund Group) (6) at the Ti Tree Shear Zone, GSWA 149010. Numbers in brackets refer to locations in Fig. 1 in the main body text.

least 0.05 (e.g., Jourdan et al., 2005). Mini-plateaus follow the same criteria except that they include between 50% and 70% of released ^{39}Ar and, as a consequence, are considered less reliable. Uncertainties include analytical and J-value errors. Plateau and mini-plateau ages from step-heated single-grain aliquots are reported with 2 sigma uncertainties.

4.2. SHRIMP U–Pb xenotime geochronology

Two samples were analysed using *in situ* U–Pb xenotime geochronology. Optical microscopy and scanning electron microscopy were used to identify suitable xenotime crystals (> 15 μm in diameter) for analysis by Sensitive High Resolution Ion Microprobe (SHRIMP). Xenotime grains > 15 μm across were drilled out in 3 mm-diameter plugs and cast in a single 25 mm epoxy mount. Xenotime reference materials were in a separate mount that was cleaned and Au-coated with the sample mounts prior to analysis.

The U–Pb data were obtained during two SHRIMP analytical sessions on the 13th and 20th October 2008. An O_2^- primary beam, with a spot size of 10–15 μm , was focussed through a 30 μm Kohler aperture with a beam intensity of 0.22–0.28 nA. The secondary ion beam was focussed through a 100- μm collector slit onto an electron multiplier to produce mass peaks with flat tops and a mass resolution (1% peak heights) of > 5000. A post-collector retardation lens was used to reduce stray ion produced from background counts. Xenotime was analysed with a 9-peak run table, and analytical procedures followed established methodologies (Fletcher et al., 2000, 2004). The primary Pb/U standard MG-1 ($^{206}\text{Pb}/^{238}\text{U}$ age of 490 Ma, $^{207}\text{Pb}/^{206}\text{Pb}$ age of 491.8 Ma, and U concentration of 1050 ppm) (Fletcher et al., 2004) was used for Pb/U, Pb/Th, and U and Th abundance calibrations. The secondary standards were z6413 (XENO1 of Stern and Rainbird, 2001) and BS-1 (Fletcher et al., 2004) used in conjunction with MG-1 for matrix corrections to Pb/U and Pb/Th. Z6413 was also used to monitor (and if necessary to correct) instrumental mass fractionation in $^{207}\text{Pb}/^{206}\text{Pb}$.

Squid-2.50.11.02.03 software (Ludwig, 2009) was used for initial data reduction, including correction for common Pb. Common Pb corrections were based on individual measured ^{204}Pb abundances and assuming crustal common Pb at the approximate age of the samples modelled by Stacey and Kramers (1975). Corrections for matrix effects

in Pb/U and Pb/Th, and for instrumental mass fractionation in $^{207}\text{Pb}/^{206}\text{Pb}$, were carried out following established protocols as described by Fletcher et al. (2004). Weighted mean dates are reported with 95% confidence limits, whereas individual analyses are presented with 1 sigma uncertainties.

5. Geochronology results

5.1. $^{40}\text{Ar}/^{39}\text{Ar}$ mica age data

Single-grain muscovite from a mylonite sample at the Collins Fault (GSWA 216540B) yielded a plateau age of 898 ± 3 Ma (mini-plateau) (mean square weighted deviation (MSWD) = 1.07, $P = 0.38$). Single-grain muscovite and biotite from a biotite–garnet gneiss (GSWA 216533), ~0.8 km west of the Collins Fault, yielded plateau ages of, respectively, 918 ± 3 Ma (MSWD = 1.44, $P = 0.13$) and 908 ± 3 Ma (MSWD = 1.35, $P = 0.24$). Single-grain biotite from a mylonite ~2 km west of the Collins Fault (GSWA 195890B), yielded a plateau age of 862 ± 4 Ma (mini-plateau) (MSWD = 0.68, $P = 0.64$). However, muscovite from the same variably deformed outcrop sample yielded plateau ages of 1642 ± 7 Ma (MSWD = 1.72, $P = 0.08$) (GSWA 195890D) and 1639 ± 8 Ma (MSWD = 1.67, $P = 0.08$) (GSWA 195890E). Two quartz–mylonite samples from the centre of the orogen yielded muscovite plateau ages of 882 ± 3 Ma (MSWD = 1.19, $P = 0.27$) (183294) and 882 ± 3 Ma (MSWD = 0.67, $P = 0.77$) (GSWA 183295).

In summary, six plateau ages were calculated from our samples with > 70% ^{39}Ar released, and two ‘mini-plateau’ ages were calculated with > 50% ^{39}Ar (Figs. 5 and 6 and Table 2). The typical mica crystals seen in thin section from samples GSWA 195890B and D, 216533 and 216540B are shown in Fig. 3. However, since the analyses were completed on single grains from mineral separates it is not known whether the typical grains shown are the ones that were analysed.

5.2. U–Pb xenotime age data

Two xenotime crystals with distinct morphologies were identified in phyllite sample GSWA 149,009 from the Ti Tree Shear Zone: a $50 \times 80 \mu\text{m}$, anhedral crystal wrapped by the main foliation and a

A.M. Piechocka et al.

Precambrian Research 310 (2018) 391–406

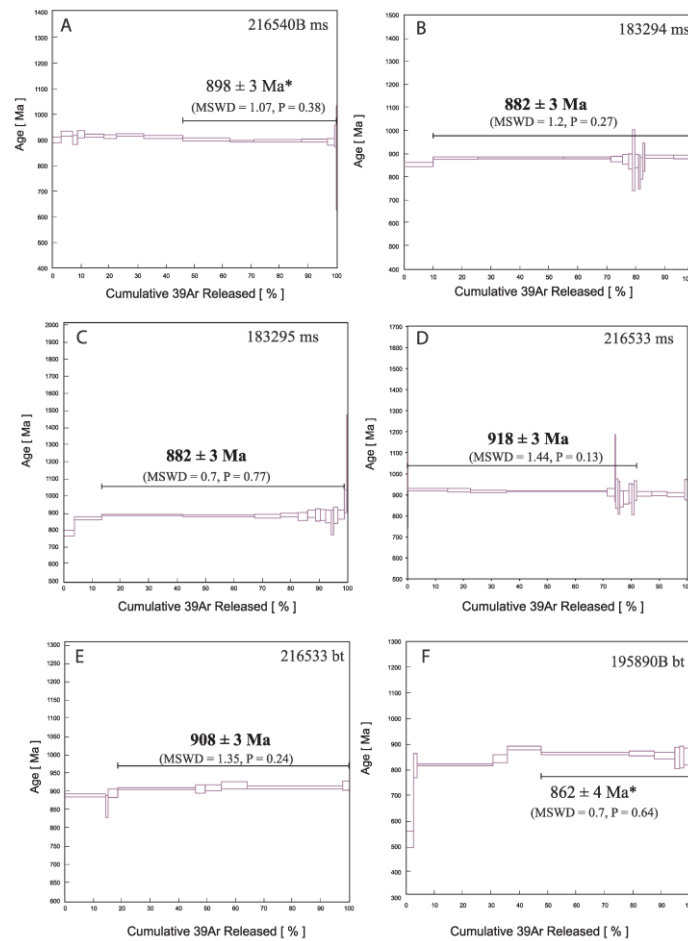


Fig. 5. A–F: $^{40}\text{Ar}/^{39}\text{Ar}$ age plateaus from mylonites within metagranites and quartz mylonites and a biotite schist from the Gascoyne Province. Asterisk indicates mini-plateau age determination. Mean ages are reported with 2 sigma uncertainty. ms = muscovite; bt = biotite.

subhedral crystal ($\sim 20 \mu\text{m}$ across) (Fig. 7A and B). Four analyses of the anhedral crystal yielded a weighted mean $^{207}\text{Pb}^*/^{206}\text{Pb}^*$ date of c. 1275 Ma and a single analysis on the subhedral crystal yielded a date of $891 \pm 26 \text{ Ma}$ (1σ) (Table 3). The second phyllite sample (GSWA 149010) contained elongate or subhedral xenotime crystals from ~ 30 to $90 \mu\text{m}$ in diameter (Fig. 7C–E). Seven analyses were carried out on five xenotime crystals (Table 3). Three statistical outliers (> 2 standard deviations from the mean) were excluded from the main group. The remaining four analyses yielded a weighted mean $^{207}\text{Pb}^*/^{206}\text{Pb}^*$ date of $887 \pm 17 \text{ Ma}$ (MSWD = 1.3) indistinguishable from the single analysis of $891 \pm 26 \text{ Ma}$ in the first sample. Combining the five analyses from the two samples yields a weighted mean $^{207}\text{Pb}^*/^{206}\text{Pb}^*$ date of $887 \pm 9 \text{ Ma}$ (MSWD = 0.96, $n = 5$) (Fig. 7F) interpreted as the age of hydrothermal xenotime growth.

6. Discussion

Our $^{40}\text{Ar}/^{39}\text{Ar}$ mica and U–Pb xenotime results of 918–862 Ma overlap with previously published total fusion $^{40}\text{Ar}/^{39}\text{Ar}$ mica dates of 960–820 Ma obtained from the Errabiddy Shear Zone in the southern Capricorn Orogen (Occhipinti and Reddy, 2009). In that study the authors interpreted their results as cooling ages related to the Edmondian Orogeny. Because mica argon dates in metamorphic terrains can either be interpreted as cooling ages (Scibiorski et al., 2015) or deformation ages (Hansma et al., 2016) we discuss the possibility of our data in terms of a new growth phase or cooling process. To assist with the interpretation we conducted diffusion modelling of muscovite. We integrate our new results with previously published geochronology to show that fault and shear zone reactivation spans not only the Gascoyne

A.M. Piechocka et al.

Precambrian Research 310 (2018) 391–406

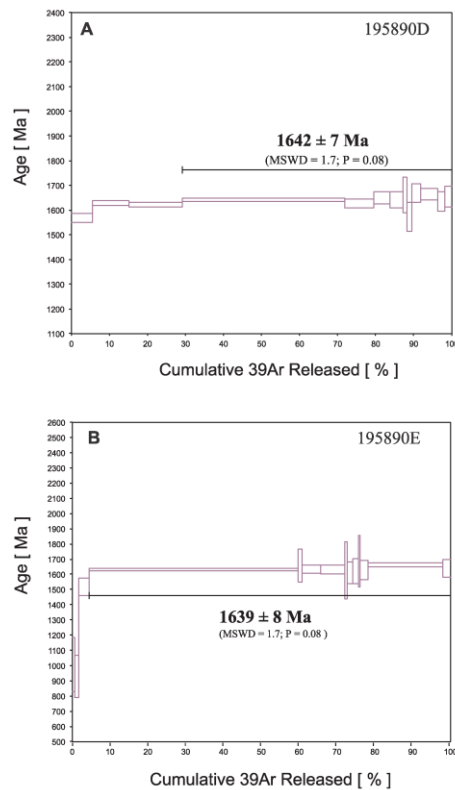


Fig. 6. A–B: $^{40}\text{Ar}/^{39}\text{Ar}$ muscovite age plateaus from a Paleoproterozoic meta-granite from the Gascoyne Province. Mean ages are reported with 2σ uncertainty.

Province but the bounding Archean cratons.

6.1. $^{40}\text{Ar}/^{39}\text{Ar}$ diffusion modelling of muscovite from the northern Gascoyne Province

Here we test whether the c. 900 Ma plateau ages are the result of

complete thermal resetting of old muscovite (c. 1600 Ma) by regional thermal metamorphism or if they arose from the shear zone reactivation at c. 900 Ma. In the northern Capricorn Orogen, the observed crystal sizes in the shear zone are around 500 μm compared to the 4 mm c. 1640 Ma muscovite crystals (Fig. 3). Since the closure temperature of muscovite is proportional to the crystal (or more accurately domain) size, it is possible that the smaller crystals within the shear zone were reset by a regional Neoproterozoic thermal event whereas the larger crystals from the country rocks remained unaffected (e.g., Dunlap et al., 1991). Therefore, we carried out diffusion simulations on the effect of regional metamorphism on synthetic $^{40}\text{Ar}/^{39}\text{Ar}$ spectra using the ArDiff algorithm (Jourdan and Erglu, 2017). The modelling parameters included the selection of three grain sizes (in radius): 125 μm , 500 μm and 1000 μm (Table 4), each assumed to have resided in the same crustal volume at c. 900 Ma with an identical P–T history during the Neoproterozoic thermal event. The crystallisation age of the host rock was set at 1650 Ma, the known age of granitic rocks in the area (Sheppard et al., 2010b). It was assumed that the temperatures were $\sim 150^\circ\text{C}$ either side of the Neoproterozoic thermal event period (they must have dropped below the muscovite closure temperature soon after igneous crystallisation since we obtained c. 1640 Ma plateau ages). The modelling comprised three time periods. Period 1 (920–880 Ma) involved heating from 150°C up to an assumed peak of 420°C , the minimum temperature needed to fully reset the small muscovite crystals for the duration used. Period 2 (880–860 Ma) involved cooling from the peak back to 150°C . Period 3 (860–0 Ma) represents slow cooling as the rock was exhumed to its present-day location at the surface. The parameters used for the muscovite and the thermal events are listed in Table 4.

The diffusion modelling results show that the conditions needed to fully reset the smallest muscovite crystals (125 μm) at 920–860 Ma (100% ^{40}Ar loss) would also substantially affect the largest muscovite crystals. Muscovite with 500 μm and 1000 μm radius in our models have lost 52% and 26% of their ^{40}Ar s (relative to their Ar contents at 920 Ma immediately before the thermal event), effectively preventing these crystals from yielding plateau or even mini-plateau ages (Fig. 8). Because our $^{40}\text{Ar}/^{39}\text{Ar}$ analyses show that the larger muscovite crystals from the surrounding country rocks do not display strong diffusion patterns but rather yield well-defined plateau ages (Fig. 6), we conclude that it is unlikely that there was a regional thermal event at c. 900 Ma exceeding the muscovite closure temperature. Alternatively, it could be that the processes responsible for the c. 900 Ma muscovite ages were restricted to within the shear zones (i.e., sample 216540B which yielded 898 ± 3 Ma) whereas muscovite in the host granite was largely unaffected by this Neoproterozoic event (i.e., samples GSWA195890D and E which yielded 1642 ± 7 Ma and 1639 ± 8 Ma, respectively). As a consequence, our results suggest that either conditions within the shear zone (Collins Fault) were above the closure temperature ($\sim 450^\circ\text{C}$) at c. 900 Ma but were much lower temperature away from the shear zone, or that regional temperatures were below the closure temperature across the entire northern Capricorn Orogen during

Table 2
 $^{40}\text{Ar}/^{39}\text{Ar}$ muscovite and biotite results from the Gascoyne Province, Capricorn Orogen.

Sample ID	Mineral	Optical properties	Size Fraction (μm)	Plateau Age (Ma $\pm 2\sigma$)	^{39}Ar (%)	MSWD	P	n
GSWA 183294	Muscovite	Aggregates of mica, yellowish color	< 355 > 212	882 ± 3	90.02	1.19	0.27	15
GSWA 183295	Muscovite	Sericitized, opaque and translucent	< 212 > 125	882 ± 3	85.49	0.67	0.77	12
GSWA 195890B	Biotite	Mostly unaltered and fresh	< 250 > 125	$862 \pm 4^*$	52.40	0.68	0.64	6
GSWA 216540B	Muscovite	Transparent, pearly luster	< 355 > 212	$898 \pm 3^*$	54.28	1.07	0.38	7
GSWA 216533	Biotite	Unaltered and fresh	< 355 > 212	908 ± 3	81.55	1.35	0.24	6
GSWA 216533	Muscovite	Transparent, pearly luster	< 355 > 212	918 ± 3	82.01	1.44	0.13	14
GSWA 195890D	Muscovite	Transparent, pearly luster	< 355 > 212	1642 ± 7	70.93	1.72	0.08	10
GSWA 195890E	Muscovite	Transparent, pearly luster	< 212 > 125	1639 ± 8	95.60	1.67	0.08	11

Notes: * indicates mini-plateau age determination (weighted mean age includes 50–70% of total ^{39}Ar . MSWD, mean squared weighted deviation; P, P-value; n, number of steps used in plateau.

A.M. Piechocka et al.

Precambrian Research 310 (2018) 391–406

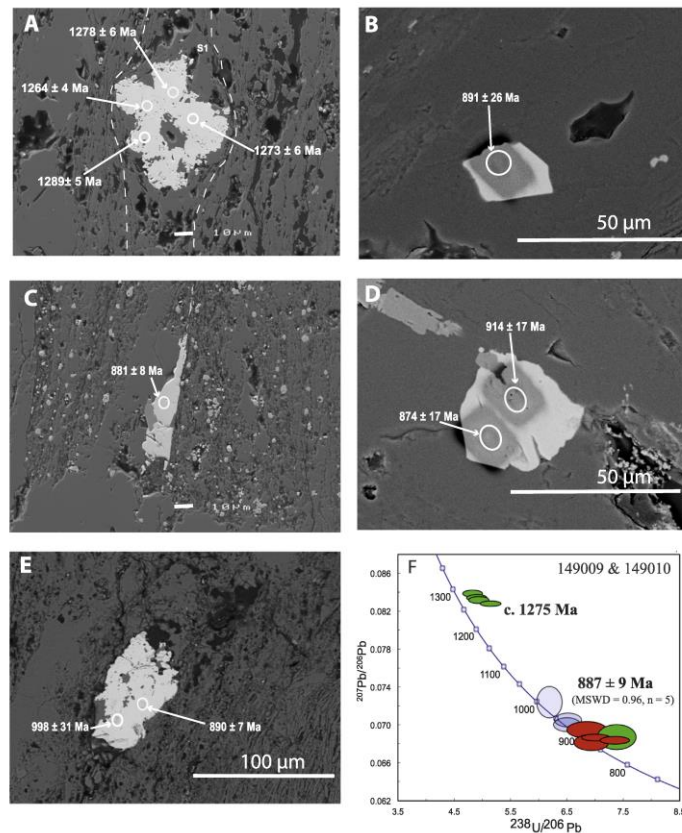


Fig. 7. A–E: Representative backscattered electron images of xenotime from siltstone/mudstone samples. A: Anhedral crystal wrapped by the 1.3–1.2 Ga quartz tectonic fabric (sample 149009). B: euhedral 25 μm xenotime crystal in quartz (Sample 149009). C: Euhedral to subhedral elongate and tabular xenotime crystal growing parallel to the adjacent quartz crystal (sample 149010) with intergrown Fe-oxide. D and E: Subhedral xenotime crystals with intergrowths and/or inclusions of Fe-oxides. F: Combined SHRIMP U-Pb xenotime results from samples 149,009 and 149010. Green ellipses denote analyses from sample 149009, red ellipses denote analyses from sample 149010, and transparent blue ellipses indicate statistical outliers excluded from the final weighted mean age calculation. Mean ages are quoted with 95% uncertainty intervals. (For interpretation of the references to color in this figure legend, the reader is referred to the web version of this article.)

Neoproterozoic reactivation, and the c. 900 Ma muscovite in the shear zone either grew or recrystallised at this time.

6.2. Ages of mica growth or cooling?

Current estimates of the closure temperature for muscovite and biotite are, respectively, $\sim 425 \pm 70^\circ\text{C}$ and $\sim 365 \pm 35^\circ\text{C}$ (Harrison et al., 1985, 2009; recalculated by Scibiorski et al. (2015)). However, there are caveats on closure temperatures which include the following variables: grain size (a reduction in grain size typically causes a reduction in closure temperature: Dodson, 1973); the rate of cooling (faster cooling rates yield higher closure temperatures: Reddy and Potts, 1999) and; temperature of deformation (in particular, greenschist facies deformation commonly causes a reduction in grain size: Dunlap et al., 1991).

Our new $^{40}\text{Ar}/^{39}\text{Ar}$ results from low-grade mylonite zones could be interpreted as ages of mica neocrystallisation or recrystallisation (i.e., reduction in grain size). Determining whether the dates represent neocrystallisation ages can be difficult to ascertain, mainly because our study involve whole-grain analysis of mineral separates, which means the ages obtained cannot be readily linked to any microstructural

observations or compositional data, unlike studies that use *in situ* laser argon analysis (e.g., Mulch and Cosca, 2004; Reddy et al., 1997). However, several mica $^{40}\text{Ar}/^{39}\text{Ar}$ studies on low-grade greenschist facies mylonite zones have demonstrated mica dates as neocrystallisation ages rather than cooling ages (e.g., Kirschner et al., 1996; Dunlap 1997).

Aggregates of muscovite within the mylonite zone at the Collins Fault (e.g., GSWA 216540B), form a well-defined foliation (Fig. 3E–F). In contrast, the Paleoproterozoic host rock sample away from the Collins Fault (GSWA 195890) consists of preserved igneous muscovite (as deformed porphyroclasts) and a foliation defined by very fine-grained biotite (Fig. 3A–D). The sizes of muscovite crystals in the shear zone have been significantly reduced compared with the large igneous muscovite crystals preserved in the host granite. The reduction in size is likely associated with low-grade deformation localised within the shear zone (Dunlap et al., 1991). In contrast, there appears to have been no new muscovite growth in the host rock away from the shear zone (sample GSWA 195890) as the muscovite yielded a Paleoproterozoic age.

Alternatively, our $^{40}\text{Ar}/^{39}\text{Ar}$ dates could be interpreted as cooling ages, an interpretation that would be consistent with that of Oechipint

A.M. Piechocka et al.

Precambrian Research 310 (2018) 391–406

Table 3
SHRIMP U-Pb xenotime data from phyllite samples central Gascoyne Province, Capricorn Orogen.

Grain	Sample	²³⁸ U ⁻	²³² Th ⁻	²³² Th	f ₂₀₆	²³⁸ U/ ²⁰⁶ Pb ⁺	²⁰⁷ Pb ⁺ / ²⁰⁶ Pb ⁺	²⁰⁶ Pb ⁺ / ²³² Th	Disc	²³⁸ U/ ²⁰⁶ Pb ⁺	²⁰⁷ Pb ⁺ / ²⁰⁶ Pb ⁺					
-spot	(ppm)	(ppm)	/ ²³⁸ U	(%)	± 1 s	± 1 s	± 1 s	(%)	date (Ma) ± 1 s	date (Ma) ± 1 s						
<i>Older group</i>																
0812E.1-3	149,009	3878	2469	0.6	0.0103	4.8242	0.1156	0.0838	0.0628	0.0094	0.0002	6	1214	26	1289	5
0812E.1-1	149,009	4058	2882	0.7	0.0058	4.9006	0.1176	0.0834	0.0624	0.0094	0.0002	6	1197	26	1278	6
0812E.1-2	149,009	3668	1633	0.4	0.0114	4.9355	0.1177	0.0832	0.0619	0.0093	0.0002	7	1189	26	1273	6
0812E.1-4	149,009	4340	3205	0.7	0.0077	5.1491	0.1244	0.0828	0.0591	0.0091	0.0002	9	1144	25	1264	4
<i>Main group</i>																
0729G.1-1	149,010	3135	1356	0.4	0.0327	6.8584	0.2335	0.0695	0.0476	0.0096	0.0006	4	877	28	914	17
0729E.1-1	149,009	2144	1423	0.7	0.1163	7.3884	0.2262	0.0688	0.0425	0.0092	0.0009	8	818	23	891	26
0812.J.1-2	149,010	3810	1077	0.3	0.0087	7.0170	0.1664	0.0687	0.0455	0.0097	0.0002	3	859	19	890	7
0812.K.1-1	149,010	2862	842	0.3	0.0219	7.3555	0.1742	0.0684	0.0409	0.0093	0.0003	7	822	18	881	8
0729G.1-2	149,010	2910	771	0.3	0.0320	21.3637	4.5330	0.0682	0.0468	0.0099	0.0006	1	868	24	874	17
<i>Statistical outliers</i>																
0812.J.1-1	149,010	1275	1117	0.9	0.2765	6.1914	0.1481	0.0724	0.0521	0.0097	0.0011	3	965	21	998	31
0812D.1-1	149,010	1232	405	0.3	0.0553	21.0674	4.3294	0.0705	0.0475	0.0098	0.0005	2	920	21	943	14
0812B.1-1	149,010	1850	808	0.4	0.0618	6.5059	0.1568	0.0702	0.0476	0.0099	0.0004	1	922	21	935	13

Notes: ⁻Indicates measured ²³⁸U and ²³²Th levels. The precisions of ²³⁸U and ²³²Th abundances measured by SHRIMP are typically 5–10%.

Pb⁺ indicates radiogenic Pb (i.e. corrected for common Pb).

f₂₀₆, proportion of common ²⁰⁶Pb in measured ²⁰⁶Pb, determined using measured ²⁰⁴Pb/²⁰⁶Pb and contemporaneous common Pb composition (Stacey and Kramers, 1975)

Disc. is apparent discordance, as D (%) = 100 × [(²⁰⁷Pb⁺/²⁰⁶Pb⁺ date) – (²³⁸U/²⁰⁶Pb⁺ date)] / [²⁰⁷Pb⁺/²⁰⁶Pb⁺ date].

Analyses are sorted by descending ²⁰⁷Pb⁺/²⁰⁶Pb⁺.

Table 4
Diffusion parameters and time-temperature history used in the ArArDiff models Jourdan and Eroglu (2017) to generate synthetic age spectra for muscovite.

Diffusion parameters		Mixed phases					
	D ₀ (cm ² /s)	E _a (J/mol)	Radius (μm)	Modal composition	%K ₂ O for each mineral	K ₂ O contribution (mixed phase)	
Muscovite	2.30E+00	264,000	125	1%	0.5%	33%	
Muscovite	2.30E+00	264,000	500	44%	0.01%	33%	
Muscovite	2.30E+00	264,000	1000	45%	0.01%	34%	
<i>Thermal history</i>							
	Crystallization age =	1650	Ma				
		Start (Ma)	End (Ma)	Duration (Ma)	Starting temp. (°C)	Ending temp. (°C)	Cooling rate (°C/Ma)
Period 1		920	880	40	150	470	–8
Period 2		880	860	20	470	150	16
Period 3		860	0	860	150	0	0
Period 4		0	0	0	0	0	

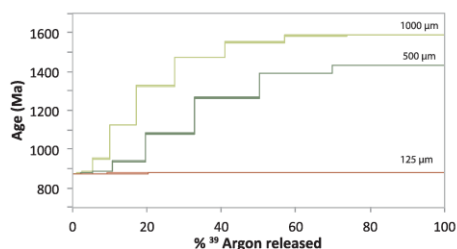


Fig. 8. Modelled ⁴⁰Ar/³⁹Ar age spectra for 125 μm, 500 μm and 1000 μm radius muscovite grains with an initial age of 1650 Ma that were later affected by a thermal overprint at 920–860 Ma that attained a maximum temperature of 460 °C (details of diffusion parameters and thermal history given in Table 4).

and Reddy (2009), who regarded their 960–820 Ma dates from the southern Errabiddy Shear Zone to represent cooling and uplift after the 1030–900 Ma Edmondian Orogeny. In particular, our mica (882 Ma) and xenotime (887 Ma) ages from the central parts of the province closely follow the end stages of reworking (c. 900 Ma) related to the Edmondian Orogeny. The xenotime interpreted as hydrothermal

growth possibly formed during exhumation along the Ti Tree Shear Zone. Therefore, our mica dates from the quartz mylonites, immediately north of the Ti Tree Shear Zone, could also be related to the post-Edmondian cooling and exhumation. Here the lineations plunge at ~30° which indicates there was a component of dip-slip movement in addition to the predominant dextral strike-slip component.

In addition to our ⁴⁰Ar/³⁹Ar dates, there are four occurrences of 920–800 Ma U-Pb phosphate ages from faults zones within the Gascoyne Province and from the bounding Archean cratons: a xenotime date of 887 ± 9 Ma (this study) interpreted to represent new growth aided by hydrothermal fluids moving along the shear zone; monazite and xenotime dates at c. 920 Ma from the Chaiba Shear Zone (Meadows et al., 2017) and; c. 850 Ma and c. 800 Ma phosphate dates, interpreted as growth from hydrothermal fluids moving along faults, from the adjacent Archean cratons (Rasmussen et al., 2007, 2010) (Fig. 9). The U-Pb phosphate ages demonstrate that there were fluids moving along pre-existing faults not only in the Gascoyne Province but within the bounding Archean cratons.

Our ⁴⁰Ar/³⁹Ar dates of 920–860 Ma could be interpreted as cooling ages, neocrystallization or recrystallization ages. However, the diffusion modelling and the petrographic evidence from the northern samples suggests that the 918–898 Ma ages represent mica growth. In contrast, interpretation of the younger muscovite dates (882 Ma), as either growth or cooling, from immediately north of the Ti Tree Shear

A.M. Piechocka et al.

Precambrian Research 310 (2018) 391–406

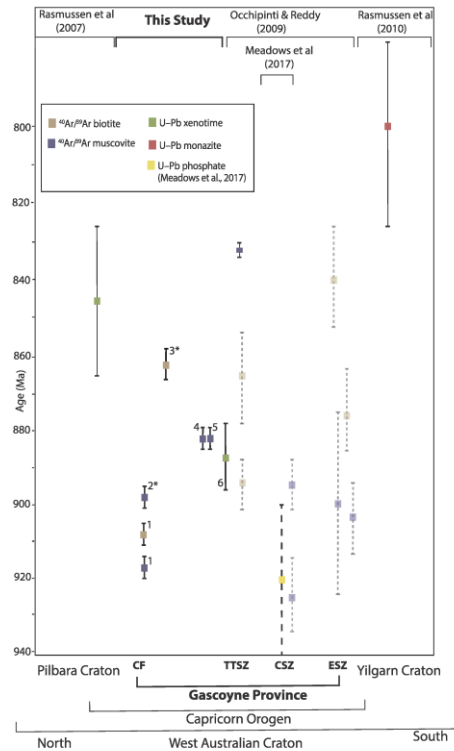


Fig. 9. Summary diagram illustrating the spread of ages defined by $^{40}\text{Ar}/^{39}\text{Ar}$ mica and SHRIMP U-Pb xenotime geochronology from major structures across the Gascoyne Province (this study) in comparison to published geochronology data in the province and from adjacent Archean Cratons. Only representative data from Occhipinti and Reddy (2009) are plotted. *Mini-plateau. (1) GSWA 216533; (2) GSWA 216540B; (3) GSWA 195890B; (4) GSWA 183294; (5) GSWA 183295; (6) GSWA 149,009 & 149101. ESZ—Errabiddy Shear Zone; CSZ—Chalba Shear Zone; TTSZ—Ti Tree Shear Zone; CF—Collins Fault.

Zone remains equivocal.

6.3. The extent of the Neoproterozoic reactivation

Muscovite and biotite from greenschist facies mylonites and shear zones in c. 1680 Ma granitic rocks from the Collins Fault in the northern part of the Gascoyne Province yielded $^{40}\text{Ar}/^{39}\text{Ar}$ dates of 918 ± 3 Ma (muscovite, GSWA 216533), 908 ± 3 Ma (biotite, GSWA 216533) and 898 ± 3 Ma (muscovite mini-plateau age, GSWA 216540B). The muscovite dates are likely to be recording a growth phase for the reasons addressed above. Therefore, the estimated temperature during the reactivation must have been below $\sim 425 \pm 70$ °C (the muscovite closure temperature, Scibiorski et al., 2015). Preliminary U-Pb monazite dating of samples GSWA 216,533 and GSWA 216540B yielded c. 1680 Ma ages (unpublished data). However, muscovite from mylonites in c. 1680 Ma granite ~ 2 km west of the Collins Fault, yielded dates of 1642 ± 7 Ma (GSWA 195890D) and 1639 ± 8 Ma (GSWA 195890E) and are interpreted as cooling ages of igneous muscovite that was

unaffected by the Neoproterozoic reactivation event. However, biotite from the same rock (GSWA 195890B), forming the very fine-grained foliation, yielded a date of 862 ± 4 Ma (mini-plateau). This suggests that the temperature away from the main shear zone was either below or above 365 ± 35 °C (biotite closure temperature) but below 425 ± 70 °C (muscovite closure temperature).

Muscovite from two quartz-muscovite mylonites (GSWA 183,294 and 183295) 14 km apart in c. 1800 Ma granitic rocks (Minnie Creek batholith) farther south in the central part of the province, immediately north of the Ti Tree Shear Zone, both yielded $^{40}\text{Ar}/^{39}\text{Ar}$ dates of 882 ± 3 Ma. These shear zones also show dextral kinematics as seen in the north. This area north of the Ti Tree Shear Zone also was likely to have been uplifted at c. 1640 Ma because of the unconformable relationship between the 1680–1465 Ma Edmund Group sediments and the Minnie Creek batholith (Sheppard et al., 2010b). In contrast to the subhorizontal lineations in the northern part of the province here lineations plunge at $25\text{--}30^\circ$ to the east-southeast which suggests there was some vertical component of movement in addition to the predominant dextral strike-slip component.

In contrast to the northern part of the province that displays consistent dextral movement along faults, the kinematics south of the Ti Tree Shear Zone are ambiguous. Our U-Pb xenotime age of 887 ± 9 Ma from the Ti Tree Shear Zone is interpreted to date hydrothermal fluids flow along the shear zone. This age overlaps with the youngest granite magmatism in this area at 899 ± 10 Ma (Piechocka et al., 2017) related to the Edmundian Orogeny. Our xenotime age may reflect growth during the uplift and exhumation during the later stages of the Edmundian Orogeny.

Our new dates overlap with poorly defined, total fusion $^{40}\text{Ar}/^{39}\text{Ar}$ mica error-dates of 925–820 Ma from the Errabiddy Shear Zone at the southern end of the Gascoyne Province (Occhipinti and Reddy, 2009). These dates were interpreted as approximate cooling ages related to a regional low-grade tectonic event associated with the Edmundian Orogeny (Occhipinti and Reddy, 2009). A single concordant plateau age of 832 ± 1.6 Ma came from a sample south of the Ti Tree Shear Zone (Fig. 1; Occhipinti and Reddy, 2009). Although many of their step-heated samples show signs of disturbance, the dataset does suggest that the Errabiddy Shear Zone was reactivated during the 920–860 Ma tectonism we have dated here. Furthermore, new U-Pb phosphate dates as young as c. 920 Ma suggest that Neoproterozoic activity also affected the Chalba Shear Zone (Meadows et al., 2017) (Fig. 9). Cutten et al. (2016) note that the 1680–1465 Ma Edmund and 1170–1070 Ma Collier Basins, present north of the Ti Tree Shear Zone are weakly metamorphosed. The Edmund Group may have been deformed either during the earlier 1320–1170 Ma Mutherbukin Tectonic Event or the Edmundian Orogeny whereas the younger Collier Group must have been affected during the Edmundian Orogeny or sometime later.

Outside of the core of the Capricorn Orogen, SHRIMP U-Pb *in situ* phosphate dates of c. 850 Ma from the southern Pilbara Craton and 800 Ma from the northern Yilgarn Craton have been interpreted as precipitation from hydrothermal fluid flow along faults (Rasmussen et al., 2007, 2010). Their regional significance was unclear, but they could be related to discrete faulting and shearing in the margins of the bounding Archean cratons in response to the reactivation of faults in the Gascoyne Province dated here at 920–860 Ma (or 920–830 Ma if the single concordant plateau age of Occhipinti and Reddy (2009) is included as part of the same event). It is also likely that at least some faults in the 1170–1070 Ma Collier Basin formed at this time. This Neoproterozoic reactivation appears to overlap with and follow on directly from the 1030–900 Ma Edmundian Orogeny as previously defined. It seems unlikely that events spanning 1030–830 Ma would represent a tectonic continuum, but there are insufficient data at present to subdivide this history into a sequence of discrete tectonic events.

A.M. Piechocka et al.

Precambrian Research 310 (2018) 391–406

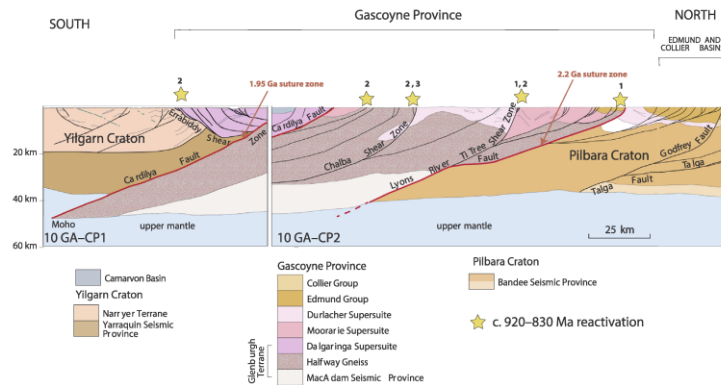


Fig. 10. Interpreted crustal geology from the seismic lines 10GA-CP3 and 10GA-CP2 (Johnson et al., 2013) highlighting the crustal architecture dominated by south dipping mantle tapping faults and shear zones that were reactivated during the 920–830 Ma Neoproterozoic event. Refer to Fig. 1 for location of seismic line. (Modified from Johnson et al., 2013). 1: Reactivation dated in this study; 2: reactivation dated by Occhipinti and Reddy (2009); 3: reactivation dated by Meadows et al., (2017).

6.4. Implications of reactivation of pre-existing crustal sutures and faults

Our results, combined with existing data, show that Neoproterozoic reactivation affected the two former suture zones in the Capricorn Orogen: the 2200 Ma Collins Fault/Lyons River Fault and the 1950 Ma Errabiddy Shear Zone/Cardilya Fault (Occhipinti et al., 2004; Selway et al., 2009; Johnson et al., 2013), as well as other major crustal structures including the Ti Tree Shear Zone and the Chalba Shear Zone (Fig. 10). The Ti Tree Shear Zone is thought to have originated during Mesoproterozoic tectonism (Sheppard et al., 2010b) with recent evidence showing that the Ti Tree Shear Zone was active during the 1320–1170 Ma Mutherbukin Tectonic Event (Korhonen et al., 2017). The Neoproterozoic reactivation is best preserved within discrete structures whereas the adjacent low-grade greenschist rocks lack any distinct Neoproterozoic deformation fabrics (Sheppard et al., 2010b). This suggests that tectonism at this time was focussed within pre-existing structures.

Unlike the Petermann and Alice Springs orogenies in central Australia (Aitken et al., 2009) and the Tien Shan Orogen in central Asia (Raimondo et al., 2014), the lack of significant metamorphic discontinuities across Neoproterozoic shear zones in the Gascoyne Province and their preservation of subhorizontal lineations (at least in the north), suggest very little exhumation or crustal thickening during reactivation. However, we do see evidence for exhumation in the central parts of the province south of the Ti Tree Shear Zone with the juxtaposition of medium-grade rocks (formed during the Edmondian Orogeny) against low-grade metasedimentary rocks of the Edmond Group (Sheppard et al., 2010b).

In this study we have presented evidence for mica growth in the northern parts of the orogen related to dextral strike-slip reactivation. The interpretation of mica ages from the quartz–muscovite mylonites immediately north of the Ti Tree Shear Zone remains equivocal, but our U–Pb xenotime age from the Ti Tree Shear Zone could reflect phosphate growth during exhumation. This interpretation would be consistent with the cooling interpreted by Occhipinti and Reddy (2009). However, our field observations do not support the earlier interpretation of regional uplift of the orogen. Occhipinti and Reddy (2009) interpreted cooling ages of mica from the Gascoyne Province, together with Gascoyne-aged detrital zircon populations in Neoproterozoic Officer Basin

to the east, to infer uplift and erosion of the western Capricorn Orogen. They suggested the cause of uplift to be collision of either Greater India or the Kalahari Craton with the West Australian Craton. However, our new geochronology data tied to dextral strike-slip kinematics of shear zones, in the northern parts of the province, along with the general lack of juxtaposition of rocks of substantially differing metamorphic grade, suggest there was no uplift in the northern part of the province. The structural interpretation of the deep seismic survey (Johnson et al., 2013) (Fig. 10) shows the boundary of the Pilbara Craton to extend at depth to the Ti Tree Shear Zone. Therefore, during north–south compression the southern part of the province may have been squeezed between the more rigid northern block and the Yilgarn Craton, which resulted in strike slip dextral faulting in the northern block and exhumation of the southern part of the orogen.

6.5. From reworking to reactivation on an orogen scale

An interesting finding of our study is that our $^{40}\text{Ar}/^{39}\text{Ar}$ mica and U–Pb xenotime dates from major shear zones and faults are only slightly younger than the youngest reworking event in the province (the 1030–900 Ma Edmondian Orogeny, Piechocka et al., 2017; Sheppard et al., 2007). The Edmondian Orogeny is largely restricted to a 20 km-wide zone in the central part of the province and is marked by greenschist to mid-amphibolite facies metamorphism and deformation. The intrusion of leucocratic granitic plutons and pegmatites in the centre of the orogen however post-dates the medium-grade reworking, which ceased at 990 Ma with magmatism having continued until 899 ± 10 Ma (Piechocka et al., 2017). The age for this youngest granitic rock is similar to our $^{207}\text{Pb}/^{206}\text{Pb}$ date of 887 ± 9 Ma for xenotime, interpreted as hydrothermal growth, from phylrites within the nearby Ti Tree Shear Zone, and to $^{40}\text{Ar}/^{39}\text{Ar}$ dates from across the Gascoyne Province recording reactivation. Therefore, from our new results and those of Piechocka et al. (2017), we show that while crustal reworking finished at 899 ± 10 Ma in the centre of the orogen (the youngest leucocratic magmatism) reactivation was occurring in the northern province at 918 ± 3 Ma. This records the transition from the final crustal reworking event in Capricorn Orogen to reactivation of crustal- and lithospheric-scale structures across the entire Gascoyne Province. Furthermore, the reworking history shows a pattern of

A.M. Piechocka et al.

Precambrian Research 310 (2018) 391–406

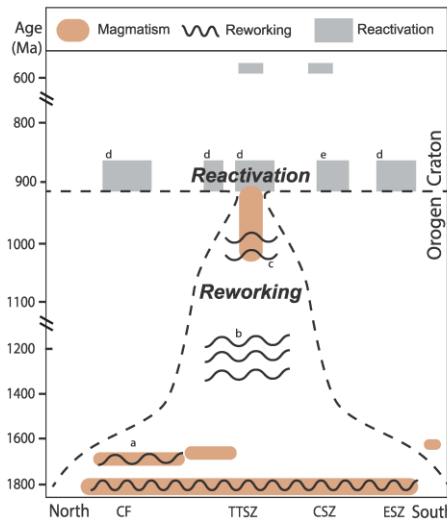


Fig. 11. Simplified time-space plot showing the distribution of reworking and reactivation events spanning the Gascoyne Province. ^a < 750 °C, > 6 kbar (Sheppard et al., 2005); ^b < 650 °C, 4.4–7 kbar (Korhonen and Johnson, 2015); ^c 500–550 °C, 3–4 kbar (Sheppard et al., 2007); ^d < 350 °C (Occhipinti and Reddy 2009; this study); ^e > 640 °C, 3–4 kbar (Meadows et al., 2017). ESZ—Errabiddy Shear Zone; CSZ—Chalba Shear Zone; TTSZ—Ti Tree Shear Zone; CF—Collins Fault.

progressive narrowing of (medium and high-grade) reworking toward the centre of the orogen (Fig. 11) as the crust became more dehydrated and refractory (Korhonen and Johnson, 2015; Johnson et al., 2017).

Our results, which combine multi-mineral geochronology techniques and field observations, demonstrate how a long-lived orogen with a complex and protracted reworking history saw a breakout in fault reactivation across the Gascoyne Province at 920–860 Ma. The footprint of the c. 920–820 Ma Neoproterozoic activity (including the one concordant plateau age from Occhipinti and Reddy (2009)) extends across much of the West Australian Craton suggesting that the far-field forces responsible reflected tectonism on a much larger scale.

7. Conclusions

Our geochronology has identified Neoproterozoic mica dates of 918–862 Ma from shear zones in the northern Gascoyne Province. In the centre of the province we obtained mica dates of 882 Ma and a U–Pb xenotime age of 887 Ma. Argon diffusion modelling and field observations suggest the muscovite ages in the north reflect growth (neocrystallisation or crystallisation) ages during dextral strike-slip reactivation related to the Edmondian Orogeny. We find no evidence of exhumation in the northern parts of the province, but our interpretation of exhumation in the south is consistent with that of Occhipinti and Reddy (2009). However, rather than uplift due to a collision from the west, tectonism may have been caused by north–south compression resulting in a rigid northern block squeezing a less competent piece of crust between the Pilbara and Yilgarn Cratons. Our results suggest that the crustal architecture of the Capricorn Orogen was effectively frozen at c. 900 Ma, with only minor localised subsequent fault-related activity recorded. The lack of evidence for any younger significant regional tectonic events suggests that the structural architecture established

during the Neoproterozoic reactivation event has essentially remained unchanged since then. Nevertheless, some of the structures that were active in the Neoproterozoic continue to be the focus of present-day seismicity (the Middalya and Mount Clere clusters in Fig. 2 of Revets et al., 2009; Keep et al., 2012).

Acknowledgments

The authors thank R. Parrish for constructive comments which have resulted in a more focussed and improved manuscript. C. Mayers of WAIF is thanked for assistance during sample preparation. ⁴⁰Ar/³⁹Ar measurements were conducted at the Western Australian Argo Facility (WAIF) and U–Th–Pb measurements were conducted using the SHRIMP ion microprobes, at the John de Laeter Centre at Curtin University, Western Australia. Simon Johnson publishes with permission of the Director of the Geological Survey of Western Australia. This PhD project was funded through an Australian Research Council (ARC) grant (LP130100922) and the Exploration Incentive Scheme.

Appendix A: Detailed analytical methods for ⁴⁰Ar/³⁹Ar geochronology

Irradiation 22: Twenty-four muscovite grains from sample 195890D were hand-picked from the < 355 μm > 212 μm fraction of which 12 were transparent with a pearly luster and chosen for irradiation. Sample 195890E yielded 30 grains from the < 212 μm > 125 μm fraction of which 25 were transparent with a pearly luster and chosen for irradiation.

Irradiation 23: Thirty muscovite grains from sample 216540B were hand-picked from the < 355 μm > 212 μm fractions and were transparent with a pearly luster. Sample 183294 hosted muscovite grains that were aggregates of mica with a distinct yellowish color, a total of 65 grains were picked from the < 355 μm > 212 μm fractions. Sample 183,295 yielded sericitized, opaque and translucent muscovite either intergrown with quartz (at the < 212 μm fraction) or free flaky mica at the > 125 μm fraction. Biotite from sample 216,533 was unaltered and fresh and 40 grains were picked at the < 355 μm > 212 μm fractions. Forty biotite crystals from sample 195890B were picked from the < 250 μm > 125 μm fractions.

For both irradiations the best grains the selected grains were loaded into discs and were irradiated for 40 h in the Oregon State University nuclear reactor in central position. The discs included a fully intercalibrated FCs standard, for which an age of 28.294 ± 0.037 Ma (± 0.13%; Renne et al., 2011) was used in I23 and a fully calibrated WA1ms standard, for which age of 2613 Ma ± 0.037 Ma (± 0.09%; Jourdan et al., 2014), used in I22. The discs were Cd-shielded (to minimize undesirable nuclear interference reactions) and irradiated in the Oregon State university nuclear reactor (USA) in central position.

For irradiation 22 the mean J-value computed from standard grains within the small pits yielded 0.01055740 ± 00000792 (± 0.075% 1 sigma) for the samples. Mass discrimination was monitored regularly through the analysis using an automated air pipette and provided a mean value of 1.00431 (± 0.04%) per dalton (atomic mass unit) relative to an air ratio of 298.56 ± 0.31 (Lee et al., 2006). The correction factors for interfering isotopes were (³⁹Ar/³⁷Ar)_{Ca} = 7.0 × 10⁻⁴ (± 1.2%), (³⁶Ar/³⁷Ar)_{Ca} = 2.6 × 10⁻⁴ (± 0.4%) and (⁴⁰Ar/³⁹Ar)_K = 7.3 × 10⁻⁴ (± 12.4%).

For irradiation 23 the mean J-value computed from standard grains within the small pits yielded 0.01085900 ± 00001466 (± 0.135% 1 sigma) for the samples. Mass discrimination was monitored regularly through the analysis using an automated air pipette and provided a mean value of 1.003996 (± 0.06%) per dalton (atomic mass unit) relative to an air ratio of 298.56 ± 0.31 (Lee et al., 2006). The correction factors for interfering isotopes were (³⁹Ar/³⁷Ar)_{Ca} = 7.0 × 10⁻⁴ (± 1.3%), (³⁶Ar/³⁷Ar)_{Ca} = 2.7 × 10⁻⁴ (± 0.84%) and (⁴⁰Ar/³⁹Ar)_K = 7.3 × 10⁻⁴ (± 12.4%).

A.M. Piechocka et al.

Precambrian Research 310 (2018) 391–406

During both analytical sessions muscovite and biotite were step-heated using a 110 W Spectron Laser Systems, with a continuous Nd-YAG (IR; 1064 nm) laser rastered over the sample during 1 min to ensure an homogeneously distributed temperature. The gas was purified in a stainless steel extraction line using two SAES AP10 getters and a GP50 getter. Ar isotopes were measured in static mode using a MAP 215–50 mass spectrometer (resolution of ~450; sensitivity of 4×10^{-14} mol/V) with a Balzers SEV 217 electron multiplier using 9 to 10 cycles of peak-hopping. The data acquisition was performed with the Argus program written by M.O. McWilliams and ran under a LabView environment. Blanks were monitored every 3–4 steps and typical ^{40}Ar blanks range from 1×10^{-16} to 2×10^{-16} mol. The raw data were processed using the ArArCALC software (Koppers, 2002) and the ages have been calculated using the decay constants recommended by Renne et al. (2011). Blanks were monitored every 3–4 steps. All parameters and relative abundance values are provided in Supplementary Tables DR S1–6 (a separate file for each sample is attached as an excel spreadsheet) and have been corrected for blank, mass discrimination and radioactive decay. Individual errors in Supplementary Tables DR S2–7 are given at the 1 σ level.

The criteria for the determination of plateau are as follows: plateaus must include at least 70% of ^{39}Ar . The plateau should be distributed over a minimum of 3 consecutive steps agreeing at 95% confidence level and satisfying a probability of fit (P) of at least 0.05 (e.g., Jourdan et al., 2005). Mini-plateaus follow the same criteria except that they include between 50% and 70% ^{39}Ar released and are considered less reliable. Uncertainties include analytical and J-value errors. All sources of uncertainties are included in the calculations.

Appendix B. Supplementary data

Supplementary data associated with this article can be found, in the online version, at <http://dx.doi.org/10.1016/j.precamres.2018.04.006>.

References

- Aitken, A.R.A., Betts, P.G., Ailleres, L., 2009. The architecture, kinematics, and lithospheric processes of a compressional intraplate orogen occurring under Gondwana assembly: the Petermann orogen, central Australia. *Lithosphere* 6, 343–357. <http://dx.doi.org/10.1130/L39.1>.
- Aitken, A.R.A., Raimondo, T., Capitanio, F.A., 2013. The intraplate character of super-continent tectonics. *Gondwana Res.* 24, 807–814. <http://dx.doi.org/10.1016/j.gr.2013.03.005>.
- Bodorkos, S., Wingate, M.T.D., 2007. The contribution of geochronology to GSWA's mapping programs: current perspectives and future directions. *Geol. Survey Western Austr.* 2007 (2), 11.
- Cawood, P.A., Tyler, I.M., 2004. Assembling and reactivating the Proterozoic Capricorn Orogen: lithotectonic elements, orogenies, and significance. *Precamb. Res.* 128, 201–218. <http://dx.doi.org/10.1016/j.precamres.2003.09.001>.
- Cutten, H.N., Johnson, S.P., Thorne, A.M., Wingate, M.T.D., Kirkland, C.L., Belousova, E.A., Blay, O.A., Zwingmann, H., 2016. Deposition, provenance, inversion history and mineralization of the Proterozoic Edmund and Collier Basins, Capricorn Orogen. *Geol. Survey Western Austr. Rep.* 127, 80.
- Dodson, M.H., 1973. Closure temperature in cooling geochronological and petrological systems. *Contrib. Mineral. Petrol.* 40, 259–274. <http://dx.doi.org/10.1007/BF00373790>.
- Dunlap, W.J., 1997. Neocrystallization or cooling? $^{40}\text{Ar}/^{39}\text{Ar}$ ages of white micas from low-grade mylonites. *Chem. Geol.* 143, 181–203. [http://dx.doi.org/10.1016/S0009-2541\(97\)00113-7](http://dx.doi.org/10.1016/S0009-2541(97)00113-7).
- Dunlap, W., Teyssier, C., McDougall, I., Baldwin, S., 1991. Ages of deformation from K/Ar and $^{40}\text{Ar}/^{39}\text{Ar}$ dating of white micas. *Geology* 19, 1213–1216. [http://dx.doi.org/10.1130/0091-7613\(1991\)019<1213:AODFKA>2.3.CO;2](http://dx.doi.org/10.1130/0091-7613(1991)019<1213:AODFKA>2.3.CO;2).
- Dyksterhuis, S., Müller, R.D., 2008. Cause and evolution of intraplate orogeny in Australia. *Geology* 36, 495–498. <http://dx.doi.org/10.1130/G24536A.1>.
- Fletcher, I.R., McNaughton, N.J., Aleinikoff, J.A., Rasmussen, B., Kamo, S.L., 2004. Improved calibration procedures and new standards for U-Pb and Th-Pb dating of Phanerozoic xenotime by ion microprobe. *Chem. Geol.* 209, 295–314. <http://dx.doi.org/10.1016/j.chemgeo.2004.06.015>.
- Fletcher, I.R., McNaughton, N.J., Rasmussen, B., 2000. SHRIMP U-Pb geochronology of authigenic xenotime and its potential for dating sedimentary basins. *Austr. J. Earth Sci.* 47, 845–859. <http://dx.doi.org/10.1046/j.1440-0952.2000.00819.x>.
- Hamner, S., Passchier, C.W., 1991. Shear sense indicators: a review. *Geol. Survey Can.* 90, 70.
- Hansma, J., Tohver, E., Schrank, C., Jourdan, F., Adams, D., 2016. The timing of the Cape Orogeny: new $^{40}\text{Ar}/^{39}\text{Ar}$ age constraints on deformation and cooling of the Cape Fold Belt, South Africa. *Gondwana Res.* 32, 122–137. <http://dx.doi.org/10.1016/j.gr.2015.02.005>.
- Harrison, T.M., G el erier, J., Aikman, A.B., Hermann, J., Heizler, M.T., 2009. Diffusion of ^{40}Ar in muscovite. *Geochimica et Cosmochimica Acta* 73, 1039–1051. <http://dx.doi.org/10.1016/j.gca.2008.09.038>.
- Harrison, T.M., Duncan, I., McDougall, I., 1985. Diffusion of ^{40}Ar in biotite: temperature, pressure and compositional effects. *Geochimica et Cosmochimica Acta* 49, 2461–2468. [http://dx.doi.org/10.1016/0016-7037\(85\)90246-7](http://dx.doi.org/10.1016/0016-7037(85)90246-7).
- Johnson, S.P., Korhonen, F.J., Kirkland, C.L., Cliff, J.B., Belousova, E.A., Sheppard, S., 2017. An isotopic perspective on growth and differentiation of Proterozoic orogenic crust: from subduction magmatism to cratonization. *Lithos* 268, 76–86. <http://dx.doi.org/10.1016/j.lithos.2016.11.003>.
- Johnson, S.P., Sheppard, S., Rasmussen, B., Wingate, M.T.D., Kirkland, C.L., Muhling, J.R., Fletcher, I.R., Belousova, E.A., 2011. Two collisions, two sutures: punctuated pre-1950 Ma assembly of the West Australian Craton during the Ophthalmanian and Glenburgh Orogenies. *Precamb. Res.* 189, 239–262. <http://dx.doi.org/10.1016/j.precamres.2011.07.011>.
- Johnson, S.P., Thorne, A.M., Tyler, I.M., Korsch, R.J., Kennett, B.L.N., Cutten, H.N., Goodwin, J., Blay, O., Blewett, R.S., Joly, A., Dentith, M.C., Aitken, A.R.A., Holzschuh, J., Salmon, M., Reading, A., Heinson, G., Boren, G., Ross, J., Costelloe, R.D., Fomin, T., 2013. Crustal architecture of the Capricorn Orogen, Western Australia and associated metallogeny. *Austr. J. Earth Sci.* 60, 681–705. <http://dx.doi.org/10.1080/08120099.2013.826735>.
- Jourdan, F., Eroglu, E., 2017. $^{40}\text{Ar}/^{39}\text{Ar}$ and (U-Th)/He model age signatures of elusive mercurian and venusian meteorites. *Meteoritics Planetary Sci.*
- Jourdan, F., Ferard, G., Bertrand, A.B., Kampunzu, K., Tshoso, M.K., Watkeys, B., 2005. Karoo large igneous province; brevity, origin, and relation to mass extinction questioned by new $^{40}\text{Ar}/^{39}\text{Ar}$ age data. *Geology* 33, 745–748. <http://dx.doi.org/10.1130/G21632.1>.
- Jourdan, F., Frew, A., Joly, A., Mayers, C., Evans, N.J., 2014. WAlms: A – 2.61 Ga muscovite standard for $^{40}\text{Ar}/^{39}\text{Ar}$ dating. *Geochimica et Cosmochimica Acta* 141, 113–126. <http://dx.doi.org/10.1016/j.gca.2014.06.010>.
- Keep, M., Hengesh, J., Whitney, B., 2012. Natural seismicity and tectonic geomorphology reveal regional transpressive strain in northwestern Australia. *Austr. J. Earth Sci.* 59, 341–354. <http://dx.doi.org/10.1080/08120099.2012.667439>.
- Kirschner, D.I., Cosca, M.A., Masson, H., Hunziker, C., 1996. Staircase $^{40}\text{Ar}/^{39}\text{Ar}$ spectra of fine-grained white mica: timing and duration of deformation and empirical constraints on argon diffusion. *Geology* 24, 747–750. [http://dx.doi.org/10.1130/0091-7613\(1996\)024<0747:AAASD>2.3.CO;2](http://dx.doi.org/10.1130/0091-7613(1996)024<0747:AAASD>2.3.CO;2).
- Korhonen, F.J., Johnson, S.P., 2015. The role of radiogenic heat in prolonged intraplate reworking: the Capricorn Orogen explained? *Earth Planetary Sci. Lett.* 428, 22–32. <http://dx.doi.org/10.1016/j.epsl.2015.06.039>.
- Korhonen, F.J., Johnson, S.P., Wingate, M.T.D., Kirkland, C.L., Fletcher, I.R., Dunkley, D.J., Roberts, M.P., Sheppard, S., Muhling, J.R., Rasmussen, B., 2017. Radiogenic heating and craton-margin plate stresses as drivers for intraplate orogeny. *J. Metamorphic Geol.* 35, 631–661. <http://dx.doi.org/10.1111/jmg.12249>.
- Lee, Y.J., Marti, K., Severinghaus, J.P., Kawamura, K., Yoo, H.S., Lee, J.B., Kim, J.S., 2006. A redetermination of the isotopic abundances of atmospheric Ar. *Geochimica et Cosmochimica Acta* 70, 4507–4512. <http://dx.doi.org/10.1016/j.gca.2006.06.1563>.
- Ludwig, K.R., 2009. *Squid 2.50, A User's Manual*. Berkeley Geochronology Centre Special Publication, pp. 95.
- Meadows, H.R., Reddy, S.M., Clark, C., Plavsa, D., Johnson, T., 2017. Localisation of High Strain and High Temperature into the Chalba Shear Zone. Specialist Group in Tectonics and Structural Geology, Gascoyne Province Conference Abstract.
- Mulch, A., Cosca, M.A., 2004. Recrystallization or cooling ages: *in situ* UV-laser $^{40}\text{Ar}/^{39}\text{Ar}$ geochronology of muscovite in mylonitic rocks. *J. Geol. Soc.* 161, 573–582. <http://dx.doi.org/10.1144/0016-764903-110>.
- Occhipinti, S.A., Reddy, S.M., 2009. Neoproterozoic reworking of the Paleoproterozoic Capricorn Orogen of Western Australia and implications for the amalgamation of Rodinia. *Geol. Soc., London, Spec. Publ.* 327, 445–456. <http://dx.doi.org/10.1144/SP327.18>.
- Occhipinti, S.A., Sheppard, S., Passchier, C., Tyler, I.M., Nelson, D.R., 2004. Paleoproterozoic crustal accretion and collision in the southern Capricorn Orogen: the Glenburgh Orogeny. *Precamb. Res.* 128, 237–255. <http://dx.doi.org/10.1016/j.precamres.2003.09.002>.
- Piechocka, A.M., Gregory, C.J., Zi, J., Sheppard, S., Wingate, M.T.D., Rasmussen, B., 2017. Monazite trumps zircon: applying SHRIMP U-Pb geochronology to systematically evaluate emplacement ages of leucocratic, low-temperature granites in a complex Precambrian orogen. *Contrib. Mineral. Petrol.* 172, 1–17. <http://dx.doi.org/10.1007/s00410-017-1386-5>.
- Raimondo, T., Hand, M., Collins, M.J., 2014. Compressional intracontinental orogens: ancient and modern perspectives. *Earth-Sci. Res.* 130, 128–153. <http://dx.doi.org/10.1016/j.earscirev.2013.11.009>.
- Raimondo, T., Collins, A.S., Hand, M., Walker-Hallam, A., Smithies, R.H., Ewins, P.M., Howard, H.M., 2010. The anatomy of a deep intracontinental orogen. *Tectonics* 29, 1–31. <http://dx.doi.org/10.1029/2009TC002504>.
- Rasmussen, B., Fletcher, I.R., Muhling, J.R., Thorne, W.S., Broadbent, G.C., 2007. Prolonged history of episodic fluid flow in giant hematite ore bodies: Evidence from *in situ* U-Pb geochronology of hydrothermal xenotime. *Earth Planetary Sci. Lett.* 258, 249–259. <http://dx.doi.org/10.1016/j.epsl.2007.03.033>.
- Rasmussen, B., Fletcher, I.R., Muhling, J.R., Wilde, A.W., 2010. *In situ* U-Th-Pb geochronology of monazite and xenotime from the Jack Hills belt: Implications for the age of deposition and metamorphism of Hadean zircons. *Precamb. Res.* 180, 26–46. <http://dx.doi.org/10.1016/j.precamres.2010.03.004>.
- Reddy, S.M., Kelley, S.P., Magennis, L., 1997. A microstructural and argon laserprobe study of shear zone development at the western margin of the Nanga Parbat-

A.M. Piechocka et al.

Precambrian Research 310 (2018) 391–406

- Haramosh Massif, western Himalaya. *Contrib. Mineral. Petrol.* 128, 16–29. <http://dx.doi.org/10.1007/s004100050290>.
- Reddy, S.M., Occhipinti, S.A., 2004. High-strain zone deformation in the southern Capricorn Orogen, Western Australia: Kinematics and age constraints. *Precamb. Res.* 128, 295–314. <http://dx.doi.org/10.1016/j.precamres.2003.09.005>.
- Reddy, S.M., Potts, G.J., 1999. Constraining absolute deformation ages: the relationship between deformation mechanisms and isotope systematics. *J. Struct. Geol.* 21, 1255–1265. [http://dx.doi.org/10.1016/S0191-8141\(99\)00032-2](http://dx.doi.org/10.1016/S0191-8141(99)00032-2).
- Renne, P.R., Balco, G., Ludwig, K.R., Mundil, R., K. Min, Response to the comment by W.H. Schwarz, et al., 2011. on "Joint determination of 40K decay constants and 40Ar/40K for the Fish Canyon sanidine standard, and improved accuracy for 40Ar/39Ar geochronology" by P. R. Renne et al. (2010). *Geochim. Cosmochim. Acta* 75, 5097–5100. <http://dx.doi.org/10.1016/j.gca.2011.06.021>.
- Revels, S.A., Keep, M., Kennett, B.L.N., 2009. NW Australian intraplate seismicity and stress regime. *J. Geophys. Res.* 114, 1–10. <http://dx.doi.org/10.1029/2008jg006152>.
- Schiborski, E., Tolver, E., Jourdan, F., 2015. Rapid cooling and exhumation in the western part of the Mesoproterozoic Albany-Fraser Orogen, Western Australia. *Precamb. Res.* 265, 232–248. <http://dx.doi.org/10.1016/j.precamres.2015.02.005>.
- Schway, K., Sheppard, S., Thorne, A.M., Johnson, S.P., Groenewald, P.B., 2009. Identifying the lithospheric structure of a Precambrian orogen using magnetotellurics: The Capricorn Orogen, Western Australia. *Precamb. Res.* 168, 185–196. <http://dx.doi.org/10.1016/j.precamres.2008.09.010>.
- Sheppard, S., Bodorkos, S., Johnson, S.P., Wingate, M.T.D., Kirkland, C.L., 2010a. The paleoproterozoic capricorn orogeny: intracontinental reworking not continent-continent collision. *Geol. Survey Western Austr.* 108, 33.
- Sheppard, S., Johnson, S.P., Wingate, M.T.D., Kirkland, C.L., Pirajno, F., 2010b. Explanatory notes for the Gascoyne Province. Geological Survey of Western Australia 1:100 000 Explanatory Notes, pp.336.
- Sheppard, S., Occhipinti, S.A., Nelson, D.R., 2005. Intracontinental reworking in the Capricorn Orogen, Western Australia: the 1680–1620 Ma Mangaroo Orogeny. *Austr. J. Earth Sci.* 52, 443–460. <http://dx.doi.org/10.1080/08120090500134589>.
- Sheppard, S., Rasmussen, B., Muhling, J.R., Farrell, T.R., Fletcher, I.R., 2007. Grenvillian-aged orogenesis in the Palaeoproterozoic Gascoyne Complex, Western Australia: 1030–950 Ma reworking of the Proterozoic Capricorn Orogen. *J. Metamorphic Geol.* 25, 477–494. <http://dx.doi.org/10.1111/j.1525-1314.2007.00708.x>.
- Stacey, J.S., Kramers, J.D., 1975. Approximation of terrestrial lead isotope evolution by a two-stage model. *Earth Planetary Sci. Lett.* 26, 207–221. [http://dx.doi.org/10.1016/0012-821X\(75\)90088-6](http://dx.doi.org/10.1016/0012-821X(75)90088-6).
- Stern, R.A., Rainbird, R.H., 2001. Advancements in Xenotime U–Pb Geochronology by ion Microprobe. Eleventh V.I. Goldschmidt Conference Lunar and Planetary Science Institute, Houston.
- Wingate, M.T.D., Giddings, J.W., 2000. Age and palaeomagnetism of the Mundine Well dyke swarm, Western Australia: implications for an Australia-Laurentia connection at 755 Ma. *Precamb. Res.* 100, 335–357. [http://dx.doi.org/10.1016/S0301-9268\(99\)00080-7](http://dx.doi.org/10.1016/S0301-9268(99)00080-7).
- Koppers, A. A. P., 2002. ArArCALC—Software for 40Ar/39Ar age calculations: *Computers & Geoscienc.* v. 28, p. 605–619, doi: 10.1016/S0098-3004(01)00095-4.

Appendix B
Supplementary Data (Chapter 3) –
SHRIMP U–Pb Monazite and Xenotime Data

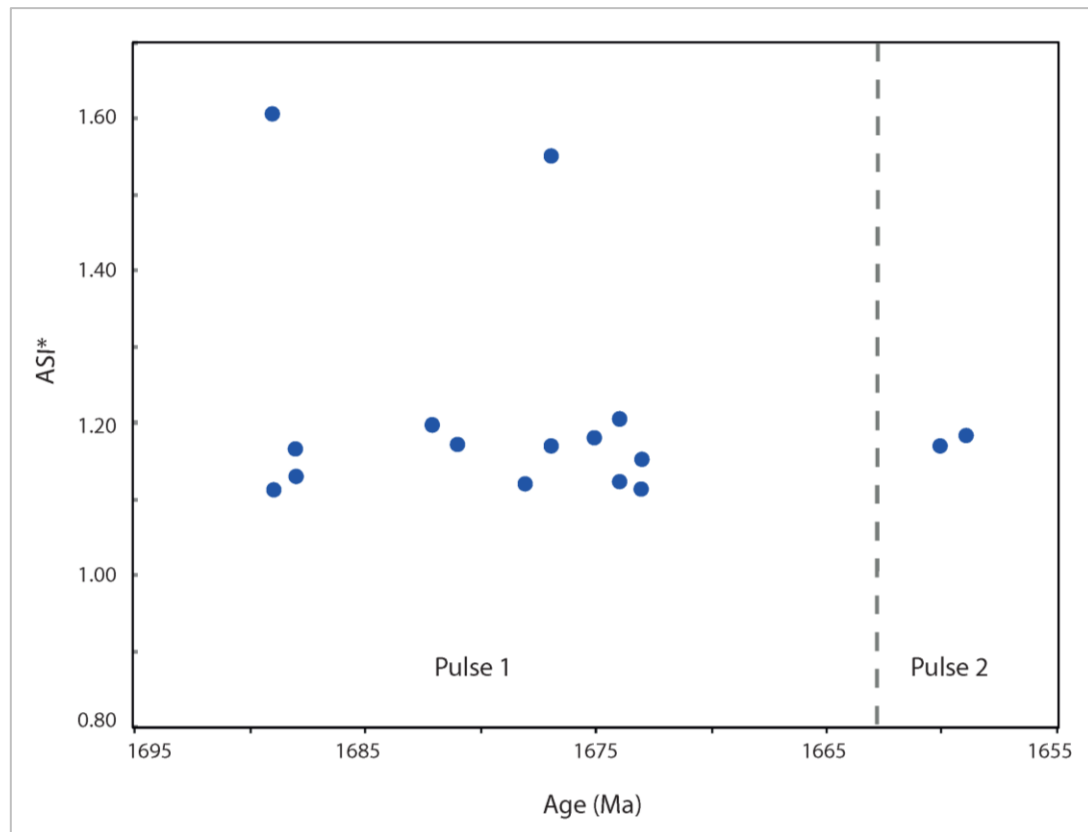


Figure B.1 Plot of ASI values for Durlacher granites from the Mangaroon Zone *
A/CNK = molar $\text{Al}_2\text{O}_3/(\text{CaO}+\text{Na}_2\text{O}+\text{K}_2\text{O})$.

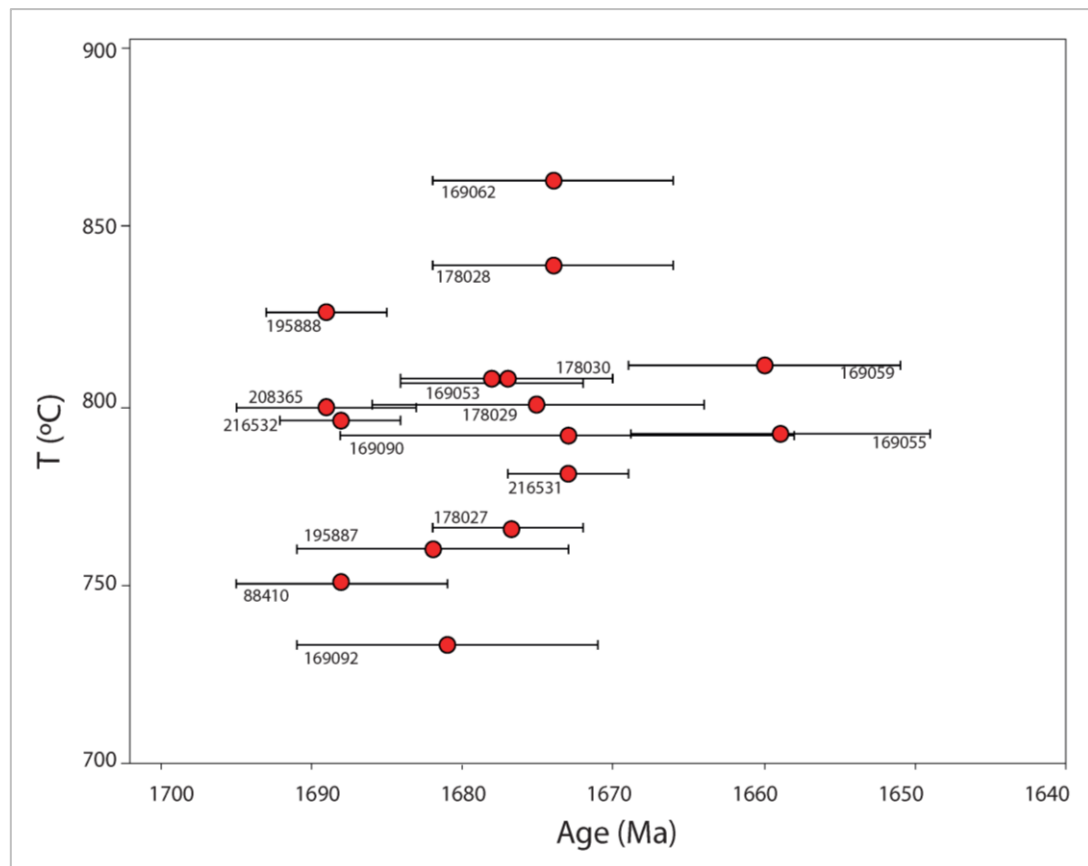


Figure B.2 Calculated zircon saturation temperatures (°C) (M parameter from Watson and Harrison 1993) plotted against igneous crystallisation ages in Ma show that Durlacher Supersuite granites were typically >750 °C. Geochemistry data is available from Table 3 and/or the Geological Survey of Western Australia WACHEM database (<http://geochem.dmp.wa.gov.au/geochem/>).

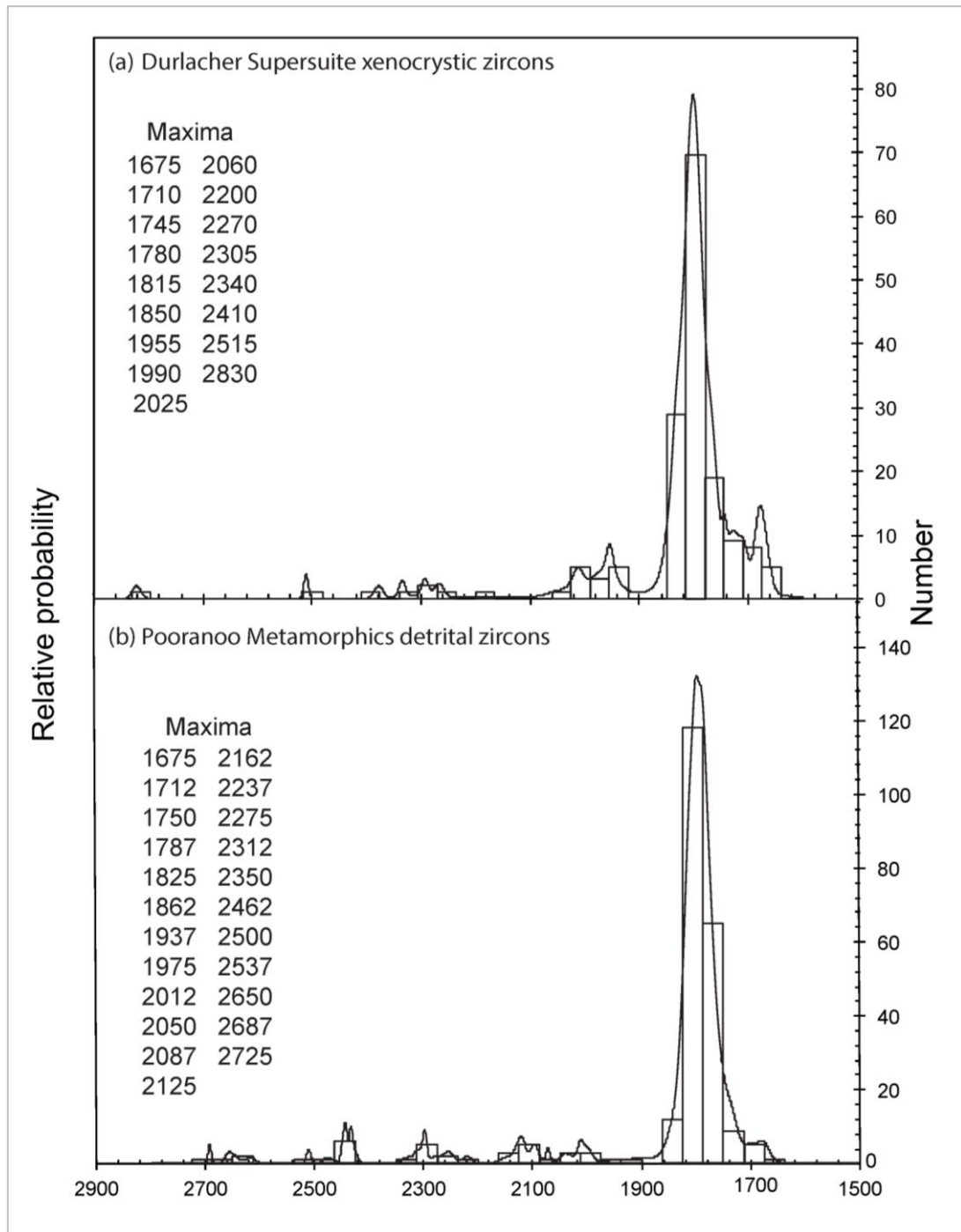


Figure B.3 Probability density diagrams and histograms of (a) xenocrystic zircons from the Durlacher Supersuite and (b) detrital zircon from the Pooranoo Metamorphics, from the Mangaroon Zone. Includes data (<5% discordant) from published data (GSWA 2016b).

Table B.1 U–Pb SHRIMP monazite and xenotime data tables

Monazite															
Grain	²³⁸ U	²³² Th	²³² Th	<i>f</i> ₂₀₆	²³⁸ U/ ²⁰⁶ Pb*	²⁰⁷ Pb*/ ²⁰⁶ Pb*	²⁰⁸ Pb*/ ²³² Th	Disc	²³⁸ U/ ²⁰⁶ Pb*	²⁰⁷ Pb*/ ²⁰⁶ Pb*					
.spot	(ppm)	(ppm)	<i>f</i> ²³⁸ U	(%)	±1σ	±1σ	±1σ	(%)	date (Ma)	±1σ	date (Ma)	±1σ			
GSWA 195890 muscovite–biotite metamonzogranite															
main group															
1612J.1-2	365	72281	198	0.24	3.29	0.06	0.1060	0.0014	0.0893	0.0036	1	1711	31	1732	24
1503F.1-2	751	90140	120	0.444	3.32	0.05	0.1055	0.0016	0.0908	0.0042	1	1697	26	1722	28
1612F.3-1	3081	74329	24	0.4	3.36	0.13	0.1053	0.0021	0.0845	0.0038	2	1679	65	1719	37
1612D.1-2	619	63627	103	0.82	3.40	0.05	0.1052	0.0020	0.0888	0.0036	3	1662	24	1717	34
1612E.1-1	514	78531	153	0.25	3.33	0.05	0.1049	0.0012	0.0859	0.0035	1	1693	25	1712	22
1612F.4-1	1038	79528	77	0.41	3.35	0.06	0.1049	0.0013	0.0871	0.0036	2	1684	30	1712	23
1502I.1-2	2789	71777	26	0.124	3.37	0.07	0.1046	0.0015	0.0900	0.0044	2	1675	35	1707	27
1612F.1-1	1258	87383	69	0.42	3.39	0.05	0.1046	0.0012	0.0828	0.0034	2	1666	25	1707	21
1612J.1-1	842	84664	101	0.93	3.36	0.05	0.1046	0.0014	0.0869	0.0036	2	1679	25	1707	25
1612B.1-2	5019	49869	10	0.13	3.41	0.06	0.1044	0.0008	0.0835	0.0034	3	1658	29	1703	14
1612B.1-1	6054	58030	10	0.24	3.43	0.05	0.1041	0.0007	0.0824	0.0033	3	1649	24	1698	12
1502C.1-1	929	70286	76	0.262	3.31	0.09	0.1038	0.0018	0.0944	0.0044	0	1702	46	1692	33
1612.A-1	1268	74811	59	0.28	3.33	0.05	0.1037	0.0009	0.0896	0.0037	0	1693	25	1691	16
1612J.1-3	608	82488	136	0.15	3.32	0.05	0.1037	0.0011	0.0836	0.0034	0	1697	26	1690	20
1503F.1-1	2810	76014	27	0.308	3.31	0.04	0.1035	0.0012	0.0919	0.0042	-1	1702	21	1688	22
1612F.3-2	2076	82760	40	0.95	3.49	0.08	0.1034	0.0020	0.0865	0.0037	4	1624	37	1686	35
1503F.1-2	2700	92923	34	0.357	3.33	0.04	0.1033	0.0008	0.0797	0.0024	-1	1693	20	1684	14
1503C.2-1	543	73266	135	0.974	3.56	0.07	0.1032	0.0021	0.0848	0.0026	5	1596	31	1682	37
1503E.1-1	453	63008	139	0.249	3.58	0.04	0.1026	0.0010	0.0905	0.0028	5	1588	18	1671	18
1502I.1-2	2475	25692	10	0.172	3.54	0.08	0.1025	0.0021	0.0878	0.0035	4	1604	36	1670	38
1612F.2-1	2005	78946	39	0.14	3.26	0.08	0.1024	0.0017	0.0848	0.0045	-3	1725	42	1669	30
1503C.2-1	771	76968	100	0.946	3.25	0.04	0.1023	0.0019	0.0930	0.0043	-4	1729	21	1667	35
1502I.1-1	2966	64896	22	0.084	3.38	0.10	0.1015	0.0033	0.0872	0.0028	-1	1671	49	1652	60
1503E.1-1	597	83993	141	0.699	3.37	0.05	0.1009	0.0018	0.0919	0.0042	-2	1675	25	1640	33
Statistical outlier															
1612F.1-2	844	87733	104	0.03	3.33	0.06	0.1054	0.0009	0.0830	0.0035	2	1693	31	1722	15
1503F.1-1	3673	96084	26	0.388	3.42	0.04	0.1013	0.0010	0.0835	0.0025	0	1653	19	1647	18
1502C.1-1	722	76359	106	0.345	3.55	0.04	0.1011	0.0008	0.0881	0.0026	3	1600	18	1644	15
1612C.1-1	330	63808	194	0.4	3.42	0.06	0.1002	0.0015	0.0896	0.0036	-1	1653	29	1629	28
disc. >5% and <i>f</i> ₂₀₆ > 1%															
1612D.3-1	493	71130	144	4.52	3.87	0.07	0.1084	0.0039	0.0831	0.0034	16	1482	27	1772	65
1612F.7-1	891	76740	86	0.86	3.53	0.05	0.1059	0.0014	0.0856	0.0035	7	1608	23	1729	24
1612F.6-1	687	82634	120	1.42	3.31	0.05	0.1054	0.0018	0.0860	0.0035	1	1702	26	1721	32
1503B.1-1	1029	69552	68	2.57	3.49	0.07	0.1050	0.0115	0.0888	0.0033	5	1624	33	1714	201
1503B.1-1	1675	69795	42	2.5	3.44	0.07	0.1048	0.0024	0.0906	0.0042	4	1645	33	1711	42
1503G.1-1	808	73344	91	1.05	3.54	0.05	0.1044	0.0023	0.0909	0.0041	6	1604	23	1704	41
1503C.1-1	1798	92879	52	2.22	3.64	0.05	0.1042	0.0016	0.0860	0.0026	8	1565	21	1700	27
1612D.1-1	973	63628	65	2.81	3.28	0.05	0.1041	0.0039	0.0881	0.0036	-1	1715	26	1698	69
1502J.1-1	1497	73405	49	4.01	4.73	0.42	0.1037	0.0078	0.0890	0.0043	27	1236	110	1692	138
1612D.2-1	644	94733	147	5.01	3.31	0.06	0.1035	0.0071	0.0725	0.0030	-1	1702	31	1688	126
1502I.1-1	3254	37296	11	0.099	3.14	0.10	0.1031	0.0017	0.0999	0.0048	-6	1782	57	1681	30
1612F.2-1a	3172	75839	24	3.32	3.52	0.06	0.1029	0.0025	0.0831	0.0034	4	1612	27	1678	45
1502C.1-2	652	76198	117	0.334	3.14	0.04	0.1028	0.0016	0.0984	0.0045	-6	1782	23	1676	29
1503E.1-2	873	61897	71	8.22	4.35	0.17	0.1028	0.0193	0.0821	0.0037	20	1334	52	1675	348
1502C.1-2	1186	57946	49	0.092	3.74	0.06	0.1024	0.0016	0.0900	0.0026	8	1527	25	1668	13
1502H.1-1	433	75399	174	2.04	3.46	0.07	0.1022	0.0026	0.0864	0.0028	2	1637	33	1665	47
1503G.1-1	670	72924	109	0.608	3.85	0.06	0.1018	0.0014	0.0844	0.0027	10	1489	23	1658	26
1503C.1-1	1191	81898	69	2.05	3.38	0.06	0.1014	0.0019	0.0924	0.0043	-1	1671	30	1651	35
1503C.2-2	276	62198	226	5.21	3.52	0.09	0.1013	0.0076	0.0748	0.0034	2	1612	41	1647	139
1502I.2-1	3643	91238	25	1.81	3.64	0.05	0.1011	0.0057	0.0866	0.0029	5	1565	21	1644	105
1502F.1-1	357	77097	216	1.08	3.78	0.06	0.1003	0.0018	0.0738	0.0021	7	1513	24	1630	33
1503A.2-1	1119	92909	83	3.21	3.79	0.06	0.0996	0.0035	0.0820	0.0026	7	1510	24	1617	66
1503E.1-2	2112	73621	35	5.41	7.49	0.76	0.0993	0.0071	0.0716	0.0027	50	808	82	1611	134
1612F.5-1	529	82364	156	0.45	3.22	0.05	0.0993	0.0015	0.0881	0.0037	-8	1743	27	1610	28
1502F.1-2	223	66512	298	1.71	3.51	0.11	0.0987	0.0025	0.0828	0.0028	-1	1616	51	1599	48
1503A.2-2	671	56919	85	5.87	4.55	0.17	0.0976	0.0087	0.0701	0.0032	19	1281	48	1578	167
P01085 biotite–muscovite syenogranite															
1009I.1-1	2420	68919	28	0.01	3.32	0.04	0.1039	0.0002	0.0927	0.0016	5	1698	18	1694	4
1009F.1-2	2355	92079	39	0.01	3.40	0.05	0.1035	0.0004	0.0868	0.0015	1	1662	22	1688	7
1009B.1-2	2956	85618	29	-0.02	3.52	0.05	0.1035	0.0006	0.0828	0.0014	0	1612	20	1688	10
1009H.1-1	2530	78833	31	-0.01	3.46	0.04	0.1034	0.0002	0.0868	0.0015	3	1636	18	1687	4
1009B.2-1	1350	81795	61	0.03	3.47	0.05	0.1034	0.0004	0.0878	0.0015	4	1634	21	1686	7
1009F.1-1	3051	83090	27	0.00	3.41	0.04	0.1032	0.0002	0.0862	0.0015	1	1657	17	1683	4
1009H.1-2	2764	68693	25	0.02	3.13	0.04	0.1031	0.0004	0.0966	0.0016	4	1789	19	1681	7
1009C.1-2	1579	87660	56	0.04	3.33	0.04	0.1031	0.0003	0.0867	0.0014	-1	1692	20	1681	6
1009F.1-3	4303	94269	22	0.02	3.55	0.05	0.1031	0.0002	0.0785	0.0014	-5	1598	19	1680	4
1009C.1-3	1083	78399	72	0.12	3.37	0.05	0.1029	0.0004	0.0877	0.0015	1	1675	22	1678	8
1009I.1-2	4632	69738	15	0.01	3.43	0.05	0.1029	0.0002	0.0878	0.0015	3	1650	19	1677	3
1009H.1-3	2757	69687	25	0.02	3.36	0.05	0.1029	0.0002	0.0886	0.0014	2	1680	20	1677	4
1009B.1-1	3798	70377	19	0.01	3.33	0.04	0.1029	0.0002	0.0886	0.0015	1	1695	18	1676	4
disc. > 5%															
1009C.1-1	2585	62216	24	0.01	3.49	0.05	0.1033	0.0002	0.0912	0.					

Grain .spot	²³⁸ U (ppm)	²³² Th (ppm)	²³² Th / ²³⁸ U	f ₂₀₆ (%)	²³⁸ U/ ²⁰⁶ Pb* ±1σ	²⁰⁷ Pb*/ ²⁰⁶ Pb* ±1σ	²⁰⁸ Pb*/ ²³² Th ±1σ	Disc (%)	²³⁸ U/ ²⁰⁶ Pb* date (Ma) ±1σ	²⁰⁷ Pb*/ ²⁰⁶ Pb* date (Ma) ±1σ					
GSWA 219741 tour-ms monzogranite															
1609F.1-2	6573	57210	9	0.03	3.19	0.05545	0.1026	0.0008	0.3136	0.0055	-5	1758	27	1671	15
1609G.1-1	767	12749	17	0.42	3.39	0.05194	0.1024	0.0010	0.2948	0.0045	0	1666	22	1668	19
1609B.1-2	1546	53460	35	0.14	3.30	0.05697	0.1023	0.0011	0.3032	0.0052	-2	1707	26	1666	19
1609C.1-2	3009	64533	21	0.02	3.28	0.06196	0.1018	0.0009	0.3045	0.0057	-3	1714	28	1658	17
1609F.1-1	7744	61064	8	0.02	3.30	0.05233	0.1015	0.0007	0.3027	0.0048	-3	1705	24	1653	12
1609E.1-1	5578	63783	11	0.02	3.38	0.05338	0.1008	0.0011	0.2957	0.0047	-2	1670	23	1639	20
<i>disc. >5% and f₂₀₆ > 1%</i>															
1609D.1-2	731	47414	65	3.21	3.45	0.05689	0.1035	0.0026	0.2899	0.0048	3	1641	24	1687	47
1609E.1-3	4266	56252	13	0.04	3.32	0.06045	0.0987	0.0010	0.3010	0.0055	-6	1696	27	1599	19
1609B.1-1	951	49490	52	0.36	3.13	0.04760	0.0984	0.0015	0.3193	0.0049	-12	1786	24	1594	28
1609A.1-1	653	53548	82	0.24	3.26	0.05037	0.0977	0.0024	0.3065	0.0047	-9	1724	23	1582	46
1609C.1-1	1576	61288	39	0.02	3.28	0.05303	0.0959	0.0016	0.3048	0.0049	-11	1715	24	1545	31
1609E.1-2	2084	61295	29	0.05	3.40	0.05296	0.0955	0.0029	0.2944	0.0046	-8	1664	23	1539	57
1609D.1-1	389	35820	92	1.15	3.60	0.06565	0.0929	0.0034	0.2780	0.0051	-6	1581	26	1485	69
GSWA 219749 cordierite-sillimanite pelitic migmatite															
<i>main group</i>															
1610I.2-1	2576	48305	19	0.03	3.35	0.05	0.1047	0.0009	0.0856	0.0035	2	1683	22	1710	15
1610G.1-2	2038	45135	22	0.03	3.41	0.07	0.1047	0.0009	0.0854	0.0035	3	1657	30	1709	15
1610C.1-1	3285	41049	12	0.04	3.37	0.07	0.1047	0.0008	0.0879	0.0036	2	1676	30	1709	15
1610B.1-3	2891	54032	19	-0.01	3.41	0.06	0.1046	0.0008	0.0826	0.0034	3	1660	25	1707	14
1610H.1-1	2369	43893	19	0.02	3.38	0.05	0.1040	0.0007	0.0871	0.0035	2	1670	22	1697	13
1610H.2-1	3175	43897	14	0.03	3.34	0.07	0.1040	0.0010	0.0880	0.0036	0	1688	30	1696	18
1610B.1-2	2345	41512	18	0.05	3.44	0.06	0.1040	0.0009	0.0850	0.0034	3	1644	24	1696	16
1610A.1-1	3824	41942	11	0.34	3.18	0.14	0.1039	0.0029	0.0871	0.0045	-4	1762	65	1695	52
1610D.1-1	3159	47355	15	0.06	3.33	0.05	0.1039	0.0013	0.0859	0.0035	0	1692	24	1695	22
1610A.1-2	4081	42355	10	0.02	3.30	0.07	0.1036	0.0008	0.0862	0.0035	-1	1706	33	1690	15
1610H.2-2	3293	48548	15	0.03	3.46	0.06	0.1036	0.0008	0.0821	0.0033	3	1635	23	1690	13
1610D.1-1a	1845	44112	24	0.03	3.37	0.06	0.1034	0.0012	0.0863	0.0035	1	1676	27	1686	21
1610D.1-2	2062	48805	24	0.05	3.47	0.05	0.1034	0.0007	0.0830	0.0034	3	1631	22	1685	13
1610D.3-1	2773	35898	13	0.05	3.27	0.06	0.1031	0.0010	0.0894	0.0036	-2	1718	27	1682	18
1610B.1-4	2357	43161	18	0.06	3.52	0.06	0.1031	0.0010	0.0777	0.0032	4	1613	23	1680	19
1610D.3-2	1770	43141	24	0.01	3.36	0.07	0.1029	0.0007	0.0870	0.0036	0	1678	31	1677	13
1610G.1-1	2122	45623	22	0.05	3.35	0.06	0.1029	0.0009	0.0880	0.0035	-1	1686	25	1676	16
1610B.1-1	2107	45150	21	0.01	3.35	0.11	0.1020	0.0017	0.0830	0.0038	-1	1684	47	1661	32
1610I.1-1	2350	41985	18	0.02	3.34	0.07	0.1015	0.0010	0.0882	0.0036	-2	1688	29	1652	18
<i>disc. > 5%</i>															
1610I.2-2	2078	45681	22	0.02	3.91	0.63	0.1099	0.0074	0.0807	0.0075	18	1468	207	1798	123
GSWA 219742 sillimanite-biotite granofels															
<i>main group</i>															
1613D.3-1	1058	56358	53	0.02	3.41	0.06	0.1049	0.0008	0.0856	0.0035	3	1657	25	1713	14
1613A.1-1	3429	47185	14	0.04	3.31	0.05	0.1046	0.0008	0.0875	0.0035	0	1701	23	1707	14
1613A.1-3	10993	45180	4	0.02	3.49	0.05	0.1042	0.0007	0.0797	0.0032	4	1626	22	1701	12
1613D.2-1	1294	54737	42	0.06	3.34	0.05	0.1042	0.0008	0.0859	0.0035	1	1689	24	1700	14
1613E.1-3	655	54434	83	0.15	3.43	0.07	0.1040	0.0017	0.0869	0.0036	3	1647	31	1697	30
1613D.1-2	8381	49798	6	0.02	3.41	0.05	0.1040	0.0006	0.0851	0.0034	2	1659	22	1697	11
1613F.1-2	659	50600	77	0.18	3.40	0.05	0.1039	0.0013	0.0855	0.0034	2	1664	23	1695	22
1613F.1-1	619	50197	81	0.16	3.41	0.06	0.1038	0.0010	0.0872	0.0035	2	1657	25	1693	17
1613C.1-2	1850	44423	24	0.06	3.33	0.07	0.1032	0.0011	0.0845	0.0034	-1	1693	30	1682	19
1613G.1-1	2231	37686	17	0.07	3.30	0.05	0.1031	0.0012	0.0877	0.0035	-2	1708	23	1681	21
1613A.1-2	869	51105	59	0.24	3.34	0.05	0.1029	0.0009	0.0861	0.0035	-1	1689	23	1678	17
1613F.2-1	566	47346	84	0.14	3.39	0.06	0.1029	0.0010	0.0869	0.0035	1	1667	27	1678	18
1613D.1-1	8912	48412	5	0.01	3.33	0.05	0.1029	0.0009	0.0881	0.0036	-1	1694	23	1677	15
1613C.1-1	1330	51442	39	0.06	3.39	0.07	0.1026	0.0010	0.0857	0.0035	0	1667	29	1673	18
1613B.1-2	4902	49154	10	0.01	3.23	0.06	0.1025	0.0011	0.0845	0.0034	-4	1739	27	1670	20
1613F.1-3	1942	44188	23	0.02	3.22	0.05	0.1025	0.0007	0.0872	0.0035	-4	1744	23	1670	12
1613E.1-2	1579	42722	27	0.07	3.36	0.05	0.1023	0.0011	0.0869	0.0035	-1	1680	23	1667	20
1613A.1-1a	8034	39299	5	0.04	3.39	0.06	0.1022	0.0008	0.0851	0.0034	0	1667	24	1665	15
1613B.1-1	668	60121	90	0.26	3.37	0.05	0.1016	0.0011	0.0864	0.0035	-1	1673	23	1653	20
1613B.2-2	1195	56324	47	-0.02	3.40	0.10	0.1000	0.0017	0.0824	0.0034	-2	1660	42	1624	31
<i>disc. > 5%</i>															
1613B.2-1	1402	55465	40	0.16	3.63	0.07	0.1025	0.0012	0.0813	0.0034	6	1570	27	1670	21
GSWA 216533 garnet-biotite-epidote pelitic gneiss															
<i>main group</i>															
1503D.1-2	4958	37658	8	0.04	3.19	0.04	0.1039	0.0012	0.0941	0.0042	-4	1756	19	1695	21
1603D.1-2	5005	47484	9	0.05	3.34	0.04	0.1036	0.0004	0.0884	0.0015	0	1689	19	1689	8
1603E.1-1	4060	48650	12	0.06	3.31	0.04	0.1033	0.0004	0.0912	0.0016	-1	1701	17	1685	6
1503D.1-1	1636	23056	14	0.21	3.23	0.04	0.1033	0.0013	0.0956	0.0042	-3	1737	19	1684	23
1603D.1-1	4278	36241	8	0.08	3.39	0.04	0.1032	0.0005	0.0902	0.0015	1	1667	17	1682	10
1603C.1-1	4851	46630	10	0.02	3.29	0.04	0.1031	0.0003	0.0899	0.0015	-2	1709	18	1681	6
1603F.1-1	2470	40983	17	0.11	3.26	0.04	0.1027	0.0006	0.0909	0.0017	-3	1726	20	1673	10
<i>disc. > 5%</i>															
NP153D.1-3	3433	34255	10	0.09	3.61	0.04	0.1028	0.0016	0.0820	0.0024	6	1576	16	1676	29

Grain spot	²³⁸ U (ppm)	²³² Th (ppm)	²³² Th / ²³⁸ U	<i>f</i> ₂₀₆ (%)	²³⁸ U / ²⁰⁶ Pb* ±1σ	²⁰⁷ Pb* / ²⁰⁶ Pb* ±1σ	²⁰⁸ Pb* / ²³² Th ±1σ	Disc (%)	²³⁸ U / ²⁰⁶ Pb* date (Ma) ±1σ	²⁰⁷ Pb* / ²⁰⁶ Pb* date (Ma) ±1σ					
P01081 quartz-biotite–tourmaline gneiss															
Main group															
1008H.1-1	720	14346	20	0.18	3.42	0.07	0.1043	0.0011	0.0861	0.0012	3	1653	32	1702	19
1008F.1-1	5077	56860	11	0.04	3.49	0.07	0.1036	0.0008	0.0849	0.0012	4	1625	27	1690	14
1008F.2-1	7388	59355	8	0.03	3.36	0.07	0.1034	0.0008	0.0881	0.0012	0	1681	29	1686	14
1008G.1-3	5124	22484	4	0.01	3.39	0.07	0.1033	0.0008	0.0868	0.0013	1	1666	28	1684	15
1008H.1-2	7271	30028	4	0.02	3.41	0.07	0.1032	0.0008	0.0843	0.0011	2	1656	29	1683	14
1008J.1-2	3598	18721	5	0.06	3.43	0.07	0.1030	0.0008	0.0877	0.0012	2	1651	28	1679	14
1008H.1-3	2232	21563	10	0.08	3.33	0.06	0.1028	0.0008	0.0856	0.0011	-1	1695	29	1675	15
1008G.1-1	14132	68536	5	0.01	3.40	0.07	0.1028	0.0007	0.0859	0.0012	1	1661	30	1675	13
1008G.1-2	1817	2454	1	0.10	3.53	0.07	0.1023	0.0009	0.0855	0.0012	3	1608	29	1666	15
disc. > 5%															
1008J.1-1	4087	21616	5	0.03	3.63	0.08	0.1035	0.0008	0.0796	0.0014	7	1569	30	1689	14
1008F.1-2	1883	41131	22	0.09	3.63	0.08	0.1031	0.0009	0.0852	0.0011	7	1568	32	1681	15
P16877 muscovite-biotite schist															
1011G.1-1	817	22584	28	0.10	3.43	0.08	0.1042	0.0010	0.0869	0.0012	3	1649	33	1701	17
1011E.2-1	1932	28917	15	0.03	3.44	0.07	0.1040	0.0009	0.0847	0.0012	3	1643	30	1696	15
1011A.1-2	2172	36238	17	0.03	3.50	0.07	0.1036	0.0008	0.0827	0.0011	4	1621	28	1690	15
1011E.3-1	7009	41167	6	0.01	3.34	0.07	0.1034	0.0008	0.0870	0.0012	0	1688	30	1687	14
1011J.1-1	6790	45374	7	0.03	3.42	0.08	0.1034	0.0008	0.0860	0.0012	2	1655	32	1685	14
1011M.1-2	3282	15080	5	0.04	3.37	0.08	0.1033	0.0008	0.0901	0.0013	0	1677	35	1684	14
1011K.1-1	7731	17848	2	0.02	3.43	0.08	0.1033	0.0008	0.0889	0.0013	2	1650	33	1683	14
1011E.1-1	3608	35214	10	0.02	3.36	0.07	0.1032	0.0008	0.0823	0.0011	0	1678	31	1683	14
1011B.1-1	3793	36477	10	0.04	3.32	0.07	0.1032	0.0008	0.0857	0.0013	-1	1698	31	1682	14
1011E.4-1	1981	25929	13	0.04	3.54	0.08	0.1030	0.0008	0.0862	0.0012	4	1604	32	1679	15
1011D.1-1	2822	38298	14	0.07	3.38	0.07	0.1030	0.0008	0.0853	0.0011	0	1671	30	1679	15
1011A.1-3	1239	36231	29	0.06	3.24	0.07	0.1028	0.0009	0.0777	0.0010	-3	1732	30	1676	16
1011H.1-1	3880	44209	11	0.03	3.46	0.06	0.1028	0.0008	0.0845	0.0012	2	1636	26	1675	14
1011A.1-1	1315	42016	32	0.14	3.37	0.07	0.1028	0.0009	0.0884	0.0012	0	1673	31	1675	17
1011K.1-2	4283	28322	7	0.03	3.44	0.07	0.1028	0.0008	0.0878	0.0013	2	1644	31	1675	14
1011C.2-1	5288	39612	7	0.00	3.42	0.07	0.1027	0.0008	0.0859	0.0012	1	1653	29	1673	14
1011E.2-2	1751	44159	25	0.10	3.36	0.07	0.1026	0.0009	0.0878	0.0012	-1	1681	30	1671	15
1011M.1-1	2824	34471	12	0.04	3.51	0.09	0.1024	0.0008	0.0813	0.0014	3	1615	35	1668	14
1011G.1-2	897	24387	27	0.13	3.39	0.07	0.1024	0.0010	0.0858	0.0011	0	1668	28	1667	17
disc. > 5%															
1011C.1-1	3448	79189	23	0.04	3.61	0.08	0.1035	0.0008	0.0865	0.0012	6	1577	31	1688	14
GSWA 216538 biotite–muscovite–tourmaline pelitic gneiss															
main group															
1602C.2-1	3321	36492	11	0.05	3.36	0.04	0.1038	0.0004	0.0899	0.0015	1	1680	18	1692	7
1602A.1-2	3541	46301	13	0.03	3.38	0.04	0.1037	0.0005	0.0873	0.0016	1	1670	19	1691	8
1602A.1-1	3413	53541	16	0.29	3.33	0.04	0.1034	0.0004	0.0903	0.0016	0	1691	16	1685	8
1602B.3-2	5137	36939	7	0.03	3.47	0.05	0.1033	0.0005	0.0855	0.0014	3	1632	21	1684	8
1602C.1-2	4669	41803	9	0.05	3.33	0.04	0.1032	0.0004	0.0883	0.0016	-1	1694	18	1682	8
1602B.3-1	5730	48386	8	0.03	3.34	0.04	0.1031	0.0004	0.0852	0.0014	0	1688	17	1681	8
1602D.1-3	2739	51213	19	0.04	3.30	0.05	0.1031	0.0004	0.0898	0.0016	-2	1709	23	1680	7
1602B.1-1	8329	56065	7	0.03	3.30	0.04	0.1030	0.0003	0.0894	0.0015	-2	1707	16	1679	6
1602D.1-2	3827	58423	15	0.04	3.29	0.04	0.1029	0.0004	0.0898	0.0015	-2	1711	19	1677	6
1602C.1-1	4428	37284	8	0.03	3.24	0.04	0.1028	0.0004	0.0899	0.0015	-3	1732	19	1675	8
1602C.1-3	4710	38681	8	0.08	3.24	0.05	0.1027	0.0009	0.0907	0.0019	-4	1734	23	1674	16
1602B.1-3	2783	42685	15	0.17	3.35	0.06	0.1027	0.0004	0.0728	0.0013	-1	1682	27	1674	8
1602D.1-1	3672	45020	12	0.03	3.33	0.05	0.1026	0.0004	0.0894	0.0015	-1	1691	21	1671	6
1602B.2-1	8384	49336	6	0.04	3.31	0.04	0.1024	0.0005	0.0892	0.0015	-2	1700	16	1668	9
round outlier															
1602B.1-2	2804	35765	13	0.11	3.53	0.04	0.1017	0.0004	0.0666	0.0013	3	1607	16	1656	8
disc. > 5%															
1606E.1-1	3836	40977	11	0.03	3.61	0.14	0.1030	0.0004	0.0766	0.0029	6	1576	53	1679	8
1602A.2-1	485	50491	104	0.33	3.77	0.05	0.0993	0.0011	0.0652	0.0011	6	1517	19	1611	21

Notes:

Pbⁱ indicates radiogenic Pb (i.e. corrected for common Pb)

*f*₂₀₆, proportion of common ²⁰⁶Pb in measured ²⁰⁶Pb, determined using measured ²⁰⁴Pb/²⁰⁶Pb and contemporaneous common Pb composition (Stacey and Kramers, 15)

Disc. is apparent discordance, as D (%) = 100 × ([²⁰⁷Pb*/²⁰⁶Pb* date] – [²³⁸U / ²⁰⁶Pb* date]) / [²⁰⁷Pb*/²⁰⁶Pb* date]

Analytical uncertainties from the multiple sessions have been applied to the data during data reduction.

Analyses are sorted by descending ²⁰⁷Pb*/²⁰⁶Pb* age for all samples

Xenotime

Grain	²³⁸ U	²³² Th	²³² Th	<i>f</i> ₂₀₆	²³⁸ U/ ²⁰⁶ Pb*	²⁰⁷ Pb*/ ²⁰⁶ Pb*	²⁰⁸ Pb*/ ²³² Th	Disc	²³⁸ U/ ²⁰⁶ Pb*	²⁰⁷ Pb*/ ²⁰⁶ Pb*					
.spot	(ppm)	(ppm)	/ ²³⁸ U	(%)	±1 σ	±1 σ	±1 σ	(%)	date (Ma) ±1 σ	date (Ma) ±1 σ					
GSWA 216538 biotite–muscovite–tourmaline pelitic gneiss															
<i>main group</i>															
NP1604A.1-	8956	1542	0.2	-0.006	3.24	0.05	0.1041	0.0005	0.0891	0.0102	-2	1736	25	1698	9
NP1604G.2-	13316	1915	0.1	0.021	3.15	0.05	0.1036	0.0005	0.0910	0.0105	-5	1775	24	1689	9
NP1604H.1-	16453	2515	0.2	0.001	3.25	0.06	0.1034	0.0002	0.0906	0.0103	-3	1731	30	1686	3
NP1604G.1-	16145	2358	0.1	0.035	3.23	0.05	0.1032	0.0003	0.0853	0.0104	-4	1741	25	1683	5
NP1604A.1-	14025	2217	0.2	0.008	3.41	0.06	0.1032	0.0002	0.0859	0.0098	2	1657	25	1683	3
NP1604C.1-	9706	2699	0.3	0.009	3.38	0.06	0.1030	0.0003	0.0852	0.0100	0	1671	25	1679	4
NP1604H.1-	13890	2154	0.2	0.005	3.53	0.06	0.1029	0.0004	0.0819	0.0096	4	1606	25	1677	6
NP1604A.1-	15927	2222	0.1	0.007	3.24	0.10	0.1027	0.0002	0.0909	0.0104	-4	1736	49	1674	3
NP1604G.2-	17799	2663	0.1	0.031	3.38	0.06	0.1027	0.0002	0.0837	0.0100	0	1671	25	1673	3
NP1604G.1-	14470	1863	0.1	0.005	3.33	0.07	0.1025	0.0008	0.0863	0.0101	-1	1691	30	1670	14
NP1604A.1-	13746	2032	0.1	0.003	3.37	0.10	0.1025	0.0006	0.0888	0.0100	0	1676	45	1670	11
<i>young outlier</i>															
NP1604G.1-	12496	1730	0.1	0.011	3.37	0.06	0.1015	0.0002	0.0844	0.0102	-2	1676	25	1653	4
<i>disc. > 5%</i>															
NP1604E.2-	10397	1578	0.2	0.003	3.12	0.09	0.1035	0.0006	0.0918	0.0106	-6	1795	44	1688	11
NP1604C.1-	15194	2405	0.2	0.006	3.13	0.05	0.1030	0.0002	0.0884	0.0107	-7	1790	24	1678	3

Notes:

Pb* indicates radiogenic Pb (i.e. corrected for common Pb)

*f*₂₀₆, proportion of common ²⁰⁶Pb in measured ²⁰⁶Pb, determined using measured ²⁰⁴Pb/²⁰⁶Pb and contemporaneous common Pb composition (Stacey and Kramers, 1972)

Disc. is apparent discordance, as $D (\%) = 100 \times ([^{207}\text{Pb}^*/^{206}\text{Pb}^* \text{ date}] - [^{238}\text{U}/^{206}\text{Pb}^* \text{ date}]) / [^{207}\text{Pb}^*/^{206}\text{Pb}^* \text{ date}]$

Analytical uncertainties from the multiple sessions have been applied to the data during data reduction.

Analyses are sorted by descending ²⁰⁷Pb*/²⁰⁶Pb* age for all samples

Appendix C

Supplementary Data (Chapter 3) – Mineral Chemistry Data and P–T Pseudosection

The following mineral chemistry data was collected during the PhD but was not used. The data presented here relates to the material in Chapter 3. Sample details and geographic locations for the samples can be found in Chapter 3.

Mineral Chemistry

Compositional (point) analyses for samples 216533, 219742 and 219749 were acquired on a JEOL 8530F electron microprobe at the Centre for Microscopy, Characterisation and Analysis (CMCA), University of Western Australia (UWA), equipped with 5 tunable wavelength dispersive spectrometers. Operating conditions used were 40 degrees take-off angle, an accelerating voltage of 15 keV, a beam current of 15 nA, and the beam fully focussed.

Elements were acquired using analysing crystals LiFH for Ti k, Cr k, LiF for Mn k, Fe k, PETJ for Ca k, K k, and TAP for Mg k, Al k, Na k, Si k. The standards were Cr₂O₃ for Cr k, Magnetite for Fe k, Periclase for Mg k, Rutile for Ti k, Mn for Mn k, Orthoclase for K k, Wollastonite for Si k, Ca k, Al k and Jadeite for Na k, except for feldspar analyses which employed Bytownite for Ca k, Al k, Na k, Si k. On-peak counting times were 30 seconds for all elements. X-ray intensity data was corrected for Time Dependent Intensity (TDI) loss (or gain) using a self-calibrated correction for Si k, Ti k, Mn k, Na k, K k and mean atomic number (MAN) background corrections were used throughout (Donovan & Tingle, 1996; Donovan et al., 2016). Unknown and standard intensities were corrected for deadtime. On-peak interference corrections were applied to Mn for interference by Cr, and to Fe for interference by Mn (Donovan et al., 1993). Detection limits ranged from 0.006 wt % for Si k to 0.006 wt % for Al k to 0.008 wt % for K k to 0.011 wt % for Ti k to 0.029 wt % for Mn k. Oxygen was calculated by stoichiometry, included in the matrix corrections and ZAF correction was applied throughout.

Elemental maps for selected garnets from sample 216533 (Figure C.1) were acquired using the Probe Image® application under identical conditions as above, but

with a beam current of 90 nA. The maps were acquired using a 1 x 1 μm pixel dimension and an 80 ms per pixel dwell time. The raw count data was processed using the Calcimage® application employing the calibration set-up and matrix correction procedures as appropriate for garnet outlined above. The processed maps were output to the Surfer® application for further enhancement. Ferric iron contents for garnet were determined using the stoichiometric method of Schumacher (1991). Table C.1 through to Table C.7 show individual point analysis for minerals analysed.

***P–T* pseudosection**

A *P–T* pseudosection was constructed for sample 216533 (Figure C.2) during the PhD but was not used. The methodology can be found in Chapter 3. The corresponding whole rock geochemistry data used to construct the pseudosection is found in Table C.8. The analytical details for the whole rock geochemistry can be found in Chapter 3.

References

- Donovan, J. J., Singer, J. W., and Armstrong, J. T., 2016, A new EPMA method for fast trace element analysis in simple matrices: *American Mineralogist* 101, 1839–1853.
- Donovan, J., D.A. Snyder, D. A., and M.L. Rivers, M. L., 1993, An Improved Interference Correction for Trace Element Analysis: *Microbeam Analysis* 2, 23–28.
- Donovan, J., & Tingle, T, 1996, An Improved Mean Atomic Number Background Correction for Quantitative Microanalysis: *Microscopy and Microanalysis* 2, 1-7.
- Schumacher, J. C., 1991, Empirical ferric iron corrections: necessity, assumptions, and effects on selected geothermobarometers: *Mineralogical Magazine* 55, 3–18.

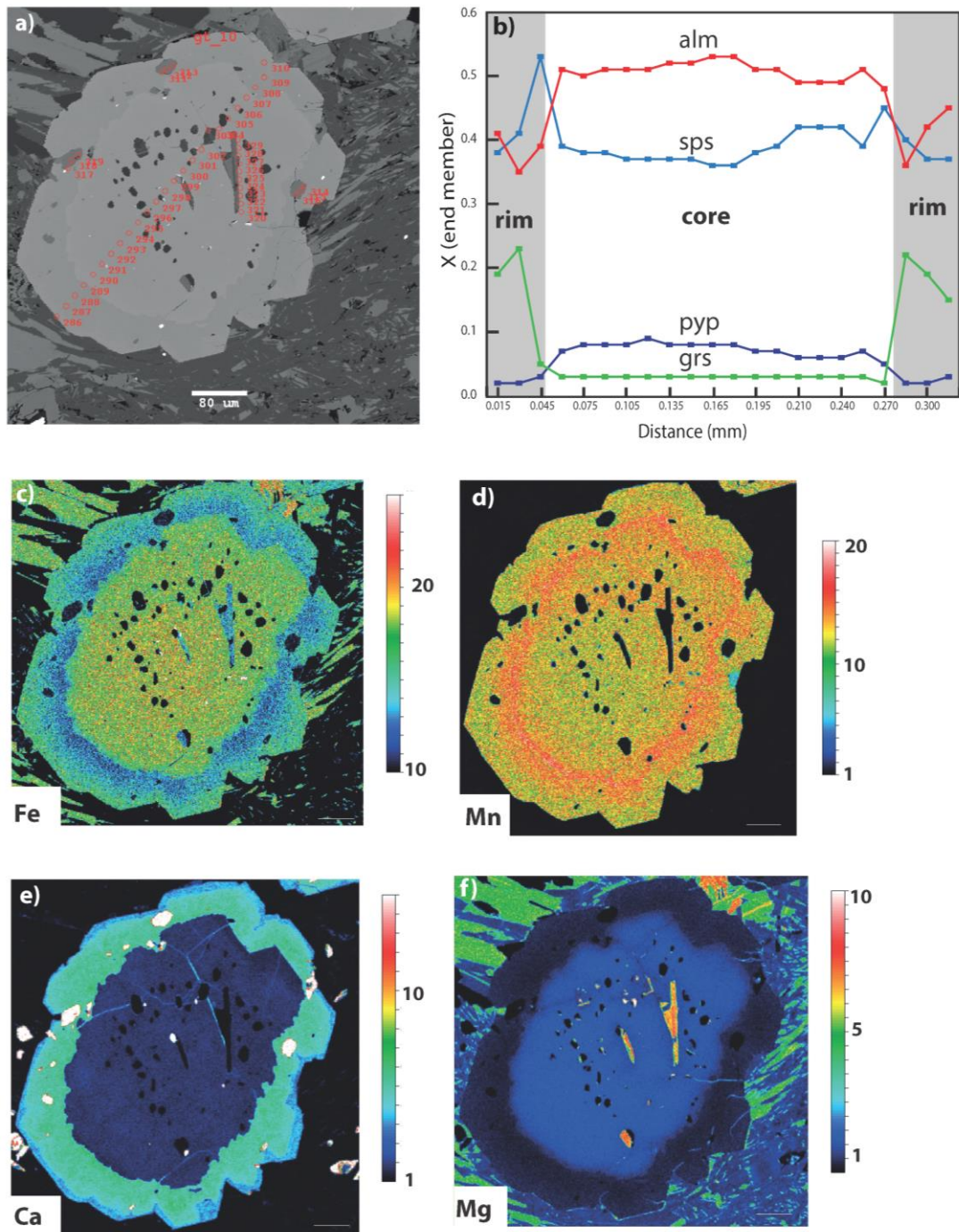


Figure C.1 Representative analysed garnet (sample 216533 garnet 11 in Table 3.2) grain showing line traverse and compositions. a) Back-scattered electron image of typical garnet from sample 216533; b) line traverse. Selected quantitative element maps for same garnet showing distinct zoning; c) Fe elemental map; d) Mn elemental map; e) Ca elemental map; f) Mg elemental map.

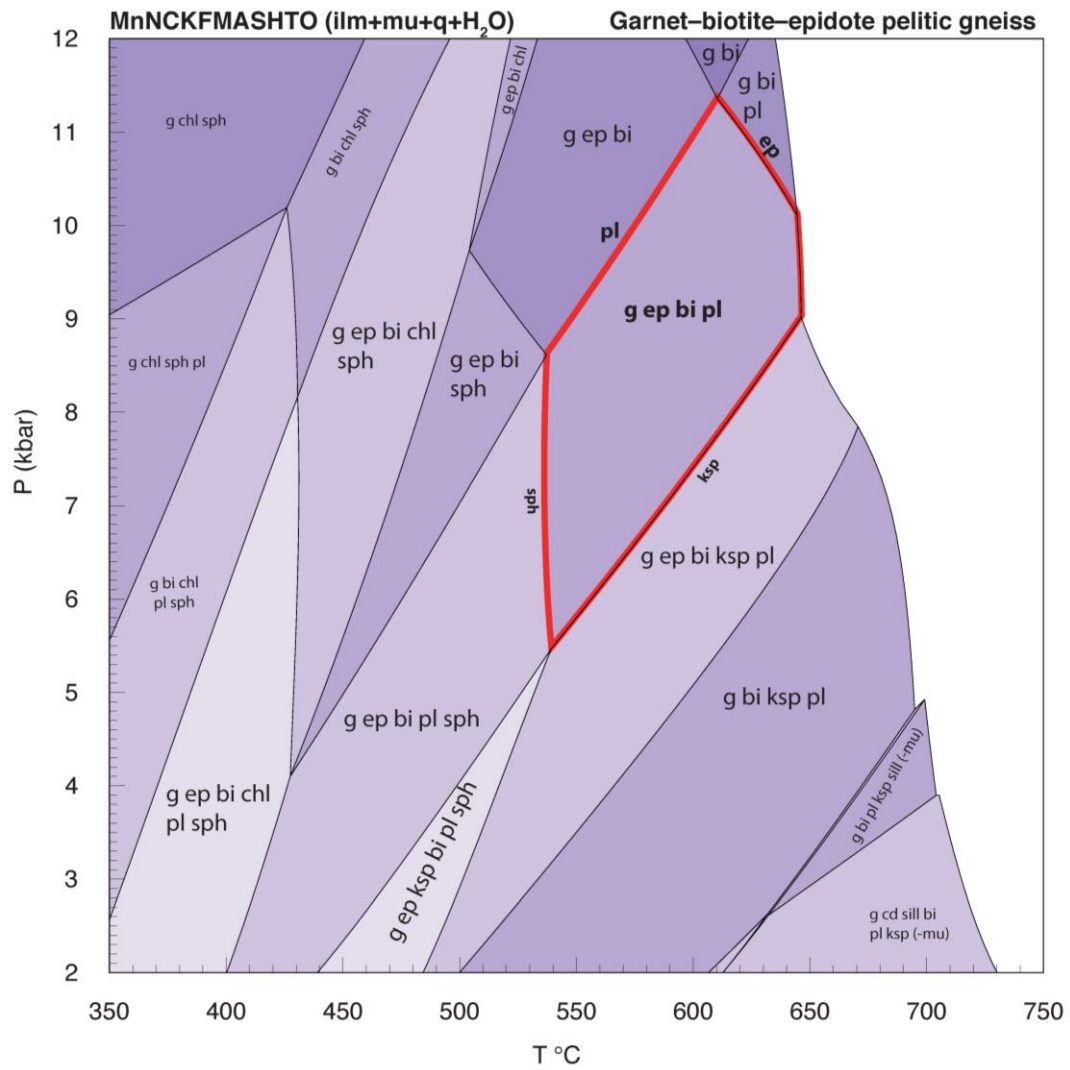


Figure C.2 P-T pseudosection for sample 216533.

Table C.1 Cordierite composition from sample 219749.

Wt%	crd_1										
SiO2	48.29	48.35	48.43	48.45	48.26	48.17	48.54	48.32	48.08	48.22	47.86
TiO2	0.00	0.00	0.00	0.01	0.00	0.01	0.00	0.01	0.00	0.00	0.00
Al2O3	32.52	33.30	33.41	33.53	33.53	33.43	33.30	33.10	33.49	33.45	33.53
Cr2O3	0.00	0.00	0.00	0.00	0.00	0.00	0.01	0.00	0.00	0.01	0.00
FeO	7.46	8.99	8.24	7.38	9.20	8.62	9.22	8.70	8.03	9.36	9.58
MnO	0.84	0.76	0.72	0.93	0.61	0.66	0.62	0.96	0.98	0.78	0.52
MgO	8.20	7.58	7.94	7.99	7.47	7.62	7.48	7.73	7.92	7.56	7.41
CaO	0.02	0.02	0.01	0.02	0.01	0.02	0.02	0.02	0.03	0.02	0.01
Na2O	0.10	0.08	0.06	0.09	0.12	0.14	0.11	0.09	0.08	0.13	0.13
K2O	0.12	0.00	0.07	0.45	0.00	0.03	0.02	0.00	0.29	0.03	0.00
TOTAL	97.54	99.08	98.90	98.85	99.20	98.69	99.32	98.94	98.89	99.55	99.04
Oxygen	18	18	18	18	18	18	18	18	18	18	18
Si	5.01	4.97	4.97	4.97	4.96	4.96	4.98	4.97	4.95	4.95	4.93
Ti	0.00	0.00	0.00	0.00	0.00	0.00	0.00	0.00	0.00	0.00	0.00
Al	3.98	4.03	4.04	4.05	4.06	4.06	4.03	4.02	4.06	4.04	4.07
Cr	0.00	0.00	0.00	0.00	0.00	0.00	0.00	0.00	0.00	0.00	0.00
Fe	0.65	0.77	0.71	0.63	0.79	0.74	0.79	0.75	0.69	0.80	0.83
Mn	0.07	0.07	0.06	0.08	0.05	0.06	0.05	0.08	0.09	0.07	0.05
Mg	1.27	1.16	1.21	1.22	1.14	1.17	1.14	1.19	1.21	1.16	1.14
Ca	0.00	0.00	0.00	0.00	0.00	0.00	0.00	0.00	0.00	0.00	0.00
Na	0.02	0.02	0.01	0.02	0.02	0.03	0.02	0.02	0.02	0.02	0.03
K	0.02	0.00	0.01	0.06	0.00	0.00	0.00	0.00	0.04	0.00	0.00
TOTAL	11.02	11.02	11.02	11.04	11.03	11.02	11.02	11.03	11.05	11.05	11.04
X _{Fe}	0.34	0.40	0.37	0.34	0.41	0.39	0.41	0.39	0.36	0.41	0.42

Cordierite composition from sample 219749. (cont)

Wt%	crd_2																		
SiO ₂	48.10	48.20	48.39	47.88	48.46	47.80	48.27	48.28	48.54	48.16	48.26	48.53	48.29	48.93	48.37	48.99	18	18	18
TiO ₂	0.00	0.00	0.00	0.00	0.01	0.00	0.03	0.00	0.00	0.00	0.00	0.01	0.00	0.00	0.00	0.00	0.00	0.00	0.00
Al ₂ O ₃	33.01	32.80	33.14	32.88	33.15	33.07	33.11	32.89	32.99	33.07	33.81	33.75	33.05	33.83	33.23	33.29	0.00	0.00	0.00
Cr ₂ O ₃	0.00	0.00	0.00	0.01	0.00	0.00	0.00	0.00	0.00	0.00	0.00	0.01	0.02	0.00	0.00	0.00	0.00	0.00	0.00
FeO	9.37	9.25	8.99	9.27	9.64	9.37	9.50	9.28	9.51	9.34	8.43	8.05	9.42	9.18	8.77	9.51	0.79	0.80	0.71
MnO	7.62	7.57	7.61	7.52	7.48	7.41	7.40	7.57	7.57	7.48	7.80	7.88	7.44	7.65	7.48	7.54	0.01	0.01	0.01
CaO	0.01	0.01	0.02	0.01	0.03	0.02	0.01	0.01	0.01	0.03	0.02	0.01	0.02	0.02	0.01	0.01	0.12	0.20	0.14
Na ₂ O	0.12	0.20	0.14	0.10	0.11	0.16	0.13	0.11	0.12	0.08	0.09	0.11	0.08	0.12	0.12	0.09	0.00	0.02	0.00
K ₂ O	0.00	0.02	0.00	0.00	0.00	0.02	0.02	0.01	0.01	0.01	0.05	0.01	0.01	0.00	0.01	0.00	99.02	98.86	99.00
TOTAL	99.02	98.86	99.00	98.41	99.56	98.58	99.05	98.90	99.37	98.85	99.44	99.57	98.87	100.33	98.86	100.11	18	18	18
Oxygen	18	18	18	18	18	18	18	18	18	18	18	18	18	18	18	18	4.96	4.98	4.98
Si	0.00	0.00	0.00	0.00	0.00	0.00	0.00	0.00	0.00	0.00	0.00	0.00	0.00	0.00	0.00	0.00	0.00	0.00	0.00
Ti	0.00	0.00	0.00	0.00	0.00	0.00	0.00	0.00	0.00	0.00	0.00	0.00	0.00	0.00	0.00	0.00	4.01	3.99	4.02
Al	4.01	3.99	4.02	4.02	4.01	4.04	4.02	4.00	3.99	4.02	4.08	4.06	4.02	4.05	4.03	4.00	0.00	0.00	0.00
Cr	0.00	0.00	0.00	0.00	0.00	0.00	0.00	0.00	0.00	0.00	0.00	0.00	0.00	0.00	0.00	0.00	0.81	0.80	0.77
Fe	0.81	0.80	0.77	0.80	0.83	0.81	0.82	0.80	0.82	0.81	0.72	0.69	0.81	0.78	0.76	0.81	0.07	0.07	0.06
Mn	0.07	0.07	0.06	0.06	0.06	0.07	0.05	0.06	0.05	0.06	0.08	0.11	0.05	0.05	0.08	0.06	1.17	1.17	1.17
Mg	1.17	1.17	1.17	1.16	1.14	1.14	1.14	1.16	1.16	1.15	1.19	1.20	1.14	1.16	1.15	1.14	0.00	0.00	0.00
Ca	0.00	0.00	0.00	0.00	0.00	0.00	0.00	0.00	0.00	0.00	0.00	0.00	0.00	0.00	0.00	0.00	0.02	0.04	0.03
Na	0.02	0.04	0.03	0.02	0.02	0.03	0.03	0.02	0.02	0.02	0.02	0.02	0.02	0.02	0.02	0.02	0.00	0.00	0.00
K	0.00	0.00	0.00	0.00	0.00	0.00	0.00	0.00	0.00	0.00	0.01	0.00	0.00	0.00	0.00	0.00	11.05	11.05	11.03
TOTAL	11.05	11.05	11.03	11.04	11.03	11.05	11.03	11.03	11.03	11.03	11.04	11.03	11.02	11.02	11.02	11.02	0.41	0.41	0.40
X _{Fe}	0.41	0.41	0.40	0.41	0.42	0.42	0.42	0.41	0.41	0.41	0.38	0.36	0.42	0.40	0.40	0.41			

Cordierite composition from sample 219749. (cont)

Wt%	crd_3																	
SiO2	48.21	48.35	48.20	48.39	48.34	48.72	48.14	48.34	48.24	47.97	48.44	48.38	48.17	48.46	48.51	48.28	48.59	
TiO2	0.00	0.01	0.02	0.05	0.00	0.00	0.00	0.00	0.00	0.00	0.00	0.02	0.00	0.00	0.00	0.00	0.01	
Al2O3	33.92	33.89	33.78	33.67	33.80	33.40	33.87	33.80	33.85	33.87	33.79	33.82	33.73	34.02	33.86	34.01	34.13	
Cr2O3	0.00	0.00	0.00	0.00	0.00	0.00	0.00	0.00	0.00	0.00	0.00	0.01	0.01	0.00	0.00	0.02	0.00	
FeO	9.17	9.03	9.22	9.16	9.21	9.32	9.37	9.35	8.95	9.05	9.15	9.58	8.72	7.75	9.16	9.06	8.93	
MnO	0.80	0.66	0.79	0.79	0.73	0.69	0.74	0.69	0.74	0.70	0.68	0.62	0.99	0.95	0.70	0.77	0.84	
MgO	7.57	7.65	7.73	7.68	7.63	7.67	7.56	7.58	7.76	7.65	7.67	7.50	7.68	8.15	7.47	7.66	7.88	
CaO	0.02	0.02	0.00	0.00	0.01	0.01	0.01	0.02	0.01	0.01	0.02	0.01	0.02	0.02	0.01	0.02	0.02	
Na2O	0.08	0.09	0.10	0.05	0.11	0.08	0.09	0.09	0.07	0.09	0.11	0.10	0.08	0.07	0.07	0.09	0.04	
K2O	0.01	0.01	0.00	0.01	0.01	0.00	0.00	0.01	0.00	0.02	0.00	0.04	0.02	0.11	0.02	0.00	0.00	
TOTAL	99.77	99.71	99.84	99.80	99.74	99.90	99.80	99.88	99.63	99.36	99.85	100.08	99.40	99.54	99.80	99.90	100.44	
Oxygen	18	18	18	18	18	18	18	18	18	18	18	18	18	18	18	18	18	
Si	4.93	4.94	4.93	4.94	4.94	4.97	4.92	4.94	4.93	4.92	4.94	4.94	4.94	4.94	4.95	4.93	4.93	
Ti	0.00	0.00	0.00	0.00	0.00	0.00	0.00	0.00	0.00	0.00	0.00	0.00	0.00	0.00	0.00	0.00	0.00	
Al	4.09	4.08	4.07	4.05	4.06	4.02	4.08	4.07	4.08	4.09	4.06	4.07	4.07	4.09	4.07	4.09	4.08	
Cr	0.00	0.00	0.00	0.00	0.00	0.00	0.00	0.00	0.00	0.00	0.00	0.00	0.00	0.00	0.00	0.00	0.00	
Fe	0.78	0.77	0.79	0.78	0.79	0.80	0.80	0.80	0.77	0.78	0.78	0.82	0.75	0.66	0.78	0.77	0.76	
Mn	0.07	0.06	0.07	0.07	0.06	0.06	0.06	0.06	0.06	0.06	0.06	0.05	0.09	0.08	0.06	0.07	0.07	
Mg	1.15	1.17	1.18	1.17	1.16	1.17	1.15	1.15	1.18	1.17	1.17	1.14	1.17	1.24	1.14	1.16	1.19	
Ca	0.00	0.00	0.00	0.00	0.00	0.00	0.00	0.00	0.00	0.00	0.00	0.00	0.00	0.00	0.00	0.00	0.00	
Na	0.02	0.02	0.02	0.01	0.02	0.02	0.02	0.02	0.01	0.02	0.02	0.02	0.02	0.01	0.01	0.02	0.01	
K	0.00	0.00	0.00	0.00	0.00	0.00	0.00	0.00	0.00	0.00	0.00	0.00	0.00	0.01	0.00	0.00	0.00	
TOTAL	11.04	11.03	11.05	11.03	11.04	11.03	11.04	11.04	11.04	11.04	11.04	11.04	11.04	11.03	11.02	11.04	11.04	
X _{Fe}	0.40	0.40	0.40	0.40	0.40	0.41	0.41	0.41	0.39	0.40	0.40	0.42	0.39	0.35	0.41	0.40	0.39	

Table C.2 Epidote composition from sample 216533.

Wt%	ep_1			ep_2			ep_3			ep_4		
SiO ₂	35.811	38.145	38.099	38.151	37.465	37.628	37.613	38.173	37.990	37.830	38.120	37.954
TiO ₂	0.038	0.040	0.000	0.031	0.036	0.059	0.030	0.034	0.055	0.000	0.044	0.024
Al ₂ O ₃	23.296	23.698	24.141	23.968	22.607	23.562	23.575	23.713	24.341	23.273	23.469	23.382
Cr ₂ O ₃	0.002	0.016	0.010	0.021	0.024	0.016	0.016	0.012	0.012	0.000	0.005	0.000
Fe ₂ O ₃	13.219	13.355	13.115	13.209	14.926	13.679	13.237	13.343	12.426	13.580	13.438	13.733
MnO	0.508	0.572	0.499	0.540	0.561	0.652	0.582	0.528	0.713	0.570	0.503	0.499
MgO	0.006	0.012	0.009	0.010	0.419	0.016	0.001	0.019	0.010	0.023	0.010	0.007
CaO	22.326	22.306	22.645	22.358	21.269	21.986	22.649	22.247	22.407	22.378	22.565	22.148
Na ₂ O	0.000	0.023	0.000	0.000	0.026	0.020	0.000	0.000	0.000	0.000	0.000	0.000
P ₂ O ₅	0.014	0.027	0.010	0.000	0.024	0.039	0.016	0.018	0.038	0.002	0.011	0.006
H ₂ O	1.884	1.893	1.894	1.894	1.885	1.890	1.889	1.894	1.897	1.889	1.891	1.891
TOTAL	97.105	100.085	100.420	100.181	99.241	99.547	99.608	99.981	99.888	99.545	100.057	99.646
Oxygen	13	13	13	13	13	13	13	13	13	13	13	13
Si	2.94	3.02	3.01	3.02	3.01	3.00	3.00	3.02	3.01	3.02	3.02	3.02
Ti	0.00	0.00	0.00	0.00	0.00	0.00	0.00	0.00	0.00	0.00	0.00	0.00
Al	2.25	2.21	2.25	2.23	2.14	2.21	2.22	2.21	2.27	2.19	2.19	2.19
Cr	0.00	0.00	0.00	0.00	0.00	0.00	0.00	0.00	0.00	0.00	0.00	0.00
Fe	0.82	0.80	0.78	0.79	0.90	0.82	0.79	0.80	0.74	0.82	0.80	0.82
Mn	0.04	0.04	0.03	0.04	0.04	0.04	0.04	0.04	0.05	0.04	0.03	0.03
Mg	0.00	0.00	0.00	0.00	0.05	0.00	0.00	0.00	0.00	0.00	0.00	0.00
Ca	1.96	1.89	1.91	1.89	1.83	1.88	1.94	1.89	1.90	1.91	1.92	1.89
Na	0.00	0.00	0.00	0.00	0.00	0.00	0.00	0.00	0.00	0.00	0.00	0.00
P	0.00	0.00	0.00	0.00	0.00	0.00	0.00	0.00	0.00	0.00	0.00	0.00
H	1.03	1.00	1.00	1.00	1.01	1.01	1.00	1.00	1.00	1.01	1.00	1.00
Total	8.01	7.97	7.98	7.97	7.97	7.97	7.99	7.97	7.98	7.98	7.97	7.97
X _{Fe}	1.00	1.00	1.00	1.00	0.95	1.00	1.00	1.00	1.00	1.00	1.00	1.00

Table C.3 Plagioclase composition from sample 216533, 219742, and 219749.

Wt%	533_pl_4										533_pl_5																			
	60.52	60.60	60.87	60.27	59.17	59.76	59.51	61.09	60.67	60.19	59.84	60.30	59.32	59.60	59.70	60.52	60.60	60.87	60.27	59.17	59.76	59.51	61.09	60.67	60.19	59.84	60.30	59.32	59.60	59.70
SiO2	0.03	0.00	0.00	0.00	0.00	0.01	0.00	0.00	0.03	0.00	0.04	0.00	0.00	0.02	0.00	0.00	0.00	0.00	0.00	0.00	0.01	0.00	0.00	0.00	0.00	0.00	0.00	0.00	0.00	0.00
TiO2	25.86	26.14	25.97	26.10	26.69	26.81	26.56	24.27	24.06	24.55	24.35	24.40	24.78	24.93	24.82	0.00	0.00	0.00	0.00	0.00	0.00	0.00	0.00	0.00	0.00	0.00	0.00	0.00	0.00	0.00
Al2O3	0.00	0.00	0.00	0.01	0.01	0.01	0.00	0.05	0.09	0.02	0.02	0.01	0.01	0.00	0.00	0.00	0.00	0.00	0.00	0.00	0.00	0.00	0.00	0.00	0.00	0.00	0.00	0.00	0.00	0.00
Cr2O3	0.08	0.03	0.01	0.03	0.00	0.04	0.02	0.00	0.00	0.00	0.00	0.00	0.00	0.00	0.00	0.00	0.00	0.00	0.00	0.00	0.00	0.00	0.00	0.00	0.00	0.00	0.00	0.00	0.00	0.00
FeO	0.01	0.00	0.00	0.00	0.01	0.00	0.00	0.00	0.00	0.00	0.00	0.00	0.00	0.00	0.00	0.00	0.00	0.00	0.00	0.00	0.00	0.00	0.00	0.00	0.00	0.00	0.00	0.00	0.00	0.00
MnO	0.00	0.00	0.00	0.00	0.02	0.00	0.00	0.00	0.00	0.00	0.00	0.00	0.00	0.00	0.00	0.00	0.00	0.00	0.00	0.00	0.00	0.00	0.00	0.00	0.00	0.00	0.00	0.00	0.00	0.00
MgO	5.87	5.99	5.92	6.37	6.78	6.64	6.78	6.00	5.98	6.31	6.34	6.33	6.62	6.93	6.79	0.00	0.00	0.00	0.00	0.00	0.00	0.00	0.00	0.00	0.00	0.00	0.00	0.00	0.00	0.00
CaO	8.00	7.35	7.79	7.90	7.46	7.74	7.37	8.10	7.83	8.04	8.00	7.91	7.76	7.78	7.73	0.00	0.00	0.00	0.00	0.00	0.00	0.00	0.00	0.00	0.00	0.00	0.00	0.00	0.00	0.00
Na2O	0.00	0.10	0.10	0.12	0.09	0.12	0.07	0.10	0.08	0.05	0.09	0.07	0.04	0.07	0.08	0.00	0.00	0.00	0.00	0.00	0.00	0.00	0.00	0.00	0.00	0.00	0.00	0.00	0.00	0.00
K2O	100.36	100.21	100.66	100.80	100.23	101.12	100.31	99.62	98.74	99.17	98.69	99.03	98.56	99.44	99.19	0.00	0.00	0.00	0.00	0.00	0.00	0.00	0.00	0.00	0.00	0.00	0.00	0.00	0.00	0.00
P2O5	2.68	2.68	2.68	2.66	2.63	2.63	2.64	2.72	2.72	2.70	2.70	2.70	2.68	2.67	2.68	0.00	0.00	0.00	0.00	0.00	0.00	0.00	0.00	0.00	0.00	0.00	0.00	0.00	0.00	0.00
O	0.00	0.00	0.00	0.00	0.00	0.00	0.00	0.00	0.00	0.00	0.00	0.00	0.00	0.00	0.00	0.00	0.00	0.00	0.00	0.00	0.00	0.00	0.00	0.00	0.00	0.00	0.00	0.00	0.00	0.00
Si	1.35	1.36	1.35	1.36	1.40	1.39	1.39	1.27	1.27	1.30	1.29	1.29	1.32	1.32	1.31	0.00	0.00	0.00	0.00	0.00	0.00	0.00	0.00	0.00	0.00	0.00	0.00	0.00	0.00	0.00
Ti	0.00	0.00	0.00	0.00	0.00	0.00	0.00	0.00	0.00	0.00	0.00	0.00	0.00	0.00	0.00	0.00	0.00	0.00	0.00	0.00	0.00	0.00	0.00	0.00	0.00	0.00	0.00	0.00	0.00	0.00
Al	0.00	0.00	0.00	0.00	0.00	0.00	0.00	0.00	0.00	0.00	0.00	0.00	0.00	0.00	0.00	0.00	0.00	0.00	0.00	0.00	0.00	0.00	0.00	0.00	0.00	0.00	0.00	0.00	0.00	0.00
Cr	0.00	0.00	0.00	0.00	0.00	0.00	0.00	0.00	0.00	0.00	0.00	0.00	0.00	0.00	0.00	0.00	0.00	0.00	0.00	0.00	0.00	0.00	0.00	0.00	0.00	0.00	0.00	0.00	0.00	0.00
Fe	0.00	0.00	0.00	0.00	0.00	0.00	0.00	0.00	0.00	0.00	0.00	0.00	0.00	0.00	0.00	0.00	0.00	0.00	0.00	0.00	0.00	0.00	0.00	0.00	0.00	0.00	0.00	0.00	0.00	0.00
Mn	0.00	0.00	0.00	0.00	0.00	0.00	0.00	0.00	0.00	0.00	0.00	0.00	0.00	0.00	0.00	0.00	0.00	0.00	0.00	0.00	0.00	0.00	0.00	0.00	0.00	0.00	0.00	0.00	0.00	0.00
Mg	0.00	0.00	0.00	0.00	0.00	0.00	0.00	0.00	0.00	0.00	0.00	0.00	0.00	0.00	0.00	0.00	0.00	0.00	0.00	0.00	0.00	0.00	0.00	0.00	0.00	0.00	0.00	0.00	0.00	0.00
Ca	0.28	0.28	0.28	0.30	0.32	0.31	0.32	0.29	0.29	0.30	0.31	0.30	0.32	0.33	0.33	0.00	0.00	0.00	0.00	0.00	0.00	0.00	0.00	0.00	0.00	0.00	0.00	0.00	0.00	0.00
Na	0.69	0.63	0.66	0.68	0.64	0.66	0.63	0.70	0.68	0.70	0.70	0.69	0.68	0.68	0.67	0.00	0.00	0.00	0.00	0.00	0.00	0.00	0.00	0.00	0.00	0.00	0.00	0.00	0.00	0.00
K	0.00	0.00	0.00	0.00	0.00	0.00	0.00	0.00	0.00	0.00	0.00	0.00	0.00	0.00	0.00	0.00	0.00	0.00	0.00	0.00	0.00	0.00	0.00	0.00	0.00	0.00	0.00	0.00	0.00	0.00
P	4.99	4.95	4.97	5.00	4.99	5.00	4.98	4.99	4.97	5.00	5.00	4.99	5.00	5.00	5.00	0.00	0.00	0.00	0.00	0.00	0.00	0.00	0.00	0.00	0.00	0.00	0.00	0.00	0.00	0.00
TOTAL	0.29	0.31	0.30	0.31	0.33	0.32	0.34	0.29	0.30	0.30	0.30	0.31	0.32	0.33	0.33	0.00	0.00	0.00	0.00	0.00	0.00	0.00	0.00	0.00	0.00	0.00	0.00	0.00	0.00	0.00
Ca albite	0.71	0.69	0.70	0.69	0.67	0.68	0.66	0.71	0.70	0.70	0.70	0.69	0.68	0.67	0.67	0.00	0.00	0.00	0.00	0.00	0.00	0.00	0.00	0.00	0.00	0.00	0.00	0.00	0.00	0.00
Na Anorthite	0.00	0.00	0.00	0.00	0.00	0.00	0.00	0.00	0.00	0.00	0.00	0.00	0.00	0.00	0.00	0.00	0.00	0.00	0.00	0.00	0.00	0.00	0.00	0.00	0.00	0.00	0.00	0.00	0.00	0.00
K Orthoclase	0.00	0.00	0.00	0.00	0.00	0.00	0.00	0.00	0.00	0.00	0.00	0.00	0.00	0.00	0.00	0.00	0.00	0.00	0.00	0.00	0.00	0.00	0.00	0.00	0.00	0.00	0.00	0.00	0.00	0.00

Plagioclase composition from sample 216533, 219742, and 219749. (cont)

Wt%	533 pl_4										533 pl_5																				
	60.52	60.60	60.87	60.27	59.17	59.76	59.51	61.09	60.67	60.19	59.84	60.30	59.32	59.60	59.70	60.52	60.60	60.87	60.27	59.17	59.76	59.51	61.09	60.67	60.19	59.84	60.30	59.32	59.60	59.70	
SiO2	0.03	0.00	0.00	0.00	0.00	0.01	0.00	0.00	0.03	0.01	0.00	0.00	0.00	0.00	0.00	0.00	0.00	0.00	0.00	0.00	0.01	0.00	0.00	0.03	0.00	0.04	0.00	0.00	0.02	0.00	
TiO2	25.86	26.14	25.97	26.10	26.69	26.81	26.56	24.27	24.06	24.55	24.35	24.40	24.78	24.93	24.82	24.27	24.06	24.55	24.35	24.40	24.78	24.93	24.82	24.27	24.06	24.55	24.35	24.40	24.78	24.93	24.82
Al2O3	0.00	0.00	0.00	0.01	0.01	0.01	0.00	0.00	0.00	0.04	0.02	0.00	0.00	0.00	0.00	0.00	0.00	0.00	0.01	0.01	0.01	0.01	0.00	0.00	0.02	0.02	0.01	0.00	0.00	0.00	
Cr2O3	0.08	0.03	0.01	0.03	0.00	0.00	0.00	0.00	0.00	0.00	0.00	0.00	0.00	0.00	0.00	0.05	0.09	0.02	0.02	0.02	0.01	0.01	0.00	0.00	0.00	0.01	0.01	0.03	0.09	0.02	
FeO	0.01	0.00	0.00	0.00	0.01	0.00	0.00	0.00	0.00	0.00	0.00	0.00	0.00	0.00	0.00	0.00	0.00	0.00	0.00	0.00	0.00	0.00	0.00	0.00	0.00	0.01	0.01	0.03	0.09	0.02	
MnO	0.00	0.00	0.00	0.00	0.00	0.00	0.00	0.00	0.00	0.00	0.00	0.00	0.00	0.00	0.00	0.00	0.00	0.00	0.00	0.00	0.00	0.00	0.00	0.00	0.00	0.00	0.00	0.00	0.00	0.00	
MgO	5.87	5.99	5.92	6.37	6.78	6.64	6.78	6.00	5.98	6.31	6.34	6.33	6.62	6.93	6.79	6.00	5.98	6.31	6.34	6.33	6.62	6.93	6.79	6.00	5.98	6.31	6.34	6.62	6.93	6.79	
CaO	8.00	7.35	7.79	7.90	7.46	7.74	7.37	8.10	7.83	8.04	8.00	7.91	7.76	7.78	7.73	8.10	7.83	8.04	8.00	7.91	7.76	7.78	7.73	8.10	7.83	8.04	8.00	7.91	7.76	7.78	7.73
Na2O	0.00	0.10	0.10	0.12	0.09	0.12	0.07	0.10	0.08	0.05	0.09	0.07	0.04	0.07	0.08	0.10	0.08	0.05	0.09	0.07	0.04	0.07	0.08	0.10	0.08	0.05	0.09	0.07	0.04	0.07	0.08
K2O	100.36	100.21	100.66	100.80	100.23	101.12	100.31	99.62	98.74	99.17	98.69	99.03	98.56	99.44	99.19	99.62	98.74	99.17	98.69	99.03	98.56	99.44	99.19	99.62	98.74	99.17	98.69	99.03	98.56	99.44	99.19
P2O5	2.68	2.68	2.68	2.66	2.63	2.63	2.64	2.72	2.72	2.70	2.70	2.70	2.68	2.67	2.68	2.72	2.72	2.70	2.70	2.70	2.68	2.67	2.68	2.72	2.72	2.70	2.70	2.68	2.67	2.68	2.68
O	0.00	0.00	0.00	0.00	0.00	0.00	0.00	0.00	0.00	0.00	0.00	0.00	0.00	0.00	0.00	0.00	0.00	0.00	0.00	0.00	0.00	0.00	0.00	0.00	0.00	0.00	0.00	0.00	0.00	0.00	
Si	1.35	1.36	1.35	1.36	1.40	1.39	1.39	1.27	1.27	1.30	1.29	1.29	1.32	1.32	1.31	1.27	1.27	1.30	1.29	1.29	1.32	1.32	1.31	1.27	1.27	1.30	1.29	1.32	1.32	1.31	
Ti	0.00	0.00	0.00	0.00	0.00	0.00	0.00	0.00	0.00	0.00	0.00	0.00	0.00	0.00	0.00	0.00	0.00	0.00	0.00	0.00	0.00	0.00	0.00	0.00	0.00	0.00	0.00	0.00	0.00	0.00	
Al	0.00	0.00	0.00	0.00	0.00	0.00	0.00	0.00	0.00	0.00	0.00	0.00	0.00	0.00	0.00	0.00	0.00	0.00	0.00	0.00	0.00	0.00	0.00	0.00	0.00	0.00	0.00	0.00	0.00	0.00	
Cr	0.00	0.00	0.00	0.00	0.00	0.00	0.00	0.00	0.00	0.00	0.00	0.00	0.00	0.00	0.00	0.00	0.00	0.00	0.00	0.00	0.00	0.00	0.00	0.00	0.00	0.00	0.00	0.00	0.00	0.00	
Fe	0.00	0.00	0.00	0.00	0.00	0.00	0.00	0.00	0.00	0.00	0.00	0.00	0.00	0.00	0.00	0.00	0.00	0.00	0.00	0.00	0.00	0.00	0.00	0.00	0.00	0.00	0.00	0.00	0.00	0.00	
Mn	0.00	0.00	0.00	0.00	0.00	0.00	0.00	0.00	0.00	0.00	0.00	0.00	0.00	0.00	0.00	0.00	0.00	0.00	0.00	0.00	0.00	0.00	0.00	0.00	0.00	0.00	0.00	0.00	0.00	0.00	
Mg	0.00	0.00	0.00	0.00	0.00	0.00	0.00	0.00	0.00	0.00	0.00	0.00	0.00	0.00	0.00	0.00	0.00	0.00	0.00	0.00	0.00	0.00	0.00	0.00	0.00	0.00	0.00	0.00	0.00	0.00	
Ca	0.28	0.28	0.28	0.30	0.32	0.31	0.32	0.29	0.29	0.30	0.31	0.30	0.32	0.33	0.33	0.29	0.29	0.30	0.31	0.30	0.32	0.33	0.33	0.29	0.29	0.30	0.31	0.32	0.33	0.33	
Na	0.69	0.63	0.66	0.68	0.64	0.66	0.63	0.70	0.68	0.70	0.70	0.69	0.68	0.68	0.67	0.70	0.68	0.70	0.70	0.69	0.68	0.68	0.67	0.70	0.68	0.70	0.70	0.69	0.68	0.67	
K	0.00	0.00	0.00	0.00	0.00	0.00	0.00	0.00	0.00	0.00	0.00	0.00	0.00	0.00	0.00	0.00	0.00	0.00	0.00	0.00	0.00	0.00	0.00	0.00	0.00	0.00	0.00	0.00	0.00	0.00	
P	4.99	4.95	4.97	5.00	4.99	5.00	4.98	4.99	4.97	5.00	5.00	4.99	5.00	5.00	5.00	4.99	4.97	5.00	5.00	4.99	5.00	5.00	5.00	4.99	4.97	5.00	5.00	5.00	5.00	5.00	
TOTAL	0.29	0.31	0.30	0.31	0.33	0.32	0.34	0.29	0.30	0.30	0.30	0.31	0.32	0.33	0.33	0.29	0.30	0.30	0.30	0.31	0.32	0.33	0.33	0.29	0.30	0.30	0.30	0.32	0.33	0.33	
Ca albite X(Alb)	0.71	0.69	0.70	0.69	0.67	0.68	0.66	0.71	0.70	0.70	0.70	0.69	0.68	0.67	0.67	0.71	0.70	0.70	0.70	0.69	0.68	0.67	0.67	0.71	0.70	0.70	0.70	0.68	0.67	0.67	
Na Anorthite X(An)																															
K Orthoclase X(Or)																															

Plagioclase composition from sample 216533, 219742, and 219749. (cont)

Wt%	742_pl_1										742_pl_2																					
	60.73	60.24	60.08	60.16	60.89	60.66	60.85	60.65	60.30	60.64	62.07	60.99	60.65	60.78	60.86	60.73	60.24	60.08	60.16	60.89	60.66	60.85	60.65	60.30	60.64	62.07	60.99	60.65	60.78	60.86		
SiO2	0.01	0.00	0.00	0.01	0.07	0.02	0.02	0.00	0.00	0.01	0.00	0.00	0.00	0.00	0.02	0.00	0.00	0.00	0.00	0.00	0.00	0.00	0.00	0.00	0.00	0.00	0.00	0.00	0.00	0.00	0.02	
TiO2	24.36	25.43	25.40	25.52	24.95	25.44	24.94	25.82	25.59	24.20	25.37	25.34	25.53	24.50	24.50	25.82	25.59	24.20	25.37	25.34	25.53	24.50	25.82	25.59	24.20	25.37	25.34	25.53	24.50	24.50	24.50	
Cr2O3	0.00	0.00	0.00	0.01	0.01	0.01	0.02	0.00	0.01	0.00	0.00	0.00	0.00	0.00	0.02	0.00	0.01	0.00	0.00	0.00	0.00	0.00	0.00	0.00	0.00	0.00	0.00	0.00	0.00	0.00	0.00	
FeO	0.14	0.01	0.01	0.06	0.05	0.00	0.02	0.05	0.06	0.06	0.02	0.04	0.04	0.11	0.02	0.05	0.06	0.06	0.02	0.04	0.02	0.04	0.02	0.00	0.00	0.00	0.00	0.00	0.00	0.00	0.00	0.00
MnO	0.04	0.00	0.00	0.00	0.03	0.00	0.07	0.01	0.01	0.00	0.00	0.00	0.00	0.00	0.02	0.01	0.01	0.00	0.00	0.00	0.00	0.00	0.00	0.00	0.00	0.00	0.00	0.00	0.00	0.00	0.00	0.00
MgO	0.00	0.01	0.00	0.00	0.00	0.00	0.00	0.00	0.00	0.00	0.00	0.00	0.00	0.00	0.00	0.00	0.00	0.00	0.00	0.00	0.00	0.00	0.00	0.00	0.00	0.00	0.00	0.00	0.00	0.00	0.00	0.00
CaO	5.17	5.76	6.15	6.05	5.50	5.95	5.43	5.96	6.15	4.53	5.75	5.57	5.73	5.06	5.43	5.96	6.15	4.53	5.75	5.57	5.73	5.06	5.96	6.15	4.53	5.75	5.57	5.73	5.06	5.06	5.06	5.06
Na2O	8.48	8.22	8.30	8.18	8.50	8.05	8.94	8.29	8.26	8.72	8.44	8.84	8.45	9.12	8.94	8.29	8.26	8.72	8.44	8.84	8.45	9.12	8.29	8.26	8.72	8.44	8.84	8.45	9.12	9.12	9.12	9.12
K2O	0.03	0.01	0.06	0.06	0.03	0.04	0.06	0.06	0.07	0.04	0.04	0.08	0.07	0.03	0.06	0.06	0.07	0.04	0.04	0.08	0.07	0.03	0.06	0.06	0.07	0.04	0.08	0.07	0.03	0.03	0.03	0.03
P2O5	98.95	99.69	99.99	100.04	100.02	100.16	100.36	100.84	100.46	100.38	100.33	100.64	100.54	100.69	99.71	100.84	100.46	100.38	100.33	100.64	100.54	100.69	99.71	100.84	100.46	100.38	100.33	100.64	100.54	100.69	99.71	99.71
TOTAL	8	8	8	8	8	8	8	8	8	8	8	8	8	8	8	8	8	8	8	8	8	8	8	8	8	8	8	8	8	8	8	8
O	2.72	2.68	2.67	2.67	2.70	2.69	2.70	2.67	2.67	2.69	2.70	2.69	2.68	2.71	2.70	2.67	2.67	2.69	2.70	2.69	2.68	2.71	2.67	2.67	2.69	2.70	2.69	2.68	2.71	2.71	2.71	2.71
Si	0.00	0.00	0.00	0.00	0.00	0.00	0.00	0.00	0.00	0.00	0.00	0.00	0.00	0.00	0.00	0.00	0.00	0.00	0.00	0.00	0.00	0.00	0.00	0.00	0.00	0.00	0.00	0.00	0.00	0.00	0.00	0.00
Ti	1.29	1.34	1.33	1.34	1.31	1.33	1.30	1.34	1.34	1.33	1.31	1.32	1.33	1.29	1.30	1.34	1.34	1.33	1.32	1.32	1.33	1.29	1.34	1.34	1.32	1.32	1.33	1.29	1.29	1.29	1.29	1.29
Al	0.00	0.00	0.00	0.00	0.00	0.00	0.00	0.00	0.00	0.00	0.00	0.00	0.00	0.00	0.00	0.00	0.00	0.00	0.00	0.00	0.00	0.00	0.00	0.00	0.00	0.00	0.00	0.00	0.00	0.00	0.00	0.00
Cr	0.00	0.00	0.00	0.00	0.00	0.00	0.00	0.00	0.00	0.00	0.00	0.00	0.00	0.00	0.00	0.00	0.00	0.00	0.00	0.00	0.00	0.00	0.00	0.00	0.00	0.00	0.00	0.00	0.00	0.00	0.00	0.00
Fe	0.01	0.00	0.00	0.00	0.00	0.00	0.00	0.00	0.00	0.00	0.00	0.00	0.00	0.00	0.00	0.00	0.00	0.00	0.00	0.00	0.00	0.00	0.00	0.00	0.00	0.00	0.00	0.00	0.00	0.00	0.00	0.00
Mn	0.00	0.00	0.00	0.00	0.00	0.00	0.00	0.00	0.00	0.00	0.00	0.00	0.00	0.00	0.00	0.00	0.00	0.00	0.00	0.00	0.00	0.00	0.00	0.00	0.00	0.00	0.00	0.00	0.00	0.00	0.00	0.00
Mg	0.00	0.00	0.00	0.00	0.00	0.00	0.00	0.00	0.00	0.00	0.00	0.00	0.00	0.00	0.00	0.00	0.00	0.00	0.00	0.00	0.00	0.00	0.00	0.00	0.00	0.00	0.00	0.00	0.00	0.00	0.00	0.00
Ca	0.25	0.28	0.29	0.29	0.26	0.28	0.26	0.28	0.29	0.29	0.26	0.28	0.26	0.24	0.26	0.28	0.29	0.29	0.26	0.28	0.26	0.24	0.26	0.28	0.29	0.29	0.26	0.27	0.24	0.24	0.24	0.24
Na	0.74	0.71	0.72	0.71	0.73	0.69	0.77	0.71	0.71	0.73	0.69	0.71	0.72	0.79	0.77	0.71	0.71	0.73	0.69	0.71	0.72	0.79	0.71	0.72	0.76	0.72	0.79	0.79	0.79	0.79	0.79	0.79
K	0.00	0.00	0.00	0.00	0.00	0.00	0.00	0.00	0.00	0.00	0.00	0.00	0.00	0.00	0.00	0.00	0.00	0.00	0.00	0.00	0.00	0.00	0.00	0.00	0.00	0.00	0.00	0.00	0.00	0.00	0.00	0.00
P	5.00	5.00	5.02	5.01	5.01	4.99	5.04	5.01	5.02	5.01	4.99	5.04	5.02	5.04	5.04	5.01	5.02	5.01	4.99	5.01	5.02	5.04	5.01	5.02	5.04	5.02	5.04	5.04	5.04	5.04	5.04	5.04
TOTAL	0.25	0.28	0.29	0.29	0.26	0.29	0.25	0.28	0.29	0.29	0.26	0.28	0.26	0.24	0.26	0.28	0.29	0.29	0.26	0.28	0.26	0.24	0.26	0.28	0.29	0.29	0.26	0.27	0.24	0.24	0.24	0.24
Ca albite X(Alb)	0.75	0.72	0.71	0.71	0.74	0.71	0.75	0.72	0.71	0.73	0.71	0.72	0.74	0.77	0.75	0.72	0.71	0.73	0.71	0.72	0.74	0.75	0.72	0.74	0.74	0.73	0.74	0.73	0.73	0.73	0.73	0.73
Na Anorthite X(An)	0.00	0.00	0.00	0.00	0.00	0.00	0.00	0.00	0.00	0.00	0.00	0.00	0.00	0.00	0.00	0.00	0.00	0.00	0.00	0.00	0.00	0.00	0.00	0.00	0.00	0.00	0.00	0.00	0.00	0.00	0.00	0.00
K Orthoclase X(Or)	0.00	0.00	0.00	0.00	0.00	0.00	0.00	0.00	0.00	0.00	0.00	0.00	0.00	0.00	0.00	0.00	0.00	0.00	0.00	0.00	0.00	0.00	0.00	0.00	0.00	0.00	0.00	0.00	0.00	0.00	0.00	0.00

Plagioclase composition from sample 216533, 219742, and 219749. (cont)

Wt%	742 pl_3										742 pl_4																			
	59.89	60.17	59.47	60.69	60.95	60.04	63.30	61.89	60.41	59.22	59.76	59.95	60.83	60.45	60.71	59.89	60.17	59.47	60.69	60.95	60.04	63.30	61.89	60.41	59.22	59.76	59.95	60.83	60.45	60.71
SiO2	0.04	0.02	0.00	0.00	0.02	0.00	0.03	0.04	0.00	0.00	0.00	0.03	0.04	0.00	0.02	0.00	0.00	0.00	0.00	0.02	0.00	0.00	0.00	0.00	0.00	0.00	0.02	0.01	0.02	
TiO2	25.25	25.22	25.39	24.62	24.49	25.17	22.58	24.07	25.22	25.13	24.55	24.35	24.46	24.21	24.41	25.13	24.55	24.35	24.46	24.35	24.46	24.35	24.46	24.35	24.46	24.35	24.46	24.21	24.41	
Al2O3	0.00	0.01	0.01	0.00	0.00	0.01	0.01	0.00	0.00	0.00	0.00	0.00	0.00	0.00	0.00	0.00	0.00	0.00	0.00	0.00	0.00	0.00	0.00	0.00	0.00	0.00	0.00	0.00	0.00	
Cr2O3	0.13	0.06	0.15	0.04	0.05	0.03	0.40	0.13	0.10	0.09	0.27	0.11	0.13	0.04	0.02	0.09	0.27	0.11	0.13	0.04	0.00	0.00	0.00	0.00	0.00	0.00	0.00	0.00	0.00	
FeO	0.00	0.00	0.00	0.00	0.00	0.00	0.00	0.00	0.05	0.00	0.00	0.00	0.00	0.00	0.00	0.00	0.00	0.00	0.00	0.00	0.00	0.00	0.00	0.00	0.00	0.00	0.00	0.00	0.00	
MnO	6.00	6.02	5.71	5.40	4.97	5.83	2.43	4.35	5.51	6.62	6.12	5.53	5.50	5.18	5.39	6.62	6.12	5.53	5.50	5.18	5.50	5.50	5.50	5.50	5.50	5.50	5.18	5.18	5.39	
CaO	8.69	8.47	8.26	8.64	9.06	8.60	10.35	9.30	8.23	8.37	8.21	8.17	8.58	8.88	8.39	8.37	8.21	8.17	8.58	8.88	8.58	8.58	8.58	8.58	8.58	8.58	8.88	8.88	8.39	
Na2O	0.08	0.03	0.28	0.06	0.05	0.02	0.02	0.05	0.21	0.06	0.03	0.05	0.08	0.02	0.04	0.06	0.03	0.05	0.08	0.02	0.05	0.05	0.05	0.05	0.05	0.05	0.02	0.02	0.04	
K2O	100.08	99.99	99.29	99.47	99.60	99.72	99.57	99.85	99.72	99.49	98.94	98.17	99.60	98.81	98.97	99.49	98.94	98.17	99.60	98.81	98.17	99.60	98.81	98.17	99.60	98.81	98.81	98.97	98.97	
P2O5																														
TOTAL	8	8	8	8	8	8	8	8	8	8	8	8	8	8	8	8	8	8	8	8	8	8	8	8	8	8	8	8	8	
O	2.67	2.68	2.67	2.71	2.72	2.68	2.81	2.75	2.69	2.66	2.69	2.71	2.71	2.72	2.72	2.66	2.69	2.71	2.71	2.72	2.71	2.71	2.71	2.71	2.71	2.71	2.72	2.72	2.72	
Si	0.00	0.00	0.00	0.00	0.00	0.00	0.00	0.00	0.00	0.00	0.00	0.00	0.00	0.00	0.00	0.00	0.00	0.00	0.00	0.00	0.00	0.00	0.00	0.00	0.00	0.00	0.00	0.00	0.00	
Ti	1.33	1.32	1.34	1.30	1.29	1.32	1.18	1.26	1.32	1.33	1.30	1.30	1.29	1.28	1.29	1.33	1.30	1.30	1.29	1.28	1.29	1.29	1.29	1.29	1.29	1.29	1.28	1.28	1.29	
Al	0.00	0.00	0.00	0.00	0.00	0.00	0.00	0.00	0.00	0.00	0.00	0.00	0.00	0.00	0.00	0.00	0.00	0.00	0.00	0.00	0.00	0.00	0.00	0.00	0.00	0.00	0.00	0.00	0.00	
Cr	0.00	0.00	0.00	0.00	0.00	0.00	0.00	0.00	0.00	0.00	0.00	0.00	0.00	0.00	0.00	0.00	0.00	0.00	0.00	0.00	0.00	0.00	0.00	0.00	0.00	0.00	0.00	0.00	0.00	
Fe	0.00	0.00	0.01	0.00	0.00	0.00	0.00	0.00	0.00	0.00	0.00	0.00	0.00	0.00	0.00	0.00	0.00	0.00	0.00	0.00	0.00	0.00	0.00	0.00	0.00	0.00	0.00	0.00	0.00	
Mn	0.00	0.00	0.00	0.00	0.00	0.00	0.00	0.00	0.00	0.00	0.00	0.00	0.00	0.00	0.00	0.00	0.00	0.00	0.00	0.00	0.00	0.00	0.00	0.00	0.00	0.00	0.00	0.00	0.00	
Mg	0.29	0.29	0.27	0.26	0.24	0.28	0.12	0.21	0.26	0.32	0.30	0.27	0.26	0.25	0.26	0.32	0.30	0.27	0.26	0.25	0.26	0.26	0.26	0.26	0.26	0.25	0.25	0.26	0.26	
Ca	0.75	0.73	0.72	0.75	0.78	0.74	0.89	0.80	0.71	0.73	0.72	0.72	0.74	0.77	0.73	0.73	0.72	0.72	0.74	0.77	0.74	0.74	0.74	0.74	0.74	0.77	0.77	0.73	0.74	
Na	0.00	0.00	0.02	0.00	0.00	0.00	0.00	0.00	0.01	0.00	0.00	0.00	0.00	0.00	0.00	0.00	0.00	0.00	0.00	0.00	0.00	0.00	0.00	0.00	0.00	0.00	0.00	0.00	0.00	
K	5.04	5.03	5.03	5.02	5.03	5.03	5.04	5.02	5.01	5.04	5.02	5.02	5.03	5.03	5.03	5.04	5.02	5.02	5.03	5.03	5.02	5.04	5.02	5.02	5.02	5.03	5.03	5.00	5.00	
P	0.28	0.28	0.28	0.26	0.23	0.27	0.11	0.21	0.27	0.30	0.29	0.27	0.26	0.24	0.26	0.30	0.29	0.27	0.26	0.24	0.26	0.26	0.26	0.26	0.26	0.25	0.25	0.26	0.26	
TOTAL	0.72	0.72	0.72	0.74	0.77	0.73	0.89	0.79	0.73	0.70	0.71	0.73	0.74	0.76	0.74	0.70	0.71	0.73	0.74	0.76	0.74	0.74	0.74	0.74	0.74	0.76	0.76	0.74	0.74	
Ca albite X(Alb)	0.00	0.00	0.02	0.00	0.00	0.00	0.00139	0.00	0.01	0.00	0.00	0.00	0.00	0.00	0.00	0.00	0.00	0.00	0.00	0.00	0.00	0.00	0.00	0.00	0.00	0.00	0.00	0.00	0.00	
Na Anorthite X(An)																														
K Orthoclase X(Or)																														

Garnet composition from sample 219742 and 216533. (cont)

Wt%	533_ft_2												533_ft_3											
	37.45	36.98	36.00	36.13	36.05	37.16	37.12	37.26	37.23	37.26	37.12	37.26	37.18	37.45	37.50	37.26	36.89	37.11	37.10					
SiO2	0.03	0.15	0.10	0.02	0.00	0.06	0.03	0.15	0.14	0.04	0.08	0.21	0.03	0.01	0.03	0.00	0.15	0.14	0.09					
Al2O3	20.57	20.34	20.32	20.38	20.42	20.58	20.75	20.33	20.17	20.30	20.67	20.13	20.62	20.83	20.87	20.68	20.02	20.37	20.45					
Cr2O3	0.02	0.01	0.02	0.00	0.01	0.01	0.02	0.03	0.03	0.02	0.00	0.01	0.03	0.00	0.01	0.01	0.02	0.02	0.03					
FeO	18.72	18.85	22.49	22.40	22.49	23.06	22.65	17.15	18.02	18.56	19.41	16.74	21.39	22.83	22.94	22.55	15.56	17.76	19.56					
MnO	15.93	15.52	17.54	16.19	16.59	16.58	17.87	16.84	15.42	15.42	15.11	17.04	18.52	16.20	16.28	17.07	18.18	16.92	15.86					
MgO	6.50	7.38	0.80	1.13	1.01	1.02	0.93	7.06	7.26	7.20	6.33	7.64	1.00	1.08	1.04	1.16	1.09	7.28	6.02					
CaO	0.00	0.00	0.01	0.00	0.02	0.00	0.00	0.01	0.00	0.00	0.00	0.00	0.00	0.00	0.00	0.01	0.00	0.00	0.00					
Na2O	0.00	0.00	0.00	0.00	0.00	0.00	0.00	0.00	0.00	0.00	0.00	0.00	0.00	0.00	0.00	0.00	0.00	0.00	0.00					
K2O	0.00	0.00	0.00	0.00	0.00	0.00	0.00	0.00	0.00	0.00	0.00	0.00	0.00	0.00	0.00	0.00	0.00	0.00	0.00					
Total	100.18	99.80	98.86	98.20	98.53	100.49	101.35	100.16	100.16	99.35	100.33	99.98	100.15	100.16	100.70	101.54	100.33	99.27	100.05	99.69				
Oxygen	12	12	12	12	12	12	12	12	12	12	12	12	12	12	12	12	12	12	12	12				
Si	3.02	3.00	2.97	2.99	2.97	3.01	2.98	3.01	3.01	3.03	3.07	3.05	3.02	3.01	3.02	3.00	3.02	3.00	3.02	3.02				
Ti	0.00	0.01	0.01	0.00	0.00	0.00	0.00	0.01	0.01	0.00	0.00	0.01	0.00	0.00	0.00	0.00	0.00	0.01	0.01	0.01				
Al	1.96	1.94	1.98	1.99	1.98	1.96	1.96	1.94	1.92	1.95	1.96	1.92	1.98	1.99	1.98	1.96	1.97	1.92	1.94	1.96				
Cr	0.00	0.00	0.00	0.00	0.00	0.00	0.00	0.00	0.00	0.00	0.00	0.00	0.00	0.00	0.00	0.00	0.00	0.00	0.00	0.00				
Fe3+	0.00	0.07	0.10	0.05	0.11	0.03	0.10	0.03	0.06	0.00	0.00	0.00	0.00	0.00	0.00	0.00	0.00	0.00	0.00	0.00				
Fe2+	1.26	1.23	1.48	1.51	1.48	1.54	1.45	1.14	1.18	1.26	1.31	1.13	1.46	1.55	1.55	1.50	1.53	1.01	1.17	1.33				
Mn	1.09	1.06	1.23	1.13	1.16	1.14	1.22	1.21	1.15	1.06	1.03	1.17	1.28	1.11	1.11	1.15	1.25	1.16	1.09	1.09				
Mg	0.07	0.07	0.19	0.24	0.24	0.25	0.24	0.06	0.06	0.07	0.07	0.06	0.17	0.25	0.25	0.24	0.24	0.06	0.05	0.07				
Ca	0.60	0.64	0.07	0.10	0.09	0.09	0.08	0.61	0.63	0.63	0.55	0.66	0.09	0.09	0.09	0.10	0.09	0.70	0.63	0.52				
Na	0.00	0.00	0.00	0.00	0.00	0.00	0.00	0.00	0.00	0.00	0.00	0.00	0.00	0.00	0.00	0.00	0.00	0.00	0.00	0.00				
K	0.00	0.00	0.00	0.00	0.00	0.00	0.00	0.00	0.00	0.00	0.00	0.00	0.00	0.00	0.00	0.00	0.00	0.00	0.00	0.00				
Total	8	8	8	8	8	8	8	8	8	8	8	8	8	8	8	8	8	8	8	8				
X _{Fe}	0.95	0.95	0.88	0.86	0.86	0.86	0.86	0.95	0.95	0.95	0.95	0.95	0.89	0.86	0.86	0.86	0.87	0.95	0.96	0.95				
End members																								
Fe X(Alm)	0.42	0.41	0.50	0.51	0.50	0.51	0.49	0.38	0.39	0.42	0.44	0.38	0.49	0.52	0.52	0.50	0.51	0.33	0.39	0.44				
Mn X(Sps)	0.36	0.35	0.41	0.38	0.39	0.38	0.41	0.40	0.38	0.35	0.35	0.39	0.43	0.37	0.37	0.39	0.38	0.42	0.39	0.36				
Ca X(Grs)	0.20	0.21	0.02	0.03	0.03	0.03	0.03	0.20	0.21	0.21	0.18	0.22	0.03	0.03	0.03	0.03	0.03	0.23	0.21	0.17				
Mg X(Py)P	0.36	0.35	0.41	0.38	0.39	0.38	0.41	0.40	0.38	0.35	0.35	0.39	0.43	0.37	0.37	0.39	0.38	0.42	0.39	0.36				
Wt% Fe+Mn+Mg	35.21	34.94	41.61	40.55	41.04	41.67	42.49	35.32	35.33	34.54	35.14	34.25	41.34	41.06	41.30	42.11	41.27	34.20	35.12	36.00				

Garnet composition from sample 219742 and 216533. (cont)

Wt%	533_gt_4												533_gt_5											
	37.72	37.40	37.40	37.32	37.21	37.22	37.23	37.10	37.57	37.43	36.42	36.12	35.86	36.04	35.87	35.81	35.82	35.88	35.87	36.38				
SiO2	0.05	0.04	0.01	0.00	0.00	0.01	0.02	0.07	0.14	0.05	0.11	0.01	0.02	0.03	0.02	0.00	0.00	0.03	0.17	0.07				
Al2O3	20.62	20.60	20.47	20.51	20.67	20.63	20.81	20.69	20.44	20.37	21.13	21.11	21.37	21.53	21.40	21.56	21.53	21.21	21.07	21.26				
Cr2O3	0.01	0.01	0.01	0.02	0.00	0.01	0.01	0.02	0.01	0.01	0.00	0.01	0.02	0.01	0.01	0.02	0.00	0.02	0.05	0.04				
FeO	19.94	19.67	19.75	23.04	23.23	23.04	23.10	22.88	18.40	17.35	20.34	17.61	21.24	23.07	23.18	23.01	22.50	21.35	16.39	19.27				
MnO	16.71	15.46	15.38	16.07	15.78	16.11	16.72	16.45	16.28	17.48	15.90	16.94	20.08	16.30	16.37	16.65	17.07	19.01	17.93	15.73				
MgO	0.66	0.65	0.64	2.04	2.17	2.10	2.15	2.03	0.51	0.48	0.64	0.46	1.38	1.95	1.66	1.87	1.87	1.28	0.43	0.59				
CaO	5.05	6.00	6.46	1.08	1.26	0.93	1.26	1.08	7.02	7.57	5.13	7.09	1.05	1.12	1.06	1.04	1.13	0.86	7.34	6.29				
Na2O	0.00	0.00	0.00	0.01	0.01	0.05	0.00	0.02	0.00	0.00	0.00	0.00	0.00	0.00	0.00	0.00	0.02	0.00	0.03	0.00				
K2O	0.00	0.00	0.00	0.00	0.00	0.00	0.00	0.00	0.00	0.00	0.00	0.00	0.00	0.00	0.00	0.00	0.00	0.00	0.00	0.00				
Total	100.76	99.84	100.16	100.08	100.35	100.09	101.29	100.29	100.30	100.82	99.62	99.46	101.01	100.05	99.58	100.10	99.94	99.65	99.30	99.63				
Oxygen	12	12	12	12	12	12	12	12	12	12	12	12	12	12	12	12	12	12	12	12				
Si	3.04	3.03	3.02	3.03	3.01	3.02	2.98	3.00	3.03	3.00	2.96	2.94	2.90	2.92	2.93	2.90	2.91	2.94	2.92	2.95				
Ti	0.00	0.00	0.00	0.00	0.00	0.00	0.00	0.00	0.00	0.01	0.00	0.01	0.00	0.00	0.00	0.00	0.00	0.00	0.01	0.00				
Al	1.96	1.97	1.95	1.96	1.97	1.97	1.97	1.97	1.94	1.93	2.03	2.02	2.04	2.06	2.06	2.06	2.06	2.05	2.02	2.03				
Cr	0.00	0.00	0.00	0.00	0.00	0.00	0.00	0.00	0.00	0.00	0.00	0.00	0.00	0.00	0.00	0.00	0.00	0.00	0.00	0.00				
Fe3+	0.00	0.00	0.00	0.00	0.03	0.00	0.10	0.02	0.00	0.07	0.06	0.14	0.25	0.14	0.12	0.19	0.19	0.11	0.19	0.08				
Fe2+	1.34	1.33	1.33	1.56	1.55	1.56	1.48	1.53	1.24	1.12	1.35	1.10	1.27	1.47	1.50	1.43	1.40	1.39	0.99	1.26				
Mn	1.14	1.06	1.05	1.10	1.08	1.11	1.13	1.13	1.11	1.19	1.10	1.17	1.37	1.12	1.13	1.14	1.17	1.32	1.24	1.08				
Mg	0.08	0.08	0.08	0.25	0.26	0.25	0.26	0.24	0.06	0.06	0.08	0.06	0.17	0.24	0.20	0.24	0.23	0.16	0.05	0.07				
Ca	0.44	0.52	0.56	0.09	0.11	0.08	0.11	0.09	0.61	0.65	0.45	0.62	0.09	0.10	0.09	0.09	0.10	0.08	0.64	0.55				
Na	0.00	0.00	0.00	0.00	0.00	0.01	0.00	0.00	0.00	0.00	0.00	0.00	0.00	0.00	0.00	0.00	0.00	0.00	0.01	0.00				
K	0.00	0.00	0.00	0.00	0.00	0.00	0.00	0.00	0.00	0.00	0.00	0.00	0.00	0.00	0.00	0.00	0.00	0.00	0.00	0.00				
Total	8	8	8	8	8	8	8	8	8	8	8	8	8	8	8	8	8	8	8	8				
X _{Fe}	0.94	0.94	0.95	0.86	0.86	0.86	0.85	0.86	0.95	0.95	0.95	0.95	0.88	0.86	0.88	0.86	0.86	0.90	0.95	0.95				
End members																								
Fe X(Alm)	0.45	0.45	0.44	0.52	0.52	0.52	0.50	0.51	0.41	0.37	0.45	0.38	0.44	0.50	0.51	0.49	0.48	0.47	0.34	0.43				
Mn X(Sps)	0.38	0.35	0.35	0.37	0.36	0.37	0.38	0.38	0.37	0.39	0.37	0.40	0.47	0.38	0.39	0.39	0.40	0.45	0.42	0.37				
Ca X(Grs)	0.15	0.17	0.18	0.03	0.04	0.03	0.04	0.03	0.20	0.22	0.15	0.21	0.03	0.03	0.03	0.03	0.03	0.03	0.22	0.18				
Mg X(Pyro)	0.38	0.35	0.35	0.37	0.36	0.37	0.38	0.38	0.37	0.39	0.37	0.40	0.47	0.38	0.39	0.39	0.40	0.45	0.42	0.37				
Wt% Fe+Mn+Mg	37.31	35.79	35.77	41.14	41.18	41.25	41.97	41.36	35.19	35.30	36.89	35.01	42.70	41.32	41.21	41.65	41.45	41.65	34.75	35.59				

Garnet composition from sample 219742 and 216533. (cont)

Wt%	533 Rt. 6															
	37.04	36.87	36.90	36.55	36.68	36.61	36.38	36.55	36.62	36.35	36.61	36.64	36.55	37.09	36.17	37.02
SiO2	37.04	36.87	36.90	36.55	36.68	36.61	36.38	36.55	36.62	36.35	36.61	36.64	36.55	37.09	36.17	37.02
TiO2	0.10	0.14	0.18	0.08	0.04	0.04	0.04	0.04	0.00	0.00	0.00	0.06	0.13	0.15	0.07	0.05
Al2O3	21.16	21.19	20.66	21.26	21.10	21.33	21.08	21.05	21.29	21.30	20.91	21.27	21.35	20.94	20.36	21.37
Cr2O3	0.00	0.01	0.01	0.01	0.02	0.00	0.01	0.00	0.00	0.00	0.01	0.02	0.03	0.00	0.01	0.00
FeO	18.60	17.10	14.51	20.03	22.33	23.00	22.51	22.83	22.88	23.01	21.82	21.82	19.46	16.29	20.14	18.46
MnO	14.76	17.05	18.74	20.64	16.81	16.86	16.55	18.18	17.06	17.58	17.18	18.43	20.70	17.39	15.59	15.59
MgO	0.56	0.40	0.34	1.03	1.65	1.70	1.65	1.29	1.29	1.45	1.69	1.56	0.93	0.41	0.66	0.54
CaO	7.23	7.19	8.04	0.77	0.95	1.00	0.92	0.90	0.93	1.01	1.00	0.78	0.83	7.30	4.19	6.45
Na2O	0.02	0.02	0.00	0.00	0.00	0.00	0.00	0.04	0.00	0.00	0.01	0.02	0.03	0.00	0.00	0.00
K2O	0.02	0.00	0.00	0.00	0.00	0.00	0.01	0.02	0.00	0.02	0.02	0.00	0.00	0.02	0.07	0.01
Total	99.49	99.98	99.39	100.36	100.57	100.20	99.10	101.04	100.21	100.71	99.25	100.59	100.00	99.64	97.26	99.48
Oxygen	12	12	12	12	12	12	12	12	12	12	12	12	12	12	12	12
Si	3.00	2.98	3.00	2.98	2.97	2.97	2.99	2.95	2.98	2.94	3.00	2.97	2.98	3.00	3.02	3.00
Ti	0.01	0.01	0.01	0.01	0.00	0.00	0.00	0.00	0.00	0.00	0.00	0.00	0.01	0.01	0.00	0.00
Al	2.02	2.02	1.98	2.04	2.03	2.02	2.04	2.03	2.05	2.03	2.02	2.03	2.05	2.00	2.00	2.04
Cr	0.00	0.00	0.00	0.00	0.00	0.00	0.00	0.00	0.00	0.00	0.00	0.00	0.00	0.00	0.00	0.00
Fe3+	0.00	0.02	0.02	0.00	0.04	0.05	0.00	0.11	0.00	0.13	0.00	0.05	0.00	0.00	0.00	0.00
Fe2+	1.26	1.14	0.97	1.36	1.53	1.52	1.53	1.54	1.47	1.47	1.49	1.45	1.33	1.10	1.41	1.25
Mn	1.01	1.17	1.29	1.42	1.15	1.16	1.15	1.24	1.17	1.20	1.19	1.26	1.43	1.19	1.10	1.07
Mg	0.07	0.05	0.04	0.12	0.20	0.21	0.20	0.14	0.16	0.17	0.21	0.19	0.11	0.05	0.08	0.07
Ca	0.63	0.62	0.70	0.07	0.08	0.08	0.08	0.08	0.08	0.09	0.09	0.07	0.07	0.63	0.37	0.56
Na	0.00	0.00	0.00	0.00	0.00	0.00	0.00	0.01	0.00	0.00	0.00	0.00	0.00	0.01	0.00	0.00
K	0.00	0.00	0.00	0.00	0.00	0.00	0.00	0.00	0.00	0.00	0.00	0.00	0.00	0.00	0.01	0.00
Total	8	8	8	8	8	8	8	8	8	8	8	8	8	8	8	8
X _{Fe}	0.95	0.96	0.96	0.92	0.88	0.88	0.88	0.91	0.91	0.89	0.88	0.88	0.92	0.96	0.94	0.95
End members																
Fe X(Alm)	0.42	0.38	0.32	0.46	0.51	0.51	0.52	0.50	0.52	0.50	0.50	0.49	0.45	0.37	0.47	0.42
Mn X(Sps)	0.34	0.39	0.43	0.48	0.39	0.39	0.39	0.42	0.40	0.41	0.40	0.43	0.49	0.40	0.37	0.36
Ca X(Grs)	0.21	0.21	0.23	0.02	0.03	0.03	0.03	0.03	0.03	0.03	0.03	0.02	0.02	0.21	0.13	0.19
Mg X(Pyph)	0.34	0.39	0.43	0.48	0.39	0.39	0.39	0.42	0.40	0.41	0.40	0.43	0.49	0.40	0.37	0.36
Wt% Fe+Mn+Mg	33.92	34.55	33.59	41.69	41.50	41.54	40.71	42.21	41.24	42.03	40.69	41.80	41.09	34.09	36.38	34.59

Garnet composition from sample 219742 and 216533. (cont)

WT%	533_#7																	
SiO2	36.45	36.74	36.90	36.40	36.73	36.65	36.61	36.59	36.63	36.77	36.73	36.76	37.21	37.05	36.97	37.04	36.90	37.00
TiO2	0.05	0.05	0.11	0.00	0.00	0.00	0.02	0.04	0.03	0.05	0.06	0.00	0.16	0.14	0.05	0.13	0.12	0.06
Al2O3	20.95	20.72	21.49	21.50	21.24	20.94	20.88	20.76	20.61	21.27	21.08	20.88	20.67	20.96	20.85	20.70	20.73	20.60
Cr2O3	0.01	0.01	0.01	0.01	0.00	0.00	0.02	0.02	0.01	0.02	0.02	0.02	0.03	0.00	0.01	0.01	0.00	0.01
FeO	20.11	19.48	16.71	19.33	22.42	23.03	23.47	22.80	23.32	23.17	23.39	23.20	15.39	16.35	16.65	16.20	17.99	19.76
MnO	16.66	15.65	17.20	21.69	16.70	15.83	16.06	15.96	16.39	15.91	16.27	16.70	16.24	16.75	17.58	17.31	15.85	15.39
MgO	0.65	0.60	0.40	0.98	1.91	1.91	2.00	1.93	1.71	1.93	1.94	1.88	0.62	0.66	0.66	0.43	0.46	0.61
CaO	4.15	5.84	7.26	0.82	0.99	0.96	0.99	1.05	0.94	0.94	0.92	0.96	9.15	7.80	6.76	7.61	6.96	5.97
Na2O	0.02	0.00	0.00	0.00	0.00	0.00	0.00	0.00	0.00	0.00	0.00	0.00	0.04	0.00	0.00	0.00	0.04	0.00
K2O	0.04	0.04	0.03	0.00	0.00	0.01	0.01	0.01	0.00	0.00	0.02	0.00	0.02	0.01	0.00	0.00	0.02	0.03
Total	99.07	99.12	100.10	100.72	100.00	99.34	100.06	99.15	99.65	100.12	100.42	100.40	99.53	99.73	99.55	99.43	99.07	99.42
Oxygen	12	12	12	12	12	12	12	12	12	12	12	12	12	12	12	12	12	12
Si	2.99	3.00	2.97	2.95	2.98	2.99	2.97	3.00	2.99	2.98	2.97	2.98	3.00	2.99	3.00	3.01	3.01	3.01
Ti	0.00	0.00	0.01	0.00	0.00	0.00	0.00	0.00	0.00	0.00	0.00	0.00	0.01	0.01	0.00	0.01	0.01	0.00
Al	2.02	1.99	2.04	2.06	2.03	2.02	2.00	2.00	1.98	2.03	2.01	1.99	1.97	1.99	1.99	1.98	1.99	1.98
Cr	0.00	0.00	0.00	0.00	0.00	0.00	0.00	0.00	0.00	0.00	0.00	0.00	0.00	0.00	0.00	0.00	0.00	0.00
Fe3+	0.00	0.00	0.00	0.06	0.01	0.00	0.08	0.00	0.04	0.03	0.06	0.07	0.03	0.01	0.01	0.00	0.00	0.00
Fe2+	1.38	1.33	1.13	1.27	1.52	1.57	1.54	1.56	1.57	1.55	1.54	1.52	1.02	1.10	1.13	1.10	1.23	1.35
Mn	1.16	1.08	1.17	1.49	1.15	1.10	1.10	1.11	1.13	1.09	1.11	1.15	1.11	1.15	1.21	1.19	1.09	1.06
Mg	0.08	0.07	0.05	0.12	0.23	0.23	0.24	0.24	0.21	0.23	0.23	0.23	0.07	0.08	0.08	0.05	0.06	0.07
Ca	0.36	0.51	0.63	0.07	0.09	0.08	0.09	0.09	0.08	0.08	0.08	0.08	0.79	0.67	0.59	0.66	0.61	0.52
Na	0.00	0.00	0.00	0.00	0.00	0.00	0.00	0.00	0.00	0.00	0.00	0.00	0.01	0.00	0.00	0.00	0.01	0.00
K	0.00	0.00	0.00	0.00	0.00	0.00	0.00	0.00	0.00	0.00	0.00	0.00	0.00	0.00	0.00	0.00	0.00	0.00
Total	8	8	8	8	8	8	8	8	8	8	8	8	8	8	8	8	8	8
X _{Fe}	0.95	0.95	0.96	0.91	0.87	0.87	0.86	0.87	0.88	0.87	0.87	0.87	0.93	0.93	0.93	0.95	0.96	0.95
End members																		
Fe X(Alm)	0.46	0.44	0.38	0.43	0.51	0.53	0.52	0.52	0.52	0.52	0.52	0.51	0.34	0.37	0.38	0.37	0.41	0.45
Mn X(Sps)	0.39	0.36	0.39	0.50	0.39	0.37	0.37	0.37	0.38	0.37	0.38	0.38	0.37	0.38	0.40	0.40	0.37	0.35
Ca X(Grs)	0.12	0.17	0.21	0.02	0.03	0.03	0.03	0.03	0.03	0.03	0.03	0.03	0.26	0.23	0.20	0.22	0.20	0.17
Mg X(Pyro)	0.39	0.36	0.39	0.50	0.39	0.37	0.37	0.37	0.38	0.37	0.38	0.38	0.37	0.38	0.40	0.40	0.37	0.35
WT% Fe+Mn+Mg	37.42	35.74	34.31	42.00	41.03	40.78	41.53	40.69	41.43	41.00	41.60	41.77	32.25	33.76	34.90	33.94	34.30	35.76

Garnet composition from sample 219742 and 216533. (cont)

WT%	533_gt_8														
SiO2	36.50	36.88	36.86	36.63	36.51	36.60	42.01	36.39	36.57	36.54	36.49	36.88	36.81	37.29	36.75
TiO2	0.05	0.05	0.09	0.10	0.04	0.00	0.00	0.03	0.00	0.03	0.00	0.09	0.18	0.04	0.04
Al2O3	20.83	20.58	20.80	20.39	21.01	20.83	19.06	20.66	20.68	20.75	20.85	20.36	20.57	20.52	20.54
Cr2O3	0.00	0.01	0.01	0.01	0.00	0.01	0.01	0.00	0.02	0.00	0.01	0.00	0.00	0.02	0.00
FeO	18.94	18.57	17.12	15.62	21.58	22.53	21.89	22.61	22.39	22.17	22.16	16.21	17.17	19.11	19.36
MnO	15.06	15.58	16.58	18.49	17.72	16.90	15.44	16.42	16.49	16.90	17.89	16.64	17.10	15.31	15.41
MgO	0.57	0.57	0.44	0.38	1.54	1.76	1.59	1.82	1.78	1.77	1.55	0.49	0.44	0.61	0.61
CaO	6.52	6.33	7.24	7.04	1.00	1.00	0.86	0.89	0.97	0.96	0.97	7.76	7.25	6.68	5.33
Na2O	0.02	0.01	0.00	0.00	0.01	0.00	0.00	0.00	0.00	0.00	0.00	0.01	0.00	0.00	0.00
K2O	0.04	0.02	0.01	0.00	0.00	0.03	0.04	0.00	0.01	0.00	0.02	0.00	0.04	0.05	0.05
Total	98.53	98.61	99.16	98.66	99.40	99.66	100.88	98.83	98.91	99.13	99.94	98.44	99.54	99.64	98.08
Oxygen	12	12	12	12	12	12	12	12	12	12	12	12	12	12	12
Si	2.99	3.02	3.00	3.00	2.99	2.99	3.39	2.99	3.01	3.00	2.97	3.02	2.99	3.03	3.03
Ti	0.00	0.00	0.01	0.01	0.00	0.00	0.00	0.00	0.00	0.00	0.00	0.01	0.01	0.00	0.00
Al	2.01	1.99	2.00	1.97	2.03	2.00	1.81	2.00	2.00	2.01	2.00	1.97	1.97	1.96	2.00
Cr	0.00	0.00	0.00	0.00	0.00	0.00	0.00	0.00	0.00	0.00	0.00	0.00	0.00	0.00	0.00
Fe3+	0.01	0.00	0.00	0.02	0.00	0.04	0.00	0.01	0.00	0.00	0.07	0.00	0.05	0.00	0.00
Fe2+	1.29	1.27	1.17	1.06	1.48	1.51	1.48	1.55	1.54	1.52	1.46	1.11	1.13	1.30	1.34
Mn	1.05	1.08	1.14	1.28	1.23	1.17	1.05	1.14	1.15	1.17	1.24	1.15	1.18	1.05	1.08
Mg	0.07	0.07	0.05	0.05	0.19	0.21	0.19	0.22	0.22	0.22	0.19	0.06	0.05	0.07	0.08
Ca	0.57	0.56	0.63	0.62	0.09	0.09	0.07	0.08	0.09	0.08	0.08	0.68	0.63	0.58	0.47
Na	0.00	0.00	0.00	0.00	0.00	0.00	0.00	0.00	0.00	0.00	0.00	0.00	0.00	0.00	0.00
K	0.00	0.00	0.00	0.00	0.00	0.00	0.00	0.00	0.00	0.00	0.00	0.00	0.00	0.00	0.00
Total	8	8	8	8	8	8	8	8	8	8	8	8	8	8	8
X _{Fe}	0.95	0.95	0.96	0.96	0.89	0.88	0.89	0.87	0.88	0.88	0.89	0.95	0.96	0.95	0.95
End members															
Fe X(Alm)	0.43	0.43	0.39	0.35	0.50	0.51	0.53	0.52	0.51	0.51	0.49	0.37	0.38	0.43	0.45
Mn X(Sps)	0.35	0.36	0.38	0.43	0.41	0.39	0.38	0.38	0.38	0.39	0.42	0.38	0.39	0.35	0.36
Ca X(Grs)	0.19	0.19	0.21	0.21	0.03	0.03	0.03	0.03	0.03	0.03	0.03	0.23	0.21	0.19	0.16
Mg X(Pyro)	0.35	0.36	0.38	0.43	0.41	0.39	0.38	0.38	0.38	0.39	0.42	0.38	0.39	0.35	0.36
WT% Fe+Mn+Mg	34.57	34.72	34.14	34.49	40.84	41.19	38.92	40.84	40.66	40.84	41.60	33.34	34.70	35.03	35.38

Garnet composition from sample 219742 and 216533. (cont)

WT%	36.61	36.43	36.64	36.62	36.33	36.63	36.58	36.44	36.41	533_gt_9	36.47	36.57	36.45	41.66	36.62	36.54	36.80	36.54	36.81
SiO2	0.05	0.04	0.09	0.15	0.00	0.00	0.01	0.00	0.00	0.00	0.02	0.04	0.00	0.00	0.00	0.00	0.17	0.06	0.02
TiO2	20.33	20.22	20.45	19.99	20.65	20.83	20.63	20.65	20.68	20.35	20.68	20.70	20.84	18.18	20.91	20.83	20.57	20.62	20.87
Cr2O3	0.08	0.05	0.12	0.17	0.01	0.02	0.02	0.02	0.01	0.02	0.01	0.00	0.01	0.01	0.00	0.00	0.02	0.00	0.01
FeO	20.38	18.97	16.09	13.02	21.96	22.98	23.14	23.73	24.07	23.58	23.26	23.20	23.91	22.16	22.97	22.55	17.12	20.50	20.48
MnO	15.74	15.60	17.04	19.90	17.93	16.41	15.67	15.61	16.67	16.56	15.99	15.60	15.61	15.56	16.30	16.62	17.62	16.13	16.56
MgO	0.62	0.54	0.36	0.22	1.59	1.94	1.90	1.75	1.58	1.83	1.84	1.84	1.98	1.35	1.92	1.76	0.48	0.68	0.70
CaO	5.77	6.37	6.98	8.72	1.11	1.02	1.09	0.94	0.84	0.93	1.01	1.04	0.90	0.90	1.00	1.09	7.27	4.30	4.19
Na2O	0.02	0.02	0.00	0.01	0.01	0.00	0.00	0.00	0.05	0.00	0.01	0.00	0.05	0.00	0.04	0.03	0.00	0.01	0.02
K2O	0.01	0.01	0.00	0.00	0.00	0.03	0.02	0.00	0.02	0.00	0.01	0.01	0.00	0.01	0.00	0.00	0.01	0.02	0.04
Total	99.61	98.25	97.77	98.82	99.60	99.85	99.06	99.14	100.34	99.31	98.68	98.98	99.75	99.83	99.76	99.42	100.07	98.86	99.70
Oxygen	12	12	12	12	12	12	12	12	12	12	12	12	12	12	12	12	12	12	12
Si	2.98	3.00	3.03	2.99	2.97	2.98	3.00	2.99	2.96	2.99	3.00	3.00	2.97	3.41	2.98	2.99	2.98	3.00	3.00
Ti	0.00	0.00	0.01	0.01	0.00	0.00	0.00	0.00	0.00	0.00	0.00	0.00	0.00	0.00	0.00	0.00	0.01	0.00	0.00
Al	1.95	1.96	1.99	1.93	1.99	2.00	1.99	2.00	1.98	1.97	2.01	2.00	2.00	1.75	2.01	2.01	1.96	2.00	2.00
Cr	0.00	0.00	0.01	0.01	0.00	0.00	0.00	0.00	0.00	0.00	0.00	0.00	0.00	0.00	0.00	0.00	0.00	0.00	0.00
Fe3+	0.12	0.05	0.00	0.09	0.10	0.06	0.01	0.03	0.16	0.08	0.00	0.00	0.11	0.00	0.06	0.04	0.10	0.00	0.01
Fe2+	1.31	1.28	1.11	0.83	1.43	1.52	1.58	1.61	1.53	1.57	1.60	1.59	1.56	1.52	1.53	1.52	1.09	1.41	1.39
Mn	1.09	1.09	1.19	1.38	1.24	1.13	1.09	1.08	1.15	1.15	1.07	1.08	1.08	1.08	1.12	1.15	1.21	1.12	1.14
Mg	0.08	0.07	0.04	0.03	0.19	0.24	0.23	0.21	0.19	0.18	0.22	0.22	0.24	0.16	0.23	0.21	0.06	0.08	0.08
Ca	0.50	0.56	0.62	0.76	0.10	0.09	0.10	0.08	0.07	0.08	0.09	0.09	0.08	0.08	0.09	0.10	0.63	0.38	0.37
Na	0.00	0.00	0.00	0.00	0.00	0.00	0.00	0.00	0.01	0.00	0.00	0.00	0.01	0.00	0.01	0.00	0.00	0.00	0.00
K	0.00	0.00	0.00	0.00	0.00	0.00	0.00	0.00	0.00	0.00	0.00	0.00	0.00	0.00	0.00	0.00	0.00	0.00	0.00
Total	8	8	8	8	8	8	8	8	8	8	8	8	8	8	8	8	8	8	8
X _{Fe}	0.95	0.95	0.96	0.97	0.88	0.87	0.87	0.88	0.89	0.89	0.88	0.88	0.87	0.90	0.87	0.88	0.95	0.94	0.94
End members																			
Fe X(Alm)	0.44	0.43	0.37	0.28	0.48	0.51	0.53	0.54	0.52	0.53	0.54	0.53	0.53	0.53	0.51	0.51	0.36	0.47	0.47
Mn X(Sps)	0.36	0.36	0.40	0.46	0.42	0.38	0.36	0.36	0.39	0.39	0.36	0.36	0.36	0.38	0.38	0.39	0.40	0.37	0.38
Ca X(Grs)	0.17	0.19	0.21	0.25	0.03	0.03	0.03	0.03	0.02	0.03	0.03	0.03	0.03	0.03	0.03	0.03	0.21	0.13	0.12
Mg X(Py)P	0.36	0.36	0.40	0.46	0.42	0.38	0.36	0.36	0.39	0.39	0.36	0.36	0.36	0.38	0.38	0.39	0.40	0.37	0.38
WT% Fe+Mn+Mg	36.74	35.11	33.49	33.15	41.48	41.32	40.71	41.09	42.32	41.64	40.48	40.63	41.50	39.07	41.19	40.93	35.22	37.31	37.73

Garnet composition from sample 219742 and 216533. (cont)

Wt%	533_ft_11																					
	36.84	36.77	36.39	36.65	36.60	36.63	36.75	36.51	36.45	36.64	41.63	36.36	36.65	36.60	36.30	36.13	36.42	36.42	36.40	36.50	36.39	36.51
SiO2	0.06	0.15	0.03	0.02	0.01	0.04	0.02	0.00	0.01	0.00	0.02	0.04	0.00	0.03	0.08	0.07	0.01	0.00	0.00	0.10	0.08	0.06
TiO2	20.43	20.36	20.81	20.79	21.00	20.62	20.93	20.92	20.87	20.75	18.40	20.63	20.88	20.88	20.61	20.41	21.15	20.87	20.74	20.55	20.61	20.39
Al2O3	0.00	0.02	0.00	0.01	0.01	0.01	0.01	0.01	0.00	0.01	0.01	0.02	0.02	0.01	0.01	0.00	0.01	0.00	0.03	0.00	0.02	
Cr2O3	18.78	16.51	18.91	22.76	22.90	23.28	23.73	23.59	23.22	23.59	22.55	23.62	23.65	22.76	22.69	22.67	22.70	22.55	21.71	16.96	18.87	20.28
FeO	16.01	17.27	22.13	16.56	16.17	15.84	15.63	15.42	15.54	15.41	14.78	15.24	16.05	16.29	17.63	17.64	17.81	16.37	18.87	16.81	15.43	15.60
MnO	0.50	0.39	0.79	1.71	1.97	2.05	2.11	2.14	1.96	1.97	1.83	1.88	1.78	1.73	1.47	1.39	1.49	1.75	1.20	0.52	0.55	0.65
MgO	6.67	7.99	1.87	1.08	1.08	1.19	1.13	0.99	1.17	0.87	0.87	1.14	1.15	1.04	0.99	0.91	0.94	0.94	0.79	7.46	6.37	5.31
CaO	0.00	0.00	0.00	0.00	0.02	0.00	0.00	0.00	0.00	0.03	0.00	0.00	0.02	0.00	0.00	0.03	0.00	0.00	0.00	0.00	0.00	0.00
Na2O	0.04	0.02	0.00	0.00	0.01	0.00	0.01	0.01	0.01	0.01	0.00	0.00	0.00	0.02	0.01	0.01	0.01	0.00	0.00	0.00	0.00	0.00
K2O	99.33	99.47	100.95	99.56	99.76	99.33	99.92	99.87	99.41	99.22	100.08	98.93	100.20	99.36	99.79	99.24	100.54	98.90	99.71	98.94	98.30	98.84
Total	12	12	12	12	12	12	12	12	12	12	12	12	12	12	12	12	12	12	12	12	12	12
Oxygen	3.00	2.99	2.95	2.99	2.98	2.99	2.98	2.97	2.98	3.00	3.39	2.99	2.97	2.99	2.97	2.97	2.95	2.99	2.98	2.98	2.99	3.00
Si	0.00	0.01	0.00	0.00	0.00	0.00	0.00	0.00	0.00	0.00	0.00	0.00	0.00	0.00	0.00	0.00	0.00	0.00	0.01	0.00	0.00	0.00
Ti	1.96	1.95	1.99	2.00	2.01	1.99	2.00	2.00	2.01	2.00	1.76	2.00	2.00	2.01	1.99	1.98	2.02	2.02	1.98	2.00	2.00	1.97
Al	0.00	0.00	0.00	0.00	0.00	0.00	0.00	0.00	0.00	0.00	0.00	0.00	0.00	0.00	0.00	0.00	0.00	0.00	0.00	0.00	0.00	0.00
Cr	0.04	0.09	0.16	0.01	0.05	0.04	0.04	0.10	0.05	0.02	0.00	0.04	0.08	0.00	0.10	0.11	0.11	0.00	0.05	0.08	0.01	0.04
Fe3+	1.25	1.06	1.17	1.55	1.52	1.54	1.55	1.55	1.57	1.57	1.53	1.60	1.55	1.56	1.48	1.49	1.47	1.55	1.46	1.11	1.29	1.37
Fe2+	1.11	1.19	1.52	1.15	1.11	1.10	1.07	1.06	1.08	1.07	1.02	1.06	1.10	1.13	1.22	1.23	1.22	1.14	1.31	1.16	1.07	1.08
Mn	0.06	0.05	0.10	0.21	0.24	0.25	0.26	0.26	0.24	0.24	0.22	0.23	0.21	0.21	0.18	0.17	0.18	0.21	0.15	0.06	0.07	0.08
Mg	0.58	0.69	0.16	0.09	0.09	0.10	0.10	0.10	0.09	0.10	0.08	0.10	0.10	0.09	0.09	0.08	0.08	0.08	0.07	0.65	0.56	0.47
Ca	0.00	0.00	0.00	0.00	0.00	0.00	0.00	0.00	0.00	0.01	0.00	0.00	0.00	0.00	0.00	0.00	0.00	0.00	0.00	0.00	0.00	0.00
Na	0.00	0.00	0.00	0.00	0.00	0.00	0.00	0.00	0.00	0.00	0.00	0.00	0.00	0.00	0.00	0.00	0.00	0.00	0.00	0.00	0.00	0.00
K	0.00	0.00	0.00	0.00	0.00	0.00	0.00	0.00	0.00	0.00	0.00	0.00	0.00	0.00	0.00	0.00	0.00	0.00	0.00	0.00	0.00	0.00
Total	8	8	8	8	8	8	8	8	8	8	8	8	8	8	8	8	8	8	8	8	8	8
X _{Fe}	0.95	0.96	0.92	0.88	0.86	0.86	0.86	0.86	0.87	0.87	0.87	0.87	0.88	0.88	0.89	0.90	0.89	0.88	0.91	0.95	0.95	0.94
End members																						
Fe X(Alm)	0.42	0.36	0.40	0.52	0.51	0.52	0.52	0.52	0.53	0.53	0.54	0.53	0.52	0.52	0.50	0.50	0.50	0.52	0.49	0.37	0.43	0.46
Mn X(Sps)	0.37	0.40	0.51	0.38	0.37	0.37	0.36	0.36	0.36	0.36	0.36	0.35	0.37	0.38	0.41	0.41	0.41	0.38	0.44	0.39	0.36	0.36
Ca X(Gr _s)	0.19	0.23	0.06	0.03	0.03	0.03	0.03	0.03	0.03	0.03	0.03	0.03	0.03	0.03	0.03	0.03	0.03	0.03	0.02	0.22	0.19	0.16
Mg X(P _{yp})	0.37	0.40	0.51	0.38	0.37	0.37	0.36	0.36	0.36	0.36	0.36	0.35	0.37	0.38	0.41	0.41	0.41	0.38	0.44	0.39	0.36	0.36
Wt% Fe+Mn+Mg	35.28	34.17	41.84	41.03	41.04	40.85	41.02	41.29	41.09	40.60	39.16	40.74	41.48	40.78	41.79	41.69	42.00	40.66	41.78	34.29	34.84	36.54

Garnet composition from sample 219742 and 216533. (cont)

Wt%	533_gt_12															
	36.00	36.32	36.41	35.96	36.50	36.33	36.11	36.62	36.39	36.34	36.30	36.73	36.85	36.81	36.90	36.94
SiO2	0.03	0.12	0.09	0.00	0.00	0.00	0.07	0.03	0.05	0.04	0.03	0.03	0.13	0.14	0.02	0.01
TiO2	20.62	20.76	20.32	20.53	20.94	20.75	20.40	21.02	20.65	20.82	20.76	20.57	20.65	21.07	20.87	21.05
Al2O3	0.01	0.00	0.00	0.00	0.00	0.01	0.00	0.02	0.01	0.00	0.01	0.03	0.00	0.00	0.00	0.00
Cr2O3	20.25	18.79	16.21	20.12	22.49	23.57	23.71	23.66	23.80	23.46	24.20	23.79	14.13	17.18	20.15	20.00
FeO	16.69	14.99	17.00	19.74	16.42	15.28	15.98	15.54	15.22	15.02	15.13	15.33	18.82	16.96	15.58	15.99
MnO	0.68	0.50	0.35	1.24	1.73	2.10	1.70	1.92	1.94	1.86	1.93	2.18	0.46	0.41	0.62	0.68
MgO	4.44	6.80	7.49	1.03	1.23	1.09	1.21	1.12	0.98	1.15	1.18	1.19	8.17	7.40	4.81	4.85
CaO	0.02	0.01	0.00	0.00	0.00	0.00	0.01	0.00	0.01	0.01	0.00	0.00	0.00	0.00	0.01	0.03
Na2O	0.06	0.00	0.00	0.00	0.00	0.00	0.01	0.01	0.00	0.01	0.00	0.00	0.00	0.00	0.05	0.02
K2O	98.80	98.30	97.87	98.63	99.31	99.13	99.19	99.94	99.04	98.71	99.54	99.86	99.21	99.98	99.00	99.56
Total	12	12	12	12	12	12	12	12	12	12	12	12	12	12	12	12
Oxygen	2.96	2.98	3.00	2.98	2.99	2.97	2.97	2.98	2.99	2.99	2.96	2.99	2.99	2.97	3.02	3.01
Si	0.00	0.01	0.01	0.00	0.00	0.00	0.00	0.00	0.00	0.00	0.00	0.00	0.01	0.01	0.00	0.00
Ti	2.00	2.01	1.98	2.00	2.02	2.00	1.97	2.01	2.00	2.02	2.00	1.97	1.98	2.01	2.01	2.02
Al	0.00	0.00	0.00	0.00	0.00	0.00	0.00	0.00	0.00	0.00	0.00	0.00	0.00	0.00	0.00	0.00
Cr	0.13	0.01	0.00	0.07	0.01	0.08	0.13	0.05	0.04	0.01	0.11	0.08	0.03	0.04	0.00	0.00
Fe3+	1.31	1.28	1.12	1.35	1.53	1.56	1.54	1.58	1.61	1.61	1.58	1.56	0.94	1.13	1.38	1.36
Fe2+	1.16	1.04	1.19	1.38	1.14	1.06	1.11	1.07	1.06	1.05	1.05	1.06	1.29	1.16	1.08	1.10
Mn	0.08	0.06	0.04	0.15	0.21	0.26	0.21	0.23	0.24	0.23	0.24	0.26	0.06	0.05	0.08	0.08
Mg	0.39	0.60	0.66	0.09	0.11	0.10	0.11	0.10	0.09	0.10	0.10	0.10	0.71	0.64	0.42	0.42
Ca	0.00	0.00	0.00	0.00	0.00	0.00	0.00	0.00	0.00	0.00	0.00	0.00	0.00	0.00	0.00	0.00
Na	0.01	0.00	0.00	0.00	0.00	0.00	0.00	0.00	0.00	0.00	0.00	0.00	0.00	0.00	0.00	0.00
K	0.01	0.00	0.00	0.00	0.00	0.00	0.00	0.00	0.00	0.00	0.00	0.00	0.00	0.00	0.00	0.00
Total	8	8	8	8	8	8	8	8	8	8	8	8	8	8	8	8
X _{Fe}	0.94	0.95	0.96	0.90	0.88	0.86	0.88	0.87	0.87	0.88	0.87	0.86	0.94	0.96	0.95	0.94
End members																
Fe X(Alrn)	0.44	0.43	0.37	0.45	0.51	0.53	0.52	0.53	0.54	0.54	0.53	0.52	0.31	0.38	0.47	0.46
Mn X(Sps)	0.39	0.35	0.39	0.46	0.38	0.36	0.37	0.36	0.35	0.35	0.35	0.35	0.43	0.39	0.37	0.37
Ca X(Grs)	0.13	0.20	0.22	0.03	0.04	0.03	0.04	0.03	0.03	0.03	0.03	0.03	0.24	0.21	0.14	0.14
Mg X(Pyg)	0.39	0.35	0.39	0.46	0.38	0.36	0.37	0.36	0.35	0.35	0.35	0.35	0.43	0.39	0.37	0.37
Wt% Fe+Mn+Mg	37.62	34.28	33.56	41.10	40.64	40.95	41.38	41.12	40.96	40.34	41.26	41.30	33.41	34.55	36.35	36.67

Garnet composition from sample 219742 and 216533. (cont)

Wt%	533_gt_13													
	36.82	36.83	37.12	36.83	36.81	36.67	36.80	36.40	36.35	36.27	36.23	36.40	36.41	36.52
SiO2	0.09	0.02	0.05	0.09	0.13	0.11	0.05	0.02	0.05	0.00	0.00	0.02	0.06	0.15
TiO2	20.81	20.77	21.05	20.82	20.79	20.64	20.60	20.51	20.76	20.66	20.79	20.76	20.51	20.96
Cr2O3	0.01	0.02	0.04	0.01	0.01	0.00	0.01	0.00	0.02	0.02	0.00	0.00	0.02	0.02
FeO	18.83	20.06	18.91	17.21	16.92	15.70	18.62	20.60	21.90	22.34	22.64	22.23	16.40	19.13
MnO	15.62	16.33	15.66	16.69	18.07	17.87	16.78	19.50	17.87	16.82	16.22	16.57	18.48	15.46
MgO	0.62	0.67	0.60	0.50	0.42	0.40	0.63	1.12	1.52	1.80	1.86	1.81	0.44	0.57
CaO	6.20	4.19	6.34	7.11	7.05	7.60	5.41	0.87	0.76	1.01	1.15	1.13	6.89	6.20
Na2O	0.00	0.02	0.00	0.01	0.00	0.00	0.00	0.00	0.00	0.00	0.00	0.03	0.02	0.00
K2O	0.02	0.01	0.01	0.02	0.01	0.00	0.00	0.00	0.00	0.00	0.03	0.00	0.01	0.01
Total	99.01	98.93	99.80	99.29	100.22	98.99	98.90	99.03	99.22	98.92	98.92	98.95	99.24	99.03
Oxygen	12	12	12	12	12	12	12	12	12	12	12	12	12	12
Si	3.01	3.02	3.01	2.99	2.97	2.99	3.02	3.00	2.99	2.98	2.97	2.99	2.97	2.98
Ti	0.01	0.00	0.00	0.01	0.01	0.01	0.00	0.00	0.00	0.00	0.00	0.00	0.00	0.01
Al	2.00	2.01	2.01	2.00	1.98	1.98	1.99	1.99	2.01	2.00	2.01	2.01	1.97	2.02
Cr	0.00	0.00	0.00	0.00	0.00	0.00	0.00	0.00	0.00	0.00	0.00	0.00	0.00	0.00
Fe3+	0.00	0.00	0.00	0.01	0.09	0.03	0.00	0.00	0.02	0.05	0.07	0.03	0.13	0.00
Fe2+	1.29	1.38	1.28	1.16	1.08	1.05	1.28	1.42	1.49	1.50	1.51	1.51	1.03	1.31
Mn	1.08	1.14	1.07	1.15	1.24	1.23	1.16	1.36	1.24	1.17	1.13	1.15	1.28	1.07
Mg	0.08	0.08	0.07	0.06	0.05	0.05	0.08	0.14	0.19	0.22	0.23	0.22	0.05	0.07
Ca	0.54	0.37	0.55	0.62	0.61	0.66	0.47	0.08	0.07	0.09	0.10	0.10	0.60	0.54
Na	0.00	0.00	0.00	0.00	0.00	0.00	0.00	0.00	0.00	0.00	0.00	0.00	0.00	0.00
K	0.00	0.00	0.00	0.00	0.00	0.00	0.00	0.00	0.00	0.00	0.00	0.00	0.00	0.00
Total	8	8	8	8	8	8	8	8	8	8	8	8	8	8
X _{Fe}	0.94	0.94	0.95	0.95	0.96	0.96	0.94	0.91	0.89	0.87	0.87	0.87	0.95	0.95
End members														
Fe X(Alim)	0.43	0.46	0.43	0.39	0.36	0.35	0.43	0.47	0.50	0.50	0.51	0.51	0.35	0.44
Mn X(Sps)	0.36	0.38	0.36	0.38	0.41	0.41	0.39	0.45	0.42	0.39	0.38	0.39	0.43	0.36
Ca X(Grs)	0.18	0.12	0.18	0.21	0.20	0.22	0.16	0.03	0.02	0.03	0.03	0.03	0.20	0.18
Mg X(Py)	0.36	0.38	0.36	0.38	0.41	0.41	0.39	0.45	0.42	0.39	0.38	0.39	0.43	0.36
Wt% Fe+Mn+Mg	35.07	37.06	35.17	34.40	35.41	33.98	36.03	41.22	41.29	40.96	40.72	40.61	35.32	35.17

Table C.5 Biotite composition from samples 216533, 219742 219749.

	742_bt_1												
SiO2	34.79	35.32	35.38	35.25	45.26	35.35	35.47	35.31	33.78	34.24	34.59	34.56	34.49
TiO2	1.09	1.12	1.07	1.02	0.93	1.09	1.15	1.12	0.88	1.05	1.13	1.10	0.91
Al2O3	20.00	19.21	19.45	19.36	16.35	19.17	19.22	19.54	20.43	19.67	19.27	19.30	19.59
Cr2O3	0.03	0.01	0.04	0.02	0.01	0.03	0.03	0.01	0.01	0.02	0.03	0.02	0.02
FeO	18.30	18.21	18.49	18.37	17.05	17.78	18.12	17.43	19.01	18.61	19.01	18.98	18.44
MnO	0.45	0.42	0.39	0.33	0.34	0.42	0.40	0.24	0.31	0.43	0.45	0.38	0.44
MgO	11.65	11.03	11.29	11.34	10.13	12.09	11.19	11.31	11.81	12.01	11.22	11.59	12.15
CaO	0.01	0.00	0.01	0.00	0.00	0.03	0.00	0.00	0.02	0.00	0.02	0.01	0.01
Na2O	0.25	0.17	0.20	0.21	0.09	0.30	0.24	0.22	0.14	0.22	0.19	0.20	0.16
K2O	8.54	9.09	8.92	8.97	7.06	9.04	9.00	9.22	7.36	7.82	8.60	8.49	8.16
H2O	4.01	4.00	4.00	4.00	4.17	4.01	4.01	4.02	4.02	4.01	3.99	3.99	4.01
TOTAL	99.11	98.58	99.25	98.87	101.40	99.30	98.82	98.42	97.78	98.09	98.51	98.63	98.41
Oxygen	24	24	24	24	24	24	24	24	24	24	24	24	24
Si	5.26	5.38	5.35	5.35	6.43	5.34	5.38	5.36	5.16	5.23	5.29	5.27	5.25
Ti	0.12	0.13	0.12	0.12	0.10	0.12	0.13	0.13	0.10	0.12	0.13	0.13	0.10
Al	3.56	3.45	3.47	3.46	2.74	3.41	3.44	3.50	3.68	3.54	3.47	3.47	3.51
Cr	0.00	0.00	0.00	0.00	0.00	0.00	0.00	0.00	0.00	0.00	0.00	0.00	0.00
Fe	2.31	2.32	2.34	2.33	2.02	2.25	2.30	2.21	2.43	2.38	2.43	2.42	2.35
Mn	0.06	0.05	0.05	0.04	0.04	0.05	0.05	0.03	0.04	0.06	0.06	0.05	0.06
Mg	2.63	2.50	2.54	2.57	2.14	2.72	2.53	2.56	2.69	2.73	2.56	2.64	2.76
Ca	0.00	0.00	0.00	0.00	0.00	0.00	0.00	0.00	0.00	0.00	0.00	0.00	0.00
Na	0.07	0.05	0.06	0.06	0.02	0.09	0.07	0.06	0.04	0.06	0.06	0.06	0.05
K	1.65	1.77	1.72	1.74	1.28	1.74	1.74	1.79	1.44	1.52	1.68	1.65	1.58
H	4.04	4.07	4.04	4.05	3.95	4.04	4.06	4.07	4.10	4.09	4.07	4.06	4.07
TOTAL	19.71	19.71	19.70	19.73	18.73	19.76	19.70	19.72	19.68	19.72	19.74	19.75	19.74
X _{Fe}	0.47	0.48	0.48	0.48	0.49	0.45	0.48	0.46	0.47	0.47	0.49	0.48	0.46

Biotite composition from samples 216533, 219742 219749. (cont)

Wt%	742_bt_2												
SiO2	35.55	36.19	35.60	35.75	35.78	35.89	35.64	35.62	35.57	35.52	35.39	34.63	35.16
TiO2	1.23	1.29	1.24	1.12	1.24	1.31	1.17	1.24	1.36	1.19	1.17	1.14	1.17
Al2O3	19.28	19.35	19.48	19.68	19.62	19.42	20.06	19.43	19.46	19.36	19.29	19.60	19.27
Cr2O3	0.02	0.02	0.02	0.02	0.04	0.03	0.01	0.03	0.03	0.02	0.03	0.03	0.03
FeO	18.75	17.17	18.39	17.90	18.19	18.29	18.36	18.55	18.10	18.19	17.59	18.14	18.36
MnO	0.32	0.34	0.36	0.41	0.43	0.29	0.37	0.41	0.39	0.33	0.38	0.27	0.34
MgO	11.14	10.88	11.03	10.93	11.06	11.15	11.19	10.94	10.66	10.96	10.86	11.19	11.10
CaO	0.00	0.01	0.00	0.01	0.00	0.00	0.00	0.01	0.01	0.00	0.01	0.00	0.01
Na2O	0.21	0.24	0.28	0.28	0.25	0.23	0.27	0.17	0.22	0.26	0.23	0.17	0.19
K2O	9.63	9.38	9.70	9.36	9.09	9.39	9.16	9.34	9.38	9.20	9.44	8.78	9.14
H2O	3.98	4.03	3.99	4.01	4.01	4.00	4.00	3.99	4.00	4.00	4.01	4.01	4.00
TOTAL	100.11	98.90	100.11	99.46	99.71	99.99	100.24	99.74	99.19	99.03	98.39	97.95	98.78
Oxygen	24	24	24	24	24	24	24	24	24	24	24	24	24
Si	5.36	5.46	5.36	5.39	5.38	5.39	5.33	5.37	5.38	5.38	5.39	5.30	5.35
Ti	0.14	0.15	0.14	0.13	0.14	0.15	0.13	0.14	0.16	0.14	0.13	0.13	0.13
Al	3.42	3.44	3.46	3.50	3.48	3.44	3.54	3.45	3.47	3.46	3.46	3.53	3.46
Cr	0.00	0.00	0.00	0.00	0.01	0.00	0.00	0.00	0.00	0.00	0.00	0.00	0.00
Fe	2.36	2.17	2.32	2.26	2.29	2.30	2.30	2.34	2.29	2.31	2.24	2.32	2.34
Mn	0.04	0.04	0.05	0.05	0.06	0.04	0.05	0.05	0.05	0.04	0.05	0.03	0.04
Mg	2.50	2.45	2.48	2.46	2.48	2.50	2.50	2.46	2.41	2.48	2.47	2.55	2.52
Ca	0.00	0.00	0.00	0.00	0.00	0.00	0.00	0.00	0.00	0.00	0.00	0.00	0.00
Na	0.06	0.07	0.08	0.08	0.07	0.07	0.08	0.05	0.06	0.08	0.07	0.05	0.06
K	1.85	1.81	1.86	1.80	1.74	1.80	1.75	1.80	1.81	1.78	1.83	1.71	1.77
H	4.00	4.05	4.00	4.03	4.02	4.01	4.00	4.02	4.04	4.05	4.07	4.09	4.06
TOTAL	19.75	19.64	19.75	19.69	19.66	19.68	19.68	19.69	19.68	19.70	19.73	19.73	19.73
X _{Fe}	0.49	0.47	0.48	0.48	0.48	0.48	0.48	0.49	0.49	0.48	0.48	0.48	0.48

Biotite composition from samples 216533, 219742 219749. (cont)

	742_bt_3																	
Wt%	34.93	35.48	35.98	34.97	35.30	35.67	35.44	35.52	35.53	35.11	35.50	36.10	36.01	35.62	35.74	36.06	35.63	35.35
SiO2	1.38	1.40	1.60	1.30	1.31	1.15	1.15	1.12	1.35	2.17	1.36	1.20	1.75	1.89	1.45	1.08	1.15	1.31
TiO2	19.23	19.27	19.45	19.11	19.51	19.43	19.93	19.34	19.30	18.73	19.35	19.81	19.41	18.89	19.58	19.58	19.43	19.08
Al2O3	0.04	0.02	0.04	0.00	0.04	0.02	0.00	0.02	0.01	0.03	0.02	0.02	0.02	0.01	0.02	0.00	0.03	0.03
Cr2O3	18.98	18.32	18.51	18.58	18.35	18.41	17.45	18.51	18.46	19.11	18.32	17.75	18.10	18.77	18.34	18.16	17.97	18.57
FeO	0.38	0.44	0.43	0.40	0.57	0.36	0.36	0.40	0.38	0.65	0.25	0.42	0.31	0.42	0.40	0.38	0.44	0.31
MnO	11.22	10.59	11.53	11.18	11.10	10.73	10.80	10.78	10.80	11.06	10.65	10.81	10.63	10.72	10.78	10.81	10.67	10.70
MgO	0.03	0.01	0.01	0.06	0.00	0.01	0.00	0.01	0.02	0.00	0.00	0.00	0.02	0.00	0.01	0.00	0.01	0.00
CaO	0.19	0.20	0.21	0.26	0.19	0.20	0.28	0.27	0.22	0.24	0.21	0.26	0.22	0.25	0.21	0.28	0.20	0.21
Na2O	9.30	9.21	9.11	9.40	9.11	9.18	9.39	9.06	9.23	9.64	9.26	9.33	9.34	9.44	9.24	9.15	9.22	8.92
K2O	3.98	4.00	4.00	3.98	4.00	4.00	4.02	4.00	4.00	3.96	4.00	4.02	4.01	3.98	4.00	4.01	4.01	4.00
H2O	99.65	98.96	100.87	99.26	99.47	99.15	98.82	99.02	99.31	100.69	98.93	99.72	99.81	100.00	99.78	99.51	98.76	98.48
TOTAL	24	24	24	24	24	24	24	24	24	24	24	24	24	24	24	24	24	24
Oxygen	5.30	5.39	5.36	5.32	5.34	5.40	5.37	5.39	5.38	5.29	5.39	5.42	5.41	5.37	5.38	5.43	5.41	5.39
Si	0.16	0.16	0.18	0.15	0.15	0.13	0.13	0.13	0.15	0.25	0.16	0.13	0.20	0.21	0.16	0.12	0.13	0.15
Ti	3.44	3.45	3.41	3.43	3.47	3.47	3.56	3.46	3.44	3.33	3.46	3.50	3.44	3.36	3.47	3.47	3.48	3.43
Al	0.00	0.00	0.00	0.00	0.00	0.00	0.00	0.00	0.00	0.00	0.00	0.00	0.00	0.00	0.00	0.00	0.00	0.00
Cr	2.41	2.33	2.30	2.36	2.32	2.33	2.21	2.35	2.34	2.41	2.33	2.23	2.27	2.37	2.31	2.29	2.28	2.37
Fe	0.05	0.06	0.05	0.05	0.07	0.05	0.05	0.05	0.05	0.08	0.03	0.05	0.04	0.05	0.05	0.05	0.06	0.04
Mn	2.54	2.40	2.56	2.53	2.50	2.42	2.44	2.44	2.44	2.48	2.41	2.42	2.38	2.41	2.42	2.43	2.41	2.43
Mg	0.00	0.00	0.00	0.01	0.00	0.00	0.00	0.00	0.00	0.00	0.00	0.00	0.00	0.00	0.00	0.00	0.00	0.00
Ca	0.06	0.06	0.06	0.08	0.06	0.06	0.08	0.08	0.06	0.07	0.06	0.08	0.06	0.07	0.06	0.08	0.06	0.06
Na	1.80	1.78	1.73	1.82	1.76	1.77	1.81	1.75	1.78	1.85	1.79	1.79	1.79	1.82	1.77	1.76	1.79	1.74
K	4.02	4.05	3.97	4.04	4.03	4.04	4.06	4.05	4.04	3.98	4.05	4.02	4.02	4.01	4.02	4.03	4.06	4.07
H	19.77	19.68	19.64	19.79	19.70	19.67	19.70	19.69	19.69	19.75	19.68	19.64	19.61	19.68	19.65	19.65	19.67	19.68
TOTAL	0.49	0.49	0.47	0.48	0.48	0.49	0.48	0.49	0.49	0.49	0.49	0.48	0.49	0.50	0.49	0.49	0.49	0.49
X _{Fe}																		

Biotite composition from samples 216533, 219742 219749. (cont)

Wt%	742_bt_4													
	34.27	34.57	34.34	34.73	34.78	34.10	34.65	34.65	35.19	35.18	34.09	35.03	34.61	
SiO2	1.10	1.36	1.18	1.38	1.26	1.15	1.20	1.28	1.26	1.14	1.29	1.25	1.32	
TiO2	19.16	19.27	19.20	19.37	19.04	19.20	19.33	19.23	19.10	18.96	19.28	19.23	19.10	
Al2O3	0.02	0.02	0.02	0.01	0.02	0.04	0.02	0.02	0.03	0.04	0.04	0.04	0.02	
Cr2O3	19.20	18.96	18.92	18.06	18.80	19.33	18.86	18.67	18.74	17.89	18.76	18.82	18.46	
FeO	0.54	0.47	0.46	0.29	0.46	0.47	0.35	0.52	0.34	0.42	0.42	0.41	0.31	
MnO	11.49	10.85	10.88	10.93	10.68	11.07	11.11	10.94	10.73	10.98	11.11	10.92	11.01	
MgO	0.00	0.02	0.02	0.02	0.02	0.00	0.00	0.02	0.01	0.00	0.01	0.00	0.02	
CaO	0.20	0.18	0.14	0.22	0.24	0.26	0.17	0.14	0.18	0.22	0.21	0.22	0.22	
Na2O	8.05	8.53	8.37	8.65	8.30	8.19	8.53	8.72	8.84	9.00	8.71	9.01	8.44	
K2O	3.99	3.99	4.00	4.01	4.00	3.99	4.00	3.99	4.00	4.01	3.99	3.99	4.01	
H2O	98.04	98.22	97.52	97.67	97.60	97.78	98.22	98.20	98.41	97.84	97.90	98.91	97.51	
TOTAL	24	24	24	24	24	24	24	24	24	24	24	24	24	
Oxygen	5.26	5.30	5.29	5.32	5.35	5.25	5.30	5.31	5.37	5.39	5.25	5.33	5.32	
Si	0.13	0.16	0.14	0.16	0.15	0.13	0.14	0.15	0.14	0.13	0.15	0.14	0.15	
Ti	3.46	3.48	3.49	3.50	3.45	3.49	3.49	3.47	3.44	3.42	3.50	3.45	3.46	
Al	0.00	0.00	0.00	0.00	0.00	0.00	0.00	0.00	0.00	0.00	0.00	0.00	0.00	
Cr	2.46	2.43	2.44	2.32	2.42	2.49	2.41	2.39	2.39	2.29	2.41	2.40	2.37	
Fe	0.07	0.06	0.06	0.04	0.06	0.06	0.05	0.07	0.04	0.05	0.05	0.05	0.04	
Mn	2.63	2.48	2.50	2.50	2.45	2.54	2.53	2.50	2.44	2.51	2.55	2.48	2.52	
Mg	0.00	0.00	0.00	0.00	0.00	0.00	0.00	0.00	0.00	0.00	0.00	0.00	0.00	
Ca	0.06	0.05	0.04	0.06	0.07	0.08	0.05	0.04	0.05	0.07	0.06	0.06	0.07	
Na	1.58	1.67	1.65	1.69	1.63	1.61	1.66	1.70	1.72	1.76	1.71	1.75	1.66	
K	4.09	4.08	4.11	4.10	4.11	4.10	4.08	4.08	4.07	4.10	4.09	4.05	4.11	
H	19.74	19.71	19.72	19.70	19.68	19.76	19.72	19.72	19.68	19.73	19.78	19.73	19.71	
TOTAL	0.48	0.49	0.49	0.48	0.50	0.49	0.49	0.49	0.49	0.48	0.49	0.49	0.48	
X _{Fe}														

Biotite composition from samples 216533, 219742 219749. (cont)

Wt%	742_bt_4 (cont)											
	33.82	34.36	35.07	35.00	34.88	35.29	34.37	35.33	35.41	35.51	35.13	35.00
SiO2	1.43	1.14	1.52	1.21	1.32	1.41	1.19	1.50	1.70	1.75	1.73	1.36
TiO2	18.82	19.24	18.94	18.96	19.07	19.31	19.18	18.80	18.65	18.67	18.69	18.88
Al2O3	0.02	0.01	0.03	0.03	0.02	0.03	0.03	0.02	0.01	0.01	0.03	0.01
Cr2O3	18.95	18.87	18.45	18.83	18.59	18.50	18.55	18.47	18.73	18.93	18.74	18.42
FeO	0.29	0.43	0.37	0.46	0.35	0.35	0.26	0.26	0.41	0.37	0.40	0.32
MnO	10.75	11.21	10.69	10.75	10.88	11.08	11.33	10.69	10.48	10.63	10.49	10.68
MgO	0.01	0.01	0.00	0.01	0.02	0.00	0.01	0.01	0.02	0.00	0.01	0.01
CaO	0.15	0.22	0.17	0.24	0.19	0.24	0.19	0.22	0.19	0.15	0.22	0.18
Na2O	9.00	8.38	9.39	8.69	8.93	8.98	8.37	9.54	9.26	9.37	9.21	8.72
K2O	3.98	4.00	3.99	3.99	3.99	4.00	4.01	3.99	3.99	3.98	3.98	4.01
H2O	97.22	97.89	98.63	98.17	98.24	99.18	97.49	98.82	98.85	99.38	98.63	97.59
TOTAL	24	24	24	24	24	24	24	24	24	24	24	24
Oxygen	5.26	5.28	5.36	5.36	5.34	5.34	5.29	5.39	5.40	5.39	5.37	5.38
Si	0.17	0.13	0.17	0.14	0.15	0.16	0.14	0.17	0.20	0.20	0.20	0.16
Ti	3.45	3.48	3.41	3.42	3.44	3.45	3.48	3.38	3.35	3.34	3.37	3.42
Al	0.00	0.00	0.00	0.00	0.00	0.00	0.00	0.00	0.00	0.00	0.00	0.00
Cr	2.46	2.42	2.36	2.41	2.38	2.34	2.39	2.35	2.39	2.40	2.40	2.37
Fe	0.04	0.06	0.05	0.06	0.05	0.04	0.03	0.03	0.05	0.05	0.05	0.04
Mn	2.49	2.57	2.44	2.45	2.48	2.50	2.60	2.43	2.38	2.41	2.39	2.45
Mg	0.00	0.00	0.00	0.00	0.00	0.00	0.00	0.00	0.00	0.00	0.00	0.00
Ca	0.05	0.07	0.05	0.07	0.06	0.07	0.06	0.06	0.06	0.04	0.06	0.05
Na	1.79	1.64	1.83	1.70	1.74	1.73	1.64	1.85	1.80	1.82	1.80	1.71
K	4.12	4.09	4.06	4.08	4.08	4.04	4.11	4.06	4.05	4.03	4.06	4.11
H	19.83	19.75	19.73	19.71	19.73	19.69	19.74	19.74	19.68	19.68	19.71	19.69
TOTAL	0.50	0.49	0.49	0.50	0.49	0.48	0.48	0.49	0.50	0.50	0.50	0.49
X _{Fe}												

Biotite composition from samples 216533, 219742 219749. (cont)

	742_bt_5											
Wt%	35.76	35.50	35.85	35.76	35.77	35.90	35.67	35.70	35.48	28.77	32.55	32.91
SiO ₂	1.24	1.32	1.48	1.35	1.26	1.26	1.19	1.37	1.49	0.64	0.81	1.07
TiO ₂	19.05	19.14	19.17	19.17	19.52	19.59	19.50	19.30	18.94	20.29	19.78	19.24
Al ₂ O ₃	0.03	0.03	0.03	0.02	0.02	0.02	0.03	0.02	0.02	0.03	0.03	0.04
Cr ₂ O ₃	19.31	18.77	18.45	18.41	18.27	18.60	17.80	18.35	18.29	21.67	20.28	20.54
FeO	0.42	0.44	0.32	0.36	0.38	0.32	0.34	0.22	0.32	1.23	0.51	0.50
MnO	10.95	10.92	10.89	10.85	11.03	11.06	10.95	11.15	11.50	12.92	12.94	12.50
MgO	0.00	0.01	0.00	0.00	0.00	0.00	0.01	0.00	0.00	0.03	0.01	0.01
CaO	0.24	0.24	0.20	0.23	0.21	0.19	0.21	0.25	0.18	0.04	0.14	0.16
Na ₂ O	9.23	9.03	9.56	9.25	9.62	9.45	9.15	9.06	9.18	3.64	6.42	7.01
K ₂ O	3.98	3.99	3.99	4.00	3.99	4.00	4.02	4.01	4.00	3.99	4.00	3.98
H ₂ O	100.21	99.40	99.95	99.41	100.07	100.39	98.87	99.44	99.40	93.24	97.46	97.95
TOTAL	24	24	24	24	24	24	24	24	24	24	24	24
Oxygen	5.39	5.37	5.40	5.40	5.38	5.38	5.40	5.38	5.36	4.65	5.02	5.08
Si	0.14	0.15	0.17	0.15	0.14	0.14	0.14	0.16	0.17	0.08	0.09	0.12
Ti	3.38	3.42	3.40	3.41	3.46	3.46	3.48	3.43	3.37	3.87	3.60	3.50
Al	0.00	0.00	0.00	0.00	0.00	0.00	0.00	0.00	0.00	0.00	0.00	0.00
Cr	2.43	2.38	2.32	2.33	2.30	2.33	2.25	2.31	2.31	2.93	2.62	2.65
Fe	0.05	0.06	0.04	0.05	0.05	0.04	0.04	0.03	0.04	0.17	0.07	0.07
Mn	2.46	2.47	2.45	2.44	2.47	2.47	2.47	2.51	2.59	3.11	2.98	2.87
Mg	0.00	0.00	0.00	0.00	0.00	0.00	0.00	0.00	0.00	0.00	0.00	0.00
Ca	0.07	0.07	0.06	0.07	0.06	0.06	0.06	0.07	0.05	0.01	0.04	0.05
Na	1.77	1.74	1.84	1.78	1.84	1.81	1.77	1.74	1.77	0.75	1.26	1.38
K	4.00	4.03	4.01	4.03	4.00	3.99	4.05	4.03	4.03	4.30	4.11	4.09
H	19.70	19.69	19.68	19.67	19.71	19.68	19.67	19.67	19.71	19.87	19.79	19.81
TOTAL	0.50	0.49	0.49	0.49	0.48	0.49	0.48	0.48	0.47	0.48	0.47	0.48
X _{Fe}												

Biotite composition from samples 216533, 219742 219749. (cont)

		749_bt_1																	
Wt%		33.90	34.96	33.36	34.65	35.03	35.14	35.58	35.45	35.35	34.97	33.93	35.05	34.66	34.78	35.31	35.21	34.32	35.19
SiO2		2.11	2.20	2.15	2.23	2.37	2.28	2.28	2.20	2.14	2.37	2.38	2.26	2.32	2.61	2.22	2.43	2.32	2.23
TiO2		18.69	19.79	19.13	18.83	19.51	19.04	19.96	19.21	19.46	18.98	18.23	19.66	18.98	19.80	20.12	19.39	18.87	19.86
Al2O3		0.04	0.04	0.05	0.05	0.05	0.04	0.04	0.03	0.04	0.04	0.03	0.04	0.05	0.05	0.03	0.05	0.05	0.05
Cr2O3		21.49	21.31	21.64	21.94	21.73	21.45	21.54	21.66	21.59	21.69	21.69	21.54	21.22	21.57	20.99	21.57	21.29	21.44
FeO		0.17	0.19	0.17	0.22	0.21	0.31	0.17	0.24	0.28	0.20	0.27	0.17	0.18	0.26	0.22	0.04	0.19	0.23
MnO		7.14	7.65	7.08	7.31	7.76	7.51	8.14	7.59	7.91	7.57	7.00	7.73	7.56	7.74	7.92	7.74	7.16	8.08
MgO		0.01	0.02	0.02	0.01	0.01	0.02	0.00	0.00	0.01	0.00	0.00	0.01	0.02	0.01	0.01	0.01	0.01	0.00
CaO		0.07	0.11	0.14	0.10	0.14	0.12	0.12	0.10	0.08	0.09	0.07	0.08	0.11	0.06	0.07	0.16	0.10	0.12
Na2O		9.86	9.83	9.64	9.85	9.86	9.67	9.58	9.82	9.66	9.90	9.78	9.79	9.81	9.80	9.62	9.92	9.74	9.71
K2O		3.91	3.93	3.91	3.91	3.92	3.93	3.94	3.93	3.93	3.92	3.91	3.93	3.93	3.93	3.95	3.93	3.92	3.94
H2O		97.39	100.04	97.29	99.09	100.59	99.49	101.26	100.24	100.45	99.74	97.30	100.25	98.85	100.62	100.45	100.45	97.99	100.84
TOTAL																			
Oxygen		24	24	24	24	24	24	24	24	24	24	24	24	24	24	24	24	24	24
Si		5.34	5.34	5.27	5.37	5.33	5.40	5.35	5.41	5.38	5.37	5.36	5.34	5.36	5.29	5.35	5.36	5.36	5.33
Ti		0.25	0.25	0.25	0.26	0.27	0.26	0.26	0.25	0.24	0.27	0.28	0.26	0.27	0.30	0.25	0.28	0.27	0.25
Al		3.47	3.56	3.56	3.44	3.50	3.45	3.54	3.45	3.49	3.44	3.40	3.53	3.46	3.55	3.59	3.48	3.48	3.54
Cr		0.00	0.00	0.01	0.01	0.01	0.01	0.01	0.00	0.00	0.01	0.00	0.01	0.01	0.01	0.00	0.01	0.01	0.01
Fe		2.83	2.72	2.86	2.84	2.77	2.76	2.70	2.76	2.75	2.79	2.87	2.75	2.75	2.74	2.66	2.75	2.78	2.71
Mn		0.02	0.02	0.02	0.03	0.03	0.04	0.02	0.03	0.04	0.03	0.04	0.02	0.02	0.03	0.03	0.01	0.02	0.03
Mg		1.68	1.74	1.67	1.69	1.76	1.72	1.83	1.73	1.79	1.73	1.65	1.76	1.74	1.75	1.79	1.76	1.67	1.82
Ca		0.00	0.00	0.00	0.00	0.00	0.00	0.00	0.00	0.00	0.00	0.00	0.00	0.00	0.00	0.00	0.00	0.00	0.00
Na		0.02	0.03	0.04	0.03	0.04	0.04	0.03	0.03	0.02	0.03	0.02	0.02	0.03	0.02	0.02	0.05	0.03	0.04
K		1.98	1.91	1.94	1.95	1.92	1.89	1.84	1.91	1.87	1.94	1.97	1.90	1.94	1.90	1.86	1.93	1.94	1.88
H		4.12	4.01	4.12	4.04	3.98	4.03	3.96	4.00	3.99	4.02	4.12	4.00	4.05	3.98	3.99	3.99	4.09	3.97
TOTAL		19.73	19.60	19.75	19.66	19.61	19.59	19.53	19.58	19.58	19.62	19.71	19.59	19.64	19.58	19.54	19.60	19.66	19.59
X _{Fe}		0.63	0.61	0.63	0.63	0.61	0.62	0.60	0.62	0.60	0.62	0.63	0.61	0.61	0.61	0.60	0.61	0.63	0.60

Biotite composition from samples 216533, 219742 219749. (cont)

		749_bt_2																																				
Wt%		34.96	35.28	34.97	34.86	34.91	35.50	34.58	35.00	35.05	35.35	35.45	34.88	35.22	34.79	34.58	35.00	34.77	34.66	34.96	35.28	34.97	34.86	34.91	35.50	34.58	35.00	35.05	35.35	35.45	34.88	35.22	34.79	34.58	35.00	34.77	34.66	
SiO2		2.32	2.32	2.35	2.57	2.30	2.32	2.21	2.05	2.11	2.31	2.23	1.98	2.09	2.14	2.35	2.02	2.48	2.24	2.32	2.32	2.35	2.57	2.30	2.32	2.21	2.05	2.11	2.31	2.23	1.98	2.09	2.14	2.35	2.02	2.48	2.24	
TiO2		19.71	19.47	19.53	19.22	19.38	19.73	19.37	19.75	19.77	19.90	19.87	19.66	19.59	19.46	19.50	19.69	19.42	19.27	19.71	19.47	19.53	19.22	19.38	19.73	19.37	19.75	19.77	19.90	19.87	19.66	19.59	19.46	19.50	19.69	19.42	19.27	
Al2O3		0.03	0.03	0.02	0.03	0.02	0.03	0.01	0.04	0.03	0.04	0.03	0.03	0.04	0.03	0.02	0.03	0.01	0.04	0.03	0.03	0.02	0.03	0.02	0.03	0.01	0.04	0.03	0.04	0.03	0.02	0.03	0.01	0.04	0.01	0.04		
Cr2O3		22.16	22.14	21.99	22.04	21.79	21.73	21.58	21.29	21.83	21.63	21.40	21.52	21.84	21.72	21.73	21.97	21.61	22.03	22.16	22.14	21.99	22.04	21.79	21.73	21.58	21.29	21.83	21.63	21.40	21.52	21.84	21.72	21.73	21.97	21.61	22.03	
FeO		0.15	0.21	0.23	0.21	0.20	0.21	0.19	0.12	0.20	0.13	0.20	0.20	0.21	0.35	0.34	0.16	0.17	0.21	0.15	0.21	0.23	0.21	0.20	0.21	0.19	0.12	0.20	0.13	0.20	0.20	0.21	0.35	0.34	0.16	0.17	0.21	
MnO		7.85	8.07	7.98	7.87	7.99	7.92	7.76	7.92	7.92	7.74	7.88	7.04	7.98	7.86	7.88	7.85	7.96	7.89	7.85	8.07	7.98	7.87	7.99	7.92	7.76	7.92	7.92	7.74	7.88	7.04	7.98	7.86	7.88	7.85	7.96	7.89	
MgO		0.00	0.01	0.01	0.01	0.01	0.02	0.01	0.00	0.02	0.01	0.02	0.01	0.01	0.00	0.00	0.01	0.04	0.00	0.00	0.01	0.01	0.01	0.01	0.02	0.01	0.00	0.02	0.01	0.02	0.01	0.00	0.00	0.01	0.04	0.00		
CaO		0.10	0.08	0.13	0.09	0.12	0.13	0.09	0.12	0.16	0.13	0.16	0.06	0.15	0.16	0.18	0.11	0.10	0.15	0.10	0.08	0.13	0.09	0.12	0.13	0.09	0.12	0.16	0.13	0.16	0.06	0.15	0.16	0.18	0.11	0.10	0.15	
Na2O		9.99	9.65	9.71	10.00	9.64	10.02	10.05	10.16	9.71	9.79	9.95	9.58	9.56	9.62	9.73	9.95	9.56	9.68	9.99	9.65	9.71	10.00	9.64	10.02	10.05	10.16	9.71	9.79	9.95	9.58	9.56	9.62	9.73	9.95	9.56	9.68	
K2O		3.91	3.92	3.92	3.91	3.93	3.93	3.92	3.93	3.93	3.93	3.93	3.94	3.93	3.92	3.92	3.92	3.92	3.92	3.91	3.92	3.92	3.91	3.93	3.93	3.92	3.93	3.93	3.93	3.93	3.92	3.92	3.92	3.92	3.92	3.92	3.92	3.92
H2O		101.19	101.18	100.85	100.80	100.29	101.53	99.77	100.38	100.71	100.95	101.11	98.88	100.61	100.05	100.22	100.71	100.06	100.08	101.19	101.18	100.85	100.80	100.29	101.53	99.77	100.38	100.71	100.95	101.11	98.88	100.61	100.05	100.22	100.71	100.06	100.08	
TOTAL		24	24	24	24	24	24	24	24	24	24	24	24	24	24	24	24	24	24	24	24	24	24	24	24	24	24	24	24	24	24	24	24	24	24	24	24	
Oxygen		5.30	5.34	5.31	5.31	5.33	5.35	5.32	5.33	5.33	5.35	5.36	5.38	5.35	5.33	5.29	5.33	5.31	5.31	5.30	5.34	5.31	5.31	5.33	5.35	5.32	5.33	5.33	5.35	5.36	5.38	5.35	5.33	5.29	5.33	5.31	5.31	
Si		0.26	0.26	0.27	0.29	0.26	0.26	0.26	0.23	0.24	0.26	0.25	0.23	0.24	0.25	0.27	0.23	0.29	0.26	0.26	0.26	0.27	0.29	0.26	0.26	0.26	0.23	0.24	0.26	0.25	0.23	0.24	0.25	0.27	0.23	0.29	0.26	
Ti		3.53	3.47	3.50	3.45	3.49	3.51	3.51	3.55	3.54	3.55	3.54	3.58	3.51	3.51	3.52	3.53	3.50	3.48	3.53	3.47	3.50	3.45	3.49	3.51	3.51	3.55	3.54	3.55	3.54	3.58	3.51	3.51	3.52	3.53	3.50	3.48	
Al		0.00	0.00	0.00	0.00	0.00	0.00	0.00	0.00	0.00	0.00	0.00	0.00	0.00	0.00	0.00	0.00	0.00	0.00	0.00	0.00	0.00	0.00	0.00	0.00	0.00	0.00	0.00	0.00	0.00	0.00	0.00	0.00	0.00	0.00	0.00	0.00	
Cr		2.81	2.80	2.79	2.81	2.78	2.74	2.77	2.71	2.77	2.74	2.70	2.78	2.78	2.78	2.78	2.80	2.76	2.82	2.81	2.80	2.79	2.81	2.78	2.74	2.77	2.71	2.77	2.74	2.70	2.78	2.78	2.78	2.80	2.76	2.82		
Fe		0.02	0.03	0.03	0.03	0.03	0.03	0.02	0.02	0.03	0.02	0.03	0.03	0.03	0.03	0.04	0.02	0.03	0.03	0.02	0.03	0.03	0.03	0.03	0.03	0.02	0.02	0.03	0.02	0.03	0.03	0.03	0.04	0.02	0.03	0.03		
Mn		1.78	1.82	1.81	1.79	1.82	1.78	1.78	1.80	1.79	1.75	1.77	1.62	1.81	1.79	1.80	1.78	1.81	1.80	1.78	1.82	1.81	1.79	1.82	1.78	1.78	1.80	1.79	1.75	1.77	1.62	1.81	1.79	1.80	1.78	1.81	1.80	
Mg		0.00	0.00	0.00	0.00	0.00	0.00	0.00	0.00	0.00	0.00	0.00	0.00	0.00	0.00	0.00	0.00	0.01	0.00	0.00	0.00	0.00	0.00	0.00	0.00	0.00	0.00	0.00	0.00	0.00	0.00	0.00	0.00	0.00	0.01	0.00		
Ca		0.03	0.02	0.04	0.03	0.04	0.04	0.03	0.04	0.05	0.04	0.05	0.02	0.04	0.05	0.05	0.03	0.03	0.05	0.03	0.02	0.04	0.03	0.04	0.04	0.03	0.04	0.05	0.04	0.05	0.02	0.04	0.05	0.05	0.03	0.03	0.05	
Na		1.93	1.86	1.88	1.94	1.88	1.93	1.97	1.98	1.88	1.89	1.92	1.89	1.85	1.88	1.90	1.93	1.86	1.89	1.93	1.86	1.88	1.94	1.88	1.93	1.97	1.98	1.88	1.89	1.92	1.89	1.85	1.88	1.90	1.93	1.86	1.89	
K		3.96	3.96	3.97	3.98	4.00	3.95	4.02	3.99	3.98	3.97	3.96	4.05	3.98	4.01	4.00	3.98	4.01	4.00	3.96	3.96	3.97	3.98	4.00	3.95	4.02	3.99	3.98	3.97	3.96	4.05	3.98	4.01	4.00	3.98	4.01	4.00	
H		19.63	19.58	19.61	19.64	19.62	19.59	19.68	19.66	19.62	19.56	19.58	19.57	19.59	19.64	19.65	19.64	19.60	19.66	19.63	19.58	19.61	19.64	19.62	19.59	19.68	19.66	19.62	19.56	19.58	19.57	19.59	19.64	19.65	19.64	19.60	19.66	
TOTAL		0.61	0.61	0.61	0.61	0.60	0.61	0.61	0.60	0.61	0.61	0.60	0.63	0.61	0.61	0.61	0.61	0.60	0.61	0.61	0.61	0.61	0.61	0.60	0.61	0.61	0.60	0.61	0.61	0.60	0.63	0.61	0.61	0.61	0.60	0.61	0.61	
X _{Fe}																																						

Biotite composition from samples 216533, 219742 219749. (cont)

Wt%	749_bt_3									
SiO ₂	35.47	35.47	35.20	35.46	35.53	35.31	35.34	35.45	35.42	35.21
TiO ₂	1.91	1.84	2.01	2.20	2.06	2.09	2.06	2.02	2.00	1.92
Al ₂ O ₃	20.34	20.19	20.13	19.96	20.06	19.88	19.79	20.09	19.99	19.97
Cr ₂ O ₃	0.05	0.04	0.03	0.03	0.04	0.03	0.04	0.04	0.04	0.05
FeO	19.99	19.99	19.80	19.99	19.75	20.07	19.85	20.08	19.88	19.78
MnO	0.30	0.24	0.31	0.33	0.31	0.26	0.25	0.16	0.29	0.19
MgO	9.36	9.30	9.30	9.30	9.36	9.37	9.17	9.06	9.35	8.94
CaO	0.00	0.01	0.01	0.01	0.00	0.01	0.00	0.01	0.01	0.01
Na ₂ O	0.08	0.14	0.13	0.13	0.12	0.08	0.11	0.13	0.09	0.10
K ₂ O	9.84	9.77	9.77	9.70	9.78	9.92	9.92	9.97	9.87	9.60
H ₂ O	3.96	3.96	3.96	3.96	3.97	3.96	3.96	3.96	3.96	3.97
TOTAL	101.30	100.95	100.66	101.08	100.97	100.98	100.49	100.97	100.89	99.74
Oxygen	24	24	24	24	24	24	24	24	24	24
Si	5.31	5.33	5.30	5.32	5.33	5.31	5.34	5.33	5.33	5.34
Ti	0.22	0.21	0.23	0.25	0.23	0.24	0.23	0.23	0.23	0.22
Al	3.59	3.57	3.57	3.53	3.55	3.53	3.52	3.56	3.54	3.57
Cr	0.01	0.00	0.00	0.00	0.00	0.00	0.00	0.00	0.00	0.01
Fe	2.50	2.51	2.49	2.51	2.48	2.53	2.51	2.52	2.50	2.51
Mn	0.04	0.03	0.04	0.04	0.04	0.03	0.03	0.02	0.04	0.02
Mg	2.09	2.08	2.09	2.08	2.09	2.10	2.06	2.03	2.09	2.02
Ca	0.00	0.00	0.00	0.00	0.00	0.00	0.00	0.00	0.00	0.00
Na	0.02	0.04	0.04	0.04	0.03	0.02	0.03	0.04	0.03	0.03
K	1.88	1.87	1.88	1.86	1.87	1.90	1.91	1.91	1.89	1.86
H	3.96	3.97	3.98	3.97	3.97	3.97	3.99	3.97	3.97	4.02
TOTAL	19.61	19.62	19.63	19.59	19.60	19.64	19.63	19.62	19.62	19.60
X _{Fe}	0.55	0.55	0.54	0.55	0.54	0.55	0.55	0.55	0.54	0.55

Biotite composition from samples 216533, 219742 219749. (cont)

		749_bt_5																																							
Wt%		34.78	35.38	35.17	35.43	35.03	35.23	35.05	34.90	34.46	34.88	34.98	34.98	34.62	35.00	35.20	35.34	35.51	34.88	35.01	34.78	35.38	35.17	35.43	35.03	35.23	35.05	34.90	34.46	34.88	34.98	34.98	34.62	35.00	35.20	35.34	35.51	34.88	35.01		
SiO2		1.93	1.96	2.11	2.23	2.04	2.20	1.97	2.08	2.21	2.37	2.11	2.13	2.02	2.12	1.99	1.76	1.95	1.92	1.73	1.93	1.96	2.11	2.23	2.04	2.20	1.97	2.08	2.21	2.37	2.11	2.13	2.02	2.12	1.99	1.76	1.95	1.92	1.73		
TiO2		19.65	20.01	19.89	19.70	19.90	19.98	19.91	19.65	19.43	19.68	19.65	19.65	19.72	19.89	20.18	19.90	20.03	19.98	19.94	19.65	20.01	19.89	19.70	19.90	19.98	19.91	19.65	19.43	19.68	19.65	19.65	19.72	19.89	20.18	19.90	20.03	19.98	19.94		
Al2O3		0.02	0.03	0.03	0.02	0.02	0.03	0.03	0.04	0.01	0.02	0.01	0.02	0.01	0.02	0.02	0.02	0.02	0.03	0.03	0.02	0.03	0.03	0.02	0.02	0.03	0.03	0.04	0.01	0.02	0.01	0.02	0.02	0.02	0.02	0.02	0.03	0.03	0.03		
Cr2O3		21.24	21.05	21.20	21.32	20.91	20.93	21.14	21.04	21.31	21.35	21.02	21.44	21.16	21.21	21.05	21.13	20.87	21.15	20.93	21.24	21.05	21.20	21.32	20.91	20.93	21.14	21.04	21.31	21.35	21.02	21.44	21.16	21.21	21.05	21.13	20.87	21.15	20.93		
FeO		0.23	0.31	0.24	0.32	0.23	0.34	0.23	0.29	0.24	0.30	0.25	0.22	0.21	0.17	0.30	0.20	0.20	0.30	0.26	0.23	0.31	0.24	0.32	0.23	0.34	0.23	0.29	0.24	0.30	0.25	0.22	0.21	0.17	0.30	0.20	0.20	0.30	0.26		
MnO		8.80	8.81	8.97	8.65	8.69	8.77	8.79	8.90	8.72	8.80	8.99	8.88	8.76	8.82	9.06	8.84	8.90	8.93	8.82	8.80	8.81	8.97	8.65	8.69	8.77	8.79	8.90	8.72	8.80	8.99	8.88	8.76	8.82	9.06	8.84	8.90	8.93	8.82		
MgO		0.00	0.00	0.01	0.00	0.01	0.00	0.00	0.00	0.02	0.00	0.00	0.00	0.01	0.00	0.00	0.00	0.01	0.01	0.00	0.00	0.00	0.01	0.00	0.01	0.00	0.00	0.00	0.02	0.00	0.00	0.00	0.00	0.00	0.00	0.01	0.01	0.00			
CaO		0.10	0.08	0.08	0.07	0.09	0.11	0.07	0.06	0.12	0.08	0.08	0.10	0.07	0.11	0.16	0.07	0.07	0.14	0.10	0.10	0.08	0.08	0.07	0.09	0.11	0.07	0.06	0.12	0.08	0.08	0.10	0.07	0.11	0.16	0.07	0.07	0.14	0.10		
Na2O		10.15	9.87	9.84	10.05	10.07	9.75	9.76	9.90	9.63	9.78	9.98	9.80	10.14	10.03	9.88	9.89	9.91	10.11	9.83	10.15	9.87	9.84	10.05	10.07	9.75	9.76	9.90	9.63	9.78	9.98	9.80	10.14	10.03	9.88	9.89	9.91	10.11	9.83		
K2O		3.92	3.94	3.93	3.93	3.93	3.94	3.94	3.93	3.93	3.93	3.93	3.93	3.92	3.93	3.94	3.94	3.95	3.93	3.94	3.92	3.94	3.93	3.93	3.93	3.94	3.94	3.93	3.93	3.93	3.93	3.92	3.93	3.94	3.94	3.94	3.95	3.93	3.94		
H2O		100.83	101.43	101.49	101.72	100.92	101.27	100.88	100.79	100.06	101.19	101.13	101.14	100.64	101.29	101.79	101.08	101.42	101.38	100.59	100.83	101.43	101.49	101.72	100.92	101.27	100.88	100.79	100.06	101.19	101.13	101.14	100.64	101.29	101.79	101.08	101.42	101.38	100.59		
TOTAL		24	24	24	24	24	24	24	24	24	24	24	24	24	24	24	24	24	24	24	24	24	24	24	24	24	24	24	24	24	24	24	24	24	24	24	24	24	24	24	
Oxygen		5.28	5.32	5.29	5.33	5.30	5.30	5.30	5.29	5.27	5.27	5.28	5.29	5.27	5.28	5.28	5.33	5.33	5.27	5.31	5.28	5.32	5.29	5.33	5.30	5.30	5.30	5.29	5.27	5.27	5.28	5.28	5.33	5.33	5.27	5.28	5.28	5.33	5.33	5.27	5.31
Si		0.22	0.22	0.24	0.25	0.23	0.25	0.22	0.24	0.25	0.27	0.24	0.24	0.23	0.24	0.22	0.20	0.22	0.22	0.20	0.22	0.22	0.24	0.25	0.23	0.25	0.22	0.24	0.25	0.27	0.24	0.24	0.22	0.22	0.20	0.22	0.22	0.22	0.20	0.20	
Ti		3.52	3.55	3.53	3.49	3.55	3.54	3.55	3.51	3.50	3.51	3.53	3.50	3.54	3.54	3.57	3.54	3.54	3.56	3.56	3.52	3.55	3.53	3.49	3.55	3.54	3.55	3.51	3.50	3.51	3.53	3.50	3.54	3.54	3.57	3.54	3.54	3.56	3.56	3.56	
Al		0.00	0.00	0.00	0.00	0.00	0.00	0.00	0.00	0.00	0.00	0.00	0.00	0.00	0.00	0.00	0.00	0.00	0.00	0.00	0.00	0.00	0.00	0.00	0.00	0.00	0.00	0.00	0.00	0.00	0.00	0.00	0.00	0.00	0.00	0.00	0.00	0.00	0.00	0.00	
Cr		2.70	2.65	2.67	2.68	2.65	2.63	2.67	2.67	2.72	2.70	2.66	2.71	2.69	2.68	2.64	2.67	2.62	2.67	2.65	2.70	2.65	2.67	2.68	2.65	2.63	2.67	2.67	2.72	2.70	2.66	2.71	2.69	2.68	2.64	2.67	2.62	2.67	2.65	2.65	
Fe		0.03	0.04	0.03	0.04	0.03	0.04	0.03	0.04	0.03	0.04	0.03	0.03	0.03	0.02	0.04	0.03	0.03	0.04	0.03	0.03	0.04	0.03	0.04	0.03	0.04	0.03	0.04	0.03	0.04	0.03	0.03	0.02	0.04	0.03	0.03	0.04	0.03	0.03	0.03	
Mn		1.99	1.97	2.01	1.94	1.96	1.97	1.98	2.01	1.99	1.98	2.02	2.00	1.99	1.98	2.03	1.99	1.99	2.01	1.99	1.99	1.97	2.01	1.94	1.96	1.97	1.98	2.01	1.99	1.98	2.02	2.00	1.99	1.98	2.03	1.99	1.99	2.01	1.99		
Mg		0.00	0.00	0.00	0.00	0.00	0.00	0.00	0.00	0.00	0.00	0.00	0.00	0.00	0.00	0.00	0.00	0.00	0.00	0.00	0.00	0.00	0.00	0.00	0.00	0.00	0.00	0.00	0.00	0.00	0.00	0.00	0.00	0.00	0.00	0.00	0.00	0.00	0.00	0.00	
Ca		0.03	0.02	0.02	0.02	0.03	0.03	0.02	0.02	0.03	0.02	0.02	0.03	0.02	0.02	0.05	0.02	0.02	0.04	0.03	0.03	0.02	0.02	0.02	0.03	0.03	0.02	0.02	0.03	0.02	0.02	0.03	0.02	0.02	0.05	0.02	0.02	0.04	0.03		
Na		1.97	1.89	1.89	1.93	1.94	1.87	1.88	1.91	1.88	1.89	1.92	1.89	1.97	1.93	1.89	1.90	1.90	1.95	1.90	1.97	1.89	1.89	1.93	1.94	1.87	1.88	1.91	1.88	1.89	1.92	1.89	1.93	1.89	1.90	1.90	1.95	1.90	1.90		
K		3.97	3.95	3.95	3.94	3.97	3.96	3.97	3.98	4.01	3.96	3.96	3.96	3.98	3.96	3.94	3.96	3.95	3.95	3.98	3.97	3.95	3.95	3.94	3.97	3.96	3.97	3.98	4.01	3.96	3.96	3.96	3.98	3.96	3.94	3.96	3.95	3.95	3.98	3.98	
H		19.72	19.62	19.64	19.62	19.66	19.60	19.64	19.67	19.69	19.64	19.67	19.66	19.72	19.67	19.65	19.64	19.61	19.71	19.67	19.72	19.62	19.64	19.62	19.66	19.60	19.64	19.67	19.69	19.64	19.67	19.66	19.72	19.67	19.65	19.64	19.61	19.71	19.67	19.67	
TOTAL		0.58	0.57	0.57	0.58	0.57	0.57	0.57	0.57	0.58	0.58	0.57	0.58	0.58	0.57	0.57	0.57	0.57	0.57	0.57	0.58	0.57	0.57	0.58	0.57	0.57	0.57	0.57	0.58	0.58	0.57	0.57	0.57	0.57	0.57	0.57	0.57	0.57	0.57	0.57	
X _{Fe}																																									

Biotite composition from samples 216533, 219742 219749. (cont)

		533_bt_1															
Wt%		35.57	35.26	35.25	35.12	35.19	35.17	34.81	35.34	35.15	34.95	35.01	35.28	35.31	35.12	35.21	
SiO ₂		1.70	1.66	1.59	1.76	1.68	1.68	1.67	1.66	1.68	1.67	1.80	1.75	1.82	1.74	1.77	
TiO ₂		16.79	16.53	16.49	16.45	16.67	16.93	16.15	16.89	16.16	16.28	16.30	16.13	16.06	15.95	16.09	
Al ₂ O ₃		0.02	0.03	0.02	0.01	0.03	0.04	0.01	0.03	0.03	0.02	0.01	0.03	0.03	0.04	0.05	
Cr ₂ O ₃		22.04	22.30	22.73	22.08	22.49	22.33	22.48	22.54	22.09	23.02	21.72	22.51	22.35	22.20	22.27	
FeO		0.37	0.33	0.32	0.37	0.34	0.35	0.33	0.42	0.40	0.45	0.37	0.41	0.32	0.31	0.20	
MnO		8.88	8.70	8.65	8.55	8.58	8.66	8.41	8.60	8.62	8.55	8.65	8.54	8.59	8.54	8.59	
MgO		0.02	0.00	0.01	0.01	0.01	0.02	0.03	0.02	0.01	0.03	0.01	0.00	0.01	0.01	0.02	
CaO		0.06	0.11	0.11	0.09	0.12	0.09	0.11	0.10	0.09	0.09	0.16	0.04	0.06	0.14	0.08	
Na ₂ O		9.91	9.79	9.99	9.76	9.83	9.61	9.39	9.56	9.67	9.65	9.84	9.76	9.77	9.75	9.81	
K ₂ O		3.90	3.90	3.88	3.90	3.89	3.90	3.90	3.90	3.90	3.88	3.90	3.89	3.90	3.90	3.90	
H ₂ O		99.27	98.61	99.04	98.10	98.83	98.78	97.30	99.05	97.80	98.59	97.77	98.33	98.23	97.69	97.99	
TOTAL		24	24	24	24	24	24	24	24	24	24	24	24	24	24	24	
Oxygen		5.52	5.51	5.50	5.52	5.50	5.48	5.52	5.50	5.54	5.49	5.51	5.54	5.54	5.54	5.54	
Si		0.20	0.19	0.19	0.21	0.20	0.20	0.20	0.19	0.20	0.20	0.21	0.21	0.22	0.21	0.21	
Ti		3.07	3.05	3.03	3.04	3.07	3.11	3.02	3.10	3.00	3.01	3.03	2.99	2.97	2.97	2.98	
Al		0.00	0.00	0.00	0.00	0.00	0.01	0.00	0.00	0.00	0.00	0.00	0.00	0.00	0.01	0.01	
Cr		2.86	2.92	2.97	2.90	2.94	2.91	2.98	2.93	2.91	3.02	2.86	2.96	2.94	2.93	2.93	
Fe		0.05	0.04	0.04	0.05	0.04	0.05	0.04	0.06	0.05	0.06	0.05	0.05	0.04	0.04	0.03	
Mn		2.05	2.03	2.01	2.00	2.00	2.01	1.99	1.99	2.02	2.00	2.03	2.00	2.01	2.01	2.01	
Mg		0.00	0.00	0.00	0.00	0.00	0.00	0.01	0.00	0.00	0.00	0.00	0.00	0.00	0.00	0.00	
Ca		0.02	0.03	0.03	0.03	0.04	0.03	0.04	0.03	0.03	0.03	0.05	0.01	0.02	0.04	0.03	
Na		1.96	1.95	1.99	1.95	1.96	1.91	1.90	1.90	1.94	1.93	1.98	1.95	1.96	1.96	1.97	
K		4.04	4.06	4.05	4.09	4.06	4.06	4.12	4.05	4.10	4.07	4.10	4.08	4.08	4.10	4.09	
H		19.76	19.79	19.82	19.79	19.80	19.76	19.80	19.75	19.80	19.82	19.82	19.78	19.78	19.82	19.80	
TOTAL		0.58	0.59	0.60	0.59	0.60	0.59	0.60	0.60	0.59	0.60	0.58	0.60	0.59	0.59	0.59	
X _{Fe}																	

Biotite composition from samples 216533, 219742 219749. (cont)

Wt%	533_bt_2												533_bt_3											
	35.05	35.18	35.09	35.20	35.06	35.12	35.31	35.20	35.12	34.59	35.09	34.95	35.06	35.06	34.36	34.93	34.81	35.02	35.00	35.06				
SiO2	1.60	1.69	1.68	1.75	1.70	1.57	1.63	1.74	1.79	1.57	2.04	1.92	1.91	1.90	1.94	1.97	1.75	1.76	1.79	1.87				
TiO2	15.92	16.68	16.23	16.74	16.56	16.36	16.61	16.46	16.81	17.12	16.02	16.20	16.31	15.95	16.10	16.30	16.56	16.48	16.58	16.75				
Al2O3	0.02	0.01	0.01	0.02	0.04	0.02	0.04	0.01	0.01	0.01	0.03	0.03	0.04	0.02	0.03	0.01	0.03	0.02	0.01	0.01				
Cr2O3	22.75	22.06	22.30	22.46	22.46	22.45	22.50	22.38	22.75	22.93	22.52	22.68	22.87	22.18	23.00	22.60	22.35	22.60	22.45	22.48				
FeO	0.41	0.20	0.20	0.26	0.48	0.33	0.37	0.54	0.34	0.41	0.45	0.29	0.31	0.42	0.47	0.36	0.52	0.28	0.43	0.39				
MnO	8.91	8.80	8.71	8.54	8.70	8.68	8.72	8.60	8.52	8.86	8.54	8.41	8.45	8.55	8.94	8.56	8.34	8.48	8.56	8.36				
MgO	0.05	0.01	0.02	0.01	0.00	0.06	0.04	0.02	0.03	0.03	0.01	0.02	0.02	0.02	0.02	0.03	0.03	0.02	0.02	0.03				
CaO	0.05	0.06	0.06	0.16	0.07	0.07	0.05	0.11	0.12	0.07	0.06	0.09	0.07	0.06	0.09	0.14	0.08	0.10	0.10	0.10				
Na2O	9.24	9.81	9.84	9.77	9.55	9.36	9.56	10.00	9.96	9.42	9.84	9.80	9.76	9.64	9.13	9.79	9.83	9.64	9.70	9.97				
K2O	3.90	3.90	3.90	3.90	3.90	3.90	3.90	3.89	3.88	3.89	3.89	3.89	3.88	3.90	3.88	3.89	3.89	3.89	3.89	3.89				
H2O	97.90	98.42	98.03	98.80	98.53	97.93	98.74	98.94	99.32	98.90	98.50	98.26	98.68	97.70	97.95	98.58	98.19	98.28	98.53	98.91				
TOTAL	24	24	24	24	24	24	24	24	24	24	24	24	24	24	24	24	24	24	24	24				
Oxygen	5.52	5.50	5.52	5.49	5.49	5.52	5.51	5.50	5.47	5.40	5.51	5.50	5.50	5.53	5.43	5.48	5.48	5.50	5.48	5.48				
Si	0.19	0.20	0.20	0.21	0.20	0.19	0.19	0.20	0.21	0.18	0.24	0.23	0.22	0.23	0.23	0.23	0.21	0.21	0.21	0.22				
Ti	2.96	3.07	3.01	3.08	3.06	3.03	3.05	3.03	3.09	3.15	2.96	3.00	3.01	2.97	3.00	3.01	3.07	3.05	3.06	3.08				
Al	0.00	0.00	0.00	0.00	0.00	0.00	0.00	0.00	0.00	0.00	0.00	0.00	0.01	0.00	0.00	0.00	0.00	0.00	0.00	0.00				
Cr	3.00	2.88	2.93	2.93	2.94	2.95	2.94	2.93	2.96	3.00	2.96	2.98	3.00	2.93	3.04	2.96	2.94	2.97	2.94	2.94				
Fe	0.05	0.03	0.03	0.03	0.06	0.04	0.05	0.07	0.04	0.05	0.06	0.04	0.04	0.06	0.06	0.05	0.07	0.04	0.06	0.05				
Mn	2.09	2.05	2.04	1.99	2.03	2.04	2.03	2.00	1.98	2.06	2.00	1.97	1.97	2.01	2.11	2.00	1.96	1.98	2.00	1.95				
Mg	0.01	0.00	0.00	0.00	0.00	0.01	0.01	0.00	0.00	0.00	0.00	0.00	0.00	0.00	0.00	0.01	0.01	0.00	0.00	0.01				
Ca	0.01	0.02	0.02	0.05	0.02	0.02	0.02	0.03	0.04	0.02	0.02	0.03	0.02	0.02	0.03	0.04	0.02	0.03	0.03	0.03				
Na	1.86	1.96	1.97	1.94	1.91	1.88	1.90	1.99	1.98	1.88	1.97	1.97	1.95	1.94	1.84	1.96	1.97	1.93	1.94	1.99				
K	4.09	4.07	4.09	4.06	4.07	4.09	4.06	4.05	4.04	4.05	4.07	4.08	4.06	4.10	4.09	4.07	4.08	4.08	4.07	4.05				
H	19.79	19.79	19.82	19.79	19.78	19.77	19.76	19.82	19.80	19.81	19.80	19.81	19.79	19.79	19.82	19.81	19.82	19.79	19.79	19.79				
TOTAL	0.59	0.58	0.59	0.60	0.59	0.59	0.59	0.59	0.60	0.59	0.60	0.60	0.60	0.59	0.59	0.60	0.60	0.60	0.60	0.60				
X _{Fe}																								

Biotite composition from samples 216533, 219742 219749. (cont)

Wt%	533_bt_4										533_bt_5									
	34.87	35.19	34.87	34.76	35.40	35.28	35.30	35.38	35.48	35.15	34.53	34.66	34.49	34.84	34.61	34.45				
SiO2	2.00	1.91	1.91	1.95	2.00	1.84	2.01	1.99	1.96	1.88	1.87	1.85	1.80	1.68	1.77	1.78				
Al2O3	15.89	16.10	15.82	15.71	16.16	16.72	16.07	15.66	15.59	16.00	16.04	15.82	16.06	16.15	16.06	16.10				
Cr2O3	0.02	0.02	0.02	0.04	0.02	0.03	0.01	0.03	0.02	0.02	0.03	0.02	0.02	0.02	0.04	0.02				
FeO	22.66	22.10	22.51	23.17	22.41	22.38	22.31	21.89	21.97	22.16	22.39	22.45	22.31	23.21	22.23	23.09				
MnO	0.59	0.40	0.36	0.35	0.37	0.37	0.51	0.35	0.38	0.32	0.32	0.40	0.45	0.30	0.32	0.35				
MgO	8.18	8.17	8.13	7.93	8.33	8.49	8.40	8.49	8.58	8.43	8.23	8.30	8.32	8.26	8.28	8.07				
CaO	0.03	0.00	0.02	0.01	0.01	0.02	0.02	0.00	0.02	0.01	0.01	0.01	0.01	0.03	0.02	0.02				
Na2O	0.09	0.07	0.09	0.05	0.09	0.08	0.05	0.05	0.07	0.08	0.07	0.08	0.11	0.13	0.07	0.11				
K2O	9.85	9.95	9.74	9.59	9.86	10.12	9.91	9.55	9.63	9.96	9.66	9.57	9.77	9.62	9.83	9.63				
H2O	3.88	3.89	3.89	3.88	3.89	3.89	3.89	3.91	3.90	3.89	3.89	3.89	3.88	3.88	3.89	3.87				
TOTAL	98.06	97.80	97.35	97.44	98.54	99.20	98.47	97.30	97.60	97.89	97.03	97.04	97.22	98.11	97.11	97.50				
Oxygen	24	24	24	24	24	24	24	24	24	24	24	24	24	24	24	24				
Si	5.51	5.55	5.54	5.53	5.54	5.49	5.54	5.59	5.59	5.54	5.50	5.52	5.49	5.50	5.51	5.48				
Ti	0.24	0.23	0.23	0.23	0.24	0.22	0.24	0.24	0.23	0.22	0.22	0.22	0.22	0.20	0.21	0.21				
Al	2.96	2.99	2.96	2.95	2.98	3.07	2.97	2.92	2.90	2.97	3.01	2.97	3.01	3.01	3.01	3.02				
Cr	0.00	0.00	0.00	0.00	0.00	0.00	0.00	0.00	0.00	0.00	0.00	0.00	0.00	0.00	0.00	0.00				
Fe	3.00	2.92	2.99	3.08	2.94	2.91	2.93	2.89	2.90	2.92	2.98	2.99	2.97	3.06	2.96	3.07				
Mn	0.08	0.05	0.05	0.05	0.05	0.05	0.07	0.05	0.05	0.04	0.04	0.05	0.06	0.04	0.04	0.05				
Mg	1.93	1.92	1.92	1.88	1.95	1.97	1.96	2.00	2.02	1.98	1.95	1.97	1.97	1.94	1.96	1.91				
Ca	0.01	0.00	0.00	0.00	0.00	0.00	0.00	0.00	0.00	0.00	0.00	0.00	0.00	0.01	0.00	0.00				
Na	0.03	0.02	0.03	0.02	0.03	0.02	0.01	0.01	0.02	0.02	0.02	0.02	0.03	0.04	0.02	0.04				
K	1.99	2.00	1.97	1.95	1.97	2.01	1.98	1.92	1.94	2.00	1.96	1.94	1.98	1.94	1.99	1.95				
H	4.09	4.10	4.12	4.11	4.07	4.04	4.07	4.12	4.11	4.09	4.13	4.13	4.12	4.08	4.13	4.11				
TOTAL	19.82	19.79	19.81	19.80	19.76	19.79	19.77	19.74	19.76	19.81	19.83	19.82	19.86	19.83	19.85	19.85				
X _{Fe}	0.61	0.60	0.61	0.62	0.60	0.60	0.60	0.59	0.59	0.60	0.60	0.60	0.60	0.61	0.60	0.62				

Biotite composition from samples 216533, 219742 219749. (cont)

Wt%	533_bt_6										533_bt_7 matrix											
	35.31	35.65	35.14	35.09	34.98	34.76	35.15	35.15	35.31	35.65	35.14	35.09	34.98	34.76	35.15	35.31	35.65	35.14	35.09	34.98	34.76	35.15
SiO ₂	1.89	1.71	1.86	1.90	1.79	1.78	1.56	1.89	1.71	1.86	1.90	1.79	1.78	1.56	1.89	1.71	1.86	1.90	1.79	1.78	1.56	1.89
TiO ₂	16.34	16.95	16.01	16.27	16.16	16.11	15.87	16.34	16.95	16.01	16.27	16.16	16.11	15.87	16.34	16.95	16.01	16.27	16.16	16.11	15.87	16.34
Al ₂ O ₃	0.00	0.01	0.00	0.00	0.01	0.02	0.00	0.00	0.01	0.00	0.00	0.01	0.02	0.00	0.00	0.01	0.00	0.00	0.01	0.02	0.00	0.00
Cr ₂ O ₃	21.70	20.94	22.73	22.71	22.56	22.02	22.46	21.70	20.94	22.73	22.71	22.56	22.02	22.46	21.70	20.94	22.73	22.71	22.56	22.02	22.46	21.70
FeO	0.43	0.41	0.38	0.38	0.38	0.63	0.21	0.43	0.41	0.38	0.38	0.38	0.63	0.21	0.43	0.41	0.38	0.38	0.38	0.63	0.21	0.43
MnO	8.77	8.51	8.53	8.45	8.64	8.52	8.60	8.77	8.51	8.53	8.45	8.64	8.52	8.60	8.77	8.51	8.53	8.45	8.64	8.52	8.60	8.77
CaO	0.03	0.02	0.03	0.01	0.01	0.03	0.01	0.03	0.02	0.03	0.01	0.01	0.03	0.01	0.03	0.02	0.03	0.01	0.01	0.03	0.01	0.03
Na ₂ O	0.07	0.02	0.04	0.05	0.02	0.07	0.05	0.07	0.02	0.04	0.05	0.02	0.07	0.05	0.07	0.02	0.04	0.05	0.02	0.07	0.05	0.07
K ₂ O	9.80	9.84	9.85	9.82	9.76	9.72	9.74	9.80	9.84	9.85	9.82	9.76	9.72	9.74	9.80	9.84	9.85	9.82	9.76	9.72	9.74	9.80
H ₂ O	3.91	3.93	3.88	3.89	3.89	3.89	3.89	3.91	3.93	3.88	3.89	3.89	3.89	3.89	3.91	3.93	3.88	3.89	3.89	3.89	3.89	3.89
TOTAL	98.23	97.99	98.46	98.57	98.18	97.55	97.55	98.23	97.99	98.46	98.57	98.18	97.55	97.55	98.23	97.99	98.46	98.57	98.18	97.55	97.55	98.23
Oxygen	24	24	24	24	24	24	24	24	24	24	24	24	24	24	24	24	24	24	24	24	24	24
Si	5.53	5.56	5.52	5.50	5.50	5.50	5.56	5.53	5.56	5.52	5.50	5.50	5.50	5.56	5.53	5.56	5.52	5.50	5.50	5.50	5.56	5.53
Ti	0.22	0.20	0.22	0.22	0.21	0.21	0.19	0.22	0.20	0.22	0.22	0.21	0.21	0.22	0.22	0.20	0.22	0.22	0.21	0.21	0.22	0.22
Al	3.02	3.12	2.96	3.01	3.00	3.01	2.96	3.02	3.12	2.96	3.01	3.00	3.01	2.96	3.02	3.12	2.96	3.01	3.00	3.01	2.96	3.02
Cr	0.00	0.00	0.00	0.00	0.00	0.00	0.00	0.00	0.00	0.00	0.00	0.00	0.00	0.00	0.00	0.00	0.00	0.00	0.00	0.00	0.00	0.00
Fe	2.84	2.73	2.99	2.98	2.97	2.91	2.97	2.84	2.73	2.99	2.98	2.97	2.91	2.97	2.84	2.73	2.99	2.98	2.97	2.91	2.97	2.84
Mn	0.06	0.05	0.05	0.05	0.05	0.08	0.03	0.06	0.05	0.05	0.05	0.05	0.08	0.03	0.06	0.05	0.05	0.05	0.05	0.08	0.03	0.06
Mg	2.05	1.98	2.00	1.98	2.03	2.01	2.03	2.05	1.98	2.00	1.98	2.03	2.01	2.03	2.05	1.98	2.00	1.98	2.03	2.01	2.03	2.05
Ca	0.00	0.00	0.00	0.00	0.00	0.01	0.00	0.00	0.00	0.00	0.00	0.00	0.01	0.00	0.00	0.00	0.00	0.00	0.00	0.01	0.00	0.00
Na	0.02	0.01	0.01	0.02	0.01	0.02	0.02	0.02	0.01	0.01	0.02	0.01	0.02	0.02	0.02	0.01	0.01	0.02	0.01	0.02	0.02	0.02
K	1.96	1.96	1.98	1.96	1.96	1.96	1.97	1.96	1.96	1.98	1.96	1.96	1.96	1.97	1.96	1.96	1.98	1.96	1.96	1.96	1.97	1.96
H	4.08	4.09	4.07	4.07	4.08	4.11	4.11	4.08	4.09	4.07	4.07	4.08	4.11	4.11	4.08	4.09	4.07	4.07	4.08	4.11	4.11	4.08
TOTAL	19.77	19.71	19.80	19.79	19.81	19.83	19.82	19.77	19.71	19.80	19.79	19.81	19.83	19.82	19.77	19.71	19.80	19.79	19.81	19.83	19.82	19.77
X _{Fe}	0.58	0.58	0.60	0.60	0.59	0.59	0.59	0.58	0.58	0.60	0.60	0.59	0.59	0.59	0.58	0.58	0.60	0.60	0.59	0.59	0.59	0.58

Biotite composition from samples 216533, 219742 219749. (cont)

Wt%	533_bt_inc_1 inclusion in garnet										533_bt_inc_2 inclusion in garnet											
	36.6817	36.16	36.43	35.97	35.91	36.08	36.37	36.24	36.05	36.00	36.09	36.26	36.15	36.22	36.38	36.24	36.05	36.00	36.09	36.26	36.15	36.22
SiO ₂	1.76383	1.79	1.73	1.53	1.59	1.69	1.58	1.45	1.52	1.40	1.50	1.57	1.43	1.45	1.58	1.38	1.45	1.40	1.50	1.57	1.43	1.45
TiO ₂	17.6823	17.13	17.68	17.07	17.49	17.23	16.93	17.58	18.01	17.42	17.42	17.11	17.39	17.17	16.93	17.80	18.01	17.42	17.42	17.42	17.11	17.39
Al ₂ O ₃	0.01	0.00	0.00	0.02	0.00	0.01	0.01	0.01	0.01	0.01	0.02	0.00	0.01	0.01	0.01	0.01	0.01	0.01	0.02	0.00	0.00	0.01
Cr ₂ O ₃	20.42	20.46	20.34	19.99	20.06	20.54	18.23	18.41	18.53	18.42	18.57	18.19	18.30	18.71	18.23	18.41	18.53	18.42	18.57	18.19	18.30	18.71
FeO	0.54	0.38	0.46	0.43	0.38	0.56	0.51	0.58	0.44	0.56	0.37	0.61	0.68	0.53	0.51	0.58	0.44	0.56	0.37	0.61	0.68	0.53
MnO	10.35	10.01	10.18	10.02	10.17	9.92	11.71	11.33	11.38	11.26	11.39	11.44	11.60	11.60	11.71	11.33	11.43	11.26	11.39	11.44	11.44	11.60
CaO	0.02	0.01	0.01	0.02	0.01	0.02	0.01	0.02	0.02	0.03	0.01	0.02	0.02	0.02	0.01	0.02	0.02	0.03	0.01	0.02	0.02	0.02
Na ₂ O	0.15	0.11	0.14	0.14	0.13	0.23	0.14	0.11	0.11	0.15	0.17	0.14	0.13	0.12	0.14	0.11	0.14	0.15	0.17	0.14	0.13	0.12
K ₂ O	9.70	9.57	9.48	9.84	9.64	9.49	9.82	9.94	9.63	9.85	9.77	10.00	9.62	9.88	9.82	9.94	9.85	9.56	9.77	10.00	9.62	9.88
H ₂ O	3.95	3.95	3.96	3.95	3.95	3.94	3.98	3.98	3.98	3.98	3.98	3.98	3.98	3.97	3.98	3.98	3.98	3.98	3.98	3.98	3.98	3.97
TOTAL	101.26	99.57	100.41	98.96	99.34	99.70	99.31	99.93	99.36	100.08	98.79	99.28	99.14	99.67	99.31	99.93	100.08	98.79	99.28	99.30	99.14	99.67
Oxygen	24	24	24	24	24	24	24	24	24	24	24	24	24	24	24	24	24	24	24	24	24	24
Si	5.51	5.53	5.51	5.53	5.49	5.51	5.53	5.50	5.50	5.44	5.50	5.52	5.50	5.50	5.53	5.50	5.44	5.50	5.49	5.52	5.50	5.50
Ti	0.20	0.21	0.20	0.18	0.18	0.19	0.18	0.16	0.17	0.17	0.16	0.18	0.16	0.17	0.18	0.16	0.17	0.16	0.17	0.18	0.16	0.17
Al	3.13	3.08	3.15	3.09	3.15	3.10	3.03	3.17	3.15	3.21	3.14	3.07	3.12	3.07	3.03	3.17	3.21	3.14	3.12	3.07	3.12	3.07
Cr	0.00	0.00	0.00	0.00	0.00	0.00	0.00	0.00	0.00	0.00	0.00	0.00	0.00	0.00	0.00	0.00	0.00	0.00	0.00	0.00	0.00	0.00
Fe	2.57	2.61	2.57	2.57	2.57	2.62	2.32	2.33	2.35	2.35	2.36	2.32	2.33	2.38	2.32	2.33	2.35	2.35	2.36	2.32	2.33	2.38
Mn	0.07	0.05	0.06	0.06	0.05	0.07	0.07	0.07	0.06	0.06	0.07	0.08	0.09	0.07	0.07	0.07	0.06	0.07	0.05	0.08	0.09	0.07
Mg	2.32	2.28	2.30	2.30	2.32	2.26	2.65	2.55	2.57	2.57	2.58	2.60	2.63	2.63	2.65	2.55	2.57	2.56	2.58	2.60	2.60	2.63
Ca	0.00	0.00	0.00	0.00	0.00	0.00	0.00	0.00	0.00	0.00	0.00	0.00	0.00	0.00	0.00	0.00	0.00	0.00	0.00	0.00	0.00	0.00
Na	0.04	0.03	0.04	0.04	0.04	0.07	0.04	0.03	0.03	0.04	0.05	0.04	0.04	0.04	0.04	0.03	0.04	0.04	0.05	0.04	0.04	0.04
K	1.86	1.87	1.83	1.93	1.88	1.85	1.90	1.92	1.87	1.90	1.90	1.94	1.87	1.91	1.90	1.92	1.90	1.86	1.90	1.94	1.87	1.91
H	3.96	4.03	3.99	4.05	4.03	4.02	4.04	4.01	4.03	4.00	4.04	4.04	4.04	4.02	4.04	4.01	4.00	4.06	4.04	4.04	4.04	4.02
TOTAL	19.65	19.69	19.65	19.75	19.72	19.71	19.76	19.74	19.73	19.75	19.75	19.78	19.75	19.78	19.76	19.74	19.75	19.75	19.77	19.78	19.75	19.78
X _{Fe}	0.53	0.53	0.53	0.53	0.53	0.54	0.47	0.48	0.48	0.48	0.48	0.47	0.47	0.47	0.47	0.48	0.48	0.48	0.48	0.47	0.47	0.47

Biotite composition from samples 216533, 219742 219749. (cont)

Wt%	533_bt_inc_3 inclusion in garnet						533_bt_inc_4 inclusion in garnet					
	35.84	35.79	35.69	35.63	36.44	35.73	35.99	35.23	35.34	33.51		
SiO2	1.36	1.40	1.53	1.52	1.27	1.31	1.44	1.41	1.53	1.64	1.55	
Al2O3	17.04	17.15	17.50	17.25	17.92	17.31	17.23	17.65	17.19	16.03	15.98	
Cr2O3	0.01	0.00	0.00	0.00	0.01	0.00	0.00	0.01	0.05	0.05	0.06	
FeO	17.67	17.91	18.11	18.14	18.02	18.00	18.20	18.07	18.98	19.51	19.01	
MnO	0.74	0.61	0.65	0.55	0.45	0.44	0.52	0.58	1.09	0.97	0.76	
MgO	12.61	12.36	12.09	12.52	13.31	12.19	12.28	12.76	10.26	10.73	10.06	
CaO	0.02	0.02	0.03	0.03	0.05	0.02	0.01	0.03	0.08	0.13	0.26	
Na2O	0.13	0.15	0.12	0.19	0.20	0.14	0.13	0.18	0.13	0.16	0.09	
K2O	8.91	9.23	9.48	8.98	8.97	9.16	9.04	9.11	9.92	9.73	8.75	
H2O	4.00	3.99	3.98	3.99	4.01	4.00	3.99	4.00	3.95	3.93	3.90	
TOTAL	98.33	98.62	99.19	98.80	100.64	98.28	98.56	100.40	99.17	98.10	97.67	
Oxygen	24	24	24	24	24	24	24	24	24	24	24	
Si	5.47	5.46	5.43	5.43	5.43	5.46	5.45	5.47	5.52	5.49	5.29	
Ti	0.16	0.16	0.17	0.17	0.14	0.15	0.17	0.16	0.18	0.19	0.18	
Al	3.06	3.08	3.14	3.10	3.15	3.12	3.10	3.11	3.11	2.94	2.97	
Cr	0.00	0.00	0.00	0.00	0.00	0.00	0.00	0.00	0.01	0.01	0.00	
Fe	2.26	2.29	2.30	2.31	2.24	2.30	2.32	2.26	2.43	2.54	2.51	
Mn	0.10	0.08	0.08	0.07	0.06	0.06	0.07	0.07	0.14	0.13	0.16	
Mg	2.87	2.81	2.74	2.84	2.96	2.78	2.79	2.84	2.35	2.49	2.37	
Ca	0.00	0.00	0.00	0.00	0.01	0.00	0.00	0.01	0.01	0.02	0.04	
Na	0.04	0.04	0.04	0.06	0.06	0.04	0.04	0.05	0.04	0.05	0.04	
K	1.74	1.80	1.84	1.75	1.70	1.79	1.76	1.74	1.94	1.93	1.76	
H	4.08	4.06	4.04	4.06	3.98	4.08	4.07	3.99	4.04	4.09	4.10	
TOTAL	19.77	19.79	19.79	19.78	19.73	19.78	19.77	19.71	19.76	19.88	19.99	
X _{Fe}	0.44	0.45	0.46	0.45	0.43	0.45	0.45	0.44	0.51	0.50	0.52	

Table C.6 Perthitic k-feldspar composition from sample 219749.

Wt%	749_kfs_1										
SiO2	65.45	65.88	65.45	65.45	64.71	64.83	66.80	66.59	65.56	64.82	65.17
TiO2	0.04	0.00	0.01	0.01	0.01	0.02	0.00	0.01	0.01	0.03	0.00
Al2O3	19.52	19.81	19.81	19.33	19.55	19.45	20.66	20.46	20.24	19.50	19.55
Cr2O3	0.00	0.00	0.00	0.01	0.00	0.00	0.00	0.00	0.00	0.01	0.01
FeO	0.13	0.04	0.03	0.02	0.00	0.00	0.03	0.14	0.00	0.18	0.01
MnO	0	0	0	0.02	0	0	0	0.04	0.04	0	0
MgO	0	0.01	0.02	0	0	0	0.03	0.04	0.03	0.00	0
CaO	0.02	0.06	0.05	0.02	0.02	0.03	0.10	0.09	0.05	0.01	0.02
Na2O	1.21	2.67	0.99	0.76	0.70	0.61	5.06	4.74	3.28	0.59	0.69
K2O	15.44	11.92	15.19	15.92	15.61	15.88	8.34	9.82	11.85	16.22	15.66
TOTAL	101.80	100.39	101.54	101.53	100.60	100.82	101.03	101.92	101.05	101.36	101.11
Oxygen	8	8	8	8	8	8	8	8	8	8	8
Si	2.96	2.98	2.96	2.97	2.96	2.97	2.96	2.95	2.95	2.96	2.97
Ti	0.00	0.00	0.00	0.00	0.00	0.00	0.00	0.00	0.00	0.00	0.00
Al	1.04	1.05	1.06	1.04	1.06	1.05	1.08	1.07	1.07	1.05	1.05
Cr	0.00	0.00	0.00	0.00	0.00	0.00	0.00	0.00	0.00	0.00	0.00
Fe	0.00	0.00	0.00	0.00	0.00	0.00	0.00	0.01	0.00	0.01	0.00
Mn	0	0	0	0.00	0.00	0.00	0.00	0.00	0.00	0	0
Mg	0	0.00	0.00	0.00	0.00	0.00	0.00	0.00	0.00	0.00	0.00
Ca	0.00	0.00	0.00	0.00	0.00	0.00	0.00	0.00	0.00	0.00	0.00
Na	0.11	0.23	0.09	0.07	0.06	0.05	0.43	0.41	0.29	0.05	0.06
K	0.89	0.69	0.88	0.92	0.91	0.93	0.47	0.56	0.68	0.94	0.91
TOTAL	5.01	4.96	4.99	5.00	5.00	5.00	4.95	5.00	5.00	5.01	4.99
Ca albite	0.00	0.00	0.00	0.00	0.00	0.00	0.01	0.00	0.00	0.00	0.00
Na Anorthite	0.11	0.25	0.09	0.07	0.06	0.05	0.48	0.42	0.30	0.05	0.06
K Orthoclase	0.89	0.74	0.91	0.93	0.93	0.94	0.52	0.57	0.70	0.95	0.94

Perthitic k-feldspar composition from sample 219749. (cont)

		749_kfs_2																		
SiO2		65.26	65.13	67.15	65.18	65.66	65.30	64.84	65.36	65.19	64.65	65.73	66.02	65.48	66.15	65.35	64.91	64.93	64.24	65.07
TiO2		0.00	0.03	0.00	0.00	0.00	0.03	0.01	0.03	0.00	0.03	0.00	0.05	0.01	0.04	0.00	0.01	0.03	0.01	0.03
Al2O3		19.47	19.45	20.52	19.32	19.63	19.54	19.57	19.80	19.17	19.23	20.01	19.77	19.85	19.77	19.94	19.51	19.45	19.49	19.61
Cr2O3		0.00	0.00	0.00	0.00	0.00	0.00	0.00	0.00	0.00	0.02	0.00	0.01	0.00	0.01	0.01	0.00	0.01	0.00	0.00
FeO		0.00	0.03	0.08	0.00	0.00	0.00	0.00	0.06	0.03	0.03	0.01	0.00	0.01	0.02	0.05	0.01	0.02	0.03	0.05
MnO		0	0.01	0	0.06	0.01	0.01	0	0	0	0.02	0	0.03	0.02	0	0.05	0	0	0.07	0.01
MgO		0	0.00	0.03	0	0	0	0.00	0.02	0	0	0.00	0.00	0.00	0.01	0.02	0	0	0.00	0
CaO		0.03	0.05	0.15	0.03	0.06	0.06	0.05	0.03	0.01	0.01	0.06	0.06	0.05	0.05	0.07	0.07	0.02	0.02	0.00
Na2O		1.39	1.31	7.20	0.80	2.19	1.45	0.80	2.32	1.09	0.64	2.80	2.66	1.86	2.86	4.61	1.00	0.66	0.63	1.10
K2O		15.01	15.24	5.67	15.45	13.77	14.61	15.61	13.44	15.51	16.00	12.41	12.61	13.47	12.31	9.11	15.50	16.01	16.26	15.34
TOTAL		101.17	101.24	100.79	100.83	101.33	101.01	100.89	101.06	101.01	100.62	101.02	101.21	100.75	101.22	99.20	101.00	101.12	100.74	101.21
Oxygen		8	8	8	8	8	8	8	8	8	8	8	8	8	8	8	8	8	8	8
Si		2.97	2.96	2.96	2.98	2.97	2.97	2.96	2.96	2.98	2.97	2.96	2.97	2.97	2.97	2.96	2.96	2.96	2.95	2.96
Ti		0.00	0.00	0.00	0.00	0.00	0.00	0.00	0.00	0.00	0.00	0.00	0.00	0.00	0.00	0.00	0.00	0.00	0.00	0.00
Al		1.04	1.04	1.07	1.04	1.05	1.05	1.05	1.06	1.03	1.04	1.06	1.05	1.06	1.05	1.07	1.05	1.05	1.06	1.05
Cr		0.00	0.00	0.00	0.00	0.00	0.00	0.00	0.00	0.00	0.00	0.00	0.00	0.00	0.00	0.00	0.00	0.00	0.00	0.00
Fe		0.00	0.00	0.00	0.00	0.00	0.00	0.00	0.00	0.00	0.00	0.00	0.00	0.00	0.00	0.00	0.00	0.00	0.00	0.00
Mn		0	0.00	0.00	0.00	0.00	0.00	0.00	0.00	0.00	0.00	0.00	0.00	0.00	0.00	0.00	0.00	0.00	0.00	0.00
Mg		0.00	0.00	0.00	0.00	0.00	0.00	0.00	0.00	0.00	0.00	0.00	0.00	0.00	0.00	0.00	0.00	0.00	0.00	0.00
Ca		0.00	0.00	0.01	0.00	0.00	0.00	0.00	0.00	0.00	0.00	0.00	0.00	0.00	0.00	0.00	0.00	0.00	0.00	0.00
Na		0.12	0.12	0.62	0.07	0.19	0.13	0.07	0.20	0.10	0.06	0.24	0.23	0.16	0.25	0.41	0.09	0.06	0.06	0.10
K		0.87	0.88	0.32	0.90	0.79	0.85	0.91	0.78	0.90	0.94	0.71	0.72	0.78	0.71	0.53	0.90	0.93	0.95	0.89
TOTAL		5.01	5.01	4.97	4.99	5.00	4.99	5.00	5.00	5.01	5.01	4.99	4.98	4.97	4.98	4.97	5.01	5.01	5.02	5.01
Ca albite	X(Alb)	0.00	0.00	0.01	0.00	0.00	0.00	0.00	0.00	0.00	0.00	0.00	0.00	0.00	0.00	0.00	0.00	0.00	0.00	0.00
Na Anorthite	X(An)	0.12	0.12	0.65	0.07	0.19	0.13	0.07	0.21	0.10	0.06	0.25	0.24	0.17	0.26	0.43	0.09	0.06	0.06	0.10
K Orthoclase	X(Or)	0.88	0.88	0.34	0.93	0.80	0.87	0.93	0.79	0.90	0.94	0.74	0.75	0.82	0.74	0.56	0.91	0.94	0.94	0.90

Perthitic k-feldspar composition from sample 219749. (cont)

Wt%	749_kfs_3																		
SiO2	65.01	65.79	66.12	67.14	66.95	64.71	66.27	65.77	65.25	65.39	64.92	65.99	65.07	65.01	66.08	65.73	65.13	64.59	64.84
TiO2	0	0.00	0.00	0.02	0.03	0.00	0.00	0.03	0.00	0.03	0.00	0.00	0.00	0.00	0.00	0.00	0.01	0.01	0.02
Al2O3	19.53	20.11	19.36	20.15	20.03	19.09	19.83	20.10	19.59	19.05	19.38	20.28	19.35	19.06	19.77	20.26	19.89	18.77	19.30
Cr2O3	0	0	0	0	0.00	0.01	0.00	0.00	0.00	0.00	0.01	0.00	0.00	0.00	0.00	0.00	0.00	0.02	0.01
FeO	0.05	0.03	0.02	0.02	0.03	0.02	0.00	0.00	0.02	0.00	0.00	0.01	0.03	0.02	0.00	0.01	0.01	0.00	0.05
MnO	0	0	0	0	0.02	0.00	0.01	0.00	0.04	0.00	0.03	0.00	0.00	0.00	0.05	0.00	0.00	0.00	0.00
MgO	0	0.01	0.00	0.00	0.00	0.00	0.00	0.01	0.00	0.00	0.00	0.01	0.00	0.00	0.00	0.02	0.01	0.00	0.00
CaO	0.01	0.05	0.04	0.21	0.05	0.02	0.05	0.07	0.01	0.02	0.02	0.02	0.02	0.01	0.08	0.04	0.04	0.00	0.03
Na2O	1.16	2.65	1.80	3.81	4.61	1.10	2.91	3.51	1.56	1.09	1.20	3.25	1.58	0.69	4.46	3.97	2.57	0.55	0.83
K2O	15.65	13.33	12.85	10.92	10.22	15.64	12.91	12.21	15.06	15.26	15.04	12.66	14.72	16.47	10.69	11.26	14.13	16.21	15.53
TOTAL	101.42	101.97	100.19	102.27	101.94	100.59	101.98	101.70	101.55	100.68	101.09	100.82	100.78	101.26	101.14	101.30	101.80	100.16	100.61
Oxygen	8	8	8	8	8	8	8	8	8	8	8	8	8	8	8	8	8	8	8
Si	2.96	2.95	3.00	2.97	2.97	2.97	2.97	2.95	2.96	2.98	2.97	2.95	2.97	2.97	2.96	2.95	2.94	2.98	2.97
Ti	0.00	0.00	0.00	0.00	0.00	0.00	0.00	0.00	0.00	0.00	0.00	0.00	0.00	0.00	0.00	0.00	0.00	0.00	0.00
Al	1.05	1.06	1.03	1.05	1.05	1.03	1.05	1.06	1.05	1.03	1.03	1.07	1.04	1.03	1.04	1.07	1.06	1.02	1.04
Cr	0.00	0.00	0.00	0.00	0.00	0.00	0.00	0.00	0.00	0.00	0.00	0.00	0.00	0.00	0.00	0.00	0.00	0.00	0.00
Fe	0.00	0.00	0.00	0.00	0.00	0.00	0.00	0.00	0.00	0.00	0.00	0.00	0.00	0.00	0.00	0.00	0.00	0.00	0.00
Mn	0.00	0.00	0.00	0.00	0.00	0.00	0.00	0.00	0.00	0.00	0.00	0.00	0.00	0.00	0.00	0.00	0.00	0.00	0.00
Mg	0.00	0.00	0.00	0.00	0.00	0.00	0.00	0.00	0.00	0.00	0.00	0.00	0.00	0.00	0.00	0.00	0.00	0.00	0.00
Ca	0.00	0.00	0.00	0.00	0.00	0.00	0.00	0.00	0.00	0.00	0.00	0.00	0.00	0.00	0.00	0.00	0.00	0.00	0.00
Na	0.10	0.23	0.16	0.33	0.40	0.10	0.25	0.30	0.14	0.10	0.11	0.28	0.14	0.06	0.39	0.34	0.23	0.05	0.07
K	0.91	0.76	0.74	0.62	0.58	0.92	0.74	0.70	0.87	0.89	0.87	0.72	0.86	0.96	0.61	0.64	0.81	0.95	0.91
TOTAL	5.02	5.01	4.94	4.98	4.99	5.02	5.01	5.02	5.02	5.00	5.00	5.02	5.01	5.02	5.01	5.01	5.05	5.01	5.00
Ca albite	0.00	0.00	0.00	0.00	0.00	0.00	0.00	0.00	0.00	0.00	0.00	0.00	0.00	0.00	0.00	0.00	0.00	0.00	0.00
Na Anorthite	0.10	0.23	0.18	0.35	0.41	0.10	0.26	0.30	0.14	0.10	0.11	0.28	0.14	0.06	0.39	0.35	0.22	0.05	0.08
K Orthoclase	0.90	0.77	0.82	0.65	0.59	0.90	0.74	0.70	0.86	0.90	0.89	0.72	0.86	0.94	0.61	0.65	0.78	0.95	0.92

Perthitic k-feldspar composition from sample 219749. (cont)

Wt%	749_kfs_4																
SiO2	65.59	64.87	64.84	64.86	65.00	65.06	65.36	65.00	65.20	65.07	65.55	65.37	64.67	65.57	65.70	66.41	65.19
TiO2	0.02	0.03	0.00	0.00	0.05	0.02	0.01	0.03	0.00	0.00	0.01	0.01	0.00	0.07	0.03	0.03	0.02
Al2O3	19.75	18.99	19.49	19.38	19.27	18.99	19.82	19.27	19.55	19.26	19.38	19.09	19.11	19.32	19.55	19.62	19.04
Cr2O3	0.00	0.00	0.00	0.00	0.00	0.01	0.00	0.01	0.01	0.00	0.01	0.00	0.00	0.00	0.00	0.00	0.01
FeO	0.06	0.03	0.00	0.06	0.07	0.00	0.02	0.02	0.03	0.05	0.09	0.07	0.02	0.05	0.01	0.05	0.00
MnO	0.02	0.00	0.04	0.00	0.05	0.00	0.00	0.00	0.01	0.00	0.00	0.00	0.01	0.00	0.04	0.04	0.00
MgO	0.00	0.00	0.00	0.00	0.00	0.00	0.00	0.00	0.02	0.01	0.00	0.00	0.00	0.00	0.00	0.00	0.00
CaO	0.06	0.02	0.01	0.04	0.02	0.03	0.03	0.04	0.05	0.00	0.00	0.00	0.02	0.02	0.03	0.02	0.01
Na2O	2.82	0.60	1.13	1.39	1.10	0.77	2.07	1.06	1.73	0.87	0.66	0.71	0.72	1.24	1.74	1.89	0.69
K2O	11.99	16.02	15.72	15.35	15.22	15.77	14.21	15.63	13.18	15.78	14.87	15.97	15.71	14.92	14.49	13.46	15.73
TOTAL	100.31	100.57	101.23	101.08	100.78	100.65	101.52	101.06	99.78	101.04	100.57	101.23	100.26	101.18	101.58	101.53	100.69
Oxygen	8	8	8	8	8	8	8	8	8	8	8	8	8	8	8	8	8
Si	2.97	2.98	2.96	2.96	2.97	2.98	2.96	2.97	2.98	2.97	2.99	2.98	2.98	2.98	2.97	2.98	2.98
Ti	0.00	0.00	0.00	0.00	0.00	0.00	0.00	0.00	0.00	0.00	0.00	0.00	0.00	0.00	0.00	0.00	0.00
Al	1.05	1.03	1.05	1.04	1.04	1.03	1.06	1.04	1.05	1.04	1.04	1.03	1.04	1.03	1.04	1.04	1.03
Cr	0.00	0.00	0.00	0.00	0.00	0.00	0.00	0.00	0.00	0.00	0.00	0.00	0.00	0.00	0.00	0.00	0.00
Fe	0.00	0.00	0.00	0.00	0.00	0.00	0.00	0.00	0.00	0.00	0.00	0.00	0.00	0.00	0.00	0.00	0.00
Mn	0.00	0.00	0.00	0.00	0.00	0.00	0.00	0.00	0.00	0.00	0.00	0.00	0.00	0.00	0.00	0.00	0.00
Mg	0.00	0.00	0.00	0.00	0.00	0.00	0.00	0.00	0.00	0.00	0.00	0.00	0.00	0.00	0.00	0.00	0.00
Ca	0.00	0.00	0.00	0.00	0.00	0.00	0.00	0.00	0.00	0.00	0.00	0.00	0.00	0.00	0.00	0.00	0.00
Na	0.25	0.05	0.10	0.12	0.10	0.07	0.18	0.09	0.15	0.08	0.06	0.06	0.06	0.11	0.15	0.16	0.06
K	0.69	0.94	0.92	0.89	0.89	0.92	0.82	0.91	0.77	0.92	0.86	0.93	0.92	0.86	0.84	0.77	0.92
TOTAL	4.97	5.00	5.02	5.03	5.00	5.00	5.02	5.01	4.96	5.01	4.95	5.00	5.00	4.99	5.00	4.96	4.99
Ca albite	0.00	0.00	0.00	0.00	0.00	0.00	0.00	0.00	0.00	0.00	0.00	0.00	0.00	0.00	0.00	0.00	0.00
Na Anorthite	0.26	0.05	0.10	0.12	0.10	0.07	0.18	0.09	0.17	0.08	0.06	0.06	0.06	0.11	0.15	0.18	0.06
K Orthoclase	0.74	0.95	0.90	0.88	0.90	0.93	0.82	0.91	0.83	0.92	0.94	0.94	0.94	0.89	0.85	0.82	0.94

Perthitic k-feldspar composition from sample 219749. (cont)

Wt%	749_kfs_5									
SiO2	66.46	66.83	64.87	66.49	64.74	65.65	65.26	65.36	65.70	64.02
TiO2	0.00	0.00	0.05	0.04	0.03	0.00	0.00	0.00	0.03	0.01
Al2O3	19.74	20.01	19.31	20.64	19.40	19.87	19.37	19.61	19.87	19.07
Cr2O3	0.01	0.00	0.00	0.00	0.00	0.01	0.00	0.01	0.01	0.00
FeO	0.02	0.00	0.01	0.00	0.04	0.06	0.00	0.05	0.07	0.16
MnO	0.00	0.06	0.06	0.00	0.00	0.00	0.00	0.00	0.02	0.00
MgO	0.00	0.01	0.00	0.01	0.00	0.03	0.00	0.01	0.00	0.00
CaO	0.05	0.11	0.04	0.11	0.02	0.08	0.02	0.05	0.05	0.00
Na2O	3.39	5.22	1.35	5.63	0.70	3.51	1.86	2.57	2.82	0.48
K2O	11.49	9.07	15.22	8.69	15.95	11.52	14.58	12.99	12.05	16.56
TOTAL	101.18	101.31	100.91	101.62	100.89	100.72	101.08	100.65	100.62	100.31
Oxygen	8	8	8	8	8	8	8	8	8	8
Si	2.98	2.97	2.96	2.94	2.96	2.96	2.97	2.97	2.97	2.96
Ti	0.00	0.00	0.00	0.00	0.00	0.00	0.00	0.00	0.00	0.00
Al	1.04	1.05	1.04	1.08	1.05	1.06	1.04	1.05	1.06	1.04
Cr	0.00	0.00	0.00	0.00	0.00	0.00	0.00	0.00	0.00	0.00
Fe	0.00	0.00	0.00	0.00	0.00	0.00	0.00	0.00	0.00	0.01
Mn	0.00	0.00	0.00	0.00	0.00	0.00	0.00	0.00	0.00	0.00
Mg	0.00	0.00	0.00	0.00	0.00	0.00	0.00	0.00	0.00	0.00
Ca	0.00	0.01	0.00	0.01	0.00	0.00	0.00	0.00	0.00	0.00
Na	0.29	0.45	0.12	0.48	0.06	0.31	0.16	0.23	0.25	0.04
K	0.66	0.51	0.89	0.49	0.93	0.66	0.85	0.75	0.69	0.98
TOTAL	4.98	4.99	5.02	5.00	5.01	5.00	5.02	5.00	4.97	5.03
Ca albite	0.00	0.01	0.00	0.01	0.00	0.00	0.00	0.00	0.00	0.00
Na Anorthite	0.31	0.46	0.12	0.49	0.06	0.31	0.16	0.23	0.26	0.04
K Orthoclase	0.69	0.53	0.88	0.50	0.94	0.68	0.84	0.77	0.74	0.96

Perthitic k-feldspar composition from sample 219749. (cont)

Wt%	749_kfs_6																			
SiO2	65.11	65.69	65.21	65.99	67.30	65.10	65.67	65.32	66.52	67.57	65.26	64.90	66.29	65.48	65.53	66.10	66.75	65.40	64.87	65.03
TiO2	0.00	0.03	0.01	0.05	0.00	0.00	0.04	0.00	0.00	0.02	0.00	0.01	0.05	0.00	0.05	0.01	0.02	0.03	0.02	0.04
Al2O3	19.06	19.76	19.32	19.07	20.32	19.58	19.60	19.17	20.61	19.91	19.39	19.22	19.58	19.55	19.09	19.47	19.59	19.24	19.13	18.92
Cr2O3	0.00	0.01	0.00	0.00	0.00	0.00	0.00	0.00	0.00	0.00	0.00	0.00	0.00	0.01	0.00	0.00	0.00	0.00	0.01	0.01
FeO	0.03	0.03	0.00	0.00	0.01	0.01	0.00	0.00	0.09	0.00	0.00	0.02	0.01	0.02	0.00	0.02	0.02	0.01	0.04	0.04
MnO	0.01	0.00	0.00	0.00	0.00	0.02	0.02	0.01	0.00	0.04	0.00	0.00	0.09	0.02	0.00	0.01	0.00	0.00	0.00	0.00
MgO	0.00	0.00	0.00	0.00	0.00	0.00	0.01	0.00	0.03	0.00	0.00	0.00	0.00	0.00	0.00	0.00	0.00	0.00	0.00	0.00
CaO	0.00	0.04	0.02	0.04	0.11	0.04	0.05	0.03	0.08	0.14	0.04	0.04	0.08	0.06	0.04	0.04	0.08	0.02	0.03	0.08
Na2O	0.95	2.58	1.27	2.29	6.06	2.46	1.91	0.95	3.42	4.09	1.09	1.48	2.36	2.02	1.01	1.90	3.36	1.22	0.75	0.53
K2O	15.48	12.90	15.32	13.84	7.90	14.54	13.84	15.55	10.99	9.34	15.56	15.11	13.28	14.16	15.27	13.68	10.87	15.50	16.14	15.26
TOTAL	100.64	101.05	101.15	101.29	101.71	101.75	101.13	101.05	101.75	101.12	101.34	100.79	101.74	101.31	100.99	101.21	100.69	101.42	101.00	99.91
Oxygen	8	8	8	8	8	8	8	8	8	8	8	8	8	8	8	8	8	8	8	8
Si	2.98	2.97	2.97	2.98	2.97	2.95	2.97	2.98	2.96	2.99	2.97	2.97	2.98	2.97	2.98	2.98	2.99	2.97	2.97	2.99
Ti	0.00	0.00	0.00	0.00	0.00	0.00	0.00	0.00	0.00	0.00	0.00	0.00	0.00	0.00	0.00	0.00	0.00	0.00	0.00	0.00
Al	1.03	1.05	1.04	1.02	1.06	1.05	1.05	1.03	1.08	1.04	1.04	1.04	1.04	1.04	1.02	1.04	1.03	1.03	1.03	1.03
Cr	0.00	0.00	0.00	0.00	0.00	0.00	0.00	0.00	0.00	0.00	0.00	0.00	0.00	0.00	0.00	0.00	0.00	0.00	0.00	0.00
Fe	0.00	0.00	0.00	0.00	0.00	0.00	0.00	0.00	0.00	0.00	0.00	0.00	0.00	0.00	0.00	0.00	0.00	0.00	0.00	0.00
Mn	0.00	0.00	0.00	0.00	0.00	0.00	0.00	0.00	0.00	0.00	0.00	0.00	0.00	0.00	0.00	0.00	0.00	0.00	0.00	0.00
Mg	0.00	0.00	0.00	0.00	0.00	0.00	0.00	0.00	0.00	0.00	0.00	0.00	0.00	0.00	0.00	0.00	0.00	0.00	0.00	0.00
Ca	0.00	0.00	0.00	0.00	0.01	0.00	0.00	0.00	0.00	0.01	0.00	0.00	0.00	0.00	0.00	0.00	0.00	0.00	0.00	0.00
Na	0.08	0.23	0.11	0.20	0.52	0.22	0.17	0.08	0.29	0.35	0.10	0.13	0.21	0.18	0.09	0.17	0.29	0.11	0.07	0.05
K	0.90	0.74	0.89	0.80	0.44	0.84	0.80	0.90	0.62	0.53	0.90	0.88	0.76	0.82	0.89	0.79	0.62	0.90	0.94	0.90
TOTAL	5.00	4.99	5.01	5.00	4.99	5.06	4.99	5.00	4.96	4.92	5.01	5.02	4.99	5.01	4.99	4.98	4.95	5.01	5.02	4.97
Ca albite X(Ab)	0.00	0.00	0.00	0.00	0.01	0.00	0.00	0.00	0.00	0.01	0.00	0.00	0.00	0.00	0.00	0.00	0.00	0.00	0.00	0.00
Na Anorthite X(An)	0.09	0.23	0.11	0.20	0.54	0.20	0.17	0.08	0.32	0.40	0.10	0.13	0.21	0.18	0.09	0.17	0.32	0.11	0.07	0.05
K Orthoclase X(Or)	0.91	0.77	0.89	0.80	0.46	0.79	0.82	0.91	0.68	0.60	0.90	0.87	0.78	0.82	0.91	0.82	0.68	0.89	0.93	0.95

Perthitic k-feldspar composition from sample 219749. (cont)

Wt%	749_kfs_7											
	65.22	65.78	65.31	65.10	66.44	65.25	66.10	66.84	65.02	65.09	64.92	63.40
SiO2	0.02	0.01	0.00	0.03	0.00	0.01	0.01	0.04	0.00	0.01	0.02	0.01
TiO2	19.43	19.38	19.70	19.63	19.88	19.36	19.71	20.35	19.50	19.03	18.92	21.58
Al2O3	0.00	0.00	0.00	0.00	0.00	0.00	0.01	0.01	0.01	0.00	0.00	0.00
Cr2O3	0.00	0.02	0.05	0.01	0.00	0.05	0.00	0.04	0.04	0.00	0.02	0.20
FeO	0.02	0.00	0.00	0.00	0.00	0.00	0.00	0.13	0.00	0.00	0.00	0.00
MnO	0.00	0.00	0.00	0.00	0.01	0.00	0.01	0.02	0.02	0.00	0.00	0.00
MgO	0.03	0.04	0.05	0.05	0.07	0.03	0.08	0.10	0.04	0.02	0.00	0.00
CaO	1.17	1.49	1.64	1.73	2.84	0.77	3.04	4.84	1.71	0.89	0.85	1.13
Na2O	15.06	14.40	14.90	14.96	12.59	15.60	12.20	8.86	14.54	15.33	15.71	15.27
K2O	100.95	101.12	101.65	101.50	101.83	101.05	101.16	101.23	100.89	100.37	100.44	101.59
TOTAL												
Oxygen	8	8	8	8	8	8	8	8	8	8	8	8
Si	2.97	2.98	2.96	2.96	2.97	2.97	2.97	2.97	2.96	2.98	2.98	2.88
Ti	0.00	0.00	0.00	0.00	0.00	0.00	0.00	0.00	0.00	0.00	0.00	0.00
Al	1.04	1.04	1.05	1.05	1.05	1.04	1.04	1.06	1.05	1.03	1.02	1.16
Cr	0.00	0.00	0.00	0.00	0.00	0.00	0.00	0.00	0.00	0.00	0.00	0.00
Fe	0.00	0.00	0.00	0.00	0.00	0.00	0.00	0.00	0.00	0.00	0.00	0.01
Mn	0.00	0.00	0.00	0.00	0.00	0.00	0.00	0.00	0.00	0.00	0.00	0.00
Mg	0.00	0.00	0.00	0.00	0.00	0.00	0.00	0.00	0.00	0.00	0.00	0.00
Ca	0.00	0.00	0.00	0.00	0.00	0.00	0.00	0.00	0.00	0.00	0.00	0.00
Na	0.10	0.13	0.14	0.15	0.25	0.07	0.27	0.42	0.15	0.08	0.08	0.10
K	0.88	0.83	0.86	0.87	0.72	0.91	0.70	0.50	0.85	0.90	0.92	0.89
TOTAL	5.00	4.98	5.02	5.03	4.99	4.99	4.99	4.96	5.01	4.99	5.00	5.03
Ca albite	0.00	0.00	0.00	0.00	0.00	0.00	0.00	0.01	0.00	0.00	0.00	0.00
Na Anorthite	0.11	0.14	0.14	0.15	0.25	0.07	0.27	0.45	0.15	0.08	0.08	0.10
K Orthoclase	0.89	0.86	0.85	0.85	0.74	0.93	0.72	0.54	0.85	0.92	0.92	0.90

Table C.7 Muscovite composition from samples 216533.

Wt%	533_ms_1 matrix										533_ms_2 matrix														
	48.91	48.84	48.76	48.04	48.04	47.74	47.95	47.66	47.87	48.39	48.53	48.99	48.54	48.91	48.84	48.76	48.04	48.04	47.74	47.95	47.66	47.87	48.39	48.53	48.99
SiO2	0.36	0.44	0.41	0.33	0.33	0.40	0.44	0.38	0.43	0.44	0.35	0.33	0.36	0.44	0.41	0.33	0.33	0.40	0.44	0.38	0.43	0.44	0.35	0.33	
TiO2	30.32	29.81	31.57	30.30	30.30	30.68	30.83	30.40	30.64	30.42	29.86	30.10	30.32	29.81	31.57	30.30	30.30	30.68	30.83	30.40	30.64	30.42	29.86	30.10	
Al2O3	0.00	0.01	0.04	0.04	0.04	0.04	0.02	0.03	0.01	0.00	0.03	0.00	0.00	0.01	0.04	0.04	0.04	0.04	0.02	0.03	0.01	0.00	0.03	0.00	
Cr2O3	3.54	3.68	3.85	4.00	4.00	3.55	3.67	3.82	3.70	3.67	3.72	3.74	3.54	3.68	3.85	4.00	4.00	3.55	3.67	3.82	3.70	3.67	3.72	3.74	
FeO	0.01	0.00	0.00	0.01	0.01	0.07	0.06	0.00	0.00	0.00	0.06	0.01	0.01	0.00	0.00	0.01	0.01	0.07	0.06	0.00	0.00	0.00	0.06	0.01	
MnO	1.23	1.32	1.13	1.25	1.25	1.08	1.03	1.09	1.13	1.12	1.47	1.19	1.23	1.32	1.13	1.25	1.25	1.08	1.03	1.09	1.13	1.12	1.47	1.19	
MgO	0.01	0.00	0.01	0.00	0.00	0.01	0.02	0.02	0.01	0.01	0.05	0.03	0.01	0.00	0.01	0.00	0.00	0.01	0.02	0.02	0.01	0.01	0.05	0.03	
CaO	0.39	0.38	0.42	0.18	0.18	0.43	0.34	0.41	0.41	0.41	0.24	0.37	0.39	0.38	0.42	0.18	0.18	0.43	0.34	0.41	0.41	0.41	0.24	0.37	
Na2O	10.85	11.19	10.76	11.07	11.07	10.86	10.82	10.74	10.87	11.07	10.26	11.14	10.85	11.19	10.76	11.07	11.07	10.86	10.82	10.74	10.87	11.07	10.26	11.14	
K2O	4.48	4.46	4.47	4.46	4.46	4.47	4.47	4.47	4.47	4.46	4.49	4.46	4.48	4.46	4.47	4.46	4.46	4.47	4.47	4.47	4.47	4.46	4.49	4.46	
H2O	100.10	100.14	101.41	99.68	99.68	99.32	100.18	99.23	100.07	100.19	99.52	99.92	100.10	100.14	101.41	99.68	99.68	99.32	100.18	99.23	100.07	100.19	99.52	99.92	
TOTAL	24.00	24.00	24.00	24.00	24.00	24.00	24.00	24.00	24.00	24.00	24.00	24.00	24.00	24.00	24.00	24.00	24.00	24.00	24.00	24.00	24.00	24.00	24.00	24.00	
Oxygen	6.56	6.57	6.46	6.50	6.50	6.46	6.43	6.46	6.50	6.52	6.59	6.54	6.56	6.57	6.46	6.50	6.50	6.46	6.43	6.46	6.50	6.52	6.59	6.54	
Si	0.04	0.04	0.04	0.03	0.03	0.04	0.04	0.04	0.04	0.04	0.04	0.03	0.04	0.04	0.04	0.03	0.03	0.04	0.04	0.04	0.04	0.04	0.04	0.03	
Ti	4.79	4.72	4.93	4.83	4.83	4.90	4.98	4.86	4.85	4.82	4.73	4.78	4.79	4.72	4.93	4.83	4.83	4.90	4.98	4.86	4.85	4.82	4.73	4.78	
Al	0.00	0.00	0.00	0.00	0.00	0.00	0.00	0.00	0.00	0.00	0.00	0.00	0.00	0.00	0.00	0.00	0.00	0.00	0.00	0.00	0.00	0.00	0.00	0.00	
Cr	0.40	0.41	0.43	0.45	0.45	0.40	0.41	0.43	0.42	0.41	0.42	0.42	0.40	0.41	0.43	0.45	0.45	0.40	0.41	0.43	0.42	0.41	0.42	0.42	
Fe	0.00	0.00	0.00	0.00	0.00	0.01	0.01	0.00	0.00	0.01	0.01	0.00	0.00	0.00	0.00	0.00	0.00	0.01	0.01	0.00	0.00	0.01	0.01	0.00	
Mn	0.25	0.26	0.22	0.25	0.25	0.22	0.21	0.20	0.23	0.22	0.29	0.24	0.25	0.26	0.22	0.25	0.25	0.22	0.21	0.20	0.23	0.22	0.29	0.24	
Mg	0.00	0.00	0.00	0.00	0.00	0.00	0.00	0.00	0.00	0.00	0.00	0.00	0.00	0.00	0.00	0.00	0.00	0.00	0.00	0.00	0.00	0.00	0.00	0.00	
Ca	0.10	0.10	0.11	0.05	0.05	0.11	0.10	0.09	0.11	0.11	0.06	0.10	0.10	0.10	0.11	0.05	0.05	0.11	0.10	0.09	0.11	0.11	0.06	0.10	
Na	1.86	1.92	1.82	1.91	1.91	1.88	1.83	1.87	1.86	1.90	1.76	1.92	1.86	1.92	1.82	1.91	1.91	1.88	1.83	1.87	1.86	1.90	1.76	1.92	
K	4.00	4.00	3.95	4.02	4.02	4.04	4.00	4.04	4.00	4.00	4.03	4.01	4.00	4.00	3.95	4.02	4.02	4.04	4.00	4.04	4.00	4.00	4.03	4.01	
H	17.99	18.04	17.97	18.04	18.04	18.06	18.00	18.04	18.02	18.03	17.93	18.05	17.99	18.04	17.97	18.04	18.04	18.06	18.00	18.04	18.02	18.03	17.93	18.05	
TOTAL	0.62	0.61	0.66	0.64	0.64	0.65	0.67	0.68	0.66	0.65	0.59	0.64	0.62	0.61	0.66	0.64	0.64	0.65	0.67	0.68	0.66	0.65	0.59	0.64	
X _{Fe}																									

Muscovite composition from samples 216533. (cont)

Wt%	533_inc_ms_1_inclusion in garnet										
SiO2	49.91	50.13	49.82	49.84	49.81	49.68	49.24	49.13	49.28	48.77	
TiO2	0.41	0.47	0.36	0.43	0.60	0.54	0.49	0.41	0.55	0.45	
Al2O3	31.32	31.04	31.25	31.44	32.08	31.63	32.40	31.68	31.23	29.79	
Cr2O3	0.06	0.04	0.05	0.07	0.07	0.05	0.05	0.07	0.04	0.05	
FeO	3.40	3.44	3.50	3.39	3.71	3.60	3.51	3.46	3.64	3.84	
MnO	0.41	0.38	0.40	0.32	0.54	0.51	0.47	0.38	0.42	0.61	
MgO	1.61	1.61	1.54	1.49	1.47	1.41	1.29	1.30	1.46	1.85	
CaO	0.03	0.04	0.01	0.03	0.01	0.03	0.02	0.02	0.02	0.03	
Na2O	0.32	0.42	0.38	0.43	0.38	0.44	0.46	0.44	0.46	0.39	
K2O	11.19	11.20	11.35	11.16	11.12	11.17	11.15	11.28	11.35	11.23	
H2O	4.46	4.46	4.46	4.46	4.45	4.45	4.46	4.46	4.45	4.44	
TOTAL	103.11	103.24	103.10	103.05	104.24	103.51	103.53	102.62	102.88	101.45	
Oxygen	24.00	24.00	24.00	24.00	24.00	24.00	24.00	24.00	24.00	24.00	
Si	6.516	6.54	6.515	6.51	6.448	6.475	6.414	6.457	6.472	6.51	
Ti	0.041	0.046	0.036	0.042	0.058	0.053	0.048	0.04	0.054	0.045	
Al	4.82	4.772	4.817	4.839	4.894	4.859	4.974	4.907	4.833	4.687	
Cr	0.006	0.004	0.005	0.007	0.007	0.005	0.005	0.007	0.004	0.006	
Fe	0.371	0.375	0.382	0.371	0.401	0.392	0.383	0.381	0.4	0.428	
Mn	0.045	0.042	0.044	0.035	0.06	0.057	0.052	0.043	0.047	0.069	
Mg	0.314	0.314	0.3	0.29	0.284	0.275	0.25	0.255	0.286	0.368	
Ca	0.003	0.005	0.001	0.004	0.002	0.004	0.002	0.003	0.002	0.005	
Na	0.081	0.105	0.095	0.108	0.94	0.111	0.117	0.113	0.116	0.1	
K	1.863	1.864	1.893	1.859	1.836	1.857	1.853	1.891	1.902	1.913	
H	3.887	3.882	3.887	3.889	3.845	3.872	3.871	3.906	3.895	3.95	
TOTAL	17.95	17.95	17.98	17.95	18.78	17.96	17.97	18.00	18.01	18.08	
X _{Fe}	0.54	0.54	0.56	0.56	0.59	0.59	0.61	0.60	0.58	0.54	

Table C.8 Data used to construct the pseudosection for sample 216533.

Sample: 216533	
<i>XRF whole rock compositions (wt%)</i>	
SiO ₂	55.57
TiO ₂	0.83
Al ₂ O ₃	18.5
Fe ₂ O ₃ ^(a)	3.10
FeO ^(a)	6.73
MnO	0.85
MgO	3.13
CaO	1.08
Na ₂ O	0.29
K ₂ O	6.63
LOI	2.01
Total	98.72
<i>Normalised molar proportions used for phase equilibria modelling (b)</i>	
SiO ₂	65.42
TiO ₂	0.74
Al ₂ O ₃	12.83
O	1.37
FeO	6.63
MnO	0.85
MgO	5.49
CaO	1.36
Na ₂ O	0.33
K ₂ O	4.98
H ₂ O	_(c)
Total	100.00

Notes:

LOI, Loss on ignition.

^(a)FeO analysed by Fe²⁺ titration; Fe₂O₃ contents calculated by difference.

^(b)Final composition used for P-T pseudosection, based on adjusted FeO:Fe₂O₃.

^(c)Assumes H₂O saturation.

Appendix D
Supplementary Data (Chapter 4) –
SHRIMP U–Pb Monazite Data

Table D.1 GSWA 139466: monazite: (Erong Granite, Moorarie Supersuite)

Grain .spot	^{238}U (ppm)	^{232}Th (ppm)	$^{232}\text{Th}/^{238}\text{U}$	f_{206} (%)	f_{208} (%)	$^{238}\text{U}/^{206}\text{Pb}^*$ $\pm 1\sigma$	$^{207}\text{Pb}^*/^{206}\text{Pb}^*$ $\pm 1\sigma$	$^{232}\text{Th}/^{208}\text{Pb}^*$ $\pm 1\sigma$	Disc (%)	$^{238}\text{U}/^{206}\text{Pb}^*$ date (Ma) $\pm 1\sigma$	$^{207}\text{Pb}^*/^{206}\text{Pb}^*$ date (Ma) $\pm 1\sigma$	$^{232}\text{Th}/^{208}\text{Pb}^*$ date (Ma) $\pm 1\sigma$
<i>main group</i>												
0902.2-1	359	24263	68	-0.16	-0.02	2.99	0.04	0.0985	0.0017	1861	23	1868
0902.2-4	345	21394	62	-0.10	-0.01	2.99	0.04	0.0968	0.0018	1861	23	1866
0902.1-1	378	33329	88	0.01	0.00	3.05	0.04	0.0971	0.0017	1827	22	1857
0902.4-1	478	37526	79	0.03	0.00	3.01	0.05	0.0968	0.0017	1847	27	1843
0902.5-1	464	30816	66	-0.09	-0.01	2.97	0.05	0.0970	0.0017	1869	26	1832
0902.6-1	412	22440	54	0.05	0.01	3.03	0.04	0.0962	0.0017	1837	22	1828
0902.2-3	355	21957	62	0.15	0.02	3.03	0.05	0.0968	0.0017	1840	29	1814
ER.1-2	370	25506	69	0.07	0.01	3.19	0.06	0.0950	0.0023	1765	27	1811
0902.2-2	418	22352	54	0.05	0.01	3.04	0.05	0.0968	0.0018	1835	25	1802
0902.3-1	442	26198	59	0.09	0.01	3.10	0.04	0.0942	0.0016	1804	22	1787
<i>outlier</i>												
0902.7-1	1964	48863	25	0.05	0.02	3.02	0.07	0.1003	0.0018	1842	37	1933
<i>Discordance > 5% and/or $f_{206} > 1\%$</i>												
ER.1-2b	302	17930	59	-0.05	-0.01	3.39	0.07	0.0998	0.0025	1672	29	1857
ER.1-1	672	40907	61	1.52	0.19	3.15	0.06	0.0937	0.0023	1783	30	1851
												1932
												1867
												1873
												1868
												1870
												1856
												1868
												1849
												1867
												1819
												1932
												1937
												1825

Table D.2 GSWA 169092: monazite: (Red Rock Bore Granite, Durlacher Supersuite)

Grain .spot	²³⁸ U (ppm)	²³² Th (ppm)	²³² Th / ²³⁸ U	f ₂₀₆ (%)	f ₂₀₈ (%)	²³⁸ U/ ²⁰⁶ Pb* ±1σ	²⁰⁷ Pb*/ ²⁰⁶ Pb* ±1σ	²³² Tl/ ²⁰⁸ Pb* ±1σ	Disc (%)	²³⁸ U/ ²⁰⁶ Pb* date (Ma) ±1σ	²⁰⁷ Pb*/ ²⁰⁶ Pb* date (Ma) ±1σ	²³² Tl/ ²⁰⁸ Pb* date (Ma) ±1σ
<i>main group</i>												
HR.3-2	4326	61195	14	0.01	0.01	3.41	0.1043	0.0008	0.0021	1665	26	1658
0904E.1-1	1067	67380	63	-0.01	0.00	3.44	0.1040	0.0005	0.0015	1645	19	1669
0902H.3-1	3501	65733	19	0.63	0.25	3.35	0.1036	0.0005	0.0016	1686	20	1705
0904E.2-2	3965	58427	15	0.03	0.02	3.42	0.1036	0.0003	0.0016	1653	21	1696
0902H.1-1	6234	64871	10	0.19	0.13	3.37	0.1035	0.0004	0.0016	1676	20	1695
HR.1-1	4357	51773	12	0.02	0.01	3.48	0.1035	0.0008	0.0021	1635	27	1687
0904E.3-1	4686	68796	15	0.00	0.00	3.37	0.1034	0.0002	0.0016	1677	20	1700
0902H.2-2	7950	64620	8	0.14	0.13	3.32	0.1032	0.0002	0.0016	1695	20	1705
HR.3-1	6828	68883	10	0.02	0.02	3.48	0.1031	0.0008	0.0021	1636	26	1655
0904E.6.1	1877	73853	39	0.00	0.00	3.43	0.1031	0.0004	0.0016	1649	21	1676
HR.1-2	3624	53080	15	0.08	0.04	3.50	0.1030	0.0009	0.0022	1627	30	1707
HR.6-1	5401	58874	11	0.03	0.02	3.47	0.1030	0.0008	0.0021	1637	27	1666
0902H.2-1	6382	63077	10	0.06	0.05	3.35	0.1030	0.0002	0.0016	1683	21	1706
0904E.5-2	5678	50603	9	0.01	0.01	3.36	0.1029	0.0002	0.0016	1681	21	1702
0904E.2-1	3580	63683	18	0.04	0.02	3.36	0.1028	0.0003	0.0016	1682	20	1686
0904E.4-1	1389	42740	31	0.04	0.01	3.39	0.1027	0.0005	0.0016	1667	22	1673
HR.5-1	978	68093	70	0.14	0.02	3.52	0.1014	0.0011	0.0020	1617	25	1613
<i>outlier</i>												
0904E.5-1	17586	34734	2	0.00	0.00	3.32	0.1021	0.0001	0.0016	1699	21	1695
<i>discordance > 5% and/or f₂₀₆ > 1%</i>												
HR.6-2	3375	53992	16	0.66	0.30	3.76	0.1064	0.0032	0.0025	1525	44	1583
HR.2-1	1134	66186	58	0.14	0.02	3.51	0.1047	0.0013	0.0021	1622	27	1658
HR.4-2	1214	61912	51	0.06	0.01	3.53	0.1046	0.0010	0.0021	1612	25	1631
HR.5-2	1180	76533	65	0.04	0.00	3.62	0.1042	0.0010	0.0020	1578	27	1581
0902H.4-1	1277	57326	45	0.74	0.12	3.56	0.1040	0.0016	0.0015	1595	39	1615
HR.4-1	1405	61231	44	0.03	0.00	3.57	0.1040	0.0009	0.0021	1597	26	1623
HR.2-2	526	68257	130	10.54	0.72	3.33	0.0957	0.0097	0.0020	1698	39	1589

Table D.3 GSWA 187401: monazite: (Perseverance Well Granite, Thirty Three Supersuite)

Grain spot	²³⁸ U (ppm)	²³² Th (ppm)	²³² Th / ²³⁸ U	<i>f</i> ₂₀₆ (%)	<i>f</i> ₂₀₈ (%)	²³⁸ U/ ²⁰⁶ Pb* ±1σ	²⁰⁷ Pb*/ ²⁰⁶ Pb* ±1σ	²³² Th/ ²⁰⁸ Pb* ±1σ	Disc (%)	²³⁸ U/ ²⁰⁶ Pb* date (Ma) ±1σ	²⁰⁷ Pb*/ ²⁰⁶ Pb* date (Ma) ±1σ	²³² Th/ ²⁰⁸ Pb* date (Ma) ±1σ
main group												
0906A.1-1	1474	75621	51	0.43	0.06	5.61	0.0738	0.0011	0.0015	1058	21	1036
0906C.1-1	1324	39962	30	0.03	0.01	5.75	0.0742	0.0007	0.0016	1033	16	1046
0906A.1-2	1369	66155	48	0.21	0.03	5.76	0.0723	0.0009	0.0013	1032	16	994
0906D.1-3	1547	66799	43	0.23	0.04	5.83	0.0717	0.0009	0.0016	1020	13	976
0906D.1-1	1524	65307	43	0.09	0.01	5.85	0.0728	0.0007	0.0016	1018	13	1009
0906E.1-2	1172	47914	41	0.66	0.11	5.87	0.0729	0.0014	0.0016	1015	11	1011
0906E.2-1	1517	62875	41	0.10	0.02	5.87	0.0728	0.0007	0.0016	1014	11	1010
0906A.1-3	1067	51269	48	0.04	0.01	5.88	0.0746	0.0008	0.0012	1012	16	1057
0906D.1-2	1785	71327	40	0.03	0.01	5.89	0.0742	0.0006	0.0016	1011	13	1047
0906E.2-2	1278	54806	43	0.03	0.00	6.04	0.0732	0.0007	0.0016	987	11	1019
0906B.1-1	1517	62940	41	0.13	0.02	6.11	0.0717	0.0008	0.0016	978	13	977
0906G.1-2	1144	80199	70	0.27	0.02	6.16	0.0731	0.0010	0.0017	970	18	1017
0906E.1-1	1934	79745	41	0.10	0.02	6.16	0.0727	0.0007	0.0015	970	11	1005
<i>discordance > 5% and/or f₂₀₆ > 1%</i>												
0906H.1-2	836	49158	59	0.77	0.09	5.55	0.0721	0.0017	0.0012	1068	17	990
0906B.1-2	1578	58115	37	0.31	0.06	5.63	0.0721	0.0009	0.0017	1053	13	988
0906G.1-1	1002	80898	81	0.27	0.02	5.70	0.0765	0.0011	0.0016	1043	16	1107
0906H.1-1	1226	55300	45	1.41	0.22	6.03	0.0742	0.0023	0.0011	989	18	1048
0906G.1-3	3878	72449	19	-0.03	-0.01	6.37	0.0759	0.0010	0.0016	941	18	1093
0906A.2-1	2587	55002	21	1.61	0.38	6.48	0.0960	0.0030	0.0034	925	132	1547
												1327
												63

Table D.4 GSWA 183287: monazite: (Perseverance Well Granite, Thirty Three Supersuite)

Grain .spot	²³⁸ U (ppm)	²³² Th (ppm)	²³⁸ U / ²³⁸ U (%)	<i>f</i> ₂₀₆ (%)	<i>f</i> ₂₀₈ (%)	²³⁸ U / ²⁰⁶ Pb* ±1σ	²⁰⁷ Pb* / ²⁰⁶ Pb* ±1σ	²³² Th / ²⁰⁸ Pb* ±1σ	Disc (%)	²³⁸ U / ²⁰⁶ Pb* date (Ma) ±1σ	²⁰⁷ Pb* / ²⁰⁶ Pb* date (Ma) ±1σ	²³² Th / ²⁰⁸ Pb* date (Ma) ±1σ			
0904A2.1-2	478	25930	54	1.18	0.17	5.90	0.0721	0.0015	0.0019	1010	27	988	43	943	36
1614E.1-1	459	23614	53	0.14	0.02	6.51	0.0684	0.0008	0.0024	922	27	880	23	943	46
1614B.1-1	465	24699	55	-0.20	-0.03	6.38	0.0699	0.0011	0.0477	939	28	927	33	942	47
0904A1.1-2	758	40534	53	-0.12	-0.02	6.27	0.0697	0.0005	0.0019	954	16	919	15	934	36
1614C.1-1	252	14830	61	0.17	0.02	6.57	0.0668	0.0010	0.0024	914	28	830	32	929	46
183287.2-1	496	24859	50	0.20	0.03	6.20	0.0652	0.0018	0.0100	964	56	782	58	920	20
1614B.1-2	377	20696	57	1.68	0.24	5.81	0.0765	0.0022	0.0463	1024	32	1108	58	914	45
183287.2-2	525	27456	52	-0.02	0.00	6.28	0.0688	0.0009	0.0457	952	11	891	26	902	10
1614E.1-2	468	24121	53	1.39	0.20	6.27	0.0753	0.0021	0.0454	954	28	1076	57	898	44
183287.2-4	435	22769	52	0.61	0.08	6.33	0.0731	0.0016	0.0453	946	11	1015	44	896	9
183287.2-3	529	27564	52	0.16	0.02	6.71	0.0707	0.0011	0.0445	896	10	948	33	879	9
0904A1.1-3	643	35713	56	-0.17	-0.02	6.43	0.0697	0.0006	0.0443	932	16	918	17	877	33
outlier															
183287.1-1a	519	23601	46	0.34	0.05	6.18	0.0675	0.0013	0.0490	967	11	853	40	967	12
<i>f</i> ₂₀₈ > 1%															
183287.1-1	538	30320	56	5.18	1.11	3.98	0.0837	0.0089	0.0314	1444	18	1285	208	881	9
Notes:															
^ Indicates measured ²³⁸ U and ²³² Th levels. The precisions of ²³⁸ U and ²³² Th abundances measured by SHRIMP are typically 5-10 %.															
Pb indicates radiogenic Pb (i.e. corrected for common Pb)															
<i>f</i> ₂₀₆ , proportion of common ²⁰⁶ Pb in measured ²⁰⁶ Pb, determined using measured ²⁰⁴ Pb/ ²⁰⁶ Pb and contemporaneous common Pb composition (Stacey and Kramers, 1975)															
<i>f</i> ₂₀₈ , proportion of common ²⁰⁸ Pb in measured ²⁰⁸ Pb, determined using measured isotope ratios and contemporaneous common Pb composition (Stacey and Kramers, 1975)															
Disc. is apparent discordance, as D (%) = 100 x [(²⁰⁷ Pb*/ ²⁰⁶ Pb* date) - (²³⁸ U/ ²⁰⁶ Pb* date)] / [²⁰⁷ Pb*/ ²⁰⁶ Pb* date]															
Analyses are sorted by descending ²⁰⁷ Pb*/ ²⁰⁶ Pb* age for samples 139466 and 169092															
Analyses are sorted by descending ²³⁸ U/ ²⁰⁶ Pb* age for sample 187401															
²⁰⁷ Pb*/ ²⁰⁶ Pb* and ²³² Th/ ²⁰⁸ Pb* analyses in grey shading (Sample 187401) were used to calculate respective weighted mean ages discussed in the text															
187401: the 1 calibration uncertainty = 0.005607 (²⁰⁶ Pb*/ ²³⁸ U) and 0.01422 (²⁰⁸ Pb*/ ²³² Th)															
Analyses are sorted by descending ²³² Th/ ²⁰⁸ Pb* age for sample 183287															
²³⁸ U/ ²⁰⁶ Pb* and ²⁰⁷ Pb*/ ²⁰⁶ Pb* analyses in grey shading (Sample 183287) were used to calculate respective weighted mean ages that are discussed in the text															
183287 calibration uncertainty = (0904) 0.005470 (²⁰⁶ Pb*/ ²³⁸ U) and 0.01081 (²⁰⁸ Pb*/ ²³² Th); (1614) 0.015519 (²⁰⁶ Pb*/ ²³⁸ U) and 0.02482 (²⁰⁸ Pb*/ ²³² Th); (183287) 0.005056 (²⁰⁶ Pb*/ ²³⁸ U) and 0.003309 (²⁰⁸ Pb*/ ²³² Th)															

Appendix E
Supplementary Data (Chapter 5) –
 $^{40}\text{Ar}/^{39}\text{Ar}$ Mica Data

Table E.1 Sample 216540B muscovite

Relative Abundances	36Ar [V]	%1σ	37Ar [V]	%1σ	38Ar [V]	%1σ	39Ar [V]	%1σ	40Ar [V]	%1σ	40(t)/39(k) ± 2σ	Age ± 2σ (Ma)	40Ar(t) (%)	39Ar(k) (%)	K/Ca ± 2σ
7M44037D	0.0000360	17.255	0.0000524	146.232	0.0000668	9.214	0.0054388	0.455	0.333990	0.110	59.43102 ± 0.88126	900.39 ± 10.52	96.78	2.91	54 ± 168
7M44038D	0.0000298	26.386	0.0000251	286.003	0.0001030	8.122	0.0075367	0.464	0.472722	0.064	61.54003 ± 0.84978	925.38 ± 10.00	98.11	4.04	156 ± 893
7M44039D	0.000068	91.048	0.000139	526.891	0.0000386	15.143	0.0032456	0.832	0.195129	0.167	59.49967 ± 1.51610	901.21 ± 18.08	98.97	1.74	121 ± 1277
7M44041D	0.000013	67.863	0.0000333	233.775	0.0000674	8.211	0.0048395	0.614	0.296646	0.108	61.34237 ± 1.22764	923.05 ± 14.40	98.87	2.58	75 ± 361
7M44042D	0.0000447	17.717	0.0000734	98.250	0.0001503	5.444	0.0078997	0.273	0.791932	0.088	60.87542 ± 0.93894	917.54 ± 6.02	98.31	6.85	91 ± 178
7M44043D	0.0000200	26.871	0.0000331	232.849	0.0000966	7.875	0.0080172	0.402	0.491174	0.090	60.51689 ± 0.64036	913.32 ± 7.59	98.78	4.29	126 ± 887
7M44044D	0.0000415	15.212	0.0001389	59.897	0.0002111	5.032	0.0079196	0.290	1.107872	0.086	61.13393 ± 0.42567	920.60 ± 5.02	98.88	9.60	67 ± 80
7M44046D	0.0000203	34.447	0.0000991	78.488	0.0003113	2.841	0.0255932	0.328	1.653326	0.036	60.46560 ± 0.63071	912.67 ± 5.11	98.61	13.71	134 ± 211
7M44047D	0.0000244	25.591	0.0000930	78.352	0.0003846	2.583	0.0325668	0.302	1.877791	0.169	59.85198 ± 0.42992	903.02 ± 5.12	99.61	16.74	175 ± 274
7M44048D	0.0000794	35.456	0.0000668	117.164	0.0001684	4.472	0.054998	0.213	0.921261	0.056	59.06232 ± 0.37165	895.98 ± 4.45	99.37	8.30	121 ± 283
7M44049D	0.0000154	46.242	0.0000109	78.469	0.0003777	3.949	0.0314010	0.307	1.662401	0.048	59.16351 ± 0.39207	897.19 ± 4.69	99.75	16.82	160 ± 251
7M44289D	0.0000034	189.203	0.0000107	878.461	0.0001226	2.582	0.072008	0.377	1.019630	0.057	59.21934 ± 0.50786	897.86 ± 6.07	99.90	9.21	837 ± 4714
7M44290D	0.0000060	106.152	0.0000041	2267.268	0.0000529	7.284	0.0044691	0.488	0.264821	0.086	58.85538 ± 1.03072	893.51 ± 12.35	99.32	2.39	569 ± 26911
7M44291D	0.0000031	232.905	0.0000037	300.531	0.0000230	12.285	0.0012365	0.938	0.074221	0.421	60.77327 ± 3.68454	916.34 ± 43.58	101.24	0.66	20 ± 122
7M44292D	0.0000047	164.137	0.0000477	192.374	0.0000052	41.323	0.0002706	3.227	0.016948	0.724	53.72810 ± 16.51046	831.14 ± 204.72	91.15	0.14	3 ± 11
Σ	0.0002807	9.459	0.0008259	38.226	0.0022695	1.339	0.1866888	0.107	11.274863	0.033					
Information on Analysis and Constants Used in Calculations															
Sample = 216540BEMUS															
Material = mus															
Location = laser															
Analyst = Fred Jourdan															
Project = GASCOYNE_NP16															
Mass Discrimination Law = POW															
Irradiation = 12940h															
J = 0.01085900 ± 0.00001466															
FCs = 28.294 ± 0.037 Ma															
(GSN = Undefined)															
Preferred Age = Undefined															
Classification = Undefined															
Experiment Type = Undefined															
Extraction Method = Undefined															
Heating = 60 sec															
Isolation = 5.00 min															
Instrument = MAP215-50															
Lithology = Undefined - Undefined															
Lab-Lon = Undefined - Undefined															
Feature = Undefined															
Results															
Age Plateau															
59.24384 ± 0.21105															
898.15 ± 3.16															
107															
38%															
2.15															
2σ Confidence Limit															
1.0351															
Error Magnification															
Total Fusion Age															
59.94485 ± 0.16868															
906.51 ± 2.69															
15															
118 ± 90															
Normal Isochron															
67.73 ± 218.49															
898.63 ± 3.75															
1.11															
35%															
2.26															
2σ Confidence Limit															
1.0543															
Error Magnification															
Number of Iterations															
1															
0.000001794															
Convergence															
Inverse Isochron															
66.68 ± 69.37															
901.38 ± 3.92															
1.31															
25%															
2.26															
2σ Confidence Limit															
1.1464															
Error Magnification															
Number of Iterations															
6															
0.0000008511															
Convergence															
2%															
Spreading Factor															

Table E.3 Sample 183295 muscovite

Relative Abundances	36Ar [V]	%1σ	37Ar [V]	%1σ	38Ar [V]	%1σ	39Ar [V]	%1σ	40Ar [V]	%1σ	40(t)/39(t) ± 2σ	Age ± 2σ (Ma)	40Ar(t) (%)	39Ar(t) (%)	K/Ca ± 2σ
7M44110D	0.0000483	13.467	0.0000745	109.607	0.0000479	17.470	0.0031685	0.992	0.1725064	0.071	49.58027 ± 1.35346	778.84 ± 17.27	91.64	3.72	22.2 ± 48.8
7M44111D	0.0000412	19.778	0.0000633	126.524	0.0000800	8.112	0.0062332	0.264	0.4778783	0.055	56.54817 ± 0.66478	865.66 ± 8.09	97.43	9.60	67.6 ± 171.1
7M44112D	0.0000076	92.590	0.0000688	99.261	0.0002852	4.281	0.0246774	0.251	1.4370909	0.051	58.14144 ± 0.34350	884.93 ± 4.13	99.84	28.77	144.5 ± 286.9
7M44114D	0.0000042	166.066	0.0007292	62.305	0.0002568	3.486	0.0276867	0.308	1.2456734	0.058	57.64137 ± 0.40971	878.91 ± 4.95	99.90	25.17	86.9 ± 106.3
7M44115D	0.0000034	211.046	0.0001005	10.059	0.0000905	10.059	0.0079399	0.440	0.4968409	0.060	57.55599 ± 0.74585	877.93 ± 9.01	99.77	3.23	41.0 ± 63.4
7M44116D	0.0000059	116.476	0.0000448	178.539	0.0000501	12.940	0.0051339	0.471	0.2967384	0.058	58.14134 ± 0.37260	884.93 ± 11.71	100.59	5.99	59.7 ± 23.0
7M44117D	0.0000036	181.279	0.0000288	74.933	0.0000283	24.514	0.0030606	0.306	0.1767070	0.095	57.42031 ± 1.80343	876.23 ± 21.81	99.13	3.66	16.2 ± 22.8
7M44119D	0.0000061	146.979	0.0000288	284.736	0.0000162	36.244	0.0022645	0.718	0.1320112	0.102	58.76241 ± 1.89921	892.39 ± 22.76	100.80	2.64	40.8 ± 232.6
7M44120D	0.0000006	1221.084	0.0000927	86.561	0.0000090	63.367	0.0014634	1.090	0.0852459	0.213	58.12848 ± 3.09437	884.78 ± 37.25	99.79	1.71	8.2 ± 14.2
7M44121D	0.0000022	306.335	0.0000776	106.624	0.0000105	61.740	0.0017517	1.065	0.1024083	0.143	58.08873 ± 2.57418	884.30 ± 30.99	99.36	2.04	11.7 ± 25.0
7M44122D	0.0000048	154.142	0.0000119	637.205	0.0000186	31.750	0.0016575	1.129	0.0914244	0.211	57.41260 ± 3.10739	876.14 ± 37.58	98.44	1.83	68.4 ± 87.5
7M44124D	0.0000078	80.534	0.0000012	7364.775	0.0000076	70.143	0.0006629	1.967	0.0396896	0.224	54.59503 ± 5.90348	841.30 ± 72.79	94.12	0.80	298.1 ± 44055.2
7M44125D	0.0000031	239.218	0.0000390	213.437	0.0000041	45.542	0.0013128	1.853	0.0769880	0.116	57.95904 ± 3.97936	882.50 ± 47.96	98.80	1.53	17.5 ± 74.7
7M44126D	0.0000065	99.864	0.0000065	305.697	0.0000239	25.231	0.0019141	0.861	0.1135701	0.265	58.32226 ± 2.28168	887.11 ± 27.43	98.29	2.23	37.0 ± 226.1
7M44127D	0.0000028	275.118	0.0000091	942.918	0.0000090	61.048	0.0008507	1.371	0.0561339	0.181	64.98513 ± 5.76702	965.49 ± 66.39	98.49	0.99	48.5 ± 95.1
7M44129D	0.0000033	206.372	0.0000039	2082.414	0.0000030	180.014	0.0001701	6.541	0.0169746	0.445	87.57448 ± 26.33819	1208.44 ± 265.07	93.85	0.20	22.8 ± 949.0
Σ	0.0001313	21435	0.0008087	40.438	0.0009800	3.003	0.0857680	0.199	4.9765814	0.025					
Information on Analysis and Constants Used in Calculations															
Sample = 183295MUS Material = mus Location = Laser Analyt = Fric Jourdan Prod = GASCOYNE NP16 Mass Discrimination Law = POW Inscat = 123400 J = 0.01096900 ± 0.00001466 FCs = 28.294 ± 0.037 Ma IGSN = Undefined Preferred Age = Undefined Classification = Undefined Extraction Type = Undefined Heating Method = Undefined Heating = 610 sec Isolation = 5.00 min Instrument = MAP215-50 Lithology = Undefined Lab-Id = Undefined Feature = Undefined															
Age Equations = Mfm et al. (2000) Negative Intensities = Allowed Decay Constant 40K = 5.531 ± 0.013 E-10 1/a Decay Constant 39Ar = 2.940 ± 0.025 E-07 1/h Decay Constant 37Ar = 6.264 ± 0.009 E-04 1/h Decay Constant 36Cl = 2.303 ± 0.045 E-06 1/h Decay Constant 40K (EC β-) = 0.576 ± 0.002 E-10 1/a Decay Constant 40K (β+) = 4.955 ± 0.013 E-10 1/a Atmospheric Ratio 40Ar/39Ar = 298.56 ± 0.30 Atmospheric Ratio 39Ar/39Ar = 0.1869 ± 0.0002 Production Ratio 39Ar/39Ar = 0.000695 ± 0.000009 Production Ratio 39Ar/39Ar = 0.000200 ± 0.000001 Production Ratio 39Ar/39Ar = 0.000255 ± 0.000002 Production Ratio 39Ar/39Ar = 0.000720 ± 0.000091 Production Ratio 39Ar/39Ar = 0.012160 ± 0.000030 Production Ratio 39Ar/39Ar = 263.00 ± 13.16 Scaling Ratio K/Ca = 0.520 Abundance Ratio 40K/K = 1.709 ± 0.0100 E-04 Atomic Weight K = 39.0983 ± 0.0001 g															
Results															
Age Plateau															
							57.9168 ± 0.23240				57.9168 ± 0.40%	882.17 ± 3.38	0.67	85.49	12.4 ± 10.5
												Full External Error ± 6.71	77%	12	2σ Confidence Limit
												Analytical Error ± 2.80	18%	10000	Error Magnification
Total Fusion Age															
							57.56473 ± 0.25434				57.56473 ± 0.44%	877.98 ± 0.41%		16	55.1 ± 44.6
												Full External Error ± 6.80			
												Analytical Error ± 3.07			
Normal Isochron															
							38.24 ± 166.78				38.24 ± 436.12%	881.36 ± 0.47%	0.28	85.49	
												Full External Error ± 7.12	99%	12	2σ Confidence Limit
												Analytical Error ± 3.69	10000	189	Error Magnification
													1	Number of Iterations	
													0.0000000754	Convergence	
Inverse Isochron															
							2058.59 ± 6368.59				2058.59 ± 303.37%	876.50 ± 12.11	0.45	85.49	
												Full External Error ± 13.8%	92%	12	2σ Confidence Limit
												Analytical Error ± 11.96	10000	189	Error Magnification
													1	Number of Iterations	
													0.0002865645	Convergence	
													3%	Spreading Factor	

Table E.5 Sample 216533 biotite

Relative Abundances	36Ar [V]	%1σ	37Ar [V]	%1σ	38Ar [V]	%1σ	39Ar [V]	%1σ	40Ar [V]	%1σ	40(t)/39(t) ± 2σ	Age ± 2σ (Ma)	40Ar(t) (%)	39Ar(t) (%)	K/Ca ± 2σ
7M44837D	614%	4	0.0000043	175.661	0.00001498	246.835	0.0000123	65.556	0.0003100	3.245	0.076183	919.71 ± 179.52	107.41	0.28	1 ± 5
7M44838D	618%	4	0.0000339	24.257	0.0000817	225.846	0.0000883	6.174	0.0153979	0.280	0.3547387	923.87 ± 5.69	98.94	14.04	44 ± 199
7M44839D	62.0%	4	0.0000014	660.512	0.0000986	173.458	0.0000952	9.098	0.0068987	0.377	0.5447500	922.14 ± 3.09	100.08	8.12	23 ± 81
7M44835D	62.2%	4	0.0000062	107.712	0.0000346	950.099	0.00004713	4.851	0.0141504	0.343	0.8578447	916.10 ± 6.01	100.21	12.91	212 ± 4036
7M44836D	62.3%	4	0.0000027	278.904	0.0000185	1842.863	0.00004811	2.365	0.0334633	0.148	2.4007661	917.33 ± 2.55	100.03	36.01	1110 ± 40904
7M44837D	62.4%	4	0.0000038	182.719	0.0000957	187.344	0.0000347	21.650	0.0030789	0.522	0.1810822	911.33 ± 18.11	100.62	2.76	8 ± 30
7M44838D	62.6%	4	0.0000084	85.805	0.0000466	70.766	0.0000044	175.474	0.0003099	2.885	0.0193856	1026.84 ± 160.39	112.67	0.28	0 ± 0
7M44840D	62.8%	4	0.0000042	192.376	0.0000335	1033.046	0.0000119	64.660	0.0006945	1.336	0.0438602	905.12 ± 63.71	102.50	0.78	13 ± 214
7M44841D	63.0%	4	0.0000037	218.045	0.0000022	1692.233	0.0000060	91.974	0.0007500	1.230	0.047815	886.21 ± 78.84	97.55	0.68	174 ± 58815
7M44842D	63.2%	4	0.0000030	244.479	0.0000046	222.750	0.0000156	49.642	0.0014023	0.533	0.0818420	879.53 ± 30.32	98.30	1.28	5 ± 21
7M44843D	63.4%	4	0.0000025	64714.095	0.0000261	1277.751	0.0000247	31.536	0.0020860	0.921	0.127033	887.26 ± 30.32	100.00	1.90	42 ± 1062
7M44845D	63.6%	4	0.0000054	271.401	0.0000105	343.137	0.0000150	48.342	0.0012701	1.740	0.0769546	907.28 ± 45.55	99.04	1.16	7 ± 45
7M44846D	63.8%	4	0.0000054	162.787	0.0000214	116.284	0.0000038	186.055	0.0008938	1.165	0.0533036	876.07 ± 72.72	96.93	0.82	2 ± 4
7M44847D	64.0%	4	0.0000055	120.299	0.0000117	20858.385	0.0000197	40.529	0.0010743	1.196	0.0640112	920.46 ± 47.23	102.58	0.98	336 ± 140030
7M44848D	65.0%	4	0.0000037	197.553	0.0000552	685.487	0.0000660	13.241	0.0058932	0.544	0.3534667	904.85 ± 1.65	99.68	5.38	56 ± 761
7M44850D	67.0%	4	0.0000060	115.827	0.0000854	425.094	0.0000719	15.106	0.0060896	0.300	0.3627037	905.48 ± 9.29	100.50	5.56	37 ± 315
7M44851D	70.0%	4	0.0000030	240.866	0.0000317	1087.862	0.0000739	9.798	0.0066389	0.441	0.3938628	900.32 ± 10.04	100.23	6.06	109 ± 2371
7M44852D	75.0%	4	0.0000019	362.717	0.0000186	281.637	0.0000125	60.307	0.0010920	1.353	0.0666261	925.46 ± 48.69	100.87	1.00	5 ± 27
Σ			0.0000048	667.312	0.0003586	417.415	0.0019163	2.751	0.1095844	0.104	6.6454211				
Information on Analysis and Constants Used in Calculations															
Sample = 216533MUSPOPPRR															
Material = mus															
Negative Intensities = Allowed															
Location = Laser															
Analyst = Fred Jourdan															
Project = GASCODY/GME_NP16															
Mass Discrimination Law = POW															
Irradiation = L234dk															
J = 0.01089500 ± 0.00001466															
GA1550 = 93.739 ± 0.100 Ma															
ICSN = Undefined															
Preferred Age = Undefined															
Classification = Undefined															
Experiment Type = Undefined															
Evaporation Method = Undefined															
Heating = 60 sec															
Isolation = 5.00 min															
Instrument = MAP-215-50															
Lithology = Undefined															
Lab-Logs = Undefined - Undefined															
Feature = Undefined															
Results															
Age Plateau															
60.50385 ± 0.2162															
± 0.35%															
917.88 ± 3.17															
Full External Error ± 6.72															
Analytical Error ± 2.50															
144															
82.01															
13%															
1.78															
2σ Confidence Limit															
12006															
Error Magnification															
Total Fusion Age															
60.62784 ± 0.21720															
± 0.36%															
914.61 ± 3.22															
Full External Error ± 6.73															
Analytical Error ± 2.57															
Normal Isochron															
28.64 ± 205.09															
± 716.20%															
58.33460 ± 0.77595															
± 1.33%															
887.26 ± 9.52															
Full External Error ± 11.2															
Analytical Error ± 3.33															
1.2908															
Error Magnification															
1832															
2σ Confidence Limit															
1															
Number of Iterations															
0.0000000977															
Convergence															
Inverse Isochron															
685.90 ± 389.27															
± 56.46%															
60.85394 ± 0.26832															
± 0.44%															
917.23 ± 0.40%															
Full External Error ± 6.99															
Analytical Error ± 3.16															
10000															
Error Magnification															
8															
Number of Iterations															
0.0000149601															
Convergence															
10%															
Spreading Factor															

Table E.6 Sample 195890B biotite

Relative Abundances	36Ar [V]	%1σ	37Ar [V]	%1σ	38Ar [V]	%1σ	39Ar [V]	%1σ	40Ar [V]	%1σ	40(r)/39(k) ± 2σ	Age ± 2σ (Ma)	40Ar(r) (%)	39Ar(k) (%)	K/Ca ± 2σ
7M44670D	0.000032	49.276	0.0000999	225.636	0.0000089	52.634	0.0000942	4.504	0.1392323	0.217	697.05250 ± 65.97666	3884.25 ± 151.18	97.19	10.16	1.0 ± 4.6
7M44670D	0.0000011	63.804	0.0001450	146.297	0.0000025	197.618	0.0000236	31.558	0.0774633	0.417	601.39394 ± 414.80459	3650.60 ± 1061.54	82.51	1.23	0.1 ± 0.3
7M44670D	0.0000011	490.215	0.0003539	55.210	0.0000106	35.817	0.0000894	1.501	0.112222	0.169	124.75659 ± 5.16866	1548.55 ± 43.25	99.73	46.55	1.3 ± 1.4
7M44670D	0.000063	80.348	0.0002467	80.226	0.0000028	131.390	0.0001263	7.306	0.0241279	0.343	175.61729 ± 36.16658	1929.54 ± 237.66	92.07	6.62	0.3 ± 0.4
7M44670D	0.000057	103.494	0.0001675	126.060	0.0000009	382.324	0.0001395	6.175	0.0469807	0.254	320.06348 ± 47.18747	2709.76 ± 207.02	96.30	7.24	0.4 ± 1.0
7M44670D	0.0000022	261.429	0.0000894	112.497	0.0000038	89.856	0.0000144	50.737	0.0160668	0.655	1293.77764 ± 1322.95723	4902.49 ± 1726.08	103.57	0.76	0.0 ± 0.1
7M44670D	0.0000097	53.596	0.0001776	104.847	0.0000089	49.984	0.0001168	8.264	0.2515632	0.140	2094.96864 ± 3170.68336	5727.42 ± 287.45	98.85	6.21	0.3 ± 0.7
7M44670D	0.000020	249.864	0.0006001	34.081	0.0000015	234.326	0.0001295	26.329	0.177414	0.182	6106.00070 ± 3470.83836	7610.66 ± 925.17	99.63	1.52	0.0 ± 0.0
7M44680D	0.0000421	15.820	0.0001688	123.182	0.0000194	24.693	0.0001826	4.748	1.1408982	0.038	6174.05574 ± 666.43829	7630.69 ± 169.22	98.90	9.57	0.6 ± 1.4
7M44682D	0.0000454	14.172	0.0000673	283.704	0.0000277	15.332	0.0001425	8.423	1.3548950	0.259	9416.32569 ± 1698.09925	8384.72 ± 302.00	99.00	7.46	0.8 ± 4.8
7M44683D	0.0000227	26.663	0.0000467	525.048	0.0000082	39.482	0.0000513	18.459	0.7781766	0.042	15049.92713 ± 6561.1165	9226.05 ± 664.07	99.13	2.68	0.6 ± 6.0
Σ	0.0001651	12.508	0.0000071	670.778	0.0000618	21.766	0.0019101	1642	4.0566675	0.089					
Information on Analysis and Constants Used in Calculations															
Sample = 195890B/CDFR Material = Dio Location = Leser Analyst = F. Leclercq Project = GASCOY/NE_NPIS Mass Discrimination Law = POW Inhibitor = 0.00001466 IG-150 = 39.73 ± 0.10 Ma IG-15N = Undefined Preferred Age = Undefined Classification = Undefined Experiment Type = Undefined Extraction Method = Undefined Heating = 60 sec Isolation = 3.00 Ma Instrument = MAP215-50 Lithology = Undefined Lat-Lon = Undefined - Undefined Feature = Undefined Age Equations = Min et al. (2000) Negative Intensities = Min et al. (2000) Decay Constant 40K = 5.531 ± 0.079 E-10 1/a Decay Constant 39Ar = 2.947 ± 0.028 E-07 1/a Decay Constant 37Ar = 8.364 ± 0.018 E-04 1/a Decay Constant 36Cl = 2.303 ± 0.046 E-05 1/a Decay Constant 40K(EG) = 0.576 ± 0.009 E-10 1/a Decay Constant 40K(E) = 4.965 ± 0.013 E-10 1/a Atmospheric Ratio 39Ar/39K = 298.65 ± 0.30 Atmospheric Ratio 39Ar/39K(g) = 0.1859 ± 0.0002 Production Ratio 39Ar/39K(a) = 0.000658 ± 0.000009 Production Ratio 39Ar/39K(s) = 0.000692 ± 0.000009 Production Ratio 39Ar/39K(l) = 0.000253 ± 0.000002 Production Ratio 39Ar/39K(K) = 0.00230 ± 0.000091 Production Ratio 39Ar/39K(R) = 0.01250 ± 0.000030 Production Ratio 39Ar/39K(c) = 263.00 ± 13.15 Scaling Ratio 39Ar/39K = 1.770 ± 0.0100 E-04 Abundance Ratio 40Ar/39Ar = 39.0683 ± 0.00019 Atomic Weight K = 39.0983 ± 0.00019															
Results															
Age Plateau Cannot Calculate															
Total Fusion Age 2100.34749 ± 69.34011 ± 3.30% Full External Error ± 64.90 Analytical Error ± 97.19															
Normal Isochron Cannot Calculate															
Inverse Isochron Cannot Calculate															
MSW															
Age ± 2σ (Ma)															
40(r)/39(k) ± 2σ															
39Ar(k) (%)															
K/Ca ± 2σ															

Table E.7 Sample 195890D muscovite

Relative Abundances	36Ar [V]	%1σ	37Ar [V]	%1σ	38Ar [V]	%1σ	39Ar [V]	%1σ	40Ar [V]	%1σ	40(r)/39(k) ± 2σ	Age ± 2σ (Ma)	40Ar(k) (%)	39Ar(k) (%)	K/Ca ± 2σ
6N422730	0.0000050	108.264	0.0000062	553.415	0.0000254	30.115	0.0022623	0.712	0.2971005	0.121	130.67202 ± 2.36488	1657.52 ± 16.37	99.50	5.60	119 ± 1317
6N422740	0.0000010	409.718	0.0000223	253.140	0.0000389	18.744	0.0038822	0.412	0.5374105	0.064	138.34905 ± 1.32825	1628.08 ± 10.30	99.94	9.60	75 ± 379
6N422750	0.0000097	717.831	0.0000217	216.051	0.0000676	11.195	0.0056075	0.399	0.7704674	0.070	137.44125 ± 1.27185	1621.02 ± 9.90	100.03	13.87	111 ± 484
6N422760	0.0000058	46.913	0.0000557	177.608	0.0002135	4.787	0.0173268	0.290	2.4304014	0.032	140.08951 ± 0.83952	1641.61 ± 6.42	99.88	42.86	290 ± 1031
6N422800	0.0000052	94.333	0.0000161	239.380	0.0000384	18.228	0.0030964	0.749	0.4297701	0.113	138.22118 ± 2.34117	1627.08 ± 16.17	99.60	7.66	74 ± 353
6N422810	0.0000035	128.821	0.0000122	234.630	0.0000215	30.085	0.0017104	0.929	0.2430988	0.096	141.16763 ± 3.19795	1649.81 ± 24.51	99.36	4.23	330 ± 15488
6N422820	0.0000033	153.037	0.0000158	375.139	0.0000126	52.566	0.0015532	1.319	0.1940229	0.169	139.93147 ± 4.22445	1640.31 ± 32.55	99.45	3.35	48 ± 357
6N422830	0.0000116	43.746	0.0000198	189.528	0.0000058	14.580	0.0004301	2.113	0.0623492	0.893	142.65652 ± 9.65311	1651.19 ± 73.53	98.41	1.06	4 ± 6
6N422850	0.0000050	119.528	0.0000098	117.154	0.0000120	53.901	0.0009258	1.057	0.1345068	0.183	131.26704 ± 7.27416	1572.28 ± 58.20	95.15	1.28	11 ± 67
6N422860	0.0000025	252.153	0.0000036	114.146	0.0000283	25.161	0.0008131	0.752	0.2858011	0.125	142.36422 ± 2.98249	1653.88 ± 22.76	100.29	4.48	20 ± 24
6N422870	0.0000007	44.981	0.0000095	84.913	0.0000129	50.293	0.0007308	1.308	0.1132734	0.219	139.16219 ± 5.19582	1634.61 ± 40.16	97.17	1.96	9 ± 8
6N422880	0.0000055	83.344	0.0000169	248.520	0.0000089	71.505	0.0007716	1.461	0.1025955	0.212	141.75703 ± 5.68781	1654.32 ± 43.49	98.40	1.76	18 ± 90
Σ	0.0000632	29.548	0.0002614	67.680	0.0004963	5.234	0.0404278	0.180	5.6410488	0.026					
Information on Analysis and Constants Used in Calculations															
Sample = 195890D															
Material = mus															
Location = Laser															
Analyst = Fred Jourdan															
Project = GASODYNE NP16															
Mass Discrimination Law = PDW															
Irradiation = 12340h															
J = 0.0165740 ± 0.00000792															
WArms = 2613.000 ± 2.352 Ma															
IGSN = Undefined															
Preferred Age = Undefined															
Classification = Undefined															
Experiment Type = Undefined															
Extraction Method = Undefined															
Heating = 500 °C															
Isolation = 5.00 h															
Instrument = MAP215-50															
Lithology = Undefined															
Lab-Long = Undefined - Undefined															
Feature = Undefined															
Results															
Age Plateau															
40(e)/39(e) ± 2σ															
140.14818 ± 0.92053															
± 0.66%															
1641.98 ± 7.27															
± 0.44%															
Full External Error ± 15.14															
Analytical Error ± 7.09															
172 70.93															
8% 10															
194 ± 2σ Confidence Limit															
13102 Error Magnification															
Total Fusion Age															
139.06795 ± 0.157669															
± 0.14%															
1633.64 ± 4.74															
Full External Error ± 14.05															
Analytical Error ± 4.46															
Normal Isochron															
8.53 ± 195.88															
#####															
1645.69 ± 6.89															
± 0.42%															
Full External Error ± 14.98															
Analytical Error ± 6.70															
10000															
± 2σ Confidence Limit															
Error Magnification															
1															
Number of Iterations															
0.000013188															
Convergence															
Inverse Isochron															
918.23 ± 1295.15															
± 141.16%															
1637.27 ± 9.44															
± 0.58%															
Full External Error ± 16.27															
Analytical Error ± 9.30															
19															
± 2σ Confidence Limit															
Error Magnification															
12101															
Number of Iterations															
0.0000601670															
Convergence															
6%															
Spreading Factor															

Table E.8 Sample 195890E muscovite

Relative Abundances	36Ar [V]	%1σ	37Ar [V]	%1σ	38Ar [V]	%1σ	39Ar [V]	%1σ	40Ar [V]	%1σ	40(r)/39(k) ± 2σ	Age ± 2σ (Ma)	40Ar(t) (%)	39Ar(k) (%)	K/Ca ± 2σ
60 °C	0.0000010	512.564	0.0000016	586.010	0.0000015	250.604	0.0000857	2.649	0.0182808	0.676	70.48431 ± 16.25873	1005.80 ± 177.95	102.24	0.71	6.9 ± 80.6
60 °C	0.0000029	183.467	0.0000495	137.100	0.0000004	946.791	0.0002714	2.145	0.081228	0.412	63.55536 ± 12.09266	928.33 ± 138.15	95.17	1.04	2.4 ± 6.5
61 °C	0.0000047	128.372	0.0000335	196.905	0.0000091	50.822	0.0006859	1.837	0.0841896	0.212	124.78941 ± 7.02264	1519.70 ± 57.85	101.68	1.64	8.8 ± 34.7
61 °C	0.0000030	188.253	0.0000164	516.887	0.0000788	5.238	0.0144033	0.353	2.0017293	0.047	138.91391 ± 1.01878	1632.45 ± 7.88	99.95	55.39	493.6 ± 5161.8
61 °C	0.0000012	468.261	0.0000003	22028.901	0.0000013	284.746	0.0002591	2.215	0.0385089	0.352	142.27311 ± 14.13904	1688.27 ± 107.87	100.96	1.00	343.8 ± 15481.1
61 °C	0.0000001	5267.272	0.0000633	103.411	0.0000085	51.259	0.0001291	0.691	0.1737400	0.088	139.12641 ± 3.16556	1634.10 ± 24.48	100.01	4.97	8.8 ± 18.1
61 °C	0.0000004	1298.732	0.0000214	308.490	0.0000174	19.856	0.0016167	1.131	0.2245861	0.101	136.84673 ± 3.64532	1631.93 ± 28.22	99.95	6.22	32.5 ± 200.7
61 °C	0.0000002	2505.110	0.0000372	178.998	0.0000012	2617.815	0.0001746	5.656	0.0240810	0.286	136.23965 ± 24.17240	1627.23 ± 187.62	100.25	0.67	2.0 ± 7.2
61 °C	0.0000012	465.639	0.0000200	330.610	0.0000066	49.350	0.0004040	0.204	0.0582593	0.204	135.92551 ± 3.13987	1608.18 ± 71.65	99.37	1.55	8.7 ± 57.4
61 °C	0.0000027	200.394	0.0000025	2790.191	0.0000008	482.764	0.0003563	1.940	0.0481960	0.180	137.53180 ± 10.149042	1621.73 ± 81.67	101.66	1.37	61.3 ± 3422.2
62 °C	0.0000040	138.943	0.0000555	115.475	0.0000016	222.865	0.0001640	3.341	0.0227803	0.376	146.19660 ± 22.62244	1687.96 ± 169.79	105.26	0.63	1.3 ± 2.9
62 °C	0.0000032	172.190	0.0000289	237.037	0.0000025	154.621	0.0005379	1.948	0.0736290	0.104	138.64186 ± 8.13709	1630.35 ± 63.05	101.29	2.07	8.0 ± 37.9
64 °C	0.0000019	310.033	0.0000112	589.501	0.0000569	10.952	0.0051495	0.586	0.7364457	0.046	142.90414 ± 1.81074	1663.07 ± 13.78	99.92	19.80	197.8 ± 2332.0
67 °C	0.0000022	232.706	0.0000655	102.225	0.0000058	69.788	0.0005027	1.504	0.0709403	0.164	139.81385 ± 7.33030	1639.40 ± 56.51	99.08	1.93	3.3 ± 6.8
Σ	0.0000056	364.542	0.00003840	65.226	0.0002849	6.161	0.0260030	0.259	3.5890122	0.031					
Information on Analysis and Constants Used in Calculations															
Sample = 195890E															
Material = mus															
Location = Laser															
Analyst = Fred Jourdan															
Project = GASCOY/GNE_NP16															
Mass Discrimination Law = POW															
Irradiation = I2340h															
J = 0.01055740 ± 0.00000732															
WArms = 2613.000 ± 2.352 Ma															
IGSN = Undefined															
Preferred Age = Undefined															
Classification = Undefined															
Experiment Type = Undefined															
Extraction Method = Undefined															
Heating = 60 sec															
Isolation = 5.00 min															
Instrument = MAP215-50															
Lithology = Undefined															
Lat-Lon = Undefined - Undefined															
Feature = Undefined															
Age Equations = Min et al. (2000)															
Negative Intensities = Allowed															
Decay Constant 40K = 5.531 ± 0.013 E-10 1/a															
Decay Constant 39Ar = 2.940 ± 0.029 E-07 1/h															
Decay Constant 37Ar = 8.230 ± 0.082 E-04 1/h															
Decay Constant 36Cl = 2.303 ± 0.046 E-06 1/a															
Decay Constant 40K(β+) = 0.576 ± 0.002 E-10 1/a															
Decay Constant 40K(ε) = 4.955 ± 0.013 E-10 1/a															
Atmospheric Ratio 40Ar/36Ar(a) = 298.56 ± 0.30															
Atmospheric Ratio 39Ar/36Ar(a) = 0.1869 ± 0.0002															
Production Ratio 39Ar/37Ar(β) = 0.000702 ± 0.000008															
Production Ratio 39Ar/37Ar(β) = 0.000023 ± 0.000002															
Production Ratio 36Ar/37Ar(β) = 0.000363 ± 0.000002															
Production Ratio 40Ar/39Ar(β) = 0.000730 ± 0.000091															
Production Ratio 38Ar/39Ar(β) = 0.012400 ± 0.000368															
Production Ratio 38Ar/39Ar(β) = 263.00 ± 13.15															
Scaling Ratio K/Ca = 0.430															
Abundance Ratio 40K/K = 1.1700 ± 0.0100 E-04															
Atomic Weight K = 39.0983 ± 0.0001 g															
Results															
Age Plateau															
139.72838 ± 0.10517															
± 0.75%															
Full External Error ± 16.62															
Analytical Error ± 8.11															
1.67															
95.60															
8%															
11															
189															
2σ Confidence Limit															
Error Magnification															
1.2904															
Total Fusion Age															
136.06392 ± 0.85959															
± 0.62%															
Full External Error ± 14.86															
Analytical Error ± 6.68															
Normal Isochron															
47.30 ± 362.90															
± 787.15%															
Overestimated Error															
139.20192 ± 1.26887															
± 0.91%															
Full External Error ± 16.95															
Analytical Error ± 9.81															
1															
Number of Iterations															
0.000005859															
Convergence															
Inverse Isochron															
15095.05 ± 134052.61															
± 888.06%															
Overestimated Error															
136.21144 ± 12.43963															
± 9.13%															
Full External Error ± 98.29															
Analytical Error ± 97.40															
1.0000															
Error Magnification															
Number of Iterations															
7															
Convergence															
0.000016586															
Spreading Factor															
6%															
MSW															
1.67															
95.60															
8%															
11															
189															
2σ Confidence Limit															
Error Magnification															
1.2904															
14															
23.1 ± 38.0															